Contemporary Topics in

Analytical and Clinical Chemistry

Volume 4

Contemporary Topics in Analytical and Clinical Chemistry

Volume 4

Edited by
David M. Hercules
University of Pittsburgh
Pittsburgh, Pennsylvania

Gary M. Hieftje
Indiana University
Bloomington, Indiana

Lloyd R. Snyder
Technicon Instruments Corporation
Tarrytown, New York

and
Merle A. Evenson
University of Wisconsin
Madison, Wisconsin

PLENUM PRESS • NEW YORK AND LONDON

Library of Congress cataloged the first volume of this title as follows:

Contemporary topics in analytical and clinical chemistry.
v. 1-
New York, Plenum Press, [c1977-
v. ill. 24 cm.
Editor: v. 1- D. M. Hercules.
Key title: Contemporary topics in analytical and clinical chemistry, ISSN 0160-3620.
1. Chemistry, Clinical. 2. Chemistry, Analytic. I. Hercules, David M.
RB40.C66 616.07'56'05 79-640979
MARC-S

ISBN-13:978-1-4613-3420-0 e-ISBN-13:978-1-4613-3418-7
DOI: 10.1007/978-1-4613-3418-7

A Division of Plenum Publishing Corporation
233 Spring Street, New York, N.Y. 10013

Contributors

BEN HAHN, Technicon Instruments Corporation, Tarrytown, New York

DAVID M. HERCULES, Department of Chemistry, University of Pittsburgh, Pittsburgh, Pennsylvania

DR. PAUL E. JOHNSON, E. I. Du Pont de Nemours & Co., Inc., Wilmington, Delaware

DR. MICHAEL P. NEARY, Los Alamos Scientific Laboratories, Los Alamos, New Mexico

BRUCE P. NERI, Abbott Diagnostics, Dallas, Texas

DR. JAGAN RAO, Technicon Instruments Corporation, Tarrytown, New York

GOPAL S. RAUTELA, E. I. Du Pont de Nemours & Co., Inc., Wilmington, Delaware

DR. ALEXANDER SCHEELINE, Department of Chemistry, University of Wisconsin, Madison, Wisconsin

DR. P. M. A. SHERWOOD, Department of Inorganic Chemistry, University of Newcastle upon Tyne, United Kingdom

PAUL L. SMOCK, E. I. Du Pont de Nemours & Co., Inc., Wilmington, Delaware

JOHN P. WALTERS, Department of Chemistry, University of Wisconsin, Madison, Wisconsin

DR. ISIAH M. WARNER, Department of Chemistry, Texas A&M University, College Station, Texas

DR. DAVID L. WITTE, Department of Pathology, University of Iowa, Iowa

Contents

1. Polychromatic Analysis Using the Technicon STAC™ Analyzer

Jagan Rao and Ben Hahn

1. Introduction 1
2. The STAC Analyzer 2
   - 2.1. Diluter/Dispenser Module 2
   - 2.2. Analytical Module 2
   - 2.3. Electronics Module 3
3. General Theory 4
4. Selection of Primary and Secondary Wavelengths 7
5. Classification of Polychromatic Analysis 8
   - 5.1. Correction for Nonreactive (Static or Time Invariant Interferences) 9
   - 5.2. Correction for Reactive (Kinetic) Interferences 10
   - 5.3. Correction for a Combination of Both Reactive and Nonreactive Interferences 10
   - 5.4. Detection of Substrate Depletion 12
6. STAC Assays 13
7. Examples of Polychromatic Analysis 14
   - 7.1. Calcium 14
   - 7.2. Total Bilirubin 17
   - 7.3. Uric Acid 19
   - 7.4. Triglycerides 22
   - 7.5. AST 23
8. Conclusion 24

References 25

2. Introduction to Multiple-Wavelength Spectrophotometric Measurements in Analytical and Clinical Chemistry

David L. Witte

1. Introduction 27

2. Definitions 28
3. Applications in Analytical Chemistry 28
4. Applications in Clinical Chemistry 30
5. Epilogue 33
References 34

3. Bichromatic Analysis: The Design and Function of the ABA-100
David L. Witte and Bruce P. Neri

1. Introduction 37
2. Design Principles 38
3. Performance of Individual Instrument Functions 46
   3.1. Photometric Uncertainty and Linearity 46
   3.2. Control of Reaction Temperature 46
   3.3. Sample Evaporation 48
   3.4. Volume Measurement 48
   3.5. Performance Characteristics Unique to Bichromatic Measurements 49
4. Automation of a Specific Method with the ABA 51
5. Quality Control 51
6. Special Applications 52
7. Epilogue 52
References 53

4. Bichromatic Analysis as Performed in the Du Pont Automatic Clinical Analyzer ('aca')
Paul E. Johnson, Paul L. Smock, and Gopal S. Rautela

1. Introduction 55
2. Analytical Test Pack 55
   2.1. Header 56
   2.2. Pack Envelope 57
3. Instrument 57
   3.1. Sample Handling/Pack Filling 57
   3.2. Timing, Temperature, Reagent Addition/Mixing, and Incubation 59
4. Measurement System 59
   4.1. Measurement Techniques 60
   4.2. Electro-Optical System Description 60
   4.3. Zero Absorbance Requirement 61
   4.4. Output Result Performance and Calibration 62

5. Measurement Principles 64
5.1. Implementation 65
5.2. Representative Examples 66
5.3. Reaction Time Courses 66
5.4. Chromophore Spectra 67
5.5. Performance 72
6. Advantages 72
6.1. Disadvantages 74
6.2. Future Applications 74
References 74

5. The Analysis of Matrix Formatted Multicomponent Data
Isiah M. Warner

1. Introduction 75
1.1. Data Reduction Strategies in Analytical Chemistry 75
1.2. Description of MFMDT 78
2. Linear Algebra Review 79
2.1. Vectors and Matrices 79
2.2. Arithmetic of Matrices 80
2.3. Matrix Solution of a System of Linear Equations 81
2.4. Basis and Rank 83
2.5. Identity and Inverse Matrices 84
2.6. Eigenvalues and Eigenvectors 85
2.7. Glossary 86
3. Theory and Application of MFMDT in Qualitative Analysis of the Fluorescence Emission–Excitation Matrix (FEEM) 87
3.1. Properties of Fluorescence Emission 87
3.2. Principles of Qualitative Analysis of the FEEM by MFMDT 88
3.3. Qualitative Analysis of Simulated Fluorescence Data 97
3.4. Qualitative Analysis of Experimental Fluorescence Data . . 101
4. Theory and Application of MFMDT in Quantitative Analysis of the FEEM 103
4.1. Theory of Least Squares Analysis of the FEEM 105
4.2. Theory of Linear Programming Analyses (Simplex Method) of the FEEM 107
4.3. Quantitative Analysis of Simulated Fluorescence Data . . . 109
4.4. Quantitative Analysis of Experimental Fluorescence Data 110
5. Summary and Conclusion 116
5.1. Effectiveness of MFMDT for Analysis of Multicomponent Fluorescence Data 116
5.2. Expansion and Future Applications of MFMDT 117

6. Appendices 118
6.1. Fortran Subroutines for Qualitative Analysis 118
6.2. Fortran Subroutines for Quantitative Analysis 123
References 139

6. Nonlinear Parameter Estimation of Convolved Excitation and Multiple Emission Response Functions

Michael P. Neary and David M. Hercules

1. Introduction 141
1.1. Luminescence Processes 143
1.2. Modern Instrumentation 145
1.3. Algorithms for Nonlinear Data Analysis 145
2. Instrumentation and Analytical Parameters 147
2.1. Time Correlated Single-Photon Method 147
2.2. Theory 148
2.3. Pile-Up 151
2.4. Time-to-Amplitude Converter 152
2.5. Excitation Source 154
2.6. Optics 155
2.7. Photomultiplier Tube 156
2.8. Start and Stop Lines 156
2.9. Timing Filter Amplifier (TFA) 157
2.10. Analytical Considerations—Intensity versus Concentration 157
2.11. Scattered Excitation Radiation 158
2.12. Analytical Wavelength and Bandpass Selection 159
2.13. Linearity versus Concentration 159
3. Data Handling 160
3.1. Theory and Description of the Algorithms 160
3.2. Grid Search Algorithms (GSA) 161
3.3. Moments Algorithm (MA) 165
3.4. Marquardt's Algorithm (MQA) 170
4. Experimental 178
4.1. Data Sources 180
5. Results and Discussion 181
5.1. Simulated Data—GSA 181
5.2. Simulated Data—MA 182
5.3. Simulated Data—MQA 185
5.4. Comparison of Convergence Characteristics for MQA and MA 193
5.5. Convergence Rate and Efficiency 196

5.6. Fluorescence Data 197
6. Summary 202
References 203

7. ESCA Studies of Electrode Surfaces
P. M. A. Sherwood

1. Introduction 205
2. Electrode Transfer 209
   2.1. The Possibilities for Film Change and Decomposition During Transfer 209
   2.2. The Anaerobic Transfer Electrochemical Cell 211
3. Data Analysis 215
4. Carbon and Related Electrodes 218
5. Electrodes Involving Magnesium and Aluminum 220
   5.1. Detection of Precipitation of Magnesium Hydroxide 220
   5.2. Effect of Ions on the Anodic Oxide Films on Aluminum . . . 220
   5.3. Anodization of Aluminum in Liquid Hydrogen Fluoride . . 223
6. Electrodes Involving Titanium 224
   6.1. Titanium Metal and Alloys 224
   6.2. Titanium Dioxide and Related Electrodes 225
7. Vanadium Pentoxide Electrodes in Reserve Cells 226
8. Electrodes Involving Chromium 227
9. The Manganese Dioxide Electrode 230
10. Electrodes Involving Iron 230
   10.1. Studies of Metallic Iron 232
   10.2. Studies of Iron Alloys 234
   10.3. Studies of Stainless Steel 235
11. Electrodes Involving Nickel 240
   11.1. Studies of Nickel Metal 240
   11.2. Studies of Molten Salt Systems 242
   11.3. Studies of Nickel Alloys 244
12. Electrodes Involving Copper 244
   12.1. Cu(I) Oxide Solar Cells 244
   12.2. Corrosion Inhibition of Copper 244
   12.3. Studies of Copper Alloys 245
13. Electrodes Involving Zinc 247
14. The Niobium Electrode 247
15. The Molybdenum Electrode 247
16. Ruthenium Dioxide-Based Film Electrodes 249
17. Electrodes Involving Tantalum 250
18. Electrodes Involving Tungsten 250

19. Electrodes Involving Tin 252
19.1. Studies of Oxidized Tin Surfaces 252
19.2. Studies of the Anodic Polarization of Metallic Tin 256
19.3. Studies of Tinplate 258
19.4. Studies of Tin Alloys 259
20. The Study of Anodic Oxide Films on Gallium Arsenide and Related Compounds 259
21. Chemically Modified Electrodes 264
21.1. Modified Electrodes 264
21.2. Modified Electrodes with Covalently Bonded Species 265
22. Studies of Solid Electrolytes 270
23. Ion-Selective Electrodes 270
24. Noble Metal Electrodes 270
24.1. Studies of Oxide Films on Platinum Electrodes 270
24.2. Studies of Sulfide Films on Platinum Electrodes 273
24.3. Studies of Platinum Electrodes in Molten Salt Systems . . . 273
24.4. Electro-Oxidation in Platinum Systems 274
24.5. Underpotential Deposition on Platinum Electrodes 275
24.6. Studies of Lead Oxidation on a Platinum Electrode 276
24.7. Studies of Oxide Films on Gold Electrodes 276
24.8. Studies of Oxide Films on Palladium Electrodes 277
24.9. Studies of Oxide Films on Iridium Electrodes 277
24.10. Studies of Mixed Noble Metal Systems 277
25. Trace Metal Analysis 277
26. Studies of Paint Films 278
27. AES Studies of Electrode Surfaces 279
28. Conclusion 279
References 279

8. Spatially Resolved Spectroscopy: Theory and Applications of the Abel Inversion

Alexander Scheeline and John P. Walters

1. Introduction 295
2. Fundamentals 297
3. Computation of Area Matrices 300
4. Abel Inversion of Strictly Emitting Profiles 308
5. Self-Absorption and the Abel Inversion—Theory 311
6. Self-Absorption and the Abel Inversion—Examples 316
7. Background Correction in the Presence of Self-Absorption 323
8. Instrumental Misalignment and Spark Wander 328
9. Summary on Wander 336

10. True Measurement Noise 337
11. Spatially Unseparated Emission and Absorption 340
12. Conclusion 350
13. Appendix 351
References 372

Polychromatic Analysis Using the Technicon STAC™ Analyzer

Jagan Rao and Ben Hahn

1. Introduction

The simultaneous use of two wavelengths for a single clinical assay goes back at least to 1954 (bilirubin analysis[1]). More recently, so-called bichromatic analysis has been incorporated into two widely used automated clinical analyzers: the DuPont 'aca' and the Abbot ABA-100. Other sections of the present chapter describe these systems and their use of bichromatic analysis in some detail. The general application of polychromatic analysis—where absorbances at two or more wavelengths are combined in optimal fashion for the analysis of multicomponent mixtures—is well understood and widely applied by analytical chemists (e.g., reference 2).

The initial adaption of bichromatic analysis for automated clinical assay procedures was determined mainly by the goal of improving instrumental precision, rather than for providing improved accuracy of final results. Later, it was appreciated that bichromatic analysis offered both possibilities, although this technique continued to be used in such fashion as to emphasize precision over accuracy. More recently, the possibility of polychromatic analysis for upgrading the quality of reported data has been discussed in connection with the Technicon STAC analyzer.[3,4] Since the STAC system is adequately precise without the use of bichromatic correction, it was possible to consider the *general* application of polychromatic analysis for the elimination of certain interferences, thereby improving accuracy rather than precision.

Jagan Rao and Ben Hahn • Technicon Instruments Corporation, Tarrytown, New York 10591.

However, since some forms of polychromatic analysis can actually degrade precision, it became necessary to evaluate the trade-offs between improved accuracy and retention of maximum precision.

In Section 2 we will provide a brief description of the STAC analyzer, and then discuss the various applications of polychromatic analysis for handling different types of assay interferences. Many options are available in this regard, and it is useful to discuss these, and to evaluate different options for specific problems. Finally, we will illustrate each of these approaches with specific examples on the STAC analyzer: the assay for calcium, total bilirubin, uric acid, triglycerides, and AST.

2. The STAC Analyzer

The STAC analyzer is designed to perform quantitative analyses of individual serum samples for a number of biochemical parameters. In order to perform random determinations for a variety of biochemical tests, the STAC system utilizes a patented cell design which functions as reagent containers, reaction vessel, and optical cuvette. The physical design of the STAC cell is the same for all chemistries. Each cell has two compartments, the optical and trigger compartment, each of which can contain lyophilized reagents. These compartments are interconnected by an inverted U-tube passage that provides separation of the reconstituted reagents until reaction is initiated by mixing on the system. The STAC system is comprised of three modules: the diluter/dispenser, the analytical module, and the electronic module. For a detailed description, see references 5 and 6.

2.1 Diluter/Dispenser Module

The purpose of the diluter/dispenser is to aspirate a selected volume of serum (either 10 or 50 μl) and then dispense the sample and 750 μl of water into the optical compartment. Simultaneously, 750 μl of diluent (either water or AMP buffer) is dispensed into the trigger compartment.

2.2 Analytical Module

The analytical module consists of a number of interacting electromechanical and electro-optical assemblies that are designed to accept, transport, and process the STAC cell within a temperature-controlled environment. The cell after reconstitution is placed on a loading tray which automatically transfers the cell to a rotating carousel. The carousel is maintained at a constant temperature by means of a plenum chamber assembly. An evenly distributed air flow provides a constant 37°C environment for the cell.

At various stations on the carousel a number of analytical functions are accomplished. Residence time at each station is 2 min.

Station 1. The cell code is read. Information as to the chemistry, the type of sample (calibrant or unknown), and the lot number are contained on the cell code.

Station 2. The cell can be mixed by an air pump if required. The reaction would be initiated at this point. A pressure transducer is used to verify if mixing occurred.

Station 3. No mechanical functions occur. Residence of the cell at this station is to allow for incubation of the reaction initiated by mixing at a previous station.

Station 4. The cell can be mixed to initiate reaction if it is not yet accomplished. Also, the reaction is measured optically. Finally, the temperature of the reaction mixture is monitored in order to apply the appropriate temperature correction.

Station 5. Cells are ejected from the carousel.

The optical assembly obtains precise absorbance readings of the reaction mixture within the optical compartment of the STAC cell. The operation of the optical system is controlled by a microcomputer which receives input from the cell code. Operator involvement is eliminated and any drift or minor changes in optical characteristics are automatically compensated.

The light source is a low-voltage tungsten halogen lamp whose intensity is controlled by a lamp stabilization circuit. A set of condenser lenses collimate the light from the lamp with an effective aperture of $f/2.0$. A set of interference filters mounted on a filter wheel is programmed by a microcomputer to provide the appropriate monochromatic light. This is accomplished by a series of stepper motor indexing commands.

The filtered light is then split, with the largest portion collected by a projection lens and focused on the STAC cell optical window. The transmitted light is then collected and projected on to a solid-state photodetector. A small portion of the filtered light is directed from the beam splitter toward a reference photodetector. The output of the reference photodetector is applied to the lamp stabilization circuit, where it is compared to a reference signal in order to maintain a constant source lamp intensity.

2.3. Electronics Module

The electronics module provides real-time control, data processing, and operator interface functions for the STAC system. The system programs consist of an organized sequence of instructions that enable the electronics module to perform the following functions:

- Control the operation of all the mechanical devices within the analytical module.

- Acquire data from the cell code reader, optics system, and temperature correction system. Data are compiled and validated to assess any system malfunction.
- Compute test results from analytical data.
- Print results, calibration data, and system status messages.
- Respond to operator-initiated instructions.

3. General Theory

In conventional colorimetric analysis, the absorbance of the reaction mixture is measured at a single wavelength (λ_1), which is usually selected for maximum sensitivity. The concentration of analyte or chromophore (x_c) in the sample is then proportional to the corrected absorbance (A_1). So-called "bichromatic analysis," which is an extension of this approach, involves the measurement of an absorbance A_2 at some second wavelength (λ_2), to give a corrected absorbance ($A_1 - A_2$). The latter absorbance difference is then similarly proportional to x_c.

If the absorptivities of chromophore (c) and blank (b) at λ_1 and λ_2 are, respectively, a_1^c, a_1^b, a_2^c, and a_2^b, and if the concentration of the blank is x_b, the following expressions apply[5]:

$$A_1 = a_1^c x_c + a_1^b x_b \tag{1}$$

$$A_2 = a_2^c x_c + a_2^b x_b \tag{2}$$

For the special case of a blank that absorbs equally at λ_1 and λ_2 (i.e., $a_1^b = a_2^b$), simple subtraction of A_2 from A_1 completely eliminates the effect of the blank, since then

$$x_c = (A_1 - A_2)/(a_1^c - a_2^c) \tag{3}$$

Figure 1 illustrates one situation where equation (3) would be applicable, although this is a special case of limited general applicability (since a_1^b/a_2^b is rarely unity, particularly for the several possible interferences that can be encountered in a given assay). The use of equation (3) (so-called "bichromatic analysis") is nevertheless attractive for some assays because it allows simultaneous correction for certain shortcomings of present analytical systems: electro-optical drift or instability, variations in reagent concentration and/or absorbance, and differences in cuvette absorbance. These advantages can be combined with partial correction for various interferences which are of minor importance in the assay.[6] However, as the possible impact of sample interferences becomes more important (i.e., larger assay errors become possible), other forms of polychromatic analysis are required (see, e.g., reference 3).

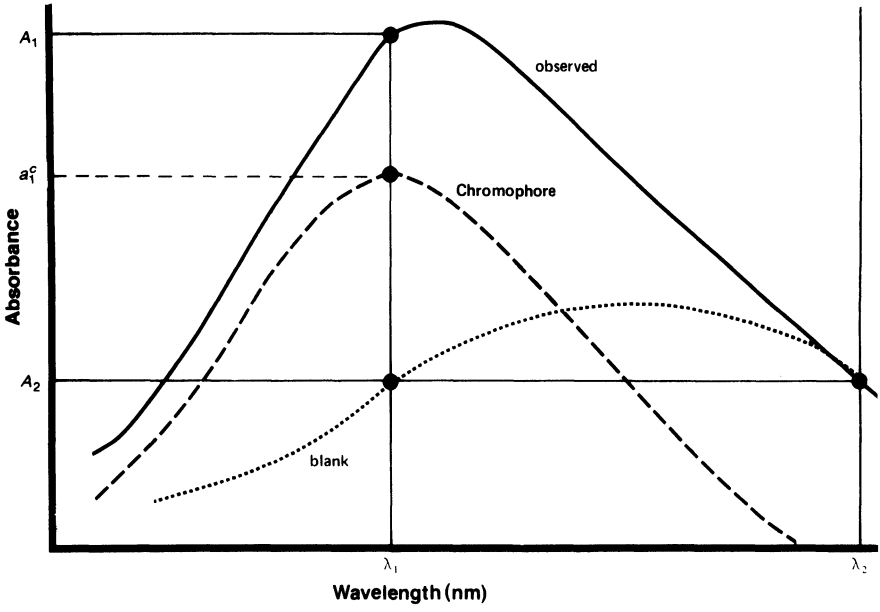

Figure 1. Curves showing a typical unity factor ($K = 1$) in polychromatic analysis.

The above approach can be expanded to allow for more general applicability, as illustrated in Figure 2. Some interferents (e.g., turbidity) do not have an absorbance spectrum that provides $a_1^b = a_2^b$ at some wavelength pair 1 and 2. From equations (1) and (2), the concentration of analyte is given as

$$x_c = \left[a_2^b / \left(a_1^c a_2^b - a_2^c a_1^b\right)\right] A_1 - \left[a_1^b / \left(a_1^c a_2^b - a_2^c a_1^b\right)\right] A_2 \tag{4}$$

or

$$x_c = R_1 A_1 - R_2 A_2 \tag{5}$$

where R_1 and R_2 are constants for a given assay. Rearranging equation (5) and introducing a sensitivity factor (S), we get

$$x_c = \frac{A_1 - R_2 / R_1 A_2}{S} \tag{6}$$

or

$$x_c = \frac{A_1 - KA_2}{S} \tag{7}$$

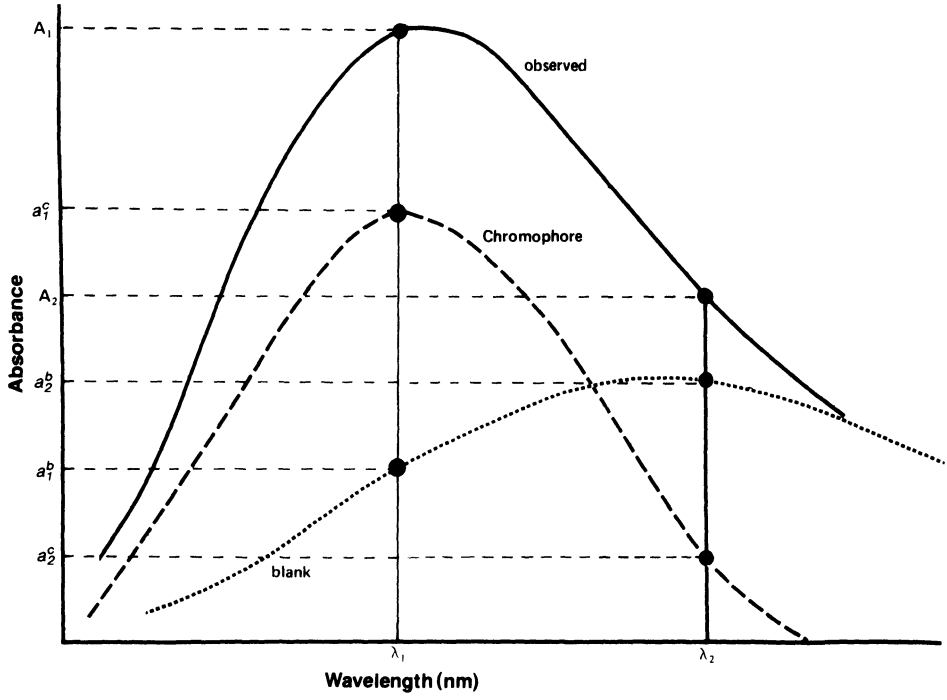

Figure 2. Curves showing a typical nonunity factor ($K \neq 1$) in polychromatic analysis.

where $R_2/R_1 = K$ is a new constant for a given assay and is equal to the ratio of absorptivities (a_2^b/a_1^b) of the particular interferents at the two wavelengths of interest. S is the sensitivity factor whose value is obtained on the STAC system using a calibration standard.

Equation (7) could be expanded and written as shown below:

$$x_c = \frac{\left(A_1^{\text{test}} - A_1^{\text{RB}}\right) - K\left(A_2^{\text{test}} - A_2^{\text{RB}}\right)}{S} \tag{8}$$

where A^{test} and A^{RB} represent the measured absorbance values at the designated wavelength using the test (sample) and reagent blank (RB), respectively.

Equation (8) represents the general form of the equations derived for bichromatic analysis on the STAC system.

Alternatively, the concentration of the interferent (x_b) can be determined:

$$x_b = \left[a_2^c/\left(a_2^c a_1^b - a_1^c a_2^b\right)\right] A_1 - \left[a_1^c/\left(a_2^c a_1^b - a_1^c a_2^b\right)\right] A_2 \tag{9}$$

Of course, equation (9) could also be written in the same form as for equation (8).

Measurement of x_b allows flagging of samples with very large specific interferences (where equation (8) might be less reliable). Many clinical assays are subject to more than one type of interference, e.g., both hemoglobin and turbidity. In some chemistries, it might not be possible to correct for all interferents present in the sample by means of a single bichromatic equation. In such cases, equation (9) could be used to determine if one or more of the interferents are present in the sample. If either interferent is present to the exclusion of the other, some form of equation (8) could be used to calculate the concentration of x_c. When both interferents are simultaneously present in the sample, a trichromatic expression based on absorbance measurements at three different wavelengths could be derived to calculate x_c. The calcium chemistry on the STAC system represents an example of this type of polychromatic analysis.

Since each additional absorbance measurement (A_2, A_3, etc.) is subject to some imprecision, overall assay precision would be expected to decrease for bichromatic versus monochromatic analysis, and for trichromatic versus bichromatic analysis. For this reason, trichromatic analysis should be restricted to those occasions where it is required, and the use of more than three wavelengths in polychromatic analysis seems not to be very useful. Either bichromatic, trichromatic analysis, or some combination, can be used to correct an assay for various interfering species. These interferents can be either nonreactive (static) or reactive (kinetic). The correction of reactive interferences differs only in requiring polychromatic absorbance measurements at more than one time during the analytical reaction.

4. Selection of Primary and Secondary Wavelengths

The selection of pertinent wavelengths λ_1 and λ_2 deserves comment. The primary wavelength is chosen for the same reasons as in classical (monochromatic) analysis. Thus, the major considerations are maximum sensitivity and minimum interference by blank. In Figures 1 and 2, λ_1 is chosen for maximum absorptivity of the chromophore. At the same time, the relative blank interference (a_1^c/a_1^b) is fortuitously minimized. In other cases, a compromise between these two factors may be required. For example, λ_1 can be selected somewhat off the chromophore absorption maximum, in order to either minimize or eliminate relative interference by the reagent blank.

The choice of the secondary (or additional) wavelength(s) is dictated by two considerations: (a) the relationship of a_1^b to a_2^b for each interferent(s), and (b) the amount of "leverage" attainable. The term leverage refers to the quantity $a_1^c a_2^b / a_2^c a_1^b$, a maximum value of which usually favors precision in

polychromatic analysis. Thus, λ_2 should be selected for maximum blank absorbance and minimum chromophore absorbance, just as the reverse is true in the selection of λ_1. The concept of leverage is further illustrated by comparing Figures 1 and 2. The more advantageous situation is seen in Figure 1, where $a_2^c = 0$ and $a_1^b = a_2^b$.

5. Classification of Polychromatic Analysis

Polychromatic analysis can generally be classified into four different groups.

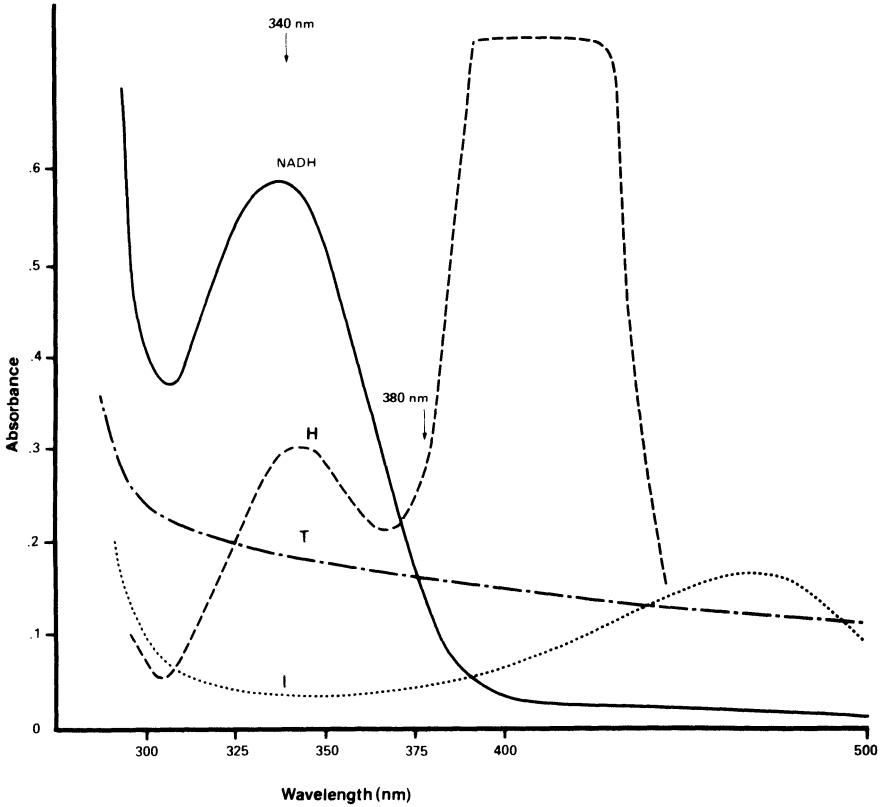

Figure 3. Scan of turbid (T), hemolyzed (H), and icteric (I) samples in glucose reagent without NAD and glucose (NADH) in reagent with NAD. The curves clearly show $K \approx 1$ at 340/380 nm wavelength pair.

5.1. Correction for Nonreactive (Static or Time Invariant) Interferences

This type of interference is caused by turbid (lipemic), hemolyzed (hemoglobin), and icteric samples.

The glucose chemistry on STAC represents an example of nonreactive interferences, with K fortuitously ≈ 1. As shown in Figure 3, the three interferents (turbidity, hemolysis, and icterus) have about the same absorbance at both primary (340 nm) and secondary (380 nm) wavelengths. Thus, conventional "bichromatic analysis" as used on the ABA or ACA is quite adequate for correcting these interferences. More commonly, as in the case of calcium (Figure 4) and total bilirubin (Figure 5), the situation is altogether different. Here, K is not equal to unity for these same three interferents at possible wavelengths λ_1 and λ_2. As discussed in Section 7.1 a more complex approach is required for calcium on STAC—although that procedure is based on the same principles discussed above.

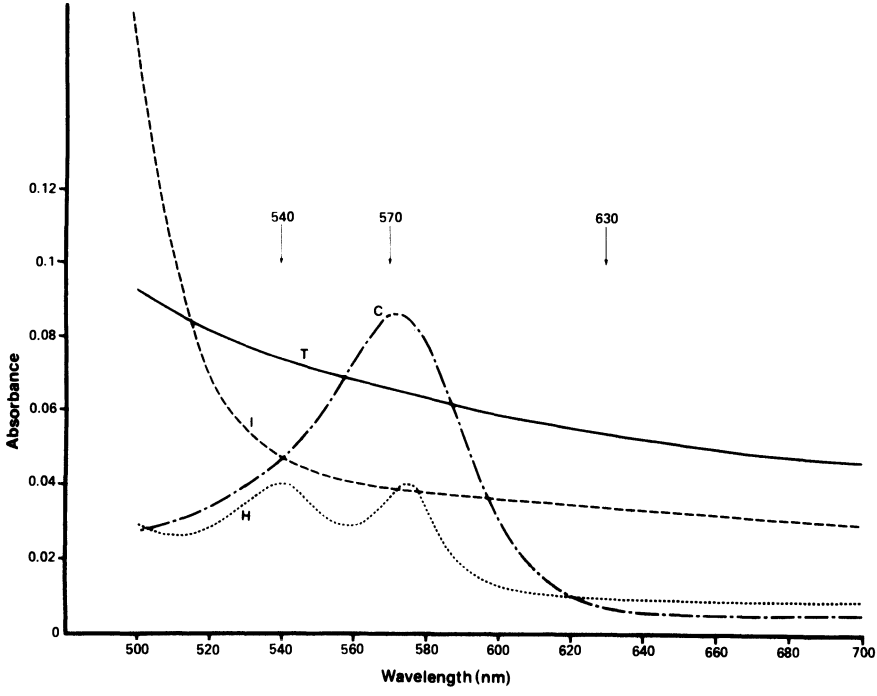

Figure 4. Scan of turbid (T), hemolyzed (H), and icteric (I) samples in calcium reagent without CPC and calcium (C) in reagent with CPC.

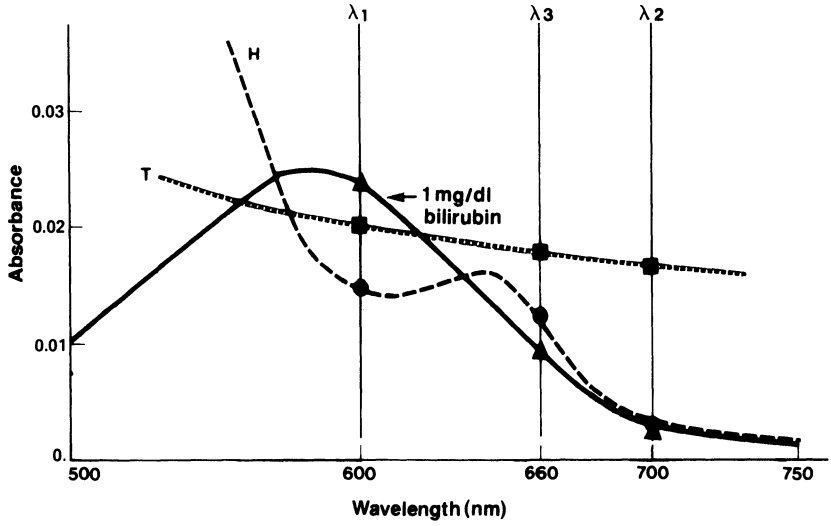

Figure 5. Scan of turbid (T) and hemolyzed (H) samples in total bilirubin reagent without fast red B. Total bilirubin in reagent with fast red B.

5.2. Correction for Reactive (Kinetic) Interferences

The interference of bilirubin in the STAC uric acid rate method (see Figure 6) provides an example of the application of polychromatic analysis to correct for reactive interferents in a clinical assay. Here, bilirubin not only absorbs at the wavelength of interest (525 nm), but also reacts with the H_2O_2 generated during the uric acid–uricase reaction, thereby, contributing to a negative interference in the uric acid assay. As shown in equation (23), a secondary wavelength (405 nm) measurement could be used to correct the uric acid values for this type of interference. As shown in Figure 7, a slightly different type of reactive interference is found in the STAC triglyceride assay due to sample clearing (due to the destruction of chylomicrons by lipase). This, too, can be corrected by a secondary wavelength measurement at 405 nm.

5.3. Correction for a Combination of Both Reactive and Nonreactive Interferences

It is possible to have a combination of both reactive and nonreactive interferences in the same sample. So far, in our work we have not encountered such combined interferences in any clinical assay for the STAC analyzer system. One would expect this type of interference to be more complicated, possibly involving measurements at three or more wavelengths. The general

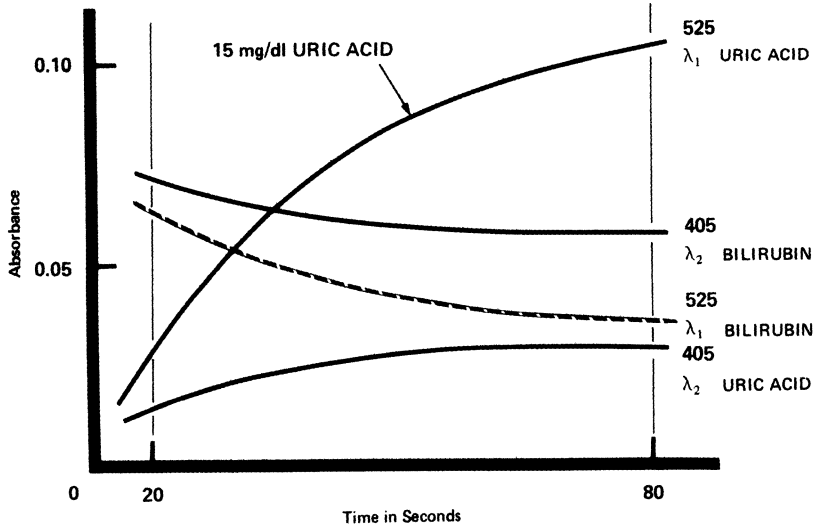

Figure 6. Typical pseudo-first-order rate curves for uric acid and bilirubin at both 405 and 525 nm in uric acid assay reagent.

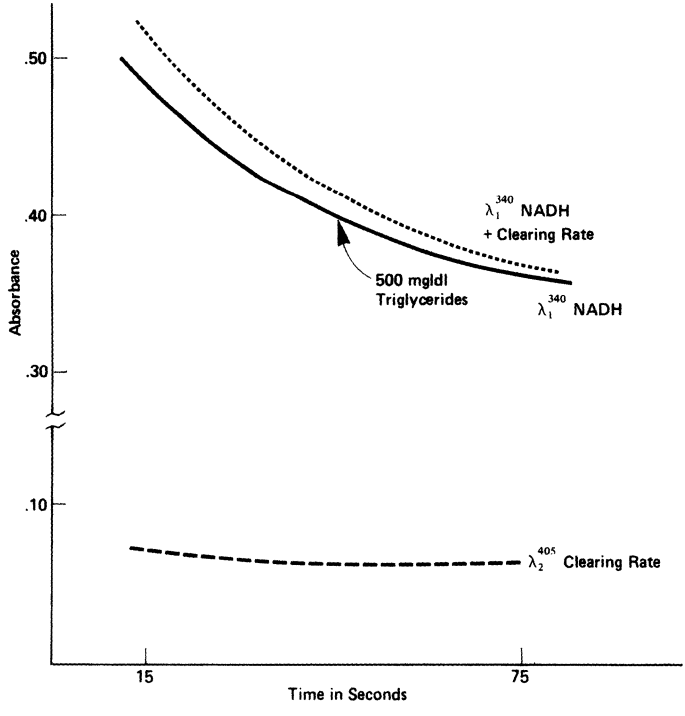

Figure 7. Typical sample clearing rate during triglyceride assay.

approach to handling such a situation can be inferred from the previous two cases.

5.4. Detection of Substrate Depletion

Polychromatic analysis can also be applied to detect substrate depletion, when the absorbance of substrate is itself subject to sample blank interferences. For example, consider the AST assay on STAC. If the rate is monitored after the *trans*-aminase reaction has been triggered, depletion of NADH can be occasionally obscured by a high absorbance of the sample at 340 nm (e.g., by turbidity, etc.). As shown in Figure 8, measurement of the reaction mixture at a second wavelength (e.g., 380 nm) allows the computa-

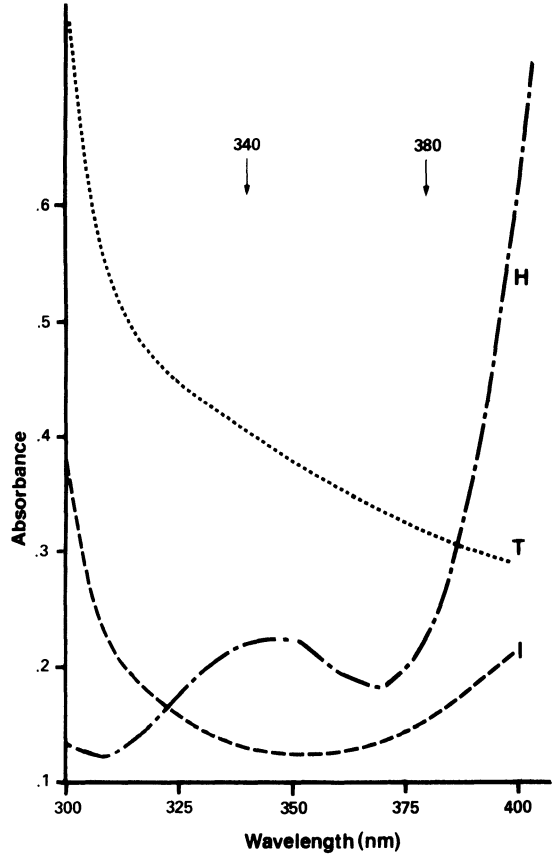

Figure 8. Scan of turbid (T), hemolyzed (H), and icteric samples in AST reagent without NADH. Comparison of curves at 340 (λ_1) and 380 nm (λ_2) clearly shows nonunity factor ($K \neq 1$) for turbid samples.

tion of absorbance at 340 nm due to NADH, thus, avoiding the problem of hidden-substrate depletion.

Polychromatic analysis generally allows at least partial correction for most sample interferences. In favorable cases, more than 90% of the most serious interferences can, thus, be corrected for. However, when such interferences are large, correction for even 90% of the interference may leave an unacceptable residual error (e.g., reference 3). In this case, the approximate magnitude of the original interference is of interest, and this can be obtained by a simple examination of the assay reaction absorbance at some third wavelength (λ_3). When the interference exceeds some critical level, the result should then be flagged as possibly invalid. For example, in the calcium determination on STAC, the sample is checked for turbidity by an absorbance measurement at 630 nm (λ_3) (at this wavelength, the chromophore has minimal absorbance). As shown in equation (10), if this absorbance after correcting for reagent blank exceeds a certain preset level, the sample would be flagged as being turbid and the results would be invalidated; if this happens, the sample has to be diluted and rerun to get a valid answer:

$$\left(A_{630}^{\text{test}} - A_{630}^{\text{RB}}\right) > 0.15\text{A} \tag{10}$$

6. STAC Assays

The various spectrophotometric absorption scans were obtained using a Perkin-Elmer, Coleman Model 124 or a Beckman Model 35 double-beam spectrophotometer, utilizing a path length of 10 mm. All other experimental data were obtained using the STAC analyzer. Human sera were used for interference studies.

Reagents for each chemistry were lyophilized in a disposable two-chamber cell. The cell is reconstituted by adding sample (10 or 50 μl) plus 0.75 ml of distilled water to the optical compartment. The trigger compartment is reconstituted with 0.75 ml distilled water or (for calcium) 1.55 *M* 2-amino-2-methyl-1-propanol (AMP) buffer (pH 10.2 at 25°C). Reaction is initiated by mixing the contents of both chambers on the system at the appropriate mixing stations. All analyses were done at 37°C.

A brief description of methodology employed is given in the following. A more detailed discussion is presented by Hahn *et al.*[4] and Morgenstern *et al.*[7]

Glucose[8–10] is determined by the hexokinase, glucose-6-phosphate dehydrogenase (G6PDH) method with ATP in the trigger compartment and the other enzymes in the optical compartment. The reaction is started with an early mix and the absorbance is measured at 340 nm after 5 min. Calcium is

determined by a modified cresolphthalein complexone (CPC) method employing AMP as the buffer[11-13] at a pH of 10.2. The total bilirubin method is based on the reaction of the sample with diazotized 5-nitro-2-aminoanisole (fast red B, $ZnCl_2$ salt) in maleic acid medium at a pH of 1.1.

The triglyceride assay is based on a modification of the Bucolo and David[14] procedure and uric acid is determined by a modified Trinder reaction.[15] Both these assays are measured as pseudofirst-order rates between 15 and 77 sec after initiation of the reaction.

The AST assay is a modification of the Henry *et al.* procedure.[16] The reaction is measured as a zero-order rate after a 2.6-min lag phase.

7. Examples of Polychromatic Analysis

7.1. Calcium

The calcium–cpc reaction illustrates the application of polychromatic analysis to correct for the three static interferents (turbidity, bilirubin, and hemoglobin), where the K values are not equal to 1. In presenting this chemistry, an effort would be made to discuss the various polychromatic-analysis options to correct for these three interferents.

The spectral absorption curves for the chromophore and the above three interferents are shown in Figure 4. Using the criteria of maximizing chromophore and minimizing blank absorbances, 570 nm represents a conventional choice for λ_1, the primary wavelength. However, the selection of λ_2, the secondary wavelength, poses some difficulty. For all wavelengths beyond 570 nm the K values for the two interferents are quite dissimilar, especially for turbidity and hemoglobin. This automatically rules out a reliable simultaneous correction for all three interferents by means of a single bichromatic equation (using a λ_2 above 570 nm).

In the calcium assay, turbidity is a more important interference than either hemoglobin or bilirubin. Also, the frequency of hemolyzed samples is generally low. If we ignore (for the moment) the possible interference of hemolyzed samples, the choice of 630 nm as λ_2 then seems reasonable. The use of the wavelength pair 570/630 nm makes it possible to correct for both turbidity and bilirubin, using a single value of K. Also, since the chromophore has minimal absorbance at 630 nm, the above wavelength pair offers maximum leverage in regard to interferences by turbidity and/or bilirubin. Using equation (8), the concentration of calcium in nonhemolyzed samples can be calculated as

$$\text{calcium}\left(\frac{\text{mg}}{\text{dl}}\right) = \frac{\left(A_{570}^{\text{test}} - A_{570}^{\text{RB}}\right) - 1.175\left(A_{630}^{\text{test}} - A_{630}^{\text{RB}}\right)}{S_1} \tag{11}$$

Equation (11) accurately corrects for both turbidity and icterus in hospital specimens,[3] but yields an average residual error of 0.36 mg/dl (1 SD) for hemolyzed samples. Since the frequency of hemolyzed samples is low, such samples can be flagged as described later on, following which they can be recalculated trichromatically to correct for hemolysis (as well as turbidity and/or icterus). In this way, the moderate loss in precision that results from trichromatic versus bichromatic analysis is confirmed to a small population of samples—those that are hemolyzed.

The flagging of hemolyzed samples is carried out as follows. As shown in Figure 4, hemoglobin absorbs strongly at 540 nm. Using the absorbance data of Figure 4 for the chromophore (calcium) and blank (average of turbidity and icterus), equation (9) can be used to calculate the "apparent" blank concentration X_b:

$$X_b = 30.2\left(A_{630}^{\text{test}} - A_{630}^{\text{RB}}\right) - 0.7\left(A_{570}^{\text{test}} - A_{570}^{\text{RB}}\right) \tag{12}$$

The same data of Figure 4 also allows us to write (for nonhemolyzed samples)

$$A_3 = A_{540}(\text{calculated}) = a_3^c x_c + a_3^b x_b \tag{13}$$

Substituting equation (11) (i.e., x_c) and equation (12) (i.e., x_b) into equation (13), then gives

$$A_{540}(\text{calculated}) = 0.455\left(A_{570}^{\text{test}} - A_{570}^{\text{RB}}\right) + 0.706\left(A_{630}^{\text{test}} - A_{630}^{\text{RB}}\right) \tag{14}$$

For nonhemolyzed samples, equation (14) will provide calculated values of A_{540} that are in close agreement with experimental values for a particular sample. However, if the sample is hemolyzed, the experimental A_{540} value will be found to significantly exceed the calculated value using equation (14) (because of the strong absorbance of hemoglobin at 540 nm). So we can write

$$\left(A_{540}^{\text{test}} - A_{540}^{\text{RB}}\right) > 0.455\left(A_{570}^{\text{test}} - A_{570}^{\text{RB}}\right) + 0.706\left(A_{630}^{\text{test}} - A_{630}^{\text{RB}}\right) \tag{15}$$

If this imbalance exceeds a certain set level (in this case $0.01A$), the samples will be flagged as hemolyzed. Thus, a comparison of calculated and experimental A_{540} values allows the flagging of significantly hemolyzed samples during the calcium assay. Samples not flagged as hemolyzed are then calculated using equation (11), while flagged samples are calculated using the trichromatic equation derived from the data of Figure 4 (see reference 3 for details):

$$\text{calcium}\left(\frac{\text{mg}}{\text{dl}}\right) = \left[\left(A_{570}^{\text{test}} - A_{570}^{\text{RB}}\right) - \left(A_{630}^{\text{test}} - A_{630}^{\text{RB}}\right)0.2234 - \left(A_{540}^{\text{test}} - A_{540}^{\text{RB}}\right)0.7686\right]/S_2 \tag{16}$$

To summarize, calcium can be assayed on STAC by taking absorbance measurements at 540, 570, and 630 nm. Then:

1. Hemolyzed samples can be flagged using equation (15).
2. Nonhemolyzed samples can be determined bichromatically using equation (11) which corrects for turbidity and/or icterus.
3. The flagged (hemolyzed) samples can be determined trichromatically using equation (16). This corrects for all three interferents.

As shown in Table 1, the above sequence of handling the data corrects for all three interferents. However, it was found experimentally that the value set for the discriminant function [i.e., the imbalance value in equation (15) set at $0.01A$ to detect hemolysis] varies for STAC from machine to machine (due to optical variations), making it difficult to detect the hemolysis of the sample accurately. Without accurate hemolysis detection, the above sequence of

Table 1. Calcium Blank Correction Using the Various Polychromatic Options

Serial number	Sample appearance	STAC assay values (mg/dl) using 570/630 nm bichromatic equation	STAC assay values (mg/dl) using 570/630/540 nm trichromatic equation (when flagged)	STAC assay values (mg/dl) using 570/540 bichromatic equation	True blank[a] corrected values	SMAC™ Triglyceride values for turbid samples
1	Normal	9.5	—	9.4	9.5	—
2	Normal	9.0	—	9.0	9.1	—
3	Normal	10.2	—	10.2	10.4	—
4	Normal	8.8	—	8.7	8.6	—
5	Normal	9.8	—	9.8	9.7	—
6	Turbid	8.8	—	8.5	8.4	888
7	Turbid	10.9	—	10.8	10.8	466
8	Turbid	10.0	—	9.8	10.0	901
9	Turbid	10.0	—	10.0	10.2	224
10	Turbid	11.1	—	10.9	11.0	838
11	Hemolyzed	9.7	9.6	9.6	9.5	—
12	Hemolyzed	11.3	11.1	11.1	10.9	—
13	Hemolyzed	6.0	5.2	5.2	5.4	—
14	Hemolyzed	9.1	7.2	7.0	7.0	—
15	Hemolyzed	8.7	8.5	8.5	8.6	—
16	Icteric	9.0	—	9.0	9.0	—
17	Icteric	9.3	—	9.2	9.2	—
18	Icteric	8.5	—	8.7	8.6	—
19	Icteric	9.5	—	9.4	9.5	—
20	Icteric	10.8	—	10.6	10.7	—

[a]Values obtained on the STAC system by running a separate blank for each sample (using calcium reagent without CPC).

equations would not be of much use in correcting for the three interferents. It is possible to overcome this variable discriminant problem by calibrating and assigning a specific discriminant value for each machine (instead of one fixed value for all machines). However, an alternate method which would be independent of system variations was considered more desirable.

Fortunately, on STAC we have been able to find a simple bichromatic equation ($K \neq 1$) to correct for all three interferents. As mentioned before, 570 nm offers the best choice for the primary wavelength and a careful reexamination of the absorbance curves of Figure 4 below 570 nm indicated the possibility of using 540 nm as the secondary wavelength. Although at 540 nm hemoglobin has strong absorptivity, the three interferents have about the same K values (using the wavelength pair 570/540 nm), thereby, making it possible to correct for all the three interferents by means of a single-bichromatic equation:

$$\text{calcium}\left(\frac{\text{mg}}{\text{dl}}\right) = \frac{1.19\left(A_{570}^{\text{test}} - A_{570}^{\text{RB}}\right) - \left(A_{540}^{\text{test}} - A_{540}^{\text{RB}}\right)}{S} \tag{17}$$

Even though the above equation has lower sensitivity (due to significant absorbance of the chromophore at 540 nm), it was found experimentally to give results similar to values calculated using the bi- and trichromatic equations with hemoglobin detection. The data are shown in Table 1.

The above example of the application of polychromatic analysis to calcium assay clearly demonstrates the various options available to correct for the three static interferences. As shown above, the final choice depends on a number of factors, e.g., maximum possible correction for blanks, ease of manipulation and independency from system variations, acceptable final precision, etc.

7.2. Total Bilirubin

The total bilirubin chemistry represents another example of the use of polychromatic analysis to correct for static interferences where the weighting factor is not equal to 1 ($K \neq 1$). The major interferents for this chemistry are turbidity and hemoglobin. The spectral absorption curves for these two interferents and the chromophore are shown in Figure 5. The absorption maxima for the chromophore is near 585 nm, but to minimize blank interferents on λ_1, the latter is selected at 600 nm.

The ratio of absorbances for the two interferents at 600/660 nm (i.e., the K values) is sufficiently similar to allow the use of 660 nm as a secondary wavelength (λ_2) for the bichromatic analysis. However, the chromophore also absorbs significantly at 660 nm, and as a result, the sensitivity of the method

would be lower (and precision poorer) using these two wavelengths (600/660 nm) for bichromatic analysis:

$$\text{total bilirubin}\left(\frac{\text{mg}}{\text{dl}}\right)=\frac{\left(A_{600}^{\text{test}}-A_{600}^{\text{RB}}\right)-1.17\left(A_{660}^{\text{test}}-A_{660}^{\text{RB}}\right)}{S_1} \tag{18}$$

An alternative approach is as follows. From data on collected samples, it was obvious that turbidity is a common and more significant interference than hemoglobin in the total bilirubin determination. A bichromatic equation was then developed using 600 nm as the primary wavelength and 700 nm as the secondary wavelength (hemoglobin has minimal absorbance at this wavelength) to correct for turbid blanks:

$$\text{total bilirubin}\left(\frac{\text{mg}}{\text{dl}}\right)=\frac{\left(A_{600}^{\text{test}}-A_{600}^{\text{RB}}\right)-K\left(A_{700}^{\text{test}}-A_{700}^{\text{RB}}\right)}{S_2} \tag{19}$$

In equation (19), K is the weighting factor for turbid samples and is assigned a value of 1.23, A^{test} is the absorbance of the sample at the designated wavelength, and A^{RB} is the absorbance of the reagent with water as sample (or reagent blank) at the designated wavelength. These blank data are stored in STAC memory and are recalled by the system for each calculation. S_2 is the sensitivity factor (i.e., A/mg/dl) and is computed on STAC by running a calibration standard. This information is also stored in the computer memory. As can be seen from the data in Table 2, the bichromatic equation (19) corrects well for turbid samples, as well as for slightly hemolyzed (up to 50 mg/dl hemoglobin) samples.

In this chemistry we now have two bichromatic equations [(18) and (19)]. The first equation corrects for both turbid and hemolyzed samples, but the sensitivity is low. The second equation corrects well for turbidity and minor hemolysis. So by using a combination of these two equations, it is possible to correct for the two interferents in all possible situations, with minimum overall loss in sensitivity and precision.

Table 2. Total Bilirubin Blank Correction

	Average error (mg/dl)		
		Bichromatic	
Sample type	Unblanked	600/700	600/660
Normal	0.44	0.05	—
Turbid	2.6	0.08	—
Slightly hemolyzed[a]	0.74	0.05	—
Grossly hemolyzed[b]	2.23	1.07	0.13

[a] < 150 mg/dl hemoglobin.
[b] > 200 mg/dl hemoglobin.

Table 3. Total Bilirubin Blank Correction

Serial number	Sample appearance	STAC Assay value (mg/dl) using 600/700 nm bichromatic equation	600/660 nm bichromatic equation	Assay value validated	True blank[a] corrected value
1	Normal	1.2	1.3	1.2	1.2
2	Normal	3.0	3.2	3.0	3.0
3	Normal	0.7	0.8	0.7	0.7
4	Normal	1.8	1.9	1.8	1.8
5	Normal	0.7	0.8	0.7	0.6
6	Turbid	0.8	0.8	0.8	0.8
7	Turbid	5.6	5.8	5.6	5.5
8	Turbid	1.3	1.2	1.2	0.9
9	Turbid	3.8	4.0	3.8	3.7
10	Turbid	1.2	1.2	1.2	1.1
11	Hemolyzed	0.8	0.8	0.8	0.8
12	Hemolyzed	0.9	0.8	0.8	0.6
13	Hemolyzed	3.4	2.1	2.1	2.0
14	Hemolyzed	3.1	1.7	1.7	1.6
15	Hemolyzed	2.3	2.1	2.1	2.0

[a]Values obtained on the STAC system by running a separate blank for each sample (using reagent without fast red B).

Case 1: *If the Sample is Not Hemolyzed.* The total bilirubin value calculated using equation (19) should be equal to the value calculated using equation (18) within experimental error. If this condition is met, the value calculated using equation (19) (more precise) is validated and printed as the correct value.

Case 2: *If the Sample is Hemolyzed.* The value calculated using equation (19) will be greater than the value obtained using equation (18)—as equation (19) does not adequately correct for hemoglobin and any absorbance contribution by hemoglobin represents a positive error [in equation (19)]. Under these conditions, the value obtained using equation (18) would be validated as the correct value.

As shown in Table 3, this double bichromatic approach works well. Thereby proving that it is possible to correct for static interferences by the use of a discriminating double-bichromatic equation.

7.3. Uric Acid

This assay on STAC represents an example of the application of polychromatic analysis to correct for reactive (kinetic) interferences. In this type of interference, the interferent reacts with one (or more) of the products

formed during the assay reaction, thereby contributing to error in the analytical determination.

The reaction of uric acid with uricase is measured on STAC as a pseudofirst-order rate using the following coupled reaction[16–18]:

$$\begin{aligned} &\text{uric acid} + O_2 + H_2O \xrightarrow{\text{uricase}} \text{allantoin} + H_2O_2 + CO_2 \\ &H_2O_2 + \text{4-aminoantipyrine} + p\text{-hydroxybenzoate} \xrightarrow{\text{peroxidase}} \\ &\text{coupled-color-product} + H_2O \end{aligned} \tag{20}$$

In kinetic determinations [such as shown in equation (20)], the subtraction of the initial from the final absorbance value (giving ΔA values) automatically corrects for static interferences (e.g., turbidity and hemoglobin in this assay). However, bilirubin represents a kinetic interference, since it reacts with hydrogen peroxide formed during the uric acid–uricase reaction and absorbs at the wavelength of interest. The peroxide-reacted bilirubin has a lower absorbance at 525 nm (the primary wavelength) than the unreacted bilirubin. As a result, bilirubin not only reduces the amount of chromophore formed (by reacting with peroxide), but also contributes to a further decrease in absorbance due to the lower absorption of the peroxide-reacted bilirubin at 525 nm. At low levels of bilirubin in the sample, its interference can be essentially eliminated by the addition of albumin to the reagent (due to binding of bilirubin with albumin, thereby preventing its reaction with peroxide). However, at higher levels of bilirubin (above 5 mg/dl), a significant interference occurs in the STAC uric acid assay.

Once again, it is possible to correct for this type of interference by the use of a bichromatic measurement. The uric acid chromophore has maximum absorbance near 505 nm. However, to minimize bilirubin interference and maximize the leverage (bilirubin has considerable absorbance at 505 nm and minimal absorbance at 525 nm), 525 nm was selected as the primary wavelength (λ_1). Although bilirubin has maximum absorbance at 450 nm, the chromophore also absorbs significantly at this wavelength. To obtain maximum leverage the secondary wavelength (λ_2) was selected at 405 nm.

Figure 6 shows the characteristic rate curves for uric acid and bilirubin at both 405 and 525 nm. Using NBS uric acid standards,[19] it was found experimentally that the ratio of $\Delta A_{405}/\Delta A_{525}$ for uric acid is about 0.2. The ΔA values refer to the difference in absorbance between reaction times of 15 and 77 sec after the initiation of the reaction at the optical read station. Thus, in the absence of bilirubin in the sample we can write

$$0.2\Delta A_{525} - \Delta A_{405} = 0 \tag{21}$$

If bilirubin is present in the sample at interfering levels, it reduces the ΔA

values at both 405 and 525 nm. Experimentally, it was found that the relative decrease in ΔA at 405 nm is greater than the relative decrease of ΔA at 525 nm. In other words,

$$0.2\Delta A_{525} - \Delta A_{405} > 0 \tag{22}$$

It is possible to relate the magnitude of change in equilibrium of equation (22) to the bilirubin interference level and calculate the corrected uric acid value by means of the following equation:

$$\text{uric acid}\left(\frac{\text{mg}}{\text{dl}}\right) = \frac{\Delta A_{525} + (0.2\Delta A_{525} - \Delta A_{405})K}{S} \tag{23}$$

In the above equation, S denotes the sensitivity factor (i.e., $\Delta A/\text{mg/dl/min}$) and is obtained on the STAC system by the use of a calibration standard.

The factor K is a constant and is assigned a value of 1.3. This value was arrived at by analyzing a large amount of bilirubin containing (varying levels of bilirubin) human sera samples on STAC and calculating the uric acid values using equation (23) with varying K values. The results obtained using the K value of 1.3 showed the best correlation with the reference method.[20]

As shown in Table 4, the above derived bichromatic equation corrects well for both normal and icteric samples. Thus, it is possible to use polychromatic analysis to correct for kinetic interference.

Table 4. Uric Acid Bilirubin Correction

Sample	Total bilirubin[a] (mg/dl)	Uric acid[b] (mg/dl)	STAC Uric acid (mg/dl)	
			Uncorrected[c]	Corrected[d]
Calibrant	2.0	5.5	—	—
1	0.8	4.8	4.7	4.7
2	3.4	5.4	5.2	5.2
3	17.9	4.9	3.5	5.3
4	7.1	6.0	5.3	5.6
5	12.5	4.7	3.9	4.7
6	21.7	4.6	2.9	5.0
7	4.2	5.6	5.3	5.3
8	2.1	5.4	5.3	5.3
9	1.7	4.2	3.9	3.9
10	2.3	8.2	8.1	8.1

[a] Total bilirubin values assayed on STAC.
[b] Uric acid values assayed by BMC procedure at 292 nm.
[c] Uncorrected = $[\Delta A_{525}]/[\Delta A_{525}^{\text{calibrant}}/\text{concentration of calibrant}]$.
[d] Corrected = $[\Delta A_{525} + (0.2\Delta A_{525} - \Delta A_{405})1.3]/\text{sensitivity}$;

$$\text{sensitivity} = \frac{\left[\Delta A_{525}^{\text{calibrant}} + \left(0.2\Delta A_{525}^{\text{calibrant}} - \Delta A_{405}^{\text{calibrant}}\right)1.3\right]}{\text{concentration of calibrant}}$$

7.4. Triglycerides

This chemistry represents another example of the application of polychromatic analysis to correct for a slightly different type of reactive interference.

The STAC triglycerides assay is based on the first-order conversion of triglycerides to glycerol (by lipase) followed by a rapid coupling of glycerol to the NADH to NAD reaction. As illustrated in Figure 7, this assay is subject to sample clearing interferences if the reaction is followed only at 340 nm. This decrease in absorbance at 340 nm due to sample clearing is attributed to the destruction of chylomicrons by the lipase reagent.

However, it is possible to correct the triglyceride values for the sample clearing effect by a bichromatic measurement at 340/405 nm.

The primary wavelength λ_1 (340 nm) is selected from the absorption maximum of NADH and the reaction is followed at this wavelength from 15 to 77 sec after initiation at the optical read station. As noted in Section 3, turbidity (T) exhibits significant absorbance at both 340 and 405 nm, but NADH has negligible absorbance at 405 nm. Thus, by the use of 405 nm as λ_2, the secondary wavelength offers maximum leverage in this bichromatic assay. Based on equation (8), it is possible to write

$$\text{triglycerides}\left(\frac{\text{mg}}{\text{dl}}\right) = \frac{(A_{340} - KA_{405})}{S} \tag{24}$$

Equation (24) actually applies to an endpoint determination of triglycerides, rather than a kinetic determination as on STAC. However, equation (24) can also be applied to the concentration of triglycerides as a function of time. Therefore, by replacing the A_{340} and A_{405} values of ΔA_{340} and ΔA_{405} values, respectively, we can make equation (25) work equally well for the kinetic assay.

$$\text{triglycerides}\left(\frac{\text{mg}}{\text{dl}}\right) = \frac{(\Delta A_{340} - K\Delta A_{405})}{S_1} \tag{25}$$

S_1 is now defined as a sensitivity factor that can be determined for the STAC assay by running a calibration standard.

The constant K was determined experimentally by measuring the actual clearing rates at 340 and 405 nm for several lipemic samples. By eliminating NADH from the reagents, the clearing reaction could be monitored separately from the glycerol reation, as shown in Table 5, columns 2 and 3. The weighted average of $(\Delta A_{340}/\Delta A_{405})$ represented by K, came out to be approximately 1.5. Substitution of this value of K in equation (25) allows the calculation of corrected triglyceride values in both clear and turbid samples.

Table 5. Triglyceride Kinetic Blank Correction

Sample	ΔA_{340}[a]	ΔA_{405}[a]	Residual error (mg/dl)	
			Uncorrected[b]	Corrected[c]
Calibrant[d]	0.0606	0.0005	—	—
1	0.0033	0.0021	14	1
2	0.0346	0.0235	143	−3
3	0.0076	0.0053	31	−2
4	0.0112	0.0074	46	0
5	0.0029	0.0021	12	−1
6	0.0101	0.0054	42	8
7	0.0078	0.0051	32	1
8	0.0032	0.0021	13	0
9	0.0219	0.0134	90	8

[a] ΔA_{340} and ΔA_{405} are measured by eliminating NADH from the reagents except for the calibrant.
[b] Uncorrected $= \Delta A_{340}/(0.0606/250$ mg/dl).
[c] Corrected $= [\Delta A_{340} - (1.5)\Delta A_{405}]/[(0.0606 - 1.5 \times 0.0005)/250$ mg/dl].
[d] Human sample assayed on SMAC (250 mg/dl triglycerides). ΔA_{340} and ΔA_{405} are actual reaction rates.

The last two columns of Table 5 compare the residual error due to clearing for the uncorrected (i.e., monochromatic) assay versus the bichromatic assay.

The above data clearly show that bichromatic (polychromatic) analysis could be used effectively to correct not only for static, but also for kinetic interferences. The only difference is the substitution of ΔA values for the absorbance values in kinetic versus endpoint determinations.

7.5. AST

The AST method represents an example where a secondary wavelength measurement can be applied to validate (not correct) an analytical result.

After an initial lag phase (during which endogenous pyruvate is consumed) the AST method follows zero-order kinetics. On the STAC system, the rate is monitored for 60 sec after a 2.6 min lag phase. Since the rate is not monitored from time zero, a significant substrate (NADH) depletion could occur with high AST samples. This could result in a severe underestimation of the activity of the high-AST samples.

However, substrate depletion could be detected by the use of a secondary wavelength measurement which would allow a correction of the primary wavelength measurement for any non-NADH absorbing components present in the sample (e.g., turbidity, bilirubin, and hemoglobin).

Figure 8 shows the characteristic curves for the three common interferents (turbidity, bilirubin, and hemoglobin) in AST reagent without NADH. As can be seen, both hemoglobin and bilirubin have approximately the same

absorbance at 340 and 380 nm, but turbidity, which is a more common interference, has higher absorbance at 340 nm than at 380 nm. Further experiments on the STAC system established the ratio A_{340}/A_{380} for turbidity as 1.2. Since NADH has minimum absorbance at 380 nm, the measured absorbance at this wavelength could be attributed almost entirely to the interferents. So we now have a means of correcting the measured absorbance at 340 nm for the above mentioned interferents by simply subtracting the weighted A_{380} nm value taken at the same time.

$$A_{340} \text{ corrected} = A_{340} \text{ measured} - 1.2 A_{380} \text{ measured} \tag{26}$$

In establishing the weighting factor K as 1.2, we have identified turbidity as a more significant interferent at 340 nm in this chemistry. The use of this factor, of course, would automatically correct and, in some cases, probably overcorrect for the other two interferences. But this situation is more desirable and assures the detection of substrate depletion even with highly turbid samples.

The above A_{340} corrected value gives the absorbance due to NADH at 2.6 min available for the AST reaction during the subsequent measurement on the STAC system. The actual procedure on STAC is to compare the A_{340} (corrected) value with a value calculated for samples of maximum activity (corresponding to the range of the AST assay on STAC). When A_{340} (corrected) is below this value, the sample will be flagged for dilution and rerunning. Equation (26) is not required to be very precise, since a further safety factor exists in the check for linearity of enzyme reaction after 2.6 min.

8. Conclusion

Polychromatic analysis is a particularly powerful technique for ensuring accurate results in certain clinical chemistry assays. However, to take full advantage of its potential, we must be free to select more than two wavelengths when this is advantageous, and to use correction factors (K values) that are different from unity. Finally, we must weigh different possible approaches within polychromatic analysis for the best overall results in terms of assay reliability, accuracy, and precision. There is no generally "best" approach to a given assay; rather, each method offers unique opportunities for the custom design of polychromatic analysis around that method.

Acknowledgments

The authors are greatly indebted to Dr. Lloyd R. Snyder for his constant encouragement and help in writing the manuscript. The authors also thank

Daniel Vlastelica for reading the manuscript and making valuable suggestions, Jana Furda for her work on uric acid, and Judy Chall and Fedela Tranzillo for their technical assistance. Finally, our sincere thanks to Linda Cirillo for her understanding and help in typing this manuscript.

References

1. G. Y. Shinowara, Spectrophotometric studies on blood serum and plasma, the physical determination of hemoglobin and bilirubin, *Am. J. Clin. Pathol.*, **24**, 696–710 (1954).
2. I. M. Kolthoff and P. J. Elving (eds.), *Treatise on Analytical Chemistry, Part I: Theory and Practice*, Vol. 5, pp. 2789–2795, Interscience, New York (1963).
3. G. Kessler and L. R. Snyder, Bichromatic analysis as applied to Technicon STAC biochemical analyzer, in: *Advances in Automated Analysis. 1976 Technicon International Congress*, pp. 28–35, Mediad Press, Tarrytown, New York (1977).
4. B. Hahn, D. L. Vlastelica, L. R. Snyder, J. Furda, and K. J. M. Rao, Polychromatic analysis: New applications of an old technique., *Clin. Chem.*, **25**, 951–959 (1979).
5. J. C. Cowles, Theory of dual-wavelength spectro-photometry for turbid samples, *J. Optical Soc. Am.*, **55**, 690–693 (1969).
6. K. L. Ratzloff and D. Natusch, Theoretical assessment of precision in dual-wavelength spectrophotometric measurements, *Anal. Chem.*, **49**, 2170–2176 (1977).
7. S. Morgenstern, B. Hahn, and D. Vlastelica, STAC rate reaction and fixed-point methods, in: *Advances in Automated Analysis. 1976 Technicon International Congress*, pp. 16–22, Mediad Press, Tarrytown, New York (1977).
8. W. Barthelmai and R. Czok, *Klin. Wochschr.*, **40**, 585 (1962).
9. W. E. Neeley, Simple automated determination of serum or plasma glucose by a hexokinase/glucose-6-phosphate dehydrogenase method, *Clin. Chem.*, **18**, 509–515 (1972).
10. M. W. Slein, *Methods of Enzymatic Analysis* (H. V. Bergmeyer, ed.), pp. 117–123, Academic Press, New York (1963).
11. G. Kessler and M. Wolfman, An automated procedure for the simultaneous determination of calcium and phosphorous, *Clin. Chem.*, **10**, 686–703 (1964).
12. H. Grittleman, An improved automated procedure for the determination of calcium in biological specimens, *Anal. Biochem.*, **18**, 521–531 (1967).
13. R. W. Morehead and H. G. Biggs, The use of 2-amino-2-methyl-1-propanol (AMP) as the alkalizing agent in an improved continuous-flow cresolphthalein complexone procedure for calcium in serum, *Clin. Chem.*, **20**, 1458–1460 (1974).
14. G. Bucolo and H. David, Quantitative determination of serum triglycerides by the use of enzymes, *Clin. Chem.*, **19**, 476–482 (1973).
15. P. Trinder, Determination of glucose in blood using glucose oxidase with an alternate oxygen acceptor, *Ann. Clin. Biochem.*, **6**, 24–27 (1969).
16. R. J. Henry, N. Chiamoni, O. J. Giolub, and S. Berkman, Revised spectrophotometric methods for the determination of glutamic-oxalacetic transaminase, glutamic-pyruvic transaminase, and lactic acid dehydrogenase, *Am. J. Clin. Pathol.*, **34**, 381–398 (1960).
17. M. B. Ettinger, C. C. Ruchhoff, and R. J. Lishka, Sensitive 4-aminoantipyrene method for phenolic compounds, *Anal. Chem.* **23**, 1783–1788 (1951).
18. E. Emerson and K. Kelly, The condensation of aminoantipyrene, *J. Org. Chem.* **13**, 532–534 (1948).
19. Standard Reference Material 913 Uric Acid, Office of Standard Reference Materials, National Bureau of Standards, Washington, D.C.
20. Boehringer-Mannheim 292 nm Uricase Method, BMC, Indianapolis, Indiana. Catalog Number 124737, Using a Gilford 2400 Spectrophotometer.

Introduction to Multiple-Wavelength Spectrophotometric Measurements in Analytical and Clinical Chemistry

David. L. Witte

1. Introduction

Spectrophotometry continues to be very important in analytical chemistry and is the single most important detection system in the clinical laboratory. Even recent clinical laboratory advances in high-pressure liquid chromatography and enzyme-linked immunochemistry depend on spectrophotometric measurements. Although measurements made at a single wavelength are most common, multiple-wavelength analyses are growing in importance and add to the capabilities of the modern laboratory. Multiple-wavelength spectrophotometry has been used to measure multiple components in a complex mixture, to correct for interferences, and to increase sensitivity. Examples of these applications will be discussed individually with special reference to their relevance in clinical chemistry. These general principles will serve as an introduction to the three following contributions which describe commercial applications of multiple-wavelength spectrophotometry in the clinical chemistry laboratory. This chapter is not intended to be an exhaustive review, but to provide the reader with general insight into clinical chemistry applications and a bibliography to guide further study. Two recent reviews[1, 2] are suggested for additional background.

David L. Witte • Department of Pathology, University of Iowa, Iowa City, Iowa 52240.

2. Definitions

Precise communication is only possible if definitions are clearly understood. Terms used in the literature of multiple-wavelength spectrophotometry are not uniform. Therefore, the following definitions will be used in this chapter.

1. *Monochromatic spectrophotometry* refers to the use of a single beam of light with a relatively narrow dispersion of wavelengths. These analytical techniques usually employ the Beer–Lambert law and separate reaction vessels for sample and either a reagent or a sample blank.
2. *Dual-beam spectrophotometry* will be used when referring to the usual scanning spectrophotometer in which a beam of monochromatic light is split in space and passed through two separate reaction vessels, one for the reference and one for the sample. This analytical technique also uses the Beer–Lambert law and provides a simultaneous blank. Obviously scanning introduces multiple wavelengths, but the principles are identical to the monochromatic measurements.
3. *Multichromatic spectrophotometry* will refer to the use of more than one wavelength of monochromatic light. The most frequent applications use a single beam which alternates among the multiple wavelengths. *Bichromatic* and *trichromatic* refer to specific examples of *multichromatic* measurements. These measurements may use the simple Beer–Lambert law, but more complex calculations will be discussed.
4. *Derivative spectrophotometry* is accomplished in several ways. One method involves scanning with two beams of light with a small fixed difference in their wavelength.[1] Therefore, this is a special application of multiple-wavelength spectrophotometry and different from bichromatics as defined above since two beams are used.
5. *Dual-wavelength spectrophotometry* will refer to the use of two beams of light with different wavelengths for the sample beam and reference beam.

The most important definition for the contributions that follow is *multichromatic spectrophotometry*; the above definitions are included to avoid confusion.

3. Applications in Analytical Chemistry

Most undergraduate analytical chemistry texts[3] discuss the use of multiple-wavelength spectrophotometry for the measurement of multiple chromophores in a mixture. This approach requires at least one wavelength per component and utilizes the same number of equations of the following

form:

$$A_\lambda = \sum_i \varepsilon_{\lambda i} b c_i$$

where A_λ denotes the observed absorbance at wavelength λ, $\varepsilon_{\lambda i}$ denotes the extinction coefficient of the ith component at wavelength λ, b the path length, and c_i the concentration of the ith component.

A logical extension of the above equation is the use of log–Gaussian mathematical functions to fit the band shape of electronic absorption spectra.[4–7] This approach has allowed the determination of tautomeric and hydration equilibrium constants from the spectral analysis of complex mixtures of aromatic molecules.[6–7] This mathematical treatment of multiple-wavelength spectral data has also aided in the demonstration of changes in vibronic fine structure during protein denaturation.[5]

Using multiple wavelengths, Fonda and Johnson[8] have shown that the contribution to light absorption due to a turbid impurity can be effectively calculated. This is possible since over a short range of wavelengths (320–530 nm) the contribution of turbidity is linearly related to either log-wavelength or the inverse of the wavelength. Therefore, if any segment of the specified spectral region has no absorbance contribution by chromophore and all absorbance is due to turbidity, the contribution due to turbidity can be calculated over the entire spectral region.

In 1950, Willard Allen published a calculational method for the subtraction of the absorption contributed by a linearly absorbing impurity.[9] This is widely known as the "Allen base line correction" and assumes that the absorption due to impurity is linear over a short range of wavelengths. Therefore, the contribution of the impurity to the absorbance at the analytical wavelength can be calculated if the absorption is known at two wavelengths equidistant above and below the analytical wavelength:

$$A_{\text{analyte},\lambda} = A_\lambda = \frac{A_{\lambda+\Delta\lambda} + A_{\lambda-\Delta\lambda}}{2}$$

A more general derivation was published by Jensen and Oliver,[10] who also assumed a linearly absorbing impurity, but the two additional measurements need not be equidistant from the analytical wavelength. The Allen baseline correction has been widely applied, but the underlying assumptions must never be forgotten.

Eugene Allen and W. Rieman III published a method to determine the concentration of one compound in a complex mixture through the use of two or three wavelengths.[11] Their method is a simplification of the multicomponent method discussed earlier and rests on the assumption that all the

interferents have the same ratio of absorbances at two wavelengths, i.e., $K = \varepsilon_{\lambda 1}/\varepsilon_{\lambda 2}$ for all impurities. Again, careful validation of this assumption is necessary. However, Allen and Rieman have shown the method is useful for mixtures containing pyridine, β-picoline, 2-aminopyridine, 2-aminopyrimidine, 2-amino-4-methylpryimidine, and 2-amino-4, 6-dimethylpyrimidine, and they present a clever graphical solution to multiple equations.

Britton Chance designed a dual-wavelength spectrophotometer for the study of pigments in turbid solutions of cytosol.[12-13] His apparatus used two beams of different but relatively close wavelengths, and measured an absorbance difference (A_d), $A_d = A_{\lambda 1} - A_{\lambda 2}$. He reports a sensitivity of 5×10^{-4} absorbance even in very turbid solutions. The use of two closely spaced wavelengths should correct for cuvette absorption and position differences as well as sample turbidity since it is assumed these properties change little over a short range of wavelengths.

Dual-wavelength spectrophotometry has seen commercial application[14-15] and Shibata *et al.*[14] lists five advantages of this equipment:

1. ability to measure a small change in absorbance in the presence of a large absorbance background;
2. colorimetry without reference if total absorbance is less than 0.01;
3. if both wavelengths are scanned derivative spectra are generated;
4. special relative spectra can be generated by scanning one wavelength with the second wavelength fixed;
5. two reactions can be followed independently in one reaction vessel.

Gerchakov[16] has published analytical methods for mixtures using a scanning sample beam with a fixed-wavelength reference beam. He feels this technique provides advantages in the analysis of mixtures. Chance and Graham[17] and others[18] have also described analytical methods that scan wavelengths in highly turbid solutions. The analysis of errors and sensitivity in dual-wavelength spectrophotometry was reviewed independently by Cowles,[19] Rikmenspoel,[20] and Hendler.[21] Whereas this instrumentation has been of great interest to biochemists who study reactions in complex cytosol suspensions, it has not received much attention in analytical or clinical chemistry. However, as the clinical laboratory becomes more involved in the measurement of cytosol binding proteins this instrumentation may find applications.

4. Applications in Clinical Chemistry

The use of multiple wavelengths in the clinical laboratory is commonplace and several representative specific examples will be discussed. Perhaps

the most widely remembered example is that of the "Allen baseline correction" in the measurement of urinary steroids, which has already been discussed.

A second well-studied example is in the spectrophotometric measurement of bilirubin in amniotic fluid for the assessment of fetal hemolytic disease. Liley's[22-23] original method used a baseline correction involving a plot of log-absorbance versus wavelength which allowed the calculation of A_{450} values in amniotic fluid samples. This method was shown to be effective in making clinical decisions. As people used the method of Liley, modifications began to appear. Burnett[24] has pointed out that erroneous decisions will result if a linear baseline correction is substituted for the logarithmic correction proposed by Liley. This is an example of how laboratorians fall into the trap of making a simplifying analytical change and fail to validate that the clinical utility of the assay has not changed. Burnett also points out that considerable error in baseline correction will occur if the zero-absorbance reference point is not carefully established.

Multiple-wavelength spectrophotometry is widely used for the specific measurement of catecholamine metabolites in urine. Pisano[25] describes a method which uses measurements at two wavelengths to correct for the interference caused by synephrine, a component of nose drops and bronchodilators. Measurements are made at 347 and 330 nm after the catecholamine metabolites and synephrine are converted to vanillin and 4-hydroxybenzaldehyde, respectively, by periodate oxidation. Vanillin absorbs maximally at 347 nm and the ratio of the extinction of vanillin (V) and 4-hydroxybenzaldehyde (4HB) at 347 and 330 nm are both known ($C_{4HB} = \varepsilon_{330\ 4HB}/\varepsilon_{347\ 4HB} = 1.90$ and $C_V = \varepsilon_{330V}/\varepsilon_{347V} = 0.686$). Therefore, the contribution of synephrine as its conversion product 4-hydroxybenzaldehyde can be subtracted from the absorbance at 347 nm to obtain the contribution due to vanillin. This analytical system makes the determination of metanephrines more specific.

Bilirubin is the most frequently measured pigment in serum. Accurate and precise measurement of the relatively high concentrations present in the serum of newborns is important for therapeutic decisions in the prevention of kernicterus. Bilirubin has a high extinction at 460 nm and the only other major absorption in newborn serum is due to contamination by hemoglobin from the sampling process. Therefore, it is obvious that a simple instrument could be designed to measure bilirubin in the presence of hemoglobin by measuring absorption at two wavelengths. One instrument, reported by Jackson[26] and Jackson and Hernandez,[27] uses 450 and 540 nm. A second instrument, manufactured by the American Optical Company, uses 461 and 551 nm since the absorption by hemoglobin is equal at those two wavelengths and simplifies the correction.[28-30] These instruments have achieved wide acceptance in the clinical laboratory and yield accurate results in the presence of hemoglobin.[29] Since the two wavelengths used in these "bilirubinometers"

are 90 nm apart one would predict that a turbid sample would cause overestimation of bilirubin due to greater absorption by turbidity at the lower wavelength. Early discussions of these instruments suggested that this would not be a problem,[28] however, later reports are contradictory.[29,31] The quantitative aspects of this problem are not readily apparent in the literature. Therefore, I present data obtained in our laboratory with the American Optical (AO) Instrument, after addition of an intravenous nutritional lipid source, Intralipid^R, to serum samples (see Table 1). Table 1 indicates that turbidity causes an overestimation, but it is not large.

The measurement of carbon monoxide in blood is most frequently accomplished with a commercially available instrument using spectrophotometric measurements at several wavelengths.[32] Instrumentation Laboratories, Lexington, Massachusetts, has marketed instruments specifically designed to measure carbon monoxide in blood, where it is present as carboxyhemoglobin. The IL182 uses three filters to measure total hemoglobin (Hb), oxyhemoglobin (HbO_2), and carboxyhemoglobin (HbCO).[33] All three pigments share an isobestic point at 548 nm, Hb and HbO_2 absorb equally at 568 nm, and Hb and $HbCO_2$ absorb equally at 578 nm. A newer instrument, the IL282, uses four cathode lamps to measure the three pigments mentioned above plus methemoglobin. The wavelengths used are 535.0, 585.2, 594.5, and 626.6 nm.[34] Dual-wavelength spectrophotometry as described by Chance[12] has also recently been used to measure HbCO.[35]

Another application of measurements at two wavelengths is the simultaneous determination of glucose-6-phosphate dehydrogenase activity and hemoglobin in red cell lysates which allows reporting results in units of enzyme activity per gram of hemoglobin.[36] Measuring both analytes in the same reaction cuvette eliminates errors due to differences in dilution when the two measurements are made in separate cuvettes.

The most frequent use of multiple-wavelength spectrophotometry in the clinical laboratory involves the use of bichromatics, as defined earlier. The general principle involves measurement of absorbance at two wavelengths and the use of the two extinction coefficients to calculate concentration. This

Table 1. Effect of Turbidity on Measurement of Bilirubin with the AO Bilirubinometer

Sample $A_{650\ nm}$	Observed bilirubin (mg/dl)
0.300	10.6
0.822	11.0
0.923	11.5
1.360	12.0
2.335	12.3
2.875	12.2

is a simple use of Beer's law, although it is frequently misunderstood or misrepresented.

Consider a reaction that converts reactant (R) to product (P) which occurs in a reaction mixture with a background color (BC). The absorbance of the reaction mixture will be monitored at two wavelengths (A_1 and A_2):

$$\mathrm{R} \rightarrow \mathrm{P} \tag{1}$$

$$A_1 = \varepsilon_{\mathrm{R}1} b c_{\mathrm{R}} + \varepsilon_{P1} b c_{\mathrm{P}} + BC_1 \tag{2}$$

$$A_2 = \varepsilon_{\mathrm{R}2} b c_{\mathrm{R}} + \varepsilon_{\mathrm{P}2} b c_{\mathrm{P}} + BC_2 \tag{3}$$

$$A_d = A_1 - A_2 \tag{4}$$

where ε_{R} denotes the extinction coefficient of R at each wavelength, ε_{P} the extinction coefficient of P at each wavelength, BC the background color at each wavelength, c_{R} the concentration of R, c_{P} the concentration of P, b the optical path length, and, A_d the absorbance difference. It follows

$$A_d = b c_{\mathrm{R}}(\varepsilon_{\mathrm{R}1} - \varepsilon_{\mathrm{R}2}) + b c_{\mathrm{P}}(\varepsilon_{\mathrm{P}1} - \varepsilon_{\mathrm{P}2}) + (BC_1 - BC_2) \tag{5}$$

This rather complex equation can be shortened by simplifying assumptions. If c_{R} is very small, as is desirable in most analytical reactions, then

$$A_d = b c_{\mathrm{P}}(\varepsilon_{\mathrm{P}1} - \varepsilon_{\mathrm{P}2}) + (BC_1 - BC_2) \tag{6}$$

Equation (6) is frequently simplified by assuming that the background color is equal at both wavelengths; then

$$A_d = b c_{\mathrm{P}}(\varepsilon_{\mathrm{P}1} - \varepsilon_{\mathrm{P}2}) \tag{7}$$

If equation (7) is to be used, care is necessary in the validation of the underlying assumptions, otherwise significant errors can result. The assumption that c_{R} is near zero is frequently true. However, the assumption that $BC_1 = BC_2$ is frequently untrue. Unless the two wavelengths are carefully chosen, the second assumption is often negated by even the most commonly encountered spectral contaminants in the clinical laboratory, i.e., hemolysis, icterus, and lipemia. Therefore, the wary analyst must be vigilant to avoid interferences.

5. Epilogue

This chapter introduces the subject of multiple-wavelength spectrophotometry as it is applied in the clinical laboratory. Some specific commercial

applications have been mentioned. Obviously, many other commercial applications were not mentioned. The selection was made only to illustrate general concepts and not intended to convey any value judgment regarding instrumentation. Discussions of rapid scanning devices were purposely omitted and are reviewed elsewhere.[37,38] The three following chapters discuss specific commercial applications. Certainly other instruments could have been included. The three chosen rely most substantially on multiple-wavelength measurements and illustrate the advantages and disadvantages of this type of spectrophotometry, i.e., enhancement of sensitivity, correction for interferences, and analysis of multiple components.

References

1. T. J. Porro, Double-wavelength spectroscopy, *Anal. Chem.*, **44**, 93A–103A (1972).
2. K. L. Ratzlaff and D. F. Natusch, Theoretical assessment of precision in dual wavelength spectrophotometric measurement, *Anal. Chem.*, **49**, 2170–2176 (1977).
3. D. A. Skoog and D. M. West, *Fundamentals of Analytical Chemistry*, p. 663, Holt, Rinehart, Winston, New York (1963).
4. D. B. Siano and D. E. Metzler, Band shapes of the electronic spectra of complex molecules, *J. Chem. Phys.*, **51**, 1856–1861 (1969).
5. D. E. Metzler, C. Harris, I. Yang, D. Siano, and J. A. Thomson, Band-shape analysis and display of fine structure in protein spectra: A new approach to perturbation spectroscopy, *Biochem. Biophys. Res. Commun.*, **46**, 1588–1597 (1972).
6. D. E. Metzler, C. M. Harris, R. J. Johnson, D. B. Siano, and J. A. Thomson, Spectra of 3-hydroxypyridines. Band-shape analysis and evaluation of tautomeric equilibria, *Biochemistry*, **12**, 5377–5392 (1973).
7. C. M. Harris, R. J. Johnson, and D. E. Metzler, Band-shape analysis and resolution of electronic spectra of pyridoxal phosphate and other 3-hydroxypyridine-4-aldehydes, *Biochim. Biophys. Acta*, **421**, 181–194 (1976).
8. M. L. Fonda and R. J. Johnson, Computer analysis of spectra of enzyme-substrate and enzyme-inhibitor complexes involving aspartate aminotransferase, *J. Biol. Chem.*, **245**, 2709–2716 (1970).
9. W. M. Allen, A simple method for analyzing complicated absorption curves, of use in the colorimetric determination of urinary steroids, *J. Clin. Endocrinol.*, **10**, 71–83 (1950).
10. S. B. Jensen and R. W. A. Oliver, A simplified general proof of the Allen correction equation and some comments concerning its applicability to the colorimetric analysis of oestriol, *Clin. Chim. Acta*, **44**, 443–448 (1973).
11. E. Allen and W. Rieman III, Determining only one compound in a mixture, *Anal. Chem.*, **25**, 1325–1331 (1953).
12. B. Chance, Rapid and sensitive spectrophotometry. III. A double beam apparatus, *Rev. Sci. Instrum.*, **22**, 634–638 (1951).
13. B. Chance, Spectrophotometry of intracellular respiratory pigments, *Science*, **120**, 767–775 (1954).
14. S. Shibata, M. Furukawa, and K. Goto, Dual-wavelength spectrophotometry, *Anal. Chim. Acta*, **46**, 271–279 (1969).
15. R. L. Sellers, G. W. Lowy, and R. W. Kane, A versatile UV-VIS spectrophotometer, *Am. Lab. (March)*, 61–68 (1973).

16. S. M. Gerchakov, Dual wavelength spectrophotometry. Determination of 1, 2, 4-benzene-tricarboxylic acid and benzenepentacarboxylic acid, *Spectros. Lett.*, **4**, 403–409 (1971).
17. B. Chance and N. Graham, A rapid scanning dual wavelength spectrophotometer, *Rev. Sci. Instrum.*, **42**, 941–945 (1971).
18. R. Szentrimay and T. Kuwana, Double wavelength spectrophotometry with a rapid scanning instrument, *Anal. Chem.*, **49**, 1348–1352 (1977).
19. J. C. Cowles, Theory of dual-wavelength spectrophotometry for turbid samples, *J. Opt. Soc. Am.*, **55**, 690–693 (1965).
20. R. Rikmenspoel, The sensitivity and accuracy of dual-wavelength spectrophotometers, *Appl. Opt.*, **3**, 351–355, (1964).
21. R. W. Hendler, Limitations on the use of and interpretation of data from the Aminco–Chance dual-wavelength split-beam recording spectrophotometer and related instruments, *Anal. Biochem.*, **94**, 450–464 (1979).
22. A. W. Liley, Liquor amnii analysis in the management of the pregnancy complicated by rhesus sensitization. *Am. J. Obstet. Gynecol.*, **82**, 1359–1370 (1961).
23. A. W. Liley, Errors in the assessment of hemolytic disease from amniotic fluid, *Am. J. Obstet. Gynecol.*, **86**, 485–494 (1963).
24. R. W. Burnett, Instrumental and procedural sources of error in determination of bile pigments in amniotic fluid, *Clin. Chem.*, **18**, 150–154 (1972).
25. J. J. Pisano, *Assay of catecholamine metabolites based on vanillin formation*, in: *The Thyroid and Biogenic Amines* (J. E. Rall and I. J. Kopin, eds.), ch. 7, pp. 474–488, North-Holland, Amsterdam (1972).
26. S. H. Jackson, A direct-reading bilirubinometer incorporating hemolysis and turbidity correction, *Clin. Chem.*, **11**, 1051–1057 (1965).
27. S. H. Jackson and A. H. Hernandez, A new "bilirubinometer" and its use in estimating total and conjugated bilirubin in serum, *Clin. Chem.*, **16**, 462–465 (1970).
28. A. H. Levkoff, M. C. Westphal, and J. F. Finklea, Evaluation of a direct reading spectrophotometer for neonatal bilirubinometry, *Am. J. Clin. Pathol.*, **54**, 562–565 (1970).
29. M. Michaëlsson, Evaluation of a method for determination of bilirubin in serum using direct spectrophotometry, *Scand. J. Clin. Lab. Invest.*, **30**, 387–390 (1972).
30. AO Bilirubinometer Model 10200 Reference Manual, Scientific Instrument Division, American Optical Corporation, Buffalo, New York (1971).
31. T. A. Blumenfeld, C. F. Steinbrink, H. S. Cheskin, J. D. George, and T. P. Vogl, Manual micromethods for bilirubin determination in sera of adults and children and investigation of reasons for observed differences, *Am. J. Clin. Pathol.*, **69**, 388–397 (1978).
32. N. W. Tietz and E. A. Fiereck, The spectrophotometric measurement of carboxyhemoglobin, *Ann. Clin. Lab. Sci.*, **3**, 36–42 (1973).
33. Instructions IL182 Co-Oximeter, Instrumentation Laboratory, Inc., Lexington, Massachusetts (1968).
34. Instructions IL282 Co-Oximeter, Instrumentation Laboratory, Inc., Lexington, Massachusetts (1980).
35. A. Ramieri, Jr., P. Jatlow, and D. Seligson, New method for rapid determination of carboxyhemoglobin by use of double-wavelength spectrophotometry, *Clin. Chem.*, **20**, 278–281 (1974).
36. E. W. Catalano, G. F. Johnson, and H. M. Soloman, Measurement of erythrocyte glucose-6-phosphate dehydrogenase activity with a centrifugal analyzer, *Clin. Chem.*, **21**, 134–138 (1975).
37. T. E. Cook, R. E. Santini, and H. L. Pardue, Design and evaluation of a vidicon based derivative spectrophotometer, *Anal. Chem.*, **49**, 871–877 (1977).
38. T. C. O'Haver, Potential clinical applications of derivative and wavelength-modulation spectrometry, *Clin. Chem.*, **25**, 1548–1553 (1979).

3

Bichromatic Analysis: The Design and Function of the ABA-100

David L. Witte and Bruce P. Neri

1. Introduction

The Abbott bichromatic analyzers are the commercial applications of the design concepts of Max Liston, Liston Scientific, Newport Beach, California. Liston conceived the ABA-100 as an ultramicro, single reagent, single channel, simultaneous bichromatic kinetic analyzer in the late 1960's. This chapter will describe the unique analytical capabilities of Liston's design and we will, therefore, emphasize the ABA-100 in our discussions. For completeness the reader should realize that Abbott Diagnostics has refined the original Liston design and subsequently introduced three other analyzers which complement the capabilities of the ABA-100. The first of these analyzers was the ABA-50, which contained the same optics and logic as the ABA-100, but was semiautomated and is no longer being manufactured. Major modifications introduced in the ABBOTT-VP included an integral syringe for a second reagent, a diluter capable of detecting liquid levels, logic to calculate results using multiple standards, additional error detection capabilities, and choices of reaction times to allow faster completion of analyses. The newest instrument, the ABA-200, has added flexibility in dilution ratios, times of reagent addition, and calculational capabilities. All these analyzers share many design features and are adaptable to perform a wide variety of spectrophotometric measurements.

The major objective of this chapter is to discuss Abbott's unique design characteristics for ultramicro chemical analysis and simultaneous bichromatic

David L. Witte • Department of Pathology, University of Iowa, Iowa City, Iowa 52220.
Bruce P. Neri • Abbott Diagnostics, Dallas, Texas.

spectrophotometry. We will also discuss general instrumental performance, the approach to automation of a new method with the ABA-100, validation procedures to ensure quality performance, and selected examples of applications. For more detailed reviews of performance characteristics for specific analyses the Reference section lists several sources.[1-5]

2. Design Principles

The Abbott ABA-100 has two modules. The smaller functions as a chemistry processing module and performs the sample and reagent dispense, reaction incubation, and sequential spectrophotometric measurements in a 32 position cuvette. The larger module is a programmer and readout device which controls the functions of the processing module (temperature, time, calibration) as well as calculates and prints results.

The design of the ABA-100 embodies several interlocking concepts. Ultramicro analysis with sample volumes of 2.5–25 μl and reagent volumes of 250–500 μl reduces reagent costs and minimizes the sample size. Accurate and precise performance at these low-sample volumes and high-dilution ratios requires meticulous attention to detail in design and operation. The dimensions and surface properties of the sample probe must be carefully controlled to minimize surface adsorption to prevent sample carry over from cuvette to cuvette. Probe bore diameter is designed to ensure adequate fluid velocity for mixing. The position of the probe in both sample and reaction mixture must be carefully monitored by the operator to minimize the wetted surface. The speed of probe movements must be controlled to minimize unwanted ejection of liquid due to inertia when the probe is stopped. Finally, in working with small sample and reaction mixture volumes the ratio of surface area to volume and the presence of air currents must be considered to reduce evaporation.[6-7]

In the late 1960's there was increased concern for interference in enzyme analysis caused by competing reactions. The interference of pyruvate in the analysis of alanine amino transferase (ALT) provides a specific example. The reaction scheme is shown below:

$$\text{alanine} + \text{alphaketoglutarate} \xrightarrow{\text{ALT}} \text{pyruvate} + \text{glutamate}$$

$$\text{pyruvate} + \text{NADH} + \text{H}^+ \xrightarrow{\text{LDH}} \text{lactate} + \text{NAD}^+$$

Incorrectly stored samples may contain considerable amounts of pyruvate which will react in the ALT reaction system and erroneously elevate the apparent ALT value for that specimen. However, since the endogenous pyruvate is present in finite amounts it will be consumed early so that late in the reaction course the only source of pyruvate is the ALT reaction. The ABA

combines a high dilution of sample (1:51 or 1:101) and long preincubation times (5 min) to minimize problems due to endogenous substrates such as pyruvate. It is important to remember that high dilutions do not alter the effects of interfering enzymes which act on the substrates present in the reagent.

Since high dilutions are used to eliminate the effects of endogenous substrates, the reactions to be monitored necessarily occur at a slow rate and, therefore, generate small changes in absorbance. To make this design concept operationally acceptable a spectrophotometric system capable of excellent stability and high resolution even at absorbances above 1.0 was needed. Liston designed the bichromatic photometric system of the ABA-100 to satisfy that need. This system provided excellent reproducibility and adequate sensitivity to small changes in absorbance, independent of the absolute absorbance. Use of two wavelengths minimizes optical errors caused by cuvette imperfections and cell to cell differences as well as Rayleigh scatter due to particulates in the reagents or Brownian motion of large lipids in the reaction mixture. The optical corrections are valid for materials which absorb equally at the two wavelengths selected for bichromatic measurement, an assumption which is more likely to be true if the two wavelengths are close together. The original ABA-100 was intended only as a kinetic enzyme analyzer and designed with two wavelength pairs: 340–380 and 450–415 for NADH and paranitrophenol (PNP), respectively.

The fundamentals of the bichromatic optics are shown in Figure 1. The heart of the system is the spinning filter wheel placed in the analytical light

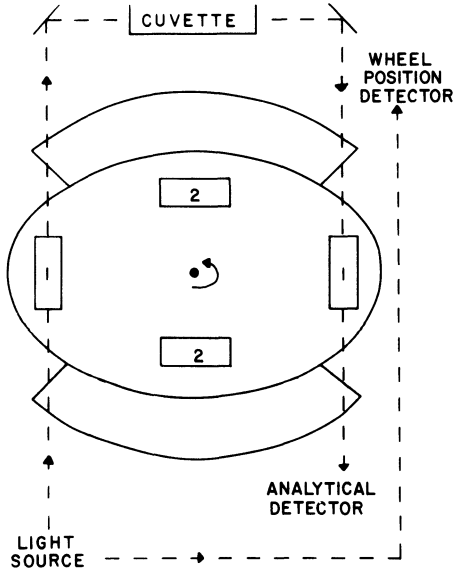

Figure 1. ABA-100 optical diagram.

beam. As shown diagrammatically, the filter wheel contains two pairs of identical filters with like filters located 180° apart. Thus, as the filter spins, the cuvette and detector are alternately traversed by the two wavelengths, two times per revolution. The outer circumference of the filter wheel has two segments with different diameters. When the filters corresponding to wavelength 1 are in the analytical beam, light will reach the wheel position optical detector, when the wheel rotates 90° filter 2 is in the analytical light beam and the wider circumference blocks the light path to the wheel position detector. Conceptually then, the analytical beam is made up of a repeating step function which corresponds to wavelength 1, the nontransmitting portion of the wheel, and wavelength 2. Simultaneously, the wheel position detector receives a repeating step function due to the chopping by the larger wheel circumference. Therefore, the instrument is able to monitor which signal is related to which wavelength.

As the reader continues it will become apparent that understanding of the ABA-100 bichromatic optics depends on careful comprehension of several timing functions. The first of these is the frequency of the step functions recorded by the optical detectors. In the ABA-100 and ABA-50 the filter wheel spins at 1800 rpm or one revolution takes roughly 33 msec. Since the bichromatic measurements are made $\frac{1}{4}$ of a revolution apart, they only differ by about 8 msec in time. The newer instruments, the VP and ABA-200, spin the filter at 3600 rpm.

Before considering the mechanism by which bichromatics increases resolution and precision, let us consider why two filter pairs were used instead of one. Passing the analytical beam through two filters of the same wavelength, one before and one after the cuvette, squares the attenuation of unwanted wavelengths and reduces the effective bandpass by $1/(2)^{1/2}$ to approximately 8 nm. Using two filters allows the ABA-100 to achieve adequate isolation of ultraviolet energy from the preponderance of visible energy in an incandescent source. The use of two filters also reduces instrument costs since the effects of tiny holes and fluorescence in inexpensive filters are also attenuated. Finally, the two filter arrangement makes it possible to make precision optical measurements in an open cuvette since room light is blocked by the second filter. The open cuvettes can be monitored visually and reagent can be added during the reaction course.

The precision of the ABA-100 optical system is primarily a result of a unique circuit for analog-to-digital (A/D) conversion. The electrical engineering of this circuitry is beyond the scope of this contribution and these authors. However, a clear concept of the bichromatic A/D conversion system used on the ABA-100 is essential to understanding the instrument and will be presented in a conceptually useful form although not electronically accurate in detail. These concepts require another understanding of time segments used during the measurement of absorbance difference (A_d) by the ABA-100, and are best explained through the use of an analogy.

The ABA-100 monitors 32 reaction cuvettes every 5 min. Therefore, each cuvette spends about 9350 msec in the analytical light path. During about the first 9000 msec of this period the instrument is charging two capacitance circuits, one for each wavelength. However, these two capacitance circuits do not completely hold their charge, therefore, the charging done at the end of the time period is more significant than the charging at the beginning of the 9000 msec period. A useful analogy is a bath tub with a leaky drain plug which is being filled with water. The water which enters early in the filling period has a greater chance of leaking out.

In the last few milliseconds, after the capacitors (one for each wavelength) are charged, a reading is taken. This is accomplished by charging a separate resistance capacitance (RC) circuit with exquisitely reproducible decay characteristics. The properties of this RC circuit are represented diagrammatically on the right half of Figure 2 and the left half represents an absorption spectrum. When the charge accumulated on the capacitance for wavelength 2 corresponds to the charge on the RC circuit a reading on a sensitive digital clock is made. A few milliseconds later, when the RC circuit charge equals the charge on the capacitor for wavelength 1 a second time reading is taken. Due to the logarithmic relation of percent transmittance versus absorbance and the RC circuit voltage versus time, these pairs of voltage and time readings convert the analog transmittance information to digital absorbance difference information.

The precision of the absorbance difference measurement results from the precision of the time measurement using a digital clock. Signal averaging is

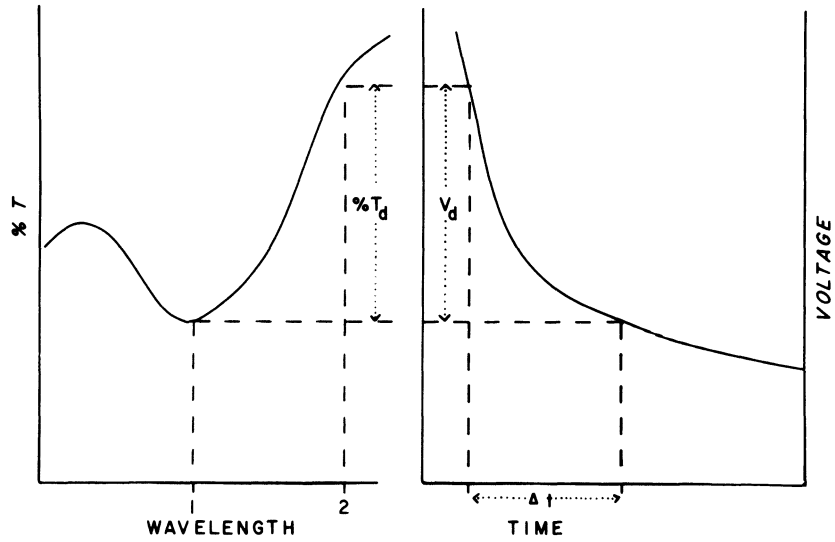

Figure 2. ABA-100 A/D conversion.

accomplished by the "leaky" capacitance circuits. The clock functions at 400,000 cycles per second. The decay time of the RC circuit corresponding to an absorbance difference of 2.0 is about 25 msec. These 25 msec are divided into 10,000 cycles by the clock. This generates a scale with a large number of divisions facilitating precise and sensitive A_d measurements. Table 1 illustrates the number of scale divisions used by some representative A/D converters.[8]

In the RC circuit the capacitance is constant, but the resistance can be varied by adjustment of the calibration setting. This adjustment effectively varies the rate of decay of the RC circuit. Therefore, this adjustment makes it possible to utilize a large number of digital clock cycles for low as well as high A_d measurements. This also allows direct conversion of results to concentration or enzyme activity units.

The more recent Abbott instruments, the VP and ABA-200, measure A_d similarly. However, the VP and ABA-200 do not average the signal with a "leaky" capacitance circuit. Instead, the newer instruments average 330 individual data points gathered over a period of 2.75 sec.

The bichromatics reduce the cost of sensitive photometry, but conceptually complicate the calibration of determinations such as enzyme rates, which derive results from the extinction coefficient of the product formed at one wavelength. Since any ABA measurement is necessarily made at two wavelengths, A_d, the calculation of concentration must involve the extinction coefficient of the product at both wavelengths or the extinction difference ε_d. These ε_d values are not readily available in the literature. In addition, since bichromatics has allowed reduced cost through the use of less expensive filters, the interinstrument variability of filter transmission and bandpass make each filter pair unique. Therefore, each filter pair must be standardized, i.e., the manufacturer derives a "filter factor" which is analogous to ε_d. The most frequently used analyte is NADH which has a molar extinction coefficient of 6.22×10^3 at 340 nm. Since the extinction at 380 nm must be subtracted from that at 340 nm, the usual filter factor for an ABA-100 340–380 filter pair is $4.5—5.0 \times 10^3$. Three common analytes in the clinical laboratory require the use of a filter factor. These are paranitroaniline (PNA), paranitrophenol (PNP), and NADH. The first two are stable and inexpensive and their filter factors are determined directly for each 450–415 filter pair. Since NADH is

Table 1. Scale Divisions of A/D Converters

A/D converter	Scale divisions
8 bit	256
9 bit	512
12 bit (e.g., ENI GEMSAEC)	4,096
ABA-100	10,000
15 bit (e.g., DuPont aca III)	32,768

more expensive and less stable its filter factor is determined using the conversion of NAD→NADH by primary standard glucose in the following reaction sequence:

$$\text{glucose} + \text{ATP} \xrightarrow{\text{hexokinase}} \text{glucose-6-phosphate} + \text{ADP}$$

$$\text{glucose-6-phosphate} + \text{NAD}^+ + \text{H}_2\text{O} \xrightarrow{\text{G6PDH}}$$

$$6\ \text{phosphogluconate} + \text{NADH} + \text{H}^+$$

Obviously, any empirical parameter has an uncertainty. The field specifications for acceptable error in filter factor are 0.1 for a NADH filter factor of about 5.0. Therefore, this calibration process has a field specification of ±2%.

All spectrophotometric measurements involve the use of appropriate blanks. In clinical chemistry these are usually reagent blanks and rarely individual sample blanks. The ABA-100 designates the 01 reaction cuvette as the reagent blank, and the absorbance change observed in the 01 cell is subtracted from the change in all other cells. The only limitation in this system is that the 01 blank must be less than 099 for kinetic methods, i.e., only reagent blanks of a certain size can be accommodated. The ABA-100 cannot perform true sample blanks without a separate blank analysis using an appropriate blank reagent.

The validation of analytical results in the clinical laboratory includes the use of known quality control specimens, and this process for the ABA-100 is similar to any other discrete chemical analyzer. In addition to the laboratory quality control program, modern instrumentation provides concrete signals to alert the operator to specific process problems. The ABA-100 provides a visual signal to the operator when the light energy reaching the analytical photodetector is below acceptable limits indicating the results for that cuvette are unreliable. Like most newer enzyme rate analyzers the ABA-100 signals the operator when reactant depletion is likely in a given reaction cuvette. This system is best described using a specific example, the measurement of alanine amino transferase (ALT) as previously described. Early in the reaction course the concentration of NADH is high, therefore, absorbance at 340 nm is high as is $A_d = A_{340} - A_{380}$. As the ALT reaction proceeds NADH is consumed and A_d decreases as shown in Figure 3, curve A. At later times, for samples with high ALT activity, the NADH is completely consumed and the reaction rate decreases (Figure 3, curve A at 20 min). Obviously, the depletion of NADH in a defined reagent system can be detected by the absorbance of the reaction mixture. The operator programs the ABA-100 with a zero offset as shown by the dotted horizontal line in Figure 3. When the A_d of the reaction mixture falls below this zero offset the instrument detects a negative number and adjusts the printer ribbon so that the result for that cuvette position is printed in red. Therefore, the operator receives a permanent record of those positions which are suspect for reactant depletion.

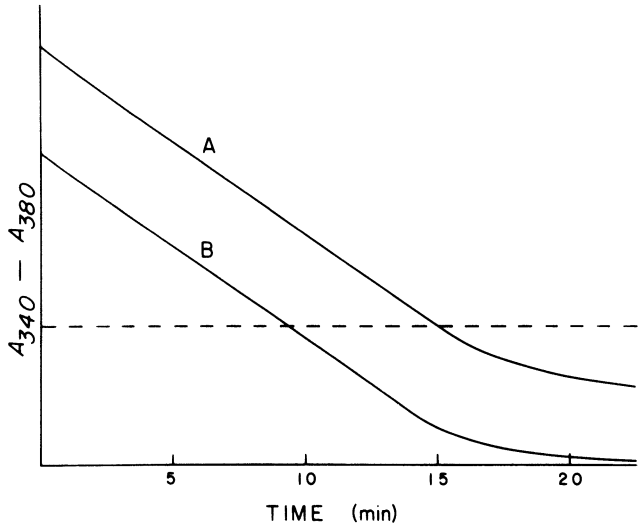

Figure 3. ABA-100 reactant depletion detection.

The system described for ALT reactant depletion is used for all the enzyme reaction rates measured by the ABA-100. However, minor alterations to filter pairs are needed to detect reactant depletion for creatine kinase (CK), lactate dehydrogenase (LD), alkaline phosphatase (ALP), and gamma glutamyltranspeptidase (GGTP). The absorbance increases during the reaction course for these four enzymes. The products are NADH, NADH, PNP, and PNA, respectively. To use the same system described for ALT, reverse filters are introduced: 380–340 for CK and LD and 450–415 for ALP and GGTP. For a reaction producing NADH the $A_d = A_{380} - A_{340}$ will increase in the negative direction, toward the zero offset. Therefore, the signal will look similar to that described for ALT and the same circuitry can be used. This requires that neutral density absorbance filters be placed in the filter pairs by the manufacturer to allow for proper offset of the zero. The same logic applies for ALP and GGTP whose products absorb maximally at about 405 nm. The ABA-100 filter pairs are adjusted to give the zero A_d values shown in Table 2.

Table 2. Zero A_d of Filter Pairs

Filter pair	Zero A_d
340–380	0.0
380–340	+1.8
380–340L	+0.5
450–415	+1.8

There is a potential problem with the reactant depletion (red print) limit on the ABA-100. The instrument assumes all the reaction mixtures begin at the same A_d, i.e., the contribution of the sample to the A_d is negligible compared to that of the reagent. This assumption is valid for the vast majority of specimens. However, again using the ALT example, let us consider a specific set of conditions which invalidate the above assumptions. Suppose a serum sample is obtained from a patient with acute hepatitis. This sample may have a very high ALT and quite likely a very high bilirubin. The ALT reaction is monitored by $A_d = A_{340} - A_{380}$. Bilirubin absorbs more at 380 than 340 nm, resulting in an initial A_d lower than most samples (Figure 3, curve B). As the reaction proceeds, the reactant depletion limit is reached before the NADH is consumed and before the reaction rate decreases. Therefore, the presence of bilirubin has caused the ABA-100 to erroneously signal reactant depletion. This example is presented to point out that the operator must be well informed of both the chemical and optical operating principles if the instrument is to be used intelligently. Obviously in the example presented no harm will result since the warning was given too early. However, one must be aware that the possibility also exists of the warning being given too late. Although we have never observed it, theoretically the sample described above could also have an elevated alkaline phosphatase and the zero time $A_d = A_{450} - A_{415}$ observed in that analysis would be higher than that for most specimens due to the bilirubin. This could shift the curve in the other direction in Figure 3 and cause a false black print. For added safety the manufacturer has suggested setting the reactant depletion limit at a point where 20% of the reactant remains.

The newer Abbott instruments (VP and ABA-200) have incorporated improved process monitoring capabilities, and those changes conceptually related to bichromatics will be discussed. In the ABA-100 the 01 reaction cuvette is the reagent blank which is subtracted from all other positions. In the newer instruments this is also true, but if the 01 cell reaction rate is outside the limits determined for each chemical reaction system the instrument will print a reagent degradation signal. In the ABA-100 the first reading of an enzyme reaction usually occurs after a 5 min preincubation period. In the newer instruments the first reading occurs within seconds after the reagent and sample are mixed. This initial reading is used to determine a reactant depletion limit for each cuvette position individually. That is, the same absorbance change from its initial reading is allowed for each cuvette. This circumvents the problem of false reactant depletion signals as described above for the ABA-100 with an icteric ALT specimen. The newer instruments are also capable of recognizing reaction direction, therefore, reverse filters are no longer necessary.

The above discussion has been qualitative and is intended to present the generalities of the Abbott bichromatic analyzer design. The reader with a

Table 3. ABA-100 Specifications[9]

Parameter	Design specification
Path length in multicuvette	1.0 ± 0.006 cm
Visible cell to cell variation at $A_d = 0.8$	$0.006A_d$
UV cell to cell variation	$0.004A_d$
Drift (15 min warm-up)	Less than $0.0004A_d$/hr
Linearity	$0.0–1.0A_d \pm 0.002$
	$1.0–1.2A_d \pm 0.005$
	$1.2–1.4A_d \pm 0.005$
	$1.4–1.6A_d \pm 0.008$
	$1.6–2.0A_d \pm 0.010$
	$2.0–2.5A_d \pm 0.005$
Noise (340–380 at $A_d = 1.8$)	Total range less than $0.004A_d$
Timing of reaction	$\pm 1\%$
Temperature	± 0.1°C
Precision of dilution ratio	$\pm 2\%$
Accuracy of dilution ratio	$\pm 2\%$
Carry over	Less than 0.05%

more quantitative interest is referred to Table 3 for pertinent instrument specifications,[9] remember, these are lower limits and the actual performance may be superior.

3. Performance of Individual Instrument Functions

3.1. Photometric Uncertainty and Linearity

One of the major contributions of the ABA-100 is bichromatic measurement which allows high-resolution absorbance measurements with low-cost components. Mercer and Varat[10] state that the ABA-100 was capable of measuring A_d with sensitivities of $\pm 0.0001A_d$.

Data from one of the authors laboratories (DLW) are shown in Figure 4. These data were collected with various concentrations of NADH in buffered aspartate aminotransferase reagent. The closed symbols show the mean absorbance for thirty-one measurements of A_d, the open symbols show the coefficient of variation derived from those thirty-one values. Figure 4 and Table 4 demonstrate that the ABA-100 is linear to at least $2.66A_d$ and that the coefficients of variation are in the range of 0.1–0.3%.

3.2. Control of Reaction Temperature

In the determination of enzyme activity the temperature in the reaction cuvette must be precisely and accurately controlled. Monitoring reaction

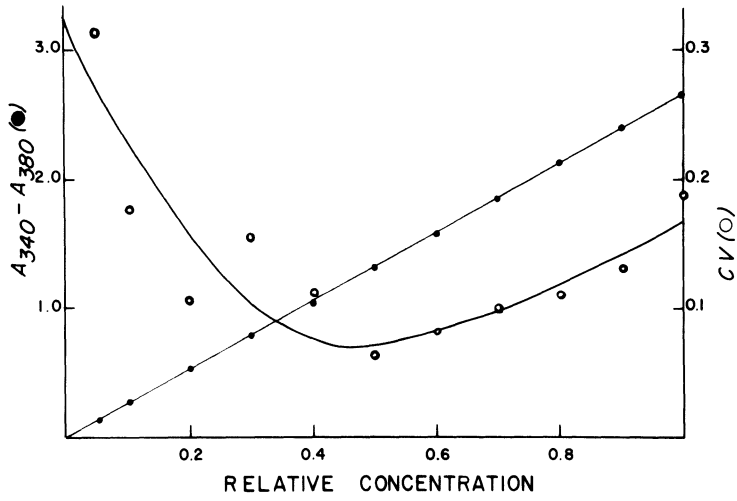

Figure 4. ABA-100 absorbance linearity and reproducibility with a 340–380 filter pair.

temperature electronically is difficult and expensive. A practical alternative is the use of a temperature sensitive spectrophotometric solution[11,12] containing cresol red in buffers with a significant temperature–pH dependency. Using these spectrophotometric monitors, temperature variability over 11 days was shown to be 0.15–0.20°C for three ABA-100's.[12] These solutions have also been used to determine the time necessary to achieve the desired temperature in the reaction cuvette. This should closely follow the time–temperature course of a reagent system. Room temperature reagents will take 4–6 min to reach a temperature of 5–7°C above ambient. This is important to note since refrigerated reagents may not reach 37° fast enough to allow efficient and accurate measurements.

Table 4. Linearity and Precision of ABA-100 with Buffered NADH Solutions

Relative concentration	Mean $n = 31$	Standard deviation (SD)
100	2.6609	0.0050
90	2.4035	0.0032
80	2.1292	0.0024
70	1.8520	0.0018
60	1.5826	0.0013
50	1.3216	0.0008
40	1.0479	0.0012
30	0.7907	0.0012
20	0.5265	0.0006
10	0.2734	0.0005
5	0.1352	0.0004

3.3. Sample Evaporation

We have previously alluded to the sample evaporation problems in ultramicro analysis. Loeb *et al.*[6] have shown that the evaporation rate of a 50 μl sample in an ABA-100 sample cup is 8% per hour. However, this rate is cut to 0.5% per hour if the sample is covered with a thin film of dimethylpolysiloxane (Sera-Seal). Liston points out that Sera-Seal also helps reduce adsorption of solutions to the probe surfaces, but cautions that water is soluble in Sera-Seal and will diffuse through it; therefore, a large volume of Sera-Seal could effectively concentrate samples by taking up water.

3.4. Volume Measurement

The importance of accurate and precise measurements of sample and reagent volumes cannot be over emphasized. The modern clinical laboratory uses aqueous primary standard solutions whenever possible. However, these aqueous solutions are less viscous than the protein containing serum specimens. Vader and Vink[13] have shown that some volume measuring devices are viscosity dependent, and comparing serum samples with high viscosity to low viscosity aqueous standards can cause a significant problem. To test the effect of viscosity on the ABA-100 diluter system we have prepared solutions of PNP in aminomethylpropanol (AMP) buffer with varying amounts of added glycerol to alter the viscosity. The results in Table 5 indicate the ABA-100 system is not significantly dependent on viscosity. Therefore, the use of low viscosity aqueous standards is not contraindicated.

In the modern laboratory small sample requirements are a desirable property in instrumentation. A more important parameter is the minimum sample needed in the sample cup for accurate aspiration. The ABA-100 will accurately and precisely aspirate 5 μl of sample from a total volume of 20 μl and dispense this sample with 250 μl of reagent. Table 6 shows the performance of the ABA-100 for this 1:51 dilution for ten replicate dilutions of PNP in AMP buffer using various sample volumes.

Table 5. Effect of Viscosity on Dilution Ratio (1:51)

% Glycerol	Mean A_d	SD
0	0.194	0.0024
25	0.196	0.0012
50	0.191	0.0042

Table 6. Dilution Ratio Precision

Volume in sample cup (μl)	Mean A_d	SD	Deviation from nominal dilution ratio (%)
50	0.925	0.0056	+1.3
25	0.931	0.0043	+1.7
20	0.927	0.0029	+1.3

3.5. Performance Characteristics Unique to Bichromatic Measurements

The purpose of the bichromatic measurements in the ABA-100 has been misrepresented by many. It should be clear now, that bichromatics was introduced to provide precise spectrophotometric measurements at low cost. Bichromatics as used on the ABA-100 was never intended to substitute for a specimen blank, even though this idea has been erroneously published in several places. The unusual problems with bichromatic measurements are most prevalent in chemical methods which involve a single spectral measurement of a reaction mixture (i.e., an endpoint or equilibrium method) where effects at the second wavelength alter the results. Kinetic methods involve multiple measurements of a reaction mixture over time so that the effects at the second wavelength subtract out and have no effect.

Careful users of the ABA-100 quickly realized that the second wavelength was not a serum blank and, in fact, was more likely to cause problems than alleviate them in endpoint methods. It was not until 5 years after the introduction of the ABA-100, that discussions of bichromatics and its effects on chemical analysis appeared in the clinical chemistry literature.[14,15] The effects of the most common interferences: lipemia, hemolysis, and icterus, were not fully appreciated until even later.

The evaluation of analytical interferences is not an easy task. The simple addition of an interferent may not exactly replicate the effect of that interferent in a real biological specimen. The pure interferent no doubt will behave differently than the natural one which is accompanied by its breakdown products as well as other less well characterized materials. Nevertheless, the addition of bilirubin, hemoglobin, and lipids to samples provides the beginnings of an understanding and each will be discussed individually.

The effects of lipemia are probably least understood. Spectrally the problem is usually considered as a simple turbidity problem and the chemical and micellar aspects of samples with high lipids are frequently ignored. Fonda and Johnson[16] have shown that turbidity is a correctable spectral interference and that the absorbance due to turbidity increases linearly with the inverse of the wavelength. Therefore, with the ABA-100 filter pairs, turbidity will cause an increase in A_d for 340–380, 500–600, and 550–650, and a

decrease for 380–340 and 450–415. Of course the effect on the final analytical result will depend on whether absorbance increases or decreases with concentration of analyte.

Turbidity is also a frequent problem in lyophilized control sera. Again the use of bichromatic measurements with the ABA or Du Pont aca will cause predictable errors in endpoint measurements. Steele *et al.*[17] have reported that turbidity in control sera can cause an overestimation of serum glucose of 60 mg/l in some control sera. This is not a major problem, but the clinical chemist must be aware of the interaction of methods and samples such as this.

Hemolysis is easier to study since hemoglobin is easily added to samples. However, this is not the same as either *in vitro* or *in vivo* hemolysis. Even the *in vitro* addition of hemolysate may not chemically and spectrally duplicate the hemolyzed specimen. With this caveat, predictable interferences can be reproduced by adding hemoglobin. Gochman *et al.* have shown that the Du Pont aca bichromatic glucose method yields falsely low results in the presence of very high hemoglobin; however, the ABA method was unaffected.[18] Gochman *et al.* explained this apparent discrepancy by careful examination of the spectra. The ABA uses 340–380 nm and hemoglobin absorbance is virtually identical at those two wavelengths and, therefore, cancels. The aca uses 340–383 nm and the hemoglobin absorbance at 383 nm is slightly higher than 340, therefore, a falsely low result is obtained. The effects of hemolysis are even more complex if one considers other secondary pigments such as methemalbumin which will cause profound problems on the ABA-100 450–415 filter pair and relatively little problem on most of the others.

The careful evaluation of the effect of bilirubin on a chemical analysis is also difficult. Bilirubin itself has a strong and broad absorption band at 460 nm and is easily oxidized to other pigments with different absorption bands. Therefore, a complex spectral mixture may be formed. It has been shown[19] that bilirubin can be oxidized to biliverdin in the presence of cholesterol and cholesterol oxidase, and the extent of oxidation of bilirubin is dependent on the contents of the reaction mixture. Thus, a material that interferes spectrally at 460 nm is converted to one that interferes at 650 and 390 nm and the extent of conversion is variable. This illustrates the complexities of understanding the interferences present in equilibrium analysis and the additional care needed if bichromatic methods are used.

Kinetic measurements using the ABA-100 are relatively unaffected by unchanging spectral sample blanks, since subsequent readings are subtracted from each other. The false signal for reactant depletion has already been discussed. The electronics of the ABA-100 exhibit a couple of unusual errors which occur rarely, but are of some importance. First when the absorbance of a reaction mixture becomes very high (i.e., >5) the ABA-100 electronics overload and print a result that is meaningless. Even rarer, if this high A_d

sample is encountered in an optically maladjusted instrument the electronic signal can cause a false black print or can carry over into the next cuvette position. These two problems are rare but worth recording for the sake of completeness.

4. Automation of a Specific Method with the ABA

Automation requires careful attention to the details of the manual method and the ABA adds a second wavelength that must be considered. Frequently, little is known about changes at this second wavelength since it was never important in the monochromatic manual methods.

The spectral properties of the product must be considered and an appropriate wavelength pair selected. Any relevant interference at either wavelength must be evaluated. The A_d of the interferent must be compared to the sensitivity of the standard curve. Obviously if the interferent yielded an $A_d = 0.010$ and the dynamic range of the method only spanned an A_d of 0.0–0.1 the interference may be quite significant. However, if the dynamic range spanned 0.0–1.5 it may be possible to ignore the interferent.

Any side reactions that will result in a change in absorbance at either wavelength must also be evaluated relative to the sensitivity of the desired reaction.

The kinetics of the reaction process must be understood to select acceptable times for spectrophotometric measurements.

Using the ABA, one of the most important questions is "What type of blank is required?" Very few automated devices are able to easily perform individual sample blanks. Therefore, all attempts are made to eliminate this need. The ABA will perform simultaneous reagent blanking, but requires a separate analytical run with a blank reagent to generate sample blanks.

5. Quality Control

The implementation of a method in a clinical laboratory is incomplete unless effective measures are introduced to ensure quality performance as well as cost effective preventative maintenance.

Several functions of the ABA-100 operation can be monitored independently. The volume dispensing system needs to be cleaned regularly and the performance validated with spectrophotometric standard solutions. This is routinely performed by diluting PNP samples with AMP buffer in the reagent vessel and recording results using the 450–415 filter pair. The optics can be checked for stray light and linearity by analyzing glucose standard solutions that yield absorbance results above $2.0A_d$. The position and condition of the probe must be carefully monitored during each run. In ultramicro volume measurements small changes in probe position or surface characteristics can

cause errors. The ABA filter pairs should be visually inspected frequently and the filter factors for NADH, PNP, and PNA checked periodically. The other filters can also be checked with spectrophotometric standard solutions or with less expensive dyes.[20] The noise of the optical and electronic systems should also be checked frequently to prevent unexpected random errors.

6. Special Applications

It is not the objective of this chapter to present specific detailed performance data. However, several interesting applications which utilize the unique features of the ABA-100, such as bichromatics and the addition of reagents during the reaction course, will be discussed briefly.

The use of a special 340–650 filter allows the application of turbidimetric methods such as lipase[21] and immunoglobulins by immunoturbidimetry.[22] The capability of adding more than one reagent using an auxiliary dispenser makes it possible to perform homogeneous enzyme multiplied immunoassays (EMIT^R) using the ABA-100. Many EMIT methods have been reported and two representative examples are given in the Reference section.[23,24] The EMIT drugs of abuse assays have been automated on the ABA-100 using a special white light–UV light filter pair. Finally, we have recently used the multiple reagent addition capability to facilitate the performance of a functional spectrophotometric assay for heparin.[25]

7. Epilogue

We have tried to present a conceptual description of the Abbott bichromatic analyzer with an emphasis on the central design features. We have alluded to specific applications only when they have added to the understanding of the instrument. This chapter is not in the jargon of the clinical laboratory and will hopefully be useful to analytical chemists interested in clinical instrumentation, industrial chemists interested in unique approaches to problems, clinical chemists interested in a more thorough understanding of a very common, but often misrepresented instrument, and, finally, to medical laboratory personnel with a desire for deeper understanding of their daily activities.

Acknowledgments

We would like to acknowledge our wives, Dorothy and Barbara, for their inspiration, encouragement and support, Max Liston for his open discussions

with us, and Linda Brown, Judy Pfohl, and Beverly Pennell for their conscientious experimental work. Finally we thank the late Paul Tramell who initiated our interest and participation in the understanding of bichromatic analysis.

References

1. G. F. Grannis, C. G. Massion, and J. G. Batsakis, The 1978 College of American Pathologists survey of analyses of five serum enzymes by 450 laboratories, *Am. J. Clin. Pathol.*, **72**, 285–298 (1979).
2. H. R. Beckala, J. Agrell, R. W. Forsman, and H. A. Homburger, Evaluation of commercial enzyme reagent kits by use of a semiautomated chemistry analyzer, *Am. J. Clin. Pathol.*, **72**, 151–155 (1979).
3. R. Haeckel, Evaluation of the Abbott bichromatic analyzer 100 (a proposal for an evaluation scheme), *J. Clin. Chem. Clin. Biochem.*, **14**, 227–237 (1976).
4. E. J. Sampson, D. D. Derck, and L. M. Demers, Comparison of results for 13 clinical laboratory determinations with three automated analytical systems, *Clin. Chem.*, **22**, 346–349 (1976).
5. D. L. Witte, D. A. Barrett II, and D. A. Wycoff, Evaluation of an enzymatic procedure for determination of serum cholesterol with the Abbott ABA-100, *Clin. Chem.*, **20**, 1282–1286 (1974).
6. H. G. Loeb, P. R. Tramell, G. Szepessy, G. Browning, and M. Liston, Effect of a sample evaporation retardant on enzyme activity results with the Abbott bichromatic analyzer-100, *Clin. Chem.*, **18**, 698 (1972).
7. C. A. Burtis, J. M. Begovice, and J. S. Watson, Factors influencing evaporation from sample cups, and assessment of their effect on analytical error, *Clin. Chem.*, **21**, 1907–1917 (1975).
8. E. Maclin, A systems analysis of GEMSAEC precision used as a kinetic enzyme analyzer, *Clin. Chem.*, **17**, 707–714 (1971).
9. ABA-100 Design Specifications, Abbott Document S9522, May 2, 1975.
10. D. W. Mercer and M. A. Varat, Detection of cardiac-specific creatine kinase isoenzyme in sera with normal or slightly increased total creatine kinase activity, *Clin. Chem.*, **21**, 1088–1092 (1975).
11. L. Bowie, F. Esters, J. Bolin, and N. Gochman, Development of an aqueous temperature-indicating technique and its application to clinical laboratory instrumentation, *Clin. Chem.*, **22**, 449–455 (1976).
12. L. F. Brown, R. D. Feld, and D. L. Witte, Spectrophotometric temperature monitoring in the ABA-100, *Clin. Chem.*, **23**, 1147 (1977).
13. H. L. Vader and C. L. Vink, The influence of viscosity on dilution methods—Its problems in the determination of serum sodium, *Clin. Chim. Acta*, **65**, 379–388 (1975).
14. J. D. Boyett and M. F. Beeler, Use of the ABA-100 in the end-point procedures, *Clin. Chem.*, **21**, 1542 (1975).
15. J. R. Pearson and T. Matsuura, Bichromatic analyses with the ABA-100—A critical assumption, *Clin. Chem.*, **22**, 559–560 (1976).
16. M. L. Fonda and R. J. Johnson, Computer analysis of spectra of enzyme-substrate and enzyme-inhibitor complexes involving aspartate aminotransferase, *J. Biol. Chem.*, **245**, 2709–2716 (1970).
17. B. W. Steele, D. F. Koehler, T. P. Blaszkowski, and M. Azar, An example of lyophilized protein-based materials not simulating patient sera, *Clin. Chem.*, **21**, 1812–1814 (1975).

18. N. Gochman, W. T. Ryan, R. E. Sterling, and G. M. Widdowson, Interlaboratory comparison of enzymatic methods for serum glucose determination, *Clin. Chem.*, **21**, 356–361 (1975).
19. D. L. Witte, L. F. Brown, and R. D. Feld, Effects of bilirubin on detection of hydrogen peroxide by use of peroxidase, *Clin. Chem.*, **24**, 1778–1782 (1978).
20. C. S. Frings, V. I. Muscat, and N. T. Waldrop, Convenient method for checking detector response of spectrophotometers at three wavelengths, *Clin. Chem.*, **22**, 101–102 (1976).
21. R. D. Feld, D. L. Witte, and D. A. Barrett II, Kinetic determination of serum lipase activity with the Abbott ABA-100, *Clin. Chem.*, **22**, 607–610 (1976).
22. D. L. McCullough, B. J. Pennell, J. A. Goeken, and D. L. Witte, Rapid turbidimetric measurement of human immunoglobulins G, A, and M by automated bichromatic analysis, *Clin. Chem.*, **26**, 1071 (1980).
23. N. Weidner, J. M. McDonald, V. L. Tieber, C. H. Smith, G. Kessler, J. H. Ladenson, and D. N. Dietzler, Assay of theophylline: Comparison of EMIT on the ABA-100 to HPLC, GLC and UV procedures, with detailed evaluation of interferences, *Clin. Chim. Acta*, **97**, 9–17 (1979).
24. A. Castro, D. Seckinger III, A. Cid, P. Buschbaum, and T. Noto, A simple automatic kinetic enzyme immunoassay for digoxin, *Clin. Chim. Acta*, **99**, 289–295 (1979).
25. G. F. Kapke, W. G. Owen, D. L. Witte, and R. D. Feld, Determination of plasma heparin with the ABA-100, *Clin. Chem.*, **26**, 1061 (1980).

Bichromatic Analysis as Performed in the Du Pont Automatic Clinical Analyzer ('aca')

Paul E. Johnson, Paul L. Smock, and Gopal S. Rautela

1. Introduction

The 'aca' system comprises an automatic clinical analyzer ('aca') and a repertoire of analytical methods for performing a variety of discrete chemical analyses of body fluid samples. Introduced in 1968, this was the first system to automate bichromatic clinical analyses. The system employs various differential absorbance techniques, including the bichromatic technique described in this chapter.

When it was introduced, the 'aca' performed eight different tests, with the bichromatic principle used for three. Of the 40 different tests presently performed, 14 employ bichromatic analysis. Specific test capacity of 30 for the first generation instruments was later increased to 62 for the second and third generation units. The latter, 'aca' III, introduced in 1978, will certainly broaden the capability of bichromatic (and other) analyses due to its flexible microprocessor-based design.

2. Analytical Test Pack

Individual tests are processed through the 'aca' in patented analytical test packs (see Figure 1). For a single specific test, the disposable test pack

Paul E. Johnson, Paul L. Smock, and Gopal S. Rautela • E. I. Du Pont de Nemours and Company, Inc., Wilmington, Delaware 19898.

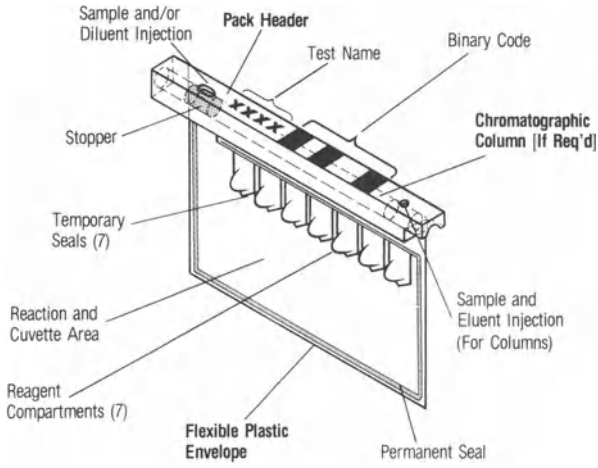

Figure 1. Analytical test pack.

serves the following functions:

1. contains the necessary chemical reagents;
2. accepts the sample and diluent;
3. encloses the chemical reaction;
4. becomes the optical cuvette for photometric analysis.

The test pack has two parts: the header and the pack envelope.

2.1. Header

The rigid header, to which the pack envelope is attached, provides the means for:

1. adding sample and diluent to the pack;
2. housing a chromatographic column, if necessary;
3. identifying the test (pack) type in both human and machine-readable forms for processing;
4. handling/transporting the pack by the instrument.

For noncolumn headers, sample and diluent injection is performed by puncturing the stopper with a hypodermic needle (at the instrument filling station) and pumping the fluid through a passageway into the pack envelope. Columns are contained in the headers for tests in which sample pretreatment is necessary. A variety of fractionation procedures can be used to separate and elute the desired analyte into the pack envelope.

One column procedure which can be used to prepare a sample for bichromatic analysis involves interaction between sample and chemical compounds loosely associated with inert column support materials. The support materials may be glass or inert organic polymer beads with acidic or basic functional groups. For instance, a column utilizing trichloroacetic acid treatment of a sample precipitates and removes proteins from the serum matrix. This prevents a secondary reaction product between an interfering serum component and chromophore precursor, thus, eliminating a spectral interference not compensable by bichromatic analysis.

2.2. Pack Envelope

The flexible plastic envelope is made of two Du Pont Surlyn® ionomer resin (registered trademark of E.I. du Pont de Nemours & Company) film layers specially heat sealed to form seven reagent compartments and the reaction/measurement cuvette chamber. The combined film properties of chemical inertness, heat sealability, strength, minimal fluorescence, and high UV/visible optical transmission optimize system performance. The sealed pack also precludes sample and diluent evaporation.

The test pack's seven reagent compartments contain either liquid or tableted reagents or a combination of both, depending on the particular test. Some methods require liquid surfactants, such as BRIJ-35 or TWEEN 20, to minimize interferences caused by bubbles and film surface attractiveness. This helps to clear the solution and, therefore, to eliminate possible photometric interference. Tablets may contain one or more reagents, along with a nonreactive, noninterfering excipient, to provide final blend properties.

3. Instrument

The 'aca' instrument automatically performs all of the necessary functions to process samples and analytical test packs. The instrument's modular design is illustrated in simplified form in Figure 2. The modules are controlled by a custom computer to provide the processing sequence.

Prior to photometric measurement, the instrument controls the critical aspects of processing, including sample handling, pack filling, timing, temperature, reagent addition, and incubation.

3.1. Sample Handling/Pack Filling

To begin processing, an operator loads the input tray with a sample cup, followed by one or more test packs (one for each test desired). Positive

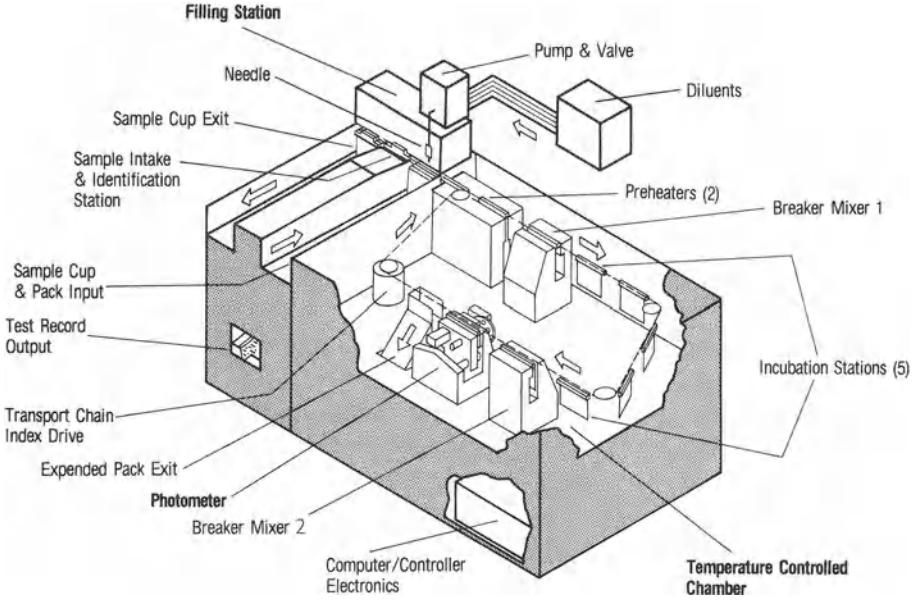

Figure 2. Operational diagram of the 'aca'.

identification of the sample is maintained by an optical transfer system which transfers the information from a card attached to the sample cup onto the report slip used for printing the results for that sample.

A shuttle mechanism moves the sample cup to the left for sample aspiration. Each test pack is decoded, filled via the needle and tubing connected to the pump, and then shuttled to the right into the main processing chamber of the instrument. The basic fill-cycle time is 37 sec. However, with column headers, a longer fill-cycle time is used (up to 296 sec), depending on the elution speed requirements of the chromatographic column.

The patented fluid metering system performs the required sample dilution with one of five diluents. The total fluid volume entered in the pack is held constant at 5 ml, with sample aliquots ranging from 20–500 μl. A typical dilution ratio precision of 0.2% is obtained at the 40 μl level.

Minimal fluid entrapment in any area of the dispensing system together with automatic flushing between cycles results in inconsequential carryover of sample or diluent. For the extremely sensitive bichromatic phosphorous test, a nonstandard extended flush cycle reduces the carryover of phosphorous (contained in one of the diluents) from the typical 0.1% to less than 0.001%.

3.2. Timing, Temperature, Reagent Addition/Mixing, and Incubation

After sample and diluent addition, pack processing continues in the processing chamber of the instrument. A pin on the transport chain holds the pack header as the transport system indexes every 37 sec to carry the pack (or packs) through the remaining processing stations or modules. At the completion of pack processing, the pack is stripped from the pin and drops into the waste container.

The preheater stations contact the pack to raise the temperature of the fluid contents to that of the processing chamber. This temperature is maintained at $37 \pm 0.2°C$ throughout the processing and $37 \pm 0.1°C$ during measurement.

At the breaker–mixer 1 module, hydrostatic force opens the temporary seals of compartments 1–4, releasing any reagents contained in them. Mixing is provided for 10 sec by a patting action on the pack. Reaction initiation for most of the current bichromatic methods is at this processing point.

After leaving breaker–mixer 1, the pack is indexed through the five delay stations allowing an incubation period of 185 sec.

At breaker–mixer 2, any reagents in pack compartments 5–7 are released and mixed by a process similar to that of breaker–mixer 1. At the completion of this cycle, the pack is advanced into the photometer for analysis. It is possible to delay the action of breaker–mixer 2 by 10 sec. There are, therefore, three well-controlled chemical reaction times available: 261.5, 39.5, and 29.5 sec.

4. Measurement System

The photometer module shown in Figure 2 is the final stage in the pack processing sequence. The complete system for pack absorbance measurements, shown in Figure 3, comprises the photometer and auxiliary computer control and signal processing electronics.

Once the test pack enters the photometer, the pack's Surlyn® envelope is formed into an optical cuvette. Two cell-forming plates close onto the pack, and the high internal fluid pressure forms the two plastic film layers into a precise cell with a 1 cm path length. Optical coupling of the film and the quartz windows housed in each cell forming plate is achieved by coating the windows with a transparent mineral oil prior to plate closure.

This process of forming the cuvette from the pack walls virtually eliminates most sources of significant error inherent in other measurement systems: "cell repositioning errors" are nonexistent; the single-test packs preclude sample carryover; and the high-internal fluid pressure serves to clear the pack solution of any bubbles.

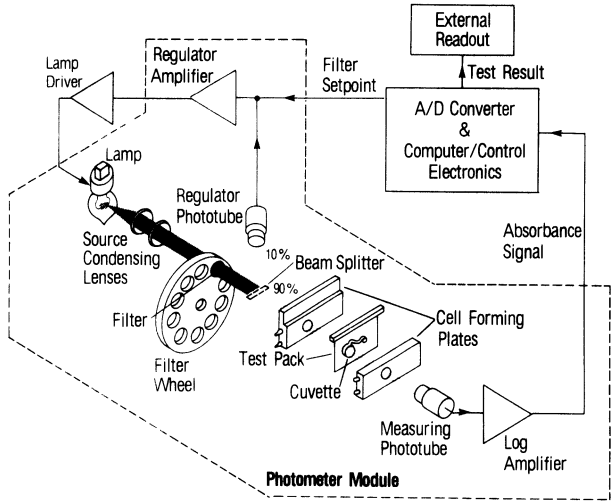

Figure 3. Measurement system of the 'aca'.

4.1. Measurement Techniques

To perform an assay, the differential absorbance ΔA is determined by one of three measurement techniques. One type involves monitoring the change in pack absorbances over a fixed time interval at a single wavelength. A second type involves making single absorbance measurements, at the same wavelength, on two successive packs; the measurement of the sample in the first pack is referenced to a blank in the second pack.

The third technique is bichromatic analysis, using a single pack, where A_{λ_1} and A_{λ_2} represent the absorbances at wavelengths λ_1 and λ_2. A_1 and A_2 are their measured values at specific points in time, such that

$$\Delta A = \Delta A_{\lambda_1, \lambda_2} = A_1 - A_2 \tag{1}$$

The $\Delta A_{\lambda_1, \lambda_2}$ form of ΔA will be used henceforth to designate this bichromatic technique in the 'aca.'

4.2. Electro-Optical System Description

The measurement system was specifically designed to perform the various ΔA determinations mentioned, and most of its features and operational parameters relate directly to bichromatic analysis. The photometer design is of the single-beam type, utilizing interference filters for wavelength selection and electro-optical feedback for light source stabilization. Nine filters in the

filter wheel provide measurement wavelengths of 293, 340, 383, 405, 452, 510, 540, 577, and 600 nm, a suitable range for clinical chemistry analyses.

For any wavelength, beam intensity incident on the pack is stabilized by feedback regulation of the quartz–halogen–tungsten light source. A phototube, detecting reflected light from the beam splitter, drives the regulator circuitry in reference to a setpoint current. Beam intensity increases or decreases to equalize the two currents. By providing a variable setpoint current, the incident beam can be adjusted for each filter.

The measuring phototube detects the transmitted light through the pack cuvette, and the absorbance relationship is obtained by logarithmic processing of the phototube current and subsequent analog-to-digital (A/D) conversion of the log voltage. The absorbance signal is measured to a high resolution of 0.1 mA (0.05 mA for 'aca' III) over a 2.5 absorbance range.

During the 37-sec cycle, the measurement proceeds in the following sequence after plate closure on the pack. After 10 sec, the A_1 measurement of A_{λ_1} is made; the 10-sec delay allows for cuvette formation, bubble clearing, and lamp stabilization on the chosen filter. The λ_2 filter is then selected for the A_2 measurement of A_{λ_2}; there is another delay to allow for filter wheel rotation to the desired filter and lamp restabilization. The delay ranges from 6 to 8 sec, depending on how far the filter wheel must rotate to reach the second filter.

4.3. Zero Absorbance Requirement

Since the A_1 and A_2 values in equation (1) represent the log ratio of transmitted (I_1, I_2) to incident (I_{01}, I_{02}) intensities at the λ_1, λ_2 wavelengths, then

$$\Delta A_{\lambda_1,\lambda_2} = -\log \frac{I_1}{I_{01}} + \log \frac{I_2}{I_{02}} \tag{2}$$

or, with rearranging

$$\Delta A_{\lambda_1,\lambda_2} = -\log \frac{I_1}{I_2} + \log \frac{I_{01}}{I_{02}} \tag{3}$$

This requires that the incident intensities be constant to yield a constant ratio term for practical use in bichromatic spectrophotometry. This is satisfied by adjusting a defined "zero absorbance" reference level for all filters (except the 293 nm wavelength), so that the constant term is zero. A dedicated pack, filled with water diluent only, is processed and the setpoint for each filter is adjusted to obtain equal zero operating levels. Since the 293 nm filter is not balanced to the operating level of the others (due to restricted output from the

lamp in the UV spectral region) its use is precluded for bichromatic tests. Subsequent stability of these "zero absorbance" levels is necessary to attain desired resolution, precision, and accuracy of bichromatic measurements.

4.4. Output Result Performance and Calibration

Total system accuracy is assured by controlling both the systematic and random error sources in three system areas: the pack and its processing factors, sample handling, and absorbance measurement. Result accuracy is maintained for a given method and/or pack lot by calibration and correlation techniques to well-assayed control materials. A brief treatment of the major photometric errors that contribute to analytical result uncertainties is appropriate to this discussion.

The derivation of each test result is based on a $y = mx + b$ linear equation in the form of

$$\text{test result} = K(\text{SF})\,\Delta A_{\lambda_1,\lambda_2} + \text{offset} \tag{4}$$

where K includes constant scaling parameters, SF is the adjustable scale factor, and the offset directly compensates for "zero analyte" blank shifts.

The photometric accuracy (and precision) of the $\Delta A_{\lambda_1,\lambda_2}$ and offset terms is determined by the individual absorbance readings. The offset value is usually small and subject to minor variability between calibration intervals (i.e., pack lot changes).

Performance and calibration of the slope and linearity for the log amplifier and A/D converter constitute the major electronic absolute error sources in processing the absorbance signal. Measuring phototube nonlinearity of photocurrent versus incident (pack transmitted) light is negligible. Therefore, by purely electronic calibration of these components, less than 0.005 A error (nonlinearity) is contributed over the 2.5 A scale.

Over the 2.5 absorbance range, the measurement precision is controlled by three predominant factors: source drift/noise, absorbance signal noise, and A/D converter quantization error.

Source drift in this context refers primarily to the differential wavelength–"zero absorbance" response variations which occur over a time period of several hours (or many packs). The net error contribution is proportional to sample transmittance, thus decreasing in importance as A_1 and A_2 (or $\Delta A_{\lambda_1,\lambda_2}$) increase in magnitude. Short-term source intensity fluctuations are negligible for a given filter positioned into the beam, due to the high-gain optical feedback stabilization. However, to minimize the long-term imprecision, the phototube pair is tightly matched for characteristics of spectral response, absolute sensitivity, and drift. Large cathode active areas allow low current-density operation, and matched beam images at both cathode

surfaces serve to reduce drift effects resulting from the discrete, heterogeneous nature of the lamp filament. Finally, to maintain the system within acceptable error limits, the "zero absorbance" levels are readjusted at least every 8 hr.

The A/D converter measurement is linear in absorbance, resulting in a constant resolution of 0.1 mA using a 15 bit design, or 0.05 mA for 16 bits in 'aca' III. The quantization error q (which is $\pm\frac{1}{2}$ of the least significant bit—the smallest resolved increment) causes uncertainty in the absorbance readings. For low absorbance conditions (<1.0), the root mean square (rms) noise content in the voltage (log amp output) signal is relatively small compared to q, such that the major uncertainty for a measured voltage (absorbance) can be as large as q. In the case of higher absorbance values the input signal rms noise is comparable to q, such that the total uncertainty is now due to the combined standard deviations in both the signal and q.

All of these factors combine to determine the relative absorbance ($\Delta A/A$) uncertainty function. For bichromatic tests, the system's typical relationship shows a 2.0% CV at the 10 mA level, decreasing to 0.3% at 100 mA, a minimum of 0.1% at 0.7 A, and only 0.3% at 2.5 A. Therefore, precise measurement capability exists for either small or large $\Delta A_{\lambda_1,\lambda_2}$ differences. Concurrently, excellent precision is retained in measuring small $\Delta A_{\lambda_1,\lambda_2}$ differences even when both A_{λ_1} and A_{λ_2} values are high.

Stray light errors, due to residual detection of undesirable filter background transmission, lead to an inconsequential discrepancy of only 0.01 A (maximum) at 2.5 A. This low error is attained by minimizing the transmission of lamp radiation, outside the filter passband, to which the detector is sensitive.

The remaining primary error contributor to test result inaccuracy in equation (4) relates to the wavelength variations from nominal for each of the interference filters. These differences, up to ± 2 nm, cause absorbance reading errors as compared to the true value obtained if nominal wavelength filters are used. A secondary error effect is related to the finite bandwidth of each filter, typically half-peak values of 4 nm for visible and 10 nm for UV wavelengths. These filter bandwidths are significant with respect to the absorption bandwidths of the measured chromophores.

The combined error effect of these filter characteristics (wavelength inaccuracy and finite bandwidth), is accounted for by correcting the theoretical SF value for each method. Essentially, two types of correction analyses are applied, dependent upon the particular chromophore characteristics and the defined wavelength reading points for λ_1 and λ_2. One case involves a relatively simple correction factor for method calibration when the λ_1 point coincides (approximately) with the chromophore peak wavelength and the λ_2 point measures a rather static portion of the chromophore.

The second case applies when the λ_1 (and possibly λ_2) reading point(s) occur on the slopes of the chromophore. Analytical expressions are developed

in terms of the wavelength deviations from nominal for each filter and the measured absorbance differences on chromophore curves for several concentrations. The measured difference in absorbance is corrected to the true λ_1, λ_2 through appropriate formulas. This is based on the principle that the slopes of the absorbance versus concentration curves vary linearly at a given wavelength. For exacting correction, the determination of the filter passband "centroid" is also required. A rather complex procedure and SF correction equation results and is, therefore, beyond the scope of this chapter. Three pertinent facts do remain: filter characteristics affect method calibration (up to 5%); correction formulas can resolve this problem; and high quality interference filters provide long-term, stable performance.

In conclusion, high photometric precision and accuracy are achieved in the 'aca' system. Electronic and optical system errors are small, resulting in minimal absorbance nonlinearity. Relatively minor imprecision is introduced in performing the two absorbance readings and calculating their difference, versus other single-point absorbance reading techniques. From an absolute viewpoint, accuracy is improved versus these single-point approaches for analyte concentration determination.

5. Measurement Principles

Bichromatic analysis involves the taking of two absorbance measurements of the reaction mixture at two different wavelengths. One wavelength is usually at or near the λ maxima, and the second at or near the λ minima of the chromophore absorbance spectra. This approach is used for methods in which the reaction reaches equilibrium. In this type of reaction, the absorbance versus time curve reaches a stage of near-zero change, i.e., reaction has reached the equilibrium region (see Figure 4).

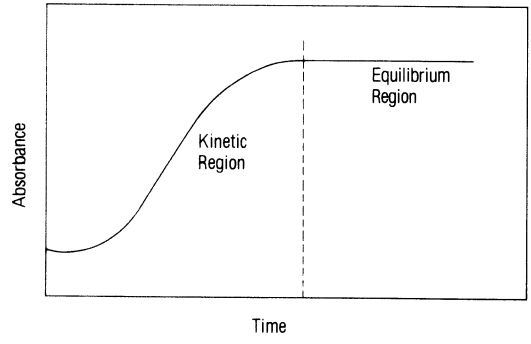

Figure 4. Theoretical method time–course reaction curve.

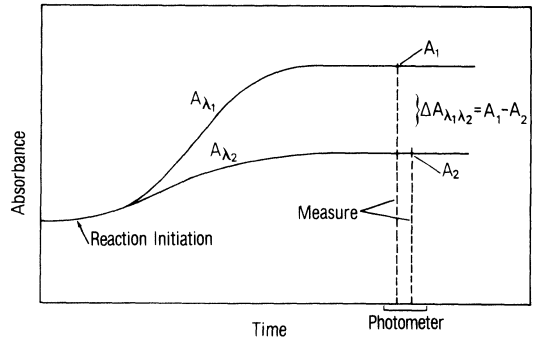

Figure 5. Absorbance versus time at two wavelengths—the 'aca' bichromatic measurement principle.

Since Beer's law holds for any point in the absorbance versus wavelength relationship (in a properly controlled system), then when equilibrium is achieved, measurement of $\Delta A_{\lambda_1,\lambda_2}$ yields a signal proportional to analyte concentration. This is represented in Figure 5, where absorbance–time relationships at both wavelengths of interest are shown to attain equilibrium before their measurement in the photometer.

In certain instances, a true equilibrium ($dA/dt = 0$) cannot be achieved. However, the dA/dt in such cases may be of insufficient magnitude to cause errors of any analytical or clinical significance.

5.1. Implementation

For a given assay, the reaction parameters such as enzyme, coenzyme, and substrate concentrations are co-optimized[1] to yield equilibrium zones at the selected time of optimization, the equilibrium is achieved by product trapping or quenching of the reaction at the appropriate time.

The most useful wavelength pair, λ_1 and λ_2, is determined from an analysis of the magnitude of:

1. nonproportionality between A_1 and A_2 over the range of analyte concentration;
2. sample-to-sample variations and their effects on A_2;
3. interference effects which cause independent changes in A_1 and A_2.

Acceptable performance with respect to these criteria is essential to bichromatic analysis. An additional requirement is adequate sensitivity for analyte quantitation. Other factors occasionally must be considered. For instance, if turbidity interference dominates then the selected wavelengths are chosen as close to each other as possible to minimize its effect.

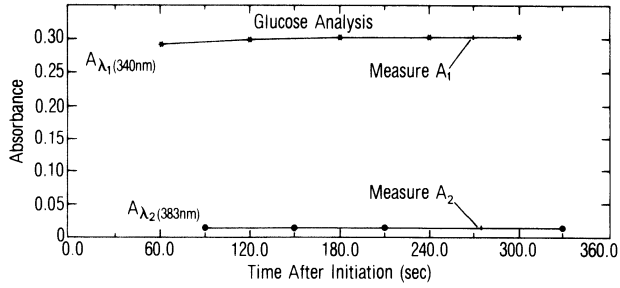

Figure 6. Absorbance of the NADPH chromophore at two wavelengths, as a function of time after reaction initiation, for the 'aca' glucose method. Specific reaction conditions: [glucose]=4.5 mmol/l, sample volume=40 μl; time to initial measurement=261.5 sec.

5.2. Representative Examples

The following examples demonstrate the application of previously described principles for 'aca' bichromatic analyses. Time–course reaction curves for selected methods, together with representative chromophore spectra for most methods are presented, along with a summary tabulation.

5.3. Reaction Time Courses

The 'aca' methods for which analytes are determined by bichromatic analysis fall into two families differentiated by the incubation time between reaction initiation and the absorbance readings taken in the photometer: 1. breaker–mixer 1 initiated; incubation time—261.5 sec; 2. breaker–mixer 2 initiated; incubation time—39.5 sec. Time–course curves for both families are shown in Figures 6–8.

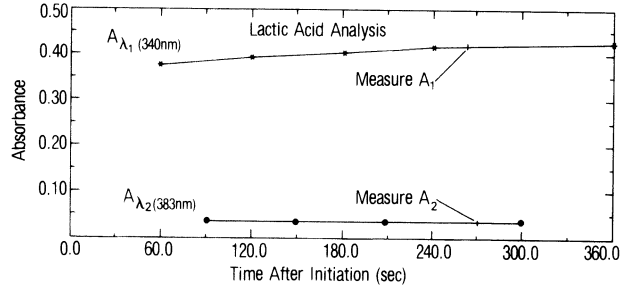

Figure 7. Absorbance of the NADH chromophore at two wavelengths, as a function of time after reaction initiation, for the 'aca' lactic acid method. Specific reaction conditions: [lactate]=1.3 mmol/l, sample volume=40 μl; time to initial measurement=261.5 sec.

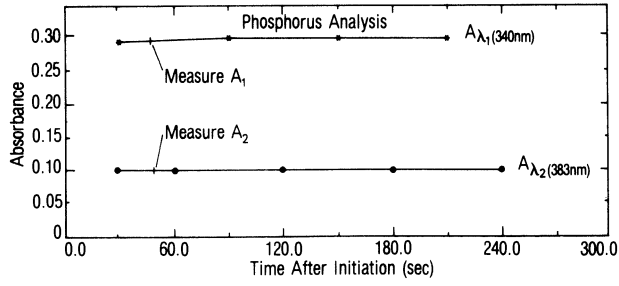

Figure 8. Absorbance of the reduced phosphomolybdate chromophore at two wavelengths, as a function of time after reaction initiation, for the 'aca' phosphorus method. Specific reaction conditions: [phosphorus] = 1.1 mmol/l, sample volume = 40 μl; time to initial measurement = 39.5 sec.

The curves shown for family 1 include those associated with the glucose and lactic acid methods. The glucose method is representative of those tests where the enzyme catalyzed formation of chromophore (NADPH) has progressed well into the equilibrium region by the time measurement is performed. For lactic acid, a secondary product trapping agent (hydrazine to trap pyruvate) has been used to facilitate attainment of reaction equilibrium within the specified time frame. A curve for the phosphorus method is included as an example of family 2. Here a rapid formation of reduced phosphomolybdate leads to the attainment of the requisite equilibrium conditions within the shorter time frame before photometric measurement. All of the curves demonstrate that equilibrium has been attained at the time of the absorbance measurements at both λ_1 and λ_2. The majority of the 'aca' bichromatic methods belongs to the 261.5-sec incubation group.

5.4. Chromophore Spectra

As a general rule, bichromatic analysis is best performed at clearly defined absorption maxima and minima. Measurements at those wavelengths maximize assay sensitivity. However, spectral interference effects associated with measurements at these wavelengths result in restricted selection for the assay. Thus, the magnitude of response across the entire range of available wavelengths is an important consideration in final λ_1 and λ_2 selection.

This type of information is shown in Figures 9–11 as chromophore spectra for most of the 'aca' bichromatic analysis methods. Two concentrations of analyte were processed normally through reaction initiation. Then, at an equivalent incubation time an aliquot was removed from each pack for spectra generation in a scanning spectrophotometer.

These figures demonstrate, in general, well-defined maxima and minima for the chromophores involved as well as proportional response at the two

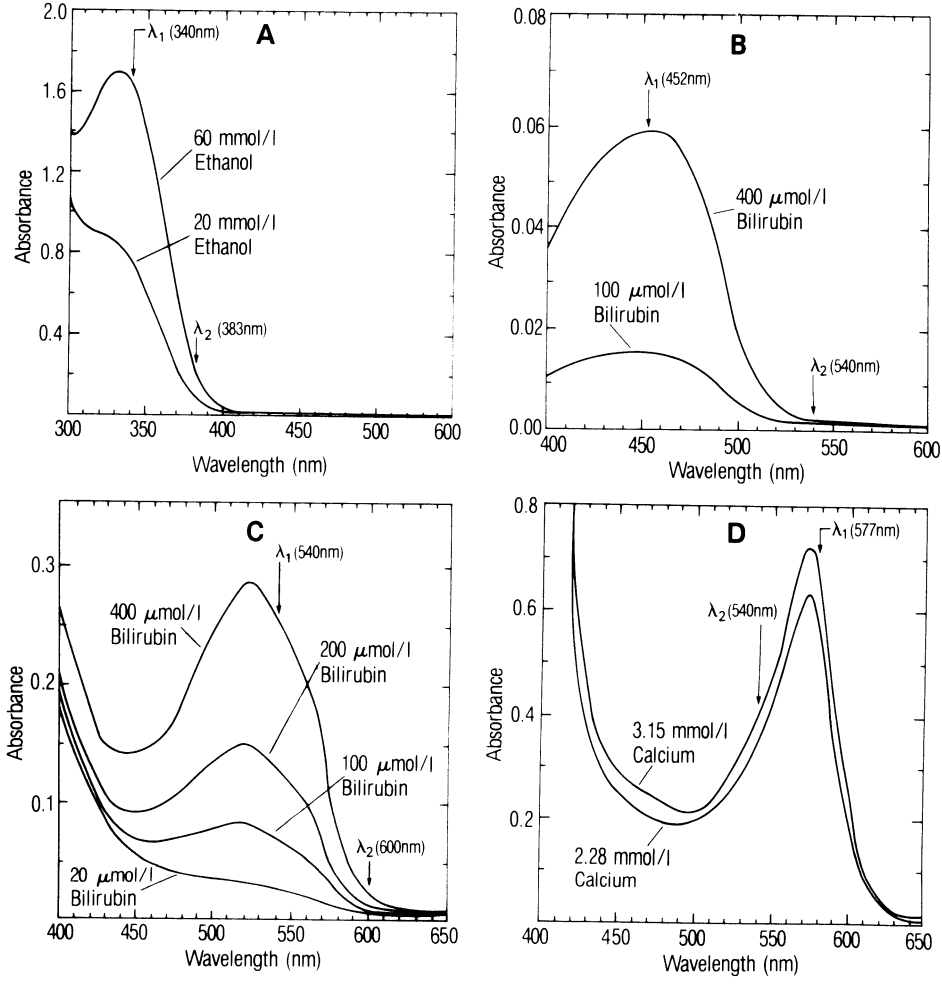

Figure 9. Absorbance spectra for reacted pack contents from the following 'aca' assay systems: A—alcohol method, NADH chromophore, sample size = 20 μl; B—neonatal bilirubin method, bilirubin chromophore, sample size = 20 μl; C—total and conjugated bilirubin methods, azobilirubin chromophore, sample size = 60 μl; D—calcium method, Ca-OCPC (OCPC—orthocresolphthalein complexone) complex chromophore, sample size = 60 μl.

wavelengths as a function of analyte concentration. Exceptions to the former observation involve 'aca' detection of chromophore at 340 nm for the alcohol, lactic acid, phosphorus and CFP (cerebrospinal fluid protein) methods. In two of these cases, lactic acid and alcohol, the shoulder of the peak for substrate NAD (λ max = 259 nm) masks the NADH chromophore peak. In the case of phosphorus, the maximum is further into the UV and cannot be detected in the 'aca' system. Lastly, the CFP "chromophore" involves turbidimetric

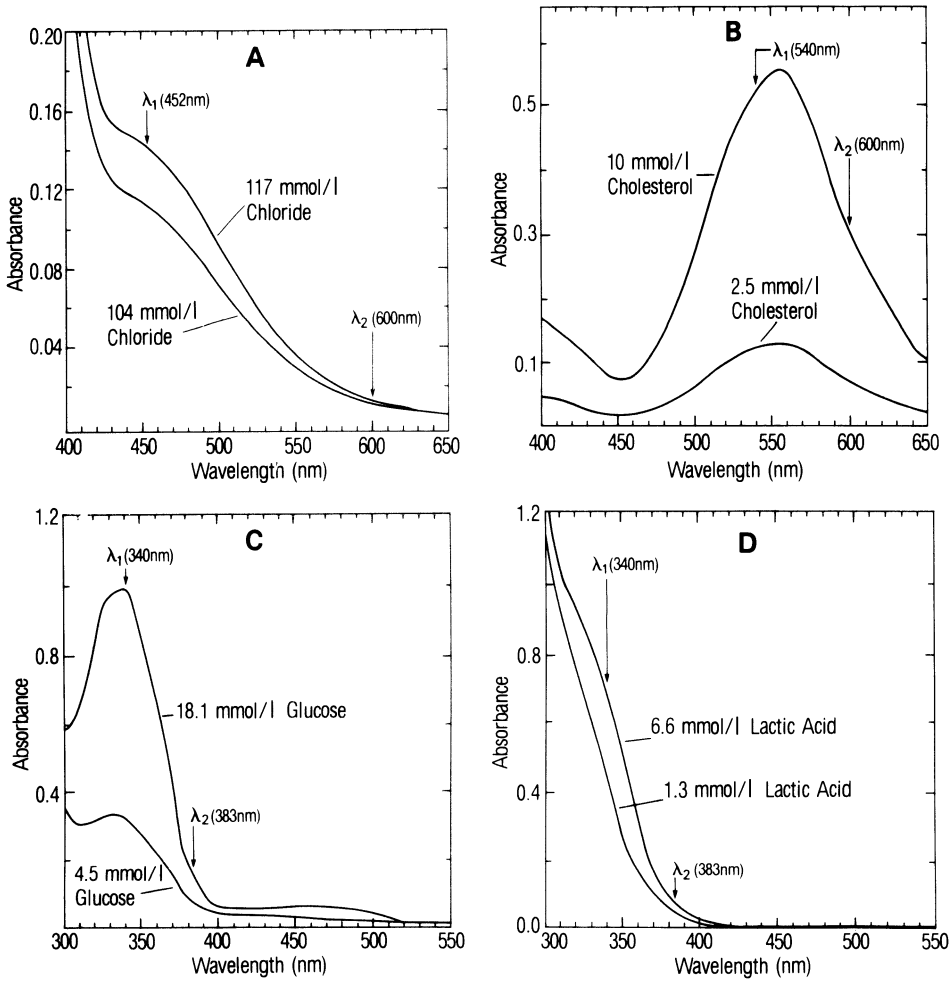

Figure 10. Absorbance spectra for reacted pack contents from the following 'aca' assay systems: A—chloride method, $Fe(SCN)^{2+}$ chromophore, sample size=60 μl; B—cholesterol method, quinoneimine chromophore, sample size=20 μl; C—glucose method, NADPH chromophore, sample size=40 μl; D—lactic acid method, NADH chromophore, sample size=40 μl.

detection; thus, a spectrum with a characteristically sharp maximum and minimum is not expected.

An exhaustive analysis for wavelength selection involves these spectra, as well as others obtained for samples containing known interferents. In each assay the chosen wavelengths represent the optimum combination of maximum sensitivity and minimum interference. In some cases, interferences may be eliminated or substantially reduced through chemical means to improve

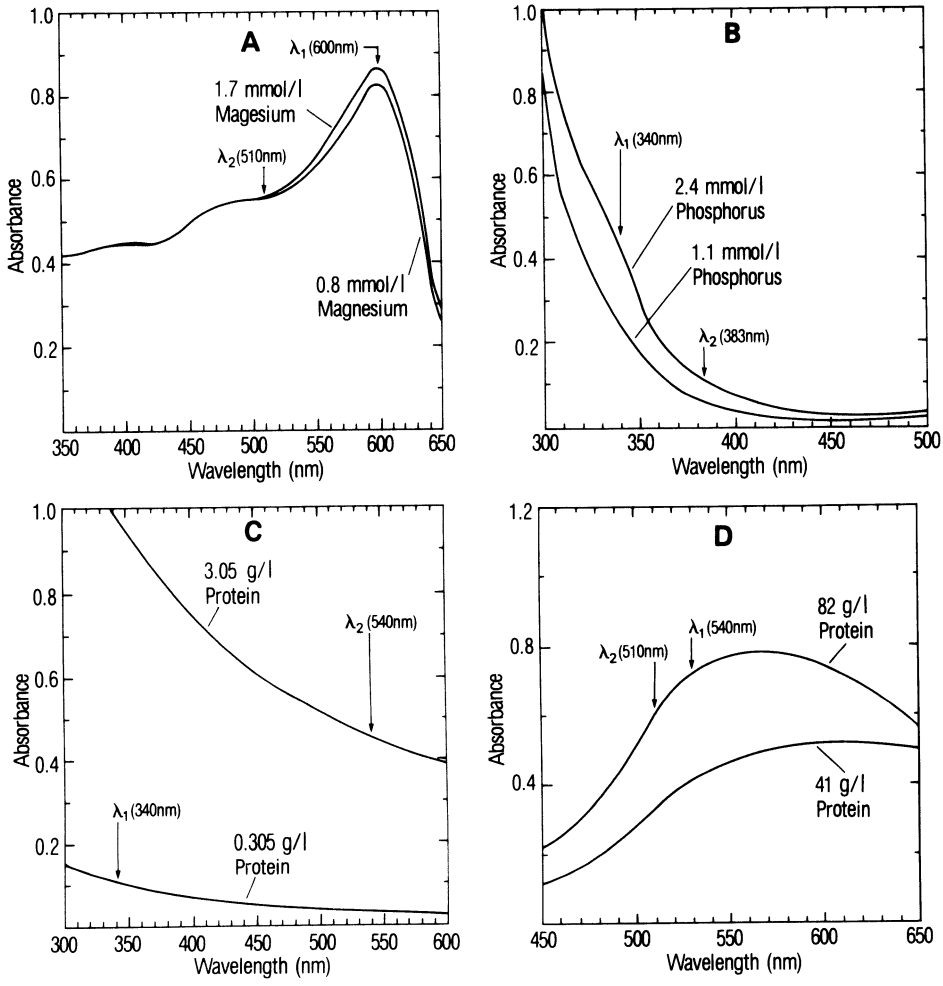

Figure 11. Absorbance spectra for reacted pack contents from the following 'aca' assay systems: A —magnesium method, Mg–MTB (MTB—methylthymol blue) chromophore, sample size = 20 μl; B—phosphorus method, reduced phosphomolybdate chromophore; sample size = 40 μl; C—CFP, turbidity response, sample size = 300 μl; D—total protein, Cu(II)-protein complex chromophore, sample size = 160 μl.

performance for a given wavelength pair selection. For example, the phosphorus method employs the addition of hypochlorite and a surfactant to eliminate interferences due to bilirubin and protein precipitation.

The data presented in Table 1 give a comparison of the wavelengths selected and observed spectral maxima/minima, as well as resulting sensitivity for the 14 'aca' bichromatic methods.

Table 1. Measurement Parameters of the 'aca' Bichromatic Methods

Method	Measurement time following reaction initiation (sec)	Wavelengths (nm)		Sensitivity	Spectral[a]		Chromophore
		Measurement	Blanking	(mA/mmol/l)	max(nm)	min(nm)	
Albumin	261.5	600	540	530.00	623	544	Albumin–BCG[b]
Alcohol	261.5	340	383	19.6	332	410	NADH
Bilirubin (conjugated)	39.5	540	600	633.00	520	630	Azobilirubin
Bilirubin (total)	261.5	540	600	633.00	520	630	Azobilirubin
Bilirubin (neonatal)	261.5	452	540	175.00	455	540	Bilirubin
Calcium	261.5	577	600	111.00	572	640	Ca–OCPC[c] complex
Cholesterol	261.5	540	452	22.81	555	452	Quinoneimine dye
Chloride	261.5	452	600	0.99	440	640	Fe $(SCN)^{2+}$
Glucose	261.5	340	383	40.17	336	400	NADPH
Lactic acid	261.5	340	383	38.26	320	400	NADH
Magnesium	261.5	600	510	47.93	600	650	Mg–MTB[d]
Phosphorus	39.5	340	383	88.28	<340	455	Phosphomolybdate
Total protein (serum)	261.5	540	510	1.37 (mA/g/l)	540–570	<450	Cu(II)-protein
CFP (CSF-protein)	39.5	340	540	83.5 (mA/g/l)	—	—	Turbidity

[a]As determined from spectral scans of chromophore in the presence of the total reagent system.
[b]Albumin–bromcresol green dye complex.
[c]Calcium-*O*-cresolpthalien complexone.
[d]Magnesium–methylthymol blue complex.

5.5. Performance

The value of any method is determined by its analytical performance. Table 2 presents relevant performance data for the 'aca' bichromatic methods. Original findings obtained in the research phase for each method have been verified during external field evaluations. The performance data shown reflect the composite results.

An in-depth discussion of the magnitude of listed interferences is beyond the scope of this chapter. In most instances where an interferent is cited, e.g., visible hemolysis, gross turbidity, etc., the interference becomes significant at high concentrations of these substances. At lower concentrations of interferents the effects are usually minimal and do not cause significant bias. The quantitative relationship between interferent concentrations and bias for all the current methods are described in the 'aca' Chemistry Instruction Manual.[2]

6. Advantages

Bichromatic analysis is well suited to the 'aca' system. This technique allows use of a single test pack for analyte quantitation, resulting in cost savings and maximum throughput, since a separate pack is not needed for a dedicated blank. Furthermore, the blank measured in the single pack is a true static blank. This is a sound blank compensation alternative because the blank and chromophore readings are measured under identical conditions for the sample plus complete reagent system. This compensates for unexpected variations in reagent and sample component interactions.

Another noteworthy point is that acceptable method performance is attainable with respect to possible interferences. The use of a column, for interference removal, has proven unnecessary to date. This presents a cost savings factor for the 'aca' methodologies using bichromatic analysis. Furthermore, due to the equilibrium requirements for bichromatic analysis, the event sequence of reaction initiation, incubation, and then photometric measurement, leads to practical instrumental design. The 'aca' system provides this sequence under very rigid automated conditions. Thus, even for those methods where a true equilibrium is not attained, this automation produces adequate reproducibility of results.

Additionally, bichromatic techniques provide the basis for practicality in photometric measurement system design. A single absorbance reading cannot adequately account for instrument and/or chemical shifts, whereas bichromatic measurement satisfactorily compensates for these effects. The 'aca' photometric system applies this technique to virtually cancel sources of error common to both wavelengths. Therefore, over reasonable time periods, the relative absorbance error, which may lead to relative concentration error, is minimal throughout a broad absorbance range.

Table 2. Analytical Performance of the 'aca' Bichromatic Methods

Method	Linearity	Precision, %CV[a]	Interferences
Albumin	116–940 μmol/l	0.5–1.3	Hemoglobin at or above 5 g/l causes about 4.0% increase in result
Alcohol	0–50 mmol/l	0.9–1.5	Visible hemolysis; isopropyl alcohol
Bilirubin (conjugated)	0–310 μmol/l	0.9–1.5	Visible hemolysis; placental blood
Bilirubin (total)	0– 430 μmol/l	0.7–4.5	Visible hemolysis
Bilirubin (neonatal)	5–390 μmol/l	0.5–5.8	Carotenoids; turbidity; umbilical cord blood
Calcium	1.25–3.75 mmol/l	0.6–2.0	Hemoglobin above 2.5 g/l
Cholesterol	1.30–21.00 mmol/l	1.2–1.5	Bilirubin above 145 μmol/l
Chloride	60–140 mmol/l	0.8–1.0	High turbidity
Glucose	0–28 mmol/l	0.8–1.9	EDTA above 24 mmol/l; bilirubin above 0.3 mmol/l
Lactic acid	0–15 mmol/l	1.3–5.6	Hemoglobin above 5 g/l
Magnesium	0–8.23 mmol/l	1.3–5.5	None
Phosphorus	0–2.90 mmol/l	0.7–1.8	Visible hemolysis; anticoagulants—fluoride, oxalate, and EDTA
Total protein (serum)	0–120.0 g/l	0.9–2.2	Visible hemolysis; carotenoids, bilirubin >20 mg/dl, plasma expanders
CFP (CSF-protein)	0–2.00 g/l	2.0–4.2	High turbidity; gross hemolysis

[a]Within run and day-to-day within the linear range.

6.1. Disadvantages

Since factors remain in the photometric system that cause independent "zero absorbance" drifts, then a possible disadvantage of bichromatics would be errors introduced by these drifts over time. However, as was pointed out, this error is minimized by periodic readjustments, i.e., filter balance.

Another drawback can be inaccuracy introduced in those cases where sample-to-sample differences cause significant blank absorbance variations. In these instances, the bichromatic approach cannot be used. This is also true when serum interferents create significant bias. Column separation techniques can be used to eliminate such biases.

6.2. Future Applications

While the bichromatic analysis technique has had wide application within the 'aca' system, several additional areas might be considered applicable. One example is the quantitation of specific serum proteins by performing a bichromatic measurement on the turbidimetric signal generated by immunoprecipitates. This technique might also be used in determination of certain coagulation factors.

Since bichromatic analysis is the simplest case of multichromatic measurement techniques, it is clear that expansion into this area enhances future potential. With the advent of the microprocessor-controlled 'aca' III instrument, applications of multichromatics are possible due to flexible software control of operational parameters. In particular, variable detection timing and more flexible wavelength selection will broaden the application of multichromatic techniques. To exemplify this enhancement, the potential now exists for detection of multiple chromophores within a single pack—for example, the various forms of hemoglobin present in a blood sample.

In conclusion, bichromatic analysis has provided the necessary foundation on which future multichromatic analysis applications will be built.

Acknowledgments

The authors express their appreciation to W. Lock, Du Pont Clinical Systems Division, for his review and valuable suggestions for this manuscript.

References

1. G. S. Rautela, R. D. Snee, and W. K. Miller, Response-surface co-optimization of reaction conditions in clinical chemical methods, *Clin. Chem.*, **25**(11), 1954–1964 (1979).
2. Automatic Clinical Analyzer, Chemistry Instruction Manual, Du Pont Company, Clinical Systems Division, Publications Department, Wilmington, Delaware, 19898.

5

The Analysis of Matrix Formatted Multicomponent Data

Isiah M. Warner

1. Introduction

During the past two decades, the mini- and microcomputer revolution has introduced a new era of computerized instrumentation capable of acquiring large amounts of data in relatively short time periods. Consequently, the analytical chemist suddenly finds that the problem of acquiring reasonable amounts of accurate data has been transformed into one of what to do with huge amounts of data. This dilemma has resulted in many analytical chemists pursuing research into areas of data reduction. The period when the only mathematical need of the analytical chemist was "basic statistics" is long past. The use of more sophisticated mathematical techniques such as factor analysis[1,2] and pattern recognition[3,4] in analytical chemistry are noticeably present in the literature.

This chapter describes a new data reduction technique which we shall call a matrix formatted multicomponent data technique (MFMDT). Before describing MFMDT, it is appropriate to describe other data reduction techniques in analytical chemistry which are also used in the analysis of data matrices.

1.1. Data Reduction Strategies in Analytical Chemistry

There are many matrix data reduction techniques employed in analytical chemistry. This discussion shall, however, be confined to the techniques of

Isiah M. Warner • Department of Chemistry, Texas A & M University, College Station, Texas 77843.

factor analysis and pattern recognition which have gained increased popularity for chemical data reduction during the past few years. However, our discussion shall be a nonmathematical description of these techniques since both use similar mathematical operations to extract data information. It is the use of this extracted information which differentiates the methods of factor analysis and pattern recognition.

Factor analysis owes much of its growth and development to statisticians associated with the social sciences. Much of the early work can be attributed to nineteenth century social scientists such as Francis Galton.[5] If one were to consult one of several texts[6–8] on factor analysis, he would encounter such linear algebra terms as basis vectors, factors, eigenvectors, dimension, and rotation just to name a few. However, complete understanding of these terms is not necessary to effectively understand the use of the technique. The primary goal of factor analysis is to "disentangle complex interrelationships... and identify the independent influences or causes at work."[8] The data to be factor analyzed are presented in tabular form and the patterned variations or factors are extracted through the mathematical procedures of linear algebra. To better understand this definition, let us examine data which might be factor analyzed. For example, suppose one were interested in evaluating a test administered to six persons whom we shall call *A*, *B*, *C*, *D*, *E*, and *F*. Let us further suppose that the examination had five questions and that the questions are worded such that the answers required a yes or no response. Regardless of the nature of the original questions, we can evaluate the responses in terms of individuals and question numbers. Table 1 provides a hypothetical table of responses that we might obtain. Depending on the information we desire from this test we might evaluate the data in terms of rows, i.e., the response of each individual to a given question. Alternatively, we might examine the columns which give us the response of each individual to a group of questions. Evaluating our data in terms of rows, we observe that the responses to questions 1, 3, and 5 were identical. If one were to numerically represent these data and factor analyze, factor analysis would uncover this interrelationship. Furthermore, a complete factor analysis would seek the underlying cause of this interdependence. For example, closer evaluation of this set of questions might indicate that they are a measure of political or religious involvement. Note that in our analysis of this data, it was not necessary to obtain specific information about the individual respondents to the questionnaire. This is because factor analysis seeks to mathematically evaluate the data without *a priori* knowledge of the independent causes or influences at work. For this example, applying factor analysis might seem like an overkill. However, consider the case where there are 100 questions to which 1,000 persons responded, then we have a table containing 100,000 responses. It would then be much easier to tabulate the responses on computer cards, input them to a computer, and then factor analyze to find the patterned variations.

Table 1. Five Question Examination Administered to Six Persons

Question number	Person tested					
	A	*B*	*C*	*D*	*E*	*F*
1	yes	yes	yes	no	yes	no
2	no	no	no	yes	no	yes
3	yes	yes	yes	no	yes	no
4	no	no	yes	yes	yes	yes
5	yes	yes	yes	no	yes	no

Our example illustrates why many of the applications of factor analysis have been in the behavioral and social sciences. It is easy to conceive of thousands of such examples in these areas of study. However, factor analysis has gradually found applications in the natural sciences. Recent applications have included factor analysis of solvent shifts in proton magnetic resonance,[9] anisotropic solvent shifts,[10] self-association of acetic acid,[11] and classification of compounds by factor analysis of their mass spectra.[12] Duewer *et al.* have also described a technique for improving the reliability of factor analysis of chemical data.[13]

In contrast to factor analysis, pattern recognition owes much of its growth and development to the engineering sciences.[14] Peter C. Jurs and Thomas L. Isenhour, two of the leading chemical investigators of pattern recognition techniques, have stated that the primary objective of pattern recognition is "to categorize a sample of observed data as a member of a class to which it belongs."[15] As an example, let us see how a pattern recognitionist might treat the data presented in Table 1. For this example, we will search for column variation. Examination of our data columns shows that four of the six examinees responded with a yes answer to questions 1, 3, and 5. Closer observation will show that the other examinees responded negatively to these three questions and positively to the remaining two questions. For graphical purposes, we can represent a negative response as a "0" and a positive response as a "1." A plot of positive and negative responses for questions 1, 3, and 5 against positive and negative responses to questions 2 and 4 is displayed in Figure 1. In this diagram, we have plotted a mixed response to questions 2 and 4 as a point midway between "0" and "1." Figure 1 shows that our examinees are grouped into three categories. Assessment of additional data on examinees *D* and *F* show that they are teenagers. Similarly, *C* and *E* are found to be middle aged, while *A* and *B* are senior citizens. It is reasonable to conclude that our graph provides us with a method for discriminating age differences based on the responses to questions 1–5. Note that in Figure 1, the *C* and *E* groups are more closely related to the *A* and *B* groups than the *D* and *F* groups. Thus, using our hypothetical example, we have graphically proven the "generation gap."

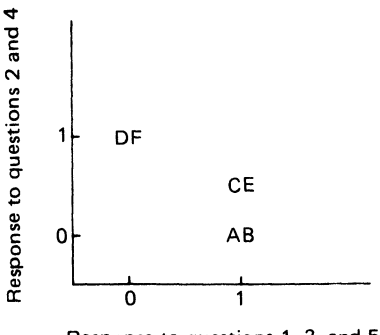

Figure 1. Graphical evaluation of questionnaire responses.

Our simple example illustrates that pattern recognition seeks to find patterns which will allow classification into categories. Pattern recognition has found increased applications in chemical data interpretation. In a recent article, Bruce Kowalski, a leading investigator in pattern recognition applications to chemical data, described the strengths, limitations, and future trends of pattern recognition.[16] Other articles describe some applications of pattern recognition to chemical data evaluation.[17-19]

The discussion above was designed to illustrate the differences in the objectives of factor analyses and pattern recognition through simple example. This example does not portray the power of factor analysis and pattern recognition. Many of the applications of these techniques are to data where the interrelationships and pattern variations are not apparent. It is these data sets which provide the most fruitful uses of pattern recognition and factor analysis. Both techniques involve an extensive use of linear algebra and statistics. Consequently, a detailed mathematical description is beyond the scope of this chapter. However, one of several texts on the topics[20-23] can be consulted if more information is desired. It should also be mentioned that factor analysis is finding increased applications in the field of pattern recognition. Consequently, the difference between the techniques in applications are becoming more diffuse.

1.2. Description of MFMDT

The technique which is described in this manuscript evolved as a result of a new development in fluorescence instrumentation.[24] This new fluorescence instrument rapidly acquires data in the form of a matrix **M**. The elements of this matrix m_{ij} represent the fluorescence intensity measured at wavelength λ_j for excitation at λ_i. The huge amount of data generated by this instrument and the unavailability of algorithms to handle such large data sets served as the rationale for exploring new methods of data reduction. The algorithms were designed to provide information about, first, the number of

component molecules contributing to the spectra, second, the composition of the solution, when the spectra of standardized solutions are known, and, third, the absorption and emission spectra of each species present in the system.

Because of two fundamental properties of most fluorescing molecules (which will be described later), linear algebra techniques were selected to extract qualitative information from the matrix **M**. For quantitative information, we use the methods of least squares and linear programming. Both of these approaches will be discussed in detail. However, it is appropriate to first briefly review linear algebra.

2. Linear Algebra Review

2.1. Vectors and Matrices

A *matrix* can be thought of as a table of numbers or a table of symbols representing numbers. Thus, an example of two matrices would be

$$\begin{bmatrix} 1 & 2 & 3 \\ 4 & 5 & 6 \\ 7 & 8 & 9 \end{bmatrix} \quad \text{or} \quad \begin{bmatrix} a_{11} & a_{12} & a_{13} \\ a_{21} & a_{22} & a_{23} \\ a_{31} & a_{32} & a_{33} \end{bmatrix}$$

The shape of these matrices is said to be 3×3 (3 by 3) indicating that the matrices have three rows and three columns. A matrix of shape $r \times 1$ or $1 \times r$ is called a *vector*. The symbol for a vector is usually a lower case underscored or boldface letter. A matrix can be said to be made up of a set of row or column vectors.

Generally, the symbol for a matrix is an upper case underscored or boldface letter and the elements of the matrix are represented by lower case, subscripted letters. The second matrix above would have the general symbol **A**. The elements are subscripted according to their position in the matrix. Thus, the element a_{ij} is the element which corresponds to the ith row position and the jth column position. Similarly, a_{12} is the element located in the first row and second column position.

The *transpose* of a matrix has the rows written as columns and the columns as rows. Thus, the transpose of the matrix **A** above is

$$\begin{bmatrix} a_{11} & a_{21} & a_{31} \\ a_{12} & a_{22} & a_{32} \\ a_{13} & a_{23} & a_{33} \end{bmatrix}$$

The symbol for this matrix is the symbol for the original matrix with the superscripted lower case t, i.e., $\mathbf{A}^t$. It should be noted that whereas **A** has shape $n \times r$, $\mathbf{A}^t$ has shape $r \times n$.

2.2. Arithmetic of Matrices

The *addition* or *subtraction* of matrices require that they be of the same shape. Once this requirement is satisfied, matrices are subtracted or added element by element. Obviously, we can have a string of additions and subtractions as in scalar arithmetic provided all matrices have the same shape.

Multiplication of matrices is of two types: scalar, and matrix multiplication. *Scalar multiplication* is as the name implies, multiplication of a matrix by a scalar. The product of scalar multiplication is the matrix obtained by multiplying each element of the original matrix by the scalar. Matrix multiplication is a more complicated process. To multiply two matrices, *the number of columns of the first matrix must equal the number of rows of the second.* The matrix product of two matrices, **B** and **C**, produces a third matrix **A** whose elements are given by

$$a_{ij} = \sum_{k=1}^{r} b_{ik} c_{kj} \tag{1}$$

This formula applies to the product of any two matrices as long as the number of columns of the first matrix equals the number of rows of the second matrix. The product of a $1 \times r$ matrix times an $r \times 1$ matrix is called a vector product. The shape of the product matrix is determined by the shape of the original matrices. In general, multiplication of an $n \times r$ matrix **B** by an $r \times m$ matrix **C** produces an $n \times m$ matrix **A**.

There is one additional point which should be brought out with regards to vector multiplication. The vector product described above is called an *inner*, *scalar*, or *dot product*. There is also another product called the *outer product* of two vectors which produces a matrix. For example, consider two vectors, **x** and **y**, with elements a_k and b_l of length n and m, respectively,

$$\begin{bmatrix} a_1 \\ a_2 \\ \vdots \\ a_n \end{bmatrix} \overbrace{\underbrace{\begin{matrix} b_1 & b_2 & \cdots & b_m \end{matrix}}}$$

then the outer product of column vector **x** and row vector **y** produces the matrix

$$\begin{bmatrix} a_1 b_1 & a_1 b_2 & \cdots & a_1 b_m \\ a_2 b_1 & a_2 b_2 & \cdots & a_2 b_m \\ \vdots & \vdots & & \vdots \\ a_n b_1 & a_n b_2 & \cdots & a_n b_m \end{bmatrix}$$

Note that the outer product does not require that the vectors be of the same length, whereas, the inner product does.

Table 2. Properties of Matrices under the Operations of Addition and Multiplication

Property	Addition	Matrix multiplication	Scalar multiplication
Associative	True $(\mathbf{A}+\mathbf{B})+\mathbf{C}=\mathbf{A}+(\mathbf{B}+\mathbf{C})$	True $\mathbf{A}(\mathbf{BC})=(\mathbf{AB})\mathbf{C}$	True $k(l\mathbf{A})=(kl)\mathbf{A}$
Commutative	True $\mathbf{A}+\mathbf{B}=\mathbf{B}+\mathbf{A}$	Not generally true $\mathbf{AB}\neq\mathbf{BA}$	—
Distributive	—	True $\mathbf{A}(\mathbf{B}+\mathbf{C})=\mathbf{AB}+\mathbf{AC}$	True $(k+l)\mathbf{A}=k\mathbf{A}+l\mathbf{A}$ $k(\mathbf{A}+\mathbf{B})=k\mathbf{A}+k\mathbf{B}$

Both the scalar and outer product of vectors will be useful to our later discussion. For example, a vector is said to be normalized to unity or of length one if the scalar product of the vector with itself gives the scalar one. Furthermore, two vectors are said to be orthogonal if both vectors are nonzero (not all elements 0) and their scalar product produces the scalar zero. We will use normalized and orthogonal vectors in discussion of the MFMDT.

We should also cite a few properties of matrices with regard to the operations of addition and multiplication. This is given in Table 2. In addition to the rules specified in Table 2, it should be obvious that if the product of two matrices produces the zero matrix (matrix with all elements zero), it is not necessarily true that one of the original matrices is the zero matrix.

Finally, we should note some properties of the transpose of matrices. First, the transpose of the product of two matrices is the reverse product of the transposed matrices, i.e.,

$$(\mathbf{AB})^t=\mathbf{B}^t\mathbf{A}^t$$

and second, the products $\mathbf{A}^t\mathbf{A}$ and $\mathbf{AA}^t$ are always defined and will produce a square matrix with the same rank (see later discussion) as $\mathbf{A}$. Furthermore, these matrices are symmetric. A symmetric matrix is defined to be a matrix $\mathbf{C}$ with elements $C_{ij}=C_{ji}$ for $i\neq j$. The rows and columns of $\mathbf{A}^t\mathbf{A}$ are a linear combination of the rows of $\mathbf{A}$. The rows and columns of $\mathbf{AA}^t$ are a linear combination of the columns of $\mathbf{A}$.

2.3. Matrix Solution of a System of Linear Equations

For our discussion, it is useful to examine the set of linear equations:

$$\begin{aligned}
a_{11}X_1+a_{12}X_2+\cdots+a_{1n}X_n&=Y_1\\
a_{21}X_1+a_{22}X_2+\cdots+a_{2n}X_n&=Y_2\\
&\vdots\\
a_{n1}X_1+a_{n2}X_2+\cdots+a_{nn}X_n&=Y_n
\end{aligned}$$

Using our knowledge of the arithmetic of matrices, we should be able to convince ourselves that this system of linear equations is equivalent to the equation

$$\mathbf{Ax}=\mathbf{y}$$

in matrix notation. The elements of each matrix are defined as follows:

$$\mathbf{A}=\begin{bmatrix} a_{11} & a_{12}\cdots a_{1n} \\ a_{21} & a_{22}\cdots a_{2n} \\ \vdots & \\ a_{n1} & a_{n2}\cdots a_{nn} \end{bmatrix}, \qquad \mathbf{x}=\begin{bmatrix} X_1 \\ X_2 \\ \vdots \\ X_n \end{bmatrix} \text{ and } \mathbf{y}=\begin{bmatrix} Y_1 \\ Y_2 \\ \vdots \\ Y_n \end{bmatrix}$$

To solve the set of linear equations, we need not consider the vector **x**, but only the elements of the matrices **A** and **y**. It is possible to incorporate **y** into **A** and form what is called the *augmented matrix*, i.e., the matrix

$$\begin{bmatrix} a_{11} & a_{12}\cdots a_{1n} & Y_1 \\ a_{21} & a_{22}\cdots a_{2n} & Y_2 \\ a_{n1} & a_{n2}\cdots a_{nn} & Y_n \end{bmatrix}$$

If we were going to solve the set of linear equations directly, we would first try to reduce the equations to a more useful form. For example it might be possible to eliminate some of the variables in an equation by subtracting a multiple of another equation or combination of equations. Then, it stands to reason that it is possible to reduce our augmented matrix in a similar fashion. This process of simplification is known as *row reduction*. To understand how row reduction works, let us consider a specific example. Consider the set of equations

$$X_1+2X_2+3X_3=16$$

$$3X_1+5X_2+X_3=8$$

$$3X_1+X_2+4X_3=23$$

Forming the augmented matrix, we obtain

$$\begin{bmatrix} 1 & 2 & 3 & 16 \\ 3 & 5 & 1 & 8 \\ 3 & 1 & 4 & 23 \end{bmatrix}$$

It is easy to show that the augmented matrix is equivalent (i.e., has the same

solution) to the matrix

$$\begin{bmatrix} 1 & 0 & 0 & 1 \\ 0 & 1 & 0 & 0 \\ 0 & 0 & 1 & 5 \end{bmatrix}$$

This matrix which is in its simplest form is called *row-reduced* because the first nonzero entry in each nonzero row is equal to one, and every other entry in the column which contains the leading one's are zero. Our system of linear equations is then equivalent to

$$X_1 + 0 \cdot X_2 + 0 \cdot X_3 = 1$$

$$0 \cdot X_1 + X_2 + 0 \cdot X_3 = 0$$

$$0 \cdot X_1 + 0 \cdot X_2 + X_3 = 5$$

or simply $X_1 = 1$, $X_2 = 0$, and $X_3 = 5$. Thus, using matrix algebra, we have found a simple process for solving a system of linear equations. Although the example given is of a set of nonhomogenous equations, we can solve a set of homogenous equations just as easily.

2.4. Basis and Rank

Before defining basis, it is useful to define the rank of a matrix. The *rank* of a matrix is the number of linearly independent rows (no row is a linear combination of the others) necessary to express every other row in the matrix. In the above example the coefficient matrix could only be reduced to a form with three rows. Thus, the matrix is said to have rank 3. The rows of the row-reduced matrix form a *basis* for the matrix, i.e., any equivalent set of rows can be expressed as a linear combination of the rows of the row-reduced matrix

$$\begin{bmatrix} 1 & 0 & 0 \\ 0 & 1 & 0 \\ 0 & 0 & 1 \end{bmatrix}$$

Note that the rows of the row-reduced matrix are linearly independent, i.e., no row is a linear combination of the other two. This requirement is necessary for vectors which form a basis. It should be obvious at this point that any three linearly independent vectors which can be obtained as a linear combination of the basis vectors (1,0,0), (0,1,0), and (0,0,1) also form a basis for the matrix. In mathematical terms, we would say that these equivalent vectors span the same space as the vectors (1,0,0), (0,1,0), and (0,0,1).

If one were to column reduce the original matrix, he would find that it requires three columns to form a basis for the columns. This fact holds true for all matrices, i.e., *column rank equals row rank*. Thus, if we have a matrix of shape 2×3 or vice versa, then the maximum rank of this matrix is 2.

2.5. Identity and Inverse Matrices

In our previous example, when we row-reduced the matrix

$$\begin{bmatrix} 1 & 2 & 3 \\ 3 & 5 & 1 \\ 3 & 1 & 4 \end{bmatrix}$$

we obtained the matrix

$$\begin{bmatrix} 1 & 0 & 0 \\ 0 & 1 & 0 \\ 0 & 0 & 1 \end{bmatrix}$$

This matrix is called the *identity* or *unity matrix*. In matrix algebra, it has the same function as the scalar "1" in scalar arithmetic. Multiplication of a matrix by the identity matrix (assuming the multiplication is defined) produces the original matrix. There are identity matrices of different sizes. The only requirements of an identity matrix is that it (a) be square, i.e., the number of rows equal the number of columns, (b) have all diagonal elements ($i = j$) of unity, and (c) have all nondiagonal elements ($i \neq j$) of zero. The symbol for the identity matrix is the symbol $\mathbf{I}$. To denote the particular identity matrix, the number of rows and columns are sometimes subscripted, e.g., $\mathbf{I}_n$.

In scalar arithmetic, the inverse of a scalar is the scalar by which you can multiply the scalar and produce the scalar 1. Similarly, in matrix arithmetic, the inverse of a matrix is the matrix by which one can multiply a matrix and produce the identity matrix. If this inverse is both the left and right inverse of a given matrix $\mathbf{A}$, then this inverse is called the *inverse* of $\mathbf{A}$ and has the symbol $\mathbf{A}^{-1}$. It can be shown that this left and right inverse is unique and applies only to square matrices.

Let us return to the system of linear equations which we solved in Section 2.3 of this chapter. The matrix of coefficients of the variables was given as

$$\begin{bmatrix} 1 & 2 & 3 \\ 3 & 5 & 1 \\ 3 & 1 & 4 \end{bmatrix}$$

There are mathematical procedures for finding the inverse of this matrix.[25]

Whatever procedure we use, we will find that the inverse of the coefficient matrix is

$$\begin{bmatrix} -19/35 & 5/35 & 13/35 \\ 9/35 & 5/35 & -8/35 \\ 12/35 & -5/35 & 1/35 \end{bmatrix}$$

We previously asserted that the system of linear equations could be represented in matrix form as

$$\begin{bmatrix} 1 & 2 & 3 \\ 3 & 5 & 1 \\ 3 & 1 & 4 \end{bmatrix} \begin{bmatrix} X_1 \\ X_2 \\ X_3 \end{bmatrix} = \begin{bmatrix} 16 \\ 8 \\ 23 \end{bmatrix}$$

If we multiply both sides of the equation on the left by the inverse matrix, we obtain

$$\begin{bmatrix} X_1 \\ X_2 \\ X_3 \end{bmatrix} = \begin{bmatrix} -19/35 & 5/35 & 13/35 \\ 9/35 & 5/35 & -8/35 \\ 12/35 & -5/35 & 1/35 \end{bmatrix} \begin{bmatrix} 16 \\ 8 \\ 23 \end{bmatrix}$$

or simply

$$\begin{bmatrix} X_1 \\ X_2 \\ X_3 \end{bmatrix} = \begin{bmatrix} 1 \\ 0 \\ 5 \end{bmatrix}$$

Thus, it is easy to find the solution to a system of equations using the inverse of the matrix of coefficients. It is true that any system of the form

$$\mathbf{Ax} = \mathbf{y}$$

can be solved by finding the inverse of **A** (if it exists).

2.6. Eigenvalues and Eigenvectors

In this section, we briefly introduce the concept of eigenvalues and eigenvectors. These concepts will be particularly important to our later discussions on the theory of MFMDT.

Consider an equation of the form

$$\mathbf{Ax} = \lambda \mathbf{x}$$

where **A** is a matrix, **x** is a vector, and λ is a scalar. Then, the vector **x** is called the eigenvector of **A** associated with the eigenvalue λ.

Given a 2×2 matrix, we can form an eigenvalue–eigenvector equation of the form

$$\begin{bmatrix} 3 & 2 \\ 1 & 2 \end{bmatrix} \begin{bmatrix} X_1 \\ X_2 \end{bmatrix} = \lambda \begin{bmatrix} X_1 \\ X_2 \end{bmatrix}$$

There are procedures to solve for the vector **x** and its associated eigenvalues which we will not discuss here. However, the solution to this equation gives $\lambda=1$ and $\lambda=4$. The associated eigenvectors are $(1,-1)$ and $(2,1)$, respectively. We can prove that these vectors are linearly independent and that they are a linear combination of the basis vectors $(1,0)$ and $(0,1)$. Consequently, *the eigenvectors form a basis for the matrix.* Note also that we have two nonzero eigenvalues. *The number of nonzero eigenvalues of a given matrix is equal to its rank.*

This brief review of linear algebra was designed to familiarize the reader with a basic knowledge necessary to understand the MFMDT. The treatment here was designed to be as brief as possible. If a more detailed treatment is desired, any of several excellent texts[25–27] can be consulted.

2.7. Glossary

This glossary is limited to those terms frequently used in the discussion of the MFMDT. Any terms used in the discussion and not defined here will be defined in the discussion.

1. *Basis.* A set of linearly independent vectors are said to form a basis of the matrix **A** if a linear combination of the vectors will reproduce any row of **A**.
2. *Diagonalization.* Any matrix **A** which satisfies the eigenvector–eigenvalue equation

$$\mathbf{Ax}=\lambda\mathbf{x}$$

   is similar to a diagonal matrix **B**. The process of finding **B** is called diagonalization. The nonzero diagonal elements of **B** are the eigenvalues λ of **A**.
3. *Eigenvalue and eigenvector.* Given an equation of the form

$$\mathbf{Ax}=\lambda\mathbf{x}$$

   then any constant λ which satisfies this equation is said to be an eigenvalue of **A**. Any vector **x**, associated with a distinct eigenvalue, and which satisfies this equation is called an eigenvector of **A**.

4. *Identity matrix.* Any $n \times n$ matrix whose diagonal elements ($i = j$) are unity and whose off-diagonal elements ($i \neq j$) are zero. (See Section 2.5.)
5. *Inner (scalar, dot) product.* The scalar assigned to two vectors **x** and **y** of length n. (See Section 2.2.)
6. *Inverse matrix.* The inverse of an $n \times n$ matrix **A**, denoted $\mathbf{A}^{-1}$, is defined to be that matrix which multiplies **A** on the left or right to produce the identity matrix.
7. *Matrix.* A table of numbers or a table of symbols representing numbers.
8. *Norm or length of a vector.* The square root of the scalar product of a vector with itself.
9. *Outer product.* The matrix formed by the product of two vectors **x** and **y**. (See Section 2.2.)
10. *Rank.* The number of vectors necessary to form a basis for a matrix **A**.
11. *Rectangular matrix.* A matrix whose number of rows does not equal its number of columns.
12. *Row-reduction.* The process of converting a matrix from one form to its simplest equivalent form. If the matrix is square and invertible, then its simplest equivalent form is the identity matrix.
13. *Shape.* The number of rows and columns of a matrix, usually specified as $n \times m$.
14. *Square matrix.* A matrix whose number of rows equals its number of columns.
15. *Transpose.* The matrix formed by writing the rows of **A** as columns and vice versa.
16. *Vector.* A matrix with one row or one column.

3. Theory and Application of MFMDT in Qualitative Analysis of the Fluorescence Emission–Excitation Matrix (FEEM)

3.1. Properties of Fluorescence Emission

A familiar form of Beer–Lambert's law states that the absorbance A for a single species absorbing monochromatic light is given by

$$A = \varepsilon bc$$

Another form of this equation provides the relationship

$$\text{intensity of absorbed light} = I_0(1 - 10^{-\varepsilon bc}) \tag{2}$$

In these relationships, I_0 is the intensity of the monochromatic light, ε is the molar extinction coefficient at the wavelength of use, b is the sample thickness

traversed by the beam, and c is the concentration of the component in units of moles per liter. An essential assumption of the Beer–Lambert equation is that multiple absorping species act independently of each other in the absorption process. Consequently, the absorbance for multiple species is the summation of the individual absorbances.

If we define a term Φ_f as the fraction of absorbed photons emitted as fluorescence, then the intensity of fluorescence I_f is given by

$$I_f = \Phi_f I_0(1 - 10^{-\varepsilon bc}) \tag{3}$$

At low absorbance ($\varepsilon bc \leqslant 0.01$) equation (3) can be approximated by

$$I_f = \Phi_f I_0 2.303 \varepsilon bc \tag{4}$$

If I_0 is normalized for nonuniform lamp output and Φ_f is assumed to be wavelength independent, then it is apparent from equation (4) that the intensity of fluorescence is directly proportional to the absorbance. Consequently, if we monitored the intensity of fluorescence at a given wavelength as a function of excitation wavelength, we would expect to obtain a profile identical to the absorption profile. For a pure component, this profile would be independent of the monitored emission wavelength.

Another property of fluorescing molecules is that emission almost always occurs from the first excited state. Even if excitation is to an excited state higher than the first, the molecule rapidly relaxes to the lowest vibrational level of the first excited state before emitting a photon. Of the many thousands of compounds that fluoresce, only a few have been found not to obey this property.

From the two properties discussed above, one can intuitively infer the multicomponent capabilities of fluorescence. For example, suppose one observes the emission spectrum as a function of several wavelengths of excitation and the relative emission profile does not change, then only one fluorescing species is present. If the profile does change with exciting wavelength, then the presence of more than one component is indicated. Conversely, if the excitation spectrum changes with monitored emission wavelength, the presence of multiple components is also indicated. The mathematical implications of these properties are discussed below.

3.2. Principles of Qualitative Analysis of the FEEM by MFMDT

The elements of the fluorescence emission matrix **M** for a pure component can be expressed as

$$m_{ij} = \alpha x_i y_j \tag{5}$$

Here, α is a concentration-dependent scalar whose value is given by $\alpha = 2.303\Phi_f bc$. The terms in the α expression were defined previously for equation (3). The parameter x_i is an element of the excitation vector given by

$$x_i = I_0(\lambda_i)\varepsilon(\lambda_i)$$

where $I_0(\lambda_i)$ is the incident intensity of monochromatic light at wavelength λ_i and $\varepsilon(\lambda_i)$ is the molar extinction coefficient of the fluorescing component at wavelength λ_i. The parameter y_j is an element of the emission spectrum and is given by the expression

$$y_j = \delta(\lambda_j)\gamma(\lambda_j)$$

where $\delta(\lambda_j)$ is the fraction of fluorescence photons emitted at wavelength λ_j and $\gamma(\lambda_j)$ accounts for instrumental artifacts such as geometry of light collection and sensitivity of the analyzing system.

The properly sequenced set of x_i's is a column vector representing the measured fluorescence excitation spectrum of the molecule and the properly sequenced set of y_j's is a row vector representing the measured fluorescence emission spectrum. Since we have previously asserted that for a pure component the fluorescence emission excitation vector is independent of the monitored emission wavelength and that the emission vector is independent of the exciting wavelength, the matrix **M** has the simple form

$$\mathbf{M} = \alpha \mathbf{x}\mathbf{y} \tag{6}$$

Thus, **M** is the outer product of the vectors **x** and **y** multiplied by our concentration dependent parameter α. Every element of **M** is assumed to obey the restrictions of equation (4).

For a sample containing n number of fluorescing species the multicomponent matrix **M** has the form

$$\mathbf{M} = \sum_{l=1}^{n} \alpha(l)\mathbf{x}(l)\mathbf{y}(l) \tag{7}$$

where l is used to denote the components. The vector $\mathbf{x}(l)$ is the excitation vector for the lth component while $\mathbf{y}(l)$ is the emission vector for the lth component. Equation (7) assumes that the solution is sufficiently dilute that the energy transfer among species can be neglected.

Analysis of the matrix of equation (7) then consists of finding n, $\alpha(l)$, $\mathbf{x}(l)$, and $\mathbf{y}(l)$. If our system were ideal, i.e., without noise, then finding n would be equivalent to determining the rank of **M**. Finding $\mathbf{y}(l)$ and $\mathbf{x}(l)$ is equivalent to finding a basis for **M** with the additional restriction that this

basis have vectors with nonnegative elements. This restriction is consistent with the fact that true spectra do not normally possess negative entries.

Weber has shown[28] that the rank of **M** defines the minimum number of independent emitters contributing to **M**. If the dimensions of **x** and **y** are large compared to n, then it is reasonable to conclude that the set of $\mathbf{x}(l)$ and $\mathbf{y}(l)$ is linearly independent. In that case, the number of fluorescing species would be given accurately by the rank if **M** were ideal. However, since **M** contains random noise, the rank of **M** will usually equal the dimension of **M**. We then have the practical problem of rejecting those vectors associated with noise. Any scheme which rejects the noise vectors will probably also reject vectors of fluorescing emitters whose intensities are below the noise level. Besides random noise, there are two additional sources of extraneous signals which occur in the matrix **M** and will, therefore, interfere with analysis. One source is signal arising from dark current in the detector or associated electronics. The second source is scattered exciting light which has a maximum on the diagonal $\lambda_i = \lambda_j$. In theory both extraneous sources can be removed by running a solvent blank to obtain a background matrix. A multiple of this matrix can then be subtracted from the mixture matrix.

If the number of fluorescing species contributing to **M** is small, then it is possible to obtain information about the individual spectra of unknown components. Suppose we are able to obtain n linearly independent vectors, $\mathbf{v}(1), \mathbf{v}(2), \cdots, \mathbf{v}(n)$, which form a basis for the rows of **M**. Then there exists some column vector $\boldsymbol{u}(l)$ such that

$$\mathbf{M} = \sum_{l=1}^{n} \mathbf{u}(l)\mathbf{v}(l) \tag{8}$$

In our review of linear algebra, we indicated that the matrices $\mathbf{M}^t\mathbf{M}$ and $\mathbf{M}\mathbf{M}^t$ had the same rank as **M**. Moreover, the rows and columns of $\mathbf{M}^t\mathbf{M}$ are a linear combination of the rows of **M** and the rows and columns of $\mathbf{M}\mathbf{M}^t$ are a linear combination of the columns of **M**. Consequently, the eigenvectors of these matrices form a basis for the matrix **M**. The eigenvectors $v(l)$ and $w(l)$ and eigenvalues $\xi(l)$ of $\mathbf{M}\mathbf{M}^t$ and $\mathbf{M}^t\mathbf{M}$ are given by the general theory of unsymmetric bilinear forms[29] as

$$\mathbf{v}(l)\mathbf{M}^t\mathbf{M} = \xi(l)\mathbf{v}(l)$$

$$\mathbf{M}\mathbf{M}^t w(l) = \xi(l)\mathbf{w}(l) \tag{9}$$

and

$$\mathbf{v}(l)\mathbf{v}(l)^t = \mathbf{w}(l)^t\mathbf{w}(l) = 1$$

$$\mathbf{u}(l) = \mathbf{w}(l)[\xi(l)]^{1/2} = \mathbf{M}[\mathbf{v}(l)]^t$$

An additional advantage of this approach is that if the eigenvalues of $\mathbf{M}^t\mathbf{M}$ are arranged in the order $\xi(1) \geq \xi(2) \geq \cdots > \xi(n)$, then $\sum_{l=1}^{n} \mathbf{u}(l)\mathbf{v}(l)$ provides the best least squares approximation to $\mathbf{M}$ of rank n. Since $\mathbf{M}$ contains noise, it is assumed that a least squares fit will give the best approximation. Note also from equation (9) that $\mathbf{v}(l)$ and $\mathbf{w}(l)$ are normalized such that their scalar products are unity. Thus, the inequality $u(l)_i v(l)_j \leq [\xi(l)]^{1/2}$ assures that the outer product $\mathbf{u}(l)\mathbf{v}(l)$ does not contribute more than $[\xi(l)]^{1/2}$ to any element of $\mathbf{M}$.

Using the above prescription, one can easily obtain $\mathbf{M}$ in the form of equation (8). However, this does not necessarily assure that our matrix is in the form of equation (7) where $\mathbf{x}(l)$ and $\mathbf{y}(l)$ are vectors with only positive or zero entries and $\alpha(l)$ is a concentration parameter. Since there is no way to determine $\alpha(l)$ without standard spectra, the factors $\alpha(l)$ can be absorbed into the definition of $\mathbf{x}(l)$ or $\mathbf{y}(l)$ such that equation (7) can be represented as

$$\mathbf{M} = \sum_{l=1}^{n} \mathbf{x}(l)\mathbf{y}(l) \tag{10}$$

For $\mathbf{M}$ of rank 1, i.e., a single fluorescing specie, there is no problem. The eigenvector $\mathbf{v}(1)$ of $\mathbf{M}^t\mathbf{M}$ is positive for $\mathbf{M}$ of rank 1 (apart from noise). For $\mathbf{M}$ of more than rank 1, the eigenvectors form an orthogonal set of basis vectors. Orthogonality guarantees linear independence of the basis vectors. Consequently, the eigenvectors greater than the first will generally have negative entries. We know that true spectral vectors should possess only nonnegative entries. We then have a problem of finding another basis which consists entirely of positive and zero entries.

For the case of two fluorescing species, it is easy to find a matrix $\mathbf{K}$ and its inverse which will transform the eigenvectors to possible spectral vectors. It is easy to show that such a matrix $\mathbf{K}$ exists if we first arrange the eigenvectors $\mathbf{u}(l)$ into a matrix $\mathbf{U}$, i.e., $\mathbf{U} = \mathbf{u}(1), \mathbf{u}(2), \ldots, \mathbf{u}(\mathbf{n})$. A similar arrangement for the eigenvectors $\mathbf{v}(l)$ into a matrix $\mathbf{V}$ gives $\mathbf{V} = \mathbf{v}(1)^t, \mathbf{v}(2)^t, \ldots, \mathbf{v}(\mathbf{n})^t$ so that

$$\mathbf{M} = \mathbf{U}\mathbf{V}^t \tag{11}$$

Then if a matrix $\mathbf{K}$ exists, the following equation is valid:

$$\mathbf{U}\mathbf{V}^t = \mathbf{U}\mathbf{K}\mathbf{K}^{-1}\mathbf{V}^t \equiv \mathbf{U}\mathbf{K}\left[\mathbf{V}(\mathbf{K}^{-1})^t\right]^t \tag{12}$$

That is, if equation (11) is true, then also

$$\mathbf{M} = \mathbf{U}'\mathbf{V}''^t \tag{13}$$

where

$$\mathbf{U}' = \mathbf{UK} \geqslant 0 \tag{14}$$

and

$$\mathbf{V}' = \mathbf{V}(\mathbf{K}^{-1})^{t} \geqslant 0 \tag{15}$$

For our two-component system, equation (12) can also be expressed for the $k \times l$ matrix $\mathbf{M}$ as

$$\left[\begin{bmatrix} u(1)_1 \\ u(1)_2 \\ \vdots \\ u(1)_k \end{bmatrix}\begin{bmatrix} u(2)_1 \\ u(2)_2 \\ \vdots \\ u(2)_k \end{bmatrix}\right] \begin{bmatrix} k_{11} & k_{12} \\ k_{21} & k_{22} \end{bmatrix} \begin{bmatrix} \dfrac{k_{22}}{|\mathbf{K}|} & -\dfrac{k_{12}}{|\mathbf{K}|} \\ -\dfrac{k_{21}}{|\mathbf{K}|} & \dfrac{k_{11}}{|\mathbf{K}|} \end{bmatrix}$$

shape: 2×2 2×2

$$\times \begin{bmatrix} \overbrace{v(1)_1 v(1)_2 \cdots v(1)_l} \\ \underbrace{v(2)_1 v(2)_2 \cdots v(2)_l} \end{bmatrix} \tag{16}$$

The quantity denoted as $|\mathbf{K}|$ in equation (16) is the determinant of $\mathbf{K}$ and has the value $(k_{11}k_{22} - k_{12}k_{21})$. The matrix product of the 2×2 matrices ($\mathbf{K}$ and $\mathbf{K}^{-1}$) produces the 2×2 identity matrix. Since multiplication by the identity matrix does not change our equality, equation (13) is indeed valid. Our procedure is then to search the elements of the eigenvectors $\mathbf{u}(l)$ and $\mathbf{v}(l)$ to find the boundary conditions on the elements of ($\mathbf{K}$ and $\mathbf{K}^{-1}$). In the evaluation of experimental data it is not always possible to satisfy equations (14) and (15) because of noise contributions to the eigenvectors. Therefore, it is necessary to relax the constraints of $\mathbf{U}'$ and $\mathbf{V}'$ so that they are allowed to have small negative elements. Using T and T' as estimates of the noise contributions to the spectral vectors, we obtain from equations (14)–(16)

$$u(1)'_i = k_{11}u(1)_i + k_{21}u(2)_i \geqslant -T \tag{17}$$

$$u(2)'_i = k_{12}u(1)_i + k_{22}u(2)_i \geqslant -T \tag{18}$$

$$v(1)'_j = \left[k_{22}v(1)_j - k_{12}v(2)_j\right]/|\mathbf{K}| \geqslant -T' \tag{19}$$

$$v(2)'_j = \left(k_{11}v(2)_j - k_{21}v(1)_j\right)/|\mathbf{K}| \geqslant -T' \tag{20}$$

Clearly, one can assume $k_{11} = k_{22} = 1$ without loss of generality. Since the first eigenvectors **u(1)** and **v(1)** have positive or zero entries (except for noise contributions) and since **u(2)** and **v(2)** have some positive entries the constraints imposed by equations (17)–(20) on the elements of **K** can be written for $|\mathbf{K}| > 0$ as

$$\min_{v(2)_p > 0} \left(\frac{T'|\mathbf{K}| + v(1)_p}{v(2)_p} \right) \geq k_{12} \geq \max_{u(2)_p > 0} -\left(\frac{T + u(2)_p}{u(1)_p} \right) \tag{21}$$

$$\min_{v(1)_p > 0} \left(\frac{T'|\mathbf{K}| + v(2)_p}{v(1)_p} \right) \geq k_{21} \geq \max_{u(2)_p > 0} -\left(\frac{T + u(1)_p}{u(2)_p} \right) \tag{22}$$

The reciprocal of the estimated signal/noise ratio provides a good estimate of $T'|\mathbf{K}|$. Since the eigenvector **u(1)** is normalized to the square root of the first eigenvalue of $\mathbf{M}^T\mathbf{M}$ an estimate of T can be acquired from the relationship $T \cong [\xi(1)]^{1/2} T'|\mathbf{K}|$. A better procedure for obtaining an estimate of $T'|\mathbf{K}|$ involves the use of a value of an order of magnitude less than the initial estimate. Then $T'|\mathbf{K}|$ is adjusted [using $T = [\xi(1)]^{1/2} T'|\mathbf{K}|$] to the smallest positive value for which the upper bounds to k_{12} and k_{21} are not less than the lower bounds. Equations (21) and (22) define the permissible range of k_{12} and k_{21} since there are no solutions to equations (17)–(20) for $|\mathbf{K}| \leq 0$. This transformation of the eigenvectors to spectral vectors is not the same as a standard oblique rotation in factor analysis. In factor analysis, the vector rotations are done independently. This technique is a dependent rotation. If **K** is used to transform the eigenvectors **u**(l), then $(\mathbf{K}^{-1})'$ must be used to transform the eigenvectors **v**(l).

While this discussion treats only the two-component case, extension to more than two components is, in principle, straightforward. However, while one continues to deal with a linear transformation given by the matrix **K**, the elements of $|\mathbf{K}|(K^{-1})'$ are now nonlinear in the elements of **K**. Consequently, finding **K** becomes a more difficult problem which must be solved iteratively.

The preceding discussion has shown how it is possible to delineate possible spectral vectors from the eigenvectors of $\mathbf{M}'\mathbf{M}$ and $\mathbf{M}\mathbf{M}'$. However, because of the inequality signs, equations (21) and (22) imply some degree of ambiguity. In essence, there is a range of possible spectra which will satisfy the constraints of equations (21) and (22). This section describes the expected degree of ambiguity based on spectral overlap. Consider the true spectral vectors **x**(l) and **y**(l). These vectors are defined to be nonnegative. Suppose we wish to find all nonnegative vectors which form a basis for the same vector

space. Then, we can find a matrix and it's inverse which satisfies the equation

$$\mathbf{M}=\left[\begin{bmatrix} x(1)_1 \\ x(1)_2 \\ \vdots \\ x(1)_k \end{bmatrix}\begin{bmatrix} x(2)_1 \\ x(2)_2 \\ \vdots \\ x(2)_k \end{bmatrix}\right]\begin{bmatrix} 1 & a_{12} \\ -a_{21} & 1 \end{bmatrix}$$

$$\times\begin{bmatrix} \dfrac{1}{(1+a_{12}a_{21})} & \dfrac{-a_{12}}{(1+a_{12}a_{21})} \\ \dfrac{a_{21}}{(1+a_{12}a_{21})} & \dfrac{1}{(1+a_{12}a_{21})} \end{bmatrix}\left[\frac{\overbrace{y(1)_1 y(1)_2 \cdots y(1)_l}}{\overbrace{y(2)_1 y(2)_2 \cdots y(2)_l}}\right] \tag{23}$$

Separating into inequality equations similar to equations (13) and (14), we have

$$\mathbf{u(1)}'=\mathbf{x(1)}-a_{21}\mathbf{x(2)}\geqslant 0$$

$$\mathbf{u(2)}'=\mathbf{x(2)}+a_{12}\mathbf{x(1)}\geqslant 0 \tag{24}$$

$$\mathbf{v(1)}'=[\mathbf{y(1)}-a_{12}\mathbf{y(2)}]/(1+a_{12}a_{21})\geqslant 0$$

$$\mathbf{v(2)}'=[\mathbf{y(2)}+a_{21}\mathbf{y(1)}]/(1+a_{12}a_{21})\geqslant 0 \tag{25}$$

Since $\mathbf{x}(l)$ and $\mathbf{y}(l)$ are nonnegative, the boundary conditions for a_{12} and a_{21} can be written as for the approximate vectors $u(l)'$ and $v(l)'$

$$\min_{x(2)_i>0}\left(\frac{x(1)_i}{x(2)_i}\right)\geqslant a_{21}\geqslant \max_{y(1)_j>0}-\left(\frac{y(2)_j}{y(1)_j}\right)$$

and

$$\min_{y(2)_j>0}\left(\frac{y(1)_j}{y(2)_j}\right)\geqslant a_{21}\geqslant \max_{x(1)_i>0}-\left(\frac{x(2)_i}{x(1)_i}\right) \tag{26}$$

Let us examine the conditions which must exist for the vectors $\mathbf{u}(l)'$ and $\mathbf{v}(l)'$ to be identical to the correct spectral vectors, i.e., the conditions under which a_{12} and a_{21} are unambiguously zero. It is evident that a_{21} will be restricted to equal zero if and only if $x(1)_i=0$ for some i such that $x(2)_i\neq 0$ and $y(2)_j=0$ for some j such that $y(1)_j\neq 0$. Similarly, a_{12} will be restricted to equal zero if and only if $x(2)_i=0$ for some i such that $x(1)_i\neq 0$ and $y(1)_j=0$ for some j such that $y(2)_j\neq 0$. Thus, a pair of spectral vectors, $\mathbf{x(1)}$ and $\mathbf{x(2)}$, are well separated if each has at least one zero entry where the other has a positive

entry. Similar reasoning can be used for the pair of spectral vectors, **y(1)** and **y(2)**.

In Figure 2, we have summarized the expected ambiguities in the 16 possible combinations of spectral range intersections in emission and excitation. For each combination, we have listed the range of values which a_{12} and a_{21} may assume, and the number of derived spectra which will be ambiguous.

We have also included in Figure 2, the implications on the spectral vectors transformed by the matrix **K**, based on the spectral overlaps. We cannot predict which element of **K** is ambiguous due to the arbitrariness in sign convention of the second eigenvector, **u(2)** and **v(2)**. For example, $-\mathbf{u(2)}$ and **u(2)** are equally valid eigenvectors orthogonal to **u(1)**. If $-\mathbf{u(2)}$ is chosen as the second eigenvector, then equations (17)–(20) can be written as

$$\frac{1}{k_{21}}u(1)' = \mathbf{u(2)} + \frac{1}{k_{21}}\mathbf{u(1)}$$

or

$$\mathbf{u(2)}'' = \mathbf{u(2)} + k'_{12}\mathbf{u(1)}' \tag{27}$$

where $\mathbf{u(2)}'' = 1/k_{21}\mathbf{u(1)}'$ and $k'_{12} = 1/k_{21}$. Using similar reasoning for $-\mathbf{v(2)}'$ and combining the results, it is easily shown that

$$\frac{1}{k_{21}\text{min}} = k'_{12}(\text{max}), \qquad \frac{1}{k_{21}\text{max}} = k'_{12}(\text{min}) \tag{28}$$

$$\frac{1}{k_{12}\text{min}} = k'_{21}(\text{max}), \qquad \frac{1}{k_{12}\text{max}} = k'_{12}(\text{min}) \tag{29}$$

These results imply that whether the correct **K** element is a maximum or minimum depends on the phase chosen for the second eigenvectors.

Six categories of spectra can be distinguished: For case I, all excitation or emission spectra are well-separated, and, thus, the derived spectra are unambiguous. For case II one of the pairs of excitation or emission spectra is well separated, but the other pair is not. Here two of the four derived spectra (one excitation and one emission) will be free of ambiguity, while the other two will be ambiguous, but the correct solution will be one of the extreme values of k_{12} or k_{21}. For case III, neither the emission nor excitation spectral ranges are well separated, but for one of the pairs, component 1 has the widest range while for the other pair component 2 is dominant. In this case, two of the four spectra will be free of uncertainty, while the other two will be ambiguous and the correct values of the uncertain coefficient k_{12} or k_{21} will be in an intermediate region. In case IV, the spectral ranges are not well-separated

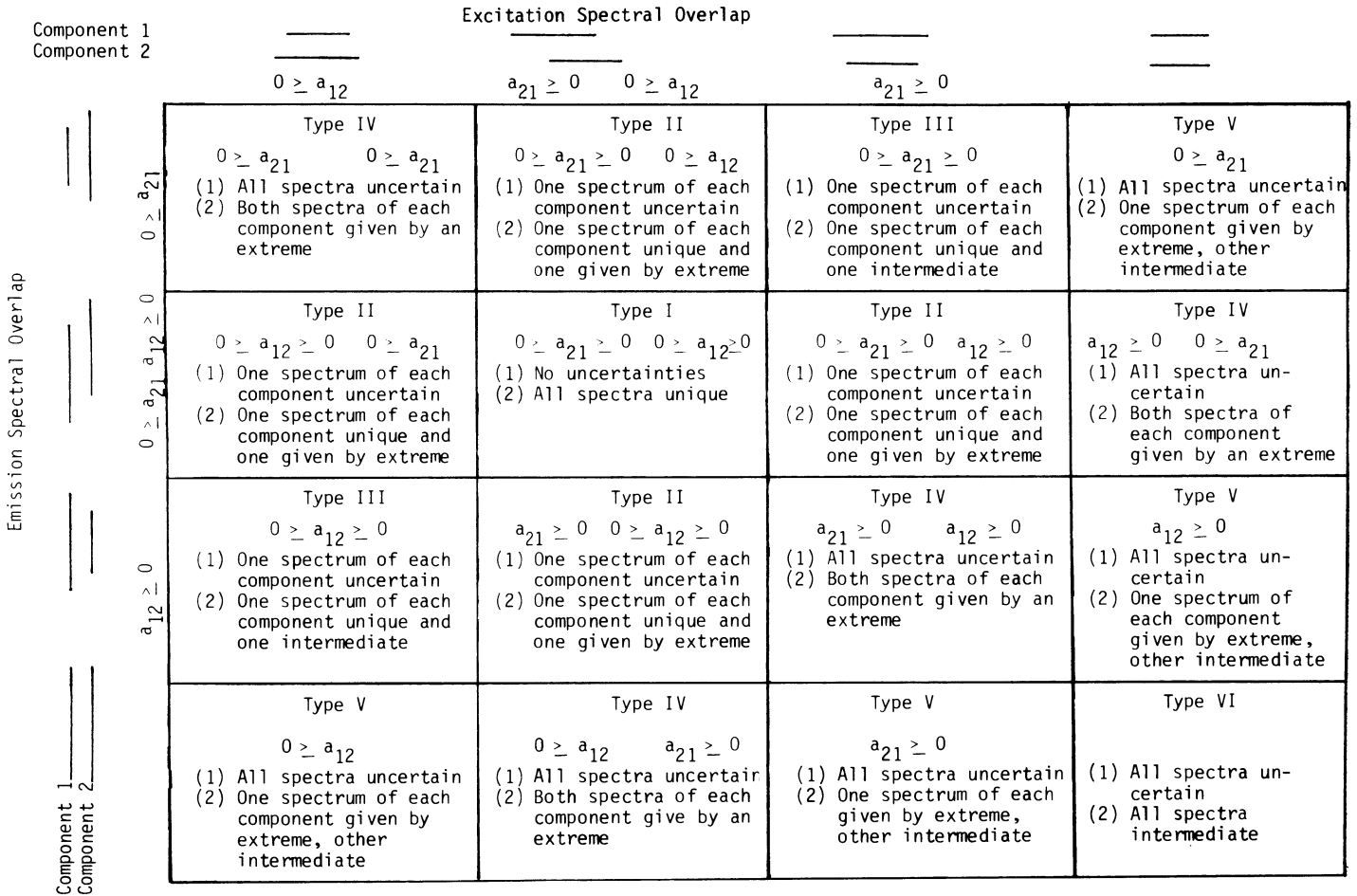

Figure 2. Ambiguity of a two-component FEEM.

and the same component dominates both spectra. In this case, all of the derived spectra will be uncertain, although the coefficient k_{12} and k_{21} will be at the extremes of their respective ranges. In case V, the spectral range for both components covers the whole range of observation in emission (or excitation), while one component dominates in excitation (or emission). In this case, all the spectra are ambiguous, but one of the k's will be at the extreme of its range. Finally, in case VI, the spectral range of all spectra cover the whole range of observation, all spectra are ambiguous, and both k's lie interior to their permitted range. Thus, in 7 of the 16 combinations, one is afforded at least two completely unambiguous "fingerprint spectra," and in only one case does none of the spectra derived from extreme values of k_{12} and k_{21} correspond to correct spectra. By examination of a wider range of wavelengths it should be possible to convert any ambiguous case into a less ambiguous (or unambiguous) one.

3.3. Qualitative Analysis of Simulated Fluorescence Data

This section uses computer synthesized data to establish the important features of the MFMDT. Table 3 shows the parameters for synthesizing this example of a binary mixture. Each component was synthesized using a single Gaussian function in both excitation and emission. The s and t values of Table 3 indicate the extent of overlap of the two components. These values are the scalar product of the excitation and emission spectra, respectively. If the excitation spectra of the two components were very similar, s would be expected to have a value close to unity. If the excitation spectra were very different, s would have a value close to zero, i.e., close to being orthogonal. A similar conclusion can be drawn about t and the emission spectra. A constant intensity matrix $\mathbf{M}^d$ was added to our synthesized spectra to simulate dark current. Photon statistical noise was then added to the synthesized mixture matrix using a random Poisson generator. The observed mixture matrix $\mathbf{M}^o$ can then be represented as

$$\mathbf{M}^o = \mathbf{M}^f + \mathbf{M}^d + \mathbf{M}^r \tag{30}$$

Table 3. Computer Synthesized Binary Mixture

Component	Emission wavelength maxima (nm)	Excitation wavelength maxima (nm)	Maximum emission intensity, photons	Matrix dimension	s/t
1	500	416	100	50×50	0.11/0.11
2	440	356	20	—	—

where $\mathbf{M}^f$ is the noise-free fluorescence matrix and $\mathbf{M}^r$ is the noise matrix. Both photon statistical noise and digitization noise are included in $\mathbf{M}^r$. Figure 3(a) shows the matrix obtained using our computer simulation. The largest component, component 1, was synthesized using 100 photons as the maximum signal. Component 2 was synthesized using 20 photons as the maximum signal. As one would expect, the second component is very much obscured by the noise from the first component and dark current.

Our $\mathbf{M}^o$ matrix was then analyzed using the MFMDT described in the previous section. The sequence followed in our qualitative analysis process are:

1. Data pretreatment. Pretreatment of data is often required before eigenanalysis. This pretreatment might be initial smoothing of data or background subtraction. In this example, no data smoothing was used. However, it was necessary to subtract background since the constant intensity of the dark current will concentrate into a single eigenvalue. For experimental data, it is a simple procedure to run a background matrix using a solvent blank. A multiple of this background matrix can then be subtracted from the observed data. In this simulated case, the known dark current of 10 photons was subtracted from the simulated mixture.

2. Eigenanalysis. The square root of the eigenvalues and eigenvectors of the matrix $\mathbf{M}^t\mathbf{M}$ were calculated using equation (9). The square roots of the eigenvalues found were 903.1, 180.1, 38.2, and 61.0. The third and fourth eigenvalues are reasonably close and smaller than the first two. Consequently, the rank of the input matrix was determined to be 2. The excitation and emission eigenvectors of the first two components are plotted in Figures 3(b) and (c). The small negative elements in $\mathbf{u}(1)$ and $\mathbf{v}(1)$ are a consequence of noise in our experimental matrix. The negative elements in $\mathbf{u}(2)$ and $\mathbf{v}(2)$ can be largely attributed to their required orthogonal relationship to $\mathbf{u}(1)$ and $\mathbf{v}(1)$.

3. Transformation of eigenvectors. The next step of the MFMDT uses equations (21) and (22) to find the matrix $\mathbf{K}$ and $\mathbf{K}^{-1}$ which transforms the eigenvectors to spectral vectors. Ambiguity results from the range of values of k_{12} and k_{21} satisfying equations (21) and (22) with $T'|K|=0.019$ and $T=17.2$ for this example. The possible spectral vectors are shown in Figures 3(d) and (e). Note that the resolved first component is not as distorted from noise as is the second component. Note also that although the second component is somewhat distorted by noise, possible identification can still be accomplished through location of excitation and emission peak maxima. The variation in ambiguity results from the extent of overlap of the two components. The transformation elements k_{12} and k_{21} may often have a relatively large range. However, regions of small ambiguities may exist due to the eigenvector associated with the other component having values close to zero in the affected region. Using Figure 2, one would have predicted a Type I overlap. However, the severe noise of this simulation caused some deviation.

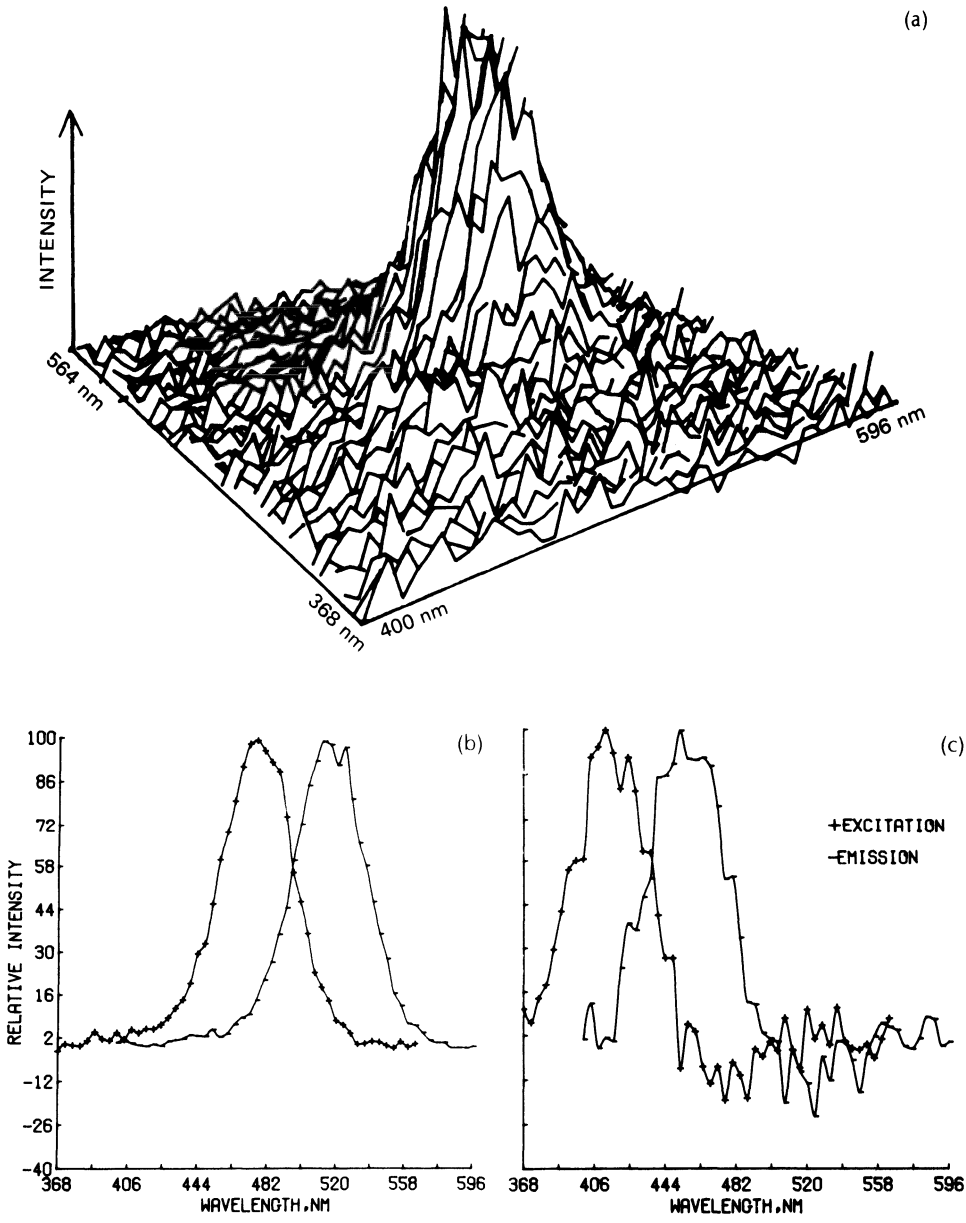

Figure 3. (a) Isometric projection of simulated two-component mixture. (b) First eigenvectors. (c) Second eigenvectors. (d) The derived spectra of component 1 (Absolute intensity = 100 photons). (e) The derived spectra of component 2 (Absolute intensity = 20 photons). (f) The resynthesized data containing only the first two components. [Reprinted with permission from *Anal. Chem.*, **49**, 564 (1977).]

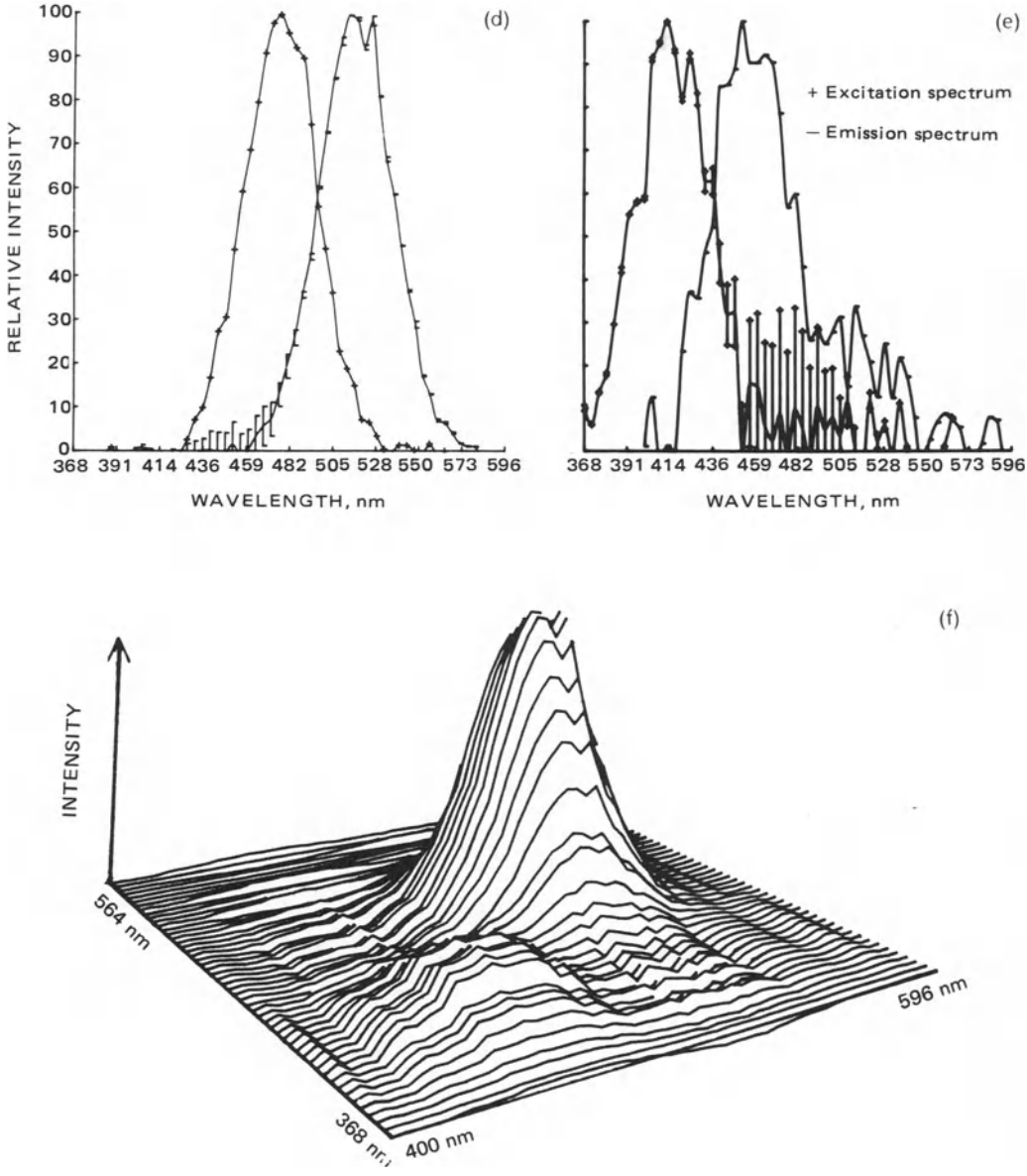

Figure 3. (*continued*).

4. Resynthesization. Figure 3(f) shows the resynthesized mixture matrix obtained by using only the first two basis vectors. Using this matrix, evaluation of the conclusion that the matrix is of rank 2 can be made. Subtraction of this matrix from the original matrix should produce only a random noise matrix.

The next simulation was designed to demonstrate the usefulness and accuracy of the ambiguity table provided in Figure 2. In this experiment, the emission and excitation spectra of the five aromatic hydrocarbons: perylene, anthracene, chrysene, pyrene, and fluoranthene were digitized. The fluorescence emission excitation matrix of ten binary mixtures of these compounds was obtained. No noise was added to the data since only the inherent ambiguity of the eigenvector transformation was being evaluated. The synthesized data were then submitted to the eigenanalysis program and the ambiguity of deconvoluted spectra was evaluated and compared to the predictions of Figure 2. Table 4 shows the nonzero spectral range of our five compounds. Experimental results agree with the prediction of Figure 2 in all cases. As examples, Figures 4(a), (b), and (c) show the results of deconvoluting the mixtures perylene/pyrene, perylene/fluoranthene, and pyrene/chrysene. The correct spectrum is drawn as a continuous curve while the range of possible spectra are displayed as error bars. Note that in the pair perylene/pyrene, partial overlap exists in emission since the emission range of perylene is 418–538 nm and the emission range of pyrene is 354–526 nm. Similarly, partial overlap exists for the excitation spectra. This corresponds to a Type I overlap and there is no ambiguity as predicted. Similar reasoning shows that the pairs perylene/fluoranthene and pyrene/chrysene are a Type II and Type III overlap, respectively. Table 5 summarizes the results of this experiment. The s and t values are as defined previously.

3.4. Qualitative Analysis of Experimental Fluorescence Data

An experimental fluorescence emission-excitation matrix was obtained using the computerized fluorometer of Gouterman *et al.*[33] This binary system

Table 4. Nonzero Spectral Range of Five Aromatic Hydrocarbons[a]

Aromatic hydrocarbons	Emission range (nm)	Excitation range (nm)
Anthracene	362–502	290–382
Chrysene	354–534	290–362
Fluoranthene	370–546	290–394
Perylene	418–538	350–450
Pyrene	354–526	290–366

[a]Reprinted with permission from *Anal. Chem.*, **49** (4), 564 (1977). Copyright by the American Chemical Society.

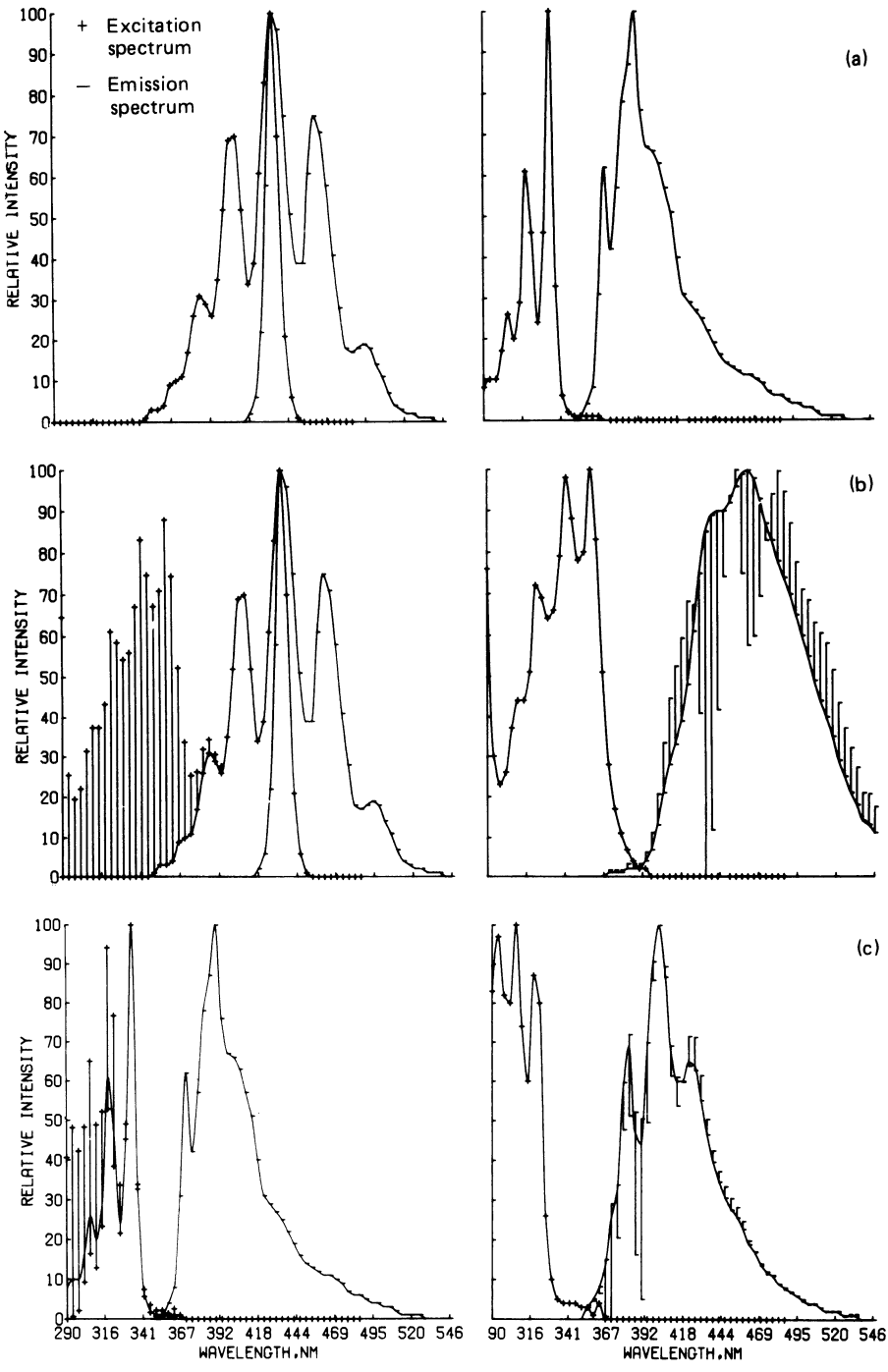

Figure 4. (a) Ambiguity of binary mixture of perylene and pyrene. (b) Ambiguity of binary mixture of perylene and fluoranthene. (c) Ambiguity of binary mixture of pyrene and chrysene.

Table 5. Spectral Ambiguity of Binary Mixtures of Aromatic Hydrocarbons[a]

Mixture	s/t values	Spectral overlap type
Anthracene/perylene	0.08/0.21	I
Perylene/pyrene	0.0006/0.24	I
Perylene/chrysene	0.0006/0.40	I
Perylene/fluoranthene	0.04/0.88	II
Chrysene/fluoranthene	0.50/0.48	II
Anthracene/fluoranthene	0.83/0.30	II
Pyrene/fluoranthene	0.59/0.31	II
Anthracene/pyrene	0.41/0.87	III
Anthracene/chrysene	0.23/0.92	III
Pyrene/chrysene	0.52/0.90	III

[a]Reprinted with permission from *Anal. Chem.*, **49** (4), 564 (1977). Copyright by the American Chemical Society.

corresponds to a mixture of the porphyrin compounds free-base octaethylporphin (H_2OEP) and zinc octaethylporphin (ZnOEP). An isometric projection of these data is shown in Figure 5(a). Note the diagonal signal with maxima at $\lambda_{ex} = \lambda_{em}$ contributed by scattered light. This interference and dark current were removed by running a solvent blank under conditions identical to the mixture matrix. This blank was then subtracted such that much of the scattered light was removed. It was found that it is not experimentally possible to substract out scattered light exactly using a solvent blank. However, for analysis purposes, it suffices to subtract enough of the scattered light such that the residual is below the noise level. Eigenanalysis of the pretreated matrix followed by eigenvector transformation produced the spectra shown in Figures 5(b) and (c). The deconvoluted spectrum is again drawn as a continuous curve while the range in ambiguity is depicted by error bars. Evaluation of spectral overlap would have indicated a Type II overlap as observed. The square roots of the first four eigenvalues of $\mathbf{MM}^t$ were 2790.2, 809.1, 167.8, and 87.6 indicating a rank 2 mixture. Much of the noise in this sample was associated with the scattered light region as displayed in the residual error matrix of Figure 5(d). For this example $T'|\mathbf{K}|$ had a value of 0.010 while T's value was 27.9.

4. Theory and Application of MFMDT in Quantitative Analysis of the FEEM

Section 3 of this chapter treated the case where the the components of the fluorescence emission–excitation matrix $\mathbf{M}$ are unknown. This section treats the circumstances where the components are all specified, but the amounts are unknown. This is quite often the analytical problem in routine analyses in chemical laboratories.

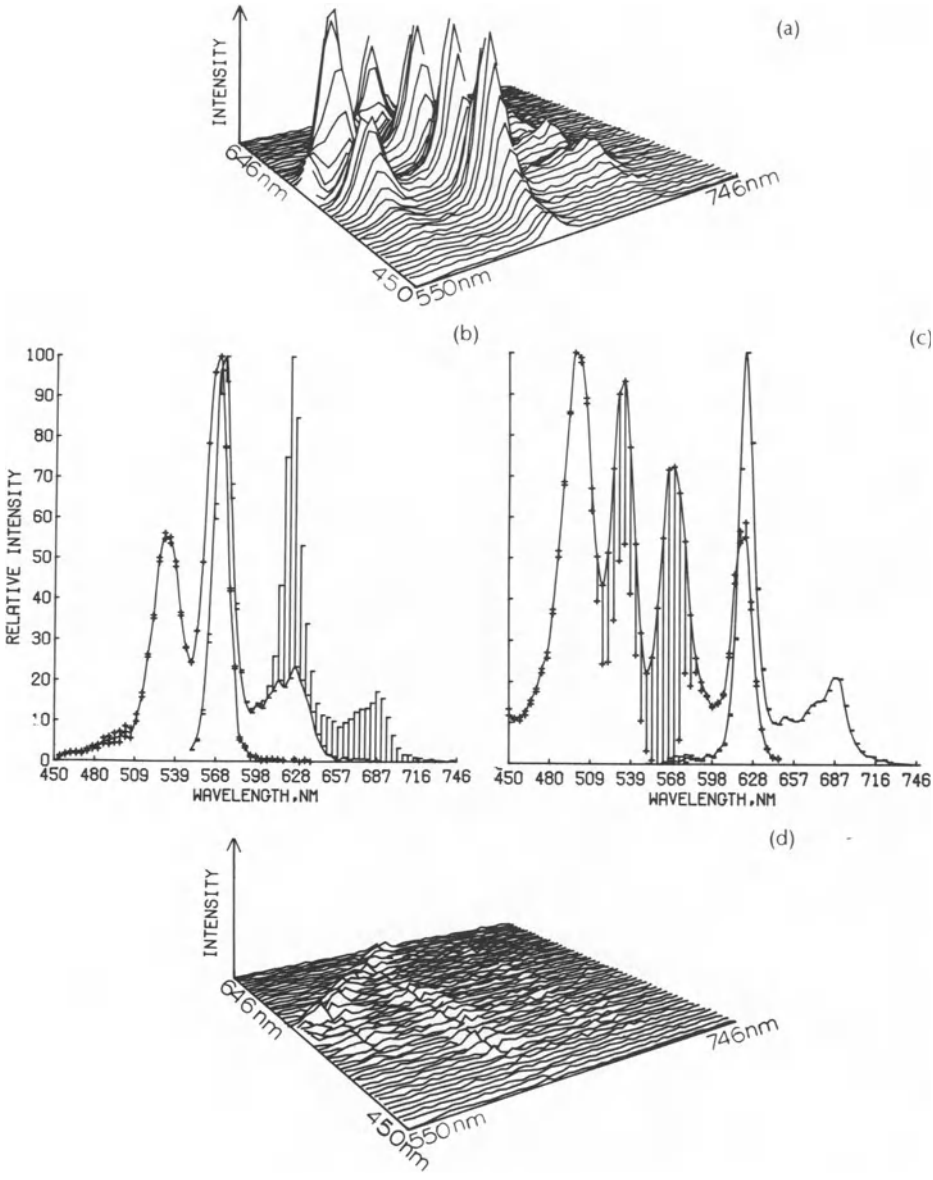

Figure 5. (a) Isometric projection of experimentally acquired two-component mixture of ZnOEP and H_2OEP. (b) Resolved two-dimensional spectra of component 1(ZnOEP). [Reprinted with permission from *Anal. Chem.*, **49**, 564 (1977).] (c) Resolved two-dimensional spectra of component 2(H_2OEP). [Reprinted with permission from *Anal. Chem.*, **49**, 564 (1977).] (d) Isometric projection of error matrix.

4.1. Theory of Least Squares Analyses of the FEEM

If the components of equation (7) are all specified, it is a simple procedure to run standard fluorescence emission–excitation matrices of each. In that case, one can represent equation (7) for n components as

$$\mathbf{M} = \sum_{i=1}^{n} c(i)\mathbf{M}(i) \tag{31}$$

where $\mathbf{M}(i)$ is the standard matrix produced by species i and $c(i)$ is its concentration divided by its standard concentration. Then the best approximation to $\mathbf{M}$, in the least squares sense, requires that the weighted sum of the squares of the elements of the error matrix $\mathbf{E}$ be a minimum. That is

$$\sum_{kl} t_{kl} e_{kl}^2 = \sum_{kl} t_{kl} \left(m_{kl} - \sum_{i} c(i) m(i)_{kl} \right)^2 = \min \tag{32}$$

where t_{kl} represent the weighting factors. To compute the minimum of $\Sigma_{kl} t_{kl} e_{kl}^2$, it is necessary to differentiate equation (32) and set the differential equal to zero to obtain the least squares condition:

$$\sum_{j} \left[\sum_{kl} t_{kl} m(i)_{kl} m(j)_{kl} \right] c(j) = \sum_{kl} t_{kl} m(i)_{kl} m_{kl} \tag{33}$$

where m_{kl} is the element in the kth row position and the lth column position of the observed fluorescence emission–excitation matrix. The parameters $m(i)_{kl}$ and $m(j)_{kl}$ are matrix elements of the standard fluorescence and emission–excitation matrices for the ith and the jth components. For n number of components, equation (33) can be expressed in matrix notation as

$$\mathbf{Wc} = \mathbf{p} \tag{34}$$

where $\mathbf{W}$ is an $n \times n$ matrix whose elements w_{ij} are given by

$$w_{ij} = \sum_{j} \left[\sum_{kl} t_{kl} m(i)_{kl} m(j)_{kl} \right]$$

The matrix $\mathbf{c}$ is an $n \times 1$ column vector containing the variables, $c(i)$ to be computed. The matrix $\mathbf{p}$ is an $n \times 1$ matrix whose elements p_i are given by $p_i = \Sigma_{kl} t_{kl} m(i)_{kl} m_{kl}$.

It should be obvious that equation (34) is of the form

$$\mathbf{Ax} = \mathbf{y}$$

i.e., a system of linear equations. The solution to equation (34) is then

$$\mathbf{c} = \mathbf{W}^{-1}\mathbf{p} \tag{35}$$

as discussed in Section 2.5 of this chapter. The parameter $\mathbf{W}^{-1}$ is the matrix inverse of the matrix $\mathbf{W}$ in equation (34).

If equation (31) were a mathematical identity, then the solutions to equations (33) would produce the correct $c(i)$'s. However, the measured fluorescence emission–excitation matrices contain random noise as we have discussed previously. Consequently, the calculated $c(i)$'s will be in error. It is desirable to compute the associated error as well as the $c(i)$'s. A calculation of the variance for $c(i)$ has been described[30] which assumes no error in the standard spectra and only error in the mixture spectra. This assumption is clearly invalid for most analytical data as well as the fluorescence emission–excitation matrices. Therefore, it is necessary to derive new formulas for computation of the variance of $c(i)$.

The unique variance of $c(i)$ contributed by the uncertainty in the experimentally measured matrix is given by

$$\sigma^2_{\text{mix}}\{c(i)\} = \sum \left(\frac{\partial c(i)}{\partial m_{kl}} \right)^2 \sigma^2_{(m_{kl})}$$

or

$$\sigma^2_{\text{mix}}\{c(i)\} = \sum_{kl} t^2_{kl} \left[\sum_r w^{-1}_{ir} m(r)_{kl} \right]^2 \sigma^2_{(m_{kl})} \tag{36}$$

where w^{-1}_{ir} are the elements of the inverse of W and $\sigma^2_{(m_{kl})}$ is the estimated variance of the klth element of the mixture matrix. The other terms have been previously defined in equation (33). A similar computation for the unique variance contributed by error in the standard matrices gives

$$\sigma^2_{\text{std}}\{c(i)\} = \sum \left(\frac{\partial c(i)}{\partial m(j)_{kl}} \right)^2 \sigma^2_{[m(i)_{kl}]}$$

or

$$\sigma^2_{\text{std}}\{c(i)\} = \sum_{kl} t^2_{kl} \sum_j \left[e_{kl} w^{-1}_{ij} - \left(\sum_r w^{-1}_{ir} m(r)_{kl} \right) c(j) \right]^2 \sigma^2_{[m(i)_{kl}]} \tag{37}$$

where $\sigma^2_{[m(j)_{kl}]}$ is the estimated variance of the klth element of the jth standard matrix. The total variance of the calculated $c(i)$'s is the sum of the individual

variances, i.e.,

$$\sigma^2_{\text{total}}\{c(i)\} = \sigma^2_{\text{mix}}\{c(i)\} + \sigma^2_{\text{std}}\{c(i)\} \tag{38}$$

For the least squares method the total variance will increase as the number of known components decreases. This is a result of the increase in variance contributed by uncertainty in the experimentally measured mixture matrix.

One final point should be made about the weighting factor t_{kl} in the least squares analysis. In analytical measurements, it is often found that the degree of uncertainty varies with the magnitude of the datum. In those cases, it is often advantageous to give certain data a higher degree of importance than others in determining the least squares fit to the data set. This process is termed "weighting" the data. It is important to correctly determine the weighting factors since different weights will give different answers. Our t_{kl}'s in equations (31)–(36) correspond to the weighting factors. For photon limited noise, the weights are usually the inverse of the magnitude of the signal.

4.2. Theory of Linear Programming Analyses (Simplex Method) of the FEEM

Quantitative analysis of the fluorescence emission–excitation matrix becomes more difficult if the components are not all specified. Suppose, for example, that the rank is large and only the standard spectrum $\mathbf{M}(1)$ is known. Then one can state that $m_{kl} - c(1)m(1)_{kl} \geqslant 0$ for all kl, where the terms are as defined previously. Since $c(1)$ cannot contribute negatively to m_{kl}, we can write

$$0 \leqslant c(1) \leqslant \min_{kl}\left[m_{kl}/m(1)_{kl}\right] \tag{39}$$

This will provide us with a range of possible values of $c(1)$. However, if there is any wavelength at which this fluorescing specie is the only emitter, then the minimum ratio of m_{kl} to $m(1)_{kl}$ will actually equal $c(1)$. Similarly, if two components are specified and the rank is large, then

$$m_{kl} - c(1)m(1)_{kl} - c(2)m(2)_{kl} \geqslant 0 \tag{40}$$

For the range of $c(1)$ and $c(2)$, we then have

$$\begin{aligned} 0 \leqslant c(1) &\leqslant \min_{kl}\left\{\left[m_{kl} - c(2)m(2)_{kl}\right]/m(1)_{kl}\right\} \leqslant \min_{kl}\left[m_{kl}/m(1)_{kl}\right] \\ 0 \leqslant c(2) &\leqslant \min_{kl}\left\{\left[m_{kl} - c(1)m(1)_{kl}\right]/m(2)_{kl}\right\} \leqslant \min_{kl}\left[m_{kl}/m(2)_{kl}\right] \end{aligned} \tag{41}$$

Again, under favorable conditions, our ratios may provide the actual values of $c(1)$ and $c(2)$.

Recently, C. N. Ho *et al.*[31] have described an alternative procedure for use when the components are not all specified. This approach uses the method of rank annihilation to determine the $c(i)$'s of the known components. Since this technique shows great promise in the cases where the components are not all specified, a brief description is given here. The rank n of the matrix $\mathbf{M}$ is determined by the number of nonzero eigenvalues of $\mathbf{M}'\mathbf{M}$, i.e., the number of eigenvalues not associated with noise. Obviously, one of the nonzero eigenvalues is associated with the known component. The technique of rank annihilation subtracts a multiple of the previously determined standard fluorescence emission–excitation matrix until the eigenvalue associated with the component disappears or minimizes. The matrix $\mathbf{M}$ is then effectively reduced to a matrix of rank $(n-1)$ and the multiple which minimizes the eigenvalue of the known is $c(1)$.

Under certain experimental conditions, it was found advantageous to employ a linear programming technique (the simplex method) rather than the conventional least squares. Linear programming is a series of mathematical techniques designed to optimize a certain linear function of unknown variables, subject to linear constraints (equalities or inequalities) that restrict the permissible values of the variables. The simplex method is one of these linear programming techniques. An excellent monograph by Noble[32] can be consulted for the general theory of linear programming and, in particular, the simplex method. Consider how a linear programming technique might relate to quantitative analyses of the fluorescence emission–excitation matrix. For instance, suppose that we have a mixture of n components of unknown concentrations and that we know the standard fluorescence emission–excitation matrix of r of them ($r \leqslant n$). Then, we can write a set of constraining equations in the form of

$$m(1)_{kl}c(1) + m(2)_{kl}c(2) + \cdots + m(r)_{kl}c(r) \leqslant m_{kl}$$

or

$$e_{kl} = m_{kl} - \sum_i c(i)m(i)_{kl} \geqslant 0 \tag{42}$$

where the symbols are as defined previously. It is possible to write an inequality in the form of equation (42) for each value of k and l. Thus, if our standard and mixture matrices have the shape $k \times l$, then "k times l" inequalities can be written. We have the additional inequalities

$$c(i) \geqslant 0 \tag{43}$$

since we should not obtain negative concentrations of our components. Then,

the linear programming problem is to maximize the expression

$$\Gamma = \sum_{i=1}^{r} a(i)c(i) \tag{44}$$

subject to the constraints of equations (42) and (43). The $a(i)$ coefficients of the $c(i)$'s must be a set of positive weights such that Γ is a maximum for the correct values of $c(i)$. The procedure used here is to sum the elements of the constraining equations such that

$$a(i) = \sum_{kl} m(i)_{kl} \tag{45}$$

In this manner, one tends to neutralize the random effects of noise in the data.

In practice, it is not always practical to use all "k times l" elements of the matrices to define the inequality constraints. For example, a "50×50" matrix would require 2500 inequalities in the form of equation (42). Thus, it is necessary to limit the number of constraining equations. We have previously indicated that the concentration of our known component is likely to be determined by a single ratio, such as $m_{kl}/m(1)_{kl}$. In the regions of our matrices where dark current is the major contributor, this ratio is essentially the ratio of two random numbers. Consequently, for the linear programming method, it is essential to use only regions of the matrices with good signal/noise ratios. The procedure used in this chapter was to divide each standard matrix into 5×5 submatrices. The 25 neighboring points in each submatrix were summed to produce a total of 36 possible $a(i)$ coefficients in equation (42) for a 30×30 matrix (100 for a 50×50 matrix). The five most intense regions from each standard were used to obtain the desired number of constraining equations by using the corresponding regions from the mixture matrix. Thus, for one-, two-, and three-component systems, five, ten, and fifteen constraining equations were used, respectively. This procedure selected regions of maximum signal/noise and reduced the wild fluctuations which would be produced by applying equation (42) in the region where **M** was entirely random.

4.3 Quantitative Analysis of Simulated Fluorescence Data

This section illustrates with some computer synthesized spectra the usefulness of the least squares and simplex approach to data reduction. Fluorescence and excitation spectra were obtained with a conventional fluorometer and absorption spectrophotometer. The data were then digitized point by point. In this manner, the spectra of nine aromatic hydrocarbons:

perylene, pyrene, anthracene, fluoranthene, chrysene, phenanthrene, fluorene, carbazole, and naphthalene were obtained. All of these compounds are significant environmental contaminants and suspect carcinogens.

A fluorescence emission–excitation matrix was formed for each component using the outer product of the digitized emission and excitation vectors. Figure 6 shows an isometric projection of the FEEM formed by a linear summation of the nine components. Photon noise was again simulated with a random number generator which produced Poisson distributed numbers.

Next, a least squares fit was performed to the FEEM according to equation (32) using as standard spectra the synthesized FEEM of each component. Table 6 lists the values of the imput concentrations, the calculated values, and the errors estimated using the method described in this chapter. This example illustrates that the least squares approach is very effective for quantitative analyses of a nine-component FEEM. Also included in Table 6 are the results of linear programming analyses of this mixture. Results comparable to those of the least squares method were obtained.

4.4. Quantitative Analysis of Experimental Fluorescence Data

The preceding section served to illustrate the potentials of the least squares and simplex method for quantitative analyses of the FEEM. However, there are certain questions such as the effect of energy transfer, reabsorption, linearity of fluorescence, etc., which can only be answered using experimental data. Therefore, these next series of experiments were designed to show the applicability of this quantitative approach to the analyses of experimental data. Data for analyses were acquired with the fluorometer of

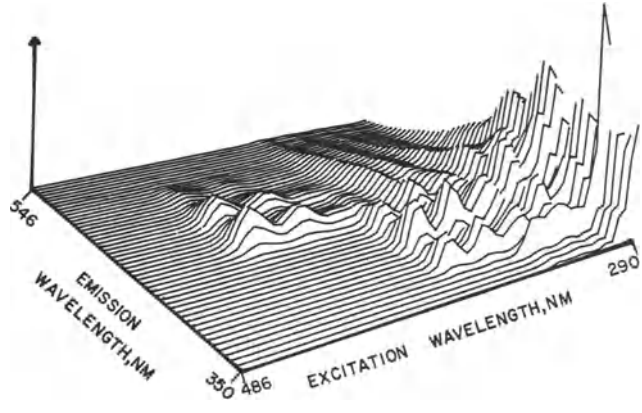

Figure 6. Simulated nine-component mixture of aromatic hydrocarbons.

Table 6. Quantitative Analyses of a Nine-Component Mixture

Component	Relative concentration	Least squares calculated concentration	Estimated SD	Simplex calculated concentration
Naphthalene	1.485	1.465	0.004	1.493
Carbazole	0.939	0.944	0.001	0.951
Fluorene	1.180	1.176	0.002	1.194
Phenanthrene	1.376	1.383	0.002	1.356
Anthracene	1.311	1.309	0.001	1.303
Pyrene	0.678	0.678	0.002	0.693
Chrysene	1.406	1.407	0.001	1.396
Perylene	0.899	0.900	0.001	0.886
Fluoranthene	0.568	0.568	0.001	0.566

Gouterman *et al.*[33] The data were acquired using the detector in the photon counting mode rather than the standard PMT mode used for the qualitative data analyses. Using this computerized instrument, standard FEEM's were obtained from previously prepared samples of known concentration using spectral grade pyridine as a solvent. Data was obtained in 6 nm intervals over a wavelength range in excitation of 470–644 nm and 550–724 nm in emission. Mixture samples were also prepared with the same stock solutions, giving mixtures of known composition,, and the FEEM was run under conditions as close to those of the standard samples as possible. The total absorbance at all wavelengths of interest was kept below 0.01. A noise matrix including scattered light and dark current was also run under the same conditions. A multiple of this matrix was subtracted from the mixture and standard matrices. The standard matrices were then smoothed by decomposition into the row and column eigenvectors according to equation (9) in Section 3.2 of this chapter.

Three sets of experiments were run corresponding to mixtures of one-, two-, and three-component systems. The first experiment was designed to show the linearity of the fluorescence intensity. Five mixtures of free base octaethylporphin (H_2OEP) were prepared at the various concentrations indicated in Table 7. The matrices were obtained over the range previously indicated giving a 30×30 matrix of 900 data points. Table 7 displays the results of these analyses using both the least squares and simplex method. A correlation curve of these data obtained by plotting volumetrically determined concentration versus calculated concentration gave a correlation coefficient of 0.9997. It is clear from these results that the fluorescence is linear and reabsorption and quenching processes are negligible under the conditions of this investigation.

The next system analyzed was a binary mixture of free base octaethylporphin (H_2OEP) and free base tetraphenylporphin (H_2TPP). There are considerable similarities between the emission and excitation spectra of these

Table 7. Least Squares and Simplex Analyses of Experimental Single Component (H_2OEP)

Input concentration (10^{-7}M)	Least squares calculated concentration (10^{-7}M)[a]	Estimated SD (10^{-7}M)	Simplex calculated concentration (10^{-7}M)[a]
1.51	1.43	0.04	1.30
2.76	2.79	0.18	2.58
5.52	5.52	0.10	5.40
11.00	11.10	0.60	10.58

[a]Calculated using the presmoothed standard spectrum of a 5.52×10^{-7}M standard.

two components. Figures 7(a), (b), and (c) show the presmoothed standard matrix of H_2OEP, H_2TPP, and the mixture matrix with the dark current and most of the scattered light subtracted. These matrices were obtained over the same wavelength region and interval as the single-component matrices in the previous discussion. Least squares and simplex fitting the presmoothed standard matrices to the mixture matrix produced the results shown in Table 8. The error in the calculated concentrations of H_2OEP and H_2TPP are 2 and 7%, respectively. These results are clearly satisfactory when one considers that each matrix is acquired in a time frame of 20 min. Dark current drift and lamp fluctuations would certainly affect the results obtained over such a time period.

The final investigation involved a ternary system of zinc octaethylporphin (ZnOEP), tin (IV) dichloro octaethylporphin ($SnCl_2OEP$), and H_2OEP. Since the ZnOEP and $SnCl_2OEP$ differed by only 3 or 4 nm in excitation, this system was obtained over a narrower wavelength interval. The excitation wavelength varied from 450 to 646 nm in 4 nm intervals and the emission varied from 550 to 746 nm in 4 nm intervals. Thus, a 50×50 matrix of 2500 data points was obtained for the mixture matrix and each standard matrix. This increased the data acquisition time to 1 hr for each matrix. Figures 8(a), (b), and (d) provide an isometric projection of the presmoothed standard matrices and the mixture matrix. Results of the analysis of this mixture are found in Table 9. Except for the 13% error in the calculated concentration of $SnCl_2OEP$, the results are satisfactory. The error in the $SnCl_2OEP$ concentration could be attributed to the severe overlap of the two components. However, the analyses of other systems point toward instrumental fluctuations as the cause of the error.

Finally, in the systems analyzed above the simplex method tended to give results somewhat lower, but comparable to the least squares results. Other experiments have shown that the selection of inequalities along with the simplex method provides better results than the least squares method when the components are not all specified. For example, Table 10 shows the results of analyzing the H_2OEP and H_2TPP binary mixture of Table 8 assuming

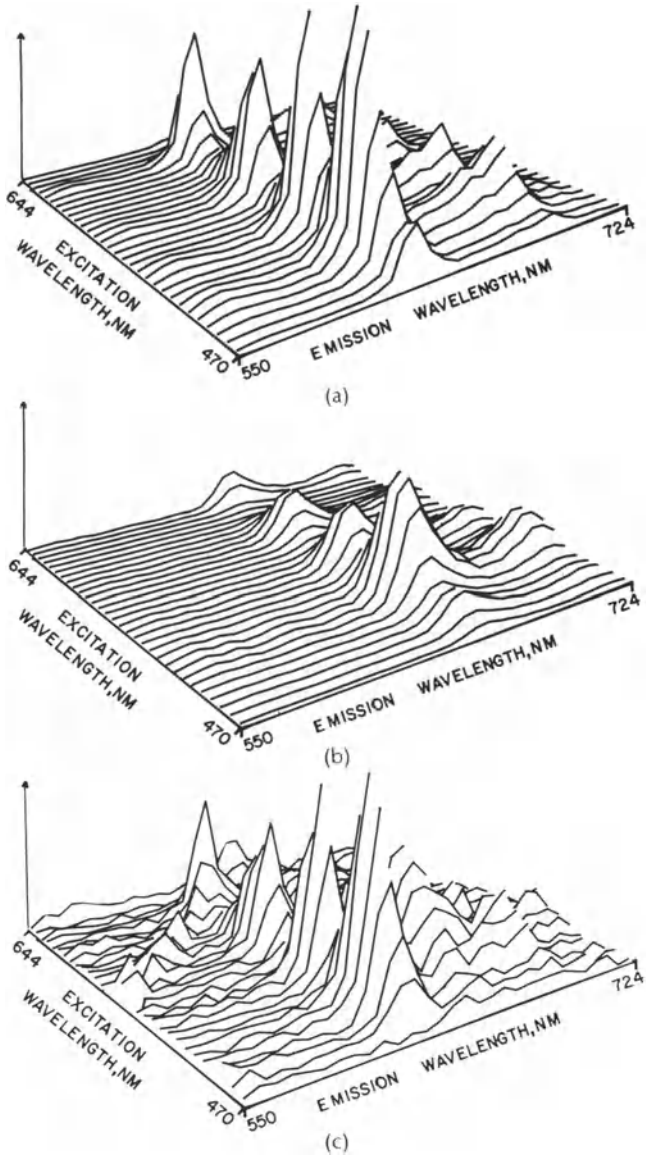

Figure 7. (a) Presmoothed H_2OEP standard with scattered light and dark current removed. (b) Presmoothed H_2TPP standard matrix. [Reprinted with permission from *Anal. Chem.*, **49**, 2155 (1977).] (c) Mixture matrix (H_2OEP and H_2TPP) with scattered light subtracted (data collected at 6 nm increments). [Reprinted with permission from *Anal. Chem.*, **49**, 2155 (1977).]

Table 8. Least Squares and Simplex Analyses of the Experimental Mixture of H_2OEP and H_2TPP

Analyte	Input concentration (10^{-7}M)	Least squares calculated concentration (10^{-7}M)[a]	Estimated SD (10^{-7}M)	Simplex calculated concentration (10^{-7}M)[a]
H_2OEP	6.21	6.26	0.19	5.96
H_2TPP	5.76	6.16	0.24	5.72

[a]Calculated using the presmoothed standard spectra of 6.21×10^{-7}M H_2OEP and 5.76×10^{-7}M H_2TPP.

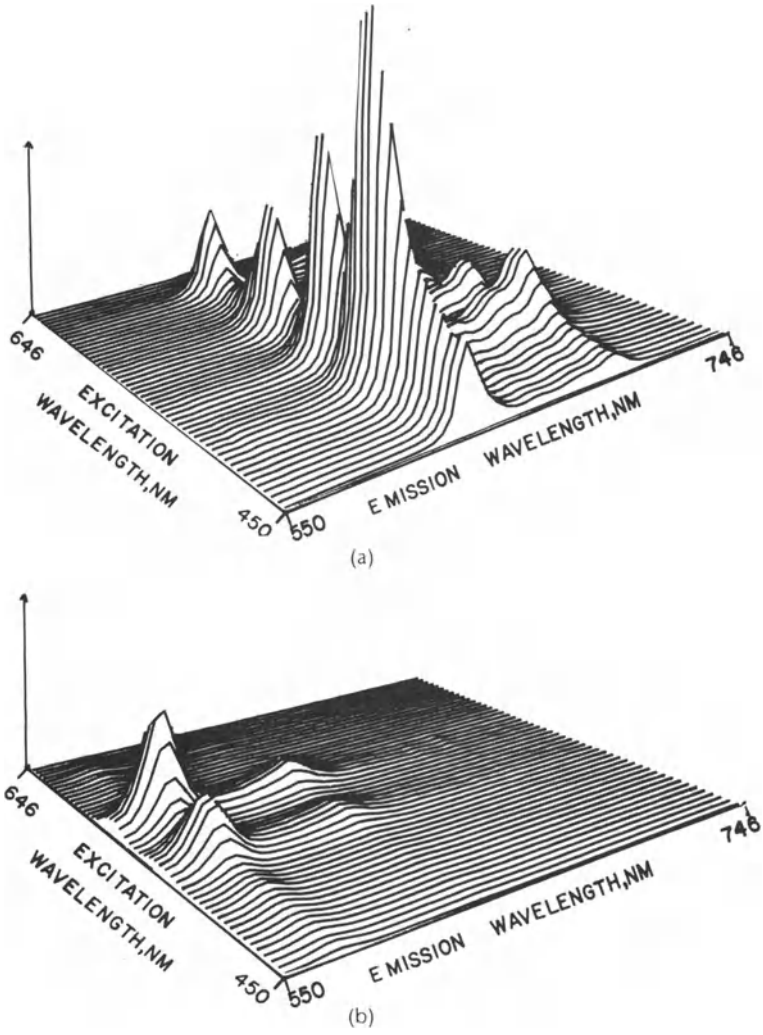

Figure 8. (a) Rank 1 H_2OEP standard matrix. (b) Rank 1 ZnOEP standard matrix. (c) Rank 1 $SnCl_2OEP$ standard matrix. (d) Mixture matrix with scattered light removed (data collected at 4 nm increments). [Reprinted with permission from *Anal. Chem.*, **49**, 2155 (1977).]

that only the H_2OEP is present in the mixtures. Since the least squares method requires that the sum of the residuals be zero, the least squares method is expected to give high results. On the contrary, the simplex method requires only that the residual matrix be nonnegative and one would expect better results using this method. These expections are clearly realized from the results of Table 10. Assuming only H_2OEP present, the least squares method gave results 11% higher and the simplex method produced results 3% lower. Clearly, the simplex method is better than the least squares method in this example when all components are not known.

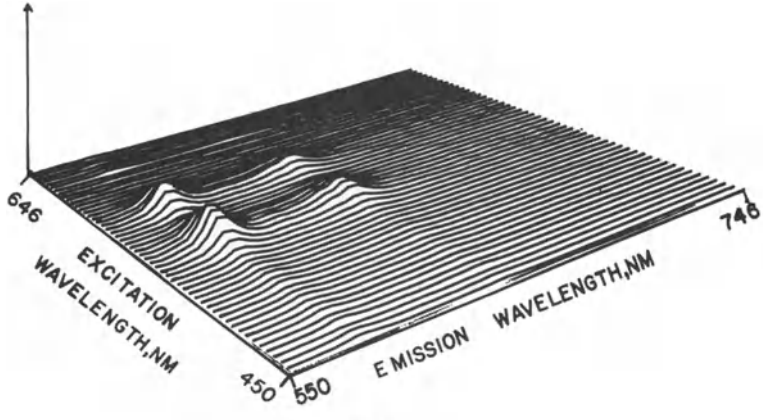

(c)

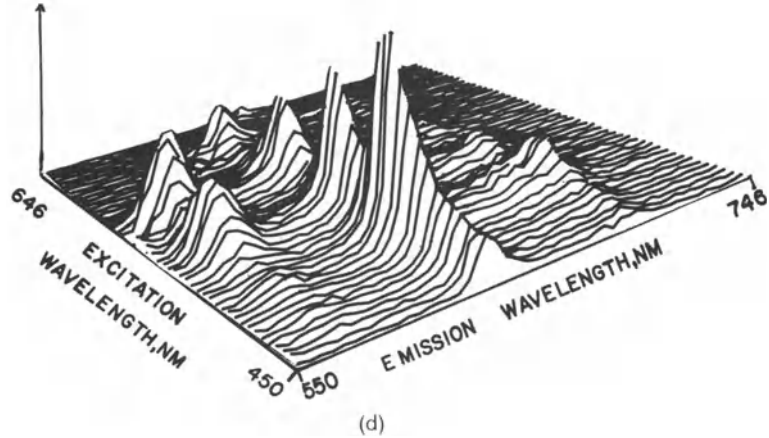

(d)

Figure 8. (*continued*).

Table 9. Least Squares and Simplex Analyses of Experimental Mixture of H_2OEP, $SnCl_2OEP$, and ZnOEP

Analyte	Input concentration (10^{-7}M)	Least squares calculated concentration (10^{-7}M)[a]	Estimated SD (10^{-7}M)	Simplex calculated concentration (10^{-7}M)[a]
H_2OEP	2.42	2.46	0.02	2.38
ZnOEP	21.4	21.6	0.5	21.0
$SnCl_2OEP$	3.04	3.44	0.23	3.22

[a]Calculated using the presmoothed standard spectra of 4.83×10^{-7}M H_2OEP, 2.14×10^{-6}M ZnOEP, and 6.07×10^{-7}M $SnCl_2OEP$

Table 10. Least Squares and Simplex Analysis of Experimental Mixture of H_2OEP and H_2TPP, Assuming That Only H_2OEP is Present

Analyte	Input concentration (10^{-7}M)	Least squares calculated concentration (10^{-7}M)[a]	Estimated SD (10^{-7}M)	Simplex calculated concentration (10^{-7}M)[a]
H_2OEP	6.21	6.89	0.32	6.02

[a]Same standard as in Table 8.

5. Summary and Conclusion

5.1. Effectiveness of MFMDT for Analysis of Multicomponent Fluorescence Data

The effectiveness of any mathematical technique can only be determined by the extent to which it accomplishes the tasks for which it was designed. Consequently, let us briefly review the goals set or the MFMDT. In the initial discussion of this chapter, it was stated that the MFMDT evolved as a result of data reduction requirements of a new rapid scanning fluorometer. It was further specified that the new algorithm had to provide information about (a) the number of fluorescent molecules contributing to the spectra, (b) the composition of the solution, when the spectra of standardized solutions are known, and (c) the absorption and emission spectra of each fluorescent species present in solution. Consider the effectiveness of MFMDT for the analyses of the fluorescence emission–excitation matrix **M** in the order in which we have listed the requirements.

1. Information about the number of fluorescent molecules contributing to the spectra. It was shown that the rank of $\mathbf{M}^t\mathbf{M}$ is a direct indication of the minimum number of fluorescing components contributing to **M**. Using the MFMDT, we were able to determine the number of eigenvalues of $\mathbf{M}^t\mathbf{M}$. If **M** were ideal,

the number of nonzero eigenvalues would indicate the rank of **M**. However, since **M** has noise, there is the problem of discriminating those eigenvalues associated with noise and those associated with the fluorescing components. In many cases, there is a clear distinction between the noise and component eigenvalues. In those cases the MFMDT can accurately determine the minimum number of fluorescing molecules contributing to the spectra.

2. The composition of the solution when the spectra of standardized solutions are known. The MFMDT uses least squares and linear programming for quantitative analysis of **M**. When all of the components are specified, both techniques tend to give comparable results. However, the linear programming method was found to give better results when all components are not specified and in the presence of instrumental fluctuations.

3. The absorption and emission spectra of each fluorescent specie present in solution. The MFMDT is limited in its capacity to handle this requirement. If the sample contains one or two components, then it is possible to derive possible spectra using the eigenvectors of $\mathbf{M}^t\mathbf{M}$ and $\mathbf{M}\mathbf{M}^t$. For a two component system, there is some degree of ambiguity. However, much of this ambiguity can be eliminated through *a priori* knowledge of the spectral overlap of the components.

In conclusion, it is reasonable to conclude that the MFMDT has satisfied much of the data reduction requirements for the rapid scanning fluorometer. However, there is still considerable room for improvement and expansion which will be discussed in the next section.

5.2. Expansion and Future Application of MFMDT

There are some obvious needs which exist for the expansion of our algorithms. First, we have to develop more reliable methods for determining the rank of **M**. There are statistical procedures for determining the rank of random matrices which need to be investigated. Methods of reducing the noise in the matrix **M** would also be helpful in the determination of the rank. We are currently investigating the use of multiplexing techniques to improve the signal/noise ratio of **M**.

Second, the reliability of the quantitative algorithms in the presence of instrumental fluctuations needs to be studied. Using a conventional fluorometer, many problems such as dark current drift and lamp fluctuations were encountered before reasonably good data could be obtained. Furthermore, improvements need to be made in the quantitative procedures when all of the components are not specified. The work of C. N. Ho *et al.*[31] is a significant step in this direction.

Third, the qualitative algorithms for extracting the absorption and emission spectra need to be expanded to more than two components. This is,

in principle, straightforward. However, as we indicated earlier, for more than two components, the elements of $|\mathbf{K}|(\mathbf{K}^{-1})^t$ are nonlinear with respect to the elements of $\mathbf{K}$. Consequently, the transformation of eigenvectors to spectral vectors requires an iterative procedure. Moreover, it is expected that the ambiguity of spectral transformation will increase with the number of components.

Finally, a wide range of applications is seen for the algorithms of the MFMDT. Since these algorithms were initially developed for the interpretation of spectral data, it is expected that the immediate applications will continue in the area of spectroscopy. One can easily conceive of using these techniques to analyze and interpret time–emission matrices, time–absorption matrices, concentration–emission matrices, and concentration–absorption matrices to name a few. In theory, any matrix which can be represented in the form of equation (7) can be analyzed by the MFMDT.

6. Appendices

6.1. Fortran Subroutines for Qualitative Analysis

```
C     SUBROUTINE EIGEN
C  IN THE FOLLOWING A ' IMMEDIATELY FOLLOWING THE NAME
C  OF A MATRIX DENOTES THE TRANSPOSE OF THAT MATRIX.
C  THIS SUBROUTINE IS FOR QUALITATIVE ANALYSIS OF
C  ONE OR TWO COMPONENT MIXTURES USING THE EIGENVALUES AND EIGENVECTORS
C  OF THE MIXTURE MATRIX. FOR EXPLANATION SEE SECTION 3.1 OF THIS CHAPTER.
      SUBROUTINE EIGEN (OM,NOT,IRX,IRY,U,V,EPS,INC,INCREM,IGEN)
C  INC,OM,NOT,IRX AND IRY ARE THE # OF COMPONENTS, THE MIXTURE MATRIX,
C  THE TOTAL # OF DATA POINTS, NUMBER OF EMISSION
C  WAVELENGTHS AND THE NUMBER OF EXCITATION
C  WAVELENGTHS, RESPECTIVELY.
C  U AND V ARE STORAGE ARRAYS FOR THE EIGENVECTORS. (THE DEFINITIONS OF THESE
C  ARRAYS WERE INADVERTENTLY INTERCHANGED FROM TEXT DISCUSSION).
C  EPS IS THE NOISE THRESHOLD EIGENVALUE.
C  ALL EIGENVALUES BELOW EPS ARE ASSUMED TO BE
C  CONTRIBUTED BY NOISE AND THE NUMBER ABOVE DETERMINES
C  THE RANK OF OM.
      DIMENSION OM(NOT),U(IRX,INC),V(IRY,INC)
      COMMON/SCRATCH/W(1325),X(50,50),T(2500),R(50),S1(50),S2(50)
      REAL NEGMAX,POSMAX
      DATA POSMAX/Z7FFFFFFF/
      DATA NEGMAX/ZFFFFFFFF/
C  W IS THE MATRIX OF "OM'OM"; SINCE THIS MATRIX
```

```
C  IS SYMMETRICAL, ONLY THE ELEMENTS ON AND ABOVE THE
C  MAIN DIAGONAL NEED TO BE STORED.
C  CONSEQUENTLY,IGEN=(IRX*(IRX+1))/2. T IS THE MATRIX OF "IRX"
C  EIGENVECTORS STORED BACK TO BACK. R IS THE
C  SET OF EIGENVALUES.
C  SET UP "OM" AS AN ARRAY "X" OF DIMENSION IRY BY IRX.
C
C  POSMAX &NEGMAX ARE RESPECTIVELY THE LARGEST POSITIVE &
C                 NEGATIVE FLOATING POINT NUMBERS THAT
C                 CAN BE STORED ON THE AMDAHL.
C
      LL=0
      DO 100 I=1,IRY
      DO 110 J=1,IRX
      LL=LL+1
      X(I,J)=OM(LL)
110   CONTINUE
100   CONTINUE
      N=IRX
      M=IRY
C  COMPUTE THE SQUARE MATRIX X'X AND STORE IN "W" USING
C  SUBROUTINE MULT.
      J=-1
      K=-1
      L=1
      CALL MULT (W,X,N,M,X,N,M,J,K,L)
C  FIND THE EIGENVALUES AND EIGENVECTORS OF W AND STORE IN R AND T,
C  RESPECTIVELY, USING THE FOLLOWING SUBROUTINES
      IJOB=2
      CALL XEIGRS(W,N,IJOB,R,TN,PERINX,IER)
C  THE EIGENVALUES ARE RETURNED BY XEIGRS ORDERED FORM LARGEST
C  TO SMALLEST. THE EIGENVALUES ARE STORED IN "R"; THE ASSOCIATED
C  EIGENVECTORS ARE STORED IN "T" IN THE SAME ORDER.
C  (NOTE: EACH EIGENVECTOR IS STORED IN T AS A COLUMN VECTOR.)
C  SINCE,AS DISCUSSED IN SECTION 3.1, THE SQUARE ROOT OF THE
C  EIGENVALUES GIVE THE RELATIVE EIGENVECTOR CONTRIBUTION IN
C  "OM", OBTAIN THE SQUARE ROOT OF EIGENVALUES.
C  DETERMINE RANK BY COMPARING WITH EPS.
C  OVERLOOK ANY NEGATIVE EIGENVALUES.
      IR=0
      DO 130 I=1,N
```

```
      IF(R(I).GT.0)R(I)=SQRT(R(I))
      IF(R(I).GT.EPS) IR=IR+1
130   CONTINUE
C  WRITE OUT THE RANK AND VALUE OF THE EIGENVALUES
      WRITE(6,*) IR,R
C  IF THE RANK IS GREATER THAN 5, LOOK AT ONLY THE TOP FIVE
C  COMPONENTS FIRST
      IF(IR.GT.5)IR=5
C  STORE THE EIGENVECTORS IN U.
      K=1
      DO 140  I=1,IR
      DO 150 J=1,N
      U(J,I)=T(K)
      K=K+1
150   CONTINUE
140   CONTINUE
C  OBTAIN THE COLUMN VECTORS BY
C  V=MU' AND STORE IN V.
      J=1
      K=1
      L=-1
      CALL MULT(V,X,N,M,U,N,IR,J,K,L)
C  IF THE RANK IS NOT EQUAL TO 2,WRITE OUT
C  THE FEEM'S FOR EACH COMPONENT. IF THE RANK EQUALS
C  TWO, FIND THE POSSIBLE SPECTRAL VECTORS ACCORDING
C  TO EQUATION 21 AND 22 IN SECTION 3.1 FIRST INITIALIZE
C  THE RANGES TO +/-INFINITY. B IS THE SAME AS K(I,U)
C  AND A IS IDENTICALLY EQUAL TO K(U,I) OF EQUATION 16.
      IF(IR-2) 21,22,23
22    CONTINUE
      BH=POSMAX
      BL=NEGMAX
      AH=POSMAX
      AL=NEGMAX
      DO 160 I=1,N
      IF (U(I,2).EQ.0.)GO TO 160
      IF(U(I,2).LT.0.) GO TO 170
      IF(U(I,1).GE.0)BH=AMIN1(BH,U(I,1)/U(I,2))
170   CONTINUE
160   IF(U(I,1).GT.0.)AL=AMAX1(AL,-U(I,2)/U(I,1))
      DO 180 I=1,M
      IF(V(I,2).EQ.0) GO TO 180
```

```
      IF(V(I,2).LT.0.)GO TO 190
      IF(V(I,1),GE.0) AH=AMIN1(AH,V(I,1)/V(I,2))
190   CONTINUE
180   IF(V(I,1)GT.0)BL=AMAX1(BL.-V(I,2)/V(I,1))
C  WRITE OUT AL,AH,BL,ANDBH
      WRITE(6,*) AL,AH,BL,BH
C  IF IT IS IMPOSSIBLE TO TRANSFORM THE EIGENVECTORS
C  USING  T=T⁻¹K⁻¹=IDENTICALLY 0, THEN CALL ALTERN WHICH
C  USES AN INCREMENTAL THRESHOLD.
      IF(AL.GT.AH.OR.BL.GT.BH) CALL ALTERN (U(1,2)
     1,U(1,1),V(1,1),V(1,2),N,M,AL,AH,BL,BH,R,INCREM)
C  IF NO INFORMATION IS KNOWN ABOUT THE SPECTRAL OVERLAP
C  BETWEEN THE COMPONENTS, USE THE MEDIAN VALUES OF "B" AND "A"
C  TO CALCULATE THE SPECTRAL VECTORS .
      AM=0.5*(AL+AH)
      BM=0.5*(BL+BH)
C  FIND THE DETERMINAT OF K AND WRITE IT OUT ALONG WITH AM AND
C  BM
      CM=1+AM*BM
      WRITE(6,*) CM,AM,BM
C  CALCULATE THE ASSUMED SPECTRAL VECTORS AND STORE IN U AND V
      DO 200 I=1,N
      Q=U(I,2)+AM*U(I,1)
      U(I,1)=U(I,1)-BM*U(I,2)
200   U(I,2)=Q
      DO 210   I=1,M
      Q=(V(I,2)+BM*V(I,1))/CM
      V(I,1)=(V(I,1)-AM*V(I,2))/CM
210   V(I,2)=Q
C  CALL SUBROUTINE TWODIM WHICH GIVES A TWO DIMENSIONAL PLOT OF THE EIGENVECTORS
C  AND COMPUTED SPECTRAL VECTORS.
C              PLOT    THE SPECTRAL VECTORS AND THE
C  RANGE OF POSSIBLE SPECTRAL VECTORS FOR EACH COMPONENT
      CALL TWODIM(AL,AH,AM,BL,BH,BM,U(1,1),U(1,2),
     1V(1,1),V(1,2))
23    CONTINUE
21    CONTINUE
C  WRITE OUT THE COMPONENTS FOUND
      DO 240 IP=1,IR
      DO 220 I=1,M
      DO 230 J=1,N
      X(I,J)=U(J,IP)*V(I,IP)
```

```
230   CONTINUE
      WRITE(6,912)(X(I,J),J=1,N)
220   CONTINUE
240   CONTINUE
912   FORMAT(2HOC,10F7.1/(2X10F7.1))
C  RESYNTHESIZE MIXTURE MATRIX AND WRITE IT OUT
      DO 250 I=1,M
      DO 260 J=1,N
      X(I,J)=0
      DO 270 IP=1,IR
270   X(I,J)=X(I,J)+U(J,IP)*V(I,IP)
260   CONTINUE
      WRITE(6,911)(X(I,I),J=1,N)
250   CONTINUE
911   FORMAT(2HOX,10F7.1/(2X10F7.1))
      RETURN
      END
C               SUBROUTINE* ALTERN
C  THROUGHOUT ´ FOLLOWING THE LETTER FOR A MATRIX DENOTES TRANSPOSE.
      SUBROUTINE ALTERN (U2,U1,V1,V2,N,M,AL,AH,BL,BH,RR,INCREM)
      DIMENSION U2(N),U1(N),V1(M),V2(M),RR(N)
      REAL POSMAX,NEGMAX
      DATA POSMAX/Z7FFFFFFF/
      DATA NEGMAX/ZFFFFFFFF/
C   TN CORRESPONDS TO T IN  EQUATIONS (17-18) AND TNV IS IDENTICALLY T ´  IKI.
      TN=0.
C  SINCE U IS NORMALIZED TO "1",TN CAN NEVER BE
C  GREATER THAN "1". IF TN EXCEEDS "1", QUIT AND  WRITE
C  OUT COMPUTED VALUES OF TN,TNV,BL,BH,AL,AND AH.
200   CONTINUE
      IF(TN.GT.1.) GO TO 30
C  COMPUTE NEW VALUES OF BL,BH,AL,AND AH BASED
C  ON INCREMENTS OF 0.001 OR ACCURACY DESIRED
72    CONTINUE
      GH=POSMAX
      BL=NEGMAX
      AH=POSMAX
      AL=NEGMAX
      TN=TN+INCREM
C  INCREM IN THE ABOVE STATEMENT IS EITHER 0.001
C  OR THE ACCURACY DESIRED
      TNV=RR(1)*TN
      DO 160 I=1,N
```

```
      IF(U2(I).EQ.0.) GO TO 160
      IF(U2(I).LT.0.) GO TO 170
      IF(U1(I).GE.0.) BH=AMIN1(BH,(TN+U1(I))/U2(I))
170   CONTINUE
160   IF(U1(I).GT.0)AL=AMAX1(AL,(TN+U2(I))/U1(I))
      DO 180 I=1,M
      IF(VI(I).EQ.0) GO TO 180
      IF(V2(I).LT.0.) GO TO 190
      IF(V1(I).GE.0.)AH=AMIN1(AH,(TNV=V1(I))/V2(I))
190   CONINTUE
180   IF(V1(I).GT.0)BL=AMAX1(BL,-(TNV+V2(I))V1(I))
C  IF BL IS GREATER THAN BH OR AL GREATER  THAN AH,
C  INCREMENT  AGAIN AND COMPUTE AL,AH,BL, AND BH
      IF(BL.GT.BH.OR.AL.GT.AH) GO TO 200
30    CONTINUE
C  WRITE OUT COMPUTED VALUES
      WRITE(6,*)  TN,TNV,BL,BH,AL,AH
      RETURN
      END
```

6.2. Fortran Subroutines for Quantitative Analysis

```
C
C                  SUBROUTINE LSQUAR
C
C  THIS SUBROUTINE IS FOR THE ANALYSIS OF MULTI-
C  COMPONENT FLUORESCENCE DATA BY THE METHOD OF LEAST SQUARES.
C  THE DESCRIPTION BELOW IS FOR THE ANALYSIS OF EXPERIMENTAL
C  DATA. THE FIRST SUBROUTINE SETS UP THE NECESSARY ARRAYS.
       SUBROUTINE LSQUAR(IRX,IRY,INC,OM,SM,NOT,ITO,W,C,
     1X,T,V,Z,WT,S,P,UNITWT)
C  UNITWT IS A PARAMETER THAT WHEN SET EQUAL TO 1
C  INDICATES THAT WE DESIRE FOR THE WEIGHT MATRIX,
C   WT, TO BE SET EQUAL TO UNITY, RATHER THAN THE
C  RECIPROCAL OF THE MAGNITUDES OF THE NUMBERS FED IN.
C
       DIMENSION OM(NOT),SM(ITO,INC),C(INC),W(INC,INC),
     1Z(IRX),V(IRY),X(NOT),WT(NOT),S(NOT),T(NOT),P(INC),
     1R(50),S1(50),S2(50),WI(1325)
C  IN THE ABOVE DIMENSION STATEMENT ,OM,SM,NOT,INC,ITO
C  IRX,AND IRY ARE THE MIXTURE MATRIX, STANDARD MATRICES STORED
C  BACK TO BACK AS EMISSION AND EXCITATION
```

```
C  VECTORS,TOTAL # OF DATA POINTS, #
C  OF COMPONENTS, SUM OF THE # OF
C  EMISSION AND EXCITATION WAVELENGTHS,
C  NUMBER OF EMISSION WAVELENGTHS AND
C  THE NUMBER OF EXCITATION WAVELENGTHS,
C  RESPECTIVELY.  W,C, AND P ARE THE MATRICES DEFINED
C  BY EQUATION 33. Z AND V ARE THE
C  ROW AND COLUMN EIGENVECTORS OF MM'. WT IS THE
C  MATRIX OF WEIGHT FACTORS AND T IS THE ARRAY
C  FOR TEMPORARY STORAGE OF THE EIGENVECTORS. R IS
C  THE ARRAY OF EIGENVALUES. S IS THE SCATTERED LIGHT ARRAY.
C  X,S1 AND S2 ARE SCRATCH ARRAYS.  WI AND MSZ ARE DEFINED
C  TO BE THE MATRIX OF MTM AND MSZ IS THE SIZE OF THE
C  ARRAY WI. SINCE WI IS SYMMETRICAL, ONLY THE DIAGONAL
C  AND THE ELEMENTS ABOVE THE
C  DIAGONAL NEED BE STORED. CON-
C  SEQUENTLY, IGEN = (IRX* (IRY+1))/2.
C  NOW CALL EXPT WHICH SETS UP THE EXPERIMENTAL
C  DATA IN PROPER FORMAT FOR DATA ANALYSIS. FR IS A CONSTANT
C  FOR CONVERTING NUMBERS TO PHOTON COUNTS.
C       MSZ = 1325
        CALL EXPT(INC,IRX,IRY,SM,NOT,OM,ITO,V,Z,WI,
     1R, S1,S2,S,X,T,MSZ,WT,FR)
        IF(UNITWT.NE.1.)GO TO 17
        DO 13 I=1,NOT
        WT(I)=1.
13      CONTINUE
17      CONTINUE
C  AFTER CORRECTLY FORMATTING THE DATA , CALL THE LEAST SQUARES
C  ANALYSIS SUBROUTINE.
        CALL LSFIT(W,OM,SM,INC,NOT,C,P,ITO,IRX,
     1IRY,WT,FR,S)
        RETURN
        END
C
C                       SUBROUTINE EXPT
C
C  THE SUBROUTINE EXPT IS FOR FORMATTING EXPERIMENTAL
C  DATA, CALCULATING FR AND SETTING UP CORRECT
C  WEIGHTING FACTORS.
        SUBROUTINE EXPT(INC,IRX,IRY,SM,NOT,OM,ITO,
     1V,Z,W,R,S1,S2,S,X,T,MSZ,WT,FR)
```

```
      DIMENSION W(MSZ),R(IRX),S1(IRX),S1(IRX),S2(IRC),
     1S(IRX,IRY,(OM(NOT),SM(ITO,INC),V(IRY),Z,(IRX),
     1X(IRX,IRY),T(NOT),WT(NOT)
900   FORMAT(  10F8.0  )
C  READ IN 50 X 50 SCATTERED LIGHT MATRIX INTO ARRAY S.
      DO 111 I=1,IRY
111   READ(5,900)  (S(J,I),J=1,IRX)
C  READ IN EXPERIMENTAL MIXTURE MATRIX.
      DO 100 I=1,IRY
100   READ(5,900)(X(J,I),J=1,IRX)
C  SUBSTRACT SCATTERED LIGHT FROM MIXTURE AND CALCULATE FR
C  (CONVERSION FACTOR FOR COUNTS TO PHOTONS) BY USING THE LAST
C  FOUR ROWS OF THE SCATTERED LIGHT MATRIX TO FIND THE AVERAGE AND
C  STANDARD DEVIATION OF THE DARK CURRENT. FR IS CALCULATED BY
C  USING THE FACT THAT THE STANDARD DEVIATION WOULD BE THE
C  SQUARE ROOT OF THE AVERAGE IF THE NUMBERS WERE IN UNITS
C  OF PHOTONS PER SECOND.
      LL=0
      SUMX=0.
      STD=0.
      IR=IRX-3
      DO 200 IM=1, IRY
      DO 250 J=1, IRX
      LL=LL+1
      WT(LL)=1/X(J,IM)
      OM(LL)=X(J,IM)-S(J,IM)
      IF(J.GE.IR) SUMX=SUMX+S(J,IM)
250   CONTINUE
200   CONTINUE
      DIV=4.0*FLOAT(IRY)
      AVG=SUMX/DIV
C  CALCULATE THE STANDARD DEVIATION (STD)
      DO 253 IS=1,IRY
      DO 255 JA=IR,IRX
      STD=STD+(AVG-S(JA,IS))**2
255   CONTINUE
253   CONTINUE
      STD=SQRT(STD/DIV)
C  CALCULATE FR AND WRITE OUT AVG,STD,AND FR
      FRS=(STD**2)/AVG
      FR=SQRT(FRS)
      WRITE(6,*)  AVG,STD,FR
C  READ IN THE STANDARD MATRICES
```

```
      DO 300 I=1,INC
      DO 400 L=1,IRY
400   READ (5,900)(X(K,L),K=1,IRX)
C  SUBTRACT OUT THE SCATTERED LIGHT FROM EACH MATRIX
      DO 500 IL=1,IRY
      DO 550 J=1,IRX
      X(J,IL)=X(J,IL)-S(J,IL)
550   CONTINUE
500   CONTINUE
C  SMOOTH OUT THE STANDARD MATRIX AND SAVE CORE BY
C  STORING  IT  AS EIGENVECTORS.
      J=-1
      K=-1
      L=1
      CALL MULT(W,X,IRX,IRY,X,IRX,IRY,J,K,L)
      IJOB=2
      CALL XEIGRS(W,IRX,IJOB,R,T,IRX,PERINX,IER)
C
C
C  THE EIGENVALUES ARE RETURNED IN DESCENDING
C  ORDER IN R;CORRESPONDING EIGENVECTORS ARE
C  STORED AS COLUMN VECTORS IN T.
C
C  SINCE EACH STANDARD MATRIX IS A SINGLE COMPONENT
C  USE ONLY THE FIRST EIGENVALUE AND EIGENVECTOR. STORE
C  EIGENVECTOR IN Z AND SM.
C
C
C
C  NOTE HERE:
C      EACH STANDARD MATRIX IS (ASSUMING NO NOISE) OF
C      RANK ONE; THUS WHEN EIGENVECTORS AND EIGENVALUES
C      ARE FOUND THE LARGEST ONE IS MOST LIKELY THE ONE
C      WHICH IS NOT CAUSED BY NOISE. THUS WE SAVE IT
C
C          AND IGNORE THE REST.
      WRITE(6,99)
99    FORMAT(1X,' THE EIGENVALUES OBTAINED FOR ONE OF THE COMPONENTS')
      WRITE(6,*) R
      DO 2 M=1,IRX
      SM(M,I)=T(M)
      Z(M)=T(M)
```

```
2      CONTINUE
C  FIND THE COLUMN EIGENVECTOR AND STORE IT IN V.
       J=1
       K=1
       L=1
       CALL MULT(V,X,IRY,IRX,Z,IRX,1,J,K,L)
C  STORE THE EXCITATION EIGENVECTOR BACK TO BACK WITH THE
C  EMISSION EIGENVECTOR.
       DO 3 N=1,IRY
       N1=IRX+N
       SM(N1,I)=V(N)
3      CONTINUE
300    CONTINUE
       RETURN
       END
C
C                    SUBROUTINE*MULT
C
       SUBROUTINE MULT(A,D,E,F,G,H,I,J,K,L)
C  SUBROUTINE MULT FORMS THE PRODUCT A=DG, OR =DG',OR=D'G,OR=D'G'
C  DEPENDING ON THE PARAMETERS K AND L;
C     K=1    FOR  D   AND =-1  FOR D'
C     L=1    FOR  G   AND =-1  FOR G'
C  J AFFECTS THE STORAGE MODE OF THE PRODUCT A:
C  FOR AN ANSWER HAVING FULL STORAGE MODE J=1,
C  FOR SYMMETRIC STORAGE MODE            J=-1.
C  SYMMETRIC STORAGE MODE IS DEFINED TO BE THE STORAGE OF ONLY
C  THE ELEMENTS WHICH WOULD LIE ON   OR ABOVE THE MAIN DIAGONAL;
C  THE VALUES ARE STORED BY COLUMN MAJOR ORDER.
C
C  THIS SUBROUTINE DOES NO CHECKING TO SEE THAT THE MATRIX D & THE
C  MATRIX G ARE, WITH THE GIVEN VALUES OF K AND L , IN FACT
C  MULTIPLIABLE. NOR IS THERE ANY CHECKING THAT THE PRODUCT MATRIX
C  WILL BE SYMMETRIC IF J=-1; THESE TASKS ARE THEREFORE THE RESPON-
C  SIBILITY OF THE USER.
C
C  FURTHER, IF J,K, OR L IS>0, THEN SUBROUTINE ASSUMES THAT 1
C  IS INTENDED.
C    &
C  IF<0, THEN -1 IS ASSUMED TO BE INTENDED.
C
C   NOTE;  DO NOT PLACE CONSTANTS OTHER THAN -1 AND +1 IN CALL
```

```
C    ----   STMT.  IF NECESSARY TO USE OTHER NUMBERS,THEN MAKE
C           THEM VARIABLES.
C      DIMENSION OM(NOT),SM(ITO,INC),C(INC),P(INC),
     1W(INC,INC),WT(NOT),S(IRX,IRY)
C  INITIALIZE W AND P TO ZERO.
       DO 10 I=1,INC
       P(I)=0
       DO 20 J=1,INC
       W(I,J)=0
20     CONTINUE
10     CONTINUE
C  CALCULATE THE VALUES OF W AND P ( EQUATION 68, CHAPTER 3)
C  USING THE MIXTURE AND STANDARD MATRICES.
       DO 100 L=1,INC
       LL=0.
       DO 150 J=1,IRY
       IM=IRX+J
       DO 200 K=1,IRX
       LL=LL+1
       X2=SM(K,L)*SM(IM,L)
       P(L)=P(L)+WT(LL)*OM(LL)*X2
       DO 250 I=1,INC
       X1=SM(K,I)*SM(IM,I)
       W(I,L)=W(I,L)+WT(LL)*X1*X2
250    CONTINUE
200    CONTINUE
150    CONTINUE
100    CONTINUE
C  SOLVE EQUATIONS SIMULTANEOUSLY,USING SUBROUTINE LIN.
C  SOLVE CALULATED CONCENTRATIONS IN C.
       CALL LIN(INC,W,MSGNOA,P,C,1)
C  WRITE OUT THE CONCENTRATIONS
       WRITE(6,18)
18     FORMAT(' ',' THE FOLLOWING IS C')
       WRITE(6,*)    C
C  CALCULATE THE ERROR IN THE CALCULATED CONCENTRATIONS USING
C  SUBROUTINE CERROR.
       CALL CERROR(C,INC,SM,IRY,IRX,P,NOT,OM,T,DC,W,ITO,S,WT,FR)
       RETURN
       END
C                        SUBROUTINE*CERROR
       SUBROUTINE CERROR(C,INC,SM,IRY,IRX,SIG,NOT,OM,T
```

```
     1,DC,W,ITO,S,WT,FR)
      DIMENSION C(INC),OM(NOT),SM(ITO,INC(,W(INC,INC)
     1,SIG(INC),DC(INC,INC),VAR(20),T(1000),S(IRX,IRY),WT(NOT)
C    FIND THE INVERSE OF W AND STORE IT IN DC USING SUBROUTINE LIN.
        CALL LIN(INC,W,MSGNDA,SIG,DC,0)
C    ZERO THE VARIABLES VAR AND SIG.
        DO 10 I=1,INC
        VAR(I)=0
        SIG(I)=0
10      CONTINUE
C    IF INC IS GREATER THAN 20, THEN THE POSSIBILITY OF BOMB EXISTS.
C
        INTEGER E,G,H,I,J,K,L
        INTEGER P,Q,R
        DIMENSION A(1),D(E,F),G(H,I)
        IX(P,R,K)=((P+R)+K*(P-R))/2
        J=ISGN(J)
        K=ISGN(K)
        L=ISGN(L)
        LL=0
        IX3=IX(I,H,L)
        DO 3 Q=1,IX3
        IX21=IX(E,F,K)
        IX2=IX(IX21,Q,J)
        DO 2 P=1,IX2
        ATEMP=0
        IX1=IX(E,F,-K)
        DO 1 R=1,IX1
        IP=IX(P,R,K)
        IQ=IX(R,Q,-L)
        IR1=IX(P,R,-K)
        IR2=IX(R,Q,L)
        ATEMP=ATEMP+D(IP,IR1)*G(IR2,IQ)
1       CONTINUE
        LL=LL+1
        A(LL)=ATEMP
2       CONTINUE
3       CONTINUE
        RETURN
        END
C               FUNCTION*ISGN
        FUNCTION ISGN(K)
        ISGN=1
```

```
      IF(K.LT.0) ISGN=-1
      RETURN
      END
C             SUBROUTINE*XEIGERS
      SUBROUTINE XEIGRS(A,N,IJOB,D,Z,IZ,PERINX,IER)
      DIMENSION A(N,N),D(N),Z ,(N),WK(1275)
      CALL EIGRS(A,N,IJOB,D,Z,IZ,WK,IER)
      CALL RESORT(D,Z,N,IZ)
      IF((IJOB.EQ.2).OR.(IJOB.EQ.3))PERINX=WK(1)
      RETURN
      END
C                SUBROUTINE*LSFIT
C  CALL THE SUBROUTINE LSFIT,WHICH PERFORMS THE LEAST SQUARES
C  ANALYSIS.
      SUBROUTINE LSFIT(W,OM,SM,INC,NOT,C,P,ITO,
     1IRX,IRY,WT,FR,S)
C  SET UP THE SCRATCH ARRAY AREA "T" AND THE ARRAY AREA
C  FOR THE INVERSE OF W, CALLED DC.
      COMMON/SCRATC/T(1000),DC(1000)
C
C  CALCULATE THE VARIANCE OF THE COMPUTED CONCENTRATIONS.
C  STORE THE COMPUTED
C  VARIANCE IN SIG.
      LL=0
      DO 15 I=1,IRY
      IM=I+IRX
      DO 20 J=1,IRX
      LL=LL+1
      OMWOS=OM(LL)
C  ESTIMATE THE ORIGINAL MIXTURE MATRIX BY ADDING THE
C  SCATTERED LIGHT BACK TO OM.
      OMRAW=OM(LL)+S(J,I)
      DO 25 K1=1,INC
      SX=0
      DO 30 K2=1,INC
      SX=SX+DC(K1,K2)*WT(LL)*(SM(J,K2)*SM(IM,K2)  )
30    CONTINUE
      VAR(K)=SX
      SIG(K1)=SIG9(K1)=(VAR(K1)**2)*OMRAW
      EPX=OMWOS-C(K1)*(SM(M,K)*SM(IM,K1))
25    CONTINUE
      DO 35 K3=1,INC
```

```
      DO 40 K4=1,INC
      XDIV=WT(LL)*DC(K3,K4)*EPX-VAR(K3)*C(K4)
      SIG(K3)=SIG(K3)+(XDIV**2)*(SM(J,K3)*SM(IM,K3)
     1+S(J,I))
40    CONTINUE
35    CONTINUE
20    CONTINUE
15    CONTINUE
C  NOW COMPUTE THE STANDARD DEVIATION FROM THE VARIANCE AND
C  WRITE IT OUT.
      DO 45 K5=1, INC
      SIG(K5)=FR*SQRT(SIG(K5)
45    CONTINUE
      WRITE(6,19)
19    FORMAT(´´ ,´ THE FOLLOWING IS SIG´)
      WRITE(6,*) SIG
      RETURN
      END

C          SUBROUTINE*LIN
C  THIS SUBROUTINE HAS AS INPUT THE VARIABLES N,A,IW, AND
C  MAYBE B.
C
C  THE OUTPUT IS X AND MSGNOA.
C
C  IF IW=1, THEN THE SYSTEM AX=B IS SOLVED AND THE SOLUTION
C  IS PLACED IN X.
C
C  IF IW´´=1,(TYP.IW=0) . THEN A**-1 IS FOUND & PLACED IN X.
C
C  IF IW=1, THEN B IS  PRESERVED
C           ELSE B IS DESTROYED.
C
C  IN ANY CASE A IS NOT AFFECTED.
C
C  IF MSGNOA = 0 ON RETURN THEN NO PROBLEM WAS RECOGNIZED.
C            = 1,          THEN A HAS A ZERO ROW, IS SINGULAR.
C            = 2,          THEN A HAS LINEARLY DEPENDENT ROWS,
C                          IS SINGULAR .
C
C IF         =1 OR 2 , THEN LIN RETURNED W/O FINDING SOLUTION.
C
```

```
C  IF MASGNOA=3 , THEN IMPROV  DID NOT CONVERGE ON ONE OR MORE
C  OF THE BASIS VECTORS; BUT SOLUTION IS RETURNED.
      SUBROUTINE LIN (N,A,MSGNOA,B,X,IW)
      DIMENSION A(N,N),B(N),X(N,1)
      DIMENSION R(50),DX(50),IPS(50),SCALES(50),UL(2500)
      CALL DECOMP(N,A,UL,IPS,SCALES,MSGNO)
      MSGNOA=MSGNO
      IF(MSGNOA.NE.0)RETURN
      IF(IW.NE.1)GO TO 1
      CALL SOLVE(N,UL,B,X,IPS)
      CALL IMPRUV(N,A,UL,B,X,IPS,R,DX,DIGITS,MSGNO)
      MSGNDA=MSGNO
      RETURN
1     CONTINUE
      DO 3 J=1,N
      DO 2 I=1,N
2     B(I)=0
      B(J)=1.0
      CALL SOLVE(N,UL,B,X(1,J),IPS)
      CALL IMPRUV(N,A,UL,B,X(1,J),IPS,R,DX,DIGITS,MSGNO)
      IF(MSGNO.NE.0)MSGNOA=MSGNO
3     CONTINUE
      RETURN
      END
C     SUBROUTINE*DECOMP (N,A,UL,IPS,SCALES,MSGNO)
C
C     THIS SUBROUTINE DECOMPOSES A ROW PERMUTATION OF A GIVEN SQUARE
C     MATRIX A INTO TWO FACTORS: P*A=L*U, WHERE P IS A PERMUTATION
C     MATRIX, L IS A LOWER TRIANGULAR MATRIX WITH 1'S ALONG THE
C     DIAGONAL, AND U IS AN UPPER TRIANGULAR MATRIX.
C     GAUSSIAN ELIMINATION WITH SCALED PARTIAL PIVOTING IS USED.
C
C     ON INPUT
C          A..... IS THE MATRIX TO BE DECOMPOSED
C          N..... IS THE ORDER OF MATRICES A AND UL
C     ON OUTPUT
C          UL.... IS THE MATRIX WHERE THE NONTRIVIAL PARTS OF U AND L,
C                 THE TRIANGULAR DECOMPOSITIONS, ARE OVERLAYED.
C                  MATRIX A MAY BE SPECIFIED IF NO LONGER NEEDED, SAVING
C                  STORAGE MEMORY
C           MSGNO. IS AN INTEGER GIVING A DIAGNOSTIC CODE:
```

```
C                =0, NO PROBLEM RECOGNIZED
C                =1, A HAS A ZERO ROW, IS SINGULAR
C                =2, A HAS LINEARLY DEPENDENT ROWS, IS SINGULAR
C                (DECOMPOSITION IS COMPLETED IN ANY CASE)
C          IPS... IS AN INTEGER N-VECTOR CONTAINING THE ROW  PERMUTATION
C                OF A USED TO GET UL, I.E., THE PIVOTING STRATEGY
C    INTERMEDIATE STORAGE
C         SCALES IS AN N-VECTOR USED FOR ROW-SCALING FACTORS
C
C    REFERENCES
C         (1). GEORGE E. FORSYTHE AND CLEVE B. MOLER, COMPUTER
C              SOLUTION OF LINEAR ALGEBRAIC SYSTEM_, PRENTICE-HALL,
C              ENGLEWOOD CLIFFS, N.J., 1967.
C         (2). JOAN R. WESTLAKE, A HANDBOOK OF NUMERICAL MATRIX
C              INVERSION AND SOLUTION OF LINEAR EQUATIONS, JOHN WILEY
C              & SONS, NEW YORK, J.Y., 1968
C         (3)  S. D. CONTE AND CARL DE BOOR, ELEMENTARY NUMERICAL
C              ANALYSIS: AN ALGORITHMIC APPROACH , MCGRAW-HILL,
C              NEW YORK, N.Y., 1972
C
C     SOURCE
C          MODIFICATION OF ROUTINE FROM REFERENCE (1).
C
C
      SUBROUTINE DECOMP (N,A,UL,IPS,SCALES,MSGNO)
      DIMENSION A(N,N),UL(N,N)SCALES(N),IPS(N)
      EQUIVALENCE(BIG,PIVOT,ROWNRM), (SIZE,TEMP)
      MSGNO = 0
C
C     INITIALIZE IPS, UL, AND SCALES
      DO 5 I=1,N
      IPS(I) = I
      ROWNRM = 0.0
      DO 2 J=1,N
      TEMP = A(I,J)
      UL(I,K) = TEMP
      TEMP = ABS(TEMP)
      IF (ROWNRM.GE.TEMP) GO TO 2
      ROWNRM = TEMP
    2 CONTINUE
      IF (ROWNRM.EQ.0.) GO TO 4
```

```
      SCALES(I) = 1./ROWNRM
      GO TO 5
    4 MSGNO=1
      SCALES(I) = 0.
    5 CONTINUE
C
C     GAUSSIAN ELIMINATION WITH PARTIAL PIVOTING
      NMI = N - 1
      DO 17 K=1,NMI
      BIG = 0.
      DO 11 I=K,N
      IP = IPS(I)
      SIZE = ABS(UL(IP,K))*SCALES(IP)
      IF (SIZE.LE.BIG) GO TO 11
      BIG = SIZE
      IDXPIV + 1
   11 CONTINUE
      IF (BIG.NE.0) GO TO 13
      MSGNO = 2
      GO TO 17
   13 IF (IDXPIV.EQ.K) GO TO 15
      J = IPS(K)
      IPS(K) = IPS(IDXPIV)
      IPS(IDXPIV) = J
   15 KP = IPS(K)
      PIVOT = UL(KP,K)
      KPI = K + 1
      DO 160 I=KPI,N
      IP = IPS(I)
      EM = -UL(IP),K)/PIVOT
      IF (EM.EQ.0.) GO TO 160
      UL(IP,K) = - EM
      DO 16 J=KPI,N
      UL(IP,J) = UL(IP,J) + EM*UL(KP,J)
   16 CONTINUE
  160 CONTINUE
   17 CONTINUE
      KP = IPS (N)
      IF (UL(KP,N).NE.0.) GO TO 19
      MSGNO=2
```

```
   19 RETURN
      END
C     SUBROUTINE*SOLVE (N,UL,B,X,IPS)
C
C     THIS SUBROUTINE OBTAINS A SOLUTION VECTOR X OF THE LINEAR SYSTEM
C     A*X=B, WHERE A IS AN INVERTIBLE N-BY-N COEFFICIENT MATRIX AND B IS
C     THE CONSTANT VECTOR OF LENGTH N, GIVEN THE LU-DECOMPOSITION OF
C     A, THE PERMUTATION USED, AND THE VECTOR B.
C     FORWARD AND BACKWARD SUBSTITUTION, RESPECTIVELY, ARE USED ON THE
C     TRIANGULAR SYSTEMS L*Y=B AND U*X=Y. WHERE L AND U ARE THE
C     TRIANGULAR FACTORS OF A, WITH U UPPER AND L UNIT-DIAGONAL LOWER.
C
C     ON INPUT
C          N..... IS THE ORDER OF THE SYSTEM
C          UL.... IS THE MATRIX CONTAINING THE NONTRIVIAL ELEMENTS OF
C                  THE FACTORS  U AND L OF A, OVERLAYED.
C                 **NOTE WELL -- A MUST HAVE BEEN NONSINGULAR OR THE
C                 ROUTINE IS LIABLE TO ABNORMAL TERMINATION**
C          B..... IS THE N-VECTOR RIGHT HAND SIDE
C          IPS... IS AN  INTEGER N - VECTOR CONTAINING THE ROW PERMUTATION
C                  OF A USED TO GET UL, I.E., THE PIVOTING STRATEGY
C     ON OUTPUT
C                  IS THE SOLUTION N-VECTOR
C
C     REFERENCES
C          (1.) GEORGE E. FORSYTHE AND CLEVE B. MOLER, COMPUTER
C               SOLUTION OF LINEAR ALGEBRAIC SYSTEMS, PRENTICE-HALL,
C               ENGLEWOOD CLIFFS, N.J., 1967
C          (2.) JOAN R. WESTLAKE, A HANDBOOK OF NUMERICAL MATRIX
C               INVERSION AND SOLUTION OF LINEAR EQUATIONS, JOHN WILEY
C               & SONS, NEW YORK, N.Y., 1968
C          (3.) S.D. CONTE AND CARL DE BOOR, ELEMENTARY NUMERICAL
C               ANALYSIS: AN ALGORITHMIC APPROACH, MCGRAW-HILL,
C               NEW YORK, N.Y., 1972.
C
C     SOURCE
C          MODIFICATION OF ROUTINE FROM REFERENCE (1).
C
C
      SUBROUTINE SOLVE (N,UL,B,X,IPS)
```

```
      DIMENSION UL(N,N),B(N),X(N),IPS(N)
      NPI = N + 1
      IP = IPS(1)
      X(1) = B(IP)
      DO 2 I=2,N
      IP = IPS(I)
      IM1 = I-1
      SUM = 0.
      DO 1 J=1,IM1
    1 SUM = SUM +UL(IP,J)*X(J)
    2 X(I) = B(IP) - SUM
      IP = IPS(N)
      X(N) = X(N)/UL(IP,N)
      DO 4 IBACK = 2,N
      I = NPI - IBACK
C     I GOES (N-1), ..., 1
      IP = IPS(I)
      IP1 = I + 1
      SUM = 0.
      DO 3 J = IP1,N
    3 SUM = SUM + UL(IP,J)*X(J)
    4 X(I) = (X(I) - SUM)/UL(IP,I)
      RETURN
      END
C     SUBROUTINE*IMPRUV (N,A,UL,B,X,IPS,R,DX,DIGITS,MSGNO)
C
C     THIS SUBROUTINE IMPROVES UPON THE SOLUTION VECTOR X OF THE LINEAR
C     SYSTEM A*X=B, GIVEN X, A, B THE U AND L FACTORS OF A, AND THE
C     PERMUTATION OF A.
C     THE METHOD OF ITERATED REDUCTION OF RESIDUALS IS USED, WITH THEIR
C     ACCUMULATION IN EXTENDED PRECISION BEING ESSENTIAL TO THE SUCCESS
C     OF THE PROGRAM. FOR EACH ITERATION, THE VECTOR R = B-A*X IS
C     COMPUTED, THEN THE SYSTEM A*DX = R IS SOLVED FOR DX, AN INCREMENT
C     VECTOR WHICH WHEN ADDED TO X GIVES A NEW, USUALLY IMPROVED,
C     SOLUTION X. THE ROUTINE TERMINATES WHEN A TEST FOR SMALLNESS OF
C     THE INCREMENT IS SATISFIED OR THE SPECIFIED MAXIMUM NUMBER OF
C     ITERATIONS HAVE BEEN PERFORMED.
C
C     ON INPUT
C          N..... IS THE ORDER OF THE SYSTEM
C          A..... IS THE ORIGINAL COEFFICIENT MATRIX
```

```
C          UL.... IS THE MATRIX CONTAINING THE NONTRIVIAL ELEMENTS OF
C                 THE FACTORS U AND L OF A, OVERLAYED
C          B..... IS THE N-VECTOR RIGHT HAND SIDE
C          X..... IS AN APPROXIMATE SOLUTION OF A*X=B
C          IPS... IS AN INTEGER N-VECTOR CONTAINING THE ROW PERMUTATION
C                 OF A USED TO GET UL, I E. , THE PIVOTING STRATEGY
C     ON OUTPUT
C          X..... IS THE CORRECT SOLUTION (TO THE LIMITS OF WORKING
C                 PRECISION), PROVIDING A WAS WELL-ENOUGH CONDITIONED
C          DIGITS IS A SCALAR GIVING THE NUMBER OF DECIMAL DIGITS OF
C                 THE INITIAL X WHICH WERE CORRECT RELATIVE TO THE FINAL
C                 IMPROVED X. THIS NUMBER CAN BE USED TO GET A ROUGH
C                 IDEA OF THE CONDITION OF A
C          MSGNO. IS AN INTEGER GIVING A DIAGNOSTIC CODE:
C                 =0, NO PROBLEM RECOGNIZED
C                 =3, MAXIMUM ITERATIONS REACHED WITHOUT CONVERGENCE --
C                 INDICATES A IS BADLY CONDITIONED
C     INTERMEDIATE STORAGE
C          R..... IS AN N-VECTOR STORING SYSTEM RESIDUALS = B-A*X
C          DX.... IS AN N-VECTOR OF INCREMENTS TO IMPROVE X
C
C     REFERENCES
C          (1.) GEORGE E. FORSYTHE AND CLEVE B. MOLER, COMPUTER
C               SOLUTION OF LINEAR ALGEBRAIC SYSTEMS-, PRENTICE-HALL,
C               ENGLEWOOD CLIFFS, N.J. , 1967.
C          (2.) JOAN R. WESTLAKE, A HANDBOOK OF NUMERICAL MATRIX
C               INVERSION AND SOLUTION OF LINEAR EQUATIONS-, JOHN WILEY
C               & SONS, NEW YORK, N.Y., 1968
C          (3.) S.D. CONTE AND CARL DE BOOR, ELEMENTARY NUMERICAL
C               ANALYSIS: AN ALGORITHMIC APPROACH-,MCGRAW-HILL
C               NEW YORK, N.Y., 1972.
C
C     SOURCE
C          MODIFICATION OF ROUTINE FROM REFERENCE (1).
C
C
      SUBROUTINE IMPRUV (N,A,UL,B,X,IPS,R,DX,DIGITS,MSGNO)
      DIMENSIONS A(N,N)UL(N,N),B(N),X(N),X(N)IPS(N),R(N),DX(N)
C     USES LIBRARY ROUTINES ABS,AMAX1,ALOG10
      DOUBLE PRECISION SUM, AIJ,XJ,XB
C     EPS IS LARGEST NUJBER FOR WHICH 1.0 + EPS = 1.0
```

```
C     FOR THE PDP EPS=2**-23  (BLUE CARD)
C     FOR THE AMDAHL EPS=1.0E-7  (YELLOW CARD)
      EPS=1.0E-7
C     EPS=1.192093E-07
C     ITMAX IS TAKEN TO BE TWICE THE NUMBER OF DECIMAL DIGITS
C     IN A FLOATING POINT NUMBER.
      ITMAX=14
      XNDRM = 0.
      DO 1 I+1,N
    1 XNORM = AMAX1(XNORM,ABS(X(I)))
      IF (XNORM.NE.0.) GO TO 3
      DIGITS = -(ALOG10(EPS))
      GO TO 10
    3 DO 9 ITER=1,ITMAX
      DO 5 I=1,N
      SUM = 0.00
      DO 4 J=1,N
      AIJ = A(I,J)
      XJ = X(J)
    4 SUM =SUM + AIJ*XJ
      XB = B(I)
      SUM = XB - SUM
    5 R(I) = SUM
C
C     IT IS ESSENTIAL THAT A(I,J)*X(J) YIELD A DOUBLE PRECISION
C     RESULT AND THAT THE ABOVE + AND - BE DOUBLE PRECISION.
C
      CALL SOLVE (N,UL,R,DX,IPS)
      DXNORM = 0.
      DO 6 I=1,N
      T = X(I)
      X(I) = X(I) + DX(I)
      DXNORM = AMAX1(DXNORM,ABS(X(I)-T))
    6 CONTINUE
      IF (ITER.NE.1) GO TO 8
      DIGITS = -(ALOG10(AMAX1(DXNORM/XNORM,EPS)))
    8 IF (DXNORM.LE.EPS*XNORM) GO TO 10
    9 CONTINUE
C
C     ITERATION DID NOT CONVERGE
      MSGNO = 3
```

```
   10 RETURN
      END
C    *SUBROUTINE*RESORT
      SUBROUTINE RESORT(R,T,IRC,IRY)
      DIMENSION R(IRX),T(IRX,IRY)
C  SUBROUTINE RESORT TAKES R AND T EACH SORTED IN EITHER
C     AN ASCENDING OR DESCENDING MANNER AND RETURNS WITH
C     THEM BOTH PLACED IN THE OTHER ORDER.
      N=IRX/2
      DO 1 I=1,N
      NI=IRX+1-I
      ATEMP=R(I)
      R(I)=R(NI)
      R(NI)=ATEMP
1     CONTINUE
      DO 2  J=1,IRY
      NJ=IRY+1-J
      DO 3 I=1,IRX
      ATEMP=T(I,J)
      T(I,J)=T(I.NJ)
      T(I,NJ)=ATEMP
    3 CONTINUE
    2 CONTINUE
      RETURN
      END
```

Acknowledgments

The author wishes to thank Dr. Thomas Wehrly and Mr. Andre Treybig of the Department of Statistics for useful discussions on factor analysis and pattern recognition. The author is also grateful to the Robert A. Welch Foundation for financial support during the preparation of this manuscript through Grant No. A-715.

References

1. M. E. Magar, *Biopolymers*, **11**, 2187 (1972).
2. D. R. Burgard, S. P. Perone, and J. L. Wiebers, *Anal. Chem.*, **49**, 1444 (1972).
3. B. R. Kowalski, *J. Chem. Inf. Comput. Sci.*, **15**, 201 (1975).
4. G. L. Ritter, S. R. Lowry, C. L. Wilkins, and T. L. Isenhour, *Anal. Chem.*, **47**, 1951 (1975).

5. C. J. Adcock, *Factorial Analysis for Non-Mathematicians*, Melbourne University Press, Carlton, N.3, Victoria, Australia (1954).
6. R. J. Rummel, *Applied Factor Analysis*, Northwestern University Press, Evanston (1970).
7. S. A. Mulaik, *The Foundations of Factor Analysis*, McGraw-Hill, New York (1972).
8. H. Harman, *Modern Factor Analysis*, University of Chicago Press, Chicago (1970).
9. P. H. Weiner, E. R. Malinowski, and A. R. Levinstone, *J. Phys. Chem.*, **74**, 4537 (1970).
10. P. H. Weiner and D. G. Howery, *Can. J. Chem.*, **50**, 448 (1972).
11. J. T. Balmer and H. F. Shurvell, *J. Phys. Chem.*, **77**, 256 (1973).
12. R. W. Rozett and E. M. Petersen, *Anal. Chem.* **48**, 817 (1976).
13. D. L. Duewer, B. R. Kowalski and J. L. Faschins, *Anal. Chem.*, **48**, 2002 (1976).
14. K. S. Fu, *Sequential Methods in Pattern Recognition and Machine Learning*, Academic Press, New York (1968).
15. P. C. Jurs and T. L. Isenhour, *Chemical Applications of Pattern Recognition*, John Wiley, New York (1975).
16. B. R. Kowalski, *Anal. Chem.*, **47**, 1152A (1975).
17. T. L. Isenhour and P. C. Jurs, *Anal. Chem.*, **43**, 20A (1971).
18. N. A. Gray, *Anal. Chem.*, **48**, 2265 (1976).
19. D. Macnaughton, L. B. Rogers, and G. Weinimont, *Anal. Chem.*, **44**, 1421 (1972).
20. J. T. Tou and R. C. Gonzales, *Pattern Recognition Principles*, Addison-Wesley, London (1974).
21. H. C. Andrews, *Introduction to Mathematical Techniques in Pattern Recognition*, Wiley–Interscience, New York (1972).
22. P. Horst, *Factor Analysis of Data Matrices*, Holt, Rinehart and Winston, New York (1965).
23. A. L. Comrey, *A First Course in Factor Analysis*, Academic Press, New York (1973).
24. I. M. Warner, J. B. Callis, E. R. Davidson and G. D. Christian, *Clin. Chem.*, **22**, 1485 (1976).
25. S. Lipschutz, *Schaum's Outline of Theory and Problems of Linear Algebra*, McGraw-Hill, New York (1968).
26. K. Hoffman and R. Kunze, *Linear Algebra*, Prentice-Hall, Englewood Cliffs (1971).
27. S. Isaak and M. N. Manougiar, *Basic Concepts of Linear Algebra*, W. W. Norton, New York (1976).
28. G. Weber, *Nature*, **190**, 27 (1961).
29. R. Courant and D. Hilbert, *Methods of Mathematical Physics*, Interscience, New York (1953).
30. A. Ralston, *A First Course in Numerical Analysis*, McGraw-Hill, New York, p. 247 (1965).
31. C. N. Ho, G. D. Christian, and E. R. Davidson, *Anal. Chem.*, **50**, 1108 (1978).
32. B. Noble, *Applied Linear Algebra*, Prentice-Hall, Englewood Cliffs (1969).
33. M. Gouterman, L. K. Hanson, G. E. Kahil, J. W. Buckler, K. Rohbock, and D. Dolphin, *J. Am. Chem. Soc.*, **97**, 3142 (1975).

6

Nonlinear Parameter Estimation of Convolved Excitation and Multiple Emission Response Functions

Michael P. Neary and David M. Hercules

1. Introduction

The purpose of the study reported in this chapter was to develop and compare different methods for the estimation of nonlinear parameters associated with response functions, which may be represented as a convolution of an excitation function with single or multiple emission function(s). Specifically, excited state lifetimes and the intensities of the corresponding luminescence were the parameters to be estimated from experimental data.

Where the lifetime and concentration of a single emitter are of interest, usually no extensive data analysis is required. If the lifetime of a single component is long relative to the excitation pulse, the lifetime may be obtained from a plot such as that shown in Figure 1. However, if the lifetime of the single component is within a factor of 5 of the decay of the excitation, deconvolution of emission and excitation functions is required to estimate the lifetime. If two emitters are present and both lifetimes are long with respect to excitation and differ from each other by a factor of 2, the lifetimes of both components can be obtained. By plotting log intensity versus time and measuring the slope of the two linear portions of the curve, as shown in Figure

Michael P. Neary • Los Alamos Scientific Laboratories, Group WX-2, M.S. 920, Los Alamos, New Mexico 87545 **David M. Hercules** • Department of Chemistry, University of Pittsburgh, Pittsburgh, Pennsylvania 15260.

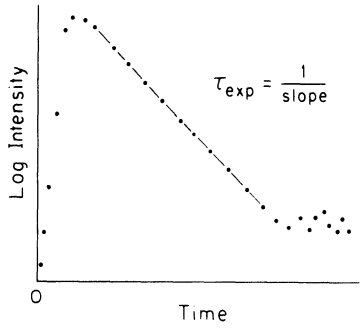

Figure 1. Log intensity versus time for decay of a single luminescent component.

2, the lifetimes are the reciprocals of the slopes. When these conditions are not met, complex numerical methods must be employed to estimate the lifetimes and concentrations. The present study addressed the latter situation.

We have confined the study to selected chemical systems which exhibit the following characteristics:

1. two fluorescent compounds having overlapping emission spectra;
2. the lifetimes of the fluorescent components are within a factor of 5 of the duration of the excitation flash, thus, application of deconvolution techniques was required along with numerical analysis of the data;
3. the lifetimes of the fluorescent components differ by no more than a factor of 2;
4. the ratios of the linear parameters of the two fluorescent components ranged from unity to 0.01.†

These restrictions were imposed so that the algorithms could be subjected to particularly rigorous conditions. In comparing the numerical algorithms used in this study, attention was given to the following considerations:

1. theoretical suitability of the numerical algorithms;
2. practical suitability of the numerical algorithms in terms of:
   a. relative differences in computer time required by the programs;
   b. sources of error in the estimates of the parameters;
3. data quality in terms of:
   a. "ill conditionedness";
   b. error.

The motivation for this study is centered about the following observations:

1. the importance of reliable estimates of fluorescent lifetimes under the conditions mentioned previously;
2. instrumentation now exists that can resolve time intervals of 0.45 nsec or better and detect single photon events;

†Linear parameters denote the parameters related to the concentration or intensity of the emitter(s); nonlinear parameters denote the parameters related to the lifetime(s) of the emitter(s).

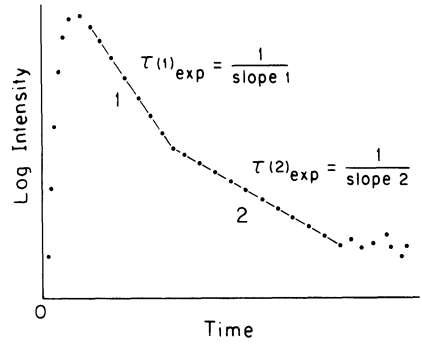

Figure 2. Log intensity versus time for decay of two luminescent components.

3. there is little understanding of the criteria by which one of the available algorithms is picked for use in the parameter estimation mentioned.

Two recent studies have addressed some of the issues raised in the present chapter. McKinnon *et al.*[1] have done extensive computational tests, including some that are discussed here, for both synthesized and real data sets. Their conclusions were that several methods are useful if the structure of the observed data is simple, namely, if the excitation cutoff is sharp or the decay is exactly exponential. They found iterative deconvolution to be best if the decay is more complicated or the excitation has a long tail. O'Connor *et al.*[2] also studied several methods for deconvoluting fluorescence decay curves. They evaluated each method in terms of its ability to deconvolate lifetimes of 1 and 5 nsec, to cope with instrumental artifacts, to analyze subnanosecond decay times, and to separate two closely spaced decays. Like McKinnon *et al.*[1] they found several methods satisfactory for undistorted, one-component decays, but least squares iterative deconvolution was most suitable when distortions were present. Only iterative deconvolution and the method of modeling functions resolved two closely spaced decays.

1.1. Luminescence Processes

Time decay measurements play a significant role in photophysical studies.[3] After excitation into its first excited singlet state, a molecule can fluoresce or undergo one of several nonradiative processes such as internal conversion, intersystem crossing, isomerization, or decomposition, as indicated by the following reactions

$A \xrightarrow{h\nu} A^*$	excitation
$A^* \xrightarrow{k_1} A + h\nu_F$	luminescence
$A^* \xrightarrow{k_2} A^3$	intersystem crossing
$A^* \xrightarrow{k_3} A$ and/or products	reactive

Assuming that A^* is in thermal equilibrium with its surroundings and that excitation is produced by a delta function, the time-dependence of A^* can be written as

$$[A^*]=[A^*]_o\exp-(k_1+k_2+k_3)t \tag{1}$$

The lifetime for A^* is

$$t_F=1/(k_1+k_2+k_3) \tag{2}$$

If the quantum yield is measured, then the natural or radiative lifetime can be obtained experimentally

$$1/t_F^\circ=k_1=\phi_F/t_F \tag{3}$$

Once k_1 and t_F are known, the sum of the rate constants for the nonradiative processes can be calculated.

Knowledge of the magnitude of t_F° can be useful in assigning the lowest excited singled state of a molecule. For example, the lowest excited state may have a low oscillator strength and be almost completely hidden under the tail of a much stronger transition. The value of t_F°, calculated for such cases from the absorption spectrum of the stronger transition, would be considerably smaller than the observed value. In cases where intersystem crossing is the only process competing with fluorescence, measurement of t_F and ϕ_F gives directly the rate constant for intersystem crossing, $k_2=(1-\phi_F)/t_F$.

The addition of bimolecular steps to the photochemical scheme can lead to complications in the decay law; however, decay kinetics can give information about bimolecular mechanisms that is difficult to obtain by steady-state techniques. Information about the radiationless path of deexcitation may be obtained indirectly from lifetime measurements. The processes that may be studied include: molecular rotation and diffusion, heavy atom effects, photochemical reaction rates, solvent interaction, energy transfer, and excited state complex formation. Molecular rotation and diffusion of large molecules ($MW\geqslant 10^4$) depend on structure and conformation. The structure and conformation of macromolecules, such as proteins and enzymes, can be determined by measuring changes in fluorescence polarization of fluorescent labels attached to selected sites on the macromolecule.

Energy transfer studies rely on knowledge of excited state lifetimes; the critical distance over which energy transfer occurs is governed by the lifetime of the donor. Knowledge of intramolecular energy transfer rates is important in studying conformation, structure, and reaction rates of biochemical macromolecules. Separate and independent systems of conjugated double bonds that can pass excitation energy from one to the other are separated by a

distance that can be estimated only by accurate measurement of the two (or more) lifetimes associated with each chromophore. The site of a conformational change can also be determined in certain cases by making reliable measurements of the change in lifetime of fluorescent probes attached to known sites on a macromolecule.

In photochemical studies, fluorescent lifetimes are useful in elucidating mechanisms of organic reactions.[4, 5] For example, because the rearrangement of certain acyclic di-II-methane compounds goes through an excited state intermediate, the fluorescent lifetimes are a direct measure of the rearrangement rates. Likewise, the photochemical formation of 9, 10-dihydroxyanthracene from 9, 10-anthraquinone goes through an excited state intermediate the lifetime of which gives a direct measure of the reaction rate.

In summary, it is clear that the need for reliable, accurate estimates of fluorescent lifetimes is both diverse and fundamental.

Only since the advent of pulsed electronics and high-quantum efficiency, short rise-time photomultipliers have lifetimes less than 5 nsec been accessible to measurement. Until that time, 5 nsec was a lower limit with an instrument that required the operator to match an electronically generated analog to the measured pulse height spectrum in real-time. The reliability and accuracy of the lifetime obtained depended largely on the competence of the operator; in fact $\pm 10\%$ variations in the estimates of a given lifetime by two different operators were not uncommon.

1.2. Modern Instrumentation

The methods underlying instrumentation that depends on modern, fast electronics may, in general, be divided into two categories[3, 6]: phase shift or modulation methods and pulsed methods. No detailed discussion will be presented for the first category; however, the second category will be dealt with extensively in the section on theory and instrumentation. However, it is noted that phase shift or modulation methods require electronics that are more complex and tempermental than those required by the pulsed method.

1.3. Algorithms for Nonlinear Data Analysis

Nonlinear data sets are the type usually acquired as instrumental responses to physico–chemical phenomena. Nevertheless, the notion persists that many nonlinear data sets are linear because they either appear to be or "should be." Certainly, many data sets, that are "near" linear, may be dealt with as linear. However, when parameters are estimated from strictly nonlinear data sets, the selection of a numerical algorithm should entail critical thought; unfortunately, in many cases the major criterion for nonlinear data analysis does not deal with the efficacy of a particular algorithm, but rather

Table 1. Methods for Nonlinear Parameter Estimation

Method	Comments
Least squares[13, 14, 20, 22, 24, 25]	Good for simple linear modeling functions or linear data
	Poor for nonlinear modeling functions, particularly where the data exhibits "ill conditionness"
	Converges rapidly
Maximum likelihood	(Same as least squares)
Gradient method (often called the method of steepest descent)[13, 14, 20, 22]	Good for simple linear modeling functions or linear data
	Poor for nonlinear modeling functions, particularly where the data exhibit "ill conditionness"
	Converges slowly, and prone to diverge
Marquardt method[17, 23]	Good for simple linear modeling functions or linear data as well as many nonlinear modeling functions or nonlinear data
	Poor for some nonlinear modeling functions particularly when the data exhibit "ill conditionness"
	Excellent convergence rate
Laplace transform method[14, 20, 26, 27]	Good for linear modeling functions or linear data as well as some nonlinear modeling functions or nonlinear data
	Has accuracy limitations due to the uncertainties introduced by forming numerical transforms and their inverses
	Extremely attractive in view of the fact that no prior information regarding the magnitudes of the parameters being estimated is required
Method of moments[9–16, 20]	Good for linear modeling functions or linear data as well as some nonlinear functions or nonlinear data
	Has accuracy limitations due to the uncertainties introduced into the parameter estimates as a result of forming numerically truncated integral estimates
	Extremely attractive in view of the fact that no prior information regarding the magnitudes of which the parameters be estimated is required
Fourier transform method[14, 20, 27, 28]	(Same as the Method of moments)

the availability of any algorithm. Table 1 lists some of the better known algorithms for linear and nonlinear data analysis along with critical comments.

In the study to be described, three significantly different numerical algorithms were examined in detail where the nonlinear modeling function, shown in equation (4), defined the data analyzed:

$$R(t) = \int_0^\infty \mathrm{EX}(u) F(t-u)\, du \tag{4}$$

where

$$F(t) = \sum_{i=1}^{2} a_i \exp(-b_i t)$$

is the emission model before convolution, $\mathrm{EX}(t)$ denotes the excitation function, t the time, u the dummy variable, a_i the linear parameters which are proportional to the intensity of the emitter, and, b_i the nonlinear scale parameter corresponding to the experimental emission decay lifetimes. Equation (4) is selected due to its wide acceptance among workers in the fields of photochemistry and analytical chemistry. A background term is not included in the modeling function. It has been omitted here because it is constant and may be dealt with in a straightforward manner. The algorithms used were as follows:

1. Grid search algorithm,[7, 8] which falls into the more general classification of steepest descent or gradient. The principal difference between steepest descent and gradient is that the gradient method requires analytical partial derivatives while the grid search requires estimated partial derivatives. In each case, the derivatives are used differently.
2. The method of moments.[9–18]
3. Marquardt's algorithm,[17–23] which is a blend of least squares and the gradient method, in which the best characteristics of both emerge.

The motivation for selecting the three algorithms listed is as follows:

1. All have either been used or suggested for use with nonlinear data sets.
2. The three exhibit dramatic conceptual differences.
3. They represent examples of simplicity (Grid Search algorithm), complexity and elegance (Marquardt's algorithm), and uniqueness (Method of Moments).

2. Instrumentation and Analytical Parameters

2.1. Time Correlated Single-Photon Method

Among the pulsed methods for measuring fluorescence lifetimes, the time correlated single-photon method gives the greatest sensitivity, reliability, and

time resolution.[3, 29, 30] The unique feature of the technique is the measurement of the time interval between the time of excitation and the time at which emission occurs; a single photon from the total emission is taken as representative. The process is repeated many times (ca. 10^8) and the result is a distribution of time intervals which is a replica of distribution of photons from each excitation. The time at which excitation occurs for each flash is arbitrarily taken as zero and is determined by either a reference photomultiplier or an electrical pulse generated by the flash lamp. In order to measure the time at which the first and only photon arrives at the photomultiplier, it is necessary to ensure that no more than one photon can be detected from each emission. Otherwise, early emission will be heavily weighted, causing a condition known as "pile-up"which is the most serious source of error for this technique.

Flash lamp repetition rates may be as high as 40 kHz for a relaxation oscillator and 20 MHz for certain Q switched lasers. Even when flash lamp excitation rates of 40 kHz are used, photon counting rates in excess of 400 counts/sec are rarely produced. The time of arrival of each photon is measured electronically by a time-to-amplitude converter (TAC) which converts the time interval into an electrical pulse with amplitude proportional to the duration of the time interval. The pulse height information from each pulse is stored in a multichannel analyzer (MCA).

To avoid "pile-up," it is necessary that the count rate be proportional to the number of photons impinging on the photocathode. This amounts to requiring a maximum of a single photon per photomultiplier output pulse. That this condition can be met experimentally is shown in the following.

2.2. Theory

Time correlated single-photon counting requires a single photon from each emission to arrive at the detector at a time proportional to the probability of emission. Statistically, this amounts to random sampling, with replacement from a known population distribution. Assuming that only one photon arrives and is sensed at the photomultiplier during any duty cycle of the flash lamp, the population distribution of the measured time intervals forms a replica of the emission probability distribution, providing that the maximum time interval to be measured is short relative to the TAC time base. Verification of the above is as follows. Let the following be necessary conditions: (a) $\Delta t_{max} \ll$ TAC time base; (b) only one photon arrives and is sensed by the photomultiplier during any duty cycle of the flash lamp. Then, the probability that the waiting time Δt until a stop pulse arrives that is not T, an arbitrary constant, is

$$P \propto \Delta t \tag{5}$$

$$P = \lambda \Delta t \tag{6}$$

where λ is the emission rate constant. The probability that $\Delta t \geqslant T$, denoted Q, is written as

$$Q = 1 - P \tag{7}$$

$$Q = 1 - \lambda \Delta t \tag{8}$$

or

$$P(T|\Delta t) = Q = 1 - \lambda \Delta t \tag{9}$$

and

$$P(T|t_i, i = 1,2,\ldots,n) = Q^n \tag{10}$$

but

$$n\Delta t = t \tag{11}$$

$$P(T|\Delta t_i, i = 1,2,\ldots,n) = (1 - \lambda t/n)^n \tag{12}$$

or as $n \to \infty$

$$P(T|\Delta t_i, i = 1,2,\ldots,\infty) = \lim_{n \to \infty} (1 - \lambda t/n)^n \tag{13}$$

Letting

$$n = 1/h \qquad \lim_{h \to 0} y = \lim_{h \to 0} (1 - \lambda t h)^{1/h} \tag{14}$$

$$\ln y = (1/h)\ln(1 - \lambda t h) = f(h)/g(h) \tag{15}$$

$$\lim_{h \to 0} \ln y = 0/0 \tag{16}$$

$$= \lim_{h \to 0} f'(h)/g'(h)$$

$$= \lim_{h \to 0} (-\lambda t)/(1 - \lambda t h)/1$$

$$= -\lambda t$$

Therefore,

$$y = \exp(-\lambda t) \tag{17}$$

Considering a large number of time intervals Δt, denoted N_o

$$y = N/N_o \tag{18}$$

or

$$N = N_o \exp(-\lambda t) \tag{19}$$

If N_o time intervals are to be measured, at any time t, N of them will have been observed and distributed according to λ. This result is reasonable since one would expect intuitively that random sampling of a known population distribution with replacement would form an image of that population distribution.

Let P_1 be the probability that n photons will be incident on the photocathode per lamp flash and $n \ll N$, where N is the total number of photons generated by the flash in the sample. Under these circumstances, Poisson distributed probability is justified since the detection of a photon is a rare event. Thus,

$$P_1 = m^n \exp(-m)/n! \tag{20}$$

where m denotes the arithmetic mean of n. Let P_2 be the probability that these n photons will cause x electrons to be ejected from the photocathode. In general, it can be assumed that P_2 is binomially distributed. Then,

$$P_2 = n!\phi^x(1-\phi)^{n-x}/x!(n-x)! \tag{21}$$

where ϕ denotes the quantum efficiency of the photocathode, i.e., the probability of response to an incident photon. The probability of x electrons being ejected from the photocathode by n incident photons is given by the joint probability summed over all n photons per flash being incident on the photocathode and x electrons being ejected from the photocathode. Thus,

$$P_x = \sum_{n=x}^{\infty} P_1 P_2 = (\phi m)^x \exp(-m\phi)/x! \tag{22}$$

With the assumption that if $x \geqslant 1$ a count will be observed at the anode of the photomultiplier, then for a count rate R at the anode of the photomultiplier to be observed for a flash lamp repetition rate of Z, the relationship between R, Z, and P_x may be written as

$$R = Z(1 - P_{x=0}) = Z[1 - \exp(-m\phi)] \tag{23}$$

$$= Z\left[m\phi - (m\phi)^2\right]/2! + (m\phi)^3/3! - \cdots \tag{24}$$

If $m\phi \gg m\phi^2/2!$, then $R = Zm\phi$ or the count rate at the anode of the photomultiplier is linearily proportional to the average number of photons striking the photocathode per unit time. Thus, with knowledge of ϕ, m can be adjusted to satisfy the inequality. Note, however, if the inequality is not satisfied then the count rate observed at the anode of the photomultiplier is not linearily proportional to the repetition rate of the flash lamp and the distribution of the emitted photons is not being randomly sampled! P_x for $m=1$, $n>1$, and $x=2$ is more probable than $m=1$, $n=1$, and $x=1$ by 0.18009 units of probability and the P_x for $m=1$, $n>1$, and $x=1$ is less probable than the P_x for $m=1$, $n>1$, and $x=2$ by 0.04228 units of probability.

The question then is for what value of m is: $P_{x>1}$ and $P_{n>1}$ sufficiently low such that the experimentalist can be assured that single photons are being measured. It is only necessary to consider $P_{n>1}$ since $P_{x>1}$ does not depend on m.

2.3. Pile-Up

It was shown above that it is desirable to have a linear relationship between the anode count rate and the average photon flux at the photocathode; however, it is important to note that, in practice, R is usually small with respect to Z. The reason is that even if the average photon flux m is one per flash of the excitation source, the probability of real photon flux $n>1$ is quite high. Thus, if $m=1$ pile-up is still observed. By picking $m=0.1$, 10% pile-up would be expected and by picking $m=0.01$, less than 1% pile-up would be expected. The later level is generally regarded as an acceptable one. By fixing $m=0.01$, only one flash in a 100 gives rise to emission that is detected at the photocathode. The only way the analysis time can be shortened is by increasing the repetition rate of the flash lamp.

Pile-up can be corrected numerically or eliminated instrumentally. The numerical procedure is as follows. If N_i is the corrected number of counts in the ith channel, n_i the number of observed counts in the ith channel, and C the total number of TAC cycles for the data under consideration, then

$$N_i = n_i \Big/ \left(C - \sum_{j=1}^{i-1} n_j \right) \tag{25}$$

One method of instrumentally correcting for pile-up involves coupling the output from the photomultiplier to a summing amplifier, the timing of which is referenced to the duty cycle of the TAC.

The output of the summing amplifier is fed to a discriminator set to pass pulses proportional to two or more photons at the photocathode. The output

of the discriminator is fed to the veto input of the TAC. The validity of the output pulse of the TAC is, thus, tested. If the TAC receives a pulse in the veto input, the output of the TAC is considered to be invalid. If no input is received at the veto input, the output pulse of the TAC is considered to be valid and is passed on to the multichannel analyzer for scaling.

2.4. Time-to-Amplitude Converter

Figure 3 is a block diagram of the single-photon counter. Two separate power supplies provide the high voltage for the photomultiplier and flash lamp. The anode output of the photomultiplier arrives at the stop input of the TAC after amplification and timing. The normal operation of the flash lamp provides a fast pulse which arrives at the start input of the TAC after timing by the constant fraction discriminator. The TAC converts the difference in time of arrival of the two pulses to a voltage proportional to the difference. The MCA sorts the TAC output pulses according to amplitude.

The detailed function of the TAC must be considered, since it is the heart of the single-photon counter. Figure 4 illustrates the TAC's operation. The TAC generates a voltage that follows a ramp versus time once it receives a start pulse. If no stop pulse is received before the end of the TAC duty cycle, the TAC produces no output. However, if a stop pulse is received within the duty cycle of the TAC, the magnitude of the ramp voltage when the stop pulse arrives is the TAC output. Once a valid start and stop pulse have been received by the TAC, the TAC's internal timer is reset at the end of the normal duty cycle. If another pulse is received after a valid start and stop pulse, but prior to the end of the normal duty cycle, it will have no effect on the TAC. In time correlated single-photon counting only pulses related to the flash lamp's operation are valid stop pulses. Thus, the output pulse from the TAC has an amplitude that is proportional to the time interval separating excitation and emission. The TAC output pulses are fed into a MCA where the pulses are sorted according to amplitude, and the channel number is directly proportional to the pulse height.

Interference in TAC operation from background is not usually significant since the on-time of the TAC, may be ca. 1 msec/sec. The TAC time base may range from 50 nsec to 30 μsec.

The range of decay times that can be measured by time correlated single-photon counting is from 1 nsec to greater than 10 μsec, this upper limit being reached when a bias amplifier is used between the TAC and the MCA to extend the range linearly. Until recently, the minimum decay time measurement was 0.45 nsec, and it was not known whether or not this was the time resolution of the instrument or a characteristic of the flash lamp. Lately, 10 psec decay times have been reported.[31]

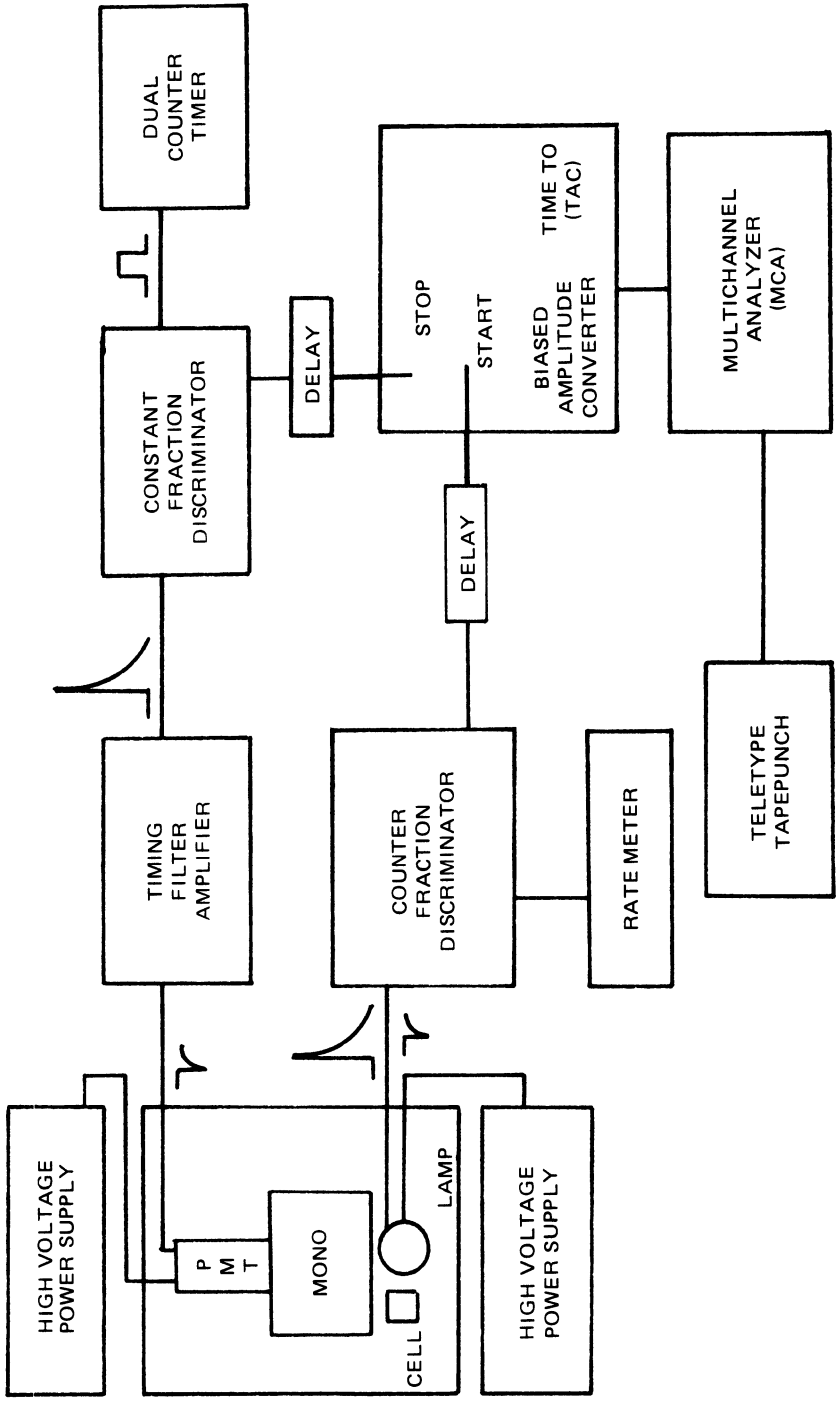

Figure 3. Block diagram of the single photon counter.

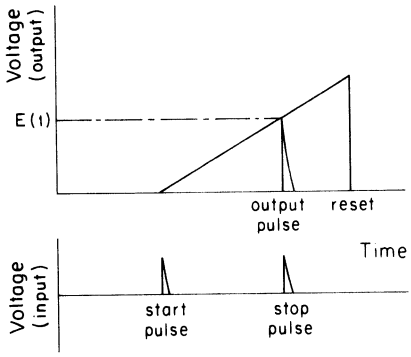

Figure 4. Voltage and timing relationships for TAC.

2.5. Excitation Source

Pulsed lifetime systems utilize short duration flash lamps that are either gated or free-running. For the present work, a free-running flash lamp was employed.

The free-running flash lamp discharges at the characteristic breakdown voltage which depends on the pressure of the fill gas and the electrode geometry. The rate at which the free-running flash lamp discharges depends on the RC time constant of the charging resistors and a capacitor across which the high voltage is applied.

The current passed during the discharge of the lamp develops a potential across a 50 Ω resistor connected between the lamp's anode and ground. The leading edge of the change in potential developed across this resistor is used as the start pulse for the TAC. The time lag between the lamp firing and the leading edge of the start pulse has been estimated at less than 10^{-11} sec. Flashing gases such as N_2, O_2, Ar, etc. can be used. Air at approximately 1 atm was used in this study. The flash emission was essentially the $C^3_{\pi u} \rightarrow B^3_{\pi g}$ transition for N_2 for which the prominent band heads are 358, 337, 316, and 298 nm. No lamp flash profile perturbation over several billion flashes was observed.

The relaxation oscillator used for this study generates light pulses by a spark discharge across tungsten electrodes. The light path in the direction of the sample is sealed with a quartz window to permit operation in the ultraviolet region. The spark chamber is fitted with inlet and outlet valves to permit operation with air or other gases at pressures up to 3 atm. The outlet valve may be fitted with a bubbler for constant flow operation, and purging is simplified by small internal volume of the spark chamber. When the flash lamp was operated with air, at 1 atm and 9 kV, the intensity of the optical light pulse incident on the sample was about 10^7 photons/flash, over all emitted wavelengths. Typical flash rates used were 20–40 kHz. The duration of the output pulse is about 2 nsec full width at half-maximum and 5 nsec at

1/10 maximum. The pulse shape could be modified by adjustment of the electrode gap which is continuously adjustable from 0 to 2 mm.

2.6. Optics

It was mentioned earlier that it is necessary to hold $m = 0.01$ or less. On the average the number of fluorescence photons per flash far exceeds 0.01 per flash. Therefore, a small aperture is placed between the sample and the entrance slit of the monochromator to ensure that $m < 0.01$. An additional benefit of using the small aperture is that scattered excitation radiation is also minimized. Much of the background observed is from scattered excitation radiation. If the instrumental method for the elimination of pile-up is being employed, some fraction of the scatter is also eliminated. However, in the absence of that capability, scatter is always early with respect to fluorescence, appearing in the leading part of the waiting time spectrum. In this study, the first four data channels were used to accumulate scatter data and were ignored for data analysis.

The monochromator shown in Figure 5 used in this study was a SPEX model 1670 minimate, a general purpose type of monochromator featuring: 0.05% scattered light and 70% blaze in the wavelength range of 175–900 nm. The optical path is basically a Czerny–Turner configuration; however, behind each slit is a 45° mirror providing an in-line path for source and output. Five pairs of fixed slits are provided, each 20 mm high. Available slit widths are 0.25, 0.50, 1.25, 2.5, and 5.0 mm corresponding to spectral bandpasses of 1, 2, 5, 10 and 20 nm, respectively. The slits slide behind light tight 0-rings when inserted into the monochromator.

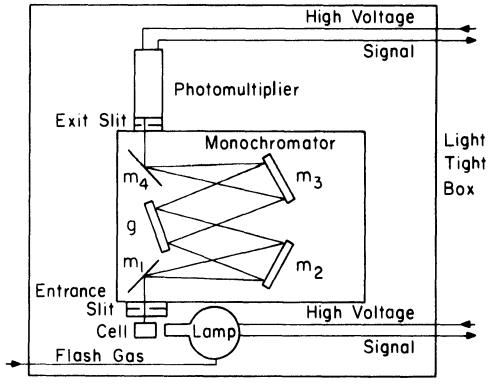

Figure 5. Diagram of the monochromator.

2.7. Photomultiplier Tube

A photomultiplier for time correlated single-photon counting should have the following characteristics: high gain, short rise-time, and a high-quantum efficiency photocathode. End window photomultiplier tubes are usually favored because of the inherent optical advantage and large photocathode. A high-gain RCA 8850 with 111 spectral response, and photocathode quantum efficiency of 31.2% at λ between 350 and 390 nm was selected.

2.8. Start and Stop Lines

The start and stop pulses received by the TAC must be well shaped and independent of the pulse shape of either the photomultiplier or flash lamp in order to accurately preserve timing information. The constant fraction discriminator and timing filter amplifier provide the necessary capability. The use of a constant fraction discriminator produces a walk-free, well-shaped negative timing pulse.

Figure 6 shows pulses of different amplitudes occurring at exactly the same time, t_{max}. The times when the pulse potential equals the lower level discriminator potential are indicated by t_1 and t_2. The time when 90% of the pulse has passed or 10% remains is indicated by t_{10}. Because photomultiplier tube pulses of different amplitudes do not cross a given discriminator level at the same point in time, an undesirable time jitter, referred to as walk $(t_2 - t_1)$, can occur.

In an ordinary discriminator the output pulse is timed from the time of crossing the lower level discriminator setting. Thus, a means of reducing walk must be employed. The means usually selected for timing fast pulses with minimum walk is a discriminator that employs the constant fraction method. The basis for its function is as follows. If two discriminator pulses in Figure 6

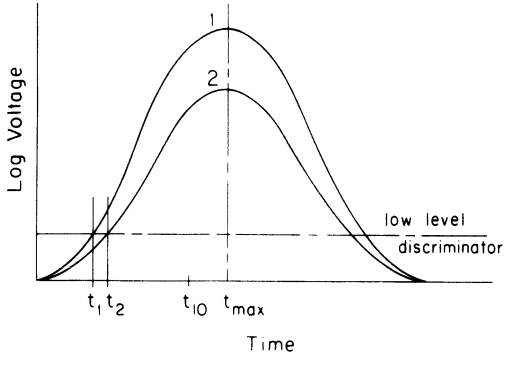

Figure 6. Method of operation of the constant fraction discriminator.

were triggered at the time when the input pulses cross the lower level discrimination setting, their leading edges would correspond to t_1 and t_2, respectively. The difference in the two times defines the magnitude of the time jitter between pulses 1 and 2 and will be incorporated into the waiting time distribution as an error. The constant fraction method eliminates such jitter by causing the output of the constant fraction discriminator to coincide with the time corresponding to a fixed fraction of the pulse amplitude as illustrated in Figure 6. Thus, the output pulse for both pulses 1 and 2 will occur at t_{10}, the time at which 90% of the maximum amplitude has been sensed by the constant fraction discriminator. The walk for the mode selected for this study was less than ± 150 psec over a 100 mV to 10 V pulse amplitude range.

2.9. Timing Filter Amplifier (TFA)

The anode output of the photomultiplier is fed into a timing filter amplifier. The timing filter amplifier is a wide-band, fast (4.5 nsec rise time), variable RC filter amplifier with high drive (up to -6 V into 50 Ω impedance with no degradation of its performance). The purpose of the timing filter amplifier is to form well shaped and amplified output pulses. The RC filter network provides the means by which a wide variety of input pulse shapes can be filtered as required for optimal timing. Amplification is usually desirable in single-photon counting so that the photomultiplier tube can be operated at lower gain where it exhibits better stability and lower background.

Usually, the smallest possible time constant is used because averaging of the differential slope is taken over the time constant. Thus, when the time constant is small, walk in the baseline crossover point will be small. Without using the differential mode, the baseline crossover time cannot be used since none exists. The time jitter in the pulse maximum is usually large, and, therefore, is not used in fast timing experiments.

2.10. Analytical Considerations—Intensity versus Concentration

The observed intensity of fluorescence is related to concentration by

$$I_{\mathrm{OBS}}(\lambda,\theta)=f(\theta)\phi_F g(\lambda)P_{\mathrm{o}}(\lambda)(1-e^{-\epsilon bc})E(\lambda)+f(\theta)g(\lambda)P_{\mathrm{o}}(\lambda)e^{-\epsilon bc}S(\lambda) \tag{26}$$

where

$f(\theta)$ = geometric efficiency related to the solid angle θ of the sample observed by the detector,

ϕ_F = fluorescence quantum efficiency,
$g(\lambda)$ = detector efficiency as a function of wavelength λ,
$P_0(\lambda)(1-e^{-\varepsilon bc})$ = fraction of incident excitation power P_0 absorbed by the fluorescer,
ε = molar absorptivity (1 M^{-1} cm^{-1}),
b = path length (cm),
c = concentration (M/l),
$P_0(\lambda)e^{-\varepsilon bc} = P_0(\lambda) - P_0(\lambda)(1-e^{-\varepsilon bc})$
$E(\lambda)$ = normalized emission as a function of wavelength λ, and,
$S(\lambda)$ = scatter efficiency as a function of wavelength λ.

For a narrow bandpass (λ_1, λ_2) and $\varepsilon bc \leq 0.05$, equation (26) becomes

$$I_{OBS} = f(\theta)\phi_F \frac{g(\lambda_1)+g(\lambda_2)}{2} P_0 \varepsilon bc \frac{E(\lambda_1)+E(\lambda_2)}{2} + f(\theta)\frac{g(\lambda_1)+g(\lambda_2)}{2} P_0(1-\varepsilon bc)\frac{S(\lambda_1)+S(\lambda_2)}{2} \tag{27}$$

2.11. Scattered Excitation Radiation

The last term in equation (27) defines the part of the observed intensity which is not due to fluorescence. In time correlated single-photon counting, scatter causes an early termination of the TAC. Scatter is indistinguishable from pile-up. Scatter of two types is significant in fluorescence measurements: secondary emission and Rayleigh scattering.

Secondary emission is the means by which light is transmitted through a transparent medium, with the exception of those wavelengths which are close to the critical wavelength. Secondary emission is the result of forced excitation of free electrons to a virtual electronic state. The lifetime of such a state is estimated as $<10^{-14}$ sec. The wavelength of the emission is the same as the incident radiation because mode equilibration is slow relative to the state lifetime. Secondary emission is linearly polarized. A major direction of secondary emission is in the plane of the incident radiation. Therefore, some secondary emission is passed into the monochromator.

Rayleigh scattering is due to local thermal perturbations in the refractive index of the media and inhomogeneities in the media. Even at low concentrations, molecules that are large with respect to the wavelength of incident radiation can cause Rayleigh scattering.

Scatter cannot be eliminated; however, it can be minimized experimentally or dealt with numerically. Experimentally, scatter can be minimized by: working at low concentrations, providing good thermal control of the sample,

and avoiding large molecules either as samples or contaminants. If the excitation emission is very intense within the fluorescence bandpass or if large molecules must be in the sample, numerical scatter corrections must be made.

The numerical correction to scatter is a careful truncation of the intensity versus time data collected. In general, the early data channels are ignored. However, because real data are in those channels as well, the factors of their convolution sums must be either estimated or eliminated from each convolution sum (data point) in the channels beyond the last channel in which scatter appears. Numerically, this procedure is not difficult.

2.12. Analytical Wavelength and Bandpass Selection

The analytical bandpass for a grating monochromator is established by: (a) the grating blaze angle; (b) the grating dispersion; (c) the angle of radiation incident on the grating; (d) the width of the exit slit. The first two items cannot be changed after the monochromator has been purchased. However, the last two can be adjusted by the experimentalist. The angle of radiation incident on the grating establishes the analytical wavelength or the wavelength at the center of the bandpass.

The analytical wavelength, in the simplest case, is that wavelength at which maximum fluorescence intensity occurs. The bandpass is all of the wavelengths of fluorescence falling on the detector, where the analytical wavelength is in the exact middle of the bandpass. The analytical wavelength and bandpass are selected so that: (a) no excitation line lies within the bandpass; (b) the excitation within the bandpass is a minimum, so that scatter is minimized.

Selection of the analytical wavelength and bandpass usually is a trade-off where the observed intensity is maximized and scatter minimized. Because of the great sensitivity of single-photon counters, scatter can always be minimized at the expense of fluorescence intensity.

2.13. Linearity versus Concentration

The condition that allows a linear relationship between concentration and observed intensity in equation (27) is that $\varepsilon bc \leqslant 0.05$. Thus, for molar absorptivities, ranging from 10^2 to 10^5 M^{-1} cm^{-1}, the concentration c may range from 5×10^{-4} to 5×10^{-7} M assuming a fixed pathlength b of 1 cm. Referring to equation (26), if $\varepsilon bc > 0.05$ the observed intensity versus concentration becomes nonlinear and follows a polynomial with significant higher order terms. If $\varepsilon bc \geqslant 5$, the observed intensity no longer increases as concentration increases. In fact, due to self-absorption, the observed intensity decreases as concentration is increased.

Linearity is an analytical convenience, not a necessity. A system that responds linearly with concentration can be characterized by a few standards and constant sensitivity. To characterize a system that responds nonlinearly with concentration, many standards are required (due to interpolation error) and varying sensitivity. In general, when using the time correlated single-photon counting technique a long time interval (several hours) is required for waiting time spectra. Therefore, if quantitative information is estimated by working at sample and standard concentrations that cause linear response, the total experiment time is minimized.

3. Data Handling

In this section, the theory and description of the algorithms used for the analysis of nonlinear data will be presented.

The algorithms and their computer programs are described in terms of the convolution integral modeling function given above, but they may be applied to virtually any linear or nonlinear data set and its modeling function. The changes required for such utilization are presented in detail below. However, for the grid search method, its use is restricted to data sets and their modeling functions which require no deconvolution. This latter point will be dealt with in detail when the results for the grid search method are discussed. Mathematically, rigorous treatments have been given for each algorithm. Detailed descriptions of the computer programs for using the algorithms have been presented elsewhere, including a step-by-step procedure for their use.[32]

3.1. Theory and Description of the Algorithms

The three algorithms used in this study are: (a) grid search algorithm (GSA); (b) moments algorithm (MA); (c) Marquardt's algorithm (MQA). The algorithms described are conceptually different from each other. However, they share the feature that they all estimate parameters of nonlinear data sets which are modeled by the convolution integral response function shown in equation (4)

$$R(t) = \int_0^\infty \mathrm{EX}(u) F(t-u)\, du \tag{4}$$

where

$$F(t-u) = \sum_{i=1}^{2} \left[a_i \Big/ \left(b_i \sum_{i=1}^{2} a_i \right) \right] \exp\left[-b_i (t-u) \right]$$

and is the model of the probability distribution function for the normalized*

emission process; EX(u) is the excitation function that depends on the excitation source characteristics and the excitation efficiency and is collected using a scattering solution; t is time, u is the dummy variable, a_i are the linear parameters which are proportional to the intensity of the emitter, and, b_i is the nonlinear scale parameter corresponding to the experimental emission decay lifetimes. The model shown in equation (4) was picked because the observed emission satisfies the definition of a convolution process. That definition is: Given any set of interactive physical processes that can be represented by a function written in closed form and sharing the same domain, the observation may be represented by the convolution of the functions regardless of their relationship on their domain. From that definition, when any physical processes are intimately related or depend on one another in some way, the observation of the interaction is regarded as a convolution.

Because the emission response function is written as shown in equation (4), allowance is made for emission decay processes having lifetimes within the full-width-at-half-maximum of the excitation function. Emission data are the convolution of the excitation and the emission probability distribution function. Thus, such a modeling function can be applied to fluorescence data without alteration.

In practice, the roles of the excitation and emission functions are reversed. That is, the excitation data set is normalized which causes the excitation function to act as the probability distribution function in terms of equation (4). The emissions function is treated as an unnormalized function. This is simply a numerical convenience, and no change in generality results.

In the modeling function shown in equation (4), no term appears that accounts for a constant background. The reasons for the omission are first, for the experimental set-up employed in this study (time correlated single-photon counting) there is an insignificant level of constant background over the time range considered, and second, the largest single contributor to the background of any kind is scattered excitation radiation which appears in the first few data channels of the multichannel analyzer.

Regardless of the source of background or the lifetimes of the emitters, the background contribution to the real data may be eliminated by running a solvent blank after the sample data have been collected. These data are subtracted from the sample data stored in the MCA memory. The difference between the two counts is formed in this way prior to using the data for parameter estimation.

3.2. Grid Search Algorithm (GSA)

The GSA is the simplest of the three algorithms and is considered by many workers to be the "best" method available for parameter estimation for either linear or nonlinear data.[7, 8, 13, 14, 20, 22, 24, 25] However, in spite of its simplicity, the GSA method has some serious shortcomings. The GSA is also

considered by some workers to be a gradient method; however, this depends on the definition of a gradient method. Gradient methods usually require that either analytical or estimated partial derivatives be formed with respect to the parameters. The magnitude and sign of each partial are analyzed so that the sign and magnitude of the parameter perturbations can be calculated or convergence decided upon. For the GSA method, however, no such partial derivatives are formed explicitly. The conditions required for the operation of the GSA are listed below.

3.2.1. Modeling Function

A well-defined modeling function is required for equation (4) that can be written in closed form. For our study, this condition was met by using

$$F(t) = a_1 \exp(-b_1 t) + a_2 \exp(-b_2 t)$$

We found that the GSA program was unable to deal with convoluted data. Thus, EX(t) above may be regarded as a Dirac delta function.

3.2.2. Initial Estimates.

Numerical initial estimates of all parameters sought are required.

Unfortunately, no set of rules, mathematical or physical, exists for deriving initial estimates of the parameters sought. A limit can be set on the maximum lifetime present and, in some cases, the maximum intensity for any sample component by using the MCA log mode so that the log of emission intensity versus time is displayed. The reciprocal of the slope, interpolated as a straight line, can then be set as the maximum lifetime that could possibly be associated with any component of the sample. The extrapolated ordinate intercept is an approximation of the maximum intensity of any component.

Usually it is possible to estimate lifetimes from prior knowledge of the compounds present in the sample. For example, it might be known that the lifetime of a fluorescent label has a certain value when present alone in a given solvent. Regardless of the chemical system into which it is introduced as a fluorescent label, a good initial estimate of its lifetime would be the one known for its pure state.

3.2.3. Data Sets Required.

Two data sets are required: (*a*) *an emission and* (*b*) *an excitation data set.*

The emission data set is composed of values of emission intensity as a function of time. The excitation data set is composed of values of the excitation intensity as a function of time.

Important statistical weighting procedures or algorithmic changes are absolutely required if data sets to be analyzed do not exhibit equal spacing of the dependent variable values.

3.2.4. Convergence Test.

An explicit test for convergence and the size of the perturbation of the parameters, referred to as the step size, is provided.

Convergence of the GSA program depends on minimizing the calculation of either the absolute or relative sum of the squared differences between the observed and calculated values of the dependent variable; the expressions for both absolute and relative error functions, $S(\text{abs})$ and $SS(\text{rel})$; respectively are

$$S(\text{abs}) = \sum_{i}^{n} [R(t_i) - Q(t_i)]^2 \tag{28}$$

or

$$SS(\text{rel}) = \sum_{i}^{n} \left\{ [R(t_i) - Q(t_i)] / [R(t_i) Q(t_i)]^{1/2} \right\}^2 \tag{29}$$

where n denotes the number of data points, $Q(t_i)$ the calculated value of the emission at t_i based on the current values of the parameters, and, $R(t_i)$ the observed value of emission at t_i.

The convergence test is the comparison of S or SS with a preselected minimum acceptable value. When S or SS is less than or equal to the minimum acceptable value program execution is terminated. For each run of the program, a value of S or SS is calculated using the current parameter set where one parameter at a time is varied, first by adding the step to the parameter and then subtracting it. The current parameter set is defined as either the initial estimates or those resulting from the previous iteration. Thus, during an iteration for each parameter, two values of S or SS are computed corresponding to each perturbation of the parameter under consideration. These are referred to as the the *peripheral error sums*. After both peripheral error sums have been calculated for a given parameter, the next parameter in the set is selected and its two peripheral error sums are calculated. This procedure begins with the first parameter of the current parameter set and ends with the last member of the set. The parameter values which exhibited the smallest peripheral error sums are retained for use during the next iteration and a new step is calculated for each new parameter. At the end of an iteration, the best current estimates of the parameters are used to calculate a central error sum. This quantity is calculated in the same manner as the

peripheral error sum; however, it is based on the best current parameter estimates which were picked by comparing the peripheral error sums for each parameter value. After the central error sum is computed, convergence is tested using the convergence criteria. If the convergence test is passed, the operation of the program is terminated. If the convergence test is not passed, the process is repeated until it is passed or a predetermined time limit is reached.

3.2.5. Convergence Criteria.

Convergence criteria must be user supplied as part of the input data set.

The convergence criteria are two numbers which define the smallest acceptable change in two consecutive central error sums and the smallest acceptable step size: $XX = 0.01\%$ change in two consecutive values of the central error sum, and $YY = 4 \times 10^{-5}$, the smallest acceptable step size. When either of the convergence criteria (but not necessarily both) is met, program operation is terminated. However, for YY to terminate operation of the program, the computed step size for all parameters must be $\leqslant YY$. When two consecutive values of the central error sum differ by less than 1×10^{-4}, XX terminates operation of the program.

A good means of selecting the magnitude of XX is to estimate (percent error) $100/(\#\text{ of counts})^{1/2}$ associated with the largest accumulated count in one of the data channels. The value obtained is a good estimate of the collective percent error in the intensity and may be regarded as the limit of precision for the calculated values of the intensity.

The manner in which YY is selected is an empirical one and depends on two factors: the required convergence rate and accuracy. One of the undesirable features of the GSA is that as the neighborhood of the true parameter values is reached the rate of convergence decreases and if the minimum step size is very small, the convergence rate will become very slow. However, by means of a very small minimum step more accuracy in the final estimates can be obtained.

Another consideration is necessary, the extent to which the data are "ill conditioned." Ill conditionedness is the ultimate limitation on accuracy in parameter estimation which relies on nonlinear data. Ill conditioned data are defined as data that can be fitted to more than one modeling function or to more than one set of parameters for a given modeling function with equal precision.

3.2.6. Convolved Data.

Usage with convolved data requires incorporation of an integration subroutine.

The subroutine used is described elsewhere.[32] An additional read statement must be added to accommodate the excitation data set as well. Our

GSA program will accommodate unconvolved data. For example, long lifetime multicomponent decay such as phosphorescence emission could be dealt with by the GSA.

3.3. Moments Algorithm (MA)

The MA is sometimes referred to as the method of moments.[9–16] Even though this method has been available for a long time, its use has been minimal due to the complex and lengthy calculations required. With the advent of high-speed digital computers, nuclear physicists revived the method in the early 1950's and applied it to regression on data sets taken from complex or multicomponent decay processes.

The only characteristic shared by the MA and the other algorithms used is that the nonlinear parameters are estimated from the same data sets. A brief description of the underlying theory of the MA is presented to emphasize the theoretical differences between the MA and the other two. A more detailed and rigorous treatment has been presented.[32]

Equation (4) defined the relationship between the observed emission or response function $R(t)$, the excitation function $\mathrm{EX}(t)$, and the modeling function $F(t)$. That relationship holds for the MA as well; however, with the modeling function written in the form shown below

$$F(t) = a_1 \exp(-t/b_1) + a_2 \exp(-t/b_2) \tag{30}$$

where the linear parameters are normalized as follows:

$$a_1 = A_1/(A_1 + A_2) \quad \text{and} \quad a_2 = A_2/(A_1 + A_2)$$

The kth moment of the response function is defined as

$$\mu_k = \int_0^\infty t^k R(t)\, dt \tag{31}$$

By substituting equation (4) into the expression for the response function moment and making the appropriate change of variables, the complete emission moment is written as

$$\mu_k = \int_{u=0}^{u=\infty} \int_{s=0}^{s=\infty} \binom{k}{p} u^p s^{k-p} \mathrm{EX}(s) F(u)\, ds\, du \tag{32}$$

where

$$p = 0, 1, 2, \ldots, k$$

Expanding equation (32)

$$\mu_k = \int_0^\infty \int_0^\infty \binom{k}{p} s^p \mathrm{EX}(s) F(u)\, ds\, du + \int_0^\infty \int_0^\infty \binom{k}{p} u s^{p-1} \mathrm{EX}(s) F(u)\, ds\, du + \cdots + \int_0^\infty \int_0^\infty \binom{k}{p} u^{k-1} s \mathrm{EX}(s) F(u)\, ds\, du + \int_0^\infty \int_0^\infty \binom{k}{p} u^k \mathrm{EX}(s) F(u)\, ds\, du \tag{33}$$

Recalling from integral calculus,

$$Y_r = \int_{u=0}^{u=\infty} u^{r-1} \sum_{i=1}^{2} a_i \exp(-b_i u)\, du = (r-1)! \sum_{i=1}^{2} a_i / b_i^r \tag{34}$$

when $k = r-1$

$$Y_r = k! G_r \tag{35}$$

where

$$G_r = \sum_{i=1}^{2} a_i / b_1^r \tag{36}$$

Now the kth moment of the excitation function is defined as

$$m_k = \int_0^\infty t^k \mathrm{EX}(t)\, dt \tag{37}$$

and the kth moment of the emission function may be written

$$\mu_k = k! \sum_{r=1}^{k+1} \left[G_r m_{(k+1-r)} \right] / (k+1-r)! \tag{38}$$

Thus, equation (38) provides a set of simultaneous equations, linear in G, for successive values of k. Each G is composed of all of the parameters associated with the modeling function. Therefore, the parameters are determined by solving the set of simultaneous equations μ_k for G_r in terms of the parameters.

Since t, the independent variable, is experimentally defined and $\mathrm{EX}(t)$ and $R(t)$ are data sets experimentally determined, the numerical values of the

response moments μ_k and the excitation moments m_k can be calculated from the data. Thus, the set of simultaneous equations shown by equation (38) can be solved for the parameters of which G is composed, by either Gaussian elimination or matrix algebra; the latter is the method of choice for the present study.

If the equations are linearly independent, an n component modeling function can be completely represented by $2n$ moments of both the response and excitation data; therefore, in the case of a two-component system, a minimum of four moments each of the response and excitation data are all that need be calculated.

As was the case for the GSA, certain conditions must be met for the successful operation of MA. These conditions are listed and discussed below.

3.3.1. Modeling Function.

A well-defined modeling function must be used in equation (4) *that can be written in closed form. For the MA program, this condition was met by equation* (30).

3.3.2. Initial Estimates.

No numerical initial estimates of the parameters being estimated are required; however, a numerical cutoff value must be carefully selected and supplied as part of the data set.

The MA is one of the few methods of nonlinear regression that does not require initial estimates. This fact makes it attractive for nonlinear data analysis, particularly for cases in which the investigator has no idea about a suitable set of initial estimates. This advantage is somewhat minimized by the requirement of a numerical cutoff value. It is shown below that in order to estimate a cutoff value, the investigator must have some idea of the parameters associated with the faster decaying component. The cutoff is defined as the value of time, beyond which only emission of a single component is significant. In order to understand the need for the cutoff value, it is necessary to consider the logic of the MA.

Parameter estimation by the MA takes place in two parts. First, the parameters of the component with the longer lifetime are estimated from those data points which are essentially free of emission from the faster decaying component. The method used to estimate those parameters is linear least squares applied to equation (40), the linear transformation of equation (39).

$$R(t_c) = a_1 \exp(-b_1 t_c) \tag{39}$$

$$\ln R(t_c) = \ln a_1 - b_1 t_c \tag{40}$$

where t_c is the cutoff value, and a_1 and b_1 are assumed to be the parameters associated with the longer-lived component. The purpose in calculating the parameters for the slower decaying component is to provide a means of extending the emission data from the last data point to infinity. The necessity for doing so is shown below.

Because emission data only go to some finite time t_s rather than to infinity, only approximate moments can be calculated from the emission data if they are not extended to infinity. Thus, since

$$\mu_k = \int_0^\infty t^k R(t)\, dt \tag{41}$$

is the exact kth moment of $R(t)$ and the kth moment of $R(t)$ calculated from the unextended data is the approximated moment of $R(t)$, denoted $\hat{\mu}_k$,

$$\hat{\mu}_k = \int_0^{t_s} t^k R(t)\, dt \tag{42}$$

the difference in the exact and approximate moments constitutes a significant source of error, or

$$e_k = \mu_k - \hat{\mu}_k = \int_{t_s}^\infty t^k R(t)\, dt \tag{43}$$

The error term e_k is most significant for the higher moments since they involve higher powers of k. Therefore, the initial estimate of the cutoff is important in determining the quality of the parameter estimates obtained by the MA. This will become clearer in the discussion of the next condition.

In general, the cutoff should be picked so that

$$t_c = [\ln a_1 - \ln R(t_c) - \ln C]/b_1 \tag{44}$$

where

$$C = [a_1 \exp(-b_1 t_c)]/R(t_c)$$

the fraction of the fast decay component in the data. If c is the relative error in $R(t_s)$, then on the average, the counts due to the fast decaying component would be indistinguishable from the relative error. Thus,

$$\text{relative error} = 1/[R(t_c)]^{1/2} = C \tag{45}$$

$$R(t_c) = 1/C^2 \tag{46}$$

then

$$t_c = (\ln a_1 + \ln C)/b_1 \tag{47}$$

An adequate signal-to-noise ratio is not assured by picking t_c as described; however, a good starting value can be determined.

The discussion above suggests one of the most serious shortcomings of the MA. If the lifetimes of the components are close together or if the slower decaying emission is much less intense than the faster decaying emission, then no "good" cutoff value exists and the MA is a poor choice.

It is usually the case that only estimates of a_1, b_1, and C are available, consequently some trial and error is required. The program is written so that more than one cutoff value can be read in with the data sets. In this way, if a bad cutoff is detected by the convergence test of the program, a new cutoff value is automatically selected.

3.3.3. Data Sets Required.

Two data sets are required: (a) an emission and (b) an excitation data set. See the remarks in Section 3.2.2. *under GSA.*

3.3.4. Convergence Test.

An explicit test for convergence must be provided.

After the MA program extends the emission data from t_c to infinity, the extended emission moments μ_k are calculated. A matrix solution to the simultaneous equations μ_k is formed in G_r for the estimated parameters, denoted $\hat{a}_i$ and $\hat{b}_i$. Using $\hat{a}_i$ and $\hat{b}_i$ for $i = 1, 2$, the estimated kth emission moment is formed, $\hat{\mu}_k$. A comparison is made of $\hat{\mu}_k$ and μ_k, the kth emission moment obtained from the data set $R(t)$, such that an error vector $\bar{\mathbf{e}}$ may be written

$$\bar{\mathbf{e}} = \mu \cdot \hat{\mu}^{-1} \tag{48}$$

If $\bar{\mathbf{e}} = \mathbf{I}$ (identity matrix), acceptable values of the emission moments have been obtained as well as acceptable values of the parameters. Ideally, if $\bar{\mathbf{e}} = \mathbf{I}$, a new cutoff would be selected and the process repeated. However, if for no other reason than the inherent Poisson distributed error associated with each member of the emission data set $R(t)$, it is unrealistic to expect $\bar{\mathbf{e}} = \mathbf{I}$ for $\bar{\mathbf{e}} = \mu \cdot \hat{\mu}$; therefore, some deviation from the identity must be allowed in practice, but specified. The analysis of the error vector follows the argument

shown below: The norm of $\mathbf{e}$, denoted $\|\mathbf{e}\|$, is defined as

$$\|\bar{\mathbf{e}}\| = \bar{\mathbf{e}}^T\bar{\mathbf{e}} = \left(\bar{e}_1^2 + \bar{e}_2^2 + \bar{e}_3^2 + \cdots + \bar{e}_{2n}^2\right) \tag{49}$$

and if $\bar{\mathbf{e}} = \mathbf{I}$ then

$$\|\bar{e}\| = 2n \quad \text{or} \quad \|\bar{e}\|/2n = 1 \tag{50}$$

Therefore,

$$1 - B \leqslant \|\bar{e}\|/2n < 1 + B \tag{51}$$

where $B < 1$ and is specified.

3.3.5. Convergence Criteria

The comments regarding "ill conditioned data" for GSA also apply here.

3.3.6. Convolved Data

Usage with convolved or unconvolved data sets requires no changes in the MA program. However, it is always necessary to provide not only an emission data set, but also an excitation data set. For convolved data, the excitation data set would be a Dirac delta function. For the first channel in which emission data appear, the corresponding excitation data channel would have 1.0. All other channels would have zeros.

3.4. Marquardt's Algorithm (MQA)

MQA is one of the newest regression methods that can be applied to nonlinear data sets, and is certainly one of the most elegant. First presented in 1958, MQA has steadily gained in popularity. The MQA is a cunning combination of the method of Gauss and the gradient method; thus, it shares some characteristics with the GSA, but none with the MA. A brief description of the underlying theory is presented in the following. A more detailed and rigorous treatment of the theory of the MQA as well as the method of Gauss and the gradient method is presented elsewhere.[32]

The MQA is a "maximum likelihood" type of algorithm and employs computational procedures for obtaining convergence and confidence intervals. The MQA exhibits the best characteristics of both the method of Gauss and the gradient method and few, if any, of their bad features.

The nonlinear modeling function shown in equation (4) is rewritten in a more general form as follows:

$$R(t) = f(t_1, t_2, \ldots, t_m; b_1, b_2, \ldots, b_k) + e \tag{52}$$

where $R(t)$ is the observed emission data set, in practice, but otherwise is regarded as the dependent variable; $R(t)$ is the convolution of $\mathrm{EX}(t)$ and $F(t)$ as shown in equation (4), t is the time in practice or the independent variable, b is the set of parameters, linear and nonlinear, m is the number of independent variables (in the case under consideration $m=1$), k is the number of parameters (in the case under consideration $k=4$), and e is the error term. In vector notation

$$\mathbf{R(t)} = f(t,\mathbf{b}) + e \tag{53}$$

and for n observations

$$\mathbf{R(t)}_u = f(\mathbf{t}_u,\mathbf{b}) + \mathbf{e}_u \tag{54}$$

for $u=1,2,\ldots,n$. The error sum of squares $S(b)$ is defined as

$$S(b) = \sum_{u=1}^{n} e_u^2 = \sum_{u=1}^{n} \left[\mathbf{R}_u - f(\mathbf{t}_u,\mathbf{b})\right]^2 \tag{55}$$

and is only a function of $\mathbf{b}$ since $\mathbf{R}_u$ and $\mathbf{t}_u$ are fixed. Letting $\mathbf{B}$ be the least squares estimate of $\mathbf{b}$ such that equation (55) is minimized, then $\mathbf{b}$ is determined by setting

$$\left[dS(b)/db_p\right]_{b_p = B_p} = 0 \tag{56}$$

thus, providing a set of normal simultaneous equations of the form

$$\left[\mathbf{R}_u - \mathbf{f}(\mathbf{t}_u,\mathbf{B})\right]\left[\mathbf{df}(\mathbf{t}_u,\mathbf{b})/db_p\right]_{b_p = B_p} = 0 \tag{57}$$

(the subscript on the last term denotes that that term is evaluated at B_p) for $p=1,2,\ldots,k$. When nonlinear modeling functions are used, it is sometimes difficult or impossible to form the set of normal equations in the manner shown previously. To solve this problem, a truncated Taylor series expansion of the nonlinear model is formed such that the approximated model is transformed into the linear domain.

Let $\mathbf{B}_0$ be the initial guesses of the parameters, carrying out a Taylor expansion of the modeling function about B_0 and truncating the series such that the terms of second order or greater are ignored, the modeling function becomes

$$\mathbf{R}(\mathbf{t}_u,\mathbf{b}) = R(\mathbf{t}_u,\mathbf{B}_0) + \sum_{p=1}^{k} \left\{\left[df(\mathbf{t}_u,\mathbf{b})/db_p\right]_{b_p = B_{p0}}\left(b_p - B_{p0}\right)\right\} \tag{58}$$

and letting

$$R_u 0 = R(\mathbf{t}_u, \mathbf{B}_0) \tag{59}$$

$$A_{p0} = (b_p - B_{p0}) \tag{60}$$

$$D_{pu0} = \left[df(\mathbf{t}_u, \mathbf{b}) / db_p \right]_{b_p = B_{p0}} \tag{61}$$

$$R_u - R_{u0} = \sum_{p=1}^{k} A_{p0} D_{pu0} + e_u \tag{62}$$

and for n data points

$$\sum_{u=1}^{n} (R_u - R_{u0}) = \sum_{u=1}^{n} \sum_{p=1}^{k} A_{p0} D_{pu0} + \sum_{u=1}^{n} e_u \tag{63}$$

Letting

$$\mathbf{D_0} = \sum_{u=1}^{n} \sum_{p=1}^{k} D_{pu0} \tag{64}$$

$$\mathbf{A_0} = \sum_{p=1}^{k} A_{p0} \tag{65}$$

$$\mathbf{R_0} = \sum_{u=1}^{n} (R_u - R_{u0}) \tag{66}$$

therefore, equation (63) may be written

$$\mathbf{R}_0 = \mathbf{D}_0 \mathbf{A}_0 \tag{67}$$

and

$$\mathbf{A_0} = (\mathbf{D}_0^T \mathbf{D}_0)^{-1} (\mathbf{D}_0^T \mathbf{R}_0) \tag{68}$$

$\mathbf{A}_0$ then is the correction vector, that is, the vector of parameter adjustments for the first iteration, and will minimize the sum of squares expression shown in equation (55). However, the MQA can be thought of as stopping at this point and forming yet another correction vector by using the gradient method as shown in the following.

In the gradient method, a correction vector is calculated as follows. The directional derivative of the quadratic form of the sum of squares of the deviations, as shown in equation (55), is formed. The directional derivative is the dot product of the gradient vector and the directional vector, or

$$dw/ds = \mathbf{u} \cdot \mathbf{v} \tag{69}$$

where w is the quadratic form of the error function, $\mathbf{u}$ is the directional vector, and $\mathbf{v}$ is the gradient vector. The directional derivative gives the instantaneous rate of change of the error function at some point on its quadratic surface. Due to the geometrical significance of the dot product, the following identity can be written

$$(dw/ds)_0 = |v_0||p| \cos\theta \tag{70}$$

at point P_0 on the quadratic error surface where θ is the angle between the two vectors $\mathbf{v}_0$ and $\mathbf{p}$ and $\mathbf{p}$ is the unit vector. Since $(dw/ds)_0$ approaches a maximum when θ approaches zero, the gradient vector of the function w at the point P_0 is a vector having direction in which $(dw/ds)_0$ has its maximum value and magnitude equal to the maximum value of $(dw/ds)_0$.

Either of the following error functions may be selected for minimization

$$S(b) = \sum_{u=1}^{n} \left[R_u - f(\mathbf{t}_u, \mathbf{b})\right]^2 \tag{71}$$

or

$$SS(b) = \sum_{u=1}^{n} \left\{ \left[R_u - f(\mathbf{t}_u, \mathbf{b})\right] - \sum_{p=1}^{k} \left[df(\mathbf{t}_u, \mathbf{b})/db_p\right]_{b_p = B_{p0}} \left(b_p - B_{p0}\right) \right\}^2 \tag{72}$$

For clarity $S(\mathbf{b}) = 0$ is picked to be minimized in terms of $\mathbf{b}$. A value of $(\mathbf{b})_0$ is picked as a first guess and $S(\mathbf{b})_0$ is calculated. If $S(\mathbf{b})_0$ is greater than zero then $S(\mathbf{b})_1$ should be diminished by the next $(\mathbf{b})_1$. Note that the gradient vector points in the direction of the most rapid *increase* in the function and is negative in the direction of the most rapid decrease. Therefore, the next approximation to $\mathbf{b}$ or $(\mathbf{b})_1$ will be of the form

$$(\mathbf{b})_1 = (\mathbf{b})_0 - h\left[dS(\mathbf{b})/db\right]_b = b_0 \tag{73}$$

where h is selected such that

$$\left[R_u - f(\mathbf{t}_u, \mathbf{b})\right]^2 - S(\mathbf{b})_0 = 0 \tag{74}$$

and

$$\mathbf{A}_0 = \mathbf{b}_0 - \mathbf{b}_1 \tag{75}$$

is the parameter correction vector for the gradient method. For convenience, the Gaussian correction vector is denoted $\mathbf{A}$, and the gradient method correction vector is denoted $\mathbf{A}_G$. The numerical subscripts refer to the iteration number.

As this point, the MQA has computed both $\mathbf{A}$ and $\mathbf{A}_G$. The angle between $\mathbf{A}$ and $\mathbf{A}_G$ denoted γ is calculated and the MQA then interpolates between the two correction vectors. The MQA correction vector, denoted $\mathbf{A}_M$, has a direction and magnitude that represents the best global strategy for minimizing $S(\mathbf{b})$. The best direction for the MQA correction vector must be within 90° of $\mathbf{A}_G$ otherwise $S(\mathbf{b})$ will increase in size. Even though the direction of $\mathbf{A}_G$ may be the best local direction in which to move to minimize $S(\mathbf{b})$, due to the attenuation of the quadratic $S(\mathbf{b})$ surface, it may be a poor global choice. The idea of interpolating between the two correction vectors $\mathbf{A}$ and $\mathbf{A}_G$ is the heart of the MQA, and is based on the inability of the gradient vector to distinguish between global and local minima. When the data exhibit "ill conditioning," severe attenuation of the quadratic $S(\mathbf{b})$ surface can occur giving rise to multiple stationary points or local minima. The theoretical basis for the MQA relies on the fact that there exists a solution $\mathbf{A}_0$ to equation (68) of the form

$$\mathbf{R}_0 = (\mathbf{D}_0 + \lambda \mathbf{I})\mathbf{A}_0 \tag{76}$$

where λ is a positive real variable and $\mathbf{I}$ the identity matrix. Thus, $\lambda\mathbf{I}$ is added to the diagonal elements of the $\mathbf{D}_0$ matrix and a solution may be found without loss of generality. The angle between $\mathbf{A}_0$ and $\mathbf{A}_G$, γ, is a continuous monotonic decreasing function of λ such that as λ increases, γ approaches 0. Since $\mathbf{A}_G$ is independent of λ, $\mathbf{A}_0$ rotates toward $\mathbf{A}_G$ as λ increases, and $\mathbf{A}_0$ approaches R_0/λ; thus, $\mathbf{A}_0$ and $\mathbf{R}_0$ become proportional in the limit and γ approaches 0. However, if $\lambda = 0$, then $\mathbf{A}_0$ and $\mathbf{R}_0$ meet at some finite angle γ where $0 \leqslant \gamma \leqslant \pi/2$. The variable is selected such that $S(\mathbf{b})_r < S(\mathbf{b})_{r-1}$. From the theory above, there always exists a sufficiently large λ such that the last inequality is satisfied unless $(\mathbf{b})_r$ already provides a minimum in $S(\mathbf{b})$. Note that given λ, $\mathbf{A}$ can be solved for by equation (76). The details of the method for selecting λ_r such that $S(\mathbf{b})_r < S(\mathbf{b})_{r-1}$ are presented in the following.

As was the case for the previous algorithms, certain conditions must be met for the successful operation of MQA. Those conditions also are listed and discussed in the following.

3.4.1. *Modeling Function*

A well-defined emission modeling function must be used with equation (4) which can be written in closed form. For the MQA program, the condition was met by

$$F(t) = a_1 \exp(-b_1 t) + a_2 \exp(-b_2 t)$$

The calculated values of the dependent variable $f(\mathbf{t},\mathbf{b})$ were formed for each value of t by convolution of the excitation data set and $F(t)$ as shown earlier. Referring to equation (4), it is necessary to realize that partial derivatives estimated from the emission data set must be used rather than analytical derivatives, since the closed form of the modeling function is unknown. The reason is that $\mathrm{EX}(t)$ is a data set the functional form of which is not known. $S(\mathbf{b})$ is formed with the observed emission data and the convolution of the excitation data set with calculated values of the normalized emission modeling function. No loss in generality is incurred.

3.4.2. *Initial Estimates*

Numerical initial estimates of all parameters must be provided as part of the input data set (see remarks under GSA).

3.4.3. *Data Sets Required*

Two data sets are required: an emission and an excitation data set (see remarks under GSA).

3.4.4. *Convergence Test*

An explicit test for the rate of convergence and a means of calculating the magnitude and direction of the perturbation of the parameters, referred to as the correction vector, must be provided.

The determination of the magnitude and direction of the parameter correction vector results from determination of λ, which depends on comparisons of consecutive numerical values of the error function $S(\mathbf{b}, \lambda)$. The means of calculating λ is shown in the following.

Let $v > 1$, $\lambda_{(r-1)}$ denote the value of λ from the previous iteration and $\lambda_0 = 10^{-2}$. $S(\mathbf{b}, \lambda/v)_{(r-1)}$ are computed and one or all of the following tests are applied:

1. if $S(\mathbf{b}, \lambda/v)_{(r-1)} \leqslant S(\mathbf{b}, \lambda)_{(r-1)}$, then $\lambda_{(r)} = \lambda/v_{(r-1)}$
2. if $S(\mathbf{b}, \lambda/v)_{(r-1)} > S(\mathbf{b}, \lambda)_{(r)}$ and $S(\mathbf{b}, \lambda)_{(r-1)} \leqslant S(\mathbf{b}, \lambda)_{(r)}$, then $\lambda_{(r)} = \lambda_{(r-1)}$

3. If $S(\mathbf{b}, \lambda/v)_{(r-1)} > S(\mathbf{b}, \lambda)_{(r)}$ and $S(\mathbf{b}, \lambda)_{(r-1)} > S(\mathbf{b}, \lambda)_{(r)}$ then λ is increased by successive multiplications by v until some smallest w is found such that

$$\lambda_{(r)} = \lambda_{(r-1)} v^w \quad \text{and} \quad S[\mathbf{b}, (\lambda v^w)]_{(r-1)} \leq S(\mathbf{b}, \lambda)_{(r)}$$

The test for convergence, when passed, causes the iteration to cease and is written as follows:

$$|a_{j(r)}| / \left[\tau + b_{j(r)}\right] < E, \qquad \text{for } j = 1, 2, \ldots, k \tag{77}$$

where $E > 0$ (5×10^{-5} is the default value), $\tau > 0$ (1×10^{-3} is the default value), and, $|a_{j(r)}|$ is the magnitude of the correction to the jth parameter on the rth iteration. The inequality in equation (77) may be stated in the following way. When correction to the absolute value of the rth estimate of the jth parameter $|a_{j(r)}|$ becomes very small with respect to the sum of the absolute value of the rth estimate of the jth parameter $|b_{j(r)}|$ and τ, then iteration will cease since the inequality is satisfied. This test is referred to as the "epsilon test."

However, when an unusually large roundoff error is present in the parameter estimates due to high correlation among the parameter estimates, the "gamma–lambda test" is passed rather than the "epsilon test" because $\lambda > 1$ when $\gamma > \pi/2$. Alternately, the "gamma–epsilon test" is passed if all a_j are small enough to pass the "epsilon test" as a result of successive halving of the increments when $\gamma < \gamma_0$. Passage of this test rather than the standard "epsilon test" indicates that the value of $S(\mathbf{b})$ is presumed minimized to within roundoff error.

3.4.5. Convergence Criteria

Numerical values of the convergence criteria must be either user supplied as part of the input data set or default values (which are part of the program) are used.

For the MQA program, the convergence criteria are either user or default supplied. The convergence criteria and default values are listed below:

$$E = 5 \times 10^{-5}$$

$$\tau = 1 \times 10^{-3}$$

$$\gamma_0 = \pi/4$$

These criteria have been discussed above.

3.4.6. Confidence Interval Criteria

Means of confidence interval calculations are provided as a measure of the quality of the parameter estimates.

Confidence interval criteria are either user or default supplied. The confidence region or interval calculations are described elsewhere[32]; however, a brief description is presented in the following.

No general theory of confidence region estimation exists for nonlinear parameters, although useful approximations based on linear theory can be calculated. The use of linear theory for these calculations is based on the fact that at convergence, the region of the $S(\mathbf{b})$ surface about the minimum is often linear. The confidence regions of a linear model are defined as a k-dimensional ellipsoid and for confidence probability $(1-a)$, the confidence region is based on all parameters b, satisfying an inequality involving the variance ratio statistic or F-distribution having a default value of 4.0. The reliability of such a confidence region calculation depends on how well the Taylor series approximates the nonlinear model in the vicinity of the minimum.

Conventional one-parameter confidence intervals can be computed for confidence probability $(1-a)$ using the estimated parameter correlation coefficients, the standard deviation in the parameter estimates, and the two-tailed $(1-a)$ point of the Student's t-distribution. However, when nonzero correlations exist, one-parameter confidence intervals will tend to underestimate the true interval within which the true jth parameter may lie and still remain within the confidence interval.

The one-parameter confidence intervals indicate a minimum length interval for each parameter assuming that the remaining simultaneous parameter estimates are the same as their corresponding population values. The intervals may be useful in determining the severity of the deviations from linearity. Otherwise stated, the parameter correlation matrix is useful in determining which parameter estimates are highly correlated, while affording probably the best single criterion of the ability of the algorithm to estimate parameters separately.

The maximum symmetric interval within which a parameter $\beta_j^{\dagger}$ lies, with probability $(1-a)$, no matter what the true values of the other parameters, is given by the interval between the two planes of support (tangent planes) of the ellipsoid which are normal to the b_j axis. The support plane confidence intervals for each parameter, although conservatively wide, are regarded by many workers as the most realistic portrayal of the precision of the individual parameter estimates.

$^{\dagger}\beta_j$ = the true value of the jth parameter.

3.4.7. Convolved Data

Usage with convolved data requires analytical partial derivatives written in closed form.

The main difference in the use of the MQA program for convolved data is the form of the modeling function and the analytical partial derivatives. If analytical partial derivatives are being used, it is always necessary that they be written in closed form and coded into the subprogram. If it is not possible to write them in closed form, then the user must resort to estimated partial derivatives as provided by the program. When the convolved data from two short lifetime process are to be processed, they must be modeled by the convolution of a two-component modeling function and the normalized excitation data set. Thus, for regression on such a data set, it is necessary to provide an additional integrating subprogram.

When analytical partial derivatives of the model function with respect to each of the parameters are used, it is necessary to convolve each of the partials evaluated at the value of the independent variable under consideration, with the appropriate values of the normalized excitation data set. The reason for this is given in the following. The Ith value of the dependent variable is written as follows:

$$R(I) = F(1)\mathrm{EX}(I) + F(2)\mathrm{EX}(I-1) + F(3)\mathrm{EX}(I-2) + F(I-1)\mathrm{EX}(2) + F(I)\mathrm{EX}(1)$$

and the partial derivatives with respect to the parameter, say $A(1)$, are written

$$dR(I)/dA(1) = \frac{dF(I)_{I=1}}{dA(1)}\mathrm{EX}(I) + \frac{dF(I)_{I=2}}{dA(1)}\mathrm{EX}(I-1) + \cdots + \frac{dF(I)_{I=I-1}}{dA(1)}\mathrm{EX}(2) + \frac{dF(I)_{I=I}}{dA(1)}\mathrm{EX}(1) \quad (78)$$

Thus, it can be seen that $dR(I)/dA(1)$ is the convolution of the partial derivative and the values of the excitation data set corresponding to the values of the independent variable at which the partial derivative was evaluated.

4. Experimental

The purpose of this work was to study means of estimating the parameters associated with two component exponential decay or emission processes, and to assess the reliability of the final parameter estimates. A strategy for

selecting the set of initial parameters was also of interest. The mathematical model for such an emission process is a sum of two simple exponential functions. This includes two linear parameters which define the maximum observable initial intensity and two-nonlinear parameters which are the rate constants for the emission processes.

The characteristic of nonlinear data that defeats parameter estimation is referred to as "ill conditionness" or "instability."† Ill conditioned data are data that can be modeled by more than one set of parameters of which the set of true values is a member. In cases of extreme ill conditionedness, the set of parameters derived at convergence may satisfy the convergence criteria to four significant figures and still differ from the true parameters by orders of magnitude!

A method exists for determining ill conditionness only in linear data, but does not apply to nonlinear data. Thus, the reliability of the final estimates depends on the extent to which the nonlinear data set is ill conditioned. Determination of the extent of ill conditionness of certain representative nonlinear data sets was the principal interest of the present study.

Methods for detecting ill conditionness are presented along with methods for assessing the reliability of the final estimates. Likewise, a strategy for selecting the best set of initial estimates was devised.

The experimental scheme included the three different algorithms for nonlinear regression just described. A nonlinear data simulator program was used to generate nonlinear data based on known parameter sets. The parameter sets were selected so that nonlinear data would exhibit varying degrees of ill conditionness. Each data set was used with each algorithm so that the capability of the algorithm to estimate the parameters could be assessed. To determine the role of the initial estimates in the success of parameter estimation, the initial estimates were varied for each data set.

In preliminary experiments, both long and short lifetime nonlinear data were considered. The central difference between the two types of data is that short lifetime data are typically more ill conditioned than long lifetime data. The reason is that short lifetime data are the convolution of the excitation and emission functions; long lifetime data need not be considered as a convolution of any kind. Thus, it is necessary to deconvolve short lifetime data, which necessitates measuring excitation data in an identical manner. Since short lifetime data are more difficult and troublesome, long lifetime data sets were not considered in detail. What was learned from short lifetime data with respect to ill conditionness, applies with little modification to long lifetime data.

†Linear data can also be ill conditioned.

Table 2. Parameters Used as the Basis for Simulated Data[a]

Data set number	Intensities		Lifetimes (nsec)	
	Compound 1	Compound 2	Compound 1	Compound 2
1	0.5	0.5	2.0	15.0
2	0.5	0.5	2.0	2.5
3	0.01	0.99	2.5	2.0
4	0.01	0.99	2.0	2.5
5	0.01	0.99	2.0	15.0
6	0.01	0.99	15.0	2.0

Values of i and τ correspond to $I_{OBS}(t) = I(1)\exp[-t/\tau(1)] + I(2)\exp[-t/\tau(2)]$.

$$\text{Normalized Intensities: Compound 1} = \frac{I(1)}{I(1)+I(2)}$$

$$\text{Compound 2} = \frac{I(2)}{I(1)+I(2)}$$

4.1. Data Sources

Both simulated and measured fluorescence data were used with the three programs. Table 2 lists the values of the parameters used with the data simulator to generate the emission data. The rationale for selecting the parameter values for each data set was to create a wide range of ill conditionedness among the simulated data sets. The intensities were selected so that the estimation process dependency on counting statistics could be evaluated. The lifetimes were selected so that they were representative of short lifetime processes.

The fluorescent compounds selected for measurement were picked on the basis of their lifetimes and fluorescence quantum efficiencies. Other factors included: emission and absorption overlap, photochemical stability, and availability. The characteristics of the fluorescent compounds used are given in Table 3.

Table 3. Characteristics of Fluorescent Compounds

Compound number	Compound name	Fluorescence data	
		λ_{max}(nm)	τ (nsec)
1	*N*-methyl-6-methoxy-quinolinium chloride[a]	440	23.7
2	*N*-methyl-quinolinium chloride[a]	400	15.0
3	Quinine sulfate[b]	450	19.5

[a] In water.
[b] In 1*N* H_2SO_4.

5. Results and Discussion

This section will be organized so that program performance with simulated and fluorescent data are separate. The simulated data were used primarily to test each program's performance, and to discover the strengths and weaknesses with respect to ill conditioned data sets.

5.1. Simulated Data—GSA

The GSA was tested with nonlinear, ill conditioned data for both short and long lifetimes. With long lifetime data sets, the GSA program sometimes converged, although the final estimates were unreliable. With short lifetime data, convergence was never observed. Thus, data sets derived from long lifetime processes are the only kind that can be dealt with effectively by the GSA program. Even with long lifetime data, considerable difficulty in parameter estimation is encountered.

It was noted that in many cases where one, two, or three of the initial parameter estimates were identical to their true values, convergence to the true values did not occur! The reason for this behavior is that each component exhibits sensitivity to a given change in its parameter values; that sensitivity depends on the various relationships that exist among all the parameters of both components.

The grid search method of determining the best current values of all parameters is to vary each parameter by a small amount, one at a time, computing the peripheral error sum, for a step in both directions about a particular parameter. The best value of each parameter is retained on the basis of the magnitude of the respective peripheral error sums and that value is used when the next parameter is considered. Consider the following situation. The first parameter is represented in the initial estimates by its true value, and one or more of the other parameters is represented by a value different from its true value. The best value selected for the first parameter by the GSA will be different from the true value, even though the true value was presented to the program initially. Thus, an adjustment to each parameter is justified even though only one may be different from its true value. This behavior is even more subtle because the amount that any parameter value is changed during any iteration depends on how much all of the current parameter values differ from their true values.

Not only was the performance of the GSA program degraded by the presence of error in the data, but the performance was unacceptable for any kind of data that are ill conditioned. The most serious shortcoming of the GSA was that the magnitudes of the standard deviation in the calculated data and the sum of squares of the residuals could be small enough to imply convergence, when the final estimates were grossly incorrect.

Despite the fact that the GSA has certain attractive features (i.e., simplicity) its drawbacks are serious enough, that on the basis of this work, it is not recommended for use with data that are ill conditioned or convolved.

5.2. Simulated Data—MA

The MA requires no set of initial estimates. The parameters are estimated on the basis of a set of simultaneous equations, linear in the parameters. After the first iteration, the current set of parameter estimates is either accepted or adjusted by a strategy designed to meet the convergence criteria. The ability of the MA program to converge to the correct parameter values depends on the accuracy of the moments, calculated for both the excitation and emission data. Any error in the calculated moments becomes very large in the higher order moments. The accuracy of any moment is critically dependent on the calculation of the extended moments or the correction to the partial moments. The corrected moments are based on the extended excitation and emission data calculated beyond the respective cutoff values. Thus, picking the excitation and emission cutoff values becomes the crucial operation when using the MA program.

Table 4 shows the importance of selecting the excitation cutoff carefully. Two excitation data sets were simulated, one with error and one without error. The parameters used to simulate the emission data set are listed in the first row of the table, labeled "True Value." The second column shows the different values of the excitation cutoff. The next four columns list the final estimates associated with each of the cutoff values. The last two columns show the standard deviation in the calculated data and the difference in the standard deviations between errorless excitation data and excitation data with error. Table 4 shows that as the excitation cutoff is increased from 1 to 40 nsec, the final estimates become increasingly inaccurate for either excitation data set. The standard deviation in the calculated data was larger when the excitation data set with error was used.

The reason for the trend shown in Table 4 is that the accuracy of the final estimates depends on the accuracy of the extended moments. The accuracy of the extended moments depends on the number of counts that are beyond the excitation cutoff. Thus, as the excitation cutoff is increased, the number of the counts beyond the excitation cutoff decreases and the accuracy of the extended excitation moments decreases.

The effect of the poorly selected emission cutoff values can also be demonstrated; however, several factors are involved. The relationship that exists between the parameters and the total number of counts collected plays a critical role in determining the quality of the fluorescence cutoff. If the lifetimes differ by less than 20%, the number of counts beyond the cutoff must be large. The counts from the fast component that occur beyond the cutoff

Table 4. Effect of Excitation Cutoff on Performance of the MA

	Excitation cutoff (nsec)[a]	Normalized intensities[b]		Lifetimes ($nsec^{-1}$)[b]		Standard deviation in calculated data (counts)[c]	Difference (counts)
		Compound 1	Compound 2	$\tau(1)$ Compound 1	$\tau(2)$ Compound 2		
True value	—	0.5	0.5	15.0	2.0	—	—
Errorless data	1	0.482	0.518	15.344	2.182	63.5	13.4
Data with error	1	0.483	0.517	15.285	2.189	76.9	—
Errorless data	10	0.483	0.517	15.346	2.184	63.9	14.7
Data with error	10	0.484	0.516	15.287	2.191	77.2	—
Errorless data	20	0.436	0.564	16.158	2.653	216.0	11.0
Data with error	20	0.436	0.564	16.122	2.653	227.0	—
Errorless data	40	0.366	0.634	17.489	3.396	424.0	11.0
Data with error	40	0.366	0.634	17.386	3.425	435.0	—

[a]The fluorescence cutoff was 50 nsec.
[b]Normalized intensities and lifetimes are defined in Table 2.
[c]Total counts $= 2.81 \times 10^5$.

must be small relative to those from the slow component. Thus, in order to select a good fluorescence cutoff, the intensity of the slow component should be greater than the intensity of the fast component. As the difference in the intensities becomes small, more total counts must be collected. When the intensity of the fast component is larger than the slow component, it is not possible to select an acceptable fluorescence cutoff. Regardless of the parameter's relationships, the maximum number of counts should be collected to ensure the best possible fluorescence cutoff value.

Table 5 shows the importance of collecting a large number of counts to ensure the best fluorescence cutoff. Three different sets of parameters (true values) were used to simulate data sets. Each parameter set was used to simulate two data sets: one with 2.81×10^5 counts and one with 5.1×10^6 counts. The counts for each data set are shown in the first column. The next four columns list the final estimates and the true values. For the data sets with 2.81×10^5 total counts, the program never sensed the presence of two components. However, for the data sets with 5.1×10^6 total counts, the program always sensed two components. Since the same fluorescence cutoff (35 nsec) was used in each case, when the total counts are increased, the quality of the fluorescence cutoff is improved.

In summary, the MA program performs well with nonlinear data from two component fluorescence processes if great care is taken to provide the best available excitation and fluorescence cutoff values. If the slow component has the largest intensity, then the cutoff values are improved by increasing the total number of counts collected. However, if the lifetimes differ by less than 20% and the intensity of the slow component is small relative to the fast component, an acceptable fluorescence cutoff cannot be obtained by any means.

Table 5. Effect of Total Counts on Performance of the MA

	Total counts	Normalized intensities[a]		Lifetimes ($nsec^{-1}$)[a]	
		Compound 1	Compound 2	$\tau(1)$ Compound 1	$\tau(2)$ Compound 2
True value	—	0.4	0.6	0.2	5.0
Computed values	2.81×10^5	—	1.0	—	3.71
	5.10×10^6	0.419	0.581	2.08	5.07
True value	—	0.6	0.4	2.0	5.0
Computed values	2.81×10^5	—	1.0	—	3.14
	5.10×10^6	0.610	0.390	2.03	5.06
True value	—	0.4	0.6	4.0	5.0
Computed values	2.81×10^5	—	1.0	—	4.56
	5.10×10^6	0.945	0.055	4.48	6.75

[a]Normalized intensities and lifetimes defined in Table 1.

5.3. Simulated Data—MQA

The extent to which emission data are ill conditioned defines the performance limits of any algorithm for regression on nonlinear data; MQA is no exception. Table 6 was formed on the basis of regression on excitation and emission data where the initial estimates were the true values. The intensity and the reciprocal lifetime of each component and the associated error are listed for six simulated data sets. The total number of counts and the standard deviation in the calculated data are shown in the last two columns. Each data set was exact (e.g., without error), therefore, the error in the parameters is regarded as roundoff and/or incomplete convergence. These results represent a best case for the performance of the MQA program and are presented for comparative purposes. It will be shown later that the relative magnitudes of the standard deviations of the calculated data and the error in the parameter estimates are helpful in assessing the reliability of the final estimates.

The MQA program computes a parameter correlation matrix at the end of each run. Table 7 presents six sets of correlation coefficients for each of the simulated data sets described in Table 2. Each correlation coefficient listed is between the two parameters shown at the head of the appropriate column. Correlation coefficients between the parameters and themselves are always unity and are not shown in the table. If a correlation coefficient is negative, the parameters probably are in an inverse relationship. If the correlation coefficient is positive, the parameters are probably in a direct relationship. The likelihood of either of these two relationships depends on the magnitude of the correlation coefficient.

The performance of the MQA program was also determined when the simulated data sets were both exact and with error, and where the initial estimates were different from the true values. Table 8 is in six parts (A–F), one for each simulated data set used. The true values of the intensities and the reciprocal lifetimes used to simulate the data are listed in the first row of each part of Table 8. The nature of convergence and the standard deviation in the calculated data are listed on the row with the computed estimates. The last two columns list the minimum error in the reciprocal lifetime final estimate and the maximum error in the intensity final estimate. In most cases where convergence is indicated, the values in the last two columns are due to roundoff and/or incomplete convergence and are not physically significant.

Referring to Table 8(A) for data set 1 (DS 1), the intensities are equal and the $1/\tau$ values differ by about an order of magnitude. Convergence only occurred when the initial estimates of the $1/\tau$ values differed in the same way as their true values, but with no restrictions on the relationship between the initial estimates of the intensities. When the ratio of the initial estimates of the $1/\tau$ values was less than 7.5, convergence never occurred.

For DS 2 the relationship between the linear parameters is the same as for DS 1; however, the $1/\tau$ values differ by about 20%. As can be seen from

Table 6. Effect of Initial Estimates on the Performance of MQA

Initial intensity (counts)[a,b]				Initial reciprocal ($nsec^{-1}$)				Total counts collected (counts ×1000	Standard deviation in calculated data (counts)
$I(1)$ Compound 1	Error	$I(2)$ Compound 2	Error	Lifetime Compound 1	Error	Lifetime Compound 2	Error		
5×10^{4}	9.255×10^{-2}	5×10^{4}	8.264×10^{-2}	5×10^{-1}	1.724×10^{-5}	6.66×10^{-2}	9.808×10^{-8}	860	6.016×10^{-2}
5×10^{4}	1.1323	5×10^{4}	1.325	5×10^{-1}	1.235×10^{-6}	4×10^{-1}	9.748×10^{-7}	225	9.238×10^{-4}
1×10^{3}	1.2702	9.9×10^{4}	1.2700	4×10^{-1}	5.267×10^{-5}	5×10^{-1}	7.505×10^{-7}	191	1.036×10^{-3}
1×10^{3}	1.5158	9.9×10^{4}	1.5160	5×10^{-1}	8.877×10^{-5}	4×10^{-1}	6.596×10^{-7}	250	1.240×10^{-3}
1×10^{3}	4.120×10^{-3}	9.9×10^{4}	3.723×10^{-3}	5×10^{-1}	3.837×10^{-6}	6.66×10^{-2}	2.205×10^{-9}	1500	2.678×10^{-3}
1×10^{3}	2.423×10^{-3}	9.9×10^{4}	2.682×10^{-3}	6.66×10^{-2}	1.421×10^{-7}	5×10^{-1}	2.523×10^{-8}	200	1.743×10^{-3}

[a] Intensities and lifetimes are defined in Table 2.
[b] Initial values = true values.

Table 7. Correlation Coefficients between the Parameters Using MQA's

Data set number[a]	$\rho[I(1)/\tau(1)]$[a,b]	$\rho[I(1)/I(2)]$	$\rho[I(1)/\tau(2)]$	$\rho[I(2)/\tau(2)]$	$\rho[I/\tau(1)/\tau(2)]$	$\rho[I(2)/\tau(2)]$
1	0.4489	−0.7956	0.7328	−0.8003	0.6494	−0.8983
2	0.9984	−1.0000	0.9986	−0.9984	0.9942	−0.9983
3	−0.9986	−1.0000	−0.9984	0.9986	0.9942	0.9984
4	0.9984	−1.0000	0.9986	−0.9984	0.9942	−0.9986
5	0.4489	−0.7956	0.7328	−0.8003	0.6494	−0.8983
6	−0.8983	−0.7956	−0.8003	0.7328	0.6494	0.4489

[a] Intensities, lifetimes, and data set parameters are defined in Table 2.
[b] $\rho[I(1)/\tau(1)]$ is the correlation coefficient between the intensity and rate constant of the first component.

Table 8. Performance of MQA with Simulated Data.

Estimate	Intensities (counts)[b] $I(1)$ Compound 1	Intensities (counts)[b] $I(2)$ Compound 2	Reciprocal[b] Lifetimes ($nsec^{-1}$) Compound 1	Reciprocal[b] Lifetimes ($nsec^{-1}$) Compound 2	Convergence	Standard deviation calculated data (counts)	Minimum standard error in reciprocal lifetimes ($nsec^{-1}$)	Maximum standard error in intensity (counts)
			(A). *Data Set 1*[a] *Total Counts* $= 8.6 \times 10^5$					
True value	5×10^4	5×10^4	5×10^{-1}	6.667×10^{-2}				
Estimates:								
Initial	5×10^4	5×10^4	5.0×10^{-1}	4.0×10^{-2}				
Computed	5×10^4	5×10^4	5.0×10^{-1}	6.67×10^{-2}	yes	5.96×10^{-2}	9.73×10^{-8}	9.18×10^{-2}
Initial	5×10^4	5×10^4	5.0×10^{-1}	4.0×10^{-1}				
Computed	*c*	*c*	*c*	*c*	no	*c*	*c*	*c*
Initial	3.0×10^4	7.0×10^4	5.0×10^{-1}	6.67×10^{-2}				
Computed	5.0×10^4	5.0×10^4	5.0×10^{-1}	6.66×10^{-2}	yes	1.52×10^{-3}	2.49×10^{-9}	2.12×10^{-3}
Initial	3.0×10^4	7.0×10^4	8.222×10^{-1}	4.0×10^{-2}				
Computed	5×10^4	5×10^4	5.0×10^{-1}	6.666×10^{-2}	yes	5.73×10^{-2}	5.73×10^{-2}	7.96×10^{-2}
Initial	4.0×10^4	6.0×10^4	1×10^{-1}	4×10^{-1}				
Computed	*c*	*c*	*c*	*c*	no	*c*	*c*	*c*
Initial	1.0×10^4	9×10^4	6.667×10^{-2}	5.0×10^{-1}				
Computed	5×10^4	5×10^4	5.0×10^{-1}	6.666×10^{-2}	yes	3.97×10^{-2}	6.47×10^{-8}	5.51×10^{-2}
Initial	1.0×10^3	$9.9\times10^{+4}$	5.0×10^{-1}	4.0×10^{-1}				
Computed	*c*	*c*	*c*	*c*	no	*c*	*c*	*c*
Initial	1×10^3	$9.9\times10^{+4}$	5.0×10^{-1}	6.667×10^{-2}				
Computed	5×10^4	9.9×10^4	5.0×10^{-1}	6.667×10^{-2}	yes	8.96×10^{-8}	1.46×10^{-8}	1.38×10^{-2}
Initial	1.66×10^4	8.33×10^4	5.0×10^{-1}	6.667×10^{-2}				
Computed	5×10^4	5×10^4	5.0×10^{-1}	6.667×10	yes	4.43×10^{-2}	7.22×10^{-8}	6.814×10^{-2}

(*continued*)

Table 8 (Cont.)

Estimate	Intensities (counts)[b] $I(1)$ Compound 1	Intensities (counts)[b] $I(2)$ Compound 2	Reciprocal[b] Lifetimes ($nsec^{-1}$) Compound 1	Reciprocal[b] Lifetimes ($nsec^{-1}$) Compound 2	Convergence	Standard deviation calculated data (counts)	Minimum standard error in reciprocal lifetimes ($nsec^{-1}$)	Maximum standard error in intensity (counts)
			(B). *Data Set 2[a] Total Counts* $= 2.25 \times 10^5$					
True value	5×10^4	5×10^4	5.0×10^{-1}	4.0×10^{-1}				
Estimates								
Initial	5×10^4	5×10^4	5.0×10^{-1}	6.667×10^{-1}				
Computed	9.45×10^4	5.5×10^4	4.58×10^{-1}	2.92×10^{-1}	no	4.61	7.59×10^{-4}	6.22×10^2
Initial	3×10^4	7×10^4	5.0×10^{-1}	4.0×10^{-1}				
Computed	3.71×10^4	6.29×10^4	5.18×10^{-1}	4.101×10^{-1}	no	6.85×10^{-1}	5.46×10^{-1}	7.44×10^2
Initial	1×10^4	9×10^4	4.0×10^{-1}	5.0×10^{-1}				
Computed	2.89×10^4	7.11×10^4	3.77×10^{-1}		no	1.17	9.46×10^{-4}	1.103×10^3
Initial	5.0×10^4	5.0×10^4	5.0×10^{-1}	4.0×10^{-2}				
Computed	9.59×10^4	4.1×10^3	4.56×10^{-1}	2.57×10^{-1}	no	5.38	6.82×10^{-4}	4.93×10^2
Initial	1.66×10^4	8.33×10^4	5.0×10^{-1}	4.0×10^{-1}				
Computed	8.92×10^2	9.81×10^4	6.50×10^{-1}	4.3×10^{-1}	no	4.1248	8.2×10^{-4}	8.99×10^2
			(C). *Data Set 3[a] Total counts* $= 1.91 \times 10^5$					
True value	1.0×10^3	9.9×10^4	4.0×10^{-1}	5.0×10^{-1}				
Initial	5.0×10^4	5.0×10^4	4.0×10^{-1}	5.0×10^{-1}				
Computed	4.49×10^4	5.51×10^4	4.86×10^{-1}	5.09×10^{-1}	no	1.00×10^{-2}	3.13×10^{-3}	1.45×10^4
Initial	3.0×10^4	7.0×10^4	5.0×10^{-1}	5.0×10^{-1}				
Computed	2.44×10^4	7.56×10^4	4.79×10^{-1}	5.05×10^{-1}	no	8.94×10^{-2}	1.52×10^{-3}	8.41×10^3
Initial	3.0×10^4	7.0×10^4	2.0×10^{-1}	6.66×10^{-1}				
Computed	7.2×10^2	9.93×10^4	3.85×10^{-1}	4.998×10^{-1}	yes	1.77×10^{-2}	9.38×10^{-6}	1.35×10^1

(D). *Data Set 4*[a] *Total Counts* $= 2.5 \times 10^5$

True value	$1.\times10^{-3}$	9.9×10^{4}	5×10^{-1}	4.0×10^{-1}				
Initial	5.0×10^{4}	5.0×10^{4}	5.0×10^{-1}	4.0×10^{-1}				
Computed	4.63×10^{4}	5.37×10^{4}	4.1×10^{-1}	3.9×10^{-1}	no	9.43×10^{-2}	2.43×10^{-3}	1.58×10^{4}
Initial	3.0×10^{4}	7.0×10^{4}	5.0×10^{-1}	4.0×10^{-1}				
Computed	2.54×10^{4}	7.46×10^{4}	4.16×10^{-1}	3.96×10^{-1}	no	8.512×10^{-2}	1.21×10^{-3}	9.39×10^{3}
Initial	3.0×10^{4}	7.0×10^{4}	5.0×10^{-1}	5.0×10^{-1}				
Computed	2.44×10^{4}	7.56×10^{4}	4.79×10^{-1}	5.054×10^{-1}	no	8.94×10^{-2}	1.52×10^{-2}	8.41×10^{3}
Initial	3.0×10^{4}	7.0×10^{4}	2.0×10^{-1}	6.66×10^{-1}				
Computed	2.94×10^{4}	7.06×10^{4}	3.88×10^{-1}	4.06×10^{-1}	no	1.04×10^{-1}	1.80×10^{-3}	1.34×10^{4}
Initial	1×10^{-3}	9.9×10^{4}	4.0×10^{-1}	5.0×10^{-1}				
Computed	*c*	*c*	*c*	*c*	no	*c*	*c*	*c*
Initial	3.0×10^{4}	7.0×10^{4}	2.0×10^{-1}	6.66×10^{-1}				
Computed	7.2×10^{2}	9.93×10^{4}	4.99×10^{-1}	3.85×10^{-1}	yes	1.77×10^{-2}	9.38×10^{-6}	1.35×10^{1}

(E). *Data Set 5*[a] *Total Counts* $= 1.5 \times 10^6$

True value	1×10^{-3}	9.9×10^{3}	5.0×10^{-1}	6.66×10^{-2}				
Initial	3.0×10^{3}	7.0×10^{3}	6.66×10^{-2}	5.0×10^{-1}				
Computed	1.0×10^{3}	9.9×10^{4}	5.0×10^{-1}	6.66×10^{-2}	yes	3.03×10^{-3}	2.50×10^{-1}	4.22×10^{-3}
Initial	3.0×10^{3}	7.0×10^{3}	6.66×10^{-1}	5.0×10^{-2}				
Computed	1.0×10^{3}	9.9×10^{4}	5.0×10^{-1}	6.66×10^{-2}	yes	2.68×10^{-3}	2.21×10^{-9}	4.12×10^{-3}
Initial	5.0×10^{4}	5.0×10^{4}	8.33×10^{-1}	4.0×10^{-2}				
Computed	1.0×10^{3}	9.9×10^{4}	5.0×10^{-1}	6.66×10^{-2}	yes	2.68×10^{-3}	2.21×10^{-9}	4.12×10^{-3}

(*continued*)

Table 8 (Cont.)

Estimate	Intensities (counts)[b] $I(1)$ Compound 1	Intensities (counts)[b] $I(2)$ Compound 2	Reciprocal[b] Lifetimes ($nsec^{-1}$) Compound 1	Reciprocal[b] Lifetimes ($nsec^{-1}$) Compound 2	Convergence	Standard deviation calculated data (counts)	Minimum standard error in reciprocal lifetimes ($nsec^{-1}$)	Maximum standard error in intensity (counts)
			(F). *Data Set 6*[a] *Total Counts* $= 2.0 \times 10^5$					
True value	1×10^{3}	9.9×10^{4}	6.66×10^{-2}	5×10^{-1}				
Initial	3.0×10^{4}	7.0×10^{4}	6.66×10^{-2}	5.0×10^{-1}				
Computed	1.0×10^{3}	9.9×10^{4}	6.66×10^{-2}	5.0×10^{-1}	yes	1.99×10^{-3}	2.87×10^{-8}	3.05×10^{-3}
Initial	3.0×10^{4}	7.0×10^{4}	2.0×10^{-1}	3.33×10^{-1}				
Computed	4.7×10^{2}	9.95×10^{4}	1.95×10^{-1}	4.958×10^{-1}	no	1.01×10^{2}	*c*	*c*
Initial	5.0×10^{4}	5.0×10^{4}	1.0×10^{-1}	2.86×10^{-1}				
Computed	2.4×10^{3}	9.76×10^{4}	1.39×10^{-1}	5.08×10^{-1}	no	3.69×10^{1}	1.01×10^{-3}	1.98×10^{2}

[a]From Table 4.
[b]Intensities and reciprocal lifetimes defined in Table 2.
[c]No computed values

Table 8(B), convergence never occurred for DS 2 unless the initial estimates were the true values. For the first, third, fifth, and sixth initial estimates, there was some tendency to propose a single exponential by estimating one very large intensity and one very small. In these cases, the values of $1/\tau$ associated with the largest intensity was intermediate between the two true values. In general, for a single component to be proposed by the MQA program, the ratio of initial estimates for the $1/\tau$ values had to be either greater than 7.0 or less than 0.5. For intermediate ratios, the MQA program proposed values for the parameters which were not much different from the initial parameter estimates. This performance was independent of the total number of counts collected during the measurement. The extent to which DS 2 is "ill conditioned" can be demonstrated by comparing the initial parameter estimates and the converged values for the third and the fifth entries. While the two sets of initial estimates differ considerably, the converged values are identical as are the standard deviations and the standard errors at convergence. Thus, an unwary experimentalist might be tempted to accept these final estimates because they were arrived at from two different sets of initial estimates.

With the MQA program, however, some indication of whether or not the final estimates are reliable is given by the magnitude of the standard deviation of the emission, coupled with the standard error in the final estimates themselves. For the cases cited, the standard deviation appears to be small, but the standard error in the parameters is moderately large. Therefore, the converged values should be suspect despite the fact that the final estimates were obtained from two different sets of initial estimates.

The MA program could resolve two components of such a data set if the total number of counts distributed among all of the data points was 5,000,000 or more. Otherwise a single exponential model was proposed. For the MQA program, however, similar behavior was not observed. Regardless of the total number of counts collected during the measurements, the presence of two components was always sensed.

In Table 8(C) and DS 3, the relationship between the $1/\tau$ values is the same as for DS 2; however, the intensities differ by about two orders of magnitude. DS 3 converged when the initial estimates were the same as the true values, and when the initial estimates were those shown as the last entry in Table 8(C). Since the faster decaying component is associated with the largest intensity and the $1/\tau$ values differ by 20%, it is expected that a single component would be proposed. This performance was never observed regardless of the initial estimates. In every case, a two component system was proposed and the final estimates were never much different from the initial estimates. Even when a single component was selected for the initial estimates [second entry in Table 8(C)], a single component was not proposed.

The standard deviation associated with each of the entries of Table 8(C) was remarkably small and the plots of the calculated and observed data

indicated acceptable final estimates. The only indication that the final estimates were unreliable was the magnitude of the standard error associated with the intensity and $1/\tau$ estimates. Convergence for DS 3 occurred when the difference in $1/\tau$ values was large. However, the standard deviation in the calculated data was larger than for sets of parameter estimates which did not lead to convergence.

Referring to Table 8(D), the difference between DS 4 and DS 3 was that the true values of the intensities were reversed. Convergence to an acceptable set of final estimates was never observed except when a large difference existed between the initial estimates or when the true values of the parameters were supplied as an initial estimate. However, in all of the cases listed, the final estimates were not much different from the initial estimates and the standard deviation in the calculated data was deceptively small. The plots of the observed and calculated emission data were coincidental and convergence was suggested. However, the standard error associated with the final estimates was large indicating the final estimates were unreliable. The fifth entry in Table 8(D) was of interest. True values of the intensities and values very close to the true values of $1/\tau$ were supplied as the initial estimates; however, the sum of squares of the difference in all of the calculated and observed values of the emission data were in excess of 10^{11}; this caused execution of the program to terminate. This is an intuitively surprising result, illustrating the care with which intuition must be applied when guessing about the performance of the programs with nonlinear data.

Referring to Table 8(E) for DS 5, the relationship between the intensities is the same as those of DS 2, 3, and 4; however, the $1/\tau$ values differ by about an order of magnitude. The DS 5 convergence characteristics are good for any reasonable set of initial estimates. The larger intensity is associated with the slower decaying component and the smaller intensity is associated with the faster decaying component. As the difference in the values of the initial intensity estimates becomes smaller ($\leqslant 50\%$) resolution of the slower component becomes more difficult.

For DS 5, the faster decaying component is never more than 1% of the total emission and as time increases the fraction of the total emission due to the fast component decreases.

DS 6 is similar to DS 5 except that the intensities are reversed. Referring to Table 8(F), convergence depended on the initial estimates being well selected. The ratio of the initial estimates of the $1/\tau$ values had to be greater than 7.5 or less than 0.5 for convergence. In general, considerable difficulty is encountered in regressing on such a data set because the slower decaying component is a small fraction of the total emission at any time. This accounts for the poor convergence of DS 5. For DS 6, the fraction of the total emission due to the slower component starts out small, but after four time intervals increases to 50% of the total emission. Thus, reliable final estimates are

expected. However, for data based on parameters similar to those of DS 5, reliable final estimates are expected most of the time. Except for intermediate values of the intensities, reliable final estimates are not usually obtained, particularly if the intensities are closer to those of DS 6 than to those of DS 5.

5.4. Comparison of Convergence Characteristics for MQA and MA

The ability of a program to resolve a two-component system depends on the relationship between the ratios of the intensities and the lifetimes. Table 9 summarizes the convergence characteristics of the MQA and the MA programs. The optimum cases are shown in the first two rows. These are when the intensity of the slow component is greater than the intensity of the fast component. When this relationship is reversed, the performance of either program is degraded. The MQA program can tolerate this unfavorable relationship better than the MA program.

The limit of resolution for a two component system may be considered in terms of Poisson distributed error. If $\tau(1)$ is larger than $\tau(2)$ and the inequality

$$I(2)\exp[-t/\tau(2)] \leqslant 3\{I(1)\exp[-t/\tau(1)]^{1/2}\} \tag{79}$$

holds for a given t, then the emission beyond t is regarded as free of the fast decaying component. If the equation (79) holds for all t's, then the fast component cannot be resolved.

This argument defines the limit of resolution for either program. Thus, if the fast component dominates the emission, it is difficult to resolve two components. Generalizations can be made for the analysis of nonlinear data sets with respect to their ill conditionedness and the likelihood of successful parameter estimation. If the fraction of the slower component emission is

$$G = \frac{1}{1 + \dfrac{I(2)\exp[-t/\tau(2)]}{I(1)\exp[-t/\tau(1)]}} \tag{80}$$

where $1/\tau(2) - 1/\tau(1) > 1$ and the value t_m is established by the duration of the measurement (usually less than 10 μsec).

The success of regression on nonlinear data sets of the summed exponential type with two components may be considered in terms of the fraction of the slow component in the data at any time interval and the magnitude of the rate of change for the same interval. Figure 7 shows four curves that approach the same limit, $G_\infty = 1$. Data that are the least ill conditioned exhibit a relatively large change in the fraction of the slow component over the time interval of the measurement.

Table 9. Comparison of MQA and MA Convergence Characteristics

Intensities ratio $I(2)/I(1)^a$	Lifetime ratio $\tau(2)/\tau(1)^a$	MQA convergence		MA convergence	
		Characteristic	No. of components	Characteristic	No. of components
$\gg 1$	>1	Excellent	2	Excellent	2
>1	>1	Good	2	Good	2
>1	<1	Fair, depends on counts	1 or 2	Poor	1
>1	<1 >0.8	Poor	1 or 2	Poor, depends on counts	1
<1	<1 >0.8	Poor	1 or 2	Poor, depends on counts	1 or 2
$\ll 1$	<1	Impossible	1 or 2	Impossible	1 or 2
$\gg 1$	$\gg 1$	Depends on 1. $\tau(2)-\tau(1)$ 2. number of counts	1 or 2	Depends on 1. $\tau(2)-\tau(1)$ 2. number of counts	1 or 2

[a]True values.

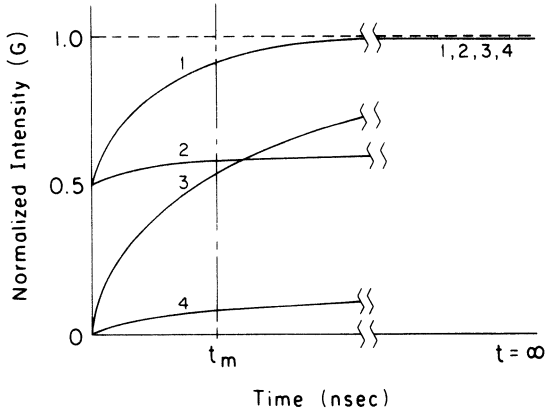

Figure 7. Change in the normalized intensity of the slow component as a function of time: curve 1: $i(2)/I(1)=1$; $|1/\tau(2)-1/\tau(1)|$ large; curve 2: $i(2)/I(1)>1$; $|1/\tau(2)-1/\tau(1)|$ large; curve 3: $i(2)/I(1)=1$; $|1/\tau(2)-1/\tau(1)|$ small; curve 4: $I(2)/i(1)>1$; $|1/\tau(2)-1/\tau(1)|$ small; t_m denotes the maximum time for measurement (usually <10 μsec).

The derivative of G with respect to time, which is the rate of change of the relative slow component emission, is given by

$$\frac{dG}{dt}=\frac{(1/\tau_2-1/\tau_1)\dfrac{I(2)}{I(1)}\exp\left[-(1/\tau_2-1/\tau_1)t\right]}{\left\{1+\dfrac{I(2)}{I(1)}\exp\left[-(1/\tau_2-1/\tau_1)t\right]\right\}^2} \tag{81}$$

When the absolute value of dG/dt is small at t_m, the data are likely to be "ill conditioned" and when the absolute value of dG/dt is large at t_m, the data are likely to be relatively well conditioned. Thus, when a set of final estimates has been obtained for the MQA program by calculating dG/dt, an estimate of the reliability may also be obtained. It was found that when a data set is "ill conditioned" there is no procedure for selecting a set of initial estimates so that reliable final estimates are guaranteed.

Figure 8 depicts regions of ill conditionedness in terms of the ratio of the intensities, $I(1)/I(2)$, and of the lifetimes $\tau(1)/\tau(2)$. By forming the indicated ratios and locating the intersections of their normal projections, a judgment can be made regarding the extent to which the data are ill conditioned. The parameter sets used in this manner may be either the final estimates or the initial estimates. By using the former, a notion of the reliability of the final estimates can be obtained and by using the latter, an estimate as to whether or not convergence can occur is obtained.

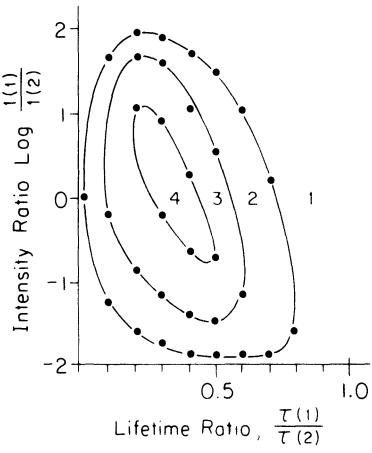

Figure 8. Ill conditionedness as a function of intensity ratio and lifetime ratio: region 1—absolutely ill conditioned; regions 2 and 3—intermediate; region 4—relatively well conditioned.

In Figure 8, parameter sets which are relatively well conditioned are defined by region 4. Parameter sets which are less well conditioned than those in region 4, but better conditioned than region 2, define region 3. The parameter sets which define region 1 are absolutely ill conditioned. Data sets derived from region 1 are impossible to regress upon.

When both the true values and the initial estimates are relatively well conditioned according to Figure 8, convergence to reliable final estimates is usually the case. If the true values are well conditioned and the initial values are poorly conditioned, convergence to reliable final estimates occurs less often. If the true values are poorly conditioned and the initial estimates are well conditioned, convergence to reliable final estimates occurs rarely. If both the true values and the initial estimates are relatively poorly conditioned, convergence to reliable final estimates never occurs. Since the degree of ill conditionedness for the true values is not known, *the best practice for selecting initial estimates is to choose a set that is relatively well conditioned.*

5.5. Convergence Rate and Efficiency

The rates of convergence for the MQA and the MA programs were found to be acceptable. The use of the MQA program with a small computer is not possible since the program employs double precision work length, Fortran system subprograms, and requires 350K of operating core. However, with little modification the MQA program could be adapted to a small computer. The same may be said of the MA program except that operating core requirements are less than 200K. The MQA program requires that the number of allowed iterations be user specified. For the data sets dealt with in this study, the iteration process never needed to be carried beyond 20

iterations. If convergence had not occurred after 20 iterations, it was unlikely that acceptable final estimates would ever be obtained. That 20 iterations are used without obtaining acceptable final estimates implies that the slope of the error ellipsoid is small in the neighborhood of the initial estimates or at the start of the regression process. The MQA exhibits the rapid convergence characteristic of the gradient algorithm in the early part of the regression and the rapid convergence characteristic of the least squares algorithm in the latter stages. Therefore, if convergence is slow at the beginning, it is unlikely that it will become more rapid later in the process. Both the MA and MQA generally used about 1 min central processing unit (CPU) time in regressing on each data set.

CPU time was used in this study as a means of assessing program efficiency. CPU time is defined as the time interval during which (a) the Fortran source program and the data sets are compiled, and (b) the compiled data are processed as dictated by the source program. Regardless of the data set processed, the GSA program was more severely limited than either of the MQA and MA programs. In fact, the GSA program failed completely to perform with short lifetime data sets and only marginally with long lifetime data sets.

5.6. Fluorescence Data

Table 10 summarizes the real fluorescence data sets run with the MQA and the MA programs. The initial estimates for the MQA program were selected so that a broad range of ill conditionedness would be represented. Table 11 shows the performance of the MA program; the true values and the final estimates are listed for each sample. The excitation cutoff value was 10 nsec in all cases.

The final estimates for the third and fifth data sets were incorrect. In both cases, the larger intensity was associated with the faster decaying component and the lifetimes differed by less than 20%. The MA program

Table 10. Data Sets for Fluorescent Compounds[a]

	Normalized intensities		Lifetimes ($nsec^{-1}$)	
Data set number	Compound 1	Compound 2	Compound 1	Compound 2
1	0.5	0.5	23.7	15.0
2	0.9	0.1	23.7	15.0
3	0.9	0.1	23.7	19.5
4	0.5	0.5	19.5	15.0
5	0.9	0.1	19.5	15.0

[a]Normalized intensities and lifetimes are defined in Table 2.

Table 11. Performance of the MA for Real Fluorescence Data

Data set number	Estimate	Fluorescence cutoff (nsec)[a]	Normalized intensities[b]		Lifetimes (nsec)[c]	
			Compound 1	Compound 2	Compound 1	Compound 2
1	True value	40	0.5	0.5	23.7	15.0
	Computed	—	0.4797	0.5203	23.995	15.110
2	True value	40	0.9	0.1	23.7	15.0
	Computed	—	0.9111	0.0889	23.610	15.780
3	True value	50	0.9	0.1	23.7	19.5
	Computed	—	—	1.000	—	21.915
4	True value	50	0.5	0.5	19.5	15.0
	Computed	—	0.8212	0.1788	20.144	13.213
5	True value	50	0.9	0.1	19.5	15.0
	Computed	—	1.000	—	16.831	—

[a]The excitation cutoff was 10 nsec in all cases.
[b]Defined in Table 2.
[c]Defined in Table 2.

sensed a single component and estimated lifetimes which were intermediate between the true values. This is the characteristic performance for the MA program under these circumstances. The parameters for the second data set were ideal because the larger intensity was associated with the slower component and the lifetimes differed by about 30%. The agreement between the final estimates and the true values for the second data set were the best observed. The first data set, though not as well conditioned as the second, was also near ideal in that the lifetimes differed by more than 30%. The final estimates were acceptable. The fourth data set was not ideal because the intensities for each component were the same and the lifetimes differed by less than 20%. The final estimates are not acceptable because the error in the intensities was as great as 60% and as great as 13% in the lifetimes.

The same fluorescence data sets were used with the MQA program. Table 12 shows the results. Each data set was run with three different initial estimates. The final or computed estimates are listed in the row below each of the initial estimates. The true values for each data set are listed in the row below each of the initial estimates. The true values for each data set are listed in the first row of each data set section. The seventh column, headed by dG/dt, lists values of the rate of change of the fraction of the slow component emission in the total emission. These values were obtained by evaluating equation (81) at some intermediate time, 100 nsecs in this case. The last column, headed by "Region of ill conditionedness," lists the numerical designation of the region in Figure 8 where the intersection of the normal projections of the ratios $I(1)/I(2)$ and $\tau(1)/\tau(2)$ falls.

Table 12. Performance of MQA for Real Fluorescence Data

Data set number[a]		Normalized intensities[b]		Lifetimes (nsec)[b]		dG/dt[c]	Region of ill conditionness[d]
		Compound 1	Compound 2	Compound 1	Compound 2		
1	True values	0.5	0.5	23.7	15	—	2
	Estimates						
	Initial	0.1	0.9	20.0	15.0	0.0020	1
	Computed	*e*	*e*	*e*	*e*	*e*	
	Initial	0.3	0.7	20.0	15.0	0.0202	2
	Computed	0.499	0.501	23.65	15.04	0.0207	
	Initial	0.9	0.1	25.0	20.0	0.009	2
	Computed	0.689	0.311	25.219	16.220	0.0298	
2	True values	0.9	0.1	23.7	15.0	—	3
	Estimates						
	Initial	0.1	0.9	25.0	20.0	0.0004	2
	Computed	0.901	0.099	23.60	15.51	0.0240	
	Initial	0.3	0.7	25.0	12.0	0.0029	3
	Computed	0.910	0.090	23.76	15.011	0.0241	
	Initial	0.5	0.5	25.0	20.0	0.0053	2
	Computed	0.923	0.077	23.66	15.23	0.0240	
3	True values	0.9	0.1	23.7	19.5	—	2
	Estimates						
	Initial	0.9	0.1	25.0	20.0	0.0092	2
	Computed	0.925	0.075	23.01	19.00	0.0080	
	Initial	0.7	0.3	25.0	20.0	0.0075	2
	Computed	0.995	0.005	24.41	18.65	0.0130	
	Initial	0.5	0.5	25.0	20.0	0.0053	1
	Computed	*e*	*e*	*e*	*e*	—	

(*continued*)

Table 12. (*Continued*)

Data set number[a]		Normalized intensities[b]		Lifetimes (nsec)[b]			
		Compound 1	compound 2	Compound 1	Compound 2	dG/dt[c]	Region of ill conditionness[d]
4	True values	0.5	0.5	19.5	15.0	—	1
	Estimates						
	Initial	0.1	0.9	20.0	12.0	0.0200	2
	Computed	*e*	*e*	*e*	*e*	—	
	Initial	0.5	0.5	20.0	14.0	0.0166	1
	Computed	*e*	*e*	*e*	*e*	—	
	Initial	0.9	0.1	20.0	14.0	0.0204	2
	Computed	*e*	*e*	*e*	*e*	—	
5	True values	0.9	0.1	19.5	15.0	—	2
	Estimates						
	Initial	0.7	0.3	20.0	14.0	0.0189	2
	Computed	0.981	0.019	18.65	16.61	0.021	
	Initial	0.5	0.5	20.0	14.0	0.0166	1
	Computed	0.999	0.001	17.80	16.98	0.0030	
	Initial	0.3	0.7	20.0	14.0	0.0127	1
	Computed	*e*	*e*	*e*	*e*	—	

[a] From Table 3.
[b] Normalized intensities and lifetimes defined in Table 1.
[c] G defined in Figure 1 caption.
[d] From Figure 2.
[e] No computed values.

The first data set, DS 1, is one in which the normalized intensities were equal and the lifetimes differed by approximately 30%. The initial estimates were selected so that there was about an order of magnitude range in the dG/dt values. The regions of ill conditionedness into which the initial estimates fell varied from 1 to 2 (Figure 8).

However, although the true values fell into region 2, they were very close to 1—the region absolute ill conditionedness. Convergence was not observed for the first initial estimate; however, as a parameter set, it was very poorly conditioned and its dG/dt was small. Considerably better conditioned data sets were represented by the second and third initial estimates, both of which shared region 2.

DS 2 was one in which the lifetimes were the same as those for DS 1; however, the normalized intensities were adjusted so that the slow component's normalized intensity was nine times larger than the fast component's. This represents an ideal condition: the lifetimes differ by about 30% and the slow component dominates the emission. Convergence occurred for all three initial estimates despite the fact that some had small dG/dt values. From the regression on this data set, it is clear that the dG/dt value and the convergence area of the initial estimates diminishes when the data set is less ideal.

For DS 3, the lifetimes differ by less than 20% and the intensity for the slow component is nine times larger than the fast component. Thus, this data set represents an ideal case in terms of the intensity–lifetime relationship, but a nonideal case for the relationship of the lifetimes. This data set was slightly ill conditioned and associated with region 3. It also has a small dG/dt value (ca. 8.3×10^{-3}). Regression on the data set was modestly successful except for the last initial estimate.

The computed values associated with the first initial estimate are slightly better than those associated with the second initial estimate. The region of ill conditionedness and the dG/dt value for the first initial estimate are better than for those of the second. Thus, in the case of this data set which is less well conditioned than the previous one, the care with which the initial estimates are selected is more important. For example, the third initial estimate is in region 1.

For DS 4, the lifetimes differed by less than 20% and the intensities were equal. The parameter relationships for this data set are not favorable. However, from the dG/dt value (ca. 1.0×10^{-2}) it was expected that convergence might occur with carefully selected initial estimates. However, successful estimation never occurred. In all cases, the dG/dt values for the initial estimates were large with respect to that of the true value, but the regions of ill conditionedness were among the worst (region 1). It is concluded that if the data set is extremely ill conditioned, then no matter how carefully the initial estimates are selected, convergence to acceptable final estimates will not occur.

For DS 5, the lifetimes were the same as those for DS 4, but the intensity of the slow component was nine times larger than that of the faster component. The value of dG/dt for this data set was considerably larger than that of DS 4 (ca. 1.5×10^{-2}). The region of ill conditionedness for this data set was 2. Though convergence occurred for the first and second initial estimates, the final estimates were not as accurate as desired. In particular, as the dG/dt value decreased the precision of the final estimates decreased as well.

6. Summary

The following points summarize the results of this study.

1. The GSA, MA, and MQA programs performed satisfactorily with long lifetime data sets provided they exhibited little ill conditionedness.

2. Only the MA and the MQA programs performed satisfactorily with short lifetime processes using data which were moderately ill conditioned.

3. If the ratio of the true values of the intensities is greater than 0.8, but less than unity, the MA program fails to converge. However, the MQA program may converge if the intensity of the longer lifetime component is very large.

4. Criteria for evaluation of the reliability of the final estimates and the ill conditionedness of the initial estimates have been established.

5. For a given data set, the precision in the estimates is usually better when the MQA program is used.

6. The chances of successful regression with either the MQA or the MA programs are greatly improved the larger the number of counts collected. The precision in the parameter estimates is likewise improved.

7. The error calculations provided by the MQA program are: standard deviation in the calculated data, standard error in the final estimates, parameter correlation matrix, support plane confidence limits, and linear confidence limits. When these were considered together relative to the final estimates, their reliability could almost always be assessed. This is not the case for the MA program.

8. Both of the MA and the MQA programs exhibited some tendency to diverge as a result of error in the data.

9. Regardless of the outcome of the regression processes, for the MQA program or any program that requires initial estimates, it is always necessary to test in some way the reliability of the final estimates.

10. In order to use the MA program with a nonlinear data set, it is necessary to supply excitation and emission cutoff values. No procedure for accurately picking these values exists: however, it is possible to calculate an estimate of the cutoff.

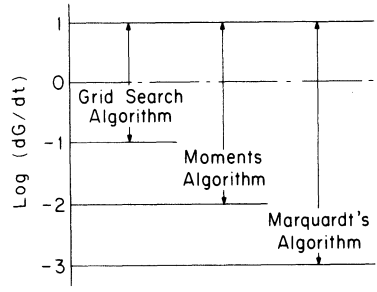

Figure 9. Ranges of application of the three algorithms.

Figure 9 summarizes the limits of application of the three algorithms used in this study in terms of the rate of change of the slow component emission in the total emission. The MQA algorithm exhibits the widest range of application with the MA algorithm range of application being nearly the same; the GSA exhibits the narrowest range. The upper limit as shown in the figure is arbitrarily picked as 1; however, in principal, this value can be much larger if the difference in the lifetimes is large.

Acknowledgments

This work was supported, in part, by Grant GM-17913 from the National Institute of General Medical Sciences.

References

1. A. E. McKinnon, A. G. Szabo, and D. R. Miller, *J. Phys. Chem.*, **81**, 1564 (1977).
2. D. V. O'Connor, W. R. Ware, and J. C. Andre, *J. Phys. Chem.*, **83**, 1333 (1979).
3. W. R. Ware, *Creation and Detection of the Excited State*, Vol. 1 (A. A. Lamola, ed.), Marcel Dekker, New York (1971), pt. A, Ch. 5.
4. W. R. Ware, S. K. Lee, G. J. Brant, and P. P. Chow, *J. Chem. Phys.*, **54**, 4729 (1971).
5. J. H. Easter and L. Brand, *Biochem. Biophys. Res. Commun.*, **52**, 1086 (1973).
6. J. B. Birks, *Progress in Reaction Kinetics*, Vol. 4, (G. Porter, ed.), Pergamon, New York, (1967).
7. T. Meites and L. Meites, *Talanta*, **19**, 1131 (1972).
8. E. Kohman, *J. Chem. Ed.*, **47**, 657 (1970).
9. Z. Bay, *Phys. Rev.*, 77, 419 (1950).
10. S. S. Brody, *Rev. Sci. Instrum.*, **28**, 1021 (1957).
11. D. Binder, *Phys. Rev.*, **77**, 856 (1950).
12. P. Wahl and H. Lami, *Biochim. Acta*, **133**, 233 (1967).
13. N. Arly and R. Buck, *Introduction to Theory of Probability and Statistics*, John Wiley, New York (1950).
14. A. Hald, *Statistical Theory with Engineering Applications*, John Wiley, New York (1956).
15. I. Isenberg and R. D. Dyson, *Biophys. J.*, **9**, 1337 (1969).

16. R. Schuyler and I. Isenberg, *Rev. Sci. Instrum.*, **42**, 813 (1971).
17. D. W. Marquardt, *J. Soc. Indust. Appl. Math.*, **11**, 431 (1963).
18. D. W. Marquardt, R. G. Bennet, and E. J. Burrell, *J. Molec. Spec.*, **7**, 269 (1961).
19. D. D. Morrison, *Proc. Jet Propulsion Lab. Seminar*, **1**, (1960).
20. R. W. Hamming, *Numerical Methods for Scientists and Engineers*, McGraw-Hill, New York, (1973).
21. H. Scheffe, *The Analysis of Variance*, John Wiley, New York (1959).
22. N. R. Draper and H. Smith, *Applied Regression Analysis*, John Wiley, New York (1967).
23. G. E. P. Box and N. R. Draper, *Univ. Wisc. Stat. Tec. Rep.*, **31** (1964).
24. A. Grinvald and I. Z. Steinberg, *Anal. Biochem.*, **59**, 583 (1974).
25. W. R. Ware, L. J. Doemeny, and T. L. Nemzek, *J. Phys. Chem.*, **77**, 2038 (1973).
26. W. P. Helman, *Int. J. Radiat. Phys. Chem.*, **3**, 283 (1971).
27. A. Gafi, R. L. Modlin, and L. Brand, *Biophys. J.*, **15**, (1975).
28. I. H. Munro and L. A. Ramsay, *J. Phys. E.*, **1**, 147 (1968).
29. L. J. Cline Love and L. A. Shaver, *Anal. Chem.*, **48**, 264A (1976).
30. Ortec Inc., Application Note AN 35, Oak Ridge, Tennessee.
31. H. E. Zimmerman, D. P. Werthemann, and K. S. Kamm, *J. Am. Chem. Soc.*, **96**, 439 (1974).
32. M. P. Neary, Ph.D. thesis, University of Georgia, 1976.
33. G. Lewis and W. R. Ware, *Rev. Sci. Instrum.*, **44**, 107 (1973).
34. R. Schuyer, I. Isenberg, and R. D. Dyson, *Photochem. Photobiol.*, **15**, 395 (1972).

ESCA Studies of Electrode Surfaces

P. M. A. Sherwood

1. Introduction

Film or adsorbed layer formation on an electrode surface has a marked effect on the behavior of that electrode. A redistribution of charge and potential occurs at the interfaces giving rise to double-layer regions. The ability of the film to transport material and charge will have important effects. The formation of the film may involve new electrode reactions; for example, for a metal M we may have

$$M \rightarrow M^{2+} + 2e$$

but formation of an oxide film is possible via the reaction

$$M + H_2O \rightarrow 2H^+ + M\text{–}O + 2e$$

It is not surprising to find, therefore, that the formation of a film on the electrode surface has a marked effect on the current–voltage curves for the electrode system concerned. For example, Figure 1 shows the current–voltage curve for a smooth platinum electrode in 0.5 mol dm^{-3} sulfuric acid.[1] As the potential is increased, the current falls initially due to oxidation of hydrogen on the electrode (formed in the return process). The current then rises sharply due to oxide formation prior to oxygen evolution (which occurs at the cusp on the extreme right-hand side of Figure 1). On decreasing the potential the current rises sharply due to oxide reduction, and then falls, rising again, with peaks due to adsorbed hydrogen formation prior to hydrogen evolution (which occurs at the cusp on the extreme left-hand side of Figure 1).

P. M. A. Sherwood • Department of Inorganic Chemistry, University of Newcastle upon Tyne, Newcastle upon Tyne NE1 7RU, England.

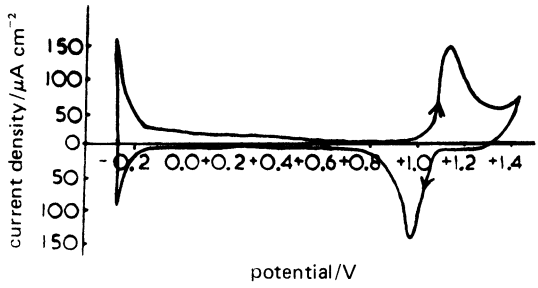

Figure 1. Current versus voltage sweeps for a smooth platinum electrode in 1 *N* sulfuric acid solution.[1]

The complete identification of the films formed on electrodes is central to a proper understanding of electrochemical systems. In addition, important information may be obtained about corrosion processes, and, in some cases, unusual compounds, not easily prepared by other methods, may be studied.

Several experimental methods have been used to study the films on electrodes. The possible presence of films is obtained from current–voltage curves, and the amount of film present may be obtained by the method of galvanostatic reduction. The film may be studied *in situ* by optical methods using ellipsometry and Raman spectroscopy (this latter method known as the hyper-Raman effect is currently the subject of great interest, though it has presently only been observed in a limited number of systems). Ellipsometry allows the optical constants of the film to be obtained from which the composition may be deduced, but the analysis is difficult and the interface between the substrate and the films must be smooth. Studies of films by infrared spectroscopy *in situ* are difficult due to sensitivity problems. There are a range of methods which involve *ex situ* analysis of the films. Microchemical analysis can be applied to thick films. X-ray and electron diffraction methods are valuable, but need thick and crystalline films (generally greater than ten monolayers thick). For example, even the thickest films that we have studied on a gold electrode by ESCA[1] are not seen by electron diffraction,[2] and in this case the films are appreciably decomposed by the electron beam. Mossbauer spectroscopy is a valuable method, but it is limited to certain elements, and again decomposition may occur.

X-ray photoelectron spectroscopy (XPS or ESCA) is a powerful method for the study of films or adsorbed layers on electrode surfaces. In ESCA the sample is subjected to almost monochromatic X-radiation which ejects both core and valence electrons from the sample. The characteristic valence bands of solids may, thus, be studied, and the binding energy of the core electrons measured. The latter depends upon the element involved, the charge on the atom or ion concerned, and upon its chemical environment. Furthermore, the

technique is especially appropriate to surface studies since the escape depth of the photoelectrons is less than 10 nm. Films of submonolayer thickness may be studied which makes the technique especially suitable for the study of submonolayer amounts of foreign atoms on electrode surfaces.

This chapter will discuss the application of ESCA to the study of electrode surfaces. Such a discussion would not be complete without a mention of the closely related technique of Auger spectroscopy (AES). Auger electrons appear in the photon excited ESCA spectrum, but most Auger spectrometers usually use electron beam excitation. The great strength of AES using electron excitation is that electron beams can be produced to very small dimensions (of the order of 5 μm and, thus, AES can provide valuable spatial information which can be used to investigate grain boundaries, fracture surfaces, or uneven surface features. Auger spectra can be collected more quickly than X-ray photoelectron spectra, but chemical shift information is often lost or difficult to interpret in Auger spectra because it involves three energy levels and the peaks are generally broader. Furthermore, the electron beam can decompose the sample. The ability of ESCA to provide information about the chemical state of the surface species for all elements in the periodic table and to identify the amount of material present makes it a very useful technique for the study of electrode surfaces. In this chapter ESCA studies of electrode surfaces will be discussed in detail, and at the end there will be a mention (and a list of references) of the electron excited AES studies of electrode surfaces.

The background of ESCA will not be explained in detail. There are now hundreds of review articles on ESCA published in many different languages. A basic background in ESCA given in such articles will be assumed. For example a review chapter by the author,[3] or for a more extensive coverage the book by Carlson[4] would be a suitable background. The application of Auger and ESCA to electrochemical problems has been reviewed,[5] and this work also gives a discussion of ESCA and Auger. Other reviews include the review by Nakajima and Watanabe[6] (written in Japanese), the review by Landolt and Mathieu[7] (written in French), and the review by Nakajima and Watanabe[8] (written in Japanese). Review articles on corrosion which include electrochemical studies have been written by Joshi,[9] Larson,[10] Castle,[11] Hashimoto and Asami[12] (written in Japanese), and Oudar[13] (written in French). The review by Larson[10] gives a review of a number of surface analytical techniques covering ellipsometry, AES, ESCA, ion scattering spectroscopy (ISS), secondary ion mass spectrometry (SIMS), electron stimulated desorption (ESD), and ion sputtering.

The number of papers using ESCA and AES for the study of electrode surfaces has increased exponentially in the last few years since the first studies in the early 1970s. In this chapter the work will be discussed on a subject basis rather than on an historical basis.

Most of the ESCA work discussed in this chapter involves core electrons and in this case the area under a given core spectral peak is proportional to the number of atoms of a particular type present, allowing the thickness of the film to be obtained. The binding energy allows the surface species to be identified by comparison with known compounds, or better by using, in addition, a suitable theoretical model to calculate the binding energy. The latter approach is valuable because the species on the electrode surface may be different from normal bulk compounds, and because the spectra of known compounds suffer from what a number of bulk compounds experience—surface decomposition—so that the spectrum of the surface is quite different from that of the bulk. For example many lithium salts contain lithium carbonate on the surface.[14] There are a number of theoretical models of varying complexity which will be found discussed in review articles on ESCA. In the types of studies discussed in this chapter the need is for a method which provides a suitably predictive model for providing comparative binding energies for a range of compounds and the author finds in this situation that approximate molecular orbital calculations and lattice potential calculations provide a suitable basis for such calculations.[15] Very few studies of the valence band of electrode surfaces have been carried out, this is partly because such spectra are generally less intense than the core levels, are more difficult to interpret, and suffer from the complication of having to unravel overlapping valence band spectra from various components including contamination. Nevertheless, the valence band spectra are important in that valuable information not available in the core region is present, especially when two different substances have little difference in their core binding energies, but substantial differences in the valence band, thus, aiding identification of the materials, are present. With the improvement in the theoretical methods available for obtaining valence band density of states, and the important developments in angle resolved photoemission experiments this region merits serious investigation. With the growing importance of single crystal electrode experiments the use of angle resolved photoemission experiments in the valence band coupled with X-ray photoelectron diffraction from the core levels becomes a valuable potential investigative method.

Electrode potentials referred to in the text are referenced to the saturated calomel electrode, and the abbreviation (SCE) follows the potentials given to indicate this. The SCE electrode has a potential of about $+0.3$ V with respect to a hydrogen electrode. A number of current–potential curves will be discussed and illustrated. These may be obtained by cyclic voltammetry, when the voltage is varied rapidly with time, or may represent curves obtained when the potential is constant for long periods of time. In general, they will show the growth of a film induced by anodic polarization. In this situation, the electrode under study is made the anode of an electrolytic cell. When a film is formed the applied current sets up an electrostatic field in the

film which may assist the growth of the film by causing ions to be pulled through the film. The situation is one of ionic conduction at high-field strengths complicated by the presence of the two interfaces: electrode/film and film/solution. When the field in the film becomes large enough for an appreciable ionic current to pass through, then the behavior becomes time-dependent since the thickness of the film is changing. Two situations may be examined experimentally: a constant ionic current situation (known as galvanostatic polarization) or a constant voltage (known as a potentiostatic polarization). In the former case, growth of the film requires a larger potential across the film for any increase in film thickness, while in the latter case, the ionic current falls with any like increase.

2. Electrode Transfer

2.1. The Possibilities for Film Change and Decomposition During Transfer

XPS studies of electrode surfaces suffer from the drawback that the electrode must be removed from the electrolyte and be transferred into the UHV chamber of the spectrometer. In the work of the author and his co-workers and of many other workers in this field, this has been done by removing the electrodes from the cell without disconnecting the potentiostat, washing in purified water, and transporting to the spectrometer in the appropriate way. In the case of the noble metals the electrode will not suffer air oxidation and the transfer is straightforward. In the case of nonnoble metals or compound electrodes special care may be necessary to ensure transfer of the electrode to the spectrometer to prevent air oxidation. In all cases it is necessary to carry out transfer in as clean a set of conditions as possible in order to reduce surface contamination during transfer.

It is necessary to examine the effect of this electrode transfer process. The result of disconnecting the potential is difficult to assess quantitatively, for the effects that this may have will depend upon the system under study. The need to transfer through the atmosphere into the spectrometer can be eliminated by methods to be described shortly. The effect of the high-vacuum system and X rays on the sample must also be considered. These problems have been discussed for particular cases by many of the investigators whose work is reviewed in this chapter. The problem of electron beam damage in AES has already been mentioned. X-ray photoreduction can also be seen, but it is generally rather slow and can be quantified and accounted for.[1] The effect of the vacuum is important. It is well known that hydrated salts tend to be dehydrated and some compounds decompose. Since the films on electrode surfaces are in solution in the cell the effect of removal into the vacuum on the composition of the surface film is important. There is much evidence that

in aqueous systems there is a strongly adsorbed layer of water on the electrode surface, which may take many hours to remove. For example in the author's apparatus which has a sample chamber fitted with a quadrupole mass spectrometer there is a strong water vapor peak for many hours. Furthermore, there is good ESCA spectroscopic evidence for the presence of bound water on the electrode surface. As expected this water film can be removed by heating, but it is still extremely tenacious. All this indicates that one can examine the film under conditions not greatly dissimilar to those in solution. Clearly, what actually happens depends upon the stability of the adsorbed film, so some unstable adsorbed intermediates might be lost either by decomposition or by removal on washing the electrode. It is encouraging to find that a large number of hydroxides have been identified on electrode surfaces, and these compounds do not generally suffer decomposition to oxides. Figure 22 illustrates how the O 1s core region allows distinction between O 1s peaks from oxide, hydroxide and water, and/or adsorbed oxygen species. A number of workers have examined the question of alteration of the film in transfer experimentally by comparison between ESCA measurements of the film and measurements of the film in the solution of the cell. For example the author and his co-workers have compared the amount of oxide formed on a gold electrode, measured by the areas under the ESCA peaks and suitable ESCA intensity expressions, with the quantity of electricity required to reduce the oxide film by galvanostatic reduction giving good agreement (Figure 2). The use of ESCA for quantitative analysis discussed in Section 25 provides another example of this agreement. Another method employed by the author and his co-workers has been the placing of the electrode into the cell again after the ESCA experiment to see if the electrode is at the same point on the current–voltage sweep.

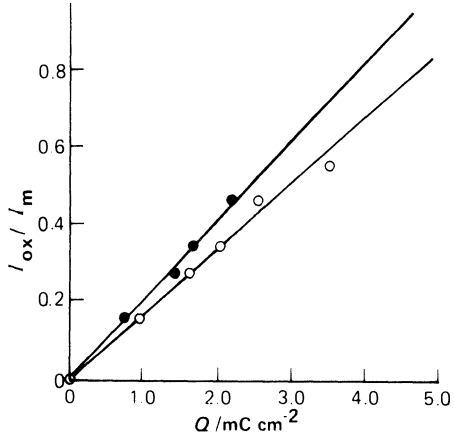

Figure 2. Comparison of galvanostatic reduction and ESCA measurements.[1]

Clearly, the possibility of film decomposition during transfer always exists and each study must try to ensure that experimental tests are carried out to evaluate the extent, if any, of such decomposition. This drawback must be balanced against the powerful information provided by the ESCA method. The next section discusses ways of reducing atmospheric oxidation and contamination to a minimum in this process.

2.2. The Anaerobic Transfer Electrochemical Cell

2.2.1. Cell Design

One method for anaerobic transfer is to place the electrochemical cell in a glove bag or glove box and carry out the electrochemistry under an atmosphere of deoxygenated nitrogen gas. Transfer to the spectrometer can be carried out using appropriate containers and glove bags and boxes.

In order to improve the technique of transfer of an electrode from an electrolyte solution to the high vacuum of the spectrometer anaerobically without decomposition or contamination, the best method is to design a cell that is attached to the spectrometer. Various groups have designed such cells for use with an ESCA spectrometer. Hammond and Winograd[16] have built miniature cells into a glove box enclosing the sample introduction probe. This design concentrates on the elimination of contamination from the solution by using a very small volume (about 250 μl) cell (Figure 3) which, with a total contaminant level of 10^{-6} M in 150 μl of electrolyte, would give 0.7 monolayers of contamination. Olefjord and Vannerberg[17] and Elfstrom and Olefjord[18] have attached an electrochemical cell via an isolation valve to a reaction chamber fitted to their ESCA instrument with a transfer system which allows the sample to be moved from the cell to the UHV chamber under protecting gas. The author and his co-workers[19, 20] have constructed

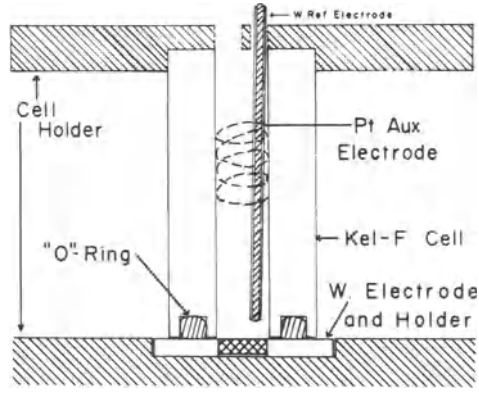

Figure 3. Miniature cell for potentiostatic oxidation.[16]

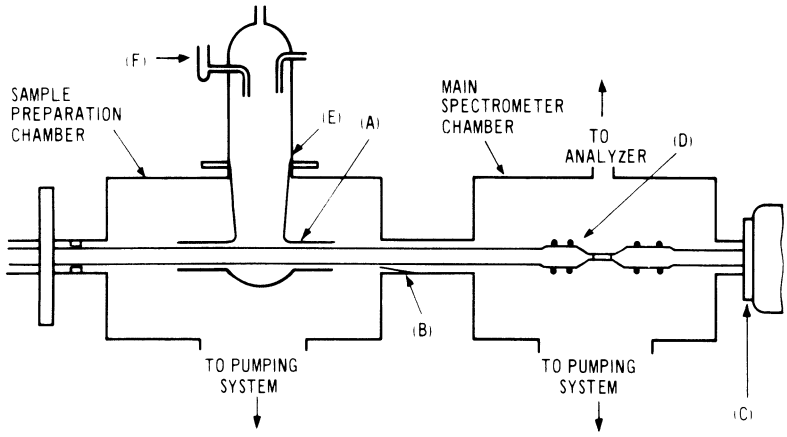

Figure 4. Schematic diagram of the spectrometer's main vacuum chamber and the sample preparation chamber containing the electrochemical cell. (A) Precision bore glass side-arms, (B) flap valve, (C) probe attached to insertion lock, (D) electrode assembly, (E) glass–metal seal, and (F) reference electrode compartment.[19]

an apparatus consisting of a high-vacuum chamber attached to the spectrometer containing a glass electrochemical cell of conventional size allowing electrodes to be studied spectroscopically and surface treated (e.g., argon-ion etched) before and after electrochemical treatment without contact with air (Figure 4).

The electrochemical cell is fitted into a separately pumped sample preparation chamber which is isolated from the main chamber by the flap valve (part B). The cell is made of glass, being connected to the sample preparation chamber via the glass–metal seal (part E). The base of the cell is fitted with precision bore glass side-arms (part A) which allow an electrode assembly to be inserted into insertion locks (part C) fitted onto both the sample preparation chamber and the main spectrometer chamber and pushed through the cell and towards the other insertion lock. This arrangement allows the electrode to be taken from the cell and into the main chamber. Figure 5 shows an exploded view of the bottom of the cell, shown containing an electrode assembly.

The electrode assembly consists of the electrode material, constructed as a metal rod which screws into an interior stainless steel shaft with a flat face cut into it (to allow angle-resolved photoemission experiments to be carried out). The electrode material is engaged on two Teflon cylinders (part A) also fitted on the brass shaft (part B), and the electrode forms a vacuum and liquid seal with the Teflon by the pressure of knife edges on the electrode material tightened by a brass locking cap on the extreme left-hand side. The Teflon cylinders seal the electrode assembly into the cell by the sealing of the

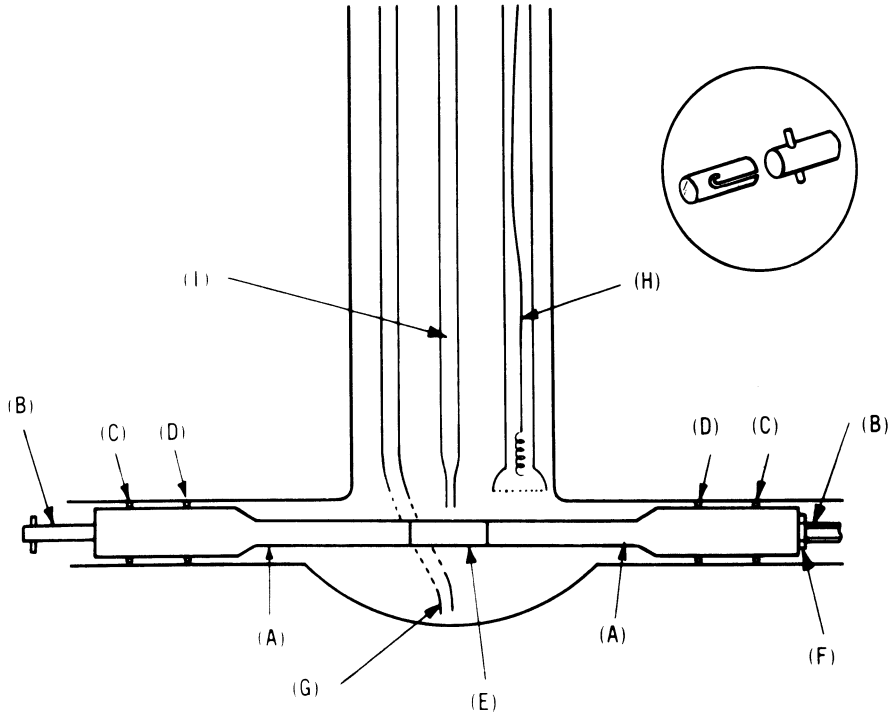

Figure 5. Diagram of the lower part of the glass electrochemical cell showing the electrode mounted on its holder in the cell. (Part A) Teflon cylinders, (part B) stainless steel smooth rod, threaded on extreme right engaging on brass end piece, (part C) Viton "O" rings, (part D) Teflon "O" rings, (part E) electrode material, (part F) stainless steel end stop, (part G) drain tube, (part H) platinum counter electrode, and (part I) Luggin capillary.[20]

two outer Viton "O" rings (part C) and the two inner Teflon "O" rings (part D) engaging on the precision bore glass side-arms of the cell. This arrangement means that when the electrode assembly is in the cell only the electrode material and Teflon are in contact with the solution and that the electrochemical experiments can be carried out with liquid in the cell and a high vacuum in the sample preparation chamber. Figure 6 shows exterior views of the cell and the rest of the apparatus. The upper part of the cell is made up of a reference electrode compartment using a standard saturated calomel reference electrode, and various inlet tubes for deoxygenated liquids, white spot nitrogen, and the evacuation of the cell. The electrode assembly can be translated from the cell through the flap valve between the two vacuum chambers and into the main spectrometer chamber. The whole electrode assembly can then be connected onto a rotatable probe fitted into an insertion lock on the main chamber, and the translation shaft removed and detached, with the flap valve

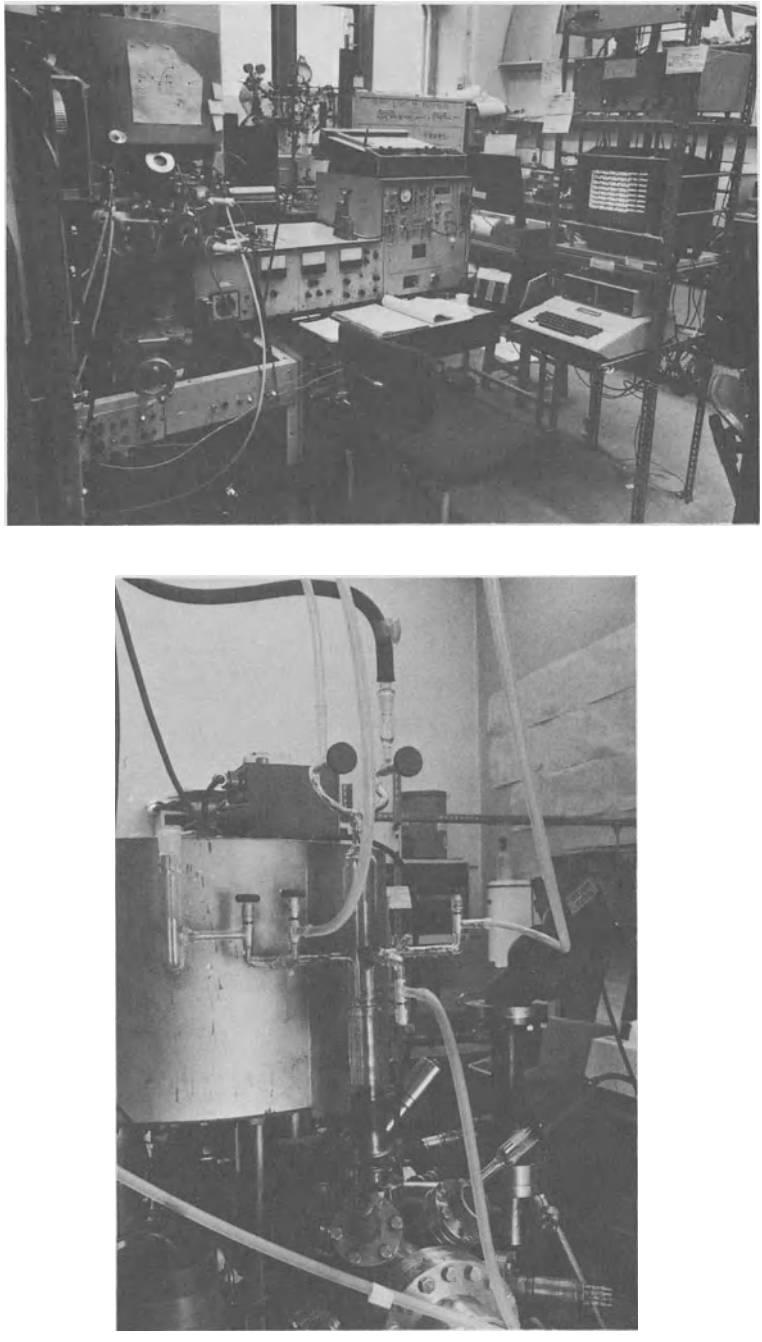

Figure 6. Views of the *in situ* electrochemical cell, insertion shaft, and the rest of the apparatus.

being closed to allow ultrahigh-vacuum conditions to be achieved in the main chamber.

This experimental design allows the surface of the electrode to be analyzed and prepared (e.g., by argon-ion etching to remove any oxide film) before any electrochemistry is carried out. The electrochemical cell is kept under vacuum except when liquid is about to be added when it is filled with white spot nitrogen. The whole arrangement allows the experiments to be carried out anaerobically with a high level of control and monitoring of surface conditions on the electrode. This apparatus also allows an investigation of the effects of bulk liquids on surfaces. Application of this and the other anaerobic transfer cells will be discussed later in this chapter.

2.2.2. Air-Formed Oxide Films

In many cases the films formed on electrode surfaces consist of metal oxides, and a useful collection of the ESCA binding energies of such oxide films has been given by Barr[21, 22] and Holm and Storp.[23] Barr provides a useful study of the room temperature air-formed oxide films on many different elemental metals.

3. Data Analysis

It has already been pointed out that most of the work described in this chapter uses core ESCA data to distinguish the chemical nature of the surface film. This sort of identification depends upon the detection of chemical shift information in the spectrum. In many cases this requires curve fitting to be carried out in order to fit a series of overlapping peaks to the data. Most ESCA data are produced in analog form and the curve fitting is generally carried out by analog methods, most commonly by using a Du Pont curve resolver. Such methods are highly subjective and, thus, often misleading. Analog data are also subject to the problems of uncertainty in peak position and peak area due to dependence upon instrument time constant and scanning speed. Analog data give essentially no idea of data quality due to the effective smoothing due to the choice of a high-time constant, and the tendency of some authors to present data which consist of a smooth curve drawn through the data. Data of high quality are needed for accurate curve fitting, although this may sometimes not be possible due to sample decomposition. In the author's laboratory recent spectra have been obtained using digital data, most recently obtained by linking the spectrometer directly to the University IBM 370/168 computer via a microprocessor link allowing extended data collection and signal averaging as well as an intermediate level computing system. The experimental arrangement is illustrated in Figure 7.

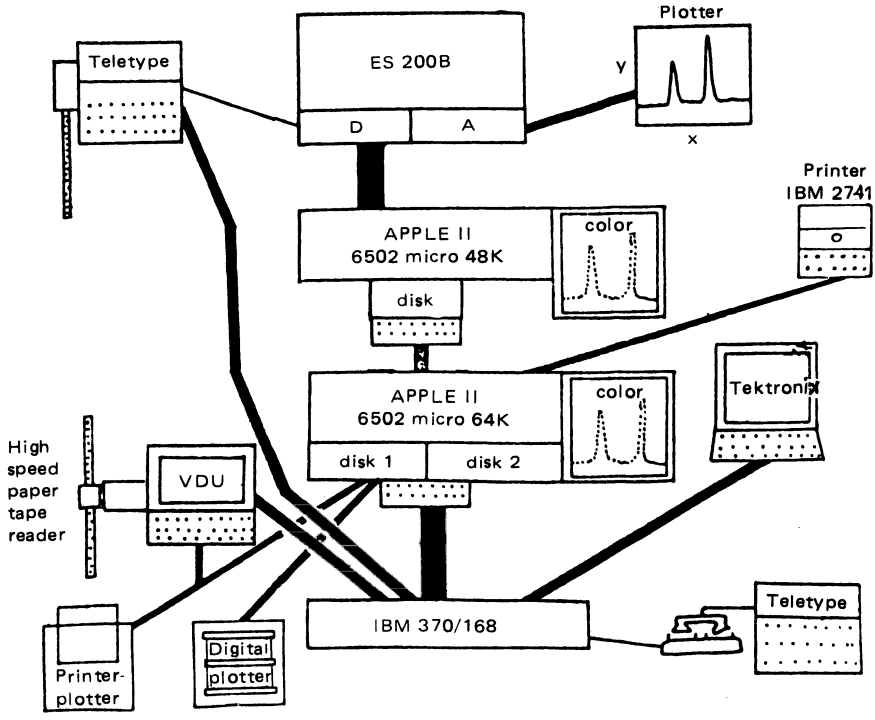

Figure 7. Schematic diagram of the data collection and data handling arrangement.

Data are collected simultaneously on an analog ratemeter (A) and a digital ratemeter (D). The analog ratemeter gives an $X-Y$ analog plot and the digital ratemeter is connected to an Apple II 6502 (48K) microprocessor system. The digital ratemeter has an additional output which allows data, when required, to be punched out on paper tape simultaneously with a transfer to the Apple II system for the rare cases when one has to monitor the collection of data with time in the case of decomposing samples. The data are stored on floppy disk on the Apple II, and can be transferred to another Apple II (64K) microprocessor for further processing so that there is no dead time in the system (i.e., the spectrometer is collecting data all the time). Either Apple II can be connected to a hard-wired high-speed line to the University IBM 370/168 computer. The 64K Apple II can act as an intermediate computing system for the plotting of data and other tasks. Data analysis is generally carried out on the IBM 370/168. This may take the form of curve fitting using nonlinear least squares fitting using a Gaussian–Lorentzian product function[20] allowing overlapping chemically shifted peaks to be analyzed with much greater accuracy. In addition, difference or differential spectra may be obtained especially in cases where small spectral changes need

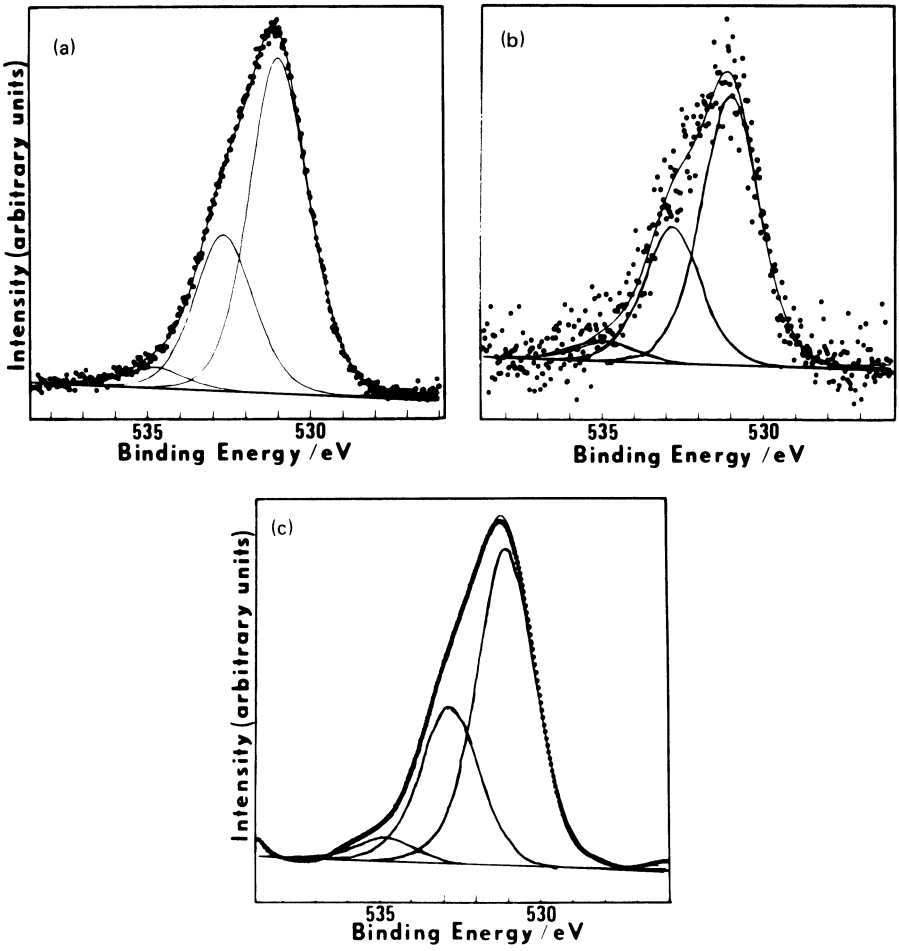

Figure 8. Oxygen 1s ESCA spectra illustrating the effect of smoothing. In all cases the spectra are fitted to three peaks, the details being given in Table 1. (a) Data for the same material obtained with good statistics by running the spectrum for a long period, (b) data for the same material with bad statistics by running the spectrum for a short period, and (c) the result of smoothing the spectrum (b) 100 times with a smoothing interval of 21.[24]

to be detected. In cases where spectra have to be run for a short time then it may be necessary to smooth the data in order to obtain any valid curve fitting. We have evaluated different methods of smoothing[24] and Figure 8 and Table 1 show how for an O 1s spectrum such smoothing allows data of poor statistics to be analyzed more successfully.

Figure 8 also shows how the nonlinear least squares curve fitting gives 95% confidence limits allowing an evaluation to be made of the significance of the fitting results. For example it is clear that the two leftmost peaks are fitted

Table 1. The Effect of Smoothing[a]

Parameter	Good statistics [Figure 8(a)]	Bad statistics [Figure 8(b)]	Bad statistics smoothed [Figure 8(c)]
Binding energy (eV)	534.81(16)	534.79(76)	534.73(12)
	532.66(04)	532.74(18)	532.71(03)
	530.95(02)	530.99(08)	530.99(01)
FWHM (eV)	2.10(04)	2.04(15)	2.10(03)
Area ratio	1:7.77:16.90	1:7.44:14.94	1:7.08:14.34
Chi squared	584.4	15636.9	321.97

[a]Figures in parentheses refer to 95% confidence limits.

with less confidence in width, height, and position than the main peak. The fitting program is also designed to fit to the minimum number of peaks consistent with obtaining the best chi-squared value (analog methods generally always give better fits with more peaks), as well as including all peaks due to satellite X-radiation.

Other workers have used Fourier transform methods for curve fitting. The whole subject is still controversial, but the main point is that good quality data and careful and critical data analysis is vital in extracting chemical information from ESCA results from the core levels of thin films on electrode surfaces.

4. Carbon and Related Electrodes

A variety of rather different carbon systems have been studied. Imoto *et al.*[25] have used ESCA to study the electrochemistry of the production of fluorine gas by the electrolysis of molten KF–2HF using a carbon anode. This process exhibits an "anode effect" which limits the electrolysis current density, for when the anode potential is raised above a certain potential there is a marked reduction of current density. The ESCA study revealed that the C 1s region showed two peaks in all cases, one due to the C–C bond in the carbon, and one due to C–F groups on the surface. The latter peak was found to grow in intensity as the anode potential was increased. This suggested that a $(CF)_n$ film was formed on the surface of the anode not only during the anode effect, but also under normal conditions of electrolysis:

$$2F^- \rightarrow F_2 + 2e$$

$$nC + nF^- \rightarrow (CF)_n + ne$$

It was suggested that the $(CF)_n$ compound reduced the wettability of the anode surface for the electrolyte. Under normal conditions of electrolysis the

$(CF)_n$ compound decomposes:

$$(CF)_n \rightarrow C + CF_4 + C_2F_6, \text{ etc.}$$

but when the rate of formation of $(CF)_n$ exceeds that of decomposition then the "anode effect" is seen.

Johansson *et al.*[26] have studied the surface of some carbon gas-diffusion air and oxygen electrodes in acid solution. The electrodes were prepared by mixing active carbon with a Teflon dispersion using different solvent mixes. The ESCA results show two different F 1s peaks, clearly separated, which the authors identify as being due to two different types of Teflon in the electrodes. They ascribe one of these peaks as being due to small Teflon particles in close contact to the active carbon (which is a good conductor) and, therefore, with a low-surface charge (for a simple discussion of surface charging see reference 3), and the other to larger Teflon particles which are, thus, further away from the active carbon particles and, being insulators, acquire a higher surface charge. This sort of differential sample charging can be demonstrated in a model system,[27] and this provides a good example of its use to identify differences in sample geometry. There are two C 1s peaks, one due to the carbon and the other due to the Teflon, the former being much more intense. As the Teflon particles became larger one would expect the free carbon surface to increase. In fact, the ratio of the total F 1s area to the active carbon C 1s area confirms the model, thus, when a large amount of small Teflon particles is present the ratio is high, and when a large amount of large Teflon particles is present the ratio is low. The ratio of the two different fluorine peaks follows the trend as well, the peak at higher binding energy increasing with respect to the lower binding energy peak as the ratio above gets smaller. The size of Teflon particles is controlled by the solvent mix. It is found that as the active carbon surface increases in area the amount of electrolyte soaked into the electrode increases and the electrochemical activity improves.

Watanabe and Morigaki[28] have investigated two kinds of graphite fluoride electrodes in the cell: graphite fluoride/1 *M* HC104-propylene carbonate solution/Li by ESCA, X-ray diffraction and DTA. In the case of the $(CF)_n$ electrode the interlayer spacing increased from 0.571 to 0.602 nm as discharging proceeded. The $(C_2F)_n$ electrode displayed more complex behavior. In both cases the ESCA spectra indicated that the discharge products were nonstoichiometric ternary intermediates CLi_xF_y for the $(CF)_n$ electrode and $C_2Li_xF_y$ for the $(C_2F)_n$ electrode, where x and y are close to unity.

Proctor and Sherwood[29] have examined the ESCA spectra of carbon fiber surfaces which have been subjected to electrochemical treatment in different electrolytes and different potentials. The C 1s and O 1s regions show clear changes in the nature of the fiber surface due to the formation of C–O and other groups.

Fujihira and Osa[30] used ESCA and electrochemical methods to study the surface of glassy carbon electrodes that were oxidized and reduced and then methylated and esterified. They found that various reactive functional groups were formed on the carbon surface.

5. Electrodes Involving Magnesium and Aluminum

5.1. Detection of Precipitation of Magnesium Hydroxide

Castle and Tremaine[31] have used ESCA as a method for detecting the initial precipitation of a tracer ion in order to determine the pH value at a cathode surface at which this precipitation occurred. These authors were concerned with the nature of the layer formed on aluminum alloys that were exposed to sea water. X-ray diffraction of thick layers has established the principal magnesium-containing component of the layer as the mineral hydrotalcite [$Mg_6Al_2(OH)_{16}CO_2 \cdot 4H_2O$], but uncertainty in the knowledge of the pH at the cathode surface complicates an understanding of the mechanism of the process. These workers investigated this problem by investigating a model system using copper and brass electrodes in magnesium chloride solution under conditions of hydrodynamically controlled exposure. Using ESCA intensity measurement for copper and magnesium lines Castle and Tremaine were able to plot the thickness of magnesium hydroxide as a function of current density at the cathode and bulk pH value (Figure 9), and found that the region within which precipitation was detected by ESCA conforms well in shape to that shape predicted from a simple hydrodynamic model [this model gives the curve OABD, the best fit being for a diffusion boundary layer thickness d of 0.3 mm, and it can be seen that below this curve the $Mg(OH)_2$ is of negligible thickness and above the curve of appreciable thickness]. The authors see this type of experiment as being useful not only for determination of the actual pH values reached at a surface by using tracer ions at varying concentrations, but also as a method for determination of effective diffusion boundary layer thicknesses in experimental systems which are not well defined hydrodynamically such as the stirred beaker arrangement.

5.2. Effect of Ions on the Anodic Oxide Films on Aluminum

A number of workers[32-39] have used ESCA to study the anodic oxide films formed on aluminum metal, and the effect that different anions have on the formation and breakdown of this passivating film. An ESCA study of aluminum alloys[40] and their anodic oxide films showed Al 2p and O 1s binding energies that were nearly identical to those of high-purity aluminum

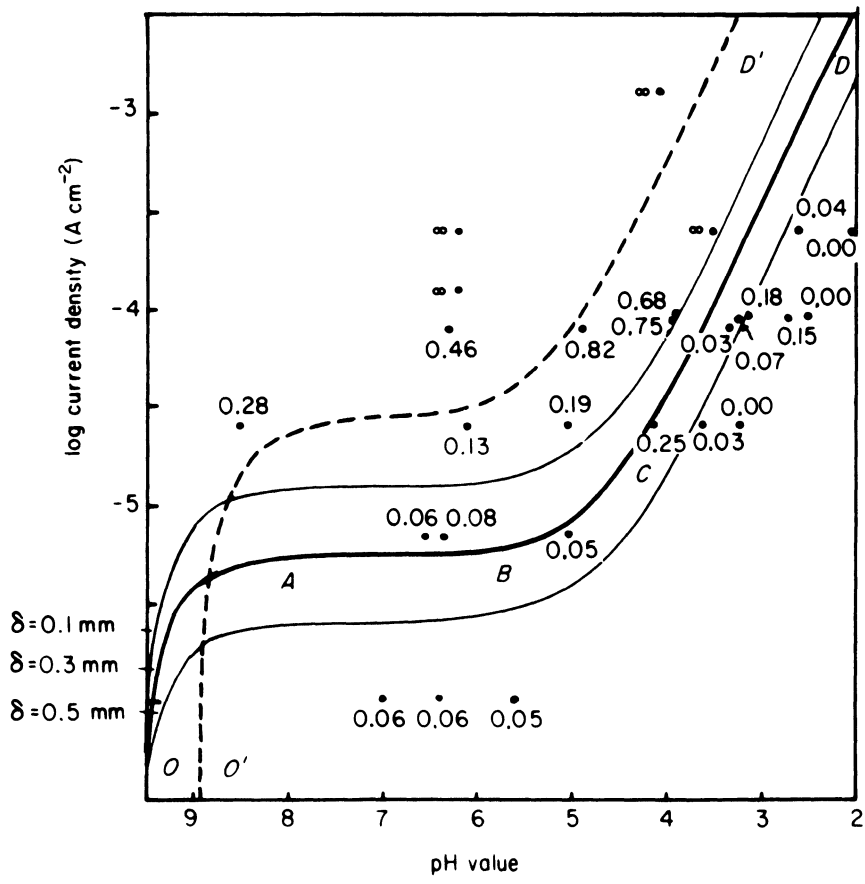

Figure 9. The thickness of magnesium hydroxide as a function of current density at the cathode and bulk pH value. Curve OD, $MgCl_2$ solution/O, D, and sea water. The number against each point is the equivalent thickness in nanometers.[31]

and its anodic oxide film. Mechanically polished aluminum metal is found by ESCA to have a thin oxide film composed of $Al_2O_3 \cdot 3H_2O$ of about 1–1.30nm thickness.[35] Eguchi *et al.*[32] studied the nature of the oxide films formed in sulfuric acid, sodium sulphate, $NH_4HB_4O_7$ and Na_2SO_3, and found sulfate incorporation. Koudelkova *et al.*[36] studied how this sulfate incorporation varied as a function of increase or decrease of anodic potential during electrolysis of aluminum in sulfuric acid. It was found that the amount of sulfate in the anodic oxide films formed during a decrease in anodic potential during electrolysis was much less than that formed during an increase in anodic potential. This result was also found by Augustynski[37] who also found that the incorporation of sulfate ions, at the rest potential, into the oxide film did not impede the simultaneous adsorption of chloride ions. Koudelkova *et*

al.[36] found that the same situation occurs for chromate solutions, and Koudelkova and Augustynski[38] have found that the same is true of nitrate solutions.

Chloride ions cause the pitting corrosion of aluminum, but the presence of other ions may inhibit this process. This is illustrated by considering the critical pitting potential (E_{cr}) of aluminum under different conditions. Figure 10 shows the potentiostatic polarization curves (polarization at 10 mV per minute) for aluminum in (curve a) 0.1 *M* NaCl solution, (curve b) 0.2 *M* Na_2CrO_4/0.1 *M* NaCl, and (curve c) 0.2 *M* $NaNO_3$/0.1 *M* NaCl solution.[38] It can be seen that the critical pitting potential is shifted to more positive potentials (i.e., in the noble direction) by the addition to the chloride solution of various anions. The amount of chloride found in the oxide film which we have seen to be unaffected by the presence of sulfate chromate or nitrate ions at the rest potential is about 3 at.% at the rest potential and in the absence of any other ions is about 12 at.% near the critical pitting potential. In all cases ESCA analysis shows that the chlorine is present in the film as chloride. Furthermore, it is surprising to find that when perchlorate ions are present[34] only chloride is found in the film because the ClO_4^- ions are quantitatively reduced inside the film:

$$3ClO_4^- + 8Al^{3+} + 24e \rightarrow 3Cl^- + 4Al_2O_3$$

with the following reaction at the metal–oxide interface:

$$Al \rightarrow Al^{3+} + 3e$$

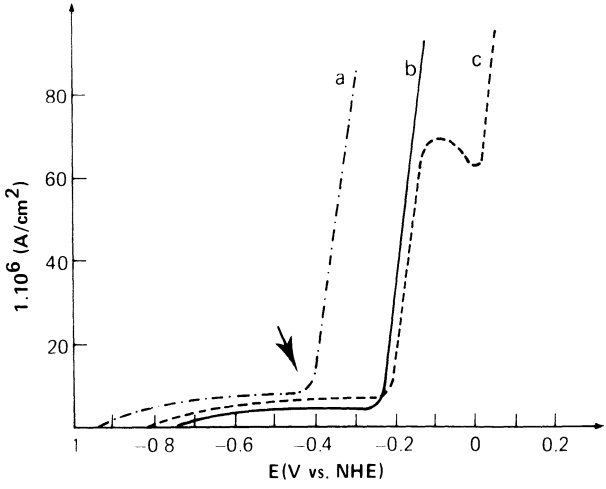

Figure 10. Potentiostatic Polarization curves for aluminum (a) in 0.1 *M* NaCl solution, (b) in 0.2 *M* Na_2CrO_4/0.1 *M* NaCl, and (c) in 0.2 *M* $NaNO_3$/0.1 *M* NaCl solutions. The arrow points to E_{cr} for 0.1 *M* NaCl solution.[38]

Despite perchlorate ions leading to the production of chloride ions, perchlorate ions act as an inhibitor with a more noble value of E_{cr}. The observation of a change in the nature of the ion when incorporated in the passive film is a general one. Thus, in the case of Na_2CrO_4 ESCA studies[36] of the film show the presence of Cr(III) in Cr_2O_3 and Cr(VI) in CrO_4^{2-}. Once again reduction is thought to occur:

$$2CrO_4^{2-} + 2Al^{3+} + 4H_3O^+ + 6e \rightarrow Cr_2O_3 + Al_2O_3 + 6H_2O$$

In the case of nitrate[35] ESCA studies show that the nitrate ions are reduced to ammonium ions:

$$NO_3^- + H_3O^+ + 3Al^{3+} + 9e \rightarrow Al\,N + Al_2O_3 + \tfrac{1}{2}H_2 + H_2O$$

Only in the case of sulfate ions is no reduction observed.

Returning to Figure 10 it is interesting to note that, in general, as soon as the E_{cr} value is passed there is a sharp increase of current, but in the case of curve c for mixed nitrate and chloride a sharp increase of current, up to 60–80 $\mu A/cm^2$, takes place about 0.2 V below the E_{cr} value. This behavior is found to be concentration dependent, and displays a strong kinetic effect since the behavior depends upon the rate of polarization. The effect is also seen in nitrate solutions with no chloride present. ESCA studies[38] show the ammonium ions mentioned above for rest potential studies of film incorporation, but an increasing amount of adsorbed nitrate ions were found as the potential was made more positive and it appears that the nitrate ions are on the surface of the film rather than being incorporated into the bulk of the film (when they would be expected to be reduced). Unlike the purely inhibiting chromate, nitrates have a partially aggressive and partially inhibiting effect on aluminum, but overall they give the largest noble shift of the critical pitting potential.

Kaneno *et al.*[39] have studied the film produced on aluminum produced in a neutral borate solution by ESCA and conventional methods. Anodic oxidation was carried out and the amount of Al^{3+} obtained from the analysis of the solution and the area of the current–time curve. A film of about 77-nm thickness was produced in this way and the film was found to contain a relatively soluble outer layer (32 nm) and an insoluble inner layer (45 nm). An ESCA depth profile was carried out of the film and the O 2s/Al 2s and B 1s/Al 2s intensity ratios were measured, and boron was found to have a depth of greater than 10 nm.

5.3. Anodization of Aluminum in Liquid Hydrogen Fluoride

Yamada *et al.*[41] have studied the anodization of aluminum in liquid hydrogen fluoride containing small amounts of water by ESCA. When the

water concentration was below 10% anodization was possible to give aluminum oxides and fluorides. When the water concentration was above 10% the aluminum dissolved rapidly.

6. Electrodes Involving Titanium

6.1. Titanium Metal and Alloys

Armstrong and Quinn[42] have used AES and ESCA to examine the electrochemical oxidation of titanium thin-film electrodes. The electrodes were prepared by electron beam evaporation onto hot (450°C) quartz disks at a pressure of 10^{-7} Torr to give films of the thickness of 20–25 nm. As a result of the reactivity of titanium these films contained a small percentage of oxide throughout the entire film and formed a thin layer of passive oxide on the exterior of the film and this affected the electrochemical behavior. AES and ESCA studies of the surface oxides formed on these films on linear potential scans in 1N $KClO_4$, 1N $HClO_4$, and 1N sulfuric acid showed a mixture of metal and metal oxides (TiO_2, Ti_2O_3, and TiO), with the higher oxides predominating with increasing electrochemical oxidation. ESCA studies showed that the oxide thickness varied from 1.23–1.4 nm for untreated electrodes and up to 2 nm for electrodes treated at potentials up to 2 V(SCE). The results are consistent with two possible interpretations. The first assumes that each electrode is covered with a thin TiO_2 layer which overlays a thin-suboxide layer (Ti_2O_3/TiO) over the reduced metal. Increasing oxidation would increase the thickness of the TiC_2 and the suboxide layers. The

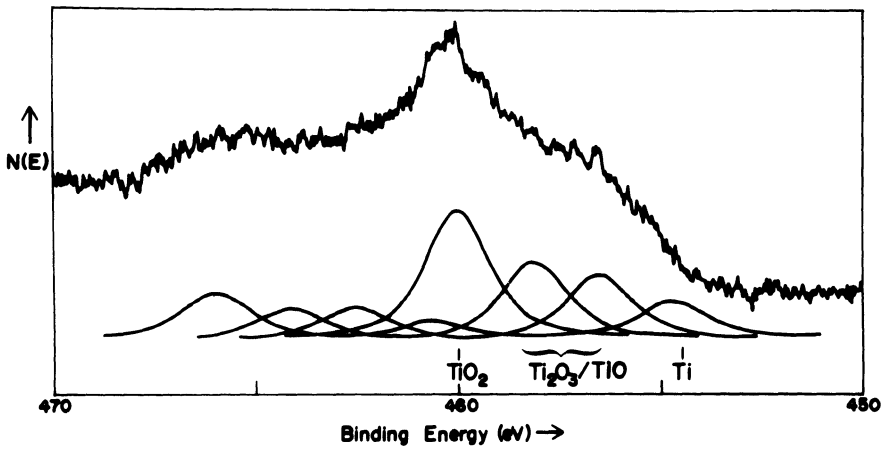

Figure 11. Curve fitted Ti ESCA spectra. The background has been subtracted for presentation of the fitted peaks.[42]

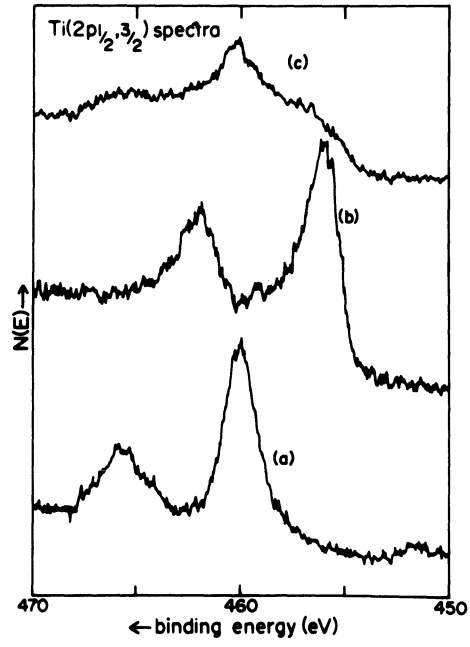

Figure 12. Titanium 2p ESCA spectra for (a) TiO_2, (b) Ti film after sputtering for about 15 nm, and (c) surface of Ti film electrode.[42]

second assumes that the TiO_2 forms islands, bordered by suboxides, which deepen and eventually coalesce as oxidation proceeds. The curve fitted ESCA data for the surface of the electrode using a computer simulation technique are shown in Figure 11, and Figure 12 shows how this spectrum compares with that of the metal (obtained by sputting 15 nm of the titanium film) and that of TiO_2. AES depth profiles were carried out to characterize the subsurface metal/metal oxide composition and to correlate the oxygen to metal atomic ratio with electrochemical pretreatment.

Dalard *et al.*[43] have used AES and ESCA to study the surface preparation of titanium and titanium alloy (TA6V4) in order to determine the factors that promote paint and glue adhesion. Thin-oxide films were made by anodic oxidation of the titanium in sulfuric acid as well as by chemical reaction. The anodic oxide films were found to be homogeneous, but were contaminated by sulfate ions.

6.2. Titanium Dioxide and Related Electrodes

There is considerable interest in titanium dioxide electrodes because water photoelectrolysis is possible without degradation or decomposition of the semiconductor electrodes. Unfortunately, titanium dioxide has too large a bandgap (3 eV which is too far into the UV region to significantly absorb solar energy) to be suitable for solar applications. Much work has been

carried out to find systems with a lower bandgap, but with a stability comparable to the titanium dioxide electrode. Another approach to this problem using chemically modified electrodes will be discussed in Section 21.2.2. Sayers and Armstrong[44] have used ESCA to monitor the surface of TiO_2 single-crystal electrodes, and $SrTiO_3$ and $BaTiO_3$ electrodes. It was found that reduction of the electrode surface in a hydrogen atmosphere resulted in an oxygen deficient surface composition which can be returned to its nearly stoichiometric oxygen-to-metal ratio by subsequent photoelectrolysis. Blondeau *et al.*[45] used ESCA, electron microscopy, microdiffraction, nuclear microanalysis, and optical measurements to study Cu^- doped titanium dioxide. Copper doping of titanium dioxide was achieved by anodic oxidation of a titanium 2.5% copper alloy which produced a better photoelectrochemical response because the doping produces a band in the bandgap of titanium dioxide, but the method of preparation lacks the control of impurities that one would desire. ESCA studies of the surface show considerable differences between mechanical surface polishing and electropolishing, thus, the electropolished sample shows no copper, but the mechanically polished sample shows a strong Cu 2p peak. When the samples are etched the mechanically polished sample shows a reduction in the copper intensity and the electropolished sample shows the appearance of a strong Cu 2p peak. Etching was found to cause reduction of titanium dioxide to metal by both groups[44, 45] of workers.

Fukuzuka *et al.*[46] have studied the relationship between corrosion resistance and the surface film of titanium coated with $PdO–TiO_2$ mixtures analyzed by ESCA and X-ray diffraction. The film was polarized in hydrochloric acid, sulfuric acid and phosphoric acid.

7. Vanadium Pentoxide Electrodes in Reserve Cells

Merriman and Vezzoli[47] have used ESCA to examine the surface of vanadium pentoxide electrodes in reserve cells. Reserve cells are designed to remain inactive for long time periods during which there is no serious loss in output capability. This is achieved by isolation of the electrolyte solution from the electrodes during the period of inactivity, the electrolyte being released by detonating a primer which releases the electrolyte contained in a glass ampule. The vanadium pentoxide electrode is made up of a mixture of V_2O_5 and graphite, and the other electrode is made up of lithium metal pressed on an expanded stainless steel screen. ESCA studies were carried out on the O 1s and vanadium core regions, and it was found that vanadium pentoxide from batteries displaying premature breakdown and irregular behavior had an oxygen content as measured by the O 1s electron region that was slightly greater than that for vanadium pentoxide from satisfactory batteries.

8. Electrodes Involving Chromium

Dickinson *et al.*[48] used ESCA to study the film formed on a gold electrode during the electrochemical reduction of chromium(VI). In the electrochemical reduction of chromium(VI) in chromic acid and mixed chromic acid and sulfuric acid solutions the open circuit potential is close to the equilibrium potential for the reaction

$$H_2CrO_4 + 6H^+ + 3e \rightarrow Cr^{3+} + 4H_2O \; E^0 = 1.36 \text{ V}$$

but no significant current flows in pure chromic acid solutions until hydrogen evolution occurs. ESCA studies showed that the reduction is prevented by the formation of a surface film. In the presence of sulfuric acid, reduction can occur, but the rate exhibits a curious dependence on potential. In both cases the films are shown to contain Cr(VI),Cr(III), chromium in an intermediate

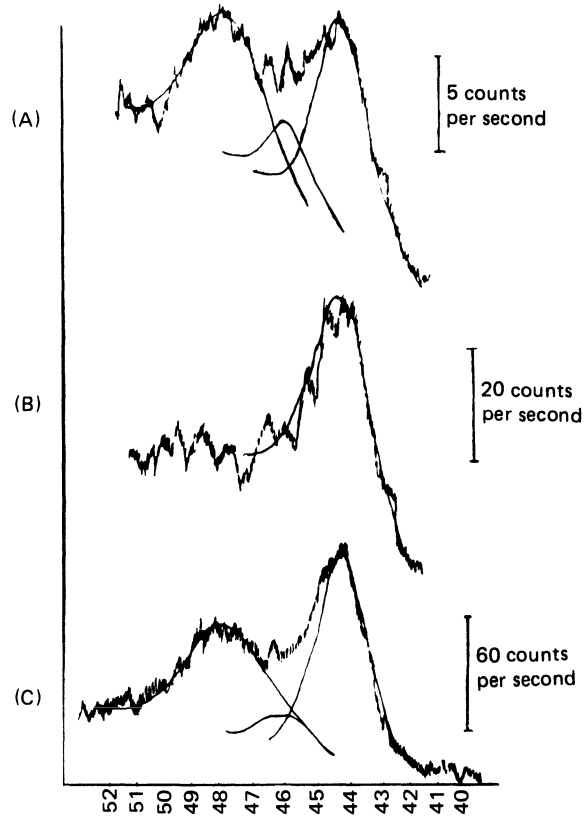

Figure 13. Cr 3p ESCA spectra for a gold electrode after polarization for 15 min at a potential of (a) +0.80 V, (b) −0.3 V, and (c) −1.20 V in 1 mol-dm^{-3} chromic acid.[48]

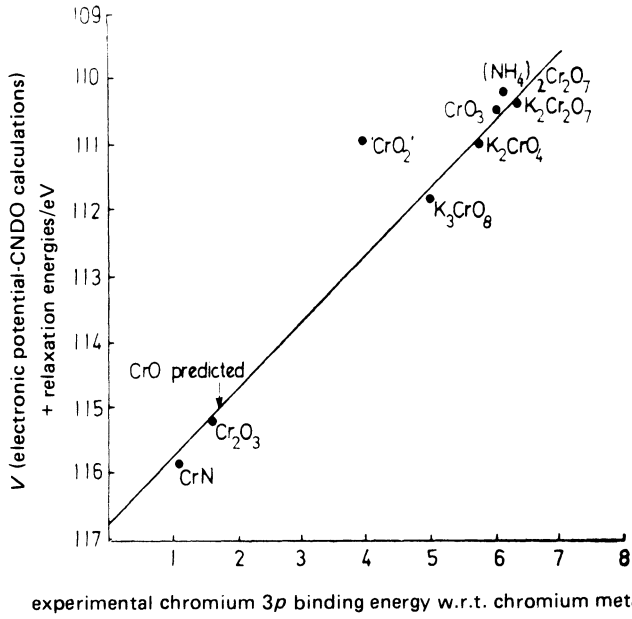

Figure 14. Plot of the sum of the electronic potential (from CNDO calculations) and the relaxation energy against the experimental difference in the binding energies of Cr 3p electrons in chromium metal and a series of chromium–oxygen compounds and CrN (line of unit slope drawn in).[15]

oxidation state, and oxygen, in varying proportions over the potential range investigated. The films had varying thicknesses, many were around 2 nm thick, but some were 6 nm or more thick. Figure 13 shows the Cr 3p electron spectrum which shows the Cr(VI) region on the left, the Cr(III) region on the right, and the substantial changes that occur in the spectrum at different potentials in chromic acid. It is interesting to examine how effective theoretical calculations[15] can be in predicting chromium core binding energies. Figure 14 shows a plot of experimental binding energies and calculated binding energies for a range of chromium compounds, showing good agreement. It will be seen that the peak that is furthest off the curve is assigned to "CrO_2." This employs the experimental value for the chromium species of the intermediate oxidation state discussed earlier. It can be seen that it certainly does not correspond to the predicted value for CrO. This intermediate oxidation state species is perhaps some hydrated form of CrO_2. It is important to point out that relaxation differences play a major role in obtaining the agreement shown in Figure 14, which is illustrated in Figure 15, which has the relaxation differences excluded.

Bouyssoux *et al.*[49] have examined the surface composition and thickness of anodic passive films formed on (111), (110), and (100) oriented chromium

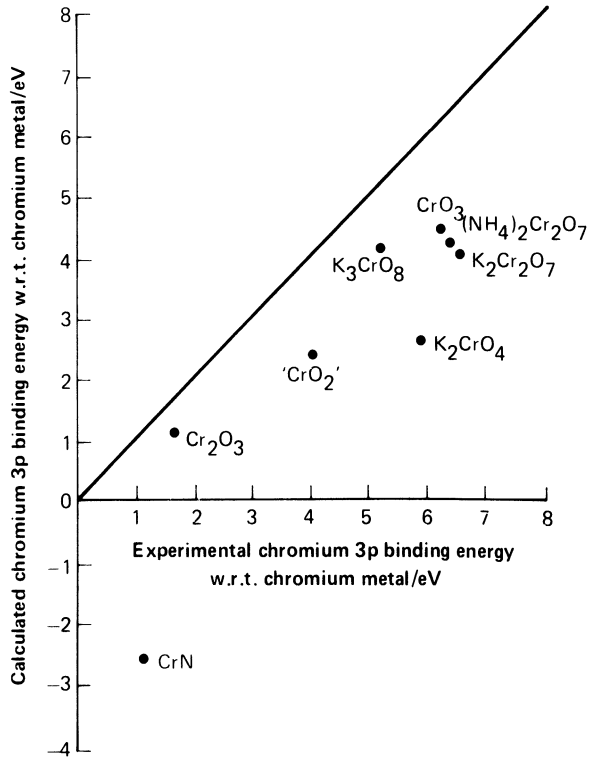

Figure 15. Plot of the calculated binding energy of Cr 3p electrons using the ground state potential model (which excludes relaxation energy) against the experimental binding energy expressed as the difference in the binding energy of Cr 3p electrons in chromium metal and a series of chromium–oxygen compounds and CrN (line of unit slope drawn in).

single-crystal electrodes in sulfuric acid baths by ESCA and AES. The films were found to contain Cr_2O_3 of 1.3–1.6-nm thickness. Sulfate adsorption was also found. AES depth profiles were carried out showing the sulfate to be in the outermost part of the passive layer, and scanning the AES it showed the sulfate to be uniformly distributed over the surface. The O 1s spectrum suggests the presence of a hydrated species on the outside of the film.

Yoshida *et al.* have examined the cathode film formed during the chromium plating process by ESCA.[50] Differences in anion distribution were found between the loose film and the compact film. There was a high-anion content on the loose film that decreased only slightly with depth into the film. There was evidence for low-valent chromium compounds on the compact film.

Hashimoto *et al.* have used ESCA to study the surface films formed on amorphous cobalt–chromium alloys in 1 *N* hydrochloric acid.[51] A hydrated

chromium hydroxide oxide was found to passivate the alloy. The surface film on Co–Cr–20B alloys was found to contain a large amount of borate together with the hydrated chromium hydroxide oxide, but only hydrated chromium hydroxide oxide was found on the surface of Co–10Cr–20B alloy. The borate was found to increase the corrosion rate.

9. The Manganese Dioxide Electrode

Lee *et al.*[52] have examined the γ-MnO_2 on a graphite support at various states of discharge by ESCA. Two different transfer procedures from the electrochemical environment to the spectrometer were used. In the first the discharged electrode was washed and stored in distilled water and dried and introduced into the spectrometer at room temperature. In the second the electrode was removed from the distilled water and placed in a dry box under dry nitrogen and then cooled to liquid nitrogen temperature. The cooled electrode was transferred and kept cool in the spectrometer, with the ice layer formed during transfer being removed by temporarily warming the sample. The former method is found to remove some weakly bound water, which is observed using the latter method. Little change was observed in the Mn 2p region for electrodes before and after discharge. Substantial changes were observed in the O 1s spectra.

10. Electrodes Involving Iron

There have been a very large number of studies of the surface of iron, iron alloys, and stainless steels. The surfaces of these essential materials will play a vital role in the general passivation of the material. Passivation means that the surface has a much lower activity or complete inertness towards its environment. This desirable situation is of course essential for effective corrosion resistance of these materials.

Faraday first discovered that iron could be passivated by placing it into concentrated nitric acid. Passivation can be achieved by electrochemical treatment. Figure 16 shows the current–voltage curve for an electropolished iron sample anodically polarized in a pH 8.41 buffer made up of a deaerated equivolume mixture of 0.15 *N* sodium borate and 0.15 *N* boric acid.[53] It is possible to identify a number of regions depending upon the applied potential (versus SCE). In the active region the current rises sharply with applied voltage, then falls sharply in the active–passive transition region staying at essentially zero in the passive region, then rising sharply in the transpassive region. In the active region the iron dissolves, leading to the formation of ferrous ions in solution[54]:

$$Fe + yH_2O \rightarrow Fe^{2+}(H_2O)y + 2e$$

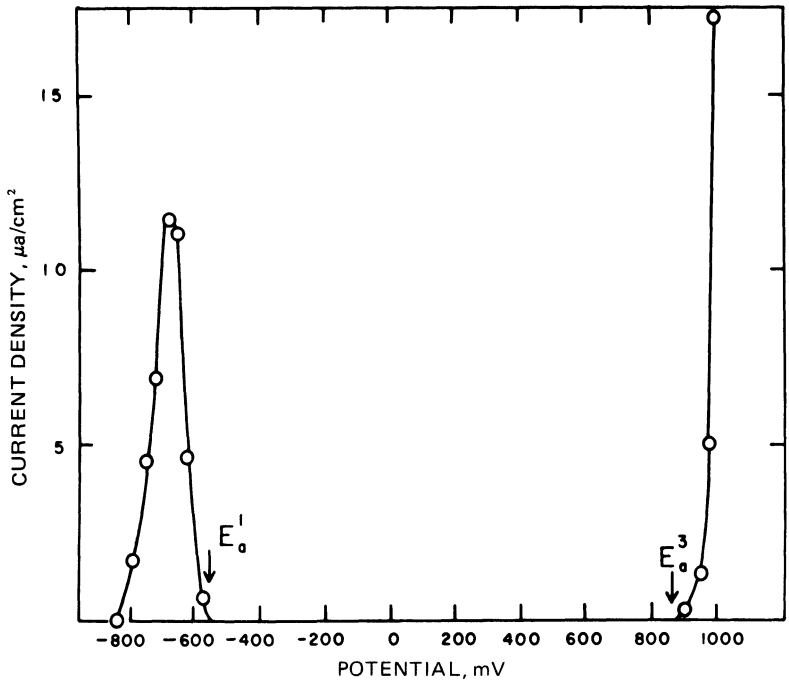

Figure 16. Anodic polarization curve for iron (pH 8.41).[53]

In the active–passive transition region various competing reactions occur concurrently at the metal–solution interface including metal dissolution and oxide film formation. In the passive region various oxide/hydroxide layers may be formed. It is these surface layers that have been the subject of extensive ESCA studies. The transpassive region will be associated with either oxygen evolution, metal dissolution or both depending upon the system studied. A potential known as the corrosion potential (E_{corr}) is often referred to. This is the potential spontaneously taken up by a metal with respect to the solution in which it is immersed.

The ESCA spectra of Fe 2p and Fe 3p core regions are unfortunately rather broad and the spectra are complicated by satellite features. Nevertheless, it is possible, using curve fitting methods, to distinguish between Fe(II) and Fe(III). Brundle *et al.*[55] have carried out a useful study of the core and valence level ESCA spectra of iron oxides. Figure 17 shows the Fe $2p_{3/2}$ and O 1s regions and Figure 18 shows the valence band spectra. These workers find that Fe(III) has a Fe $2p_{3/2}$ binding energy of about 711.2 eV and a peak width of about 4.5 eV and Fe(II) has a binding energy of around 709.6 eV and the same peak width. In addition, a broad satellite centered at around 719.8 eV is found in Fe(III) containing species and centered at around 715 eV in Fe(II) containing species. Asami *et al.*[56] have discussed the quantitative

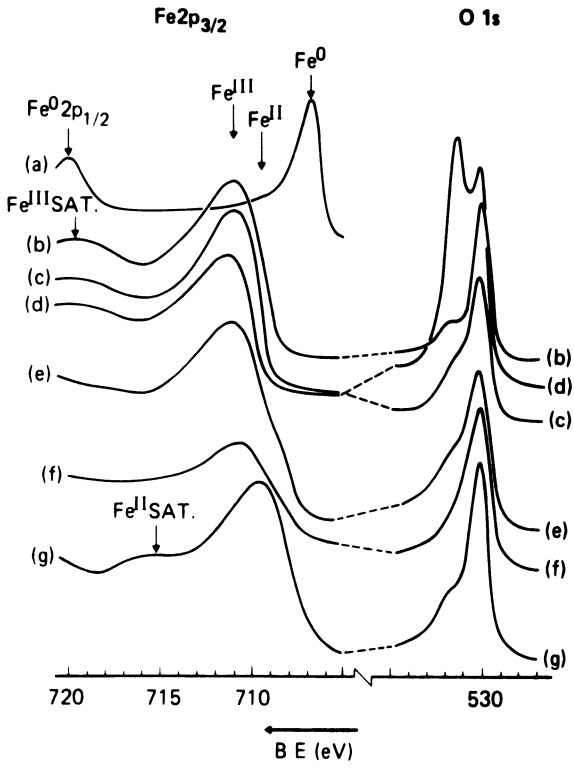

Figure 17. Fe $2p_{3/2}$ and O 1s ESCA spectra from iron oxide surfaces. Relative intensity scales are arbitrary. (a) Argon-ion cleaned Fe foil. (b) Freshly crushed α-Fe_2O_3 power (c) Freshly crushed γ-Fe_2O_3 power (d) Freshly crushed FeOOH powder. (e) Single-crystal Fe_3O_4, crushed and inserted under argon. (f) Single crystal Fe_xO, crushed and inserted under argon. (g) Sample in curve (f) briefly sputtered.[55]

ESCA determination of Fe(II) and Fe(III) in iron oxides using intensity expressions and discussed the application of these expressions to thin-amorphous passive films involving these oxides.

10.1. Studies of Metallic Iron

A number of workers have studied the surface film on pure iron electrochemically treated.[17, 57-63]

Hoar *et al.*[57] used surface charging differences to distinguish between Fe_2O_3 and Fe_3O_4. They found that the air-formed oxide film on pure iron was Fe_2O_3, and that anodic polarization into the passive region produced a surface film that contained Fe_3O_4 underneath the air-formed oxide films of Fe_2O_3. Olefjord and Vannerberg[17] examined the corrosion film formed on

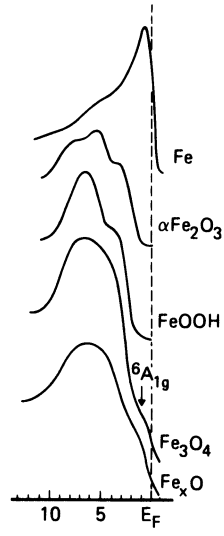

Figure 18. Valence band ESCA spectra of iron and its oxide surfaces.[55]

pure iron exposed to oxygenated water and the passive film formed chemically by treatment of iron with sodium chloride solution containing Na_2CrO_4 and KNO_2 inhibitors. In the former case the film was found to contain an Fe_2O_3 outer layer (probably in the form of the oxy–hydroxide FeOOH), and in the latter case the outer layer was found to contain $Cr(OH)_3$ for about 1 nm of the surface with a layer of the spinel $Fe_{1+x}Cr_{2-x}O_4$ of about 3-nm thickness lying below this, the chromium concentration falling with depth into the film. Asami *et al.*[58] found that the Fe(II)/Fe(III) ratio increased with anodic polarization of pure ion. Szklarska-Smialowska *et al.*[59] used ESCA and AES to examine the passive layers on iron in chloride containing solutions and found that no chloride was detected in the passive film. Wood and Vannerberg[60] correlated the passivation and inhibition properties of the surface oxide and benzoic acid films formed on iron with ESCA results. They found hydroxyl groups on surfaces that had good passivation properties. Chen *et al.*[61] studied the passive film on iron by *in situ* ellipsometric methods and *ex situ* ESCA measurements. They examined the film on pure iron polarized to 0.35, 0.65, 1.35, and 1.55 V (SCE) in a borate buffer (pH = 8.4). The ESCA spectra showed metallic iron on the electropolished iron, which disappeared due to the formation of a layer predominantly of Fe(III) as the polarization potential increased. Akimov *et al.*[62] have also studied iron passivation by ellipsometry and ESCA.

Olefjord[63] has examined the surface of an electrode made up of an iron–magnetite(Fe_3O_4) powder to which about 8% CdO powder was added. The electrodes were studied in their discharged state by X-ray diffraction and ESCA. There electrodes were charged and discharged for a number of cycles.

This process was found to produce a coarsening and a change in phase composition of the electrode. ESCA studies showed a thin cadmium-rich surface film of poor electronic conductivity formed on the surface after prolonged cycling.

10.2. Studies of Iron Alloys

There have been a number of ESCA studies of iron alloys.[57, 58, 61, 64–72]

Hoar *et al.*[57] found that the air-formed oxide film on an iron–1.56 wt.% aluminum alloy is largely Fe_3O_4. Chen *et al.*[61] have found that there is a nickel oxide and hydroxide layer thicker than that found for metallic nickel as the passive layer on 50% nickel iron alloys.

Lee *et al.*[64] have used ESCA and AES in addition to electrochemical and other measurements to study 100 nm thick films of $Fe_{1-x}Pd_x$ alloys codeposited on Si or SiO_2. These films are of interest because very small concentrations of noble metals can increase the corrosion resistance of active bulk alloys such as stainless steel. They find that iron preferentially oxidizes to Fe_2O_3 at the air–oxide interface when the films are oxidized at moderate (160–225 °C) temperatures. This leaves a localized palladium enriched region under the oxide layer. This oxidation treatment is found to increase the corrosion resistance due to the dense and protective Fe_2O_3 layer and the thickened Pd enriched layer.

Hashimoto *et al.*[65] have examined a range of iron base alloys using ESCA and electrochemical methods. The purpose of the study was to investigate the role of alloying elements in improving the corrosion resistance of the resulting alloy. The effect of adding Ni, Nb, Pd, Pt, V, and Zr to amorphous iron alloys containing 13 at.% phosphorous and 7 at.% carbon was investigated. It was found that the added alloying elements more easily corroded than iron assisted the formation of a passive hydrated Fe oxy–hydroxide film by decreasing the dissolution rate of the alloys prior to passive film formation. As given earlier, in the case of elements less easily corroded than iron these elements were found concentrated in the alloy surface immediately under the surface film.

Hashimoto *et al.*[66, 67] and Stout *et al.*[68] have examined iron–molybdenum alloys. These studies have been of interest because it well known that the addition of molybdenum to stainless steels improves their resistance to attack by chloride and acid solutions. ESCA studies of the films on Fe–Mo–C alloys[66, 67] facilitates the formation of the passive hydrated Fe oxy–hydroxide film discussed earlier. In addition studies of the film formed in the active region[66] show a large amount of molybdenum present [mainly as Mo(IV)], which is not found for the passive region. Fe–Mo–P–C alloys show similar results,[67] except that the ESCA results show the molybdenum present to be Mo(VI). ESCA, AES, and electrochemical studies of Fe–Mo binary alloys[68]

anodically polarized in a pH 8.4 borate buffer show again that molybdenum is depleted in the passive region, ESCA showing the molybdenum to be in the form of Mo(VI) and metallic Mo. The passive film was found to be less protective than that on pure iron.

Iron–chromium alloys have been the subject of many studies,[58, 69–72] for these alloys are especially important since they contain the fundamental materials of stainless steels. It is very interesting to find that the corrosion resistance of the alloy increases abruptly when the chromium content rises to 12.5 at.% or greater. Asami *et al.*[58] found that the binding energy of the Fe $2p_{3/2}$ electrons shifted abruptly from the Fe(II) value to the Fe(III) value corresponding to a sharp increase in the Fe(II)/Fe(III) ratio when the chromium content passed the above limit. Olefjord and Elfstrom[69] examined the passive film formed on this type of alloy in an acidic medium and in dry oxygen. ESCA studies showed that passivation at 0.1, 0.5, and 0.9 V(SCE) produced a homogeneous film enriched in chromium. After many hours the steady-state film was found to consist of a top layer of $Cr(OH)_3$ with iron and chromium oxides underneath. Asami *et al.*[70] studied the composition of the alloy surface that had been mechanically polished in trichloroethylene, and ESCA revealed that there were oxides and hydroxides present though the surface film had the same cationic composition as the bulk alloy. The same workers studied the anodic polarization of the alloy in sulfuric acid[71] and found that the surface films in the passive region showed a chromium enrichment together with the abrupt change in the Fe $2p_{3/2}$ binding energy discussed earlier when the chromium content of the alloy exceeded 12.5 at.%. The excess chromium in the film was found to be in the form of chromium oxy–hydroxide and it was this substance that was thought to be effective in passivation and corrosion protection. Hashimoto *et al.*[72] investigated the effect of P, C, B, and Si additives to the corrosion behavior of the alloy. Phosphorous was found to accelerate the dissolution of the alloy in the active region prior to passivation leading to a rapid enrichment of Cr(III) in the surface film leading to a good passive film. Silicon and boron, on the other hand, both do not facilitate dissolution of the film in the active region and they interfere with the formation of the Cr(III) passive film by incorporation of silicates and borates into this film forming an unsatisfactory passive film.

10.3. Studies of Stainless Steel

There have been a very large number of ESCA studies of the electrochemical behavior and passivation of stainless steel.[18, 61, 73–94] The ESCA spectra may be quite complex due to the presence of a large number of elements in the steel studied. In general, the passive layer contains Cr(III) oxide–hydroxide in all chromium containing steels. Oxides and hydroxides

are distinguished on the basis of their O 1s spectrum (discussed in Section 2.2 of this chapter).

10.3.1. Surface Treatment

There have been a number of studies of the effect of surface treatment on stainless steels, for this will greatly effect the corrosion resistance of these materials. ESCA is clearly an invaluable technique for such studies. Olefjord[78] studied the oxidation of stainless steel in oxygen at temperatures ranging from 25–800°C and oxidation times of between 1/4 and 70 hr. He found from the ESCA spectrum at low temperatures and short oxidation times that the oxide layer is mainly iron oxide, but at high temperatures and long oxidation times higher concentrations of chromium and manganese are found in the oxide layer. Elfstrom and Olefjord[18] studied the surface compositions of stainless steels that had been scraped in vacuum, mechanically polished in air, electropolished, and ion etched by ESCA. The most representative surface was found to be obtained by scraping the sample with a diamond tool in ultrahigh vacuum, the other methods producing some surface enrichment. Thus, mechanical polishing in air was found to lead to preferential iron and chromium oxidation with Mo and Ni accumulating under the oxide film. Electropolishing in $HClO_4$ lead to selective iron dissolution and metallic chromium and molybdenum surface enrichment. Argon-ion etching was found to lower the chromium and nickel content in the outermost layer due to selective sputtering.

Olefjord and Fischmeister[79] have studied the passive films formed on chromium steels when they are exposed to oxygenated water. ESCA depth profiles were carried out by stripping the film by argon-ion bombardment. After prolonged exposure chromium enrichment was found to occur to give a Cr(III) hydroxide passive layer with an underlying $Fe_{1+x}Cr_2O_4$ layer as found for pure iron by Olefjord and Vannerberg.[17] Furthermore, following the pattern seen in the other studies discussed steels with a low-chromium content (3.9 and 7.8%) suffered breakdown of the chromium rich layer to give an unprotective layer of FeOOH. Castle and Clayton[80] studied the development of oxide on commercial grade 18% Cr–8% Ni steel in low-conductivity deoxygenated water as a function of time, temperature, and solution refreshment rate. The steel surface was prepared by *in situ* ion cleaning using ESCA as a monitor of the contamination level. Samples were considered satisfactory when the contamination due to carbon and oxygen was less than 6 at.%. Samples were translated with a very brief exposure to air (about 30 sec) into the aqueous environment, and with a further brief exposure to air back into the spectrometer after treatment. It is considered that the results are not seriously effected by the brief transfer through air, but the loss of ESCA peak intensity was found due to hydrocarbon pick-up during transfer. This work

used the angular dependence of ESCA core peaks (see Section 19.1) together with argon-ion depth profiling in order to obtain depth information requiring the collection of a large number of spectra. It was concluded that the outermost layer was especially rich in OH^- ions (from the O 1s spectrum) which might be due to a layer of bound water, a situation reported earlier by Okamoto.[73] This outer layer increased in thickness when the samples were exposed to greater volumes of water and was found to contain organic molecules (see in the C 1s spectrum) which might play a role in stabilizing the film and would explain the dependence upon volume. The films were found to be less than 3 nm thick and contained Cr(III), Fe(II), and Fe(III) in the proportions found in the steel suggesting no selective oxidation or dissolution.

Diekmann *et al.*[81] find that ESCA studies of the passive films formed on stainless steel have outer layers consisting of SiO_2 on top of a chromium oxide layer containing Mo(IV) and Mo(VI), but no nickel. 10% nitric acid solution gives Mo(IV) and 98% nitric acid gives Mo(VI). The ratio of chromium oxides to molybdenum oxides can vary by a factor of 10 depending upon the nature of the nitric acid treatment. Asami and Hashimoto[82] have studied the surface film formed on types 304 and 306 stainless steels by ESCA for surface treatments involving dry polishing, wet polishing, HF treatment, and 10 and 30% nitric acid treatment. It is found that passivation of the steel follows this order of treatment. The amount of chromium and iron in the film was dependent upon the treatment method.

10.3.2. Anodic Polarization Studies

Asami *et al.*[83] found hydrated Cr(III) oxy–hydroxide to be the passive film on the extremely corrosion-resistant 10% Fe–13% Cr–7% P alloy in 0.1 *N* HCl. Akimov *et al.*[84] found that anodic polarization of 1.05 V(SCE) for chromium steels was needed in order that the ratio of the amounts of metallic iron to iron oxides approach that of air-formed oxide films. An ESCA examination[85] of 25% Cr–20% Ni stainless steel electrodes treated chemically and electrochemically showed metallic chromium produced in the film which was absent from the received sample, together with overall chromium enrichment. The metallic chromium probably arises from incomplete passivation following cathodic stripping of the existing film in the electrochemical case, and etching of the existing film in the chemical treatment sense. Hashimoto *et al.*[86] have investigated the role of molybdenum in increasing the corrosion resistance of chromium molybdenum stainless steels. ESCA studies show the film to be Cr(III) oxy–hydroxide in the passive region with a large amount of Mo(VI) in the film formed in the active region. This result is similar to the study of iron–molybdenum alloys discussed in Section 10.2. Hashimoto and Asami[87] found that the passive film on 19% Cr and 19% Cr–2% Mo stainless steels in 0.1N HCl was again hydrated Cr(III) oxy–hydroxide, but the film is

not uniform and contains micropores, some of which grow into much larger pits. Leygraf *et al.*[88, 89] have used radioisotopic γ-spectroscopic methods and AES in addition to ESCA to study the surface layers on 18% Cr and 18% Cr–3% Mo stainless steels in the passive and transpassive regions in 1 *N* sulfuric acid, and to investigate the mechanism of the dissolution of components in the steel. Molybdenum enrichment is found in the active region.

Ansell *et al.*[90] have used ESCA to study the colored films formed on stainless steel and Nilomag alloy 771. These films were produced by immersing the samples in a chromic acid/sulfuric acid solution at 70°C for various amounts of time. The color of the specimen was monitored by measuring the potential of the specimen with respect to a reference electrode when a characteristic potential–time curve was obtained. The film on stainless steel was composed principally of Fe(III), Fe(II), elemental iron, Cr(VI), chromium in an intermediate oxidation state, Cr(III), and an O 1s peak that indicated the presence of oxides and hydroxides. The type of iron and chromium species was dependent upon film preparation.

Povey *et al.*[91] have studied the surface of 18% Cr–10% Ni stainless steel after anodic polarization in the regions of transpassivity and secondary passivity. Transpassivity is the region in the current–voltage curve (shown in Figure 19 for a sweep rate of 30 $mV \cdot s^{-1}$) when the current rises sharply from the passive region (above 1 V SCE in this case). Metal dissolution occurs in this region. This is followed by a region of secondary passivity [between 1.3 and 1.6 V (SCE)]. ESCA studies showed that the film contained a hydrated Cr(III) oxy–hydroxide, with a little Cr(VI) in the transpassive region, Fe(III), Fe(II), and a variety of silicon species. The film had a lower thickness, chromium content, proportion of oxygen present as hydroxide in the transpassive region, and region of secondary passivity as compared to the passive region. Large changes were observed in the binding energies of the silicon

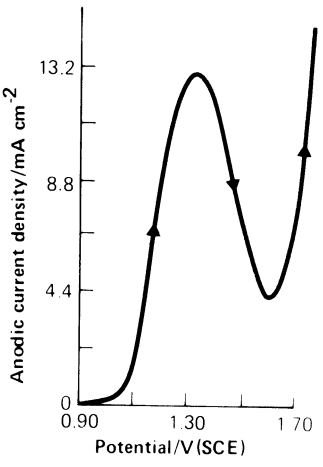

Figure 19. Current density versus potential curve for stainless steel in 1 *N* sulfuric acid at a sweep rate of 30 mV sec^{-1}.[91]

species in the film (Figure 20) corresponding to a range of species from elemental silicon to SiO_2. These changes in the silicon spectra do not necessarily indicate that silicon plays a major role in the electrochemical behavior, but that the silicon changes mirror the change in structure of the layer.

Asami *et al.*[92] have used ESCA to study the transgranular stress corrosion cracking of mild steel in sulfuric acid to which a little potassium iodide solution had been added. The surface film was found to contain FeOOH with small amounts of sulfur and I^-, the latter varying with the polarization potential with a critical potential at the same potential (0.06 V relative to the corrosion potential) when stress corrosion cracking susceptibility was found to be at a maximum. Spitz *et al.*[93] have used ESCA to study the surface of steel and copper substrates for black chrome electroplating. Agarwal *et al*,[94] have characterized the surface alloy formed by multiple implantation of Ni^+ into annealed 430 stainless steel by ESCA using argon-ion etching to obtain depth profiles.

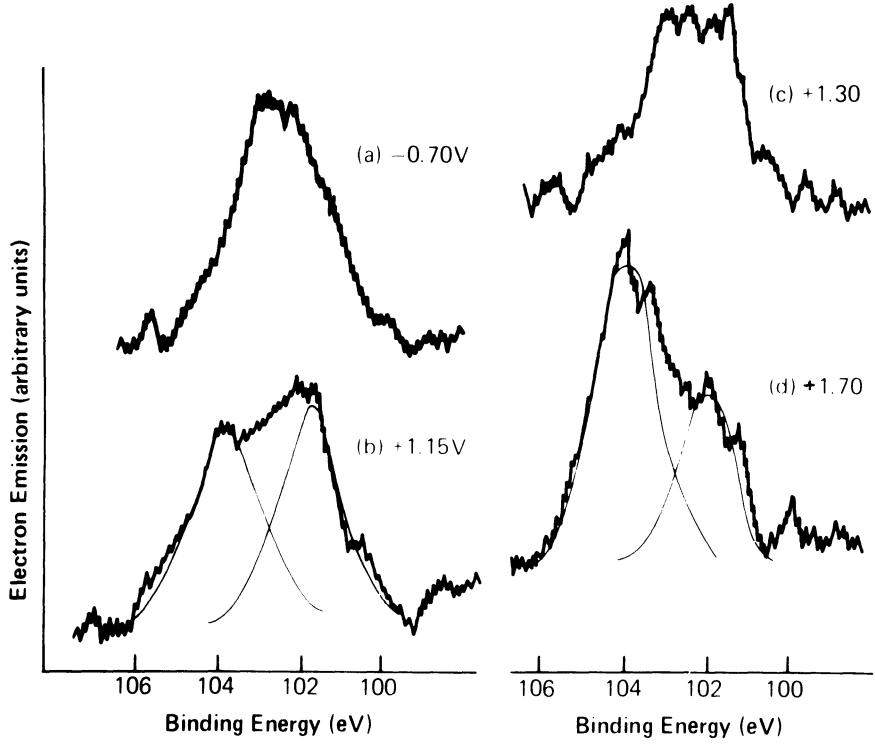

Figure 20. Si 2p ESCA spectra of the stainless steel electrode after polarization in 1 *N* sulfuric acid.[91]

11. Electrodes Involving Nickel

11.1. Studies of Nickel Metal

Nickel is a basic element of many alloy systems due to its relative noncorrodibility. Identification of the composition and structure of the passive film is clearly of great importance. Dickinson *et al.*[95] have used ESCA to investigate the film produced at a large number of potentials in the active, prepassive, passive, and transpassive regions and for various polarization times. These regions are shown on the current–voltage curve shown in Figure 21 for polarization in 0.5 mol dm^{-3} sulfuric acid. The electrochemical behavior was found to depend upon the time of polarization and the pretreatment of the electrode. In the passive region the film on the electrode surface is probably composed of NiO and $Ni(OH)_2$ with a thickness in the range of 1.1–1.7 nm over the potential range where passivation occurs. NiO was the passivating species. A precursor film of $Ni(OH)_2$ was found and this has little, if any, passivating action and is, therefore, probably porous. Some sulfate was present on the electrode at almost all potentials and a very small amount of sulfide was found in the active and prepassive regions. Figure 22 shows the O 1s region which shows how three peaks can be clearly resolved. The peak at 532.8 being due to water and or adsorbed oxygen species, the peak at 531.2 being due to hydroxyl oxygen and the peak at 529.3 being due

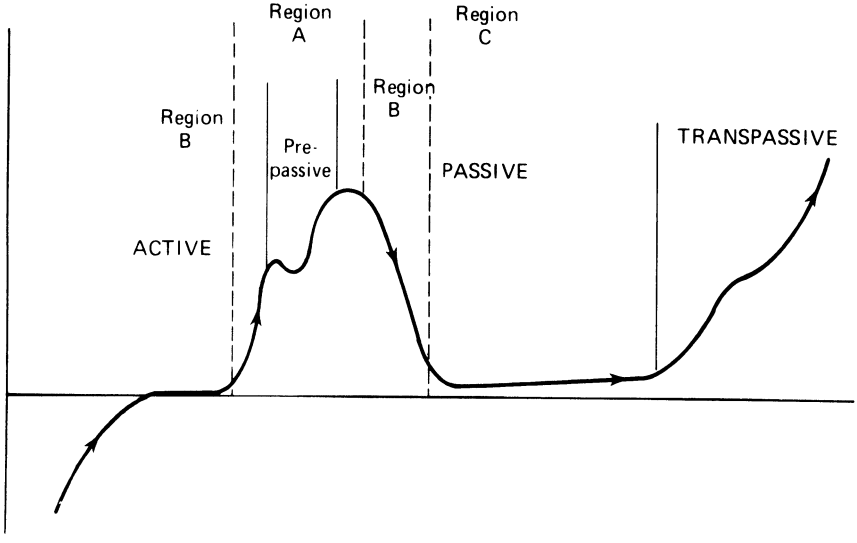

Figure 21. Diagrammatic current voltage curve showing the following regions. (a) active, (b) prepassive, (c) passive, and (d) transpassive.[95]

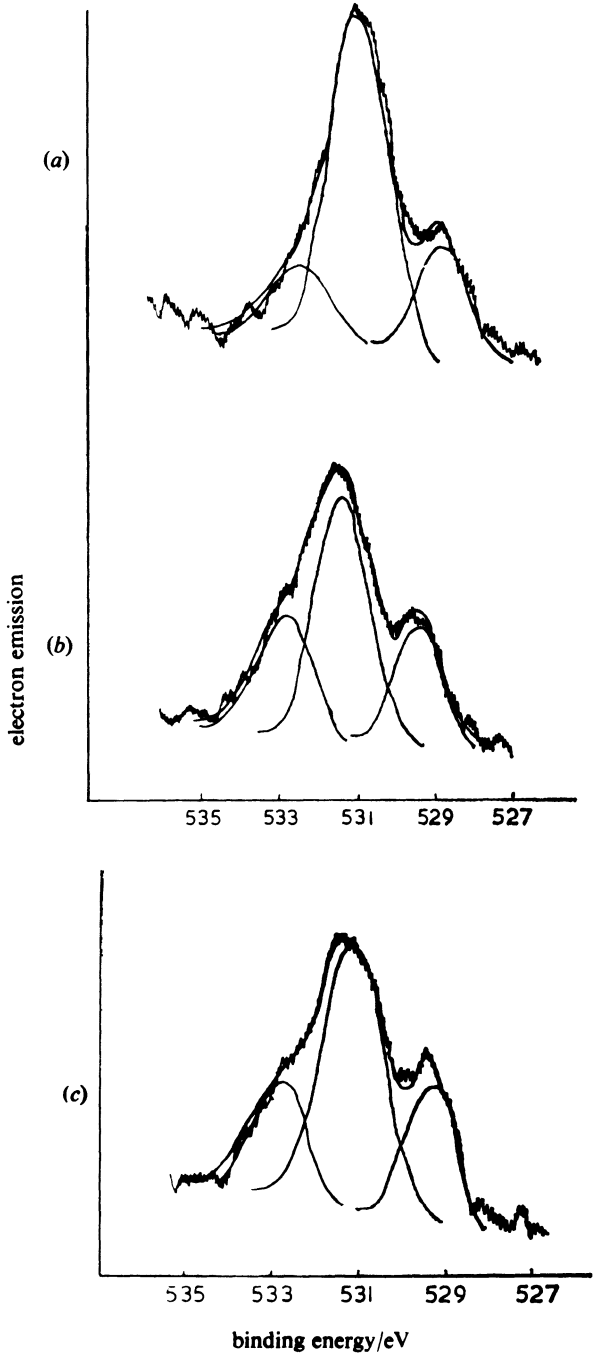

Figure 22. O 1s ESCA spectra for a nickel electrode after polarization in 1 *N* sulfuric acid for 15 min at a potential of (a) +2.30 V, (b) +1.10 V, (c) +0.80 V (SCE).[95]

to oxide oxygen. Marcus *et al.*[96] examined the composition and thickness of the passive film formed on single-crystal nickel (100) in 0.5 mol dm^{-3} sulfuric acid in the passive region at 0.54 V (SCE). They find that ESCA shows the film has a total thickness of 1 nm. Argon-ion etching showed that the sulfate is only a surface contaminant and that the outer layer of the passive film consisted of 0.6 nm thickness of $Ni(OH)_2$ with a 0.4-nm inner layer of NiO. This suggests the following model for the passive film (nickel substrate):

	OH		OH		OH
	|		|		|
OH	Ni	OH	Ni	OH	Ni
Ni	O	Ni	O	Ni	O
O	Ni	O	Ni	O	Ni

The Ni 2p spectra are complex, due to a rich satellite structure leading to a complex peak envelope caused by a large number of overlapping peaks. Thus, reliable data analysis is especially important. The marked dependence of the electrochemical behavior upon the pretreatment of the electrode[95] means that careful control of the surface state of the electrode and anaerobic transfer conditions are especially important. The anaerobic transfer cell in the author's laboratory (Section 2.2.1) is being used for a reexamination of the nickel system. The anaerobic conditions of the cell are illustrated by Figure 23 which shows the Ni 2p electron region of the electrode after argon-ion etching and before transfer into the cell, and the same electrode after insertion into deoxygenated water and into dilute deoxygenated sulfuric acid in the cell. Polarization to 0 V (SCE) shows a substantial change due to the formation of oxide and hydroxide. No change will be noted in the case of deoxygenated water, and little change [perhaps some Ni(II) sulfate is formed on the surface] in the case of deoxygenated sulfuric acid, showing that no nickel oxidation has occurred. Chen *et al.*[61] have studied the ESCA spectra of the film formed by polarizing pure nickel in a borate buffer (pH = 8.4) finding nickel oxide/hydroxide in the film. Marcus *et al.*[97] have studied the effect of sulfur on the passivation of nickel by AES and ESCA. Sulfur doped nickel shows selective dissolution of nickel and surface segregation of sulfur. Inhibition of passivation resulted when the sulfur concentration was above a critical concentration due to the formation of an adsorbed sulfur layer and the subsequent growth of Ni_3S_2 which attains a stationary thickness of about 3 nm.

11.2. Studies of Molten Salt Systems

Sabbatini *et al.*[98] and Desimoni *et al.*[99] have examined the surface of nickel electrodes in molten salt systems by ESCA. Time and temperature dependent electrode potentials in the system $Ni/CO_2 + CO_2/CO_3^{2-}$ in

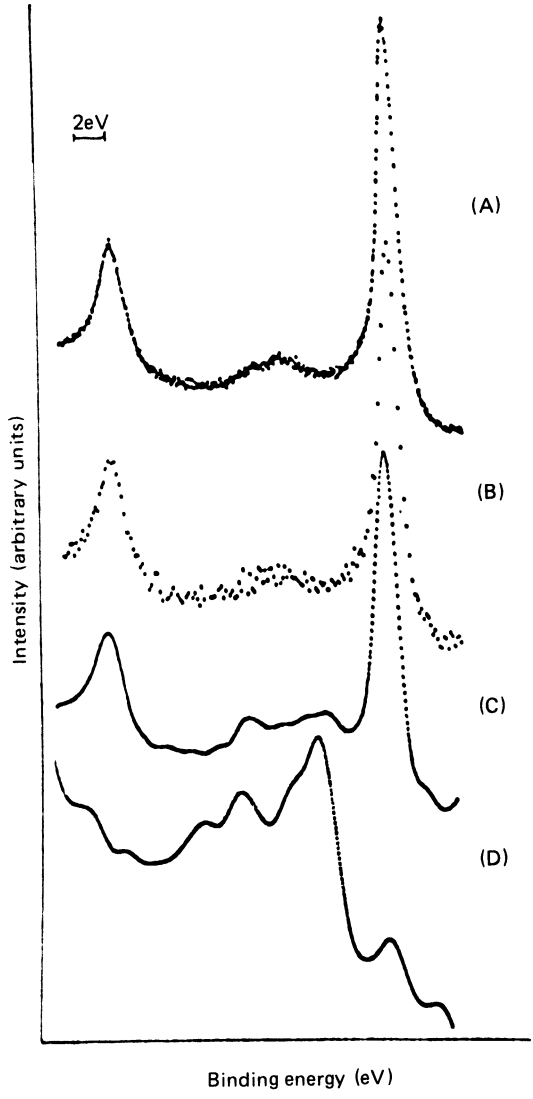

Figure 23. Ni 2p ESCA spectra for a nickel electrode that has been etched to remove any oxide film and then transferred in the anaerobic cell and exposed to deoxygenated dilute sulfuric acid with and without anodic polarization. (a) shows the spectrum immediately after etching, and (b) shows the spectrum after exposure to deoxygenated sulfuric acid. No change can be seen in the case of (b), and little change in (c). (d) shows the spectrum after the electrode is pulsed to 0.0V(SCE) for 15 min when large amounts of Ni(II) are seen. (H. Y. Hall, D. M. Hercules, P. M. A. Sherwood, and I. Welsh, unpublished results).

equimolar KNO_3–$NaNO_3$ melts were compared with ESCA studies of nickel sheets maintained under the same conditions as the electrodes. Large changes in the ESCA spectra corresponding to formation of different nickel species were found to correspond to potential variations. Plots were obtained of the variation of the potential as a function of the composition of oxygen and carbon dioxide at different temperatures for a fixed carbonate concentration. The ESCA results supported the proposed mechanistic model for the system.

11.3. Studies of Nickel Alloys

There have been a number of ESCA studies of the electrochemical behavior of nickel alloy electrodes.[61, 100–105] Copper–nickel alloys are discussed in Section 12.3.

Hashimoto *et al.*[100] found the passive film on amorphous 15% P 5% B 3% Cr to 9% Cr to be deficient in nickel and enriched in phosphorous. Schlecker *et al.*[101] found that the passive film on nickel–palladium alloys (10% palladium) examined by SIMS and ESCA consisted of nickel and palladium oxides with marked palladium enrichment, the films containing 80–90% palladium. Akimov *et al.*[102] have examined the anodic oxide coatings on titanium–nickel alloys by ESCA, electroreflection, and electrochemical methods, and Kolotyrkin *et al.*[103] have examined the corrosion resistance of nickel–molybdenum alloys by ESCA, electrochemical methods, and γ-spectroscopic methods. Hashimoto and Asami[104] used ESCA to examine the surface film on high-nickel alloys in hot concentrated sodium hydroxide solution for anodic polarization in the primary passive–transpassive region and the region of secondary passivity. These alloys are used in heat exchangers and various elements of pressurized water reactors, but may suffer from stress corrosion cracking. Susceptibility to stress corrosion cracking is affected by the surface films on the alloys. It was found that the chromium content [in the form of hydrated Cr(III) oxy–hydroxide] of the passive film increased with the rise in potential, but in the transpassive region abruptly decreased with a sharp increase in nickel content. The secondary passive films were almost exclusively composed of hydrated nickel hydroxide which transformed to hydrated nickel oxy–hydroxide with an increase in potential. Blondeau *et al.*[105] have studied the films on nickel–silicon alloys polarized in sulfuric acid by ESCA and electron diffraction. In the transpassive dissolution region the NiO films are perturbed by the incorporation of silicon. Chen *et al.*[61] found that ESCA studies of the film formed on 50% iron–nickel alloys was thicker than that formed on pure nickel.

12. Electrodes Involving Copper

12.1. Cu(I) Oxide Solar Cells

Herion *et al.*[106] have used AES and ESCA to study Cu_2O thin-film solar cells made by partial thermal oxidation of copper foil.

12.2. Corrosion Inhibition of Copper

ESCA has been combined with electrochemical and other methods to examine the inhibition of the corrosion of copper by the addition of various

organic compounds. These compounds produce a protective surface film on the copper. Fox *et al.*[107] have examined the inhibition caused by benztriazole. The presence of metal oxide is a key factor in the mechanism for it provides a pH dependent concentration of copper ions in solution. The benztriazole is found to be lightly adsorbed on the surface until at a sufficiently high concentration of benztriazole bulk precipitation of a Cu(I) benztriazole complex occurs which protects the surface by formation of a water insoluble barrier layer. Ohsawa and Suetaka[108] used UV-visible reflection spectroscopy and IR-reflection spectroscopy in addition to ESCA to study the corrosion inhibition of copper by mercaptobenzothiazole. In this case the surface is protected by a water insoluble barrier layer of Cu(I) mercaptobenzothiazole complex.

12.3. Studies of Copper Alloys

Electrochemical and ESCA studies have been carried out on a number of copper alloy systems.[109-113]

Petit *et al.*[109] have studied the dissolution of titanium–copper alloys in the active and passive regions. In the active region cathodic dissolution of copper occurs. In copper rich alloys large amounts of copper in the form of metallic copper and Cu_2O are found on the surface, and TiO_2 is found as well on the less copper rich alloys. It is thought that copper dissolution goes through an intermediate copper hydride reaction product which occurs simultaneously with the anodic dissolution of titanium. In the passive region a TiO_2 passive film is formed, through which copper can pass to give active anodic copper dissolution.

Hulett *et al.*[110] have studied the films on copper–nickel alloys (30% nickel) in the active and passive regions in 1.2 *M* sodium chloride solution at 100°C. In the active region the surface shows little difference from the bulk composition. In the passive region a passivating film of NiO was found which was similar to that of a pure nickel specimen passivated under the same conditions. Takasu *et al.*[111] examined copper–nickel alloys by AES and ESCA and found that the passive film formed by anodic polarization in 0.5 *M* perchloric acid consisted of NiO and a copper oxide with nickel and copper in the same ratio as in the bulk of the alloy. Takasu *et al.*[112] examined the surface of electropolished copper–nickel alloys by AES and ESCA. They found that the surface contained nickel and copper oxides with the same nickel and copper composition as the bulk after electropolishing, though the surface electropolished in the transpassive region was slightly enriched in copper.

Castle and Epler[113] have studied the changes in the surface composition of aluminum brass when subjected to electrochemical polarization in sea water in order to determine the behavior of condenser tube surfaces in marine

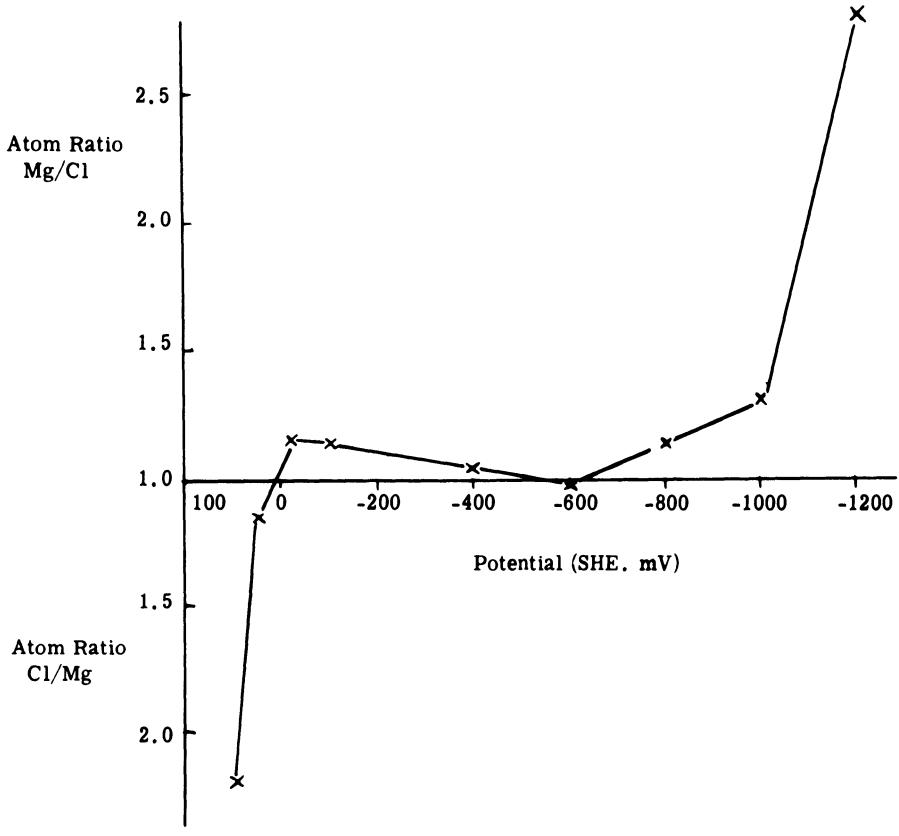

Figure 24. Correlation of magnesium and chloride pick-up on the surface with potential for polarization of aluminum brass in sea water.[113]

environments. Polarization at 100-mV intervals was carried out between −0.1 and −1.2 V (SCE). Argon-ion etching was used to remove carbon contamination picked up from the solution. Figure 24 shows the steady increase of magnesium concentration caused by the generation and deposition of $Mg(OH)_2$ at the cathode on the surface as the potential is increased. When the chloride concentration is greatest there is also a sharp increase in copper relative to zinc on the surface due to the possible formation of $Cu_2(OH)_3Cl$ on the surface. The one-to-one correspondence of magnesium and chloride ion concentrations over a wide range of potential suggests the formation of a basic chloride of the type Mg(OH)Cl perhaps in the form of a mixed magnesium–zinc hydroxy chloride. Aluminum is not found on the surface.

13. Electrodes Involving Zinc

Povey and Turner[114] used angular variation core ESCA studies and argon-ion etching to examine the surface of modified zinc primary battery anodes. It is found that porous zinc anodes used in primary batteries rarely allow complete use, and that their efficiency is improved by the incorporation of metallic lead. The electrodes were treated by immersion of zinc foil into solutions of lead acetate in sodium hydroxide, ranging in composition from 10^{-2} to 10^{-6} mol dm^{-3} lead (II). The results suggest that lead is not evenly distributed over the surface, but remains as agglomerates within the zinc matrix, penetrating to a depth of about 45 nm into the zinc substrate.

14. The Niobium Electrode

Sugimoto *et al.*[115] have studied the changes on the niobium electrode surface when it is subjected to strong cathodic polarization in 25% potassium hydroxide solutions at 24–82°C. ESCA studies of the cathodically polarized electrode indicated that the oxide layer underwent partial reduction, and showed the presence of hydroxide ions.

15. The Molybdenum Electrode

Ansell *et. al.*[20] examined the oxidation of molybdenum by oxygen and deoxygenated and oxygenated water using the *in situ* electrochemical cell discussed in Section 2.2.1. It is found that molybdenum metal (etched to remove any oxide) shows no surface oxidation when exposed to dry oxygen at room temperature, even when the spectra are run at low take-off angles to improve surface sensitivity.[116] Figures 25(a) and (b) compare the spectrum of clean molybdenum in the Mo 3d electron region for molybdenum metal with that of the same metal exposed to 1 atmosphere of oxygen for 10 min. Little oxidation of the etched metal is found when exposed to deoxygenated water or sulfuric acid solution [Figure 25(c)], however, considerable oxidation with the formation of Mo(VI) is found when the water is oxygenated [Figure 25(d)]. The reduction of the "as received" material with its oxide film was investigated after polarization at -0.9 V (SCE) in deoxygenated sulfuric acid, but complete reduction to the metal is not found, the Mo 3d spectrum (Figure 26) showing the presence of both metal and a lower oxide, perhaps Mo(III) oxide. These spectra also illustrate the value of digital curve fitting methods. Thus, the fitted spectra use different peak shapes and include satellite peaks from the nonmonochromatized X-radiation used in the author's instrument. Thus, it is noted that the metal peaks have an exponential tail

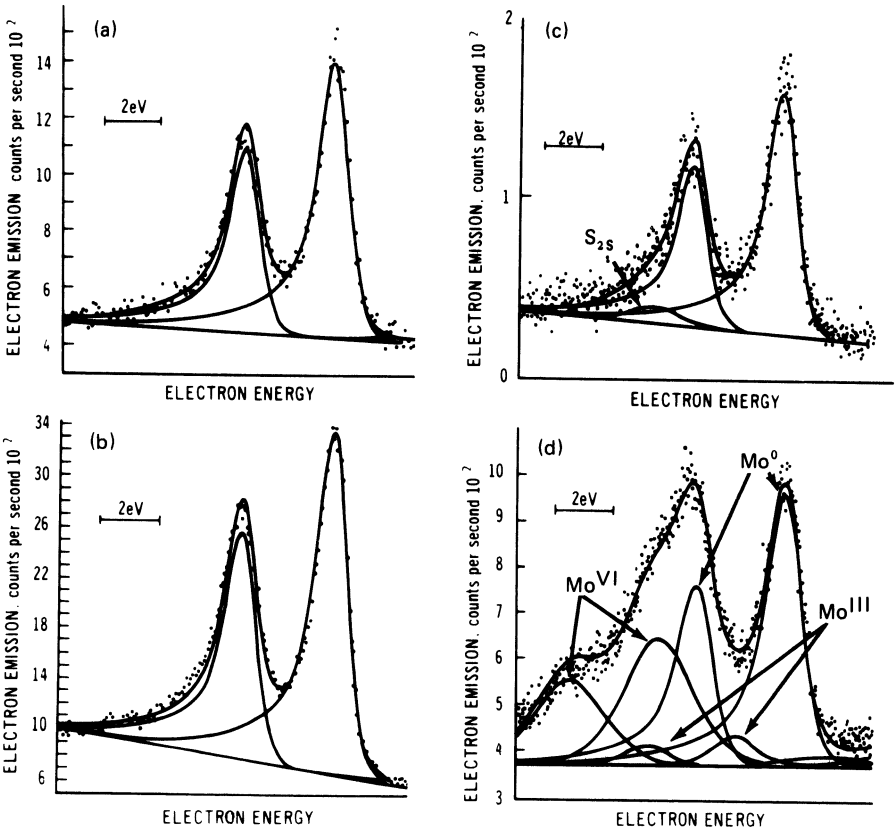

Figure 25. Mo 3d ESCA spectra for molybdenum metal subjected to various surface treatments. (a) Argon-ion etched metal, (b) etched metal exposed to oxygen (1 at. for 10 min), (c) etched metal exposed to deoxygenated dilute sulfuric acid in an anaerobic cell, and (d) etched metal exposed to oxygenated water.

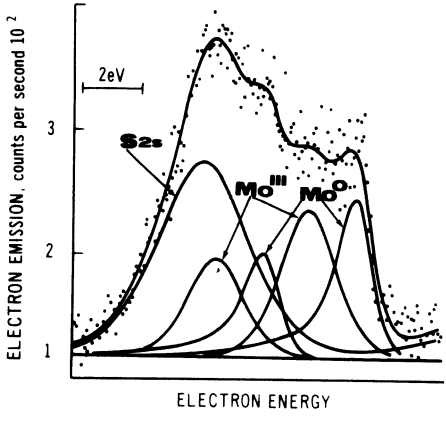

Figure 26. Mo 3d ESCA spectra of a molybdenum, as received, electrode subjected to a polarization of −0.90 V(SCE) for 5 min in 1 *N* sulfuric acid.[20]

(due to conduction band interaction) that is experimentally determined by fitting the spectrum of the clean metal surface. The spectra show $3d_{3/2}$ and $3d_{5/2}$ peaks, and the fitting process fixes the separation and area ratios for these two peaks, for the area ratio is fixed by the multiplicity, and the separation should be constant for such deep lying core levels. The spectrum in Figure 25(d) shows some Mo(III) for its inclusion into the fit causes a substantial reduction in the statistical chi square (from 836 to 673), although the error in peak position (expressed as 95% confidence limits) is much higher (± 0.28 eV) than for the Mo(VI) peaks (± 0.10 eV).

Povey and Metcalfe[117] have studied molybdenum electrodes polarized in 0.5 mol dm^{-3} sodium hydroxide solution. ESCA studies showed the presence of the molybdenum species of increasing oxidation state as the potential was increased, with Mo(VI) as the highest oxidation state detected.

16. Ruthenium Dioxide-Based Film Electrodes

RuO-based film electrodes find successful application in chlor–alkali cells. The surface of RuO_2 and RuO_2 deposited on TiO_2 film electrodes was investigated by Augustynski *et al.*[118] using ESCA. Electrodes that had just been prepared and electrodes that had undergone prolonged electrolysis in 4 *M* NaCl solution were examined. In both cases, the Ru 3p spectra showed the presence of RuO_2 and a higher oxidation state Ru compound assigned to RuO_3. Preferential diffusion was found for the RuO_2–TiO_2 electrodes, with surface enrichment of TiO_2. Electrodes that had been electrolyzed showed the presence of two different chlorine species, one due to chloride ions and the other due to adsorbed atomic chlorine or ClO^- ions.

Rolison *et al.*[119] have studied RuO_2 electrodes, made by spraying a dilute butanol solution of $RuCl_3$ onto a Ti disk heated to evaporate the solvent, and then baking to 400–450°C, in a range of nonaqueous solvents. They have found that the electrode behaves well in methyl cyanide, dimethylsulfoxide, propylene carbonate, and dimethylformamide solutions of metal bipyridyls, methyl viologen, ferrocene, tetrathiafulvalene, and nitroaromatics. ESCA was used to study the surface of the RuO_2 spray electrodes. The Ru 3d spectra showed RuO_2 and in some cases RuO_3. The relative amounts of ruthenium and oxygen suggest an oxygen richness consistent with the presence of RuO_3 on the surface. A Cl 2p band due to chloride ions was nearly always seen. A multiple O 1s band, similar to that seen by Augustynski *et al.*[118] was also seen. Many of the electrodes exhibited a Ti 2p band, which may be due to events during the baking process.

There have been a number of studies of chemically modified RuO_2 electrodes, and these will be discussed in Section 21.2.4.

17. Electrodes Involving Tantalum

Bispinck *et al.*[120] have investigated tantalum oxide layers formed either by anodic oxidation of tantalum metal foil in 1 *N* sodium hydroxide at a polarization voltage of 120 V or by heating a tantalum metal specimen for 10 min at 1200 K in a high vacuum and then for 3 min at 900 K in an oxygen atmosphere. The oxide layers were studied by SIMS, AES, and ESCA combined with argon-ion depth profiling. Both preparation methods lead to an amorphous layer of Ta_2O_5 on the metal. The anodically produced film was estimated to be about 200-nm thick since there is a linear relationship (about 1.67 nm/V) between oxide thickness and voltage in this case. The thermally grown oxide layer was found to be 2000 nm thick. The oxide specific ions $TaO_n^{\pm}$ and O^+ were followed by SIMS, the ESCA O 1s signal and valence band, and the AES O KLL, Ta MNN, and OVV, and C KLL peaks were also recorded. The anodic oxide film consisted of a contamination layer, an oxygen-rich reactive interface, and a thick homogeneous oxide layer followed by a sharp interface to the metal. In contrast, the thermal oxide film consisted of a film where the oxygen concentration decreased steadily in going into the bulk and there was a broad interface with the metal.

18. Electrodes Involving Tungsten

Carlson and McGuire[121] in an important paper examined the thickness of the WO_3 layer formed on a tungsten electrode that was anodically polarized in a solution of 0.4 *M* KNO_3 and 0.04 *M* HNO_3. Polarization was carried out at various increasing potentials, while the electrode was being held at the potential for 3 min. This process led to the formation of a uniform oxide layer. The amount of oxide was determined by dissolving the oxide layer in potassium hydroxide and counting the radioactive ^{187}W with the aid of a NaI crystal gamma spectrometer. ESCA studies showed the increasing intensity of the WO_3 peaks with increasing WO_3 thickness produced by increasing the anodization voltage (Figure 27). It was found that the thickness so obtained could be plotted against the ratio of photoelectron intensity arising from tungsten relative to those arising from WO_3 to give the plot shown in Figure 28. The theoretical line drawn through the data was obtained by analysis of the data by assuming that the X-ray beam was essentially unattenuated over the range of surface thickness from which the photoelectron can emerge, and that elastic scattering could be neglected. The photoelectron intensity dI was taken to have an exponential decay with the thickness of the film:

$$dI = F\alpha Dk e^{-\sigma x} dx$$

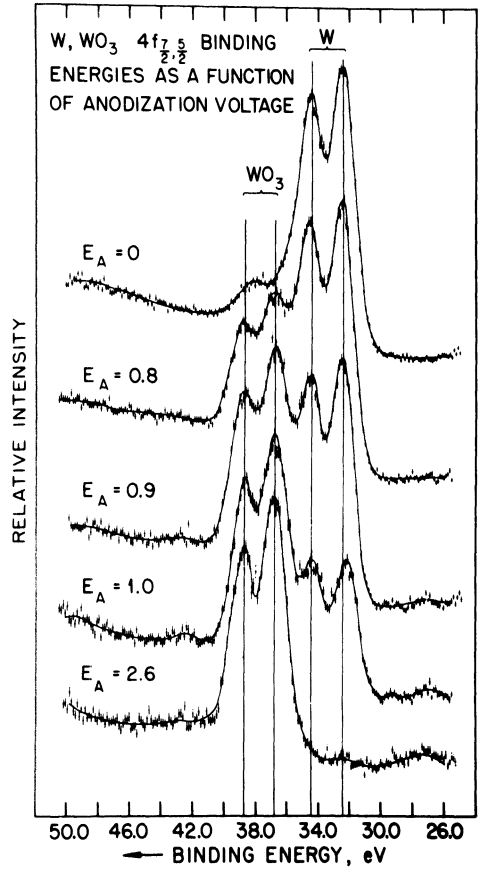

Figure 27. W 4f ESCA spectra of tungsten polarized to different anodization voltages (E_A).[121]

where F is the X-ray flux, α the photoionization cross section for a given atom in a given shell for a particular X-ray energy, D the density of the given atom, k a spectrometer factor, σ the attenuation coefficient (the inverse of the escape depth) for the inelastic collision of the electron which depends upon the photoelectron energy and the nature of the material, and x the distance through the material traveled by the photoelectrons. This distance will depend upon the take-off angle of the photoelectrons and, thus, small take-off angles lead to larger values of x and, thus, greater surface sensitivity. Equations that express film thickness in terms of the photoelectron intensity ratio (expressed as the ratio of ESCA peak areas) using this equation have been used by numerous workers to obtain information about the thickness of surface films by ESCA, and the demonstration of its validity in this paper, thus, made a substantial contribution to the use of ESCA for the study of surface films.

Denisov *et al.*[122] have used ESCA to study the changes in the surface of WO_3 films during electrocoloring.

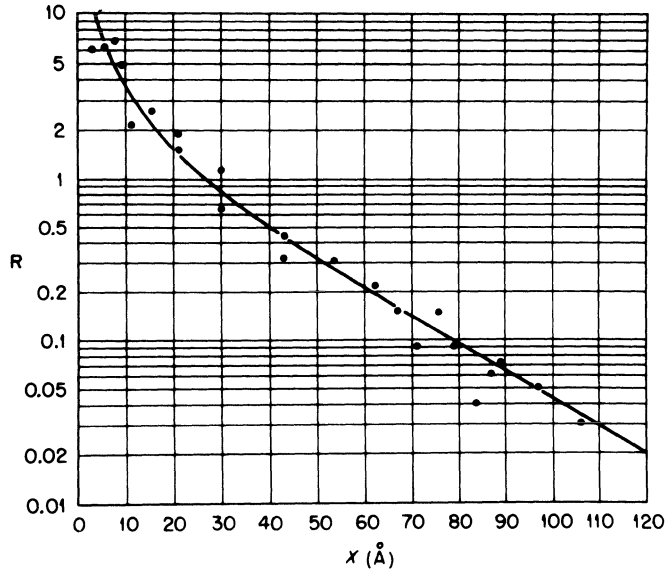

Figure 28. Plot of the ratio of intensities of photoelectrons arising from W relative to those arising from WO_3 as a function of the thickness (Å) of the WO_3 film. The solid line is the theoretical curve derived using the equation described in the text.[121]

19. Electrodes Involving Tin

19.1. Studies of Oxidized Tin Surfaces

Ansell *et al.*[123] studied the surface of "as received" metallic tin by angle resolved core ESCA and argon-ion etching. This study aimed to obtain the relative photoionization cross sections and escape depths (or inelastic mean free paths) for thickness measurements (see Section 18). Argon-ion etching of the surface was found to produce a triple layer, the surface containing a layer of metallic tin formed by reduction of the tin oxide over a layer of tin oxide which covered the substrate tin metal. This was shown by angle resolved studies which showed that the metallic tin was on the surface. Figure 29 shows the spectra obtained after argon-ion etching (Figure 30) is carried out to remove the oxide layer. As the take-off angle is made smaller the distance that the electrons have to travel before leaving the surface is increased (see Section 18), thus, electrons that leave from any inner component of the layer must travel further and their intensity will be reduced. Thus, etching causes not only removal of material, but also reduction of oxide. Reduction and decomposition during argon-ion etching represents a major problem in the use of argon-ion etching for depth profile studies. Castle[11] has pointed out that the presence of a substantial contamination layer will complicate the situation. If

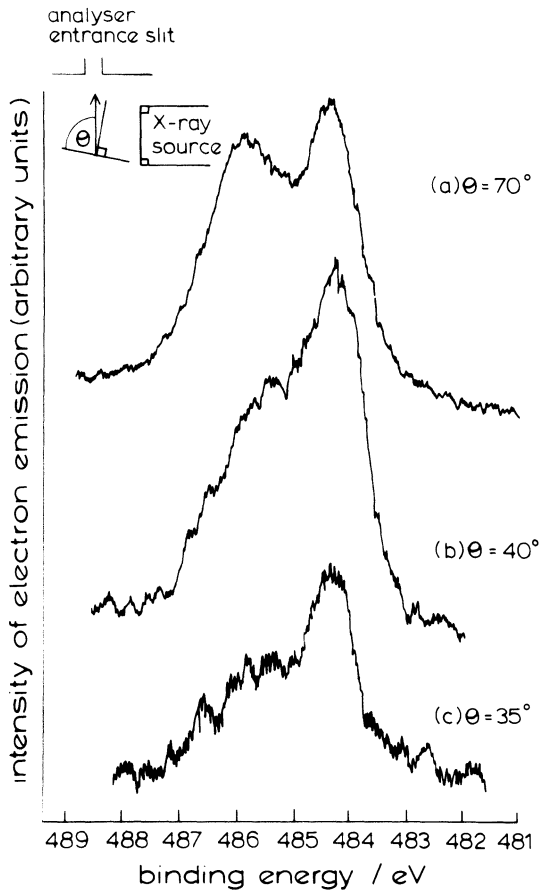

Figure 29. Sn $3d_{5/2}$ ESCA spectra of an etched tin sample (Figure 30) showing how the intensity (the ordinate in arbitrary units) varies with the angle of electron emission. The abscissa represents the binding energy (eV).[123]

I_θ represents the intensity of an outer oxide layer (of thickness d2) covered with a contaminating layer that reduces its intensity, and if I_∞ represents the intensity from infinite oxide then the intensity ratio of these two quantities will vary with the thickness of the outer contamination layer as shown in Figure 31, which shows that as the thickness of the contamination layer (d_1) increases this ratio is not necessarily going to be at a maximum at a low take-off angle.

Lin *et al.*[124] have studied the surface of tin and indium foils by AES and ESCA. The foils were argon-ion etched to remove the oxide. In addition the SnO_2 and SnO powders were subjected to argon-ion etching. SnO_2 powder was found not to change with etching, but SnO decomposed to give metallic tin. One particular problem with tin is that while there is a large difference

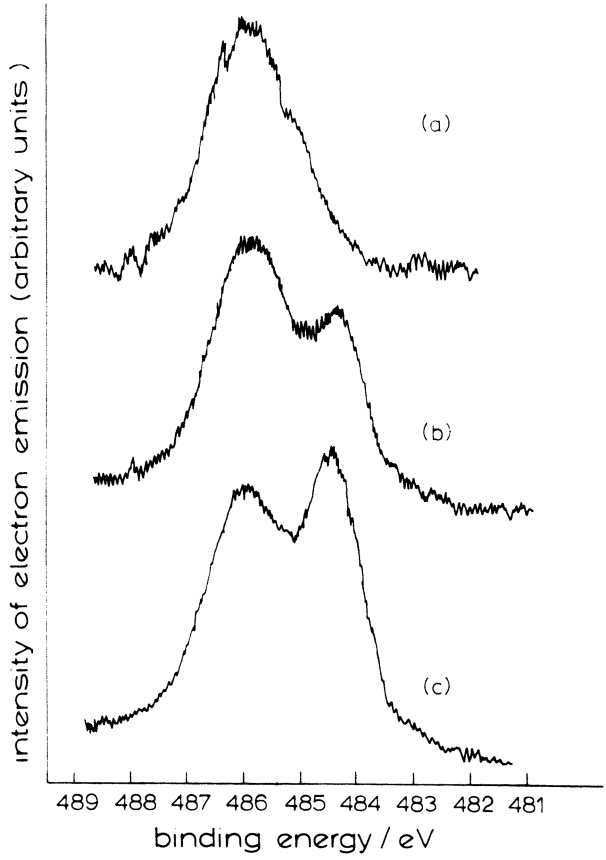

Figure 30. Sn $3d_{5/2}$ ESCA spectra of (a) tin foil prior to argon-ion bombardment, (b) after the first period of argon-ion bombardment, and (c) after the second period of argon-ion bombardment (scales as in Figure 29).[123]

between the Sn 3d binding energy between metallic tin and tin oxides, there is a very small difference in the binding energies between the tin oxides themselves. Indeed, Ansell *et al.*[125] found that the Sn 3d to O 1s separation for SnO and SnO_2 is about the same, though the difference in the Sn 3d binding energy between SnO and SnO_2 is about 0.5 eV. It is interesting that Lin *et al.*[124] find that their tin had SnO_2 on the surface and suffered no argon-ion reduction, while Ansell *et al.*[123] had a tin binding energy closer to that found for bulk SnO on their sample. As discussed previously this did suffer decomposition, just as Lin *et al.*[124] found out that SnO powder suffered decomposition. However, both groups of workers had the same oxide–metal separation on the foils (1.7 eV), and bearing in mind the closeness of the tin oxide binding energies and the problems of calibration that are present for

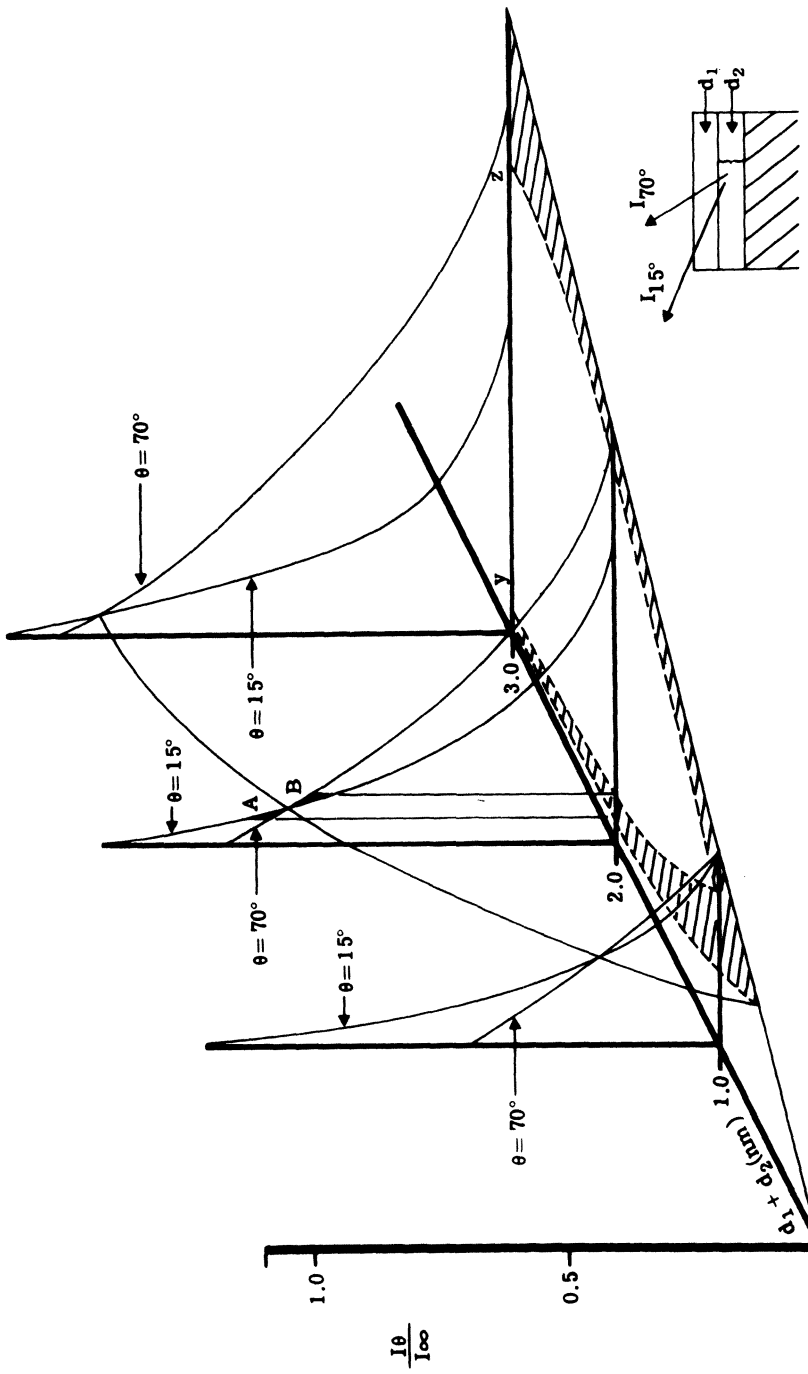

Figure 31. Plot showing how the signal strength from an oxide layer (relative to that for an infinitely thick clean oxide) covered with a contaminent layer varies with the thickness of the oxide and contaminant layer. It is seen that low collection angles only enhance the oxide signal on clean surfaces. In the hatched field the oxide signal is invariant with the angle.[11]

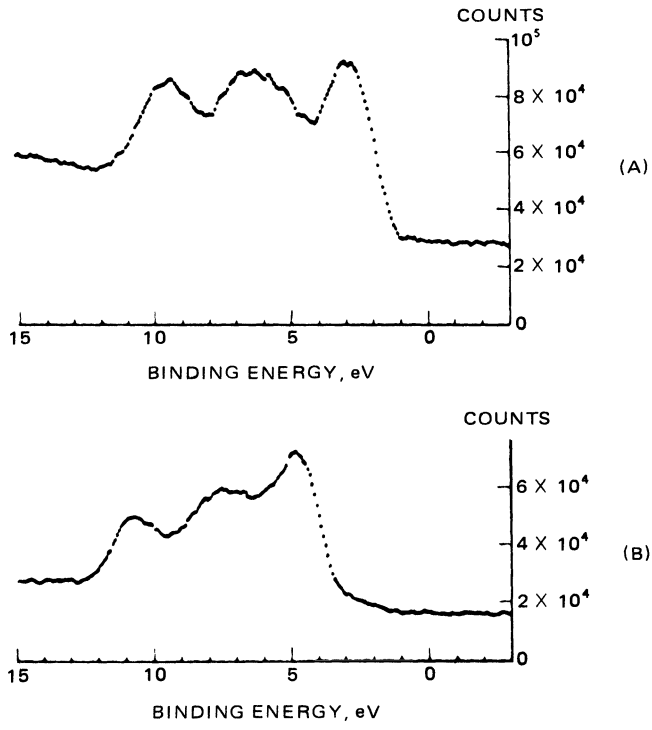

Figure 32. Valence band ESCA spectra of (a) SnO and (b) SnO_2.[126]

obtaining absolute binding energies for insulators, it can be concluded that while the foils show the same spectra in both studies, the relation of these results to the ESCA results for the oxide powders is not certain. It is interesting to note that Lau and Wertheim[126] have identified both SnO and SnO_2 on the surface of metallic tin oxidized by exposure to dry oxygen at 100°C, and there are indications that the oxide layer may consist of an SnO layer lying underneath an SnO_2 layer. This study illustrates the importance of an examination of the valence band region, for it can be seen (Figure 32) that there are substantial differences in the valence band of SnO and SnO_2, even though there is only a small difference in their Sn 3d core ESCA binding energies.

19.2. Studies of the Anodic Polarization of Metallic Tin

Ansell *et al.*[125] have studied the anodic polarization of metallic tin in the active and passive regions in 0.5 mol dm^{-3} sodium hydroxide solution. Sn(II) species, stannous oxide, and hydroxide, with a thickness of the order of 2–2.6 nm, were found in the prepassive region and increasing amounts of Sn(IV),

again in the form of oxide and hydroxide, were found at more positive potentials. Sn(IV) is the only species in the film in the passive region when the layer is found to steadily increase in thickness and the amount of oxide increase is relative to the hydroxide as the potential becomes more positive until no underlying metallic tin can be observed. In the region where both Sn(II) and Sn(IV) are present there is good reason to suppose that the film consists of an inner layer of Sn(II) below an upper layer of Sn(IV). In view of the closeness of the Sn 3d binding energies for SnO and SnO_2 it is important to discuss the validity of the distinction between Sn(II) and Sn(IV) found in this study. It is significant to note that many of the spectra show a peak due to tin oxide and a peak due to metallic tin in the same spectrum, and the difference between the metal and oxide peak is seen to change as the conditions change. It is clear from Figure 33 that while the difference is small [curve b shows Sn(IV) and tin metal and curve c shows Sn(II) and tin metal] it is significant and can be measured with some accuracy.

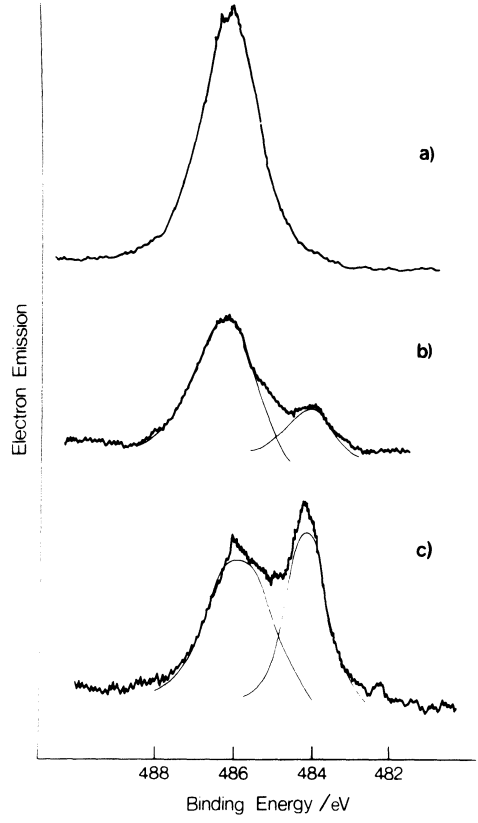

Figure 33. Sn $3d_{5/2}$ ESCA spectra of tin electrodes after-polarization at a potential of (a) −0.90 V, (b) −0.10 V, and (c) +1.50 V(SEC) in 0.5 mol dm^{-3} sodium hydroxide solution.[125]

19.3. Studies of Tinplate

The resistance of tinplate to oxidation and staining by sulfur is improved commercially by treating the tinplate by a solution that contains sodium dichromate, normally using a cathodic charging process that leads to the deposition of chromium containing species on the surface. A number of workers have used ESCA to study the passive layers on tinplate.[127-131]

Coad *et al.*[127] found that tinplate that had undergone cathodic dichromate treatment had an appreciable amount of metallic chromium on the surface in addition to Cr(III) oxide or hydroxide. In addition argon-ion depth profiles were carried out (Figure 34) which showed that the chromium metal was present over a large depth range (20 nm). It was, thus, assumed that the chromium was present in discrete regions rather than as a continuous film because a uniform layer would be expected to be about 1-nm thick. Very small amounts of tin oxide were found on the surface. Riviere[128] found that different depth profiles were obtained using argon-ion bombardment with 1- and 5-keV argon ions, in particular the Cr(III) composition profile was completely altered. The high-energy ions were found to cause greater reduction of Cr(III) oxide. Similar results to those given earlier[127] were obtained by Aubrun *et al.*[129] Leroy *et al.*[130] and Servais *et al.*[130, 131] have studied the passivation layers on tinplate by AES and SIMS as well as ESCA,[130] and have examined the effects on lacquer adhesion of the passive films using ESCA.[131]

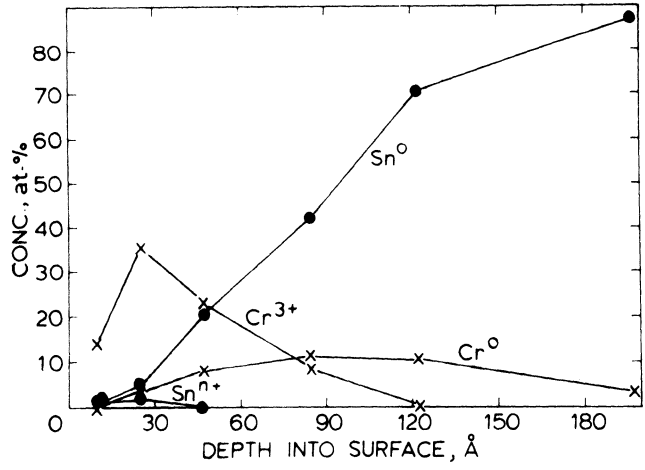

Figure 34. Argon-ion depth profile of a tinplate surface. The percent at.% concentrations of chromium metal (Cr^0), trivalent chromium (Cr^{3+}), tin metal (Sn^0), and tin oxide (Sn^{4+}) as a function of depth are shown.[127]

19.4. Studies of Tin Alloys

Thomas and Sharma[132] have examined the passive film on an electroplated tin–nickel alloy by using argon-ion depth profiles combined with ESCA. The passive film was found to contain a hydrated surface layer containing Sn(IV) and Ni(II) oxides and hydroxides with an SnO_2-rich region below. The film was found to have a thickness of about 3 nm.

20. The Study of Anodic Oxide Films on Gallium Arsenide and Related Compounds

There has been considerable interest in the anodic oxidation of gallium arsenide and related materials as a simple technique for producing barrier-type insulating films on this semiconductor. Films of this sort are of considerable importance for the construction of MOS (metal–oxide-semiconductor) devices. Transistors have been produced on gallium arsenide and there is a strong possibility that gallium arsenide may replace silicon as the material for the fabrication of microprocessor chips. There is still much work to be done in the improvement of the anodization techniques used for preparation of the MOS devices, and in order that this can be done effectively, it is important that detailed structural information be obtained on the films and their interface with the substrate gallium arsenide. The factors which affect the growth and properties of the anodic oxide films on GaAs have been discussed in the literature.[133, 134]

ESCA, generally combined with argon-ion etching in order to get a depth profile through the films (which are generally much thicker than the sampling depth of ESCA, so that the substrate gallium arsenide cannot be seen without etching) has been used to examine these films.[133–141] Bilz *et al.*[135] examined the anodic oxide films on GaP, GaAs:Te, GaSb, and InSb in $KMnO_4$ or $KMnO_4$–KOH–H_2O_2 electrolytes. Wilmsen and Kee[136] used AES and ESCA to study anodic oxide films and thermally grown oxide films on InP and GaAs. It was found that Ga–O bonding extended deeper into the GaAs than As–O bonding, and that there was a possibility which could be neither proved nor disproved (because of the closeness in core binding energy of the As 3d peak in GaAs and metallic arsenic) that elemental arsenic was present at the anodic oxide/GaAs interface. In InP both P–O and In–O bonding penetrated to the same depth and elemental phosphorous was found at the thermal oxide InP interface. Mizokawa *et al.*[137] studied two types of 40 nm thick anodic oxide films formed using a 3% tartaric acid/propylene glycol, and using an electrolyte of $K_2Cr_2O_7$/$HOCH_2CH_2OH$. ESCA depth profiles were carried out. It was found out that the film formed in the first electrolyte was homogeneous with a Ga(III)/As(III) ratio of about unity

throughout the oxide film except in the interface region, while in the second electrolyte ($K_2Cr_2O_7$) it was inhomogeneous with a Ga(III)/(oxidized As) ratio of about 3 at the surface, and it was about unity in the bulk of the film. The surface region (about the first 10 nm) had arsenic in the form of As_2O_5 rather than As_2O_3 and had a large quantity of oxygen present. The interface region (which was about 10 nm thick) between the film and the GaAs substrate in the films formed in both electrolytes showed an excess of arsenic present in this region in an amount approximately equal to the difference in the concentration between Ga_2O_3 and As_2O_3. Preferential sputtering and ion damage was taken into account. Schwartz *et al.*[138] studied anodic oxide and thermal oxide layers on GaAs by ESCA, argon-ion etching, and low-angle electron diffraction techniques. Anodic films were prepared in an electrolyte of $(NH_4)_2HPO_4$ at pH 6.7 saturated with As_2O_3 to prevent the possible leaching of As_2O_3 from the films. Again, the anodic oxide films were found to consist of As_2O_3 and Ga_2O_3 in approximately equal amounts with a film/GaAs interface of about 10-nm thickness. The effect of solubility, reduction, and differential sputtering from the argon-ion etching process were investigated. Figure 35 illustrates how the As 3d and Ga 3d regions change when the anodic film is etched and rinsed. Thus, a quick methanol rinse gives the spectrum in curve A, while the etching of 10 nm of the surface causes reduction of the As_2O_3 to give metallic arsenic (indicated by the arrow). Curves B–D illustrate how the As_2O_3 film is soluble in water. The decomposition of the As_2O_3 into metallic arsenic during etching complicates the situation for metallic arsenic produced in this way must be distinguished from excess metallic arsenic at the oxide/GaAs interface. Nishino *et al.*[139] have used ESCA depth profiles to investigate anodic oxide and plasma-produced oxide films on GaAs. Similar results to those described above were found for the anodic oxide films. The plasma produced oxide films were found to have a higher concentration of Ga_2O_3 than the anodic oxide films. Breeze *et al.*[140] have studied the anodic oxide films produced in two different electrolytes, namely $(NH_4)H_2PO_4$/glycol (giving 100-nm thick films) and tartaric acid/glycol (giving 50-nm thick films). In addition the anodic films formed on a GaAs sample with 20 nm of aluminum deposited on the surface were examined in the tartaric acid/glycol electrolyte (giving 90-nm thick films). Digital curve fitting methods were used to analyze the spectra, and, in particular, to separate the As 3d region at the interface into As from GaAs and As from metallic arsenic (Figure 36). Reduction of the As_2O_3 by the argon beam was taken into account. It was discovered that the amount of metallic arsenic formed by beam reduction (it should be noted that the extent of this reduction will depend upon the argon-ion etching conditions and these will vary considerably between different studies depending upon the beam operating potential and the argon-ion gun design) had about one third of the intensity of the As_2O_3 peak. The uniformity of ion etching by the mechanically scanned saddle field ion source used in this study was confirmed by the

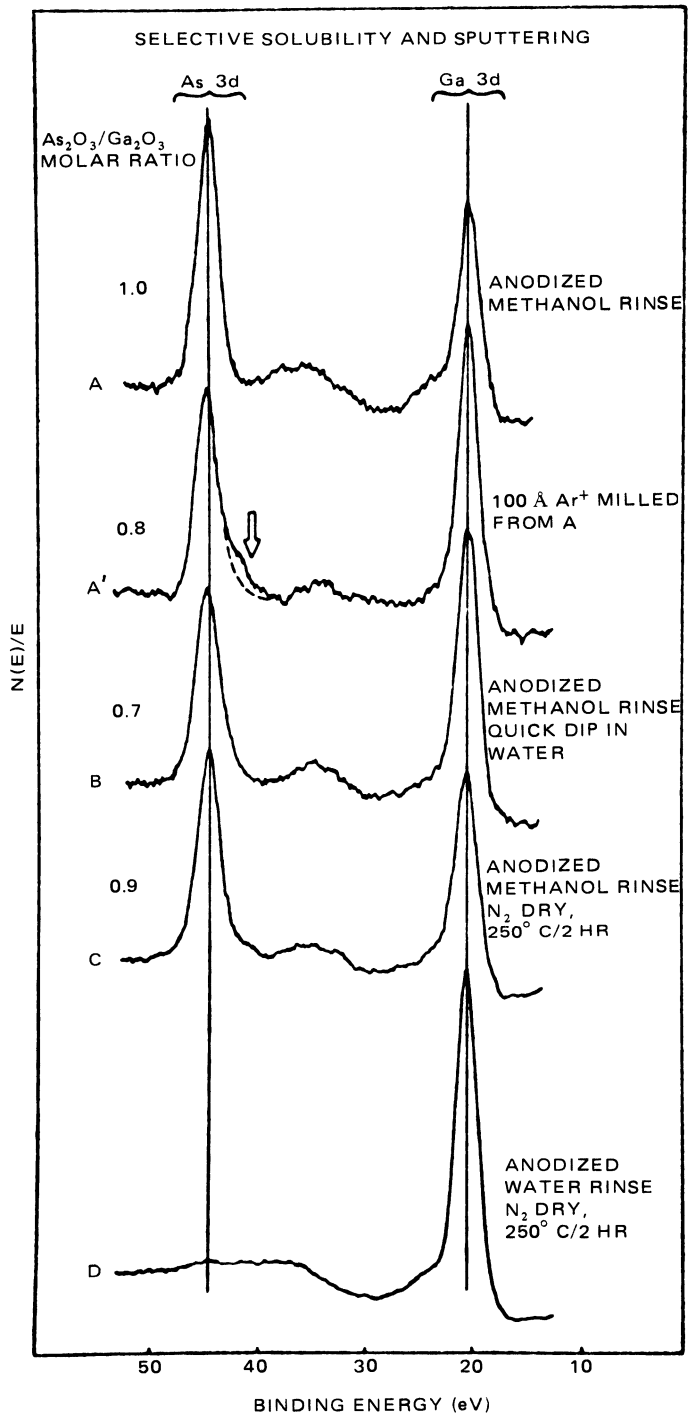

Figure 35. As 3d and Ga 3d ESCA spectra showing postanodization effects of rinsing (methanol and water) and drying (250°C/N_2/2 h) cycles on the As_2O_3 and Ga_2O_3 composition of the native oxide. The solid vertical lines indicate the binding energies of the oxides.[138]

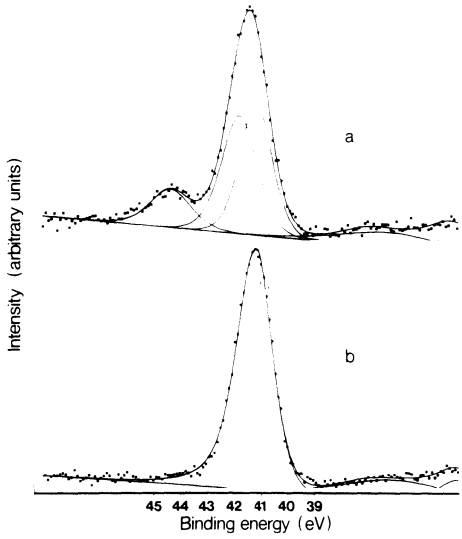

Figure 36. As 3d ESCA spectra (a) at the interface and (b) in the GaAs substrate showing nonlinear least squares curve fitting to the data.[140].

uniform interference colors seen in the film after etching. Figure 36 shows that at the interface the arsenic metal peak (the middle peak) is much more intense than that of the As_2O_3 (the peak on the left) suggesting a genuine excess of metallic arsenic at the interface. Figure 37 illustrates a depth profile through the 100-nm thick film. It will be noted that the surface is arsenic deficient, with only Ga_2O_3 being found, though in the tartaric acid glycol electrolyte the surface region is arsenic rich (in the form of As_2O_3) compared to the bulk.

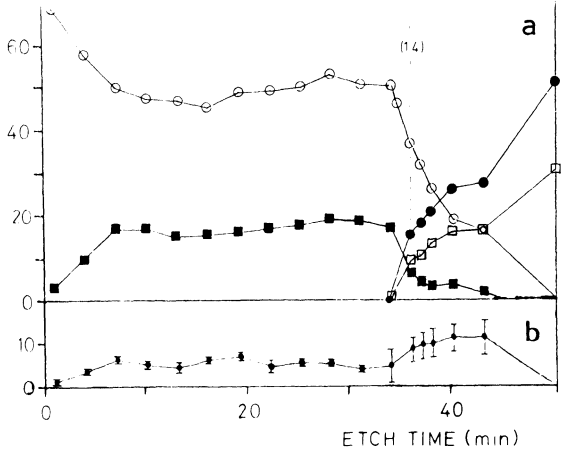

Figure 37. Argon-ion depth profile of oxide films on gallium arsenide for a 100-nm thick oxide film grown on GaAs in $(NH_4)H_2PO_4$/glycol electrolyte at 50 $\mu A\ cm^{-2}$. Argon-ion etching is carried out at 8 kV. (a) shows: ○, Ga in Ga_2O_3; ●, Ga in GaAs; ■, As in As_2O_3; □, As in GaAs. (b) The variation of the concentration of the metal. The vertical scale is in arbitrary units.[140]

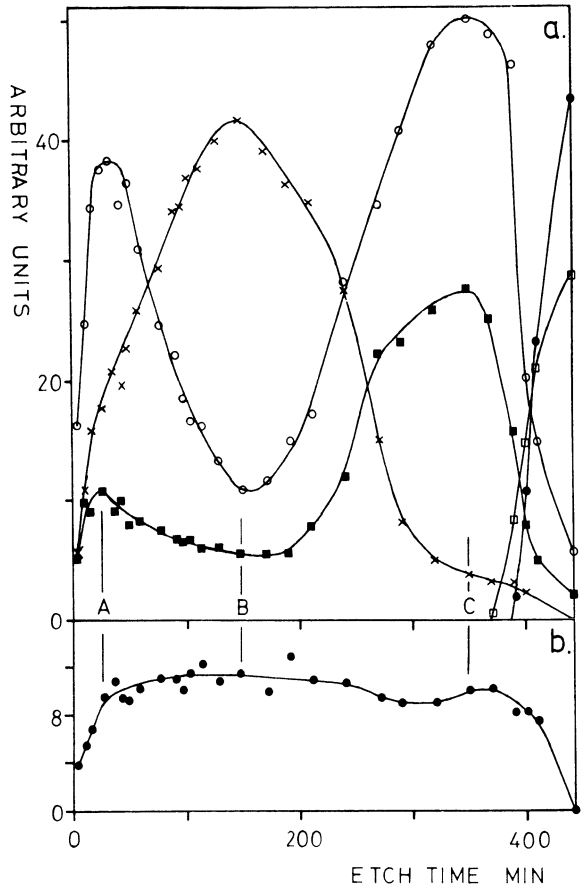

Figure 38. Argon-ion depth profile of oxide films on gallium arsenide for an oxide film grown on GaAs + 20 nm aluminum in tartaric acid/glycol electrolyte at 100 A cm^{-2}. Argon-ion etching is carried out at 5 kV. The same symbols are used as in Figure 37, together with × to represent half of the Al 2p ESCA intensity in Al_2O_3.[140]

In both cases the oxide/GaAs interface is Ga_2O_3 rich. It is interesting to note the triple-layer structure of the anodic oxide film formed from the aluminum containing sample (Figure 38). The outermost part of the film can be seen to contain Ga_2O_3 and As_2O_3, the middle of the film mainly Al_2O_3, and the inner part of the film Ga_2O_3 and As_2O_3. The inner part of the film is similar in all respect to the anodic oxide films formed on GaAs alone, but the outer part of the film is very arsenic deficient and the As_2O_3 is more susceptible to argon-ion beam reduction to metallic arsenic (the ratio of the peak areas of metal to oxide being about 1 : 1 rather than 4 : 1 in the normal film), though it is possible that metallic arsenic is produced by the reaction of unoxidized aluminum with the As_2O_3. Wilmsen *et al.*[141] have studied the oxide/GaAs

interface for thin (2.1–8.5 nm) thermal and anodic oxide films. The progress of film growth was followed by ESCA depth profiles. It was found that as the film grows the arsenic oxides are leached out leaving a continuous layer of Ga_2O_3. Oxide growth then proceeds by galliun and arsenic diffusion to the surface where they oxidize leaving the inner layer of Ga_2O_3 unchanged. The anodic oxide/GaAs interface is formed during the first 4 nm of oxide growth. Once the Ga_2O_3 layer is formed, the elemental arsenic is excluded from entering the continuous Ga_2O_3 layer and collects at the oxide/GaAs interface with the process beginning after about 4 nm of oxide growth. There is considerable interest in the electrical effect that the elemental arsenic excess might have on the MOS characteristics.

21. Chemically Modified Electrodes

There are many materials that have potentially useful properties as an electrode, but which do not behave well as an electrode material. It is possible to use these materials by modification of the surface of well-behaved electrode materials by the deposition of the desired material onto the electrode surface. In this way the electrode will display the chemical and electrochemical properties of the deposited material as if this material were itself a well-behaved electrode material. Deposition can be carried out in a number of ways, such as:

(i) weak reversible adsorption onto the electrode material,
(ii) irreversible adsorption onto the electrode material,
(iii) deposition of a film of material onto the electrode material, and
(iv) the formation of covalent chemical bonds between the electrode material and the deposited material.

The latter method, known as chemical modification, has received the most attention. In all cases it is clear that ESCA will provide a very suitable method for the investigation of the nature of the surface after modification. The last method has the advantage of potentially greater stability and predictability. I have separated discussion of work in this area into those studies that fall broadly into categories (i)–(iii) (Section 21.1) and those that show evidence of covalent bonding (Section 21.2). Such a separation does not imply that the surface interaction is fully understood in all these cases, which would allow a definite separation in this way, but it is done for the convenience of the reader.

21.1. Modified Electrodes

Savy *et al.*[142] examined the surfaces of gold electrodes modified by 2-iron phthalocyanine either by vacuum deposition using electron bombardment or slow thermal desorption at 400°C by visible and X-ray spectroscopy

and by ESCA. The behavior of the modified electrode for oxygen reduction was studied and found to be different for the two different methods of preparation of the modified electrode.

Tourillon *et al.*[143] used electrochemical methods and IR, SIMS, and ESCA to study platinum electrodes that had been modified by electrochemical deposition of a thin solid polyacetonitrile polymer film. It was found that the film consisted of polyacetonitrile doped with ClO_4^- or BF_4^- depending upon whether the experiments were carried out in 0.1 *M* solutions of chlorates in methyl cyanide or $LiBF_4^-$ in methyl cyanide. Partial destruction of the polymer chains occurs when the film is left in a moist atmosphere. Out of solution the films are nonconductive, but they become highly conductive when placed in an electrolytic medium due to the easy permeation by ions in solution. It is found[144] that the aged film in the solution containing chlorates is composed of $CH_3COHNH_2^+ ClO_4^-$ compounds. Tourillon *et al.*[145] used ESCA and SIMS to examine thin films of poly(tetrahydrofuran) on a platinum electrode formed by electrochemical deposition from solutions of 0.3 *M* LiClO and 0.1 *M* $N(Bu_4)ClO_4$ in tetrahydrofuran. It is found that the film is doped by ammines and ammonium salts in the former solution, and by an ammonium salt in the latter solution.

Albery *et al.*[146] have examined the electrode kinetics of platinum and SnO_2 electrodes modified by the irreversible adsorption of up to 20 monolayers of thionine on the surface by electrodeposition. The kinetic behavior of the modified electrode suggests that it is the ideal electrode for a photogalvanic cell using the iron thionine system. In this system light drives the following reaction:

$$2Fe(II) + Th \rightarrow 2Fe(III) + L$$

the leucothionine produced in the process does not react with the Fe(III) because this reaction is sufficiently blocked by the fast electrode kinetics of the thionine/leucothionine reaction. ESCA studies clearly show the presence of thionine on the electrode surface, the C 1s, N 1s, S 2s, and S 2p spectra of the modified electrode being extremely similar to those from a sample of thionine chloride.

21.2. Modified Electrodes with Covalently Bonded Species

Many studies[147–173] have been carried out in electrodes modified in such a way that the material forms strong covalent bonds with the substrate electrode surface. Lenhard *et al.*[163] have found that the effect of covalent anchoring of redox reagents to electrode surfaces causes little change in the redox potential compared to the solution analogs.

21.2.1. Modified Tin Oxide Electrodes

Tin oxide provides a very useful substrate for such studies. Moses *et al.*,[147] Moses and Murray,[149] Untereker *et al.*,[153] Davis and Murray,[157] Moses *et al.*,[161] Lenhard *et al.*,[163] White and Murray,[166] Wier and Murray,[167] and Willman *et al.*,[169] Armstrong *et al.*,[150] and Hawn and Armstrong[165] Fujihira *et al.*[151] and Fujihira,[152] and Lin *et al.*[159] have investigated different materials on this substrate. In most cases the electrodes are prepared as antimony-doped thin transparent films on glass. Reaction occurs between the material and a hydroxyl group on the tin oxide surface:

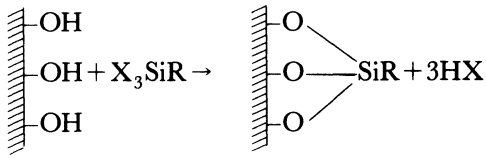

Tin oxide electrodes derivatized with 3-chloroproyltrichlorosilane,[147] 3-(2-aminoethylamino)propyltrimethoxysilane,[147, 153, 161] β-trichlorosilyl-2-ethylpyridine,[147, 153] γ-amonopropyltriethoxysilane,[152, 153] cyanuric chloride[159] which can react with a variety of substances, attachment to 1, 1-bis(hydroxymethyl)-ferrocene being studied, 3-aminopropyltriethyloxysilane,[161] mercaptopropyltrimethoxysilane to which erythrosin has been attached,[165] alkylaminesilane to which dansyl chloride has been attached,[166] oxalyl, malonyl, succinyl, glutaryl, and sebacoyl chlorides attached to 3-(2-aminoethylamino)propyltrimethoxysilane[169] have had their surfaces studied by ESCA and their electrochemical behavior studied. The study of the attachment of erythrosin to modified SnO_2 electrodes[165] provides an interesting comparison between covalently attached molecules and adsorbed dye molecules. While both provided photocurrent response of SnO_2 to visible wavelength light, enhanced stability and efficiency were found for the covalently attached dye molecules. Attempts to form amide linkages between iron porphyrins and tin oxide electrodes, silanized with an ethylenediamine reagent, lead to strong chemisorption of the porphyrin and Fe(III) on the SnO_2 surface.[157] Untereker *et al.*[153] has pointed out that the presence of moisture can cause partial hydrolysis of a polyfunctional X_3SiR (or X_2SiR_2) reagent either before or after formation of a surface bond, leading to surface bonded polymer structures such as

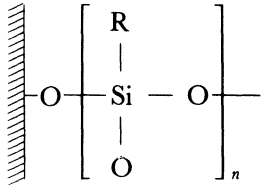

Moses and Murray[149] have produced a chemically modified electrode with a covalently anchored electroactive reagent by silinating SnO_2 with β-trichlorosilyl(2-ethyl)pyridine in benzene under anhydrous conditions and refluxing with methyl iodide, and they observed the electrochemical reduction of the immobilized methylpyridinium. The surface consists of:

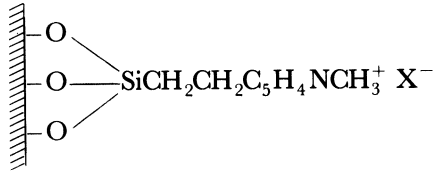

Armstrong *et al.*[150] also used ESCA to study the surface of underivatized tin and indium oxide electrodes.

21.2.2. Modified Titanium Dioxide Electrodes

Titanium dioxide has also been used as a substrate electrode material for such studies [Moses and Murray,[149] Untereker *et al.*,[153] and Moses *et al.*[161]]. TiO_2 films (of an estimated thickness of 100 nm) on titanium were prepared by anodization of polished titanium followed by heating in a 10% hydrogen 90% nitrogen mixture for several hours, by chemical vapor deposition, or by heating titanium metal in a Bunsen burner flame. The electrode was derivatized with the electroactive reagent described previously,[149] with β-trichlorosilyl-2-ethylpyridine,[153] and 3-(2-aminoethylamino)-propyltrimethoxysilane.[153, 161] The electrodes were studied by ESCA and electrochemical methods.

The use of titanium dioxide as an electrode for photoelectrolysis has been discussed in Section 6.2. Tomkiewicz[172] has modified the surface states by chemical modification of the TiO_2 electrode with diethyl((β-triethoxysilyl)-ethyl)phosphonate. The results are encouraging for the use of chemically modified TiO_2 electrodes for solar energy conversion. ESCA studies were used to characterize the surface coverage and the stability of the modified electrode.

21.2.3. Modified Indium Oxide Electrodes

Lin *et al.*[159] have used ESCA and electrochemical methods to study the surface of tin doped indium oxide(In_2O_3) electrodes as thin films on glass. The electrodes were derivatized by treatment with cyanuric chloride to which 1,1-bis(hydroxylmethyl)-ferrocene had been attached.

21.2.4. Modified Ruthenium Dioxide Electrodes

Moses and Murray,[154] Moses *et al.*,[161] and Lenhard *et al.*[163] examined chemically modified RuO_2 electrodes prepared by atomizing a dilute solution of $RuCl_3 \cdot 3H_2O$ in *n*-butylacetate onto a polished hot titanium metal disk, heating it to 475°C, and exposing it to 3-(2-aminoethylamino)-propyltrimethoxysilane,[154, 161] or 3-aminopropyltriethoxysilane.[161] ESCA and electrochemical measurements were carried out.

Wier and Murray[167] investigated SnO_2 electrodes (prepared as described previously) exposed to $RuCl_3$ solutions by electrochemistry and ESCA. Both native SnO_2 and SnO_2 derivatized with alkylaminosilane showed a strongly adsorbed ruthenium species consistent with a Ru(III) oxidation state. Argon-ion ESCA depth profiles were carried out showing considerable penetration of ruthenium into the SnO_2 lattice. The behavior is different from that of bulk RuO_2 electrodes.

21.2.5. Modified Carbon Electrodes

Carbon has also been used as a substrate for many studies. Elliot and Murray,[148] Untereker *et al.*,[153] Lennox and Murray,[155, 162] Lenhard *et al.*,[163] Evans *et al.*,[158] Lin *et al.*,[159] and Matsue *et al.*[171] have studied modified electrodes prepared by covalent attachment of various materials. Carbon has a coverage of surface oxides formed by chemical or air oxidation to form groups such as phenolic (–OH), carboxylic acid, and quinone groups depending upon the source and history of the carbon used. The phenolic groups are suitable for reaction with silanes and other materials in a similar manner shown for SnO_2 in Section 21.2.1. All of the electrodes were studied by ESCA and electrochemical methods.

Carbon surfaces have been reacted with 3-(2-aminoethylamino) propyltrimethyloxysilane,[148, 153] 3-chloropropyltrichlorosilane,[148, 153] γ-aminopropyltriethoxysilane,[148, 153] dinitrophenylhydrazine,[148] benzidine,[158] cyanuric chloride to which hydroxymethylferrocene is attached,[159] tetra(aminophenyl)prophyrin,[161] tetra(aminophenyl)porphyrin,[155] and cyclodextrin.[171]

21.2.6. Modified Gold, Platinum Metal, and Oxide Electrodes

There have been a number of studies of modified electrodes using noble metal or noble metal oxide substrates consisting of gold or platinum electrodes. Lenhard and Murray,[156] Moses *et al.*,[161] Lenhard *et al.*,[163] Fischer *et al.*,[168, 170] Allred *et al.*,[160] Knecht and Stork,[173] and Miller and Van De Mark[164] have studied such modified electrodes using ESCA and electrochemical methods.

In most studies the noble metal was anodically oxidized to form an oxide film which could be derivatized in a similar manner to that described previously. Lenhard and Murray[156] examined the amidization reaction of alklamine silanes derivitized to an oxidized platinum electrode in this way. The surface species was

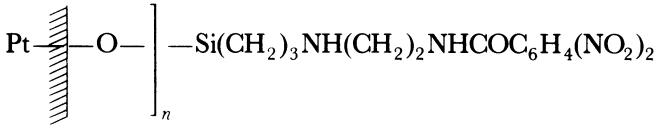

Moses *et al.*[161] studied oxidized platinum electrodes derivatized with 3-(2-aminoethylamino)propyltrimethoxysilane. Fischer *et al.*[168, 170] also studied the surface formed by derivatization of oxidized platinum and gold surfaces by (1,1,-ferroxenediyl)dichlorosilane. The electrochemically measured coverage was correlated with the ratio of Fe/Pt and Fe/Au ESCA intensities. Assuming a homogeneous bonded ferrocene multilayer, ESCA intensity expressions then give a good correlation (Figure 39) suggesting that all of the iron present is ferrocene iron, and that all of the ferrocene iron is electroactive in the electrochemical experiment. If ESCA intensities are calculated using a model that considers nonuniformity in the form of metal exposing pores, then the data could accommodate pores up to 10% of the total area. Allred *et al.*[160] have studied the attachment of permethylpolysilane groups to platinum by the electroreduction of chloropermethylpolysilanes.

Miller and Van De Mark[164] have studied the surface modification of a platinum electrode by polymer adsorption. Strong polymer adsorption was achieved by dipping platinum wire or sheet into trifluoroacetic acid solution containing small amounts of ethylene glycol terephthalate polymer or a copolymer of 60% lysine and 40% alanine. It is not clear from the results

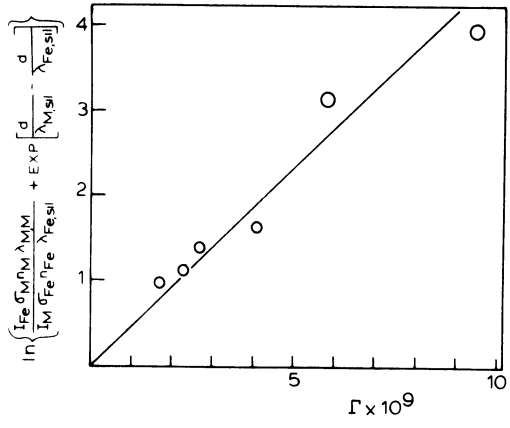

Figure 39. Plot of the Fe $2p_{3/2}$ and $M_{5/2+7/2}$ relative ESCA intensities from an intensity equation against the electrochemically measured coverage Γ.[168]

whether the adsorption actually involves covalent bond formation, but the electrochemical behavior of the modified electrodes is dominated by the polymer. AES and ESCA studies were carried out on the electrode.

Knecht and Stork[173] coated a platinum electrode electrolytically with thallium oxide in an ammoniacal Tl(I) solution. A Fourier transform curve analysis of the ESCA Pt 4f electron region showed only one platinum oxidation state corresponding to partial oxidation of the platinum in addition to the deposition of thallium oxide.

22. Studies of Solid Electrolytes

Solid electrolytes are believed to exhibit their high-ionic conductivity because of the possibility of the mobile cation being able to occupy different sites in the crystal lattice. Dickinson *et al.*[174] investigated two classes of solid electrolytes by ESCA. Solid electrolytes involving Ag(I) and Cu(I) compounds showed that shifts in ESCA core binding energies were very small, and different sites could not be distinguished. ESCA was able to distinguish different sites in β-alumina solid electrolytes, silver β-alumina showing a Ag 3d electron peak that could be fitted to two peaks with an intensity ratio of 2:1 corresponding to the ratio of different sites expected from X-ray crystallography. These experimental results were compared with lattice energy calculations.

23. Ion-Selective Electrodes

Wilson and Pool[175] have used ESCA to study the surface of a monohydrogen phosphate-selective electrode based upon $[Cu(thiourea)_3]HPO_4$ and Ag_2S. There is clearly a considerable scope for the application of ESCA in this area.

24. Noble Metal Electrodes

The first application of ESCA to electrode surfaces was the study of oxide layers on platinum electrodes by Kim *et al.*[176] Since then there have been a number of studies of noble metal electrodes involving mainly platinum, but also gold, palladium, and iridium electrodes.[177–192]

24.1. Studies of Oxide Films on Platinum Electrodes

The current–voltage curve for this electrode has already been discussed in Section 1, and shown in Figure 1. Kim *et al.*,[176] Kim *et al.*,[177] and

Winograd[181] examined the ESCA spectrum of a platinum electrode polarized at 0.7, 1.2, and 2.2 V in 1 *M* $HClO_4$ solution, which showed the progressive growth of the oxide with increasing potential. A similar overall result was obtained by Allen *et al.*[179] who carried out ESCA combined with argon-ion etching and electrochemical studies of platinum electrodes in 0.5 *M* sulfuric acid, but this work showed a difference in the identification of the species present and the potentials at which these species were formed. Dickinson *et al.*[1] examined ESCA spectra of this system at 24 potentials in 0.5 *M* sulfuric acid. This study gave results which agreed with those of Kim *et al.*,[176] Kim *et al.*,[177] and Winograd,[181] but showed marked disagreement with the study by Allen *et al.*[179] In particular, two platinum oxide species were detected: the one at low-binding energy (oxide I) corresponding to a lower platinum oxide which begins to form at about 0.73 V (SCE) and the one at high-binding energy (oxide II) corresponding to PtO_2 which begins to form at about 1.25 V (SCE). Figure 40 shows a representative spectra curve fitted by analog

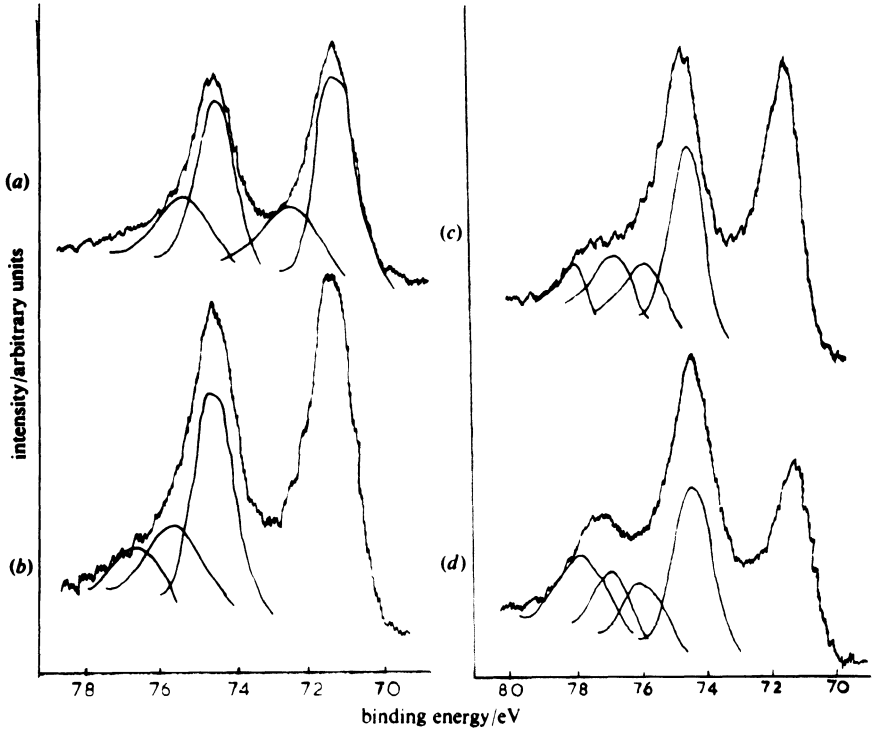

Figure 40. Pt 4f ESCA spectra for a platinum electrode after polarization for 15 min (a) at +0.15 V, (b) at +1.00 V, and (c) at +2.00 V in 1 *N* sulfuric acid. The curves are only shown fitted to the $4f_{5/2}$ peak in (b)–(d) for the sake of clarity.[1]

methods. While the curve fitting is complex, interpretation is assisted by the need to obtain consistent results over 24 continuously changing spectra, although as explained in Section 3 much more accurate methods are now available for this type of analysis. Peaks are only fitted to the Pt $4f_{5/2}$ peak for clarity, and are located right to left of the metal peak in this order: the metal satellite peak which is due to conduction band interaction, the oxide I peak, and finally on the extreme left the oxide II peak. It was also found that the platinum oxides were slowly photoreduced, as shown in Table 2, by the X-radiation, although this was already measured and accounted for. In contrast, Allen *et al.*[179] obtain a different binding energy for oxide I (76 rather than 77.1 eV for Pt $4f_{5/2}$) and both oxides are found to form at much higher potentials. The system was reexamined by Hammond and Winograd[16] in both $HClO_4$ and sulfuric acid media. They compared the results of potentiostatic oxidation at increments of increasing anodic potential and galvanostatic oxidation using current densities of 100 mA cm^{-2} for 1 hr. It is suggested that the main difference in the studies above, namely the nature of oxide I can be explained on the basis of the difference in conditions. The severe galvanostatic conditions (1 A cm^{-2} for up to 48 hr) lead to the formation of a different oxide I species which has a binding energy corresponding to PtO and $Pt(OH)_2$ which is produced chemically. The oxide I which is produced under potentiostatic conditions by Kim *et al.*,[176] Kim *et al.*,[177] Winograd,[181] and Hammond and Winograd[16] and Dickinson, *et al.*[1] is suggested to be a Pt(II) species, but neither PtO nor $Pt(OH)_2$ are. In addition, X-ray photoreduction and decomposition by argon-ion bombardment were investigated. X-ray photoreduction of PtO_2 was found to yield a product with the same binding energy as oxide I formed under galvanostatic conditions, and it is suggested that this may also account for appreciable intensity of the oxide I peaks found by Allen *et al.*[179] Argon-ion etching was found to cause substantial decomposition of PtO_2, forming PtO and metallic Pt, so that any argon-ion depth profile studies of this system are likely to be invalid. The electrodes were analyzed for the presence of electrolyte ions. Adsorbed sulfate and perchlorate ions were found on the surface of the electrodes treated in the appropriate electrolyte. It was found that after

Table 2. X-Ray Photoreduction of Platinum Species

Irradiation time (min)	Relative peak areas of Pt $4f_{5/2}$ peaks		
	Pt(metal)	PtO	PtO_2
1	56	16	28
5	62	20	20
35	65	21	14
110	76	19	5

oxidation to form oxide I, more anodic potentiostatic or galvanostatic oxidation will produce either unlimited growth of oxide II(PtO_2 in all cases) in solutions of limited acid concentration or a limited growth $PtO_x(anion)_y$ structure in which the incorporated anion changes the partition of current density from bulk PtO_2 oxide growth to oxygen evolution which limits the oxide growth. Kover *et al.*[187, 189] have examined the preparation of platinum surfaces, and the effects of air exposure. It was found that the platinum surfaces were insensitive (in terms of ESCA spectral changes) to air. Galvanostatic oxidation at 0.01 A cm^{-2} in $HClO_4$ at concentrations between 1 and 8 *M* produced an oxide I peak similar to that described previously for potentiostatic conditions, but PtO_2 was not observed under these conditions.

Turner[185] has studied the surface of electrodes made of platinum paste on stabilized ZrO_2 by AES and ESCA. Platinum oxides and C, O, Ag, S, and Cl were found on the surfaces.

24.2. Studies of Sulfide Films on Platinum Electrodes

Evans *et al.*[180] had surfaces of platinum electrodes exposed to methyl cyanide solutions containing hydrogen sulfide. At potentials greater than 1.25 V (SCE) the surface is modified by the formation of platinum sulfide, which can be removed by reduction at -0.7 V (SCE).

24.3. Studies of Platinum Electrodes in Molten Salt Systems

Sabbatini *et al.*[184] and Sabbatini *et al.*[188] have examined the surface of platinum electrodes in molten salt electrolytes. ESCA measurements were carried out on platinum foils cleaned by polishing in hot aqua regia followed by heating in dry hydrogen, and then exposing them to molten electrolytes at the same temperatures and gas pressures as used for potentiometric investigations. The samples were then cooled and washed with distilled water before introduction to the spectrometer. Platinum oxides were found on samples that had been exposed to molten KNO_3 at 673 K.[183] More oxidation and the formation of higher oxidation state oxides were found to occur as the exposure time was increased. Potentiometric measurements were carried out for the system (Pt)CO_2, O_2/CO_3^{2-} for platinum electrodes in equimolar sodium nitrate–potassium nitrate at 523 and 623 K or in pure potassium nitrate at 670 K containing 2×10^{-3} *M* sodium carbonate and controlled carbon dioxide–oxygen atmospheres. Figure 41 compares the potential versus time plot with the corresponding plot of the peak areas of the species Pt, PtO, and PtO_2. Rapid potential changes are observed at the beginning of the experiments when the oxidation of the first atomic layer of platinum occurs.

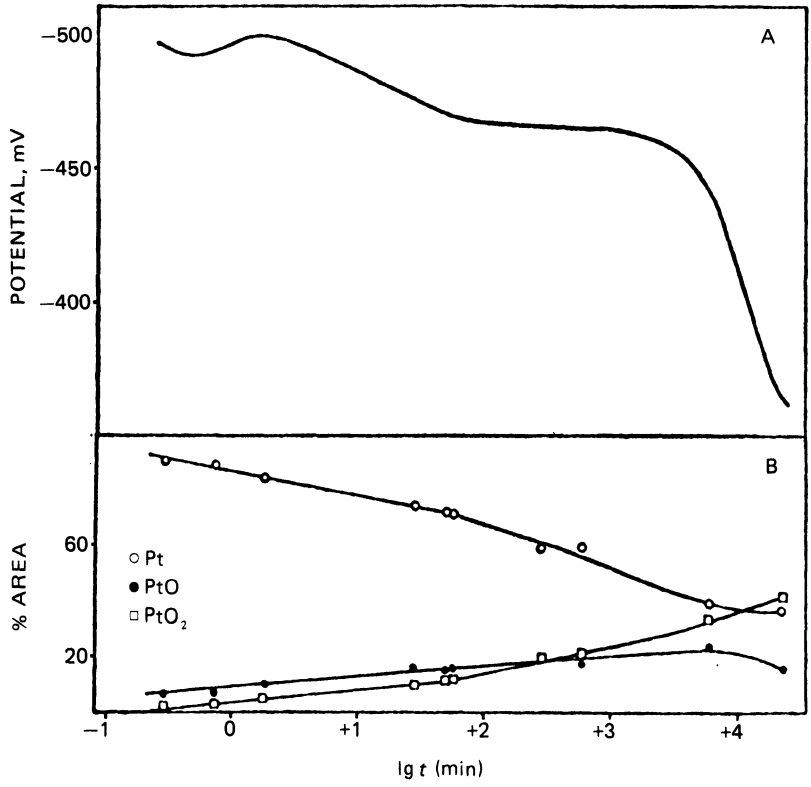

Figure 41. (A) Plot showing the comparison between the potential versus l_g time plot recorded at 670 K and (B) the corresponding plot of the peak area percent versus l_g time obtained for the species Pt, PtO, and PtO_2.[184]

24.4. Electro-Oxidation in Platinum Systems

Heitbaum[186] studied the surface of platinum electrodes during the anodic oxidation of phenylhydrazine and *p*-nitrophenylhydrazine in sulfuric acid by IR, Raman, and ESCA. It was found that the species were strongly adsorbed onto the platinum during the anodic oxidation process, which had a strongly inhibiting effect on the electrochemical process. Phenol and *p*-nitrophenol were found to be the species that were strongly adsorbed onto the surface.

Katayama[191] studied the oxidation of methanol on a platinum–tin oxide electrode in sulfuric acid media. Platinum–tin oxide was chosen because of the enhanced catalyatic activity for electro-oxidation of methanol compared with platinum metal. ESCA studies showed the surface to contain Pt(IV) and Pt(II) oxides. The Sn 3d spectrum combined with argon-ion etching suggested that Sn(IV) was present, but not in the same form as SnO_2, since it was more easily reduced by argon-ion etching.

24.5. Underpotential Deposition on Platinum Electrodes

Underpotential deposition is a phenomenon that arises when monolayer quantities of metal cations on a foreign metal substrate electrode are deposed at applied potentials that are more anodic than the reversible thermodynamic Nernstian potential. Hammond and Winograd[182, 183] have studied the underpotential deposition of silver and copper on platinum electrodes with results that are most interesting from both the electrochemical and ESCA points of view. Figure 42 shows the ESCA spectrum of the Cu 2p region of bulk copper metal and the underpotential deposited copper, together with the cyclic voltammagrams with and without the presence of copper ions. The ESCA spectra show a shift of about 1 eV to lower binding energy for the underpotential deposited copper. It is clear that the binding energy corresponds to copper atoms, for the spectrum has none of the intense satellite features associated with Cu(II), and has a binding energy that is too low to correspond to any known Cu(I) compound. Furthermore, it was shown that a similar shift could be obtained by vacuum evaporation of copper atoms,

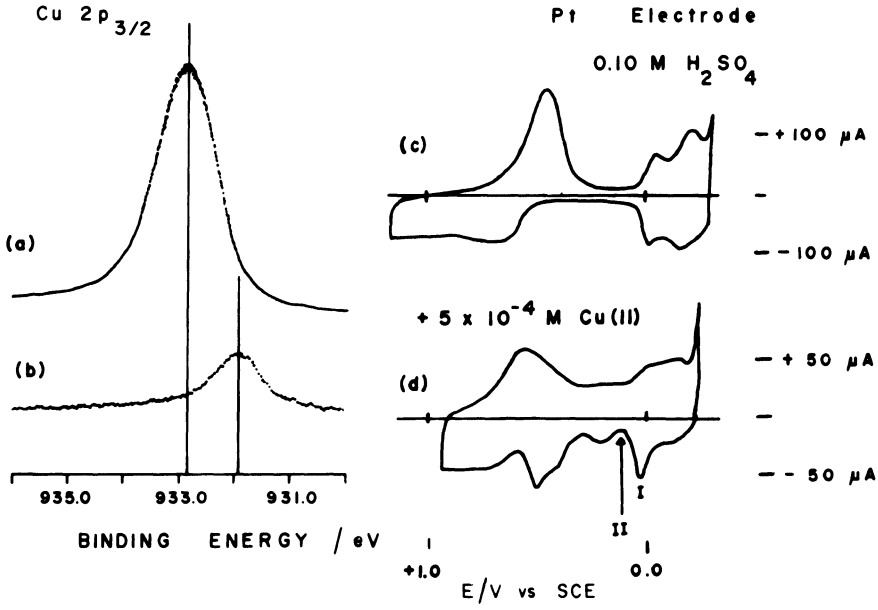

Figure 42. Cu $2p_{3/2}$ ESCA spectra and cyclic voltammagrams for underpotential deposition of copper on a platinum substrate. (a) Cu $2p_{3/2}$ ESCA spectra of bulk Cu metal, argon-ion cleaned *in situ*; (b) Cu $2p_{3/2}$ ESCA spectra of Cu underpotential deposited on platinum [aspiration of electrolyte (5×10^{-4} *M* $CuSO_4$/0.1 *M* sulfuric acid) at a potential +0.08 V relative to bulk Cu anodic stripping peak]; (c) cyclic voltammagram of a platinum electrode in 0.1 *M* sulfuric acid, at a 100 mV sec^{-1} scan rate; (d) cyclic voltammagram of a platinum electrode in 0.1 *M* sulfuric acid/5×10^{-4} *M* $CuSO_4$, at a 20 mV sec^{-1} scan rate (aspiration potential indicated by the arrow).[183]

although the shift falls as the thickness increases for this situation since, unlike the underpotential distributed layer which is two dimensional, the evaporated layer can form atom clusters. It was found that the shift was independent of position in the underpotential region, which can be seen (Figure 42) to show substantial structure. The possible explanation of this negative ESCA shift has been discussed in reference 182.

24.6. Studies of Lead Oxidation on a Platinum Electrode

Kim *et al.*[192] have monitored the oxidation of Pb(II) in the form of $Pb(NO_3)_2$ to PbO_2 on a platinum electrode by anodic polarization at 1.5 V (SCE) by ESCA. Two hydrates were found on the electrode surface as is indicated by the O 1s spectrum.

24.7. Studies of Oxide Films on Gold Electrodes

Kim *et al.*[177] examined the surface of gold foils anodized in 1 *N* sulfuric acid at 1.8 and 1.9 V (SCE) and found large changes in the ESCA spectrum associated with the formation of an Au(III) oxide. Dickinson *et al.*[1] examined the gold electrode system at 19 different potentials in 1 *N* sulfuric acid, and found a steadily increasing amount of gold oxide as the potential was increased (Figures 2 and 43) above about 1.0 V (SCE). X-ray photoreduction

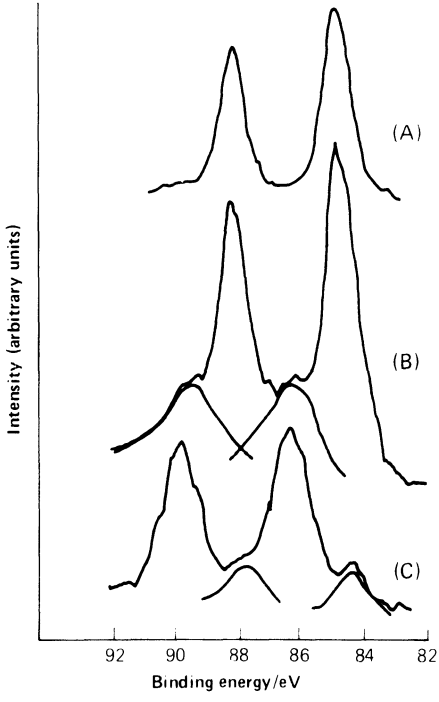

Figure 43. Au 4f ESCA spectra of a gold electrode after 15 min polarization at a potential of (a) +0.20 V, (b) +1.50 V, and (c) +1.70 V in 1 *N* sulfuric acid.[1]

of the gold oxide was also found, and this was taken into account which is shown by the crosses in Figure 2. The ESCA data were also used to obtain a roughness factor of the electrode from 2.0 to 2.4.

24.8. Studies of Oxide Films on Palladium Electrodes

Kim *et al.*[177] and Kim *et al.*[178] have studied the surface of the palladium electrode oxidized at various potentials in 1 *N* sulfuric acid. As in the case of the platinum system two different oxides are observed: PdO and PdO_2. Electrodes oxidized at 0.7 V (SCE) had an oxide film of about 0.5 nm, and those at 1.4 V (SCE) had an oxide film of about 4 nm thickness.

24.9. Studies of Oxide Films on Iridium Electrodes

Kim *et al.*[177] have studied the anodic oxides formed on an iridium electrode by ESCA. It is found that IrO_2 is formed on the electrode surface, and it is suggested that a small amount of Ir(VI) may also be present.

24.10. Studies of Mixed Noble Metal Systems

Srinivasan *et al.*[190] have reported an evaluation of materials for advanced water electrolyzers. They report that they plan to use used a LEED, AES, and ESCA combined system to study a variety of mixed noble metal electrode systems. They find that the mixed ternary oxide system (Ru–Ir–Ta) shows the most promise as an anode electrocatalyst in 1 *N* sulfuric acid.

25. Trace Metal Analysis

ESCA has been used for trace element analysis using the inherent surface sensitivity of the technique in conjunction with electrochemical deposition (accumulation of the species under investigation on the electrode surface).

Brinen amd McClure[193] used this approach for the analysis of microgram quantities of lead, cadmium, and bismuth deposited on a mercury-coated platinum electrode. The same workers[194] used this approach to analyze for lead at the parts per billion (10^{-9}) level by depositing lead onto a rotating disk electrode assembly using a glassy carbon rod electrode. Figure 44 shows the linear relationship obtained between the total amount of lead deposited on the electrode and the area under the Pb 4f ESCA lines. Brinen[195] shows an ESCA spectrum for a rotating glassy carbon electrode onto Mn, Co, Ni, Cu, Zn, Cd, Tl, Pb, and Bi which have been deposited from a solution containing these elements at a concentration of only 0.5 parts per million.

Briggs *et al.*[196] describe a method which does not use electrochemistry, but should be mentioned in this context. It involves producing a wettable surface on aluminum by etching and syringing a small quantity of solution

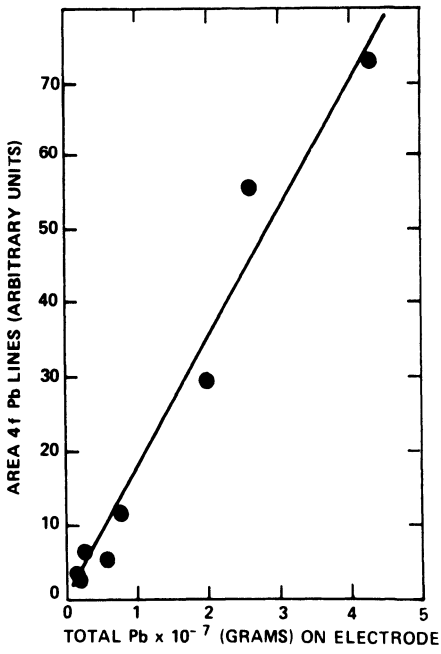

Figure 44. Plot illustrating the linear relationship between the total amount of lead deposited on a carbon electrode and the area under the Pb 4f ESCA peaks.[194].

onto the surface, and then drying the surface to give a thin film. It is found that 10 g of Pb can be detected in this way by the evaporation of 10 μl of a 1 ppm lead nitrate solution.

Sabbatini *et al.*[197] have used a rotating disk electrode assembly using a glassy carbon rod electrode to obtain a simultaneous analytical detection of tin and lead at the parts per billion (10^{-9}) level. The analysis of tin and lead in a chloride matrix presents particular problems in differential pulse anodic stripping voltammetry because tin and lead give rise, in all acidic supporting electrolytes, to stripping peaks at almost exactly the same potential. Electrochemical microdeposition allowed tin and lead to be distinguished by ESCA and detected at the parts per billion level. A linear relationship was obtained between the concentration and the area under the relevant Pb 4f and Sn 3d peaks.

The analytical use of the area under ESCA peaks used in the above studies is valuable, but it must be made clear that certain assumptions must be made about the film,[197] and analysis carried out using this method should consider the factors in the appropriate ESCA intensity expressions[121] used in each case in order to justify the approximations made.

26. Studies of Paint Films

Piens[198] has considered whether the action of an oxidizing pigment or passivation, in general, is possible under a paint film. The experiment that

was required had to demonstrate that a passive state could be achieved on a painted electrode. The simple measurement of corrosion potential (Section 10) can provide no valid conclusion concerning the state of the metal in this case because of the high value that this potential has when an oxidizing pigment is present in the paint even though the substrate metal may be in an active state. ESCA was used as a method for measurement of the state of the substrate metal after paint containing chromate oxidizing pigment was applied on iron plates that had been previously polished with emery paper. Electrochemical measurements were also carried out. It was found that there was an extremely small corrosion rate under an undamaged paint film, but it is not reduced by the oxidizing action of the pigment.

See Sections 6.1 and 19.3 for other relevant studies.

27. AES Studies of Electrode Surfaces

A number of the studies discussed in this review have involved AES studies as well as ESCA studies. There have been many studies that have involved just AES investigations. Space does not allow a full discussion to be given of these studies. However, this review would not be complete without making these references available to the reader, and so they are given at the end of the list of references.[199–278]

28. Conclusion

I feel that the application of ESCA to electrode surfaces has provided invaluable information that has added to the understanding of electrochemical systems. I have tried to illustrate the many powerful ways in which ESCA can be used to tackle a wide range of different electrochemical problems, and I have emphasized different aspects of the application of ESCA for different examples. I hope that I have made clear the problems and limitations associated with the technique. The steady development of the application and understanding of ESCA, in general, continues to open up new possibilities for its application to electrode surfaces. In association with other *ex situ* and *in situ* surface methods I am sure that it will make a substantial contribution to electrochemical studies for many years to come.

References

1. T. Dickson, A. F. Povey, and P. M. A. Sherwood, X-ray photoelectron spectroscopic studies of oxide films on platinum and gold electrodes, *J. Chem. Soc., Faraday I*, **71**, 298–311 (1975).
2. D. Clark, T. Dickson, and W. N. Mair, The interaction of oxygen and hot gold. Pt. 2. Electron-diffractrion, X-ray and electrochemical studies, *Trans. Faraday Soc.*, **55**, 1937–1946 (1959).

3. P. M. A. Sherwood, in: *Spectroscopy* (B. P. Straughan and S. Walker, eds.), Vol. 3, pp. 240–296, Chapman and Hall, London (1976).
4. T. A. Carlson, *Photoelectron and Auger Spectroscopy*, Plenum Press, New York (1975).
5. J. Augustynski and L. Balsenc, in: *Modern Aspects of Electrochemistry* (B. E. Conway and J. O'M. Brockris, eds.), Vol. 13, pp. 251–360, Plenum Press, New York (1979).
6. T. Nakajima and N. Watanabe, Surface analysis of electrode materials with ESCA, *Yoyuen*, **19**, 239–261 (1976).
7. D. Landolt and H. J. Mathieu, Application of electron spectroscopic methods to study electrochemical problems, *Oberflaeche-Surf*,. **21**, 8–15 (1980).
8. T. Nakajima and N. Watanabe, Surface analysis of electrode materials with ESCA, *Yoyuen*, **19**, 239–261 (1976).
9. A. Joshi, Investigations of passivity, corrosion and stress corrosion cracking phenomena by AES and ESCA, *Rev. Coat. Corros.*, **3**, 51–77 (1979).
10. D. T. Larson, Surface analytic techniques in corrosion science, *Corros. Sci.*, **19**, 657–673 (1979).
11. J. E. Castle, The use of X-ray photoelectron spectroscopy corrosion science, *Surf. Sci.* **68**, 583–602 (1977).
12. K. Hashimoto and K. Asami, X-ray photoelectron spectroscopy applied to the analysis of metal surfaces, *Boshoku Gijutsu*, **26**, 375–387 (1977).
13. J. Oudar, Applications of Auger spectroscopy and ESCA to the study of thin films formed on metals, *J. Microsc. Spectrosc. Electron.*, **4**, 439–450 (1979).
14. A. F. Povey and P. M. A. Sherwood, the covalent character of lithium compounds studied by X-ray photoelectron spectroscopy, *J. Chem. Soc., Faraday II*, **70**, 1240–1246 (1974).
15. P. M. A. Sherwood, Analysis of the X-ray photoelectron spectra of transition metal compounds using approximate molecular orbital theories, *J. Chem. Soc., Faraday II*, **72**, 1791–1804 (1976).
16. J. S. Hammond and N. Winograd, XPS spectroscopic study of potentiostatic and galvanostatic oxidation of platinum electrodes in sulfuric acid and perchloric acid, *J. Electroanal. Chem. Interfacial Electrochem.*, **78**, 55–69 (1977).
17. I. Olefjord and N. G. Vannerberg, ESCA studies of passive films formed on steels by oxidizing inhibitors, *Scand. Corros. Congr. (Proc), 7th*, 434–443, (1975).
18. B. O. Elfstrom and I. Olefjord, Preparation of alloys for ESCA investigation, *Phys. Scr.*, **16**, 436–441 (1977).
19. R. O. Ansell, T. Dickinson, A. F. Povey, and P. M. A. Sherwood, X-ray photoelectron spectroscopic studies of electrode surfaces using a new controlled transfer technique. Part I. Description of apparatus and preliminary studies, *J. Electroanal. Chem. Interfacial Electrochem.*, **98**, 69–77 (1979).
20. R. O. Ansell, T. Dicksinson, A. F. Povey, and P. M. A. Sherwood, X-ray photoelectron spectroscopic studies of electrode surfaces using a new controlled transfer technique. Part II. Results for a molybdenum electrode and the curve fitting procedure, *J. Electroanal. Chem. Interfacial Electrochem.*, **98**, 79–89 (1979).
21. T. L. Barr, An ESCA study of the termination of passivation of elemental metals, *J. Phys. Chem.*, **82**, 1801–1810 (1978).
22. T. L. Barr, ESCA studies of naturally passivated metal foils, *J. Vac. Sci. Technol.*, **14**, 660–665 (1977).
23. R. Holm and S. Storp, ESCA studies of chemical shifts for metal oxides, *Appl. Phys.*, **9**, 217–222 (1976).
24. A. Proctor and P. M. A. Sherwood, *Anal. Chem.*, **52**, 2315–2321 (1980).
25. H. Imoto, T. Nakajima, and N. Watanabe, Anode effect in the potassium fluoride-2 hydrogen fluoride system. I. ESCA spectra of carbon and graphite anode surfaces, *Bull. Chem. Soc. Jpn.*, **48**, 1633–1634 (1975).

26. L. Y. Johansson, J. Mrha, M. Musilova, and R. Larsson, Electrochemical measurements and surface studies on acid oxygen carbon electrodes by the use of the ESCA method, *J. Power Sources*, **2**, 183–190 (1977).
27. T. Dickinson, A. F. Povey, and P. M. A. Sherwood, Differential sample charging in ESCA, *J. Electron Spectrosc. Relat. Phenom.*, **2**, 441–447 (1973).
28. N. Watanabe and K. Morigaki, Changes in the structure of two kinds of graphite fluoride electrodes, (CF)*n* and (C2F)*n* with discharging, *Denki Kagaku Oyobi Kogyo Butsuri Kagaku*, **47**, 174–177 (1979).
29. A. Proctor and P. M. A. Sherwood, to be published.
30. M. Fujihira and T. Osa, Chemical modification of carbon electrodes, *Prog. Batteries Sol. Cells*, **2**, 244–248 (1979).
31. J. E. Castle and R. T. Tremaine, Interface analysis for the determination of the pH within the boundary layer at a cathode surface, *Surf. Interf. Anal.*, **1**, 49–52 (1980).
32. S. Eguchi, T. Hamaguchi, S. Sawada, A. Aoki, and Y. Sato, X-ray photoelectron spectra of anodic oxide films of aluminum I, *Kinzoku Hyomen Gijutsu*, **25**, 428–437 (1974).
33. S. Eguchi, T. Hamaguchi, S. Sawada, T. Mizuno, and Y. Sato, X-ray photoelectron spectra of anodic oxide films of aluminum II, *Kinzoku Hyomen Gijutsu*, **25**, 437–442 (1974).
34. J. Painot and J. Augustynski, Potentiostatic and spectroscopic study of aluminum covered with a layer of oxide: Effect of different anions, *Electrochim. Acta*, **20**, 747–752 (1975).
35. J. Augustynski, H. Berthou, and J. Painot, XPS study of the interactions between aluminum metal and nitrate ions, *Chem. Phys. Lett.*, **44**, 221–224 (1976).
36. M. Koudelkova, J. Augustynski, and H. Berthou, On the composition of the passivating films formed on aluminum in chromate solutions, *J. Electrochem. Soc.*, **124**, 1165–1168 (1977).
37. J. Augustynski, in: Passivity of Metals (R. P. Frankenthal and J. Kruger, eds.), pp. 989–1020, The Electrochemical Soc. Inc., Princeton (1978).
38. M. Koudelkova and J. Augustynski, Some aspects of the anodic behavior of aluminum in nitrate-choride solutions, *J. Electrochem. Soc.*, **126**, 1659–1661 (1979).
39. H. Kaneno, S. Kobayashi, H. Takahashi, and M. Nagayama, Depth profile of barrier-type aluminum anodic oxide films formed in a neutral borate bath, *Aruminyumu Kenkyu Kaishi*, **137**, 40–41 (1979).
40. S. Eguchi, T. Hamaguchi, S. Sawada, T. Mizuno, and Y. Sato, X-ray photoelectron spectra of aluminum alloys and their anodic oxide films, *Kinzoky Hyomen Gijutsu*, **25**, 492–498 (1974).
41. H. Yamada, T. Nakajima, and N. Watanabe, Aluminum anodic coating formation in liquid hydrogen fluoride and the ESCA spectrum of the coatings, *Aruminyumu Kenkyu Kaishi*, **118**, 19 (1977).
42. N. R. Armstrong and R. K. Quinn, Auger and x-ray photoelectron spectroscopic and electrochemical characterization of titanium thin film electrodes, *Surf. Sci.*, **67**, 451–468 (1977).
43. F. Dalard, C. Montella, and J. Gandon, Adherence of paints on titanium. III. Study and characterization of oxide films, *Surf. Technol.*, **8**, 203–224 (1979).
44. C. N. Sayers and N. R. Armstrong, X-ray photoelectron spectroscopy of titanium dioxide and other titanate electrodes and various standard titanium oxide materials: Surface compositional changes of the titanium dioxide electrode during photoelectrolysis, *Surf. Sci.*, **77**, 301–320 (1978).
45. G. Blondeau, M. Froelicher, M. Froment, A. Hugot-Le Geoff, and J. Zerbino, Influence of copper addition on optical properties of titanium dioxide, *J. Electrochem. Soc.*, **126**, 1592–1596 (1979).
46. T. Fukuzuka, K. Shimogori, H. Satoh, and F. Kamikubo, The relationship between the corrosion resistance and the surface film structure of noble metal oxide coated titanium,

Boshoku Gijutsu, **28**, 429–436 (1979).
47. M. Merriman and G. C. Verroli, Materials characterization of vanadium pentoxide utilized in Li-V205 reserve cells, *Mater. Res. Bull.*, **14**, 77–84 (1979).
48. T. Dickinson, A. F. Povey, and P. M. A. Sherwood, X-ray photoelectron spectroscopic study of the film formed on a gold electrode during the electrochemical reduction of chromium (VI), *J. Chem. Soc., Faraday Trans. I.*, **72**, 686–705 (1976).
49. G. Bouyssoux, M. Romand, H. D. Polaschogg, and J. T. Calow, XPS and AES studies of anodic passive films grown on chromium electrodes in sulfuric acid baths, *J. Electron Spectrosc. Relat. Phenom.*, **11**, 185–196 (1977).
50. K. Yoshida, Y. Tusukahara, and K. Koyama, ESCA analysis of cathode film by chromium plating, *Kinzoku Hyomen Gijutsu*, **30**, 457–461 (1979).
51. K. Hashimoto, K. Asami, M. Naka, and T. Masumoto, Surface films formed on amorphous cobalt–chromium alloys in 1N hydrochloric acid, *Boshoku Gijutsu*, **28**, 271–277 (1979).
52. C. H. Lee, E. Yeager, and B. D. Cahan, Optical and ESCA studies of the manganese dioxide electrode, *Managanese Dioxide Symp. (Proc.)*, **1**, 349–372 (1975).
53. M. Nagayama and M. Cohen, The anodic oxidation of iron in a neutral solution, *J. Electrochem. Soc.*, **109**, 781–790 (1962).
54. J. O'M. Bockris, D. Drazic, and A. R. Despic, The electrode kinetics of the deposition and dissolution of iron, *Electrochim. Acta*, **4**, 325–361 (1961).
55. C. R. Brundle, T. J. Chuang, and K. Wandelt, Core and valence level photoemission studies of iron oxide surfaces and the oxidation of iron, *Surf. Sci.*, **68**, 459–468 (1977).
56. K. Asami, K. Hashimoto, and S. Shimodaira, Quantitative ESCA determination methods of iron(2+) and iron(3+) in iron oxides, *Nippon Kinzoku Gakkaishi*, **40**, 438–444 (1976).
57. T. P. Hoar, M. Talerman, and P. M. A. Sherwood, Electron spectra of oxide films on pure iron and an iron–aluminum alloy, *Nature Phys. Sci.*, **240**, 116–117 (1972).
58. K. Asami, K. Hashimoto, and S. Shimodaira, an ESCA study of iron(2+)/iron(3+) ratio in passive films on iron–chromium alloys, *Corros. Sci.*, **16**, 387–391 (1976).
59. Z. Szklarska-Smialowska, H. Viefhaus, and M. Janik-Czachor, Electron spectroscopy analysis of in-depth profiles of passive films formed on iron in chloride-containing solutions, *Corros. Sci.*, **16**, 649–652 (1976).
60. J. C. Wood and N. G. Vannerberg, An x-ray photoemission spectroscopy study of iron-oxide, iron-benzoic acid inhibitor films, *Corros. Sci.*, **18**, 315–321 (1978).
61. C. T. Chen, B. D. Cahan, and E. Yeager, Passivation studies of iron, nickel and their alloys by, *in situ*, ellipsometry and, *ex situ*, ESCA techniques, *Gov. Rep. Announce. Index (U.S.)*, **79**, 132 (1979).
62 A. G. Akimov, N. P. Andreeva, and I. L. Rozenfel'd, Study of iron passivation in a neutral electrolyte by an ellipsometric method, *Elektrokhimiya*, **15**, 1888–1892 (1979).
63 I. Olefjord, Application of electron spectroscopy for chemical analysis to the study of iron-based battery electrodes, *J. Appl. Electrochem.*, **5**, 145–150 (1975).
64. W.-Y. Lee, G. Scherer, J. M. Eldridge, M. H. Lee, and R. H. Geiss, Oxidation and corrosion studies of iron–palladium ($Fe_{1-x}Pd_x$) films, *J. Electrochem. Soc.*, **126**, 547–555 (1979).
65. K. Hashimoto, K. Asami, M. Naka, and T. Masumoto, The role of alloying elements in improving the corrosion resistance of amorphous iron base alloys, *Corros. Sci.*, **19**, 857–867 (1979).
66. K. Hashimoto, K. Asami, M. Naka, and T. Masumoto, Effect of molybdenum on the corrosion behavior of amorphous iron–molybdenum–carbon alloys in 1N hydrochloric acid, *Sci. Rep. Res. Inst., Tohoku Univ., Ser. A*, **27**, 237–245 (1979).
67. K. Hashimoto, M. Naka, K. Asami, and T. Masumoto, An x-ray photoelectron spectroscopy study of the passivity of amorphous iron–molybdenum alloys, *Corros. Sci.*, **19**, 165–170 (1979).

68. D. A. Stout, J. B. Lumsden, and R. W. Staehle, An investigation of pitting behavior of iron–molybdenum binary alloys, *Corrosion(Houston)*, **35**, 141–147 (1979).
69. I. Olefjord and B. O. Elfstrom, The corrosion resistance of iron–chromium alloys as studied by ESCA, *React. Solids*, (*Proc. Int. Symp.*), *8th*, 1976, 791–796 (1977).
70. K. Asami, K. Hashimoto, and S. Shimodaira, XPS determination of compositions of alloy surfaces and surface oxides on mechanically polished iron–chromium alloys, *Corros. Sci.*, **17**, 713–723 (1977).
71. K. Asami, K. Hashimoto, and S. Shimodaira, An XPS study of the passivity of a series of iron–chromium alloys in sulfuric, *Corros. Sci.*, **18**, 151–160 (1978).
72. K. Hashimoto, M. Naka, K. Asami, and T. Masumoto, XPS and electrochemical studies of the effect of metalloid additives on corrosion behaviors of amorphous iron–chromium alloys, *Boshoku Gijutsu*, **27**, 279–283 (1978).
73. G. Okamoto, passive film of 18–8 stainless steel structure and its function, *Corros. Sci.*, **13**, 471–478 (1973).
74. S. Kimitaka and S. Funaki, ESCA studies of the surface film on tin free steel, *Bunko Kinkyu*, **22**, 143–150 (1973).
75. K. Sugimoto, K. Kishi, S. Ikeda, and Y. Sawada, ESCA studies of passivated chromium nickel(18 CR 8Ni) stainless steels, *Nippon Kinzoku Gakkaishi*, **38**, 54–59 (1974).
76. G. Okamoto, K. Tachibana, T. Shibata, and K. Hoshino, Analysis of passive films on stainless steel by ESCA, *Nippon Kinzoku Gakkaishi*, **38**, 117–124 (1974).
77. R. Holm and E. M. Horn, Study of the oxide layer on metals and alloys by ESCA, Metalloberflaeche–Angew. Elektrochem., **28**, 490–495 (1974).
78. I. Olefjord, Application of ESCA to oxide films formed on stainless steels at intermediate and high temperatures, *Metal Sci.*, **9**, 263–268 (1975).
79. I. Olefjord and H. Fischmeister, ESCA studies of the composition profile of low temperature oxide formed on chromium steels-II. Corrosion in oxygenated water, *Corros. Sci.*, **15**, 697–707 (1975).
80. J. E. Castle and C. R. Clayton, The use of x-ray photoelectron spectroscopy in the analyses of passive layers on stainless steel, *Corros. Sci.*, **17**, 7–26 (1977).
81. H. Diekmann, H. Graefen, R. Holm, E. M. Horn, and S. Storpp, ESCA investigations of the passive films formed on austenitic stainless steels in nitric acid, *Z. Werkstofftech.*, **9**, 37–45 (1978).
82. K. Asami and K. Hashimoto, An x-ray photoelectron spectroscopic study of surface treatments of stainless steels, *Corros. Sci.*, **19**, 1007–1017 (1979).
83. K. Asami, K. Hashimoto, T. Masumoto, and S. Shimodaira, ESCA study of the passive film on an extremely corrosion-resistant amorphous iron alloy, *Corros. Sci.*, **16**, 909–914 (1976).
84. A. G. Akimov, I. L. Rozenfel'd, L. P. Kazanskii, and G. V. Machavariani, X-ray electron study of the surface of chromium steels, *Dokl. Akad. Nauk SSSR*, **230**, 1363–1365 (1976).
85. A. K. Covington, A. Knowles, and P. M. A. Sherwood, unpublished results.
86. K. Hashimoto, K. Asami, and K. Teramoto, An x-ray photoelectron spectroscopic study on the role of molybdenum in increasing the corrosion resistance of ferritic stainless steels in hydrochloric acid, *Corros. Sci.*, **19**, 3–14 (1979).
87. K. Hashimoto and K. Asami, An x-ray photoelectron spectroscopic study of the passivity of ferritic 19-chromium stainless steels in 1N hydrochloric acid, *Corros. Sci.*, **19**, 251–260 (1979).
88. C. Leygraf, G. Hultquist, I. Olefjord, B. O. Elfstroem, V. M. Knyazheva, A. V. Plaskeev, and Ya. M. Kolotyrkin, Study of the mechanism of disolution of components and the formation of a surface layer on single crystal alloys FeCr18 and FeCr18Mo3 in the passive state, *Zashch. Met.*, **15**, 395–407 (1979).
89. C. Leygraf, G. Hultquist, I. Olefjord, B. O. Elfstroem, V. M. Knyazheva, A. V. Plaskeev,

and Ya. M. Kolotyrkin, Selective dissolution and surface enrichment of alloy components of passivated Fe18Cr and Fe18CrMo single crystals, *Corros. Sci.*, **19**, 343–357 (1979).
90. R. O. Ansell, T. Dickinson, and A. F. Povey, An x-ray photoelectron spectroscopic study of the films on colored stainless steel and colored, Nilomag, alloy 771, *Corros. Sci.*, **18**, 245–256 (1978).
91. A. F. Povey, R. O. Ansell, T. Dickinson, and P. M. A. Sherwood, An x-ray photoelectron spectroscopic study of stainless steel electrodes after polarization in the regions of transpassivity and secondary passivity, *J. Electroanal. Chem. Interfacial Electrochem.*, **87**, 189–201 (1978).
92. K. Asami, N. Totsuka, and M. Takano, Transgranular stress corrosion cracking of mild steel in 0.5N sulfuric acid$^+$ 0.005N potassium iodide solution—XPS observation of the surface film, *Corrosion (Houston)*, **35**, 208–211 (1979).
93. J. Spitz, T. Van Danh, and A. Aubert, Chromium black coatings for photothermal conversion of solar energy, part I: Preparation and structural characterization, *Sol. Energy Mater.*, **1**, 189–200 (1979).
94. S. B. Agarwal, Y. F. Wang, C. R. Clayton, H. Herman, and J. K. Hirvonen, Interpretation of electrochemical behavior of nickel-implanted type-430 stainless steel using x-ray photoelectron spectroscopy and transmission electron microscopy, *Thin Solid Films*, **63**, 19–25 (1979).
95. T. Dickinson, A. F. Povey, and P. M. A. Sherwood, Dissolution and passivation of nickel. An x-ray photoelectron spectroscopic study, *J. Chem. Soc., Faraday Trans. 1*, **73**, 327–343 (1977).
96. P. Marcus, J. Oudar, and I. Olefjord, XPS-study of the passive film on nickel, *J. Microsc. Spectrosc. Electron.*, **4**, 63–72 (1979).
97. P. Marcus, J. Oudar, and I. Olefjord, Studies of the effect of sulfur on the passivation of nickel by auger electron spectroscopy and electron spectroscopy for chemical analysis, *Mater. Sci. Eng.*, **42**, 191–197 (1980).
98. L. Sabbatini, B. Morelli, P. Zambonin, and B. A. DeAngelis, Oxygen electrodes in fused salts. Potentiometric and x-ray photoelectron spectroscopic (ESCA) findings on the system nickel dicarbonyl$^+$ dioxygen/carbonate ion in molten nitrates, *J. Chem. Soc., Faraday Trans. I*, **75**, 2628–2637 (1979).
99. E. Desimoni, B. Morelli, F. Palmisano, L. Sabbatini, and P. G. Zambonin, Electrochemical and spectroscopic (ESCA) aspects of the (nickel) carbon dioxide, oxygen/carbonate system in fused nitrates, *Ext. Abstr. Meet.—Int. Soc. Electrochem. 30th*, 88–89 (1979).
100. K. Hashimoto, M. Kasaya, K. Asami, and T. Masumoto, Electrochemical and XPS studies on corrosion behavior of amorphous nickel–chromium–phosphorous–boron alloys, *Boshoku Gijutsu*, **26**, 445–452 (1977).
101. H. Schlecker, P. Blank, and H. G. Feller, Examination of the anodic behavior of nickel–palladium alloys. Part II. Examination of the formation and composition of passive films on nickel–palladium surfaces by electrochemical methods. SEM, SIMS and XPS, *Z. Metallkd.*, **70**, 638–645 (1979).
102. A. G. Akimov, E. N. Paleolog, A. Z. Fedotova, V. G. Dagurov, V. D. Manskaya, B. A. Goncharenko, V. S. Mikheev, and N. D. Tomashov, Study of the composition of anodic oxide coatings on titanium–nickel alloys, *Elektrokhimiya*, **15**, 1089–1094 (1979).
103. Ya. M. Kolotyrkin, V. M. Knyazheva, T. E. Tsenta, V. B. Kozhevnikov, D. S. Zakhar'in, and T. V. Svistunova, Study of the mechanism of corrosion resistance of nickel–molybdenum alloys, *Fiz.-Khim. Mekh. Mater.*, **16**, 7–13 (1980).
104. K. Hashimoto and K. Asami, XPS study of surface film on nickel alloys in hot concentrated sodium hydroxide, *Corros. Sci.*, **19**, 427–435 (1979).
105. G. Blondeau, M. Froelicher, M. Froment, A. Hugot-Le Goff, and C. Vignaud, Growth of an oxide film formed by anodic polarisation of nickel–silicon alloys in a sulfuric acid medium, *C.R. Acad. Sc. Paris*, **282C**, 407–410 (1976).

106. J. Herion, B. Natsch, E. A. Niekisch, and G. Schari, Preparation and analysis of copper(I) oxide thin-film solar cells, *Comm. Eur. Communities* (Rep.), *EUR* 6376, (1979).
107. P. G. Fox, G. Lewis, and P. J. Boden, Some chemical aspects of the corrosion inhibition of copper by benztriazole, *Corros. Sci.*, **19**, 457–467 (1979).
108. M. Ohsawa and W. Suetaka, Spectroelectrochemical studies of the corrosion inhibition of copper by mercaptobenzothiazole, *Corros. Sci.*, **19**, 709–722 (1979).
109. J. A. Petit, P. Lafargue, L. Porte, and T. Minh Duc, Dissolution processes of titanium–copper alloys. ESCA studies of surface layers in active and passive states, *Electrochim. Acta*, **24**, 1023–1028 (1979).
110. L. D. Hulett, A. L. Bacarella, L. LiDonnici, and J. C. Griess, Analysis of protective oxide films on copper–nickel alloys by photoelectron spectroscopy, *J. Electron Spectrosc. Relat. Phenom.*, **1**, 169–178 (1972/73).
111. Y. Takasu, S. Maru, Y. Matsuda, and H. Shimizu, Analysis of the surface composition of passive films on copper–nickel alloys by Auger electron spectroscopy and x-ray photoelectron spectroscopy, *Bull. Chem. Soc. Jpn.*, **48**, 219–221 (1975).
112. Y. Takasu, H. Shimizu, S. Maru, M. Tomori, and Y. Matsuda, Surface composition of electropolished copper–nickel alloys, *Corros. Sci.*, **16**, 159–162 (1976).
113. J.E. Castle and D. C. Epler, The correlation of XPS analysis with electrochemical history in aqueous corrosion, *Surf. Sci.*, **53**, 286–296 (1975).
114. A. F. Povey and J. Turner, X-ray photoelectron spectroscopic studies of modified zinc anodes, *J. Electroanal. Chem. Interfacial Electrochem.*, **92**, 203–213 (1978).
115. K. Sugimoto, G. Belanger, and D. L. Piron, Changes in the niobium electrode surface induced by strong cathodic polarization, *J. Electrochem. Soc.*, **126**, 535–541 (1979).
116. H. Y. Hall and P. M. A. Sherwood, unpublished results.
117. A. F. Povey and A. A. Metcalfe, The anodic dissolution of molybdenum in alkaline solutions—x-ray photoelectron spectroscopic studies, *J. Electroanal. Chem. Interfacial Electrochem.*, **84**, 73–81 (1977).
118. J. Augustynski, L. Balsenc, and J. Hinden, X-ray photoelectron spectroscopic studies of ruthenium dioxide-based film electrodes, *J. Electrochem. Soc.*, **125**, 1093–1097 (1978).
119. D. R. Rolison, K. Kuo, M. Umana, D. Brundage, and R. W. Murray, Properties of ruthenium oxide(RuO_x) working electrodes in nonaqueous solvents, *J. Electrochem. Soc.*, **126**, 407–414 (1979).
120. H. Bispinck, O. Ganschow, L. Wiedmann, and A. Benninghoven, Combined secondary ion mass spectrometry(SIMS), Auger electron spectroscopy (AES), and x-ray photoelectron spectroscopy (XPS) investigations of tantalum oxide layers, *Appl. Phys.*, **18** 113–117 (1979).
121. T. A. Carlson and G. E. McGuire, Study of the x-ray photoelectron spectrum of tungsten–tungsten oxide as a function of thickness of the surface-oxide layer, *J. Electron Spectrosc. Relat. Phenom.*, **1**, 161–168 (1972/1973).
122. E. P. Denisov, V. I. Kruglov, Yu. A. Salganik, N. A. Tikhonov, and N. P. Sergushin, X-ray electron spectra of tungsten in electrochromic layers of tungsten trioxide, *Izv. Akad. Nauk SSR, Neorg. Mater.*, **15**, 171–172 (1979).
123. R. O. Ansell, T. Dickinson, A. F. Povey, and P. M. A. Sherwood, Quantitative use of the angular variation technique in studies of tin by x-ray photoelectron spectroscopy, *J. Electron Spectrosc. Relat. Phenom.*, **11**, 301–313 (1977).
124. A. W. C. Lin, N. R. Armstrong, and T. Kuwana, X-ray photoelectron/Auger spectroscopic studies of tin and indium metal foils and oxides, *Anal. Chem.*, **49**, 1228–1235 (1977).
125. R. O. Ansell, T. Dickinson, A. F. Povey, and P. M. A. Sherwood, X-ray photoelectron spectrosopic studies of tin electrodes after polarization in sodium hydroxide, *J. Electrochem. Soc.*, **124**, 1360–1364 (1977).
126. C. L. Lau and G. K. Wertheim, Oxidation of tin: An ESCA study, *J. Vac. Sci. Technol.*, **15**, 622–624 (1978).

127. J. P. Coad, B. W. Mott, G. D. Harden, and J. F. Walpole, Nature of chromium on passivated tinplate, *Br. Corros. J.*, **11**, 219–221 (1976).
128. J. C. Riviere, Effect of ion bombardment conditions on the chemical profile through the surface of tinplate, *Mater. Sci. Eng.*, **42**, 49–54 (1980).
129. P. J. Aubrun, G. A. Pennera, C. Legras, and D. Courteix, Evidence of metallic chromium in a passivation film of tin plate by electron spectrosopy (ESCA), *J. Microsc. Spectrosc. Electron.*, **1**, 43–52 (1976).
130. V. Leroy, J. P. Servais, L. Habraken, L. Renard, and J. Lempereur, Secondary ion mass analysis, Auger and photoelectron spectrometry of passivation layers on tinplate, *I.T.R.I. Publ.*, **530**, 399–416 (1976).
131. J. P. Servais, J. Lempereur, L. Renard, and V. Leroy, Examination by ESCA of the constitution and effects on lacquer adhesion of passivation films of tinplate, *Br. Corros. J.*, **14**, 126–132 (1979).
132. J. H. Thomas, III and S. P. Sharma, ESCA study of the passive layer on tin–nickel alloy, *J. Vac. Sci. Technol.*, **14**, 1168–1172 (1977).
133. B. Bayraktaroglu, P. A. Breeze, A. Colquhoun, A. F. A. B. El-Safti, and S. J. Hannah, New passivation methods of gallium arsenide, *Gov. Rep. Announce. Index (U.S.)*, **79**, 193 (1979).
134. P. A. Breeze and H. L. Hartnagel, An assessment of the quality of anodic native oxides of gallium arsenide for MOS devices, *Thin Solid Films*, **56**, 51–61 (1979).
135. H. J. Bilz, G. Leonhardt, G. Kuehn, K. Loeschke, and A. Meisel, ESCA studies on anodically oxidised A III B V compounds, *Krist. Tech.*, **13**, 363–368 (1978).
136. C. W. Wilmsen and R. W. Kee, Analysis of the oxide/semiconductor interface using Auger and ESCA as applied to indium phosphide and gallium arsenide, *J. Vac. Sci. Technol.*, **15**, 1513–1517 (1978).
137. Y. Mizokawa, H. Iwasaki, R. Nishitani, and S. Nakamura, Quantitative chemical depth profiles of anodic oxide on gallium arsenide obtained by x-ray photoelectron spectroscopy, *J. Electrochem. Soc.*, **126**, 1370–374 (1979).
138. G. P. Schwartz, G. J. Gualtieri, G.W. Kammlott, and B. Schwartz, An x-ray photoelectron spectroscopy study of native oxides on gallium arsenide, *J. Electrochem. Soc.*, **126**, 1737–1749 (1979).
139. M. Nishino, M. Hashiba, K. Watanabe, T. Yamashina, and K. Yabe, In-depth profile of oxide films on gallium arsenide studies by ESCA, *Hokkaido Daigaku Kogakubu Kenkyu Hokoku*, Part 95, 101–115 (1979).
140. P. A. Breeze, H. L. Hartnagel, and P. M. A. Sherwood, An investigation of anodically grown films on GaAs using x-ray photoelectron spectroscopy, *J. Electrochem. Soc.*, **127**, 454–461 (1980).
141. C. W. Wilmsen, R. W. Kee, and K. M. Geib, Initial oxidation and oxide/semiconductor interface formation on gallium arsenide, *J. Vac. Sci. Technol.*, **16**, 1434–1438 (1979).
142. M. Savy, C. Bernard, and G. Magner, Oxygen reduction on monomeric and polymeric phthalocyanines. III. Thin monomeric iron phthalocyanine layers on gold, *Electrochim. Acta.*, **20**, 383–391 (1975).
143. G. Tourillon, P. C. Lacaze, and J. E. Dubois, Electrochemical formation of thin polyacetonitrile films on a platinum surface. P.M.T., I.R., X.P.S. and SIMS analyses and study of formation mechanism, *J. Electroanal. Chem. Interfacial Electrochem.*, **100**, 247–262 (1979).
144. P. C. Lacaze and G. Tourillon, Spectroscopic study (XPS–SIMS) of the aging of polyacetonitrile thin films electrochemically deposited on a platinum electrode, *J. Chim. Phys. Phys.-Chim. Biol.*, **76**, 371–374 (1979).
145. G. Tourillon, J. E. Dubois, and P. C. Lacaze, Electrochemical doping of poly(THF) thin films deposited on the platinum electrode: XPS and SIMS spectroscopic study, *J. Chim. Phys. Phys.-Chim. Biol.*, **76**, 369–370 (1979).

146. J. W. Albery, R. W. Bowen, F. S. Fisher, A. W. Foulds, K. J. Hall, A. R. Hillman, R. G. Egdell, and A. F. Orchard, Photogalvanic cells. Part XI. The thionine-coated electrode, *J. Electroanal. Chem. Interfacial Electrochem.*, **107**, 37–47 (1980).
147. P. R. Moses, L. Wier, and R. W. Murray, Chemically modified tin oxide electrode, *Anal. Chem.*, **47**, 1882–1886 (1975).
148. C. E. Elliott and R. W. Murray, Chemically modified carbon electrodes, *Anal. Chem.*, **48**, 1247–1254 (1976).
149. P. R. Moses and R. W. Murray, Chemically modified electrodes. 3. SnO2 and TiO2 electrodes bearing an electroactive reagent, *J. Am. Chem. Soc.*, **98**, 7435–7436 (1976).
150. N. R. Armstrong, A. W. C. Lin, M. Fujihira, and T. Kuwana, Electrochemical and surface characteristics of tin oxide and indium oxide electrodes, *Anal. Chem.*, **48**, 741–750 (1976).
151. M. Fijihira, M. Masamichi, and T. Osa, Organo-modified metal oxide electrode. I. Studies of the modified layer by capacitance measurements and ESCA, *Chem. Lett.*, Part 8, 875–880, 1976.
152. M. Fujihira, T. Matsue, and T. Osa, Tin oxide electrode modified by organic substances. Study of a modified layer by capacitance method and an x-ray photoelectron spectroscopy method, *Elektrokhimiya*, **13**, 1679–1684 (1977).
153. D. F. Untereker, J. C. Lennox, L. M. Wier, P. R. Moses, and R. W. Murray, Chemically modified electrodes. Part IV. Evidence for formation of monolayers of bonded organosilane reagents, *J. Electroanal. Chem.*, **81**, 309–318 (1977).
154. P. R. Moses and R. W. Murray, Chemically modified electrodes. Part V. Covalent binding of a reversible electrode reactant to RuO2 electrodes, *J. Electroanal. Chem.*, **77**, 393–399 (1977).
155. J. C. Lennox and R. W. Murray, Chemically modified electrodes. Part VI. Binding and reversible electrochemistry of tetra-(aminophenyl)porphyrin on glassy carbon, *J. Electroanal. Chem.*, **77**, 395–401 (1977).
156. J. R. Lenhard and R. W. Murray, Chemically modified electrodes. Part VII. Covalent bonding of a reversible electrode reactant to Pt electrodes using an organosilane reagent, *J. Electroanal. Chem.*, **78**, 195–201 (1977).
157. D. G. Davis and R. W. Murray, Surface electrochemistry of iron porphyrins and iron on tin oxide electrodes, *Anal. Chem.*, **49**, 194–198 (1977).
158. J. F. Evans, T. Kuwana, M. T. Henne, and G. P. Royer, Electrocatalysis of solution species using modified electrodes, *J. Electroanal. Chem.*, **80**, 409–416 (1977).
159. A. W. C. Lin, P. Yeh, A. M. Yacynych, and T. Kuwana, Cyanuric chloride as a general linking agent for the attachment of redox groups to pyrolytic graphite and metal oxide electrodes, *J. Electroanal. Chem.*, **84**, 411–419 (1977).
160. A. L. Allred, C. Bradley, and T. H. Newman, Attachment of permethylpolysilane groups to platinum by electroreduction of chloropermethylpolysilanes. X-ray photoelectron spectroscopy of permethylpolysilanes chemically bound to electrode surfaces, *J. Am. Chem. Soc.*, **100**, 5081–5084 (1978).
161. P. R. Moses, L. M. Wier, J. C. Lennox, H. O. Finkles, J. R. Lenhard, and R. W. Murray, X-ray photoelectron spectroscopy of alkylaminesilans bound to metal oxide electrodes, *Anal. Chem.*, **50**, 576–585 (1978).
162. J. C. lennox and R. W. Murray, Chemically modified electrodes. 10. Electron spectroscopy for chemical analysis and alternating current voltammetry of glassy carbon-bound tetra(aminophenyl)porphyrins, *J. Am. Chem. Soc.*, **100**, 3710–3714 (1978).
163. J. R. Lenhard, R. Roklin, H. Abruna, K. Willman, K. Kuo, R. Nowak, and R. W. Murray, Chemically modified electrodes. 11. Predictability of formal potentials of covalently immobilized charge-transfer reagents, *J. Am. Chem. Soc.*, **100**, 5213–5215 (1978).
164. L. L. Miller and M. R. Van de Mark, Electrode surface modification via polymer adsorption, *J. Am. Chem. Soc.*, **100**, 639–640 (1978).
165. D. D. Hawn and N. R. Armstrong, Electrochemical adsorption and covalent attachement

of arythrosin to modified tin dioxide electrodes and measurement of the photocurrent sensitization to visible wavelength light, *J. Phys. Chem.*, **82**, 1288–1295 (1978).
166. H. S. White and R. W. Murray, Fluorescence and x-ray photoelectron spectroscopy surface analysis of metal oxide electrodes chemically modified with densylated alkylaminesilanes, *Anal. Chem.*, **51**, 236–239 (1979).
167. L. M. Wier and R. W. Murray, Chemically modified electrodes. VIII. The interaction of aqueous ruthenium trichloride with native and silanized tin dioxide electrodes, *J. Electrochem. Soc.*, **126**, 617–723 (1979).
168. A. B. Fischer, M. S. Wrighton, M. Umana, and R. W. Murray, An x-ray photoelectron spectroscopic study of multilayers of an electroactive ferrocene derivative attached to platinum and gold electrodes, *J. Am. Chem. Soc.*, **101**, 3442–3446 (1979).
169. K. W. Willman, E. Greer, and R. W. Murray, An x-ray photoelectron spectroscopy study of the spacing of amine groups on alkylaminesilanized tin oxide electrode surfaces, *Nouvo J. Chim.*, **3**, 455–461 (1979).
107. A. B. Fischer, M. S. Wrighton, M. Umana, and R. W. Murray, An x-ray photoelectron spectroscopic study of multilayers of an electroative ferrocene derivative attached to platinum and gold electrodes, *Gov. Rep. Announce. Index (U.S.)*, **79**, 91 (1979).
171. T. Matsue, M. Fujihira, and T. Osa, Selective electrosyntheses on a chemically modified electrode. II. Anodic chlorination of anisole with cyclodextrin on electrode surfaces and in solution, *Bull. Chem. Soc. Jpn.*, **52**, 3692–3696 (1979).
172. M. Tomkiewicz, The nature of surface states on chemically modified TiO2 electrodes, *J. Electrochem. Soc.*, **127**, 1518–1525 (1980).
173. J. Knecht and G. Stork, X-ray photoelectron spectroscopic study of the thallium oxide electrode, Fresenius, *Z. Anal. Chem.*, **289**, 206 (1978).
174. T. Dickinson, A. F. Povey, and P. M. A. Sherwood, X-ray photoelectron spectroscopic studies of solid electrolytes, *J. Solid State Chem.*, **13**, 237–244 (1975).
175. A. C. Wilson and K. H. Pool, Potentiometric behavior and surface composition of a prototype monohydrogen phosphate-selective electrode, *Anal. Chim. Acta.*, **109** 149–155 (1979).
176. K. S. Kim, N. Winograd, and R. E. Davis, Electron spectrosopy of platinum–oxygen surfaces and application to electrochemical studies, *J. Am. Chem. Soc.*, **93**, 6296–6297 (1971).
177. K. S. Kim, C. D. Sell, and N. Winograd, ESCA study of metal and metal electrode surfaces, *Proc. Symp. Electrocatal.*, 242–257 (1974).
178. K. S. Kim, A. F. Gossmann, and N. Winograd, X-ray photoelectron spectroscopic studies of palladium oxides and the palladium–oxygen electrode, *Anal. Chem.*, **46**, 197–200 (1974).
179. G. C. Allen, P. M. Tucker, A. Capon, and R. Parsons, X-ray photoelectron spectroscopy of adsorbed oxygen and carbonaceous species on platinum electrodes, *J. Electroanal. Chem. Interfacial Electrochem.*, **50**, 335–343 (1974).
180. J. F. Evans, H. N. Blount, and C. R. Ginnard, Electrochemical formation and electron spectroscopic characterization of the platinum sulfide electrode, *J. Electroanal. Chem. Interfacial Electrochem.*, **59**, 169–175 (1975).
181. N. Winograd, Electrode mechanisms using reflection and electron spectroscopy, *Gov. Rep. Announce. Index (U.S.)*, **76**, 102 (1976).
182. J. S. Hammond and N. Winograd, X-ray photoelectron and Auger spectroscopic study of the underpotential deposition of silver and copper on platinum electrodes, *J. Electrochem. Soc.*, **124**, 826–833 (1977).
183. J. S. Hammond and N. Winograd, X-ray photoelectron spectroscopic evidence of distinctive underpotential deposition states of silver and copper on platinum substrates, *J. Electroanal. Chem. Interfacial Electrochem.*, **80**, 123–127 (1977).
184. L. Sabbatini, P. G. Zambonin, E. Desimoni, and B. De Angelis, An x-ray photoelectron spectroscopic study on platinum–oxygen surfaces obtained by molten nitrate treatment.

Preliminary note, *Chim. Ind.* (*Milan*), **59**, 493–495 (1977).
185. N. H. Turner, Investigation of the surface of platinum paste electrodes, *J. Electroanal. Chem. Interfacial Electrochem.*, **87**, 67–72 (1978).
186. J. Heitbaum, XPS, Raman, and IR analysis of a surface product formed within the electrooxidation of phenylhydrazine, *Z. Phys. Chem.* (*Wiesbaden*), **105**, 307–317 (1977).
187. L. Kover, C. Ujhelyi, D. Berenyi, D. Varga, I. Kadar, A. Kover, and J. Miller, Photoelectron spectroscopic investigation of oxidized platinum surfaces, *Izotoptechnika*, **20**, 363–367 (1977).
188. L. Sabbatini, F. Palmisano, P. Zambonin, and B. De Angelis, A combined potentiometric–ESCA investigation of the electrode system (platinum)carbon dioxide, oxygen/carbonate ion in molten salts, *Ann. Chim.* (*Rome*), **67**, 525–534 (1978).
189. L. Kover, C. Ujhelyi, D. Berenyi, D. Varga, I. Kadar, A. Kover, and J. Miller, X-ray photoelectron spectroscopic investigation of electrochemically oxidized and reduced platinum surfaces, *J. Electron Spectros. Relat. Phenom.*, **14**, 201–214 (1978).
190. S. Srinivasan, R. S. Yeo, G. Kissel, E. Gannon, F. Kulesa, J. Orehotsky, and W. Visscher, Selection and evaluation of materials for advanced water eletrolyzers, *Energy Res. Abstr.*, **5**, abstr. no. 329 (1980).
191. A. Katayama, Electrooxidation of methanol on a platinum–tin oxide catalyst, *J. Phys. Chem.*, **84**, 376–381 (1980).
192. K. S. Kim, T. J. O. Leary, and N. Winograd, X-ray photoelectron spectra of lead oxides, *Anal. Chem.*, **45**, 2214–2218 (1973).
193. J. S. Brinen and J. E. McClure, Trace analysis by ESCA-electrochemical measurements, *Anal. Lett.*, **5**, 737–743 (1972).
194. J. S. Brinen and J. E. McClure, Application of ESCA to analytical chemistry. I. Electrochemical concentration of metals for trace quantitative analysis by ESCA, *J. Electron Spectrosc. Relat. Phenom.*, **4**, 243–248 (1974).
195. J. S. Brinen, Applications of ESCA to industrial chemistry, *J. Electron Spectrosc. Relat. Phenom.*, **5**, 377–400 (1974).
196. D. Briggs, V. A. Gibson, and J. K. Becconsall, Analysis of trace elements in water by ESCA, *J. Electron Spectrosc. Relat. Phenom.*, **11**, 343–347 (1977).
197. L. Sabbatini, T. Dickinson, and P. M. A. Sherwood, Simultaneous analytical detection of tin and lead at ppb level in acidic solutions by combining electrodeposition and x-ray photoelectron spectroscopy, *Ann. Chim.* (*Rome*), **70**, 137–146, 1980.
198. M. Piens, Importance of diffusion in the electrochemical action of oxidizing pigments, *J. Coat. Tech.*, **51**, 66–72 (1979).
199. J. B. Lumsden and R. W. Staehle, Applications of Auger electron spectroscopy to the determination of the composition of passive films of type 316 SS, *Scr. Metall.*, **6**, 1205–1208 (1972).
200. M. Seo, J. B. Lumsden, and R. W. Staehle, Chemical shifts in the Auger spectra of passive films, *Surf. Sci.*, **42**, 337–339 (1974).
201. W. C. Johnson and L. A. Heldt, Composition of platinum anode surfaces by Auger spectroscopy, *J. Electrochem. Soc.*, **121**, 34–36 (1974).
202. M. Seo, J. B. Lumsden, and R. W. Staehle, and R. W. Staehle, An AES analysis of oxide films on iron, *Surf. Sci.*, **50**, 541–552 (1975).
203. R. W. Revie, B. G. Baker, and J. O'M Bockris, Passive film on iron. Application of Auger electron spectroscopy, *J. Electrochem. Soc.*, **122**, 1460–1466 (1975).
204. R. W. Revie, J. O'M Bockris, and B. G. Baker, Degraded passive films on iron. Application of Auguer electron spectroscopy, *Surf. Sci.*, **52**, 664–669 (1975).
205. R. K. Quinn, N. R. Armstrong, and N. E. Vanderborgh, Electrochemistry at thin solid films, *J. Vac. Sci. Technol.*, **12**, 160–168 (1975).
206. R. M. Ishikawa and A. T. Hubbard, Study of platinum electrodes by means of thin layer electrochemistry and low-energy electron diffraction. Part I. Electrode surface structure

after exposure to water and aqueous electrolytes, *J. Electroanal. Chem. Interfacial Electrochem.*, **69**, 317–338 (1976).

207. H. G. Tompkins and J. E. Bennett, Investigations of an electrodeposited tin–nickel alloy. II. Surface passivity studied with Auger electron spectroscopy, *J. Electrochem. Soc.*, **123**, 1003–1006 (1976).
208. M. Romand, G. Bouyssoux, J. S. Solomon, and W. L. Baun, Auger spectrometric study of passive films formed on tantalum in phosphoric acid solution, *J. Electron Spectrosc. Relat. Phenom.*, **9**, 41–50 (1976).
209. A. E. Yaniv and J. B. Lumsden, The composition of passive films on ferritic stainless steels, *Passivity: Its Breakdown in Iron and Iron Base Alloys, USA–Japan Seminar*, 72–74 (1976).
210. J. B. Lumsden and R. W. Staehle, The effect of surface treatment on the composition of films on austenitic stainless steels, *Passivity: Its Breakdown in Iron and Iron Base Alloys, USA–Japan Seminar*, 75–76 (1976).
211. M. Romand, J. S. Solomon, and W. L. Baun, Concentration profiles of passive films formed on niobium metal and niobium-base alloys by Auger electron spectrometry, *Mater. Res. Bull.*, **11**, 517–524 (1976).
212. H. Okada, H. Ogawa, I. Itoh, and H. Omata, Auger electron spectroscopic analysis of the passive film of stainless steels, *Passivity: Its Breakdown in Iron and Iron Base Alloys, USA–Japan Seminar*, 82–84 (1976).
213. B. Rondot, F. Pons, J. Le Hericy, M. Da Cunha Belo, and J. P. Langeron, Auger spectrometric study of passive films formed on the surface of stainless steels, *Vide*, **30A**, 48–53 (1975).
214. R. K. Quinn, M. L. Knotek, and N. R. Armstrong, Studies of the Ag–Pt interface formed by Ag deposition from sulfolane solutions on thin film electrodes, *J. Electrochem. Soc.*, **123**, 1794–1799 (1976).
215. M. Seo, M. Sato, J. B. Lumsden, and R. W. Staehle, Auger analysis of the anodic oxide film on iron in neutral solution, *Corros. Sci.*, **17**, 209–217 (1977).
216. A. E. Yaniv, J. B. Lumsden, and R. W. Staehle, The composition of passive films on ferritic stainless steels, *J. Electrochem. Soc.*, **124**, 490–495 (1977).
217. H. Viefhaus and M. Janik-Czachor, AES investigations on passive layers on iron specimens, *Werkst. Korros.*, **28**, 219–226 (1977).
218. R. Bador, G. Bouyssoux, M. Romand, J. S. Solomon, and W. L. Baun, Characterization by Auger spectrometry of anodic films formed on aluminum, *Mater. Res. Bull.*, **12**, 197–204 (1977).
219. B. G. Baker, The application of Auger electron spectroscopy to the study of electrode surfaces, *Trends Electrochemistry, Plenary Invited Contributors Austrian Electrochem. 4th Conference*, 233–239 (1976/1977).
220. W. E. O'Grady, M. Y. C. Woo, P. L. Hagans, and E. Yeager, Electrode surface studies by LEED-Auger, *J. Vac. Sci. Technol.*, **14**, 365–368 (1977).
221. M. L. Knotek, R. K. Quinn, N. R. Armstrong, and N. E. Vanderborgh, Auger electron spectroscopic depth profiling techniques applied to ultrathin electrochemically deposited metal layers, *J. Vac. Sci. Technol.*, **14**, 705–710 (1977).
222. B. Rondot, F. Pons, J. Le Hericy, M. Da Cunha Belo, and J. P. Langeron, Auger spectrometric study of passivation films formed on the surface of stainless steel, *Vide*, **30**, 70–75 (1975).
223. C. C. Chang, B. Schwartz, and S. P. Murarka, Anodic oxide on gallium arsenide: Quantitative chemical depth profiles obtained using Auger spectroscopy and neutron activation analysis, *J. Electrochem. Soc.*, **124**, 922–926 (1977).
224. M. Da Cunha Belo, B. Rondot, F. Pons, J. Le Hericy, and J. P. Langeron, Study by Auger spectrometry and cathodic reduction of passive films formed on ferritic stainless steels, *J. Electrochem. Soc.*, **124**, 1317–1324 (1977).

225. W. C. Fort, III and E. D. Verink Jr., Elucidation of the mechanism of dezincification by Auger electron spectrosopy in combination with electrochemical methods, *C. R. Congr. Int. Corros. Mar. Salissures, 4th*, 179–185 (1976/1977).
226. J. A. Schoeffel and A. T. Hubbard, Quantitative elemental analysis of substituted hydrocarbon monolayers on platinum by Auger electron spectroscopy with electrochemical calibration, *Anal. Chem.*, **49**, 2330–2336 (1977).
227. C. E. Locke, J. H. Peavey, O. Rincon, and M. Afzal, A study of the passive film using Auger electron spectroscopy, *Charact. Met. Polym. Surf.*, (*Symp.*), 155–179 (1976/1977).
228. D. A. Stout, G. Gavelli, J. B. Lumsden, and R. W. Staehle, Galvanic cells for in-situ AES study of metal oxide surfaces, *Surf. Sci.*, **69**, 741–744 (1977).
229. J. B. Lumsden and R. W. Staehle, Composition of protective films formed on iron and stainless steels, *ASTM Spec. Tech. Publ. 1975, STP 596, Surf. Anal. Tech.-Metall. Appl.*, 39–51 (1976).
230. C. E. Locke, J. H. Peavey, O. Rincon, and M. Afzal, A study of the passive film using Auger electron spectroscopy, *Pap. Meet.—Am. Chem. Soc., Div. Org. Coat. Plast. Chem.*, **36** 51–54 (1976).
231. J. B. Lumsden and Z. Szklarska-Smialowska, The properties of films formed on iron exposed to inhibitive solutions, *Corrosion (Houston)*, **34**, 169–176 (1978).
232. V. V. Shalaginov, I. D. Belova, Yu. E. Roginskaya, and D. M. Shub, Nonstoichiometry, structural defects, and electrochemical characteristics of cobalt oxide (Co_3O_4) film electrodes, *Elektrokhimiya*, **14**, 1708–1712 (1978).
233. J. B. Mathieu, H. J. Mathieu, and D. Landolt, Electropolishing of titanium in perchloric acid–acetic acid solution. I. Auger electron spectroscopy study of anodic films, *J. Electrochem. Soc.*, **125**, 1039–1043 (1978).
234. H. Ogawa, H. Omata, I. Itoh, and H. Okada, Auger electron spectroscopic and electrochemical analysis of the effect of alloying elements on the passivation behavior of stainless steels, *Corrison (Houston)*, **34**, 52–60 (1978).
235. M. Seo and N. Sato, Differential composition profiles in depth of passive films on iron-base alloys, *Boshoku Gijutsu*, **27**, 647–652 (1978).
236. W. Wall, J. R. Stevenson, J. Larsen, M. W. Ribarsky, and K. Legg, Optical reflectivity of Auger spectroscopy of titanium surfaces with controlled exposures to oxygen and nitrogen, *Ext. Abstr.—Int. Conf. Vac. Ultraviolet Radiat. Phys., 5th*, **2**, 101–103 (1977).
237. A. Okada, Y. Ohnuki, and T. Inada, Auger-electron spectroscopy (AES) measurements on anodically oxidised layers of single-crystal gallium phosphide, *Appl. Phys. Lett.*, **33**, 447–449 (1978).
238. C. Plog, Analysis of metal surfaces. Composition and properties of raw and treated metal surfaces, demonstrated with practical examples, *Galvanotechnik*, **69**, 777–783 (1978).
239. G. E. McGuire, A. L. Bacarella, J. C. Griess, Jr., R. E. Clausing, and L. D. Hulett, Analysis of protective oxide films on copper–nickel alloys by Auger spectroscopy, *J. Electrochem. Soc.*, **125**, 1801–1804 (1978).
240. H. Konno and M. Nagayama, The role of pyrophosphate in copper deposition from cupric pyrophosphate solutions, *Electrochim. Acta.*, **13**, 1001–1007 (1978).
241. B. G. Baker, D. A. J. Rand, and R. Woods, A comparison of electrochemical and Auger analysis of the surface composition of platinum–rhodium alloys, *J. Electroanal. Chem. Interfacial Eletrochem.*, **97**, 189–198 (1979).
242. J. Clavilier and J. P. Chauvineau, The use of Auger electron spectrosopy for the characterization of the surfaces of spherical gold electrodes, *J. Electroanal. Chem. Interfacial Electrochem.*, **97**, 199–210 (1979).
243. J. B. Lumsden, R. W. Staehle, and L. Abrego, Fundamental studies of dissolution and passivity of alloys and compounds, *Gov. Rep. Announce. Index (U.S.)*, **78**, 158 (1978).
244. T. J. Magee and J. Peng, Solid–solid reactions in metal films on silicon, *Gov. Rep. Announce.*

Index (*U.S.*), **79**, 157 (1979).
245. J. W. Dini and H. R. Johnson, Optimization of gold plating for hybrid microcircuits, *Plat. Electron. Ind. 7*, paper no. 16 (1978).
246. K. Watanabe, M. Hashiba, Y. Hirohata, M. Nishino, and T. Yamashina, Oxide layers on gallium arsenide prepared by thermal, anodic and plasma oxidation: In-depth profiles and annealing effects, *Thin Solid Films*, **56**, 63–73 (1979).
247. S. L. Suib, L. R. Faulkner, G. D. Stucky, and R. J. Blattner, Chemical analysis and structural characterization of transition metal disulfide intercalates, *Anal. Chem.*, **51**, 1060–1064 (1979).
248. M. Seo and N. Sato, Surface polishing and surface composition of iron–chromium alloys, *Boshoku Gijutsu*, **27**, 172–178 (1978).
249. V. Ashworth, C. G. Googan, and J. D. Scantlebury, Intergranular dissolution of zinc alloy sacrificial anodes in sea water at elevated temperature, *Br. Corros. J.*, **14**, 46–50 (1979).
250. J. F. Evans, M. G. Albrecht, D. M. Ullevig, and R. M. Hexter, The physical and chemical characterization of electrochemically reformed silver surfaces, *Gov. Rep. Announce. Index* (*U.S.*), **79**, 138 (1979).
251. D. Eyre and D. R. Gabe, AC anodizing of aluminum in sulfuric acid, *Trans. Inst. Met. Finish.*, **57**, 38–42 (1979).
252. D. W. Endicott and G. J. Casey Jr., High speed gold plating from dilute electrolytes. Part I. Solution development and functional testing, *Annu. Tech. Conf.—Am. Electroplat. Soc.*, **66**, D-3 (1979).
253. G. J. Casey, Jr. and D. W. Endicott, High speed gold plating from dilute electrolytes, Part II. Control of surface quality utilizing Auger electron spectroscopy, *Annu. Tech. Conf.—Am. Electroplat. Soc.*, **66**, D-4 (1979).
254. R. Weil, Some property–structure relationships in electrodeposits. AES research project No. 38, *Annu. Tech. Conf.—Am. Electroplat. Soc.*, **66**, L-1 (1979).
255. K. J. McNulty, Reverse osmosis field test: Closed loop recovery of zinc cyanide rinsewaters. AES research project No. 45., *Annu. Tech. Conf.—Am. Electroplat. Soc.*, **66**, L-4 (1979).
256. W. R. Bitler, Grain boundary diffusion in gold electrodeposits. AES research project No. 50., *Annu. Tech. Conf.—Am. Electroplat. Soc.*, **66**, 0-1 (1979).
257. E. Maguire and L. Donovan, A mini-peel test for measuring adhesion of an electroplate to ABS substrate. AES research project No. 42, *Annu. Tech. Conf.—Am. Electroplat. Soc.*, **66**, L-3 (1979).
258. J. Clavilier and J. P. Chauvineau, Chemical characterization by Auger electron spectroscopy and voltammetry of platinum electrode surfaces prepared in the gas phase, *J. Electroanal. Chem. Interfacial Electrochem.*, **100**, 461–472 (1979).
259. J. W. Dini and H. R. Johnson, Gold plating for hybrid microcircuits, *Energy Res. Abstr. 4*, abstr. no. 30793 (1978).
260. T. E. Felter and A. T. Hubbard, LEED and electrochemistry of iodine on platinum(100) and platinum(111) single-crystal surfaces, *J. Electronal. Chem. Interfacial Electrochem.*, **100**, 473–491 (1979).
261. H. J. Hunger, J. Kloeber, G. Marx, W. Sommer, and H. Wicht, Study on the surface of electrochemically treated steel specimens by Auger electron spectroscopy, *Neue Huette*, **24**, 228–231 (1979).
262. M. Janik-Czachor, AES investigations of passive films on iron and iron base alloys (review with 55 references), *Corrosion* (*Houston*), **35**, 360–366 (1979).
263. G. J. Moody, N. S. Nassory, J. D. R. Thomas, D. Betteride, P. Szepesvary, and B. J. Wright, Interference films on the sensor membranes of solid-state copper(II) ion-selective electrodes, *Analyst* (*London*), **104**, 348–357 (1979).
264. C. Vazquez-Lopez, F. Sanchez-Sinencio, J. S. Helman, J. L. Pena, A. Lastras-Martinez, P. M. Raccah, and R. Triboulet, Study of the interface changes during operation of n-cadmium telluride-electrolyte solar cells, *J. Appl. Phys.*, **50**, 5391–5396 (1979).

265. S. Masshiro and N. Sato, Estimation of surface excess from compositional depth profiles of iron-base alloys passivated in sulfuric acid solution, *Trans. Iron Steel Inst. Jpn.*, **19**, 504–508 (1979).
266. M. Seo, Y. Matsumura, and N. Sato, An Auger analysis of passive films formed on iron–5% molybdenum alloy and pure iron in neutral aqueous solution, *Trans. Jpn. Inst. Met.*, **20**, 501–506 (1979).
267. D. D. Macdonald, B. C. Syrett, and S. S. Wing, The corrosion of copper–nickel alloys 706 and 715 in flowing sea water. II. Effect of dissolved sulfide, *Corrosion (Houston)*, **35**, 367–378 (1979).
268. W. L. Baun, Formation of porous films on titanium alloys by anodization, Tech. Rep. AFML-TR-Air Force Mater. Lab. (U.S.), AFML-TR-79-4133 (1979).
269. T. J. Driscoll, B. S. Covino, Jr., and M. Rosen, Electrochemical corrosion and film analysis studies of iron and iron-18 wt% chromium in 1N sulfuric acid, *Rep. Invest.—U.S. Bur. Mines*, RI 8378 (1979).
270. M. Da Cunha Belo, B. Rondot, and E. Navarro, Study of the corrosion of amorphous binary alloys: Metal–metalloid and metal–metal, *Colloq. Metall.*, 21*st Meeting* 285–299 (1978).
271. M. Datta, H. J. Mathieu, and D. Landolt, Anodic film studies on nickel under high rate transpassive dissolution conditions, *Electrochim. Acta*, **24**, 843–850 (1979).
272. Ya. M. Kolotyrkin, Some characteristics of the selective dissolution of iron and nickel alloys, *Abh. Saechs. Akad. Wiss. Leipzig, Math.-Naturwiss. Kl.*, **53**, 131–140 (1979).
273. J. W. Dini and H. R. Johnson, Optimization of gold plating for hybrid microcircuits, *Plat. Surf. Finish.*, **67**, 53–57 (1980).
274. N. Kanani, Corrosion behavior of AlMn and AlMg3 in supply water, *Aluminium (Duesseldorf)*, **55**, 724–727 (1979).
275. S. Matsuszawa, N. Baba, and S. Tajima, In-depth composition profile of anodic oxide films on aluminum studied by Auger electron spectroscopy, *Electrochim. Acta*, **24**, 1199–1202 (1979).
276. R. L. Chance and S. W. Gaarenstroom, Characterization of surface films on an anodically polarized ferritic stainless steel, *Corrosion (Houston)*, **36**, 94–101 (1980).
277. W. L. Baun, Formation of porous films on titanium alloys by anodization treatments, *Gov. Rep. Announce. Index (U.S.)*, **80**, 998 (1980).
278. B. MacDougall, D. F. Mitchell, and M. J. Graham, Galvanostatic oxidation of nickel in borate buffer solution, *J. Electrochem. Soc.*, **127**, 1248–1252 (1978).

8

Spatially Resolved Spectroscopy: Theory and Applications of the Abel Inversion

Alexander Scheeline and John P. Walters

1. Introduction

In this chapter, we present work which was done to clarify and enhance the technique of spatially resolved spectroscopy. The work accompanied our exploration of the chemistry and spectroscopy of spark discharge. It arose because more tools were needed to follow vapor from the cathodic (sample) electrode as it traveled into and through the interelectrode space in a current-carrying spark. Although our experimental and optical procedures were adequate for this job, we felt that the equivalent mathematical tools warranted further development.

The primary mathematical tool that we use in spatially resolved spectroscopy is known as the "Abel inversion." It is a process of matrix inversion where the matrix cells correspond to spatially discrete collections of atoms, ions, electrons, or molecules. It is used to numerically distinguish between light emitted in (or absorbed by) the outer cylinders of a co-axially wrapped vertical discharge from that in the inner cylinders.

To make this tool more useful, we modified the way it is programmed, the type and number of experimental parameters entered into it, and, in part, the calculational procedure itself. In the process, we discovered that the modified inversion made an excellent diagnostic tool. When used in an interactive simulation mode, it allowed the prediction of effects that were

Alexander Scheeline and John P. Walters • Department of Chemistry, University of Wisconsin, Madison, Wisconsin 53706.

difficult to control or measure experimentally. Both the modifications and some of the new insights predicted are reported here.

We modified the Abel inversion procedure itself by avoiding the use of any special mathematical functions, power-series, or curve fitting routines to describe either postulated or detected arrays of species or intensities. Instead, we used calculus to determine a large number of geometrical areas, spatially matched in number and size to a typical spark. The areas then are used to operate on up to fifty discrete experimental (or simulated) intensities and return a species distribution. Alternatively, they may operate on a postulated species distribution of any sort in the spark and return an expected laboratory view. Additionally, we provided a "line-of-sight" multiplier for the areas to allow compensation for such experimental complications as changes in the optical depth-of-field along the viewing path. While our present program considers only cylindrical discharges, elliptical forms would be usable with only a recalculation of the area matrices.

Because we formulated the inversion in terms of a common geometrical model for all discharge phenomena, it was possible to program the inversion as only one of a set of selectable options in an interactive program. As an extrapolation of standard good programming practices, we structured the program to be a centrally connected series of independent subroutines, which we call a "pinwheel" structure. Instructions within the program are simplified to single commands, so that it may be used on site with a functioning experiment in a simulation mode for intelligence enhancement. By programming in BASIC, it has been possible to load the fully interactive program into a "personal" microcomputer for operation as an integral part of an emission spectrometer. The program is very deliberately structured to answer the question "I wonder what would happen if...?" no matter where or when it arises.

The types of interactive decisions that can be made with the program are diverse. We include a routine that allows prediction of the effects of instrument misalignment and/or discharge wander (positional instability). Also included is the ability to add regulated amounts of "noise" to simulated or experimental data. While these program features address very common experimental problems, their insertion into the calculation routine to gain knowledge of their impact on experimental data is unique.

A particularly revealing feature of the interactive program is the inclusion of variable amounts of absorption to the discharge emission. For line emission, self-absorption is added, in geometrical discharge regions that are either spatially coincident with or separate from the source of emission. The absorption can have surprising effects on the emission signals, which we feel would be quite difficult to predict without controlled simulation. This program feature also allows evaluation of the effects of correcting for spatially resolved background emission in the presence of self-absorption. One effect

was discovered to be the calculation of "negative emissivities" if the background was subtracted from line emission intensity without prior absorption correction. Such negative numbers usually are considered errors. In fact, they may be a diagnostically useful tool for detecting absorption.

In developing and using this mathematical tool, we were consistently surprised at the magnitude of the changes caused in calculated emissivities by modest changes in the simulated laboratory parameters. Such knowledge lends caution to the interpretation of inverted experimental data. But it also is exciting. A simulation procedure can give provocative insights, if it returns strongly identifiable responses to postulates. These insights, while themselves subject to cautious physical interpretation, can be just the catalyst needed for designing a refreshingly new experiment, or bold modifications in existing ones. This certainly has been one of our uses of the tool. Hopefully, this description will provide the same means and incentives to other experimental spectroscopists.

2. Fundamentals

The essential problem in spatially resolved spectrometry is to determine the distribution in space of the species giving rise to emitted light and of the species perturbing that emitted light by absorption or scattering. For a plasma discharge (spark, arc, etc.), two factors determine the distribution of these species: (1) the geometry of the plasma and vapor clouds incident to that plasma and (2) the excitation conditions within the plasma as it intersects the vapor cloud. If the excitation conditions in the plasma are completely understood, the geometry of the discharge can be readily determined; similarly, if the geometry is known, excitation conditions may be ascertained. For the present, it will be assumed (1) that one wishes to determine the excitation conditions within a discharge so as to understand its behavior and (2) that the geometry is fixed so that all properties of the discharge are cylindrically symmetrical about the discharge axis. It will be evident shortly that the latter assumption is not overly restrictive.

A plasma discharge may be spatially resolved in several dimensions, as shown in Figures 1(B) and (C). The discharge [part 5 in Figure 1(C)] takes place between two electrodes [part 4 in Figure 1(C)]; resolution along that axis, i.e., parallel to arrow 6, is axial resolution, and a single resolution element in this direction is an axial slice through the discharge [for example, the disk-shaped region in Figure 1(C)]. The only other dimension usually viewable directly in the laboratory is a lateral dimension, shown by arrow 7 in Figure 1(C). The distribution of observed intensity across the inhomogeneous discharge in a lateral direction may be termed a lateral intensity profile, and may, in turn, be viewed in a wavelength-resolved or wavelength-integrated

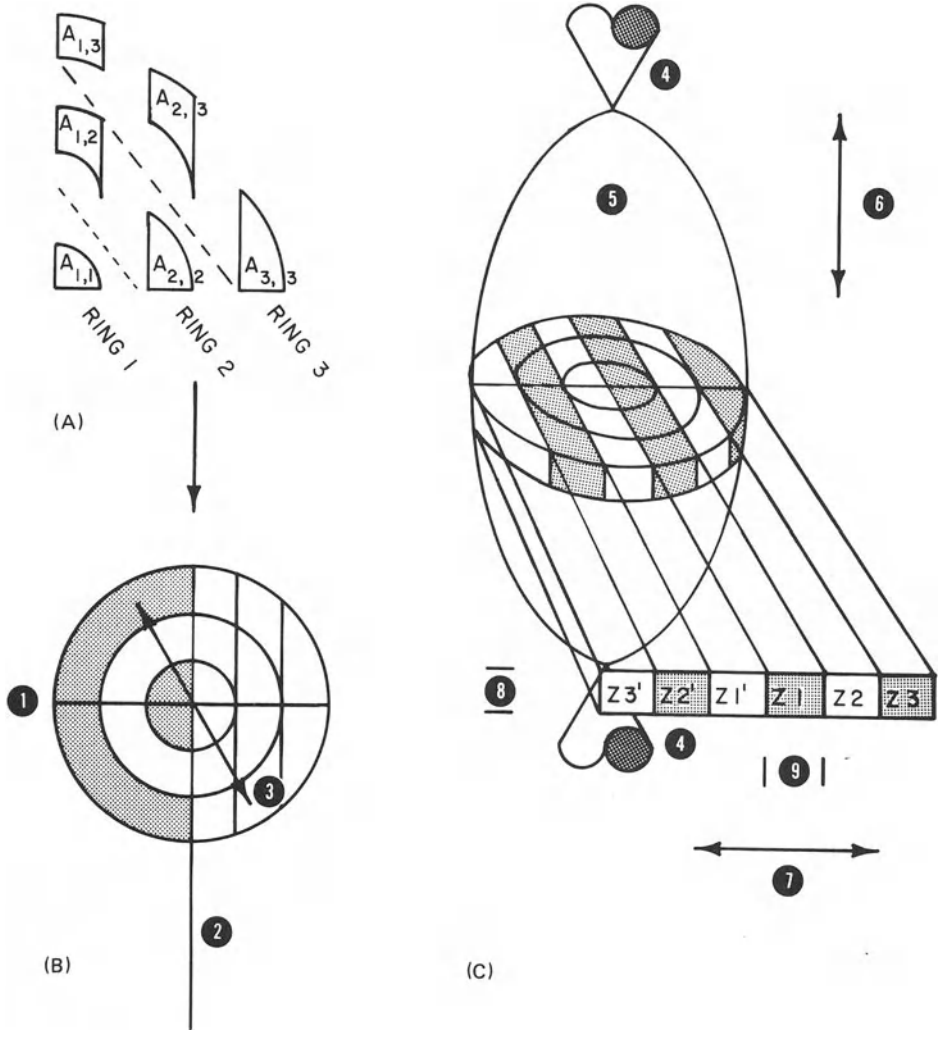

Figure 1. Spatial resolution of a plasma discharge. Components used in creating the concentric ring/lateral zone/axial slice discharge model are shown. (A) Area segments displayed by radial ring and lateral zone for shape and size comparison. (B) Combination of segments to form a cylindrical discharge model; both rings and zones are shown. (C) Three-dimensional view of a glowing discharge: (1) Object focal plane; (2) optical axis; (3) radial dimension; (4) electrodes; (5) discharge; (6) axial dimension; (7) lateral dimension; (8) axial slice thickness; (9) zone width.

fashion. As the discharge is presumed cylindrically symmetric, the chemical processes occurring within the plasma are unique in a radial direction [arrow 3, Figure 1(B)] and radial information is not directly viewable in the laboratory (at least when the plasma is viewed edge on). To obtain fundamental chemical and physical information, one must convert laterally and axially resolved data into radially resolved information (radial emission profiles).

Conceptually, one can think of the conversion from a lateral view to a radial view as a peeling process. One must look through the outer layers of the discharge to see into the center. By looking laterally far from the discharge axis, one will see processes which occur radially far from the axis as well. Due to the discharge symmetry, the contribution of the off-axis processes to on-axis signals is established geometrically. The on-axis contribution of off-axis processes may be stripped from on-axis composite information, revealing processes closer to the center of the discharge. Mathematically, this peeling or stripping process is known as the Abel inversion.

Various computational methods for performing the Abel inversion have been reviewed by Stanisavljevic and Konjevic.[1] A very thorough article by Bracewell[2] not only enumerates various inversion techniques, but also contains tables and figures showing pairs of lateral and radial profiles. A spatially resolved study of an arc discharge has been performed by Olsen,[3] and the method of Cremers and Birkebak[4] has been employed in studying inductively coupled plasmas.[5] Analog as well as digital inversion techniques have been designed.[6,7] Maldonado *et al.*[8] and Maldonado and Olsen[9] have developed a technique for performing the Abel inversion on asymmetric sources using a series expansion of the emission intensity in terms of Hermite polynomials. The authors indicated that this schema gave excellent results when applied to light emitted from an argon arc which was deflected by a magnetic field.

Additional work which has employed the Abel inversion or results thereof includes studies of the spatially heterogeneous structure of dc arcs,[9–14] inductively coupled plasmas,[5,15] and stabilized spark discharges.[16] The latter led to recommendations and procedures for reducing background contribution and noise in the use of spark discharge for spectrochemical analysis[17,18] and gave impetus to recent work on differentiation of stable and unstable spark discharges for alloy analysis.[19]

The technique upon which this discussion is based can be found in Boumans[10] and has been expanded upon by Sacks and Walters,[16] Sacks,[20] and Goldstein.[21] The method assumes that stigmatic optics[22,23] are used throughout the spectrometric observation system so that a single-axial slice may be further resolved into its lateral components [the lateral zones labeled Z1–Z3 and Z1′–Z3′ in Figure 1(C)]. If astigmatic optics are used, one obtains axial resolution [slits aligned parallel to arrow 7, Figure 1(C)] at the expense

of lateral data ("edge-on" observation). For the apparatus as described by Klueppel and Walters[25] axial resolution in combination with temporal resolution is obtained by focusing the image of a discharge on a bilateral slit so as to obtain an axial slice at the desired height above one electrode at a given time following ignition of the discharge. The thickness of the axial slice is determined by the slit width [part 8 in Figure 1(C)], and the maximum width of the discharge that may be observed is set by the height of the slit. Lateral resolution is determined arbitrarily within the limits imposed by instrumental optical abberrations by choosing a zone width [part 9 in Figure 1(C)]. If the zone width equals the instrument's lateral resolving power, it may be assumed that the emission taking place in any ring is constant across that ring. Because of the discharge symmetry, one need only collect data on one side of the system optical axis [part 2 in Figure 1(B)] to totally determine the chemical and spectroscopic properties of the discharge. It will be assumed that the discharge axis and instrumental optical axis intersect at the instrument object focal plane [part 1 in Figure 1(B)] until otherwise noted. A full description of an instrument capable of resolving a spectrum spatially and temporally as required in the models to be discussed has appeared in the literature.[24] A photographic plate is used in obtaining lateral resolution, although use of a photodiode array has been considered.[25]

As is evident in Figure 1, the radial ring width and the zone width are the same. The overlap of a given radial ring with a particular lateral zone will be termed A_{ij}, the i index indicating zone number and the j index indicating ring number. For any known controlled geometry, A_{ij} or segment areas may be computed; Figure 1 shows how the area segments may be combined to form the axial slice, and how that slice is viewed in the laboratory. The segment areas may be computed as a square array or *area matrix*. If the optical system employed in observing the discharge can be assumed to give point-to-point imaging of the discharge under observation, the A_{ij} are directly computable using analytic geometry. However, if any departure from this ideal picture occurs (as it will in any real optical system), then different regions of the discharge will be imaged with varying fidelity. Distortions which may arise due to variations in image quality parallel to the system optical axis may be called depth-of-field effects. A geometric weighting factor may be applied to compensate for these depth-of-field effects. Discrete depth-of-field regions are defined perpendicular to the optical axis and are of thickness equal to the width of the lateral zones. Depth-of-field regions and the relationship to rings, zones, and axial slices are illustrated in Figure 2.

3. Computation of Area Matrices

For simplicity, the calculations will be described in two stages: (1) the procedure for computing areas without accounting for the depth-of-field

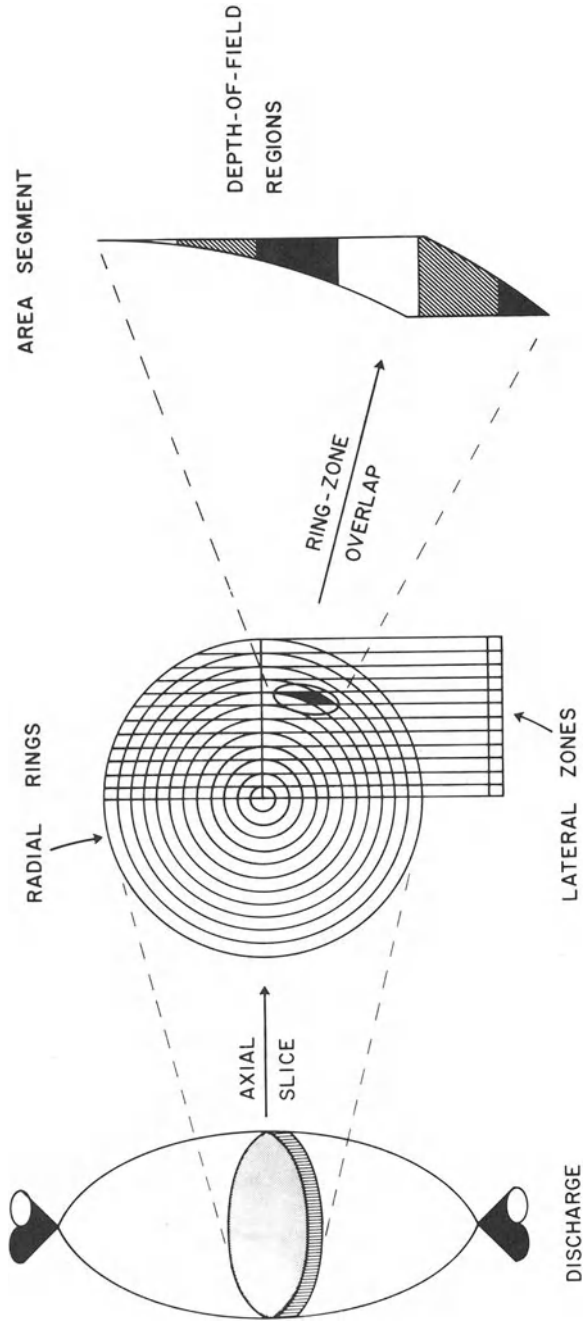

Figure 2. Definition of terms describing the spatially resolved observation of a plasma discharge.

weighting factors and (2) the method for including such weighting. The area of overlap between lateral zone i and radial ring j is symbolized as A_{ij}. Explicitly, A_{ij} is the area bounded by two circles, one of radius j and one of radius $j-1$, and is further bounded in a direction perpendicular to, and coplanar with, the viewing direction by zonal boundaries at lateral displacements i and $i-1$ from the optical axis.

The above areas are taken as unitless and may be scaled to any desired dimension. Thus, in general,

$$A_{ij} = \int_{i-1}^{i} \int_{[(j-1)^2 - x^2]^{1/2}}^{(j^2-x^2)^{1/2}} dy\, dx, \qquad i < j \tag{1}$$

In the special case where $i = j$, i.e., for those area segments having one edge along the diameter of the cylindrical discharge perpendicular to the optical axis, the area is

$$A_{ij} = \int_{i-1}^{i} \int_{0}^{(j^2-x^2)^{1/2}} dy\, dx, \qquad i = j \tag{2}$$

If $i > j$, lateral zone i never overlaps ring j, so that

$$A_{ij} \equiv 0, \qquad i > j \tag{3}$$

Table 1 gives the general form for the above integrals. The matrix of area segments was evaluated up to $i = j = 50$. This size was arrived at by considering: (1) the resolution and field size of optical systems envisaged for use with the Abel algorithm, (2) the resolution deemed necessary to resolve spatially the salient spatial features of the spark discharges under study, and (3) to a limited extent, the core size of digital computers readily accessible for use. Consideration (3) should not override consideration (1) or (2), as this would

Table 1. General Form of the Integrals Used (Angles in Radians)

Case A: $i > j$

$$A_{ij} = 0$$

Case B: $i = j$

$$A_{ij} = \frac{j^2}{2}\left\{\cos^{-1}\left(\frac{i-1}{j}\right) - \frac{i-1}{j}\left[1-\left(\frac{i-1}{j}\right)^2\right]^{1/2}\right\}$$

Case C: $i < j$

$$A = \frac{j^2}{2}\left\{\cos^{-1}\left(\frac{i-1}{j}\right) - \cos^{-1}\left(\frac{i}{j}\right) + \frac{i}{j}\left[1-\left(\frac{i}{j}\right)^2\right]^{1/2} - \frac{i-1}{j}\left[1-\left(\frac{i-1}{j}\right)^2\right]^{1/2}\right\} - \frac{(j-1)^2}{2}$$
$$\times\left\{\cos^{-1}\left(\frac{i-1}{j-1}\right) - \cos^{-1}\left(\frac{i}{j-1}\right) + \frac{i}{j-1}\left[1-\left(\frac{i}{j-1}\right)^2\right]^{1/2} - \frac{i-1}{j-1}\left[1-\left(\frac{i-1}{j-1}\right)^2\right]^{1/2}\right\}$$

guarantee that information from laboratory data would be degraded in processing. In the system in use, a cylinder 5 mm in diameter can be viewed experimentally with 50-μm resolution; thus, consideration of each side of the vertically symmetric discharge axis separately is precisely compatible with a 50 zone/50 ring discharge model.

A full listing of the 2500 area matrix coefficients is given in Appendix A. Here, those portions of the matrix thought to be most indicative of its properties are shown in Figure 3. The inverse matrix, whose use will be described in a subsequent section, is also presented.

The most readily evident property of the area matrix is that it is upper triangular. This is a general restatement of equation (3). The value of the matrix elements increases along any upper-left-to-lower-right diagonal, indicating that zone–ring overlap areas are largest in those regions of the discharge laterally farthest removed from the vertical discharge axis. In any row (along any lateral zone), the largest overlap is found for the element on the matrix diagonal. There is, however, one exception to this general observation: In lateral zone 1 ($i=1$), the largest area value is for $j=2$. Thus, the observation of the properties of the innermost ring of the discharge is complicated not only by having to look through all the surrounding discharge layers, but also by the small overlap between zone 1 and ring 1, leading to small signals related to ring 1 properties. A final property is that matrix elements in the upper right-hand corner of the matrix approach 1.0 as a limit, i.e., the overlap between zones near the optical axis and the outer rings approaches a square in shape; the apparent curvature of the discharge is largest at the core of the discharge and off-axis.

The area matrix may be used to compute expected intensities from predetermined radial emission distributions. The inverse of the area matrix may be used to compute radial emission profiles from lateral intensity information. This latter operation is most commonly employed in the laboratory and will be described below. For the moment, only the mechanics of the inverse matrix need to be of concern. The inverse matrix is most conveniently computed at the same time as the area matrix, with both matrices being made available for later computations. Although the method for computing the matrices is described in detail, this computation need be done only once; the same matrices can be used for any discharge system of any dimension and with any number of rings and zones up to the rank of the matrix. Thus, the matrices for use with a ten ring–ten zone model would be the region of intersection of the first ten rows and first ten columns in the upper left corners of the 50 ring–zone model matrices.

Properties of the inverse matrix (general element A_{ji}^{-1}, $j=$row, $i=$ column) (Figure 3) include the following. First, as was the case with the area matrix, the inverse matrix is upper triangular. Secondly, along any upper-left-to-lower-right diagonal, the absolute values of the numbers decrease; thus,

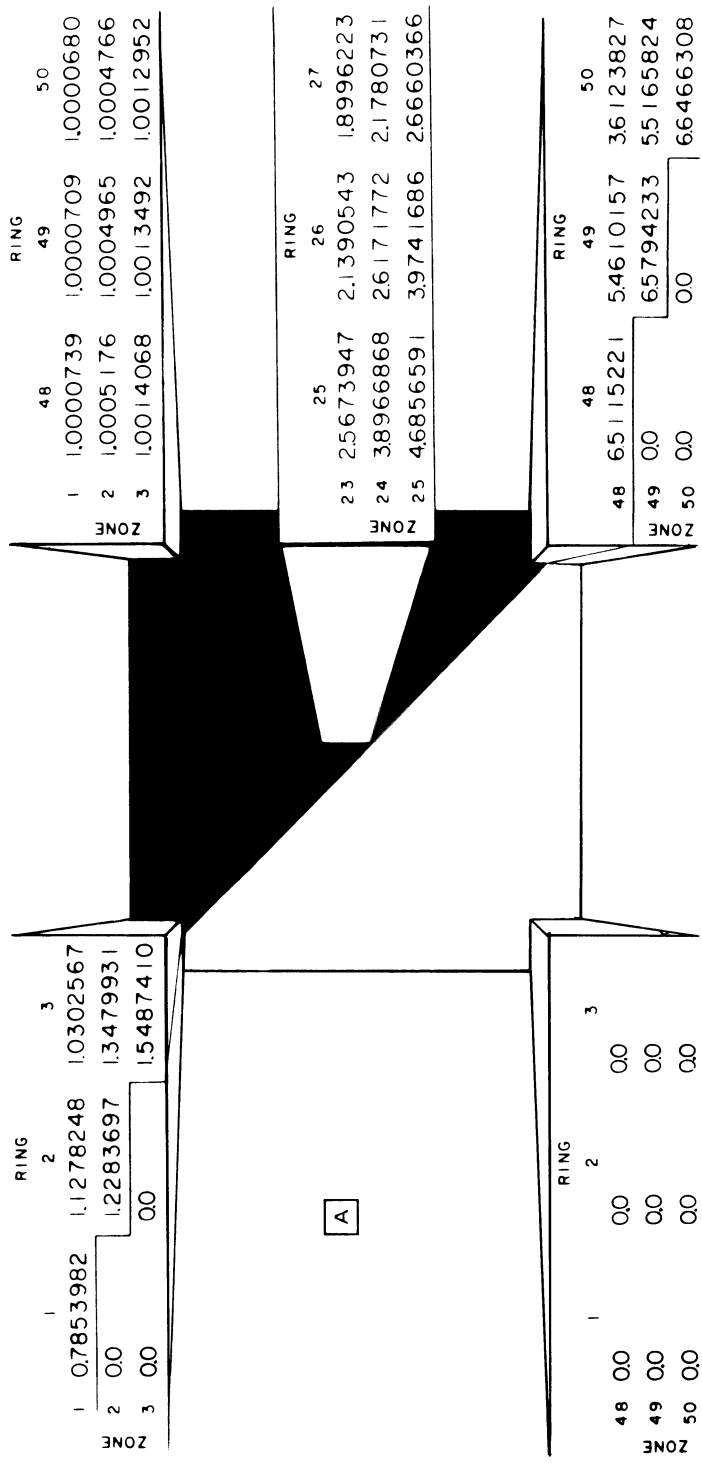

Figure 3. Salient features of the area (**A**) and inverse area ($\mathbf{A}^{-1}$) matrices. (45 of the 2500 elements in each matrix are shown. All elements below the diagonal of each matrix are 0.0.)

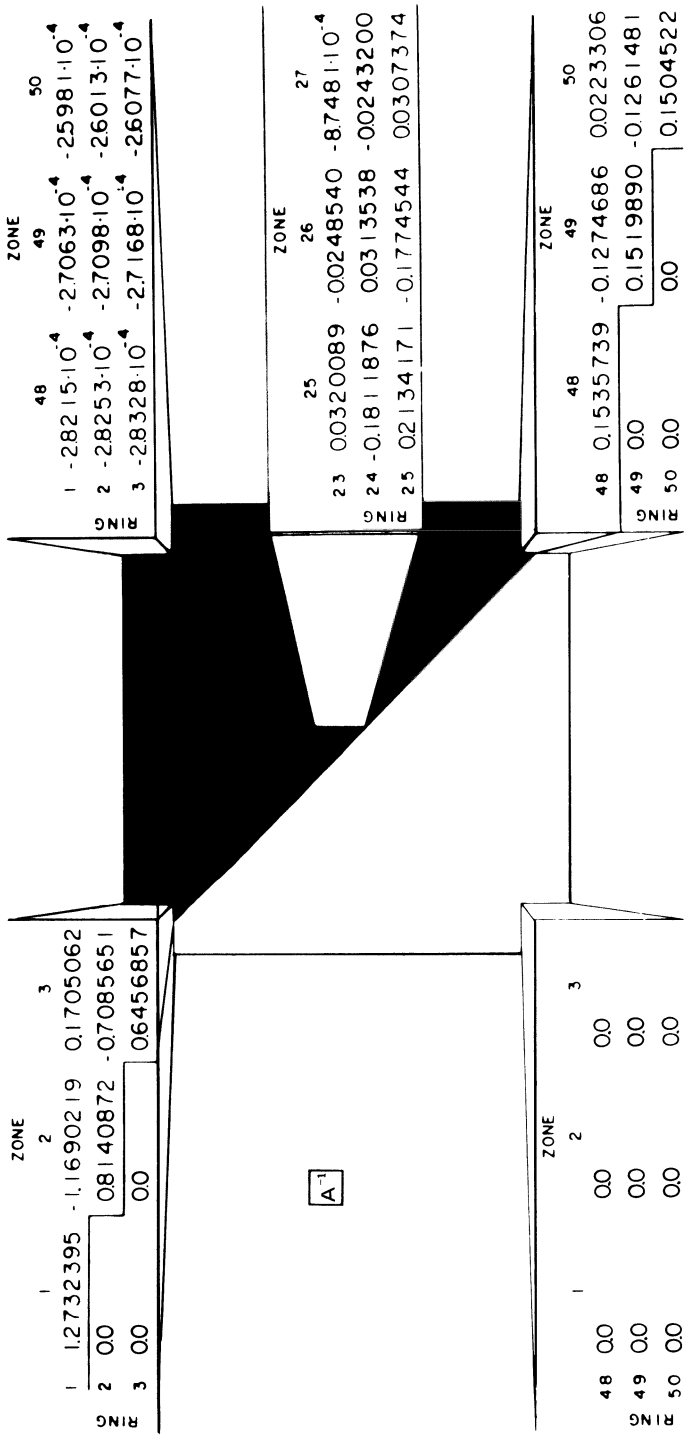

Figure 3. (*Continued*).

in processing data by the inverse matrix, information gathered in nearby zones farther from the discharge axis than the zone under consideration has a pronounced effect on any given zone computations, with the strongest interaction occurring near the discharge axis. Thirdly, aside from elements A_{jj}^{-1} and A_{jj+2}^{-1} (row j and columns j and $j+2$, respectively), all inverse matrix elements are negative. The physical effect of the inverse matrix is to "peel away" the light emitted in outer discharge layers to obtain information on the inner discharge structure; thus, subtraction of outer ring phenomena is the predominant operation carried out by $\mathbf{A}^{-1}$, which is the reason that most off-diagonal elements are negative. Fourthly, although matrix elements get smaller toward the upper right-hand corner, they never become zero. There is always a small but finite contribution of an outer ring to the intensity observed in an inner zone.

For all calculations leading to the area and inverse area matrices, double-precision calculations were performed, with single-precision output available for use with processors lacking double precision (e.g., BASIC, in which the general usage programs were written). If single-precision calculations are used, rounding errors of several tenths percent are observed in the inverse matrix. So that processing may be done confidently without inherent errors from the matrices, double-precision matrix calculation followed by the output of as many digits as the applications program can handle is recommended. For the BASIC processor employed, 8 significant figures, as shown for most matrix elements in Figure 3, were output, even though the confirmed precision of the matrix calculations was 14 digits. When the BASIC processor was used to multiply the area matrix by the inverse matrix, there were no errors larger than 1 part in 10^7. Thus, imprecision in laboratory data is expected to be sufficiently large ($\geqslant 0.1\%$) that imprecision in the area matrices is negligible.

The above computation of the area matrix presumes that the observational optical system ideally projects the three-dimensional discharge onto a two-dimensional focal plane. In fact, imaging changes can be seen as the discharge is moved along the optical axis,[22] and so it would be expected that some depth-of-field modification to the Abel inversion procedure would be necessary. As the imaging changes are a function of the geometry of the optical system, the depth-of-field modifications can be applied most easily by combining the depth-of-field corrections with the area and inverse area coefficients, which are also geometric correction factors. For such modifications, the area matrices must be calculated once for each optical system rather than once for all systems as described earlier.

The correction procedure assumes that the resolution of the optical system parallel to the optical axis is the same as the resolution perpendicular to that axis. Thus, in addition to the radial ring–lateral zone coordinate system previously used, a grid of depth-of-field regions is added in the plane of the rings and lateral zones, but perpendicular to the lateral zones.

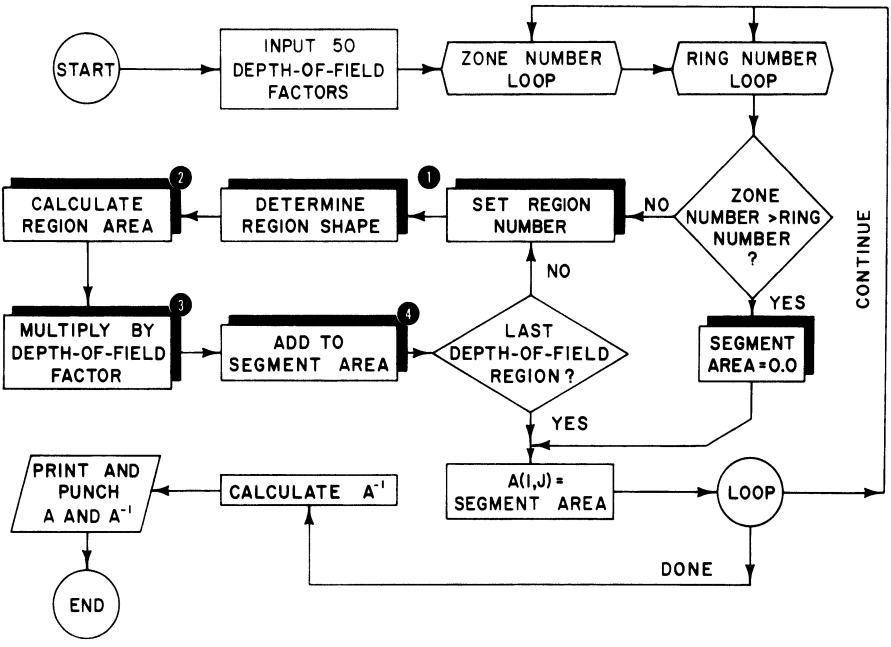

Figure 4. Flowchart for program to calculate area matrices including depth-of-field weighting.

As illustrated in Figure 4, the area matrix with depth-of-field correction is computed as follows: (1) the area segment is split into the various depth-of-field regions; (2) the area bounded by the zone, ring, and region under consideration is computed; (3) the regional area is multiplied by a depth-of-field weighting factor, specific to the region considered; (4) the overall area computed is the sum of the weighted regional areas. Thus

$$A_{ij} = \sum_{k=1}^{50} A_{ijk} F_k \tag{4}$$

where F_k is the depth-of-field correction factor for region k and A_{ijk} is the area of overlap of zone i, ring j, and region k. For many regions, A_{ijk} may be 0 (e.g., in computing A_{45}, A_{45k} for $k \geqslant 5$ would be 0). Furthermore, if F_k is set to 1.0 for all k, the area coefficients calculated without considering depth-of-field are recovered.

Table 2 and Figure 5 show the calculation of the regional areas A_{ijk}. As before, unitless areas are computed. In Figure 5, the area pairs (I,IV), (II,V), (III,VI), and (VII,VIII) are complementary, i.e., the area computed for I is 1 —(area computed for IV) etc. In the area segment shown in Figure 5, the overlap types are: A_{451}, type VI; A_{452}, type VI; A_{453}, type IV; A_{454}, type I.

Table 2. Calculation of the Regional Areas A_{ijk}[a]

Region type (as in Figure 5)	Area of region[b]
I	$[1/2(C+D)-Y(K-1)]_{I-1}^{F}$
II	$[1/2(C+D)-Y(K-1)]_{E}^{F}+E-I+1$
III	$[1/2(C+D)-YG]_{I-1}^{I}+G-K+1$
IV	$1-[YK-1/2(C+D)]_{I-1}^{I}$
V	$[YK-1/2(C'+D')]_{E'}^{F'}+1-F'$
VI	$[YH'-1/2(C'+D')]_{I-1}^{I}+K-H'$
VII	$1-[1/2(C'+D')-Y(K-1)]_{I-1}^{F'}$
VIII	$[YK-1/2(C'+D')]_{E'}^{I}$
IX	$1-[YK-1/2(C+D)]_{E}^{I}-[1/2(C'+D')-Y(K-1)]_{I-1}^{F'}$
$B=(J^2-Y^2)^{1/2}$	$B'=[(J-1)^2-Y^2]^{1/2}$
$C=Y(J^2-Y^2)^{1/2}$	$C'=Y[(J-1)^2-Y^2]^{1/2}$
$D=J^2\sin^{-1}(Y/J)$	$D'=(J-1)^2\sin^{-1}[Y/(J-1)]$
$E=(J^2-K^2)^{1/2}$	$E'=[(J-1)^2-K^2]^{1/2}$
$F=[J^2-(K-1)^2]^{1/2}$	$F'=[(J-1)^2-(K-1)^2]^{1/2}$
$G=(J^2-I^2)^{1/2}$	$G'=[(J-1)^2-I^2]^{1/2}$
$H=[J^2-(I-1)^2]^{1/2}$	$H'=[(J-1)^2-(I-1)^2]^{1/2}$

[a] Definitions are (21). Y denotes the integration variable with range parallel to the optical axis; final variable for integral limits insertion. $[f(Y)]_{Q}^{R}=f(R)-f(Q)$. I denotes the lateral zone number, J the radial ring number, and K the depth-of-field region number.
[b] B, B', G', and H arise in deriving these formulas, but do not appear in them.

The problem of which depth-of-field weighting factors to use remains. Sacks[20] and Goldstein[21] determined both experimentally and theoretically that for their optical systems ($f/27$ and $f/17.5$, respectively) weighting factors of 1.0 were indeed correct to a first-order of approximation. However, neither found this conclusion totally satisfactory, and the weighting factor framework has been retained pending further insights. A promising approach[26] concluded that for radial profiles which were either uniform or peaked near the discharge axis, errors from ignoring depth-of-field effects were less than 0.25%. It remains to be seen if off-axis profiles are distorted by assuming that all depth-of-field weighting factors equal 1.0.

4. Abel Inversion of Strictly Emitting Profiles

Based on the ring/zone discharge model and the area matrices it is possible to compute lateral profiles from radial data, and vice versa. This approach has been taken several times previously.[10,16,20,21,27] Viewing down some lateral zone through all of the discharge, the total intensity viewed is the sum of the intensities emitted in each ring/zone overlap segment viewed

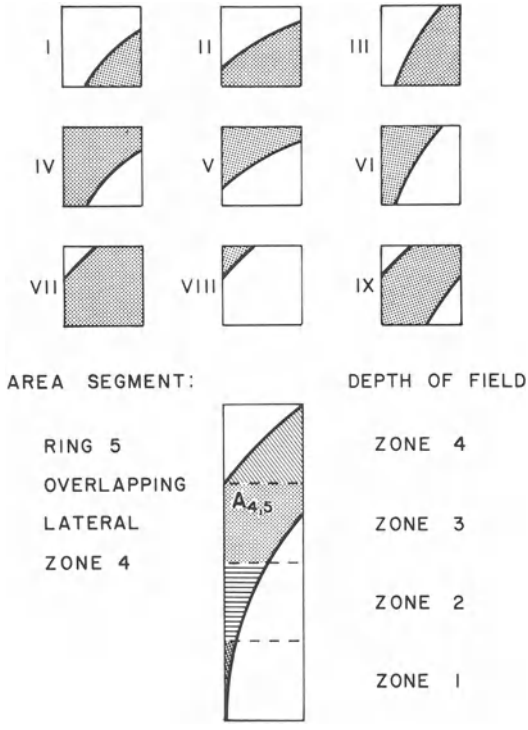

Figure 5. Shapes possible for overlap of radial rings, lateral zones, and depth-of-field regions. An example is given of the construction of one area matrix element from several overlap regions.

(assuming emission is the only optically significant phenomenon in the discharge). If each ring j has the emission coefficient J_j (ergs cm^{-3} sr^{-1} nm^{-1}), then the intensity viewed in zone i is given by

$$I_i = 2 \sum_{j=1}^{j_{\max}} A_{ij} J_j \tag{5}$$

where $j_{\max}$ is the number of the outermost ring. Note that the number of rings in the model equals the number of zones, so that if $i_{\max}$ is the total number of zones, $i_{\max} = j_{\max}$. Equation (5) could be restated in matrix form as

$$\mathbf{I} = 2 \cdot \mathbf{A}\mathbf{J} \tag{6}$$

where $\mathbf{I}$ and $\mathbf{J}$ are vectors and $\mathbf{A}$ is the area matrix with elements A_{ij} as computed in the previous section.

Some authors combine the factor of 2 used in equations (5) and (6) with the area matrix values.[10,27] The factor indicates that each ring is viewed twice, once on the "front" side of the discharge, and once on the "rear" side (away from the observer). For purely emitting sources, either convention may be used with equal ease. However, when other processes such as absorption are of importance, it becomes more convenient to have the factor of 2 separate from the A_{ij}.

Equation (5) indicates how known J_j values may be used to predict I_i values. In the laboratory, one observes I_i and wishes to calculate J_j. As the A_{ij} form a square matrix, equation (5) may be inverted to give

$$J_j = \frac{1}{2} \sum_{i=1}^{i_{\max}} B_{ji} I_i \tag{7}$$

The B_{ji} are the elements of the matrix inverse to **A** so that

$$\mathbf{A} \cdot \mathbf{B} = \mathbf{B} \cdot \mathbf{A} = \mathbf{1} \text{ (the identity matrix)} \tag{8}$$

Both matrices are listed in Appendix A.

The tabulated A_{ij} values are based on a 1-cm zone (ring) width. Segment area is proportional to the square of the zone width. Thus,

$$A_{ij} \text{ (real discharge)} = A_{ij} \text{ (tabulated)} \cdot W_i^2 \tag{9}$$

where W_i is the zone width in centimeters. Similarly,

$$B_{ji} \text{ (real discharge)} = \frac{B_{ji} \text{ (tabulated)}}{W_i^2} \tag{10}$$

A full table of symbols appears in Table 3. For all the examples which follow except those dealing with discharge wander, W_i will be taken as 1 cm. Equations (9) and (10) state that this is not a limitation to generality, as other situations may be handled by supplying the appropriate W_i scale factor. The zone width for laboratory use is determined by the lateral resolution of the observing optical train. If this resolution is 0.005 cm (50 μm), then this too should be the zone width.

Equations (5) and (7) may be modified slightly if correction for continuum background is desired. If I_i is the gross observed intensity in a given zone and I_{ib} is the intensity in the same zone at an adjacent wavelength, then

$$I_{ic} = I_i - I_{ib} \tag{11}$$

where I_{ic} is the background-corrected intensity. Then, since the Abel inversion

Table 3. Definition of Terms

A_{ij}	Area of overlap of zone i with ring j
A_{ji}^{-1}	Inverse area matrix element applicable to ring j, zone i
L_{ij}	Mean absorption pathlength in zone i through ring j
W_i	Zone width
M_{ji}	Elements of the matrix inverse to L_{ij}
I_i	Observed or observable intensity in zone i
I_i'	Intensity calculated to be observed where self-absorption is not present. Nonobservable quantity
I_{i0}	Backlight intensity for absorption experiment in zone i
J_j	Emission in ring j
K_j	Absorption in ring j
i_{max}, j_{max}	Maximum ring or zone index ($\leqslant 50$ for the matrices available)
i_{emax}, j_{emax}	Maximum ring or zone index applicable to emission portion of discharge
I_{ib}	Background intensity in zone i
I_{ic}	Intensity corrected for background

is linear when only emission occurs, either

$$J_i = \frac{1}{2} \sum_{i=1}^{i_{emax}} A_{ji}^{-1} I_{ic} \tag{12}$$

or

$$J_i = \frac{1}{2} \sum_{i=1}^{i_{emax}} A_{ji}^{-1} I_i - \frac{1}{2} \sum_{i=1}^{i_{emax}} A_{ji}^{-1} I_{ib} \tag{13}$$

The first term on the right-hand side of equation (13) performs a lateral-to-radial conversion on the total radiation observed at the wavelength of interest; the second term inverts the background radiation. When only emission occurs, background may be subtracted either before or after inversion with numerically identical results. Also, radial profiles may be modeled or computed for the continuum radiation.

5. Self-Absorption and the Abel Inversion—Theory

In the simple picture presented in the last section, a glowing discharge is assumed to be purely emitting. In such instances, there is a one-to-one

correspondence between lateral and radial profiles. However, if this simple model is applied to systems where other nonradiative spectroscopic processes are occurring, calculated radial profiles may show great discrepancies from physical reality. A case in point is self-absorption [or its limiting condition, self-reversal[28]], which alters the amount of light escaping from the discharge and the amount impinging on the detection device. For present purposes, the discharge will be modeled as being electronically hot in its interior, and electronically cooler in its outer reaches, so that the core of the discharge emits light and the fringes of the discharge absorb light. In this case, there is a complete separation of the regions in space which emit and absorb light (henceforth referred to as the "hot core" model). Thus, the emitting discharge is contained in an absorbing cylindrical shell.

The above absorbing shell will have two effects on observed lateral profiles: first, the observed intensity will be attenuated relative to its value in the absence of self-absorption and second, the shape of the lateral intensity profile will be distorted which, in turn, will distort the calculated radial emission profile. In addition, if an attempt is made to map the spatial distribution of species in the discharge, absorption may be a tool to expand the number of species which may be mapped and the regions in which they may be mapped.

If an experiment is performed employing a low-resolution spectrometer, the fact that self-absorption is occurring may not be readily apparent. Among the effects discussed herein will be the types of profile shapes which would be observed if self-absorption were present in a discharge, but the absorption was either not measured or its presence ignored in performing calculations. It is to be emphasized that if absorption is measured, its effects can be compensated, and correct radial emission and absorption profiles may be computed.

The relationship between observed absorption in the laboratory (which will be a lateral view) and the *radial absorption profile* is very similar to the relationship between the lateral intensity profile (in the absence of self-absorption) and the radial emission profile discussed in the previous section. Just as absorption measurements may be made on solutions by backlighting the solution and invoking Beer's law to determine solute concentrations, so absorption profiles in plasmas may be determined by backlighting the discharge and observing the attenuation of the backlight. (See the comments given later concerning the difficulty of this experiment.) In addition, if the "hot core" model of the discharge is correct, a particularly bright backlighting source need not be used to measure self-absorption; since absorption is measured as a ratio, the backlight need only be bright enough to be observed over background light levels, and these background intensities are low in the outer absorbing regions of the discharge. [Absorption determination techniques which do not use backlights have been described in the literature,[29,30] but generally require that the reflectivity of a mirror be known as a function

of wavelength. One method which does not require knowledge of the mirror reflectivity[31] has been proposed.]

Similar models have also been used by Dieke and Cowan[32] and Braun *et al.*[33] In both cases, however, a spatial model for the discharge was postulated and integrated, so that observations could be made on a spatially integrated basis. They allowed for line shape explicitly in all expressions. In contrast, the work reported here assumes constant optical properties within the bandpass of the observing instrument, but explicitly looks at spatial variations in the discharges. Dieke demonstrated that in on-axis observation (viewing the discharge through lateral zone 1), details of radial structure have weak influence on observed spectral line profiles. As will be demonstrated below, such is not the case for off-axis observation.

Explicit mathematical expression for dealing with self-absorption will now be presented. An approach very similar to that used for a strictly emitting source may be employed for sources subject to self-absorption by a spectroscopically cool cylinder surrounding the spectroscopically hot emitting core. The absorption pathlength through ring j as viewed in zone i, L_{ij}, may be computed as

$$L_{ij} = A_{ij}/W_i \tag{14}$$

where W_i is the zone width, area is in cm^2, and the other quantities are in cm. If A_{ij} is unitless, then $L_{ij} = A_{ij}$. Similarly, if M_{ji} is the inverse of the L_{ij} matrix

$$M_{ji} = W_i A_{ji}^{-1} \tag{15}$$

If only emission or only absorption takes place in a given radial ring, then there will be a ring $j_{e\max}$ and a zone $i_{e\max}$ such that all information contained in rings or zones numbered higher than these indices will contain information on absorption only. For these zones and rings, the inversion may be described as

$$\log_{10}\frac{I_{i0}}{I_i} = 2\sum_{j=j_{e\max}+1}^{j_{\max}} L_{ij}K_j \tag{16}$$

$$K_j = \frac{1}{2}\sum_{i=i_{e\max}+1}^{i_{\max}} M_{ji}\log_{10}\frac{I_{i0}}{I_i} \tag{17}$$

where I_{i0} is the intensity of a backlighting source viewed through zone i in the absence of self-absorption and K_j is the total absorbance, divided by the absorption pathlength in ring j. If Beer's law is stated $A = \varepsilon cb$, K corresponds to $\varepsilon \cdot c$. The factor of 2 arises because the light from the backlight passes

through a given ring of the discharge twice, once behind the object focal plane of the instrument and once in front of the object focal plain (again Figures 1 and 2 may be helpful in conceptualizing this point).

For $i \leqslant i_{e\max}$ and $j \leqslant j_{e\max}$, the emitting portion of the discharge is viewed through the absorbing shell. Thus, the discharge acts as a light source viewed through an absorption cell. Overall, the observed intensity (with no external backlight employed) can be described as

$$I_i = \left(2 \sum_{j=1}^{j_{e\max}} A_{ij} J_j \right) \cdot 10^{-} \left(\sum_{j=j_{e\max}+1}^{j_{e\max}} L_{ij} K_j \right) \tag{18}$$

As only one pass through the absorber is made by the observed light, no factor scaling the absorption pathlength (the $L_{ij}K_j$ sum) by 2 is warranted. Conversely, the emission in any emitting ring inside the absorber may be calculated by

$$J_j = \frac{1}{2} \sum_{i=1}^{j_{e\max}} A_{ji}^{-1} I_i \cdot 10 \left(\sum_{j=j_{e\max}+1}^{j_{\max}} L_{ij} K_j \right) \tag{19}$$

A tacit assumption in the above analysis is that an appropriate backlight exists which can give reproducible intensities I_{i0} in zone i. This intensity must be characterized not only in space, but also in wavelength and time. Furthermore, it must be of such level that it is readily detected instrumentally, yet does not perturb the plasma system. Furthermore, there may arise situations where the backlighting beam causes stimulated emission which, upon inversion, would appear as "negative absorptivity." Thus, while the mathematical formalism given in equations (16)–(19) is correct in principle for mapping emission and absorption, there may arise practical laboratory situations in which its use is difficult or impossible.

For modeling and data analysis, it is often desirable to be able to examine intermediate steps in the calculation as well as the final results. For determining the emission in the emitting rings, equation (19) does not allow intermediate inspection, but goes directly from observation to ring emission.

Equation (19) may be broken into two steps to clarify the calculation and permit intermediate examination of the intensity data after compensation for self-absorption. If I_i' is the intensity which would be observed in zone i in the absence of self-absorption then

$$I_i' = I_i \cdot 10 \left(\sum_{j=e_{\max}+1}^{j_{\max}} L_{ij} K_j \right) \tag{20}$$

and equation (19) may be rewritten

$$J_j = \frac{1}{2} \sum_{i=1}^{i_{max}} A_{ji}^{-1} I_i' \tag{21}$$

which is identical to equation (7) if all of the K_j values are zero, i.e., in the absence of self-absorption.

For designing algorithms to allow facile conversion from radial profiles to lateral (observable) profiles and vice versa, the equations found to be most comprehensive and yet to allow full study of intermediate calculation steps are (5), (16)–(18), (20), and (21). The flowchart in Figure 6 shows how these equations are grouped in modeling software. Figure 6(A) is for conversion of radial profiles to lateral profiles, and Figure 6(B) is for lateral-to-radial profile conversion; the multiple entry structure provides flexible computation and interaction. The equations are arranged one to a block. Block 1 corresponds to equation (5), block 2 to equation (16), and block 3 to equation (17).

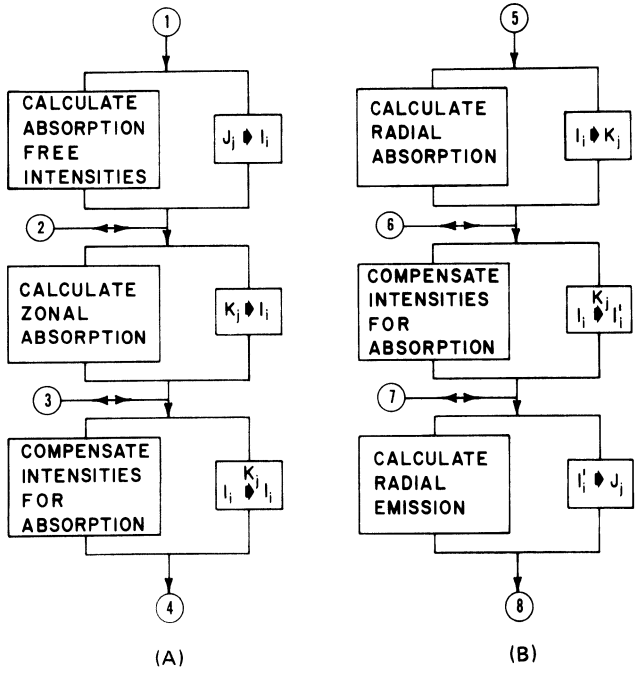

Figure 6. Multiple-entry routines for interconversion of radial and lateral spatially resolved information. (A) Radial-to-lateral profile conversion, (B) Lateral-to-radial profile conversion.

Similarly, block 5 corresponds to equation (18), block 6 to equation (20), and block 7 to equation (21) or, when no absorption is present, to equation (7). Because of the multiple-entry structure, other data manipulations such as background subtraction or data smoothing may be performed at any desired step in the procedure, and, with appropriate choice of language and control statements, in real time. All the modeling software is written in BASIC, and may be found in reference 34.

As lateral zones progressively farther away from the discharge axis are considered, the average absorption pathlength through a given ring (L_{ij}) tends to increase [see Figure 1(A)]. As self-absorption is a logarithmic process, this means that a drastically greater fraction of the emitted light is absorbed in the wings of a discharge than near the optical axis or center of the discharge. As a result, when self-absorption occurs, the spatially integrated observed intensity is diminished and, of equal consequence, truly off-axis lateral intensity profiles appear as on-axis profiles. The discussion in the next section emphasizes examples of lateral intensity profiles which would result if only a single ring of the discharge emitted, if only a single ring absorbed light, and either the concentrations of absorbing atoms or the location of the absorbing ring (or both) were to vary. In addition, calculated radial profiles will be shown and discussed, as these give insight into the experimental detection of self-absorption when high-resolution instrumentation is unavailable. Furthermore, the effects of self-absorption on calculated species distributions in a discharge will be shown. Use of single-ring profiles is a definitive case for all possible profiles for which this model can account; more involved profiles are simply combinations of several rings emitting and absorbing to various degrees. Data in the literature (reference 19 and references therein) show that extreme inhomogeneities in both time and space in spark discharges may approximate single-ring emission behavior. In the examples to follow, it will be evident that a lateral intensity profile can be singularly distorted by self-absorption, even with only a single ring of absorbers present, making it prudent to study such single-ring models as a first step in diagnosing other situations.

6. Self-Absorption and the Abel Inversion—Examples

Figure 7 shows the general procedure used to study the effects of self-absorption. First, the lateral intensity profile corresponding to a single ring of emission in ring 25 is calculated. Note that while the radial profile is strictly of an off-axis nature, one sees some intensity even on-axis, since one must look through the emitting ring when viewing the discharge through any lateral zone numbered less than or equal to the number of the emitting ring. Next, the single ring of absorption is taken into account to generate the true

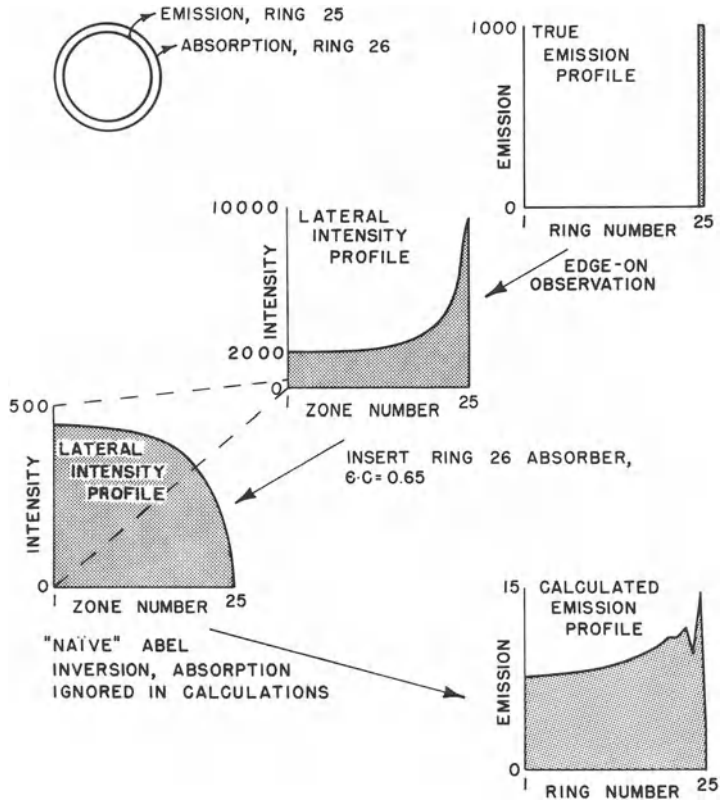

Figure 7. Procedure for modeling the effects of self-absorption on lateral and calculated radial profiles.

lateral profile which would be observed in the presence of self-absorption [in this case $K_{26} = 0.65 = (\varepsilon C)_{26}$ = absorptivity times species concentration in ring 26]. Both of the attenuation and profile shape distortion effects previously mentioned are easily seen, i.e., instead of observing an off-axis peaking lateral profile, a much weaker on-axis peaking lateral profile can be seen. Of course, in the laboratory, all that would be observed is the on-axis lateral profile; there would then be two ways to interpret that profile: (1) measure the absorption profile as given in equation (17), compensate for the self-absorption, and work back towards the top of Figure 7, thus obtaining the correct radial emission profile; or (2) either ignore the presence of self-absorption or admit its presence, but do not compensate for it. In this case, an erroneous radial emission profile would be calculated as shown at the bottom of Figure 7. Comparison of the top and bottom plots in Figure 7 clearly reveals why self-absorption must be compensated in order to get meaningful radial

emission profiles: the presence of self-absorption not only reduces the maximum calculated emission, but also makes the radial profile appear to be either on-axis or essentially uniform in nature, when, in fact, it is both off-axis and nonuniform. As the Abel inversion is highly noise sensitive (see the following), it is tempting to look at the outer zones of the calculated radial profile, attribute the jagged character of the profile to noise, and resort to data smoothing. Noise is not the cause of the jaggedness! Rather, failing to account for a physical phenomenon, i.e., self-absorption, causes error in computing the radial structure of the discharge.

Even if the lateral profile is not inverted, error may occur if the presence of self-absorption is overlooked. If a discharge is "hotter" in the center than in the wings, it would be expected that "hot" or "spark" lines would be emitted by species close to the center of the discharge, giving an on-axis type lateral profile; similarly, lines emitted by less excited species (so-called "arc lines") should be concentrated towards the wings of the discharge and give off-axis peaked lateral and radial profiles. However, as shown in Figure 7, an "arc" line subject to self-absorption can give the appearance of being a "spark" line. While careful wavelength measurement and identification should prevent misidentification of the line, cursory examination of a self-absorbed "arc" line at low resolution might lead to the belief that either (a) the discharge is fairly cool in the center, when in actuality it is the wings which are extraordinarily cool and self-absorbing, or (b) a temperature inversion exists in the discharge wherein the core is cool, and is surrounded by a hotter region (i.e., nonself-absorbed lines of higher excitation might display some slight off-axis character). A final impression would be that the discharge has a sharp physical boundary where it meets the ambient surroundings, which, in fact, is where the absorbing rings of atoms exist. It would be expected that at least some anomalous results in spatially resolved spectrometry could be explained by the previously undetected effects of self-absorption.

A systematic look at the effects of concentration on profile shape distortion is shown in Figures 8 and 9. In Figure 8, the amount of absorption, i.e., K_j, the molar concentration of the absorbing species times molar absorptivity in ring 26, is varied from 0 to 1.00. Recall that the zone width is taken as 1 cm for comparison purposes. If the zone width were 0.1 mm, then K_{26} would need to vary from 0 to 100 to effect the same distorting and attenuating effects. Insets in Figure 8 show how drastically the off-axis intensity falls off compared to the on-axis intensity, even at small absorbances. Figure 9 shows systematically the changes which would be calculated in the radial profile if absorption to the extent listed were present and not taken into account (again, if absorption were taken into account, the correct radial emission profile, as seen for $\varepsilon c = 0$ in Figure 9, would be the radial emission profile which would be calculated; the true physical radial emission profile is, in fact, unchanged throughout Figures 8 and 9, even though the calculated profiles vary widely).

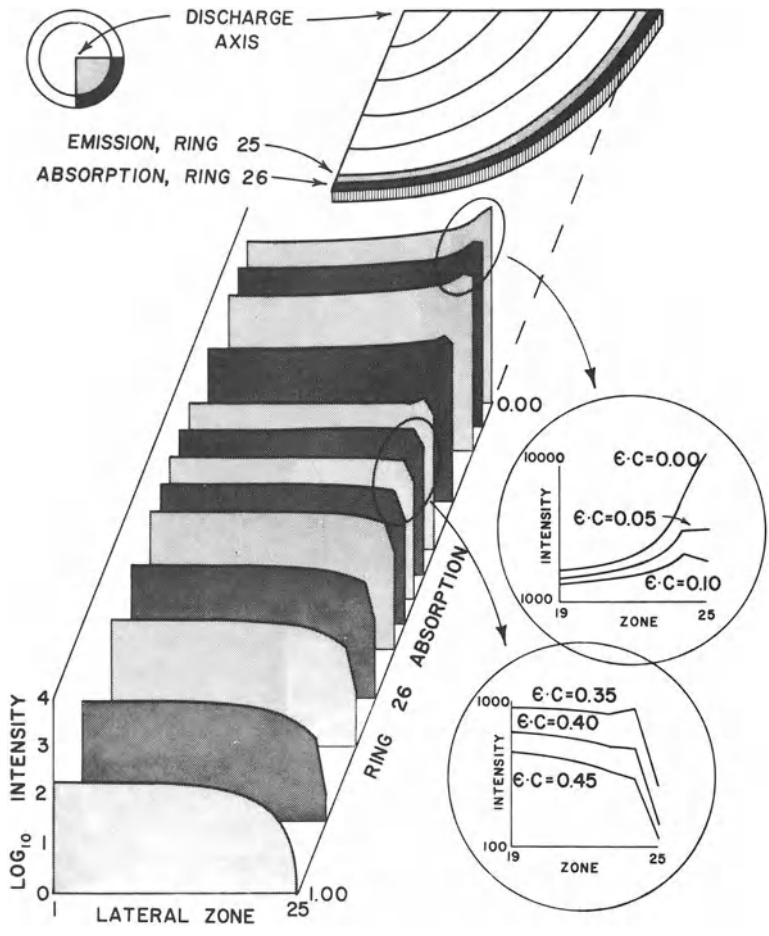

Figure 8. Effect of single-ring absorber on observed lateral intensity profile from single-ring emitter as a function of ring 26 K_j.

Figure 10 exhibits the lateral profiles which result from fixing the absorption in the absorbing ring, but varying the relative placement of the absorbing ring and emitting core of the discharge. The same radial emission profile as used previously, i.e., $J_{25} = 1000$ is employed in this figure. The K_j value was chosen so that a wide range of profile shapes was in evidence as the absorber was placed in each of the rings from 26–50. As the location of the single-ring absorber is moved farther from the discharge axis, the degree of profile distortion decreases rapidly. This is because the apparent curvature of the absorbing ring decreases as the ring radius increases. When the absorbing ring is close to the emitting ring, the absorption pathlength varies substantially with the lateral zone number whereas, when the absorbing ring has a

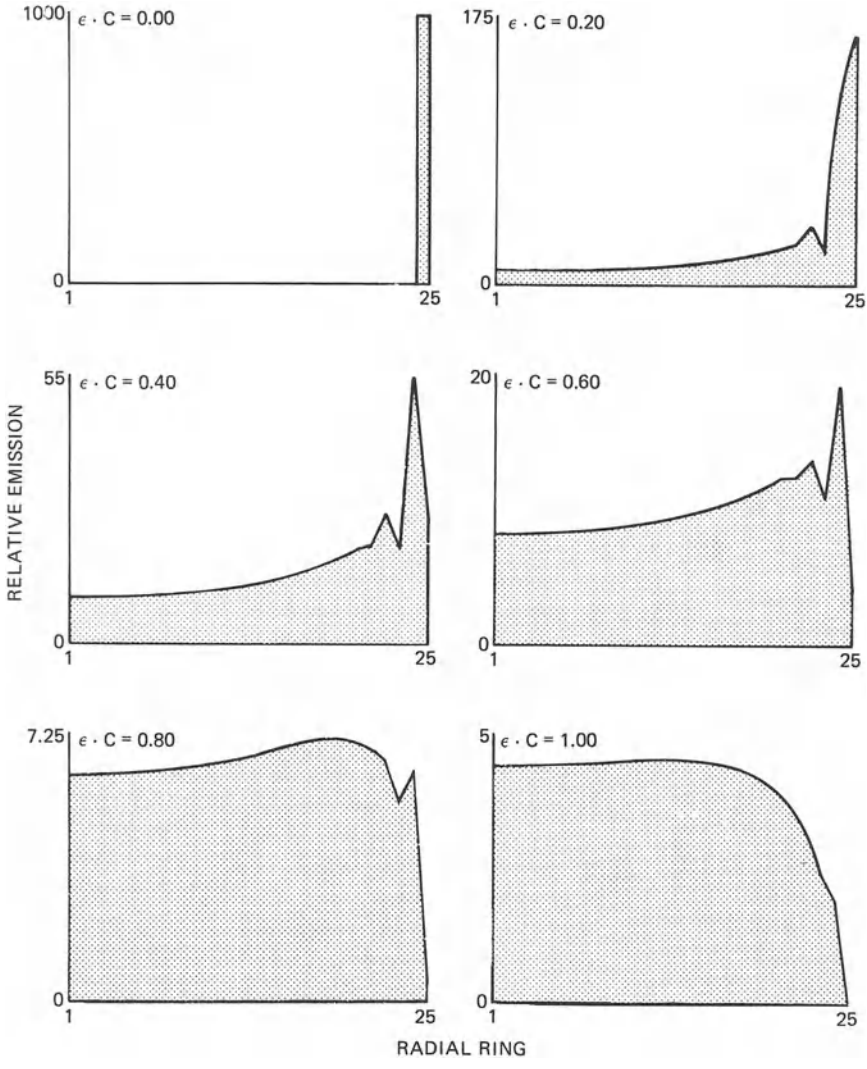

Figure 9. Calculated radial profiles. Profiles calculated by inverting several lateral profiles from Figure 8, assuming the lateral profiles were due solely to emission, even though absorption was involved. In all cases the true radial emitting species distribution is as shown for $\varepsilon \cdot c = 0$. Note how as $\varepsilon \cdot c$ (in ring 26) increases, peak calculated emission decreases, the calculated profile becomes jagged, and, finally, assumes an on-axis character.

radius much larger than that of the emitting ring, absorption pathlength differences are much smaller. As the absorber recedes from the emitter, the calculated radial emission profile shape becomes less and less affected by the presence of self-absorption, even though the intensity observed is still less than it would be in the absence of self-absorption.

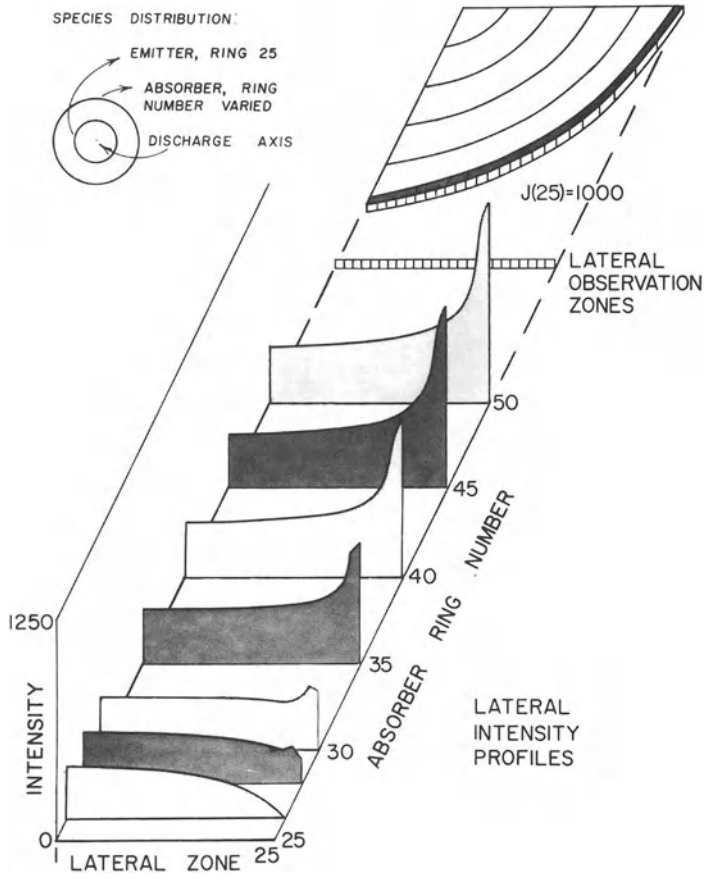

Figure 10. Effect of single-ring absorber ($\varepsilon \cdot c = 0.80$) in various rings on the observed lateral intensity profile from a fixed single-ring emitter.

If a single absorbing ring actually were propagating away from the center of a discharge (perhaps propagating with a shock front), then it would be expected that the concentration of absorbing species would decrease as the absorbing ring expanded, i.e., as the absorbing species spreads away from the discharge axis and becomes more dilute. If the conditions used in creating Figure 10 are again employed (single-ring emission in ring 25 and single-ring absorption starting in ring 26 with K_{26} or εc in ring $26 = 0.80$), but the effects of dilution are included in the model, then the lateral intensity profiles shown in Figure 11 are obtained. Note the similarity between the plots in Figures 10 and 11. Although there is less profile shape distortion in Figure 11 than in Figure 10, and although the amount of light attenuation is reduced when dilution of the absorbing species occurs, it should be evident that the

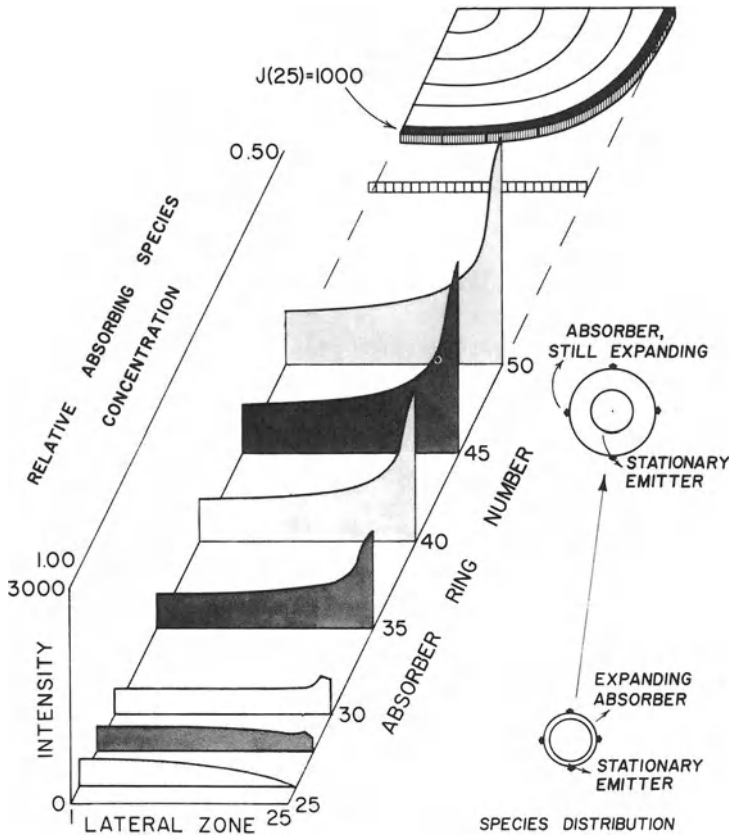

Figure 11. Dilution effects on observed lateral intensity profiles. The absorber propagates outward, with concentration reduced as r^{-2}. The condition when the absorber is in ring 26 is identical to conditions in Figure 10 when the absorber is also in ring 26.

geometric location of absorption relative to emission is of greater importance in determining lateral profile shape than is the absorbing species concentration, at least for the absorption value illustrated.

In summary, failure to account for self-absorption, when present in a discharge, can radically distort both the observed data and the calculated emission species distribution. Besides attenuating the emitted light, self-absorption may make truly off-axis emission profiles appear to be on-axis profiles, as off-axis intensity is attenuated to a greater extent than on-axis intensity. Furthermore, if the presence of self-absorption is ignored, calculated quantities such as radial emission or temperature assume progressively smaller amounts of physical significance as mathematical treatment is applied to the raw intensity data. However, when absorption is measured and taken into

account, various calculated quantities may be accurately derived from the observed data.

7. Background Correction in the Presence of Self-Absorption

Upon examination of a spectrally and spatially resolved spectrum emitted by a spark or arc discharge, one of the most striking features is the existence of a continuum background spectrum on which the line emission spectra of the atoms in the discharge are superimposed. To a first approximation, the background emission may be considered to be independent of the line emission; it is, thus, desirable to subtract background emission from the observed intensity at a line in order to find the spatially resolved emission due only to the atomic species giving rise to the line. In addition, if quantitative analysis is attempted on the atomic species giving rise to the line, then it is essential to subtract the background emission. In the absence of self-absorption, this is a straightforward process. One measures the background emission at a wavelength close to the line and simply subtracts the background intensity from the line intensity, in a zone-for-zone fashion in the spatially resolved experiment or as an integrated quantity in the spatially integrated case. If self-absorption occurs, however, the background should not be simply subtracted. Failure to account for self-absorption will lead to overcompensation for the background.

The essential cause of background overcorrection when self-absorption occurs is that light is absorbed solely as a function of wavelength; the nature of the species giving rise to the light which is absorbed is immaterial (this is also the reason for spectral interferences in atomic absorption spectrometry). Thus, continuum background radiation emitted within the line width of an absorbing species will be absorbed just as line radiation emitted at the same wavelength would be absorbed.

Figure 12 illustrates, for a spatially integrated, spectrally resolved experiment, the types of effects anticipated. The bandpass of the observing instrument is held constant at $\Delta\lambda$ throughout; the regions numbered 1 in the figure show the amount of background emission I_b emitted in the absence of self-absorption and within the instrument bandpass. Region 3 is the emission line profile in the absence of self-absorption. If one wished to determine the amount of emission attributable to region 3, i.e., the line intensity over background, the background emission (region 1) could be directly subtracted from the total emission observed at the wavelength of the line emission to determine the amount of emission attributable to the line. But if the line is self-absorbed (or self-reversed as shown at the bottom of Figure 12), then not only is a portion of the light emitted within the line self-absorbed, but also

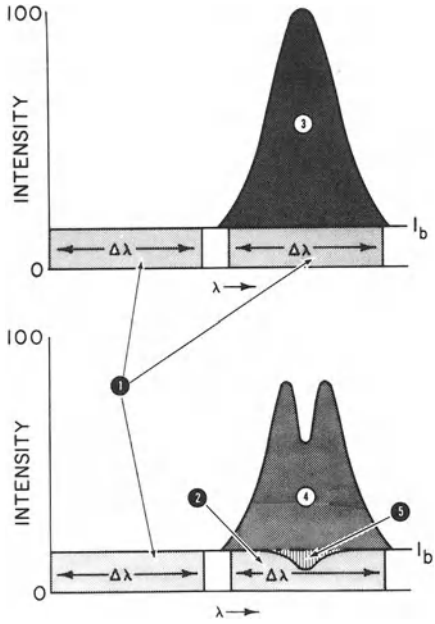

Figure 12. Background correction for spatially integrated spectra as affected by self-absorption. (1) Background in one instrument bandwidth when not subject to self-absorption. (2) Background subject to self-absorption. (3) Line radiation without self-absorption. (4) Line radiation with self-absorption. (5) Amount of background oversubtraction in the presence of self-absorption.

some of the background continuum that happens to fall within the absorption line width of the profile is absorbed.

Although self-absorption reduces the amount of emitted light observed, the misapplication of background subtraction may accentuate the apparent intensity diminution. If background emission were subtracted prior to compensating for self-absorption, background oversubtraction, to an extent shown by region 5 in the figure, would occur.

When spatial resolution of the spectrum is attempted, correction for background remains a critical problem; inadequate background subtraction may lead to the calculation of "negative emissivities," i.e., calculation that some rings of the discharge which should be emitting light are actually absorbing light, and in a linear rather than a logarithmic manner! The concept of negative emission contrasts sharply with experience and intuition; while it is likely that processes other than incorrect background subtraction could cause the calculation of negative emission, incorrect background subtraction is one method by which such negative emission may be derived.

An example illustrating processing of given data in various ways may serve to demonstrate some of the nuances of background correction. Conditions were chosen to be compatible with the examples given in the previous section, i.e., the line profile was taken as being a single-ring emitter in ring 25 and a single-ring absorber of $K_{\gamma} = 0.10$ in ring 26. Note from Figure 8 that

this is a small value for K_j, where little distortion of the lateral or radial profiles occurs.

A correct method for background subtraction in the presence of self-absorption is shown in Figure 13. One first observes the line lateral profile (plot 1) and the background lateral profile (plot 2) in an emission experiment. With the use of a backlight, a lateral absorption profile at the line wavelength is then measured. One could also measure a lateral absorption profile away from the line to observe background (continuum) absorption. In this discussion, it will be assumed that there is no background absorption.

The line lateral absorption profile is inverted using equation (17), and the radial profile so determined is used to deconvolute the line lateral intensity profile of absorption effects. This employs equation (20) and gives plot 3 in Figure 13. Only *after* so compensating for self-absorption, may the background lateral profile be subtracted, giving line intensity over background (plot 4). Finally, the Abel inversion is performed on plot 4 to give the radial line profile over background, the correct desired quantity in Figure 13, plot 5. The essential point is that self-absorption was accounted for by removing its effects upon emission data *before* background was subtracted.

As pointed out previously [equations (16) and (17)], determination of a lateral or radial absorption profile is an experiment distinct from measuring a lateral intensity profile due to the need for a backlighting source. Difficulties in measuring absorption profiles may preclude quantitative compensation for self-absorption and, consequently, prevent correct background subtraction. The backlight must have well-characterized spatial and temporal characteristics, which may be difficult to achieve except with lasers with stable mode structure. Intensity must be repeatable or a monitor provided to compensate for irreproducibility. Perhaps most difficult, the light source must be bright enough to observe a strong low-noise signal even in the presence of strong absorption, yet weak enough so as not to perturb the atomic populations in the plasma being probed. These may be mutually contradictory requirements. Even a moderately intense backlight might cause stimulated emission, giving rise to "negative absorptivity" and negating several assumptions used in the present model. These comments apply to absorption measurements even in the absence of background emission, but background adds an extra phenomenon, and, thus, extra measurements and manipulations, to the characterization of the discharge.

Two other ways in which background emission in the presence of self-absorption could have been (incorrectly) analyzed are shown in Figure 14. Using the same initial data as were used in Figure 13, background is subtracted from the line profile; then either of two courses are available. If it is not realized that self-absorption is present, data processing proceeds to plot 5, where some slight negative emission is calculated and the "spiked" ap-

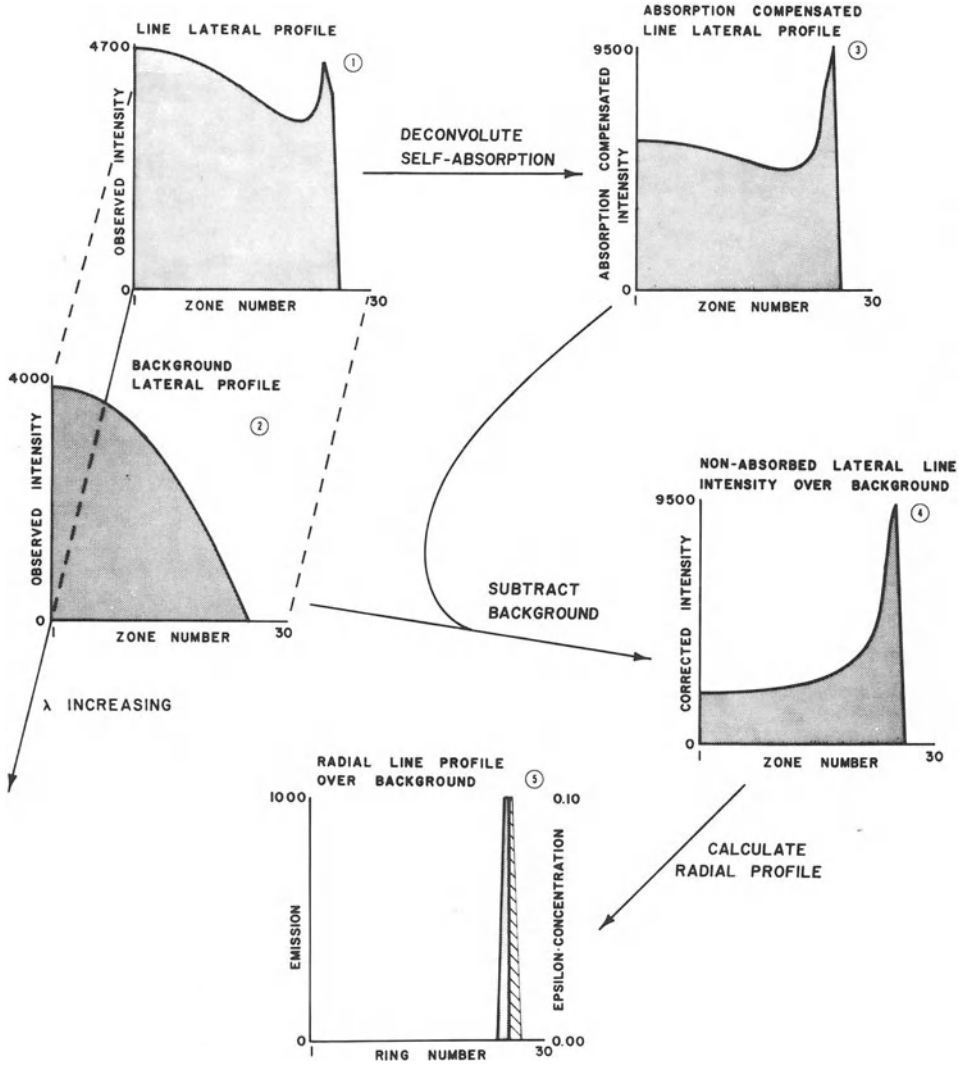

Figure 13. Proper method for background correction in the presence of self-absorption (spatially resolved case). (1) Lateral line emission as viewed through an absorber. (2) Background emission (no self-absorption at this wavelength). (3) Region (1) compensated for self-absorption. (4) Lateral profile at line wavelength corrected for absorption and background. (5) True radial species profile for species giving rise to line radiation and absorption.

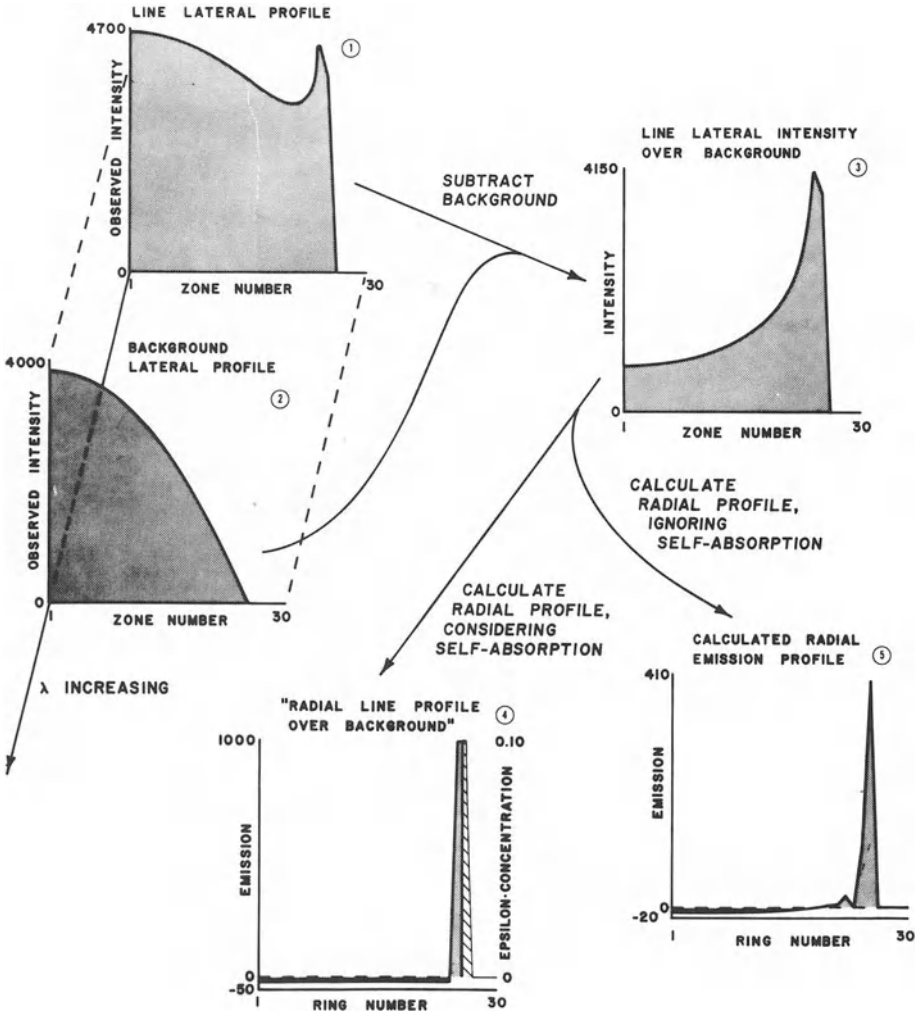

Figure 14. Improper methods for background subtraction in the presence of self-absorption (spatially resolved case). (1) and (2) as in Figure 13. (3) Line intensity over background. (4) Calculated radial profile, self-absorption not considered during lateral-to-radial calculation. (5) Radial profile, absorption accounted for after background subtraction, i.e., in improper order.

pearance of the calculated radial profile indicates, as in the previous section, that self-absorption is present and not taken into account. If, however, self-absorption is compensated in performing the Abel inversion, the calculations yield plot 4 in which the correct J_j and K_j values are calculated in rings 25 and 26, respectively, but negative emission is calculated for all rings from 1 through 24 inclusive.

Recalling that a small K_{26} was used in this example, it should be evident that, at higher K_j values, background overcorrection will be more severe, causing larger amounts of negative emission to be calculated unless the proper sequence of calculational steps is followed. If self-absorption can be compensated as discussed in the previous section, background correction is sufficiently simple that overcompensation need not be a problem.

Oversubtraction of background with consequently calculated "negative emissivities" may be used as a diagnostic for the presence of self-absorption. Earlier work by Goldstein[21] shows calculated negative emissivities for several lines. While it is possible that some mechanism other than self-absorption may have given rise to these calculated results, only the path of overcompensating for background while ignoring self-absorption fits both the procedure of data analysis used by Goldstein and the variety of processes considered by the present authors. Experimental observation of discharge conditions similar to Goldstein's using a backlight to map any absorption present would be necessary to confirm this hypothesis.

8. Instrumental Misalignment and Spark Wander

Regardless of the physical model assumed for a discharge, if valid measurements of the properties of the discharge cannot be made (for example, because of measurement noise or discharge instability), then the model is of little practical utility. If a radial model is assumed as in the preceding discussion, then the lateral zones and radial rings must be well defined, both with respect to the discharge and with respect to the observing instrument. Thus, the meaning of "lateral zone 15" must be well characterized and time-invariant in both the discharge and laboratory reference frames, and refer to a particular spatial location. If either the discharge wanders (that is, the discharge axis is located at various positions as a function of time), the instrument alignment drifts, or the discharge axis and the system optical axis are nonintersecting to begin with, then the data may be of reduced quality or invalid altogether for purposes of spatially resolving the spectroscopic data. Furthermore, if similar misalignments or nonrepeatabilities are viewed in a spatially integrated manner, as is common in spectrochemical analysis, degraded signal-to-noise ratios and worsened sensitivity may result.

Discharge wander may be regarded as an irreproducible optical misalignment in which each discharge passes through a unique spatial path, and

the observed light intensity is spatially averaged as a result. Thus, modeling of wander may be performed by an algorithm consisting of three parts: (1) an algorithm which operates on lateral data as it would be viewed in a properly aligned, spatially stable system to produce data laterally displaced from proper alignment, i.e., shifted with respect to the instrument optical axis; (2) a routine to vary the amount by which the data are shifted so that various distribution patterns for the wander may be modeled; and (3) a normalization routine to give a properly scaled value in each zone for the time-integrated observed intensity. This allows comparison on the same scale as the number of discharges used in modeling changes. To model instrument misalignment, the same procedure may be used except that in step (2), the amount of the shift is set to the amount of instrumental misalignment rather than being varied over a distribution. If the instrument vibrates, misalignment might also be a statistically distributed property. From an observational viewpoint, wander of the discharge or movement of the instrument may have similar consequences.

The routines described here will work only for purely emitting species distributions. Reasons for difficulties in modeling self-absorbed systems will be discussed later. Material illustrating the algorithm is shown in Figure 15.

In view of the assumed cylindrical (or at least bilateral) symmetry of the discharge, observation of the discharge on only one side of the discharge/optical axis should suffice to elucidate fully the discharge structure. Thus, for the radial profile shown in Figure 15, plot 1, it is sufficient in a stable discharge to look only at that portion of the lateral profile shown in Figure 15, plot 2, where the vertical axis in the inset corresponds to both the discharge and instrument optical axes. In such a case it is assumed that the mirror image of the lateral profile (plot 2) would appear on the other side of the axis. Thus, when wander or misalignment occurs, either portions of the lateral profile observed in a stable aligned discharge are obscured as they pass to the left of the axis, or portions of the discharge normally not viewed appear in the viewing field so that the apparent diameter of the discharge increases.

Figure 15, plot 3, shows three lateral profiles which would result from various amounts of wander in a single discharge. If the lateral profile has to be shifted by S zones, then the intensity in zone N after the shift is completed may be determined from the unshifted data as follows:

$$I_S(N) = I(N-S) \qquad \begin{matrix} S \leqslant 0 & \text{and} & N-S \leqslant i_{\max} \\ \text{or} \\ S \geqslant 0 & \text{and} & N-S \geqslant 1 \end{matrix} \tag{22}$$

$$I_S(N) = 0 \qquad S \leqslant 0 \quad \text{and} \quad N-S > i_{\max} \tag{23}$$

$$I_S(N) = I(S-N+1) \qquad S \geqslant 0 \quad \text{and} \quad N-S < 1 \tag{24}$$

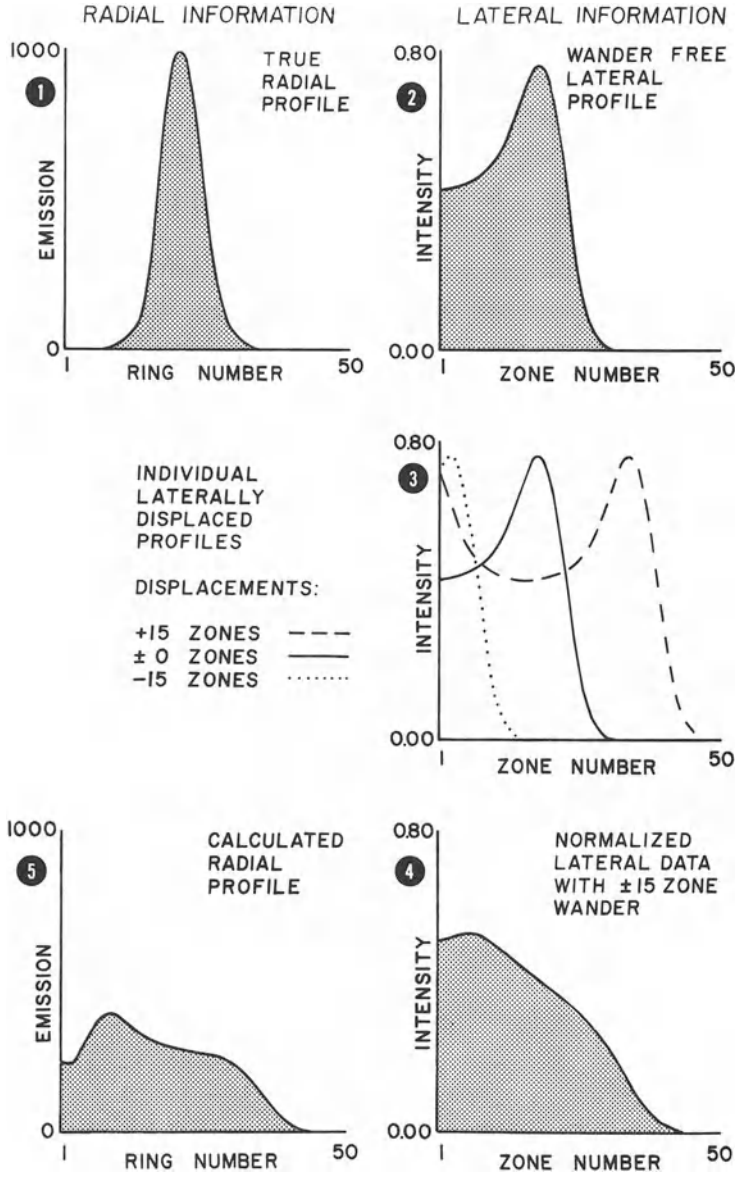

Figure 15. Computational steps in modeling discharge wander for a purely emitting source.

In all cases, S and N are integers and N may range from 1 to $i_{e\max}$; I and I_S are, respectively, the intensities before and after shifting in the zone indicated within the parentheses. These formulas account not only for shifting and for the symmetry axis, but also assume for a negative shift [e.g., Figure 15, plot 3)] that there is no intensity beyond zone $i_{e\max}$.

If the wander distribution is such that the discharge axis for any random discharge is uniformly distributed ± 15 zones from the optical axis, the total intensity distribution is as shown in Figure 15, plot 4. The uniform distribution was obtained by scaling and offsetting the pseudorandom numbers calculated by the RND function in Univac BASIC. Figure 15, plot 5 shows the radial profile obtained by inverting the lateral profile in Figure 15, plot 4. Inversion was performed by using entry point 7 as shown in Figure 6. The qualitative differences between plots 1 and 5 in Figure 15 are readily evident. Thus, manipulation of lateral data by appropriate shifting of subscripts clearly shows the effects of unstable discharges on the inversion of lateral information to radial information.

Many distributions besides the uniform pseudorandom one shown here may be used. If the lateral distribution is merely offset by S zones, the effect of gross optical misalignment may be modeled. A Gaussian random distribution may be obtained by using appropriate software as well.

The wander algorithm may be applied to radial data as well as to lateral data. However, the resulting manipulation does not model spark wander. Rather, variable apparent expansion and contraction of the radial species distribution about the discharge axis are modeled. Experimentally such a phenomenon might be observed in a time gated spectrometer [25] if there was substantial gate jitter at a point of rapid change in discharge current.

The effects that wander and misalignment may have on data quality will be illustrated by using the example of a train of spark discharges. The zone width applicable to a single such discharge is typically 0.05 mm, and it will be assumed that only emission takes place. First, the question of proper system alignment will be addressed, and then the problem of discharge or spark wander will be treated.

Figure 16 details the adverse effects that even minor misalignment may have on the determination of radial structure in a spark discharge. In the first two plots, the system is assumed to be properly aligned; the spark axis coincides with the system optical axis. Labeling the lateral zones on the left-hand side of the discharge with an L and the right-hand lateral zones with an R for easier reference, it may be seen that for both observed and inverted profiles, the left-hand and right-hand views of the discharge are identical (the fact that symmetry across the discharge and optical axes could be expected was used in deriving the formulation of the Abel inversion used in this discussion). In the second two plots, the system has been assembled such that the spark axis is two zones (e.g., 0.1 mm or 0.004 in.) to the right of the

optical centerline. If one again uses the optical centerline as the division point between the left-hand and right-hand observation zones and performs the Abel inversion separately on each set of zones, asymmetry in the calculated radial profile is readily evident. Note specifically that maximum calculated emission differs for the left-hand and right-hand calculations, and that the ring in which maximum emission occurs appears to be ring 18 for the left-hand calculation and ring 22 for the right-hand calculation. Note also that "negative emission" is calculated near the "spark axis" for the left-hand radial profile and positive emission near the axis for the right-hand radial profile. Although the true physical situation is as portrayed in plot 2 in Figure 16, plot 4 is the set of profiles which is obtained upon Abel inversion of the data in plot 3. Thus, a seemingly minor misalignment may, depending on which half of the discharge is observed, give rise to physically unreal and disparate views of where emission is taking place and to what extent.

The question then arises as to when misalignment might be noticeable. If a photographic plate is used for a detector, no centerline is etched onto the plate; the centerline is determined experimentally in each spectrum. Thus, various points in the line profile may be tentatively chosen as the centerline, finally employing that point which gives a symmetrical calculated radial profile (if the line itself is asymmetric, then either wander is occurring as discussed below or the cylindrical model of the discharge is inadequate). If a diode array or vidicon detector is used, suitable computer routines can be envisaged that would choose the centerline based on the incoming intensity data. Where problems would be most likely to occur would be in situations where the centerline is simply assumed to be in a particular location and uncritically used. For example, such problems could occur if the 55th diode in a diode array were observed to be the centerline in one experiment and then assumed to be the centerline for all later experiments. In this case, small changes in system alignment could render the calculation of a radial profile from the lateral intensity data to be little more than a mathematical exercise. As shown in Figure 16, a precision of better than ± 2 zones is necessary in setting the spatial location of the spark axis and optical centerline.

While Figure 16 shows the effect of a displacement of the spark axis from the optical axis, it does not address the problem of discharge instability or wander. If careful attention is not paid to the spark environment and source design, the spark will not occur repeatedly in the same spatial location relative to the optical axis and object focal plane, but rather will wander, either by anchoring to various locations on the cathode electrode or by "kinking" and following tortuous paths between the electrodes. As the coincidence of the spark axis and the system optical axis may be random throughout a given train of sparks, the concept of "lateral zone" becomes ill-defined; a particular zone when viewed from the spark axis reference frame has a random counterpart in the laboratory reference frame. So that the effects of

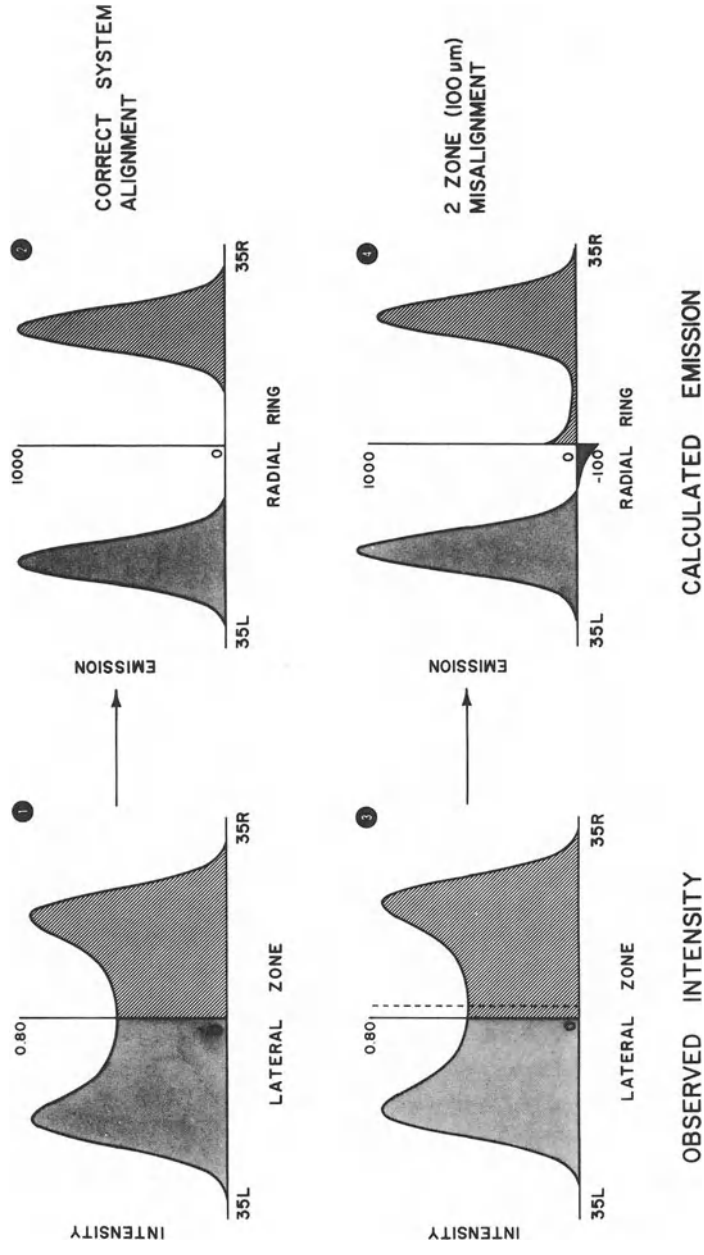

Figure 16. Effect of system alignment on the Abel inversion.

wander may be discussed in an internally consistent manner, the lateral zones will be frozen in the laboratory frame in the position they would occupy if the spark were stable and properly aligned with the system optical axis. Thus, when wander occurs, the spark can be said to move across the (laboratory fixed) lateral zones, and the extent of the wander can be expressed in terms of the number of zones traversed by the spark axis. Wander in a positive direction will be taken as movement of the spark axis to the right, and negative wander will be taken as movement of the axis to the left. Zone (and ring) size may be set at 0.05 mm. The composite view of numerous discharges which wander will be a blurred picture of the processes occurring as different parts of the discharge are viewed through a given lateral zone with each firing of the discharge.

Figure 17 illustrates the distressing effects wander can have on both observed intensity and inverted profiles. To produce this series of plots, the lateral profile which would be observed for an off-axis Gaussian radial emission profile [as would be expected for emission lines of neutral species [16,18,20,21]] centered in ring 20 and with a half-width of four rings was computed. This is the profile one would observe if no wander occurred. The first four steps shown in Fig. 15 were then performed, allowing varying degrees of wander, to produce the left-hand three-dimensional plot in Figure 17. Note that as the maximum extent of wander varies from ± 5 zones (± 0.25 mm) to ± 40 zones (± 2 mm), the off-axis character of the intensity profile is lost, and an on-axis apparently structured profile appears. At sufficiently high degrees of wander, some intensity data are lost as portions of the imaged discharge are vignetted by the edge of the optical window. Here, a spectrometer slit height of 5 mm has been assumed, such that light incident on the slit more than ± 2.5 mm removed from its centerline would be lost. If this particular line profile were viewed in a spatially integrated manner, then the line intensity would appear to decrease as wander increased beyond ± 25 zones, simply because of vignetting by portions of the instrument, e.g., slits, aperture masks, or the grating.

But, even more dramatic than the distortions occurring in the lateral intensity profiles in the presence of wander is the distortion of the radial profiles computed using the Abel inversion. With only ± 5-zone wander, the apparent maximum peak height (in zone 20) has been reduced from its correct value by 25%; the half-width of the emission profile has also increased by 50% to six rings instead of four. And with only ten zones of wander present, the Gaussian nature of the radial profile is no longer evident. As wander continues to increase, the quality of the calculated radial data continues to decrease. Furthermore, and most unfortunately, the apparent fine structure in the calculated radial profile increases with increasing wander, incorrectly indicating that complicated chemistry is occurring in the discharge.

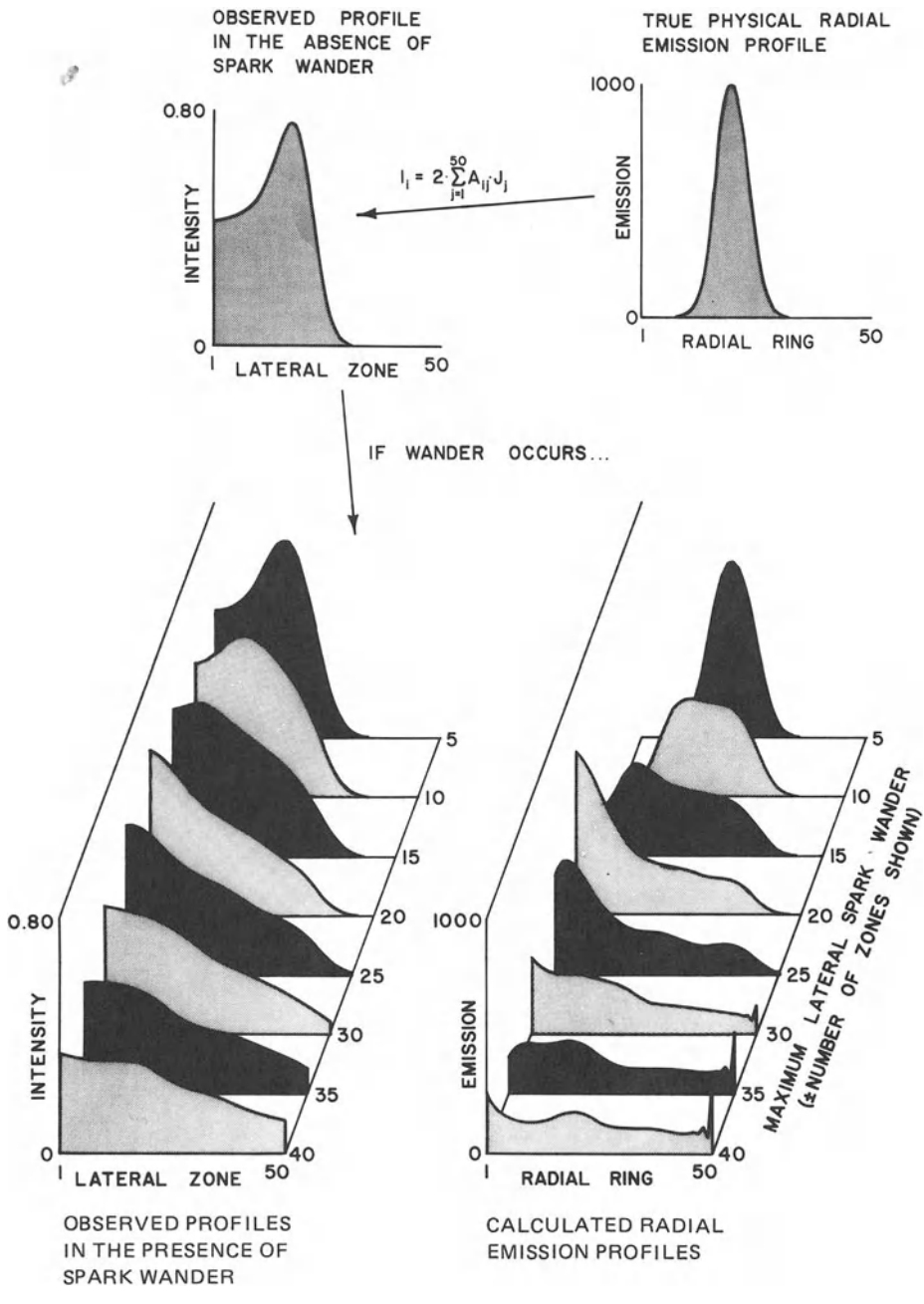

Figure 17. Effect of spark wander on lateral and calculated radial profiles.

At high degrees of wander, when light is being lost off the edge of the viewing window, jagged spikes appear at the outer edge of the calculated radial profiles. This phenomenon is similar to that observed when self-absorption took place and was not properly taken into account. While superficially it might appear that data smoothing is necessary to remove these spikes, in fact, the problem once again is that a physical phenomenon (in this case wander) is occurring which is not being taken into account in the Abel calculations. Rather than smoothing data to get rid of unwanted "noise," the fundamental cause of the problem should be alleviated, i.e., the discharge should be stabilized. Indeed, this is the major conclusion to be drawn from all the modeling thus far presented: various nuances and anomalies seen in lateral and radial views of a discharge are just as likely to have arisen from processes other than emission affecting the lateral profile as they are to have arisen from spatial variations in emission processes. Ignoring these anomalies or attributing them categorically to noise not only weakens the quality of the data so treated, but, moreover, obscures the nature of nonradiative processes taking place in the discharge. In some cases (such as discharge wander), the irregularities in the data may be removed by suitable control of the discharge; in others (for example, self-absorption), experimental procedures must be adjusted to adequately observe the phenomenon in question. Critical evaluation of which parameters need to be monitored in studying a given discharge is necessary, so that an accurate picture of the processes active in the discharge may be generated.

9. Summary on Wander

These algorithms in combination contain several limitations. First, there is no provision for wander in a direction parallel to the optical axis in addition to the situation modeled, i.e., wander perpendicular to the axis. This stems from the uniform processing of data regardless of relative position along the optical axis, a circumstance derived from the use of all depth-of-field weighting factors equal to 1.0 in the area matrix calculation. In a related limitation, there is no provision for modeling a tilt of the discharge with respect to the line formed by instrumental slits. This nonideality could be modeled if the area matrix were calculated for an ellipsoidal discharge rather than a cylindrical one (a plane slicing through a cylinder traces out an ellipse in general; a cylindrical slice is obtained only when the plane is perpendicular to the cylinder axis).

Self-absorption effects can be modeled only to a limited extent. If self-absorption is the only process occurring, shifting as described above could be used with little modification to model the effects of wander. However, if both emission and absorption occur, the modeling procedure breaks down. No longer is there a defined boundary to the emission or an inner spatial limit to

the absorption. This violates the assumption of spatial segregation of emission and absorption required by the equations given previously. By implication, even ± 1 zone wander is sufficient to preclude valid use of the spatially segregated emission–absorption model for the discharge if self-absorption is present. Analysis of emission and absorption in an unstable discharge demands a model which allows both emission and absorption in the same spatial region.

Finally, there are the implicit assumptions that no chemical changes occur which would change the radial profiles when wander occurs, and that wander is a discharge property which has no effect on any other property and is not influenced by any other characteristic. In fact, observable changes in discharge properties occur in conjunction with changes in the degree of discharge wander.[35,36] Distortions in radial and lateral profiles as a result of wander are, therefore, expected to be greater in experimental work than is demonstrated by the present modeling procedure.

10. True Measurement Noise

Whereas many phenomena occurring in a discharge may give rise to features within lateral and radial profiles which masquerade as noise, in fact, noise in the measurement of intensities in each lateral zone can lead to the catastrophic failure of the Abel inversion. The problems associated with noise have been generally recognized and treated in the literature.[37–39] Apparently the problem is fundamental, and measurement noise can lead to the highly inaccurate computation of emission, particularly in rings near the discharge axis. The problem stems from the fact that observations on regions of a discharge near the discharge axis usually are only made by looking through the outer rings of the discharge. To "peel away" the effects of these outer rings demands that information on those outer rings, collected in zones far removed from the optical axis, be employed. Thus, calculational and measurement errors made on the outer reaches of the discharge accumulate to degrade information quality on the center of the discharge.

Various data smoothing schemes have been proposed in the articles previously referenced, but no totally satisfactory noise elimination method has yet been proposed. In this discussion, no new proposals will be made concerning solution of the "noise problem" beyond suggesting that data collection systems be used which allow for signal averaging and, thus, improved signal-to-noise ratios. Our efforts will be directed instead to demonstrating the effects of measurement noise on lateral and radial profiles for a specific set of experimental conditions; e.g., that of a spectrometric system employing photographic detection. Whereas numerous other detection systems could be modeled, photographic detection was chosen, as this particular means of detection has been used extensively in our previous

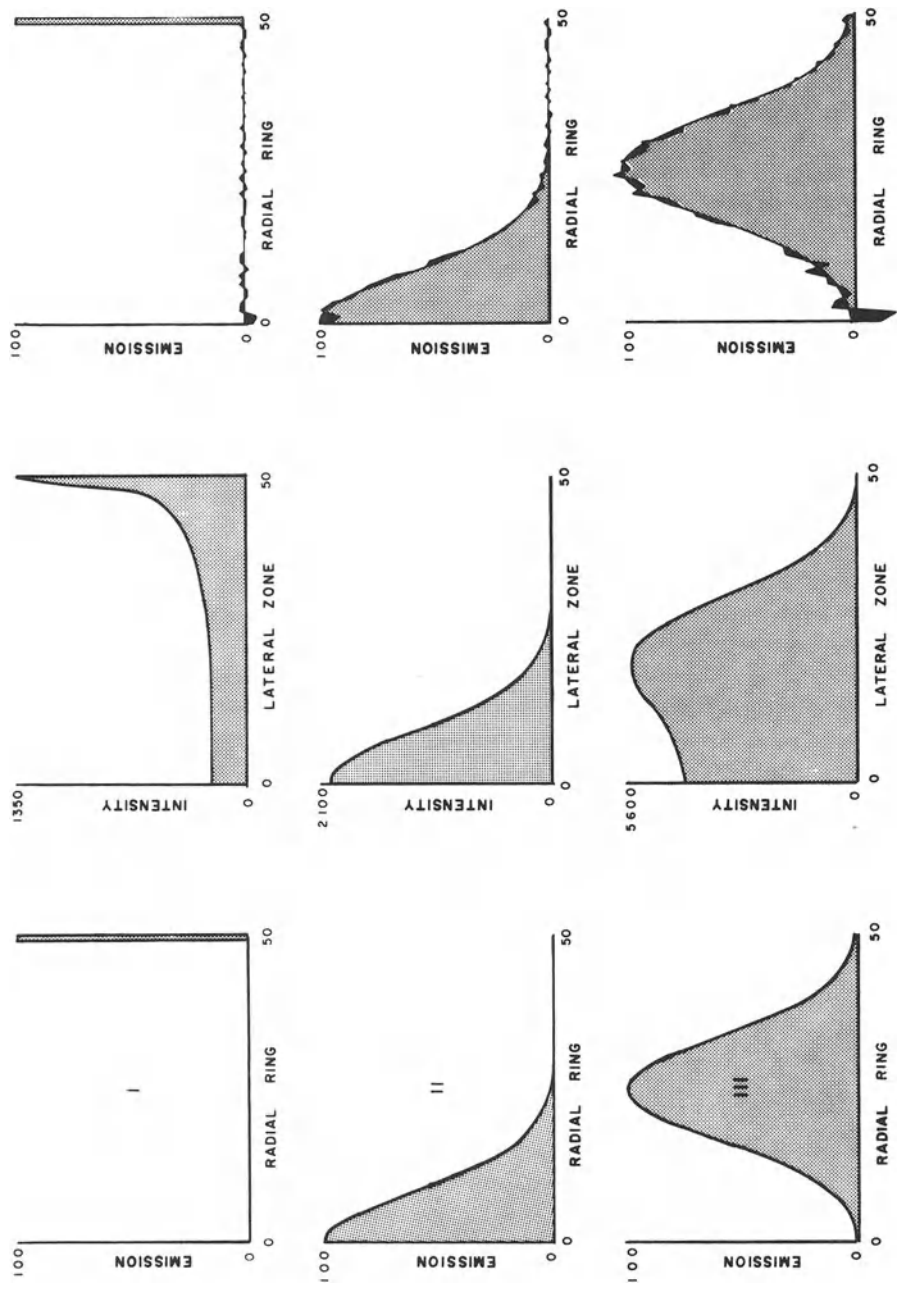
EMISSION
100
0
0
RADIAL RING
50
I
INTENSITY
1350
0
0
LATERAL ZONE
50
EMISSION
100
0
0
RADIAL RING
50
II
INTENSITY
2100
0
0
LATERAL ZONE
50
EMISSION
100
0
0
RADIAL RING
50
III
INTENSITY
5600
0
0
LATERAL ZONE
50

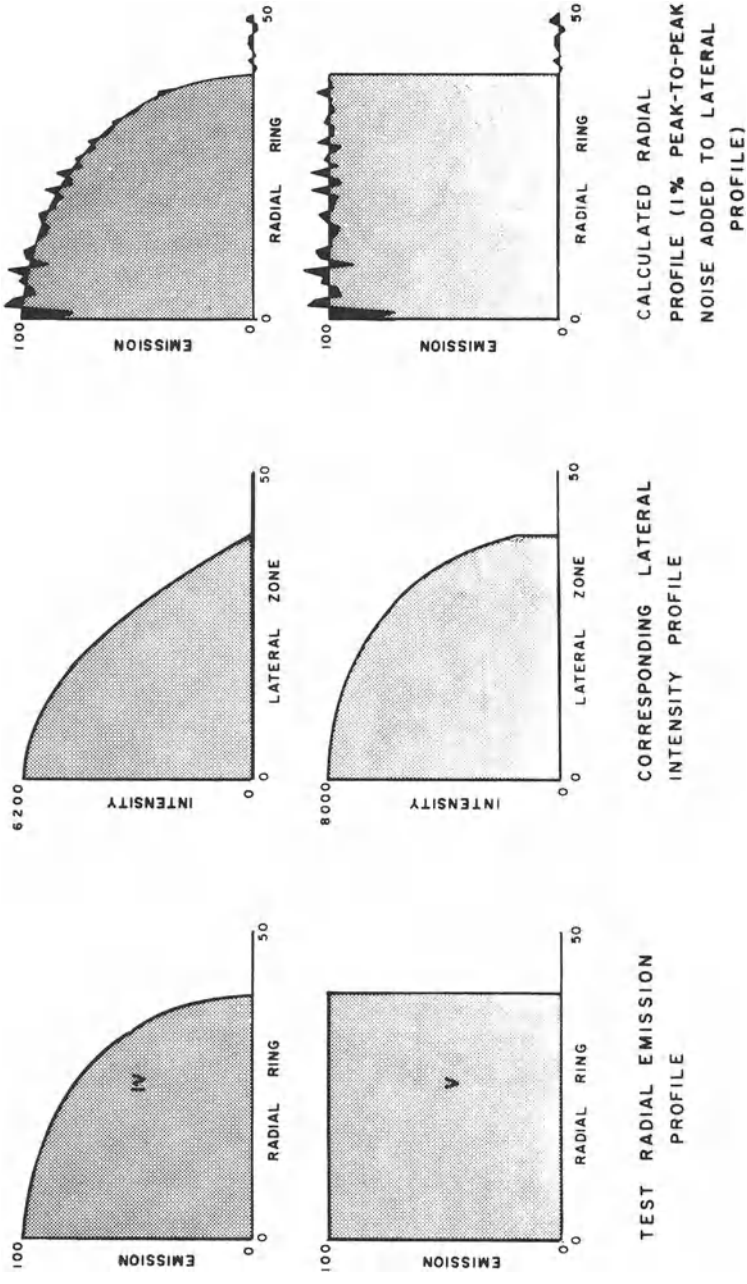

Figure 18. Effect of noise on the Abel inversion as a function of the profile shape.

research.[16,18,20,21]. If graininess in the emulsion is taken as the major contributor to noise in a system with photographic detection, then the noise amplitude is independent of the observed intensity and is dependent instead on the choice of the photographic plate grain size. By choosing exposure times appropriately, the maximum plate density (corresponding to the maximum light intensity within a particular line profile) can be sufficiently high so that the best signal-to-noise ratio within the line profile is some constant independent of the line shape.

For modeling purposes, it has been assumed that the signal-to-noise ratio of the most intense zone within a line is 100 in a square on a photographic plate 0.05 mm on a side. An optimum signal-to-noise ratio of 100 is sufficiently high so that the noise is essentially invisible on a plot of the lateral intensity profile. Nevertheless, upon Abel inversion, the radial profile may be extremely noisy. It would appear, to a first approximation, that if the noise in a density plot of a line profile obtained photographically is visible, then the Abel inversion cannot accurately be performed. Smoothing may be of assistance in alleviating the problems caused by measurement noise, but with at most 50 points in the data set to be smoothed, care must be taken that the smoothing operation does not distort the line profile.

Figure 18 is a demonstration of noise effects for radial profiles of various shapes. Here, noiseless intensity profiles are plotted with their corresponding noisy and noiseless radial profiles. The signal-to-noise ratio in the zone with the highest observed intensity was set to 100, and the same sequence of pseudorandom numbers was used to generate the noise for each profile. As the amount of internal structure in the radial profile decreases, the noise susceptibility of the Abel inversion increases. Also note that noise is more of a problem on-axis than off-axis. This is particularly frustrating as one is generally performing the Abel inversion in order to get information about the core of the discharge!

Although the problem of noise sensitivity of the Abel inversion in the presence of self-absorption has not been addressed, it may be surmised that noise will cause no less of a problem when self-absorption complicates the physical situation than it does without such complications. It also would seem reasonable that discharge wander could only amplify the deleterious effects of intensity measurement noise.

11. Spatially Unseparated Emission and Absorption

While the physical separation of emission and absorption into concentric rings may be used to describe some spectral lines in electrical discharges, there are situations[40] where such segregation does not occur. Furthermore, unless spatially concommitant emission and absorption are prohibited in a discharge

model, modeling or the description of discharge wander is severely restricted. A model is derived in the following for spatially unseparated emission and absorption deconvolution, in which it is assumed that both emission and absorption take place in a cylindrically symmetrical manner, but without separation of the two processes (necessarily) into separate rings. In the limit of process segregation or in the absence of one of the two processes, the formulas reduce to those already derived. While no discharge modeling has been performed to date using these formulas, they do provide a theoretical framework for expansion of the modeling procedures described earlier.

The model will be derived in two stages: (a) derivation of light exiting from a rectangular region in which both emission and absorption occur, and (b) application of the results of (a) to the modeling of a cylindrical discharge in which the ring/zone/area segment geometry is the same as that described previously.

The first stage of the problem has previously been addressed[41] using notation which is slightly different from that employed here. An additional assumption needed here is that a high-dispersion spectrometer is used so that there is no variation in spectral properties across the bandpass of the instrument.

A rectangular homogeneously emitting/absorbing region is shown in Figure 19. Over a pathlength b, the region emits with emissivity ηc and absorbs with absorptivity εc per unit length. The region is broken into N equal subunits of length Δx so that

$$N\Delta x = b \tag{25}$$

The assumption is now made that a particular subunit emits light and absorbs light which was emitted by subunits farther from the observer. Thus, subunit 1 emits but does not absorb. The intensity leaving subunit 1 towards the observer (in the direction shown by the arrow in the figure) is

$$I_1 = \eta c \Delta x \tag{26}$$

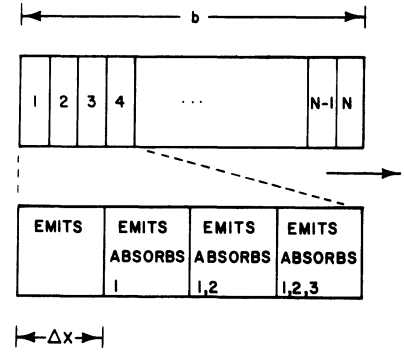

Figure 19. Homogeneous rectangular emitter/absorber, disected for numerical modeling.

Subunit 2 emits light and transmits some of the light impinging on it from subunit 1:

$$I_2 = \underbrace{\eta c \Delta x}_{\text{from subunit 2}} + \underbrace{\eta c \Delta x \, 10^{-\varepsilon c \Delta x}}_{\substack{\text{transmitted} \\ \text{from subunit 1}}} \tag{27}$$

which is

$$I_2 = \eta c \Delta x + I_1 10^{-\varepsilon c \Delta x} \tag{28}$$

or

$$I_2 = \eta c \Delta x (1 + 10^{-\varepsilon c \Delta x}) \tag{29}$$

Similarly,

$$I_3 = \eta c \Delta x + I_2 10^{-\varepsilon c \Delta x} \tag{30}$$

$$I_3 = \eta c \Delta x (1 + 10^{-\varepsilon c \Delta x} + 10^{-2\varepsilon c \Delta x}) \tag{31}$$

[Equation (31) is obtained from equation (30) by inserting I_2 as expressed in equation (29) into equation (30).] This may be continued until

$$I_N = \eta c \Delta x (1 + 10^{-\varepsilon c \Delta x} + \cdots + 10^{-(N-1)\varepsilon c \Delta x}) \tag{32}$$

$$I_N = \eta c \Delta x \sum_{i=0}^{N-1} 10^{-i\varepsilon c \Delta x} \tag{33}$$

When $i = 0$, $i\Delta x = 0$; when $i = N-1$, $i\Delta x = b - \Delta x$. In the limit as $\Delta x \to 0$, the summation in (33) becomes an integral:

$$I_N = I_{\text{observed}} = \eta c \int_0^b 10^{-\varepsilon c x} \, dx \tag{34}$$

From a table of integrals this may be evaluated

$$I_{\text{observed}} = \frac{\eta c}{2.3026 \varepsilon c} (1 - 10^{-\varepsilon c b}) \tag{35}$$

Note that ηc and εc should be regarded as grouped quantities. By analogy to earlier equations, $\eta c = J$ and $\varepsilon c = K$. In addition, the fraction in (35) may be

multiplied by 1 in any form, here taken as b/b:

$$I_{\text{observed}} = \frac{Jb}{2.3026Kb}(1-10^{-Kb}) \tag{36}$$

In all equations from (26) through (36), the width of the region in question was ignored. Absorption is independent of dimensions not parallel to the line of sight. Specifically, absorption is independent of zone width. Total emitted light is proportional to zone width. Further total emission is proportional to axial slice thickness whereas absorption is independent of this thickness:

$$V = \text{region volume} = b \cdot W \cdot Z = A \cdot Z \tag{37}$$

where Z is the axial slice thickness as defined by dimension 8 in Figure 1. Finally,

$$I_{\text{observed, 3-dimensional emitter}} = \frac{JV}{2.3026Kb}(1-10^{-Kb}) \tag{38}$$

The second part of the problem can now be tackled. If each segment of ring/zone overlap as shown in Figures 1 and 2 is taken as a homogeneous emitting/absorbing medium the logic outlined previous can be extended to the deconvolution of spatially concomitant emission and absorption. Each ring j has the emission coefficient J_j and the absorption coefficient K_j. Based on the area matrices discussed earlier, emission volume is $A_{ij} \cdot Z$ for each segment [in general, Z is a constant and may be factored out of the expressions below; in formulas prior to (37) Z was taken as 1 and tacitly ignored]. The absorption pathlength (analogous to b, defined earlier) is still described by the L_{ij} matrix.

Total light output expressions will now be derived for zones 49 and 50; a general formula will then be derived, followed by a description of a plausible experiment/computational sequence for using the formulas.

Figure 20 shows the geometry and properties of the outer zones of a discharge. In zone 50, observed intensity is that which emerges from the front of ring 50 and consists of all the intensity escaping from the front part of $A_{50,50}$ plus the portion of light emitted in the rear section of $A_{50,50}$ which is transmitted by the front section.

Light emerging from the front section only, based on equation (38) is given by

$$I_{50}(\text{front only}) = \frac{J_{50}A_{50,50}Z}{2.3026\,K_{50}L_{50,50}}(1-10^{-K_{50}L_{50,50}}) \tag{39}$$

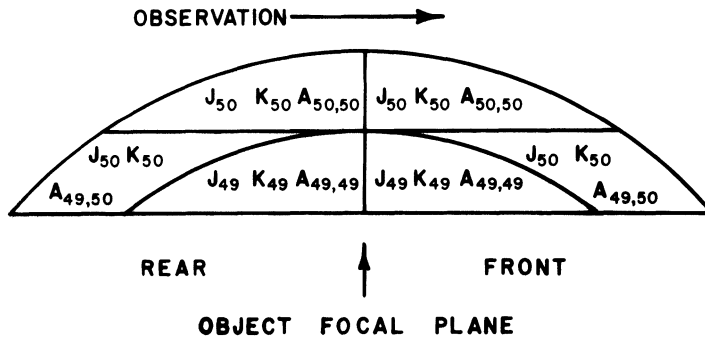

Figure 20. Geometry and properties of outer rings used to illustrate spatially simultaneous emission and absorption.

As the quantity

$$\frac{1-10^{-K_jL_{ij}}}{2.3026\,K_jL_{ij}}$$

will appear repeatedly, label it F_{ij}, the *fraction* of light emitted *within* one area segment which successfully escapes from that segment. Also by analogy to Beer's law, define

$$T_{ij}=10^{-K_jL_{ij}} \tag{40}$$

(Beer's law states $I/I_0=T=10^{-\varepsilon cb}$.) Thus,

$$F_{ij}=\frac{T_{ij}-1}{2.3026\log_{10}T_{ij}} \tag{41}$$

So in shorthand notation, equation (39) becomes

$$I_{50}(\text{front only})=A_{50,50}J_{50}ZF_{50,50} \tag{42}$$

If the discharge could be sliced at the object focal plane, it would be possible to observe the light coming only from the rear of the discharge. By the same logic as above

$$I_{50}(\text{rear only, at object focal plane})=A_{50,50}J_{50}ZF_{50,50} \tag{43}$$

What is actually observed is the intensity computed in equation (42) plus the fraction of the intensity given in equation (43) which penetrates the front half

of the discharge. The front half of the discharge acts as a Beer's law cell to the rear half of the discharge, so the fraction of the rear half's light which escapes is simply $T_{50,50}$ in this case. Thus,

$$I_{50}(\text{observed}) = A_{50,50}J_{50}ZF_{50,50}(1 + T_{50,50}) \tag{44}$$

which is equation (42) plus $T_{50,50}$ times equation (43).

Note that if there is no absorption, $T_{50,50} = F_{50,50} = 1$, $I_{50} = A_{50,50}J_{50}Z \cdot 2$, and the result from equation (5) is recovered.

For zone 49, a similar procedure may be used. A total of four area segments are involved, two on each side of the object focal plane:

$$I_{49}(\text{observed}) = I_{49,50}(\text{rear}) + I_{49,49}(\text{rear}) + I_{49,49}(\text{front}) + I_{49,50}(\text{front}) \tag{45}$$

where each I term on the right refers to the intensity generated in a given segment which escapes the discharge:

$$I_{49,50}(\text{front}) = A_{49,50}J_{50}ZF_{49,50} \tag{46}$$

$$I_{49,49}(\text{front}) = A_{49,49}J_{49}ZF_{49,49}T_{49,50} \tag{47}$$

$$I_{49,49}(\text{rear}) = A_{49,49}J_{49}ZF_{49,49}T_{49,49}T_{49,50} \tag{48}$$

$$I_{49,50}(\text{rear}) = A_{49,50}J_{50}ZF_{49,50}T_{49,49}T_{49,49}T_{49,50} \tag{49}$$

Each equation from (46) through (50) gives the value of a term in equation (45) in terms of the emission escaping from a given segment [as in equation (42) times the transmission of all the absorption cells between the emitter and the observer. Combining equations (45) – (49) gives

$$I_{49} = Z\{A_{49,50}J_{50}F_{49,50}(1 + T_{49,50}T_{49,49}^2) + A_{49,49}J_{49}F_{49,49}[T_{49,50}(1 + T_{49,49})]\} \tag{50}$$

This sequence could be continued, but a pattern is developing. A general formula can now be developed by breaking the problem in half. First, a general formula for I_i will be developed for the front half of the discharge only, then the contribution from the rear half will be added.

Let the number of rings or zones in the model be $i_{\max}$ and/or $j_{\max}$. Let the subscript f stand for something occurring in the front of the discharge and

the subscript r stand for something occurring in the rear of the discharge. In general,

$$(I_{i,j})_f = A_{ij}J_jZF_{ij}T_{i,j+1}T_{i,j+2}\cdots T_{i,j_{\max}} \tag{51}$$

[Comparison to equation (47) may be helpful.] Equation (51) could be used in general except that the case $j = j_{\max}$ gives an undefined expression (the first T employed is $T_{i,j+1}$; up to this point $j > j_{\max}$ has been disallowed. If $j = j_{\max}$, $T_{i,j+1} = T_{i,j_{\max}+1}$ is undefined). So a new definition is needed:

$$T_{i,j_{\max}+1} \equiv 1 \tag{52}$$

This allows equation (51) to be rewritten

$$(I_{i,j})_f = A_{ij}J_jZF_{ij}\prod_{l=j+1}^{j_{\max}+1} T_{il} \tag{53}$$

Or, adding all of the contributions from the front rings together

$$(I_i)_f = \sum_{j=i}^{j_{\max}} A_{ij}J_jZF_{ij}\prod_{l=j+1}^{j_{\max}+1} T_{il} \tag{54}$$

Equation (54) is obtained by summing equation (53) over all of the plausible values of j. As illustrated in Figures 1, 2, and 19, the smallest value of j for which there is ring zone overlap is for $j = i$. See also the discussion concerning equations (1)–(3).

Looking only at the rear half of the discharge up to the object focal plane, the order in which absorption occurs is reversed compared to that in the front half of the discharge. In the front half, the ring whose output passes through the most absorption cells is that closest to the object focal plane; in the rear half of the discharge the light most subject to absorption, as viewed by an observer, is that farthest from the object focal plane. This emission occurs for light emitted in the outermost ring. Thus, up to the object focal plane, absorption occurs in rings $i, i+1, \ldots, j-1$. Again the innermost ring which has $A_{ij} \neq 0$ is for $i = j$. Again a problem occurs if an analog to equation (51) is written, in that an undefined subscript may arise. The analog to (51) is

$$(I_{i,j})_{r,\text{ to object focal plane only}} = A_{ij}J_jZF_{ij}T_{i,j-1}T_{i,j-2}\cdots T_{i,i} \tag{55}$$

If $j = i$, then $T_{i,j-1}$ is undefined. So again by definition

$$T_{i,i-1} \equiv 1 \tag{56}$$

and

$$(I_i)_{r,\text{ to object focal plane only}} = \sum_{j=i}^{j_{\max}} A_{ij} J_j F_{ij} Z \prod_{l=i-1}^{j-1} T_{il} \tag{57}$$

[This is analogous to equation (54). The only change is in the range over which the transmission product is taken.]

The light from the rear half of the discharge sees the front half of the discharge as a pure Beer's law cell of transmission:

$$(T_i)_r = \prod_{m=i}^{j_{\max}+1} T_{im} \tag{58}$$

This is because the net transmission of a region is the product of the transmissions of each segment through which the light passes. Thus,

$$(I_i)_r = \left(\prod_{m=i}^{j_{\max}+1} T_{im} \right) \left(\sum_{j=i}^{j_{\max}} A_{ij} J_j F_{ij} Z \prod_{l=i-1}^{j-1} T_{il} \right) \tag{59}$$

Finally, in any zone i

$$I_i = (I_i)_f + (I_i)_r = \text{equation (54)} + \text{equation (59)}$$

$$= \sum_{j=i}^{j_{\max}} A_{ij} J_j F_{ij} Z \left[\prod_{l=j+1}^{j_{\max}+1} T_{il} + \left(\prod_{m=i}^{j_{\max}+1} T_{im} \right) \left(\prod_{l=i-1}^{j-1} T_{il} \right) \right] \tag{60}$$

While equation (60) is a complete description of how an intensity I would appear in zone i based on emissivity J_j and absorptivity K_j in each ring j, it has some computational redundancy. Specifically, the term

$$\prod_{m=i}^{j_{\max}+1} T_{im}$$

may be split up as follows:

$$\underset{a}{\prod_{m=i}^{j_{\max}+1} T_{im}} = \underset{b}{\prod_{m=i-1}^{j_{\max}+1} T_{im}} = \underset{c}{\prod_{m=i-1}^{j-1} T_{im} \cdot T_{ij} \cdot \prod_{m=j+1}^{j_{\max}+1} T_{im}} \tag{61}$$

Going from step a to step b in equation (61) employs only equation (56). The conversion from step b to step c breaks up the product into subproducts

Table 4. Definition of Terms in Equation (62)

Item	Definition	Unit
A_{ij}	Area of overlap between ring j and zone i	cm^2
L_{ij}	Absorption pathlength	cm
Z	Slice thickness	cm
J_j	Emission coefficient in ring j	$W \cdot cm^{-3} \cdot nm^{-1} \cdot sr_{-1}$
I_i	Observed intensity in zone i	$W \cdot cm^{-2}$
K_j	Absorption coefficient in ring j	cm^{-1}
T_{ij}	Transmission through zone i ring j intersection $T_{ij} = 10^{-L_{ij}K_j}$	Unitless
F_{ij}	Fraction of light emitted within A_{ij} which escapes. Defined in equation (41).	Unitless

with the goal of obtaining expressions matching other terms in equation (60). Inserting step c into equation (60) and regrouping terms gives

$$I_i = \sum_{j=i}^{j_{\max}} A_{ij} J_j F_{ij} Z \prod_{l=j+1}^{j_{\max}+1} T_{il} \left[1 + T_{ij} \left(\prod_{m=i-1}^{j-1} T_{im} \right)^2 \right] \tag{62}$$

A summary of term definitions, including units, for use with equation (62) appears in Table 4.

The terms included in equation (62) may be individually interpreted. The terms between the summation and the first product symbol arise from emission only except for the F_{ij} term. All properties in these terms occur within a fixed area segment. The other terms describe how the light emitted in the first term leaves the discharge to be seen by an observer. The first product, outside the parentheses, describes absorption which occurs to all light leaving a particular ring, whether in the front or rear of the discharge. The squared term in parentheses states that light emitted in the rear of the discharge is absorbed by inner rings twice, once in the rear half of the ring and once in the front half. The lone T_{ij} accounts for the light emitted in the rear of ring j which is absorbed on the way out of the discharge through the front of ring j.

The use of equation (62) would require two experiments to be performed in order to determine J_j and K_j, the unknown radial quantities in a discharge. In the first experiment, an absorption profile would be determined and in the second experiment, an emission profile obtained. Data from both experiments would be needed to obtain radial absorption and emission distributions.

In each zone i, suppose that a backlight has an intensity I_{i0}. In the first experiment, intensity in each zone is determined with the backlight on. In the second experiment, intensity is determined with the backlight off. In the first experiment, the intensity measured in each zone is I_{iw}, in the second, I_i [the second experiment is a pure emission experiment in the manner of Goldstein,[21] Sacks,[20] etc.]. The transmission observed in each zone T_i is given by

$$T_i = \text{transmittance in zone } i = \frac{I_{iw} - I_i}{I_{i0}} \tag{63}$$

By the logic which led to equations (16) and (17)

$$\log_{10} T_i = 2 \sum_{j=i}^{j_{\max}} L_{ij} K_j \tag{64}$$

and

$$K_j = \frac{1}{2} \sum_{i=j}^{i_{\max}} M_{ji} \log_{10} T_i \tag{65}$$

Thus, the K_j become known.

Whereas the T_i are measurable by simply combining observable quantities as in equation (63), the T_{ij} needed to use equation (62) are not directly observable. Recall that T_{ij} is the transmittance through a single segment of ring/zone overlap whereas T_i is the transmittance observed in a given zone i.

From measuring the K values

$$T_{ij} = 10^{-L_{ij} K_j} \tag{66}$$

These can be inserted into equation (62). Lumping all absorption terms together and calling them τ_{ij}

$$\tau_{ij} \equiv F_{ij} \prod_{l=j+1}^{j_{\max}+1} T_{il} \left[1 + T_{ij} \left(\prod_{m=i-1}^{j-1} T_{im} \right)^2 \right] \tag{67}$$

equation (62) becomes

$$I_i = \sum_{j=i}^{j_{\max}} Z A_{ij} \tau_{ij} J_j \tag{68}$$

This is similar to equation (5) except that the factor τ_{ij} appears. Thus, an

analog to equation (7) (solving for the J_j) requires not the inverse of the **A** matrix, but the inverse of the $\mathbf{A}\tau$ matrix. In a matrix notation equation (68) is

$$I = Z(\mathbf{A}\tau)J \tag{69}$$

so that

$$J = \frac{1}{Z}(\mathbf{A}\tau)^{-1} I \tag{70}$$

[note how $(\mathbf{A}\tau)^{-1}$ in equation (70) replaces the **B** matrix in equation (7)].

Thus, to apply equation (62) to real discharge analysis requires that a matrix be inverted for each lateral-to-radial conversion. The inversion would be unstable, as the τ_{ij} in some cases could be quite small (in situations of strong self-reversal). It would also be anticipated that the whole process would be very noise sensitive due to the large number of calculations involved. However, equation (62) in combination with a stable discharge and backlight should allow the deconvolution of spatially unseparated emission and the absorption of radiation.

12. Conclusions

The Abel inversion, when critically and carefully employed, has the ability to give radial information about a discharge from lateral observations. Care must be taken as the inversion is only a mathematical tool and cannot give information about a discharge that is not built into a model. However, seemingly erroneous results may indicate that some physically significant process has been left out of the model.

Whereas many possible discharge properties have been discussed in terms of the inversion, many avenues for further exploration are open. Each may have relevance to a particular discharge system. Among these are: (1) use of the modeling for nonsegregated emission and absorption to determine simple routes for diagnosing such situations and for analyzing systems in which atomic fluorescence may be significant; (2) exploration of instrumental transfer function (depth-of-field) effects. In converting emission to intensity, two units changes are performed exclusively by the observing instrument; J_j is in units of W cm^{-3} nm^{-1} sr^{-1}, and I_i in W cm^{-2}. The wavelength and angular units conversions are exclusively functions of instrument design and performance; (3) scattering effects; (4) effect on refractive index inhomogeneities within the discharge on light propagation away from or through the

discharge; (5) discharge geometry other than cylindrical geometry; and (6) effect of spectral line shape on inversion. This step is necessary before one can perform the inversion with confidence using data from low-resolution instrumentation.

Other problems may be of importance in various spectroscopic systems. On a positive note, however, provided that all of the physically relevant phenomena are accounted for, the Abel inversion should indeed be useful for elucidating the radial structure of plasma discharges, and, thus, their chemistry as well.

ACKNOWLEDGMENTS

Support for the work described was obtained in part from the National Science Foundation (Grant Numbers GP-35602X, CHE76-17557, CHE77-05294) and the University of Wisconsin Graduate School. Fellowship support for Alexander Scheeline was given by the National Science Foundation, Analytical Division of the American Chemical Society, and Dow Chemical Company.

Assistance in designing and implementing computer software was given by Dr. D. T. Stueland, Albert Christoph, Charles Green, and Charles Hutchins. Patricia Brinkman assisted in drawing the figures.

Portions of this work originally appeared in Doctoral theses by S. A. Goldstein and R. D. Sacks; the work, in its present form, was incorporated in the Doctoral thesis of A. Scheeline. Portions of this work have previously appeared in references 17, 21, 22, and in the following articles: A. Scheeline and J. P. Walters, *Anal. Chem.*, **48**, 1519 (1976), and A. Scheeline and J. P. Walters, *Anal. Chim. Acta*, **95**, 59 (1977). Both of these articles were incorporated into this chapter in their entirety, by permission of the copyright holders, the American Chemical Society and Plenum Press, respectively.

13. Appendix

Matrices are given rowwise. For A_{ij}, i may be found by deleting the 0 in the line number of the last row in each block of 10 lines. $j = 1$ is the first entry in each block, $j = 50$ is the last entry.

AREA MATRIX 1

1	7.8539816E-1	1.1278248E+0	1.0302567E+0	1.0144541E+0	1.0085300E+0
2	1.0056416E+0	1.0040117E+0	1.0030005E+0	1.0023295E+0	1.0018612E+0
3	1.0015214E+0	1.0012670E+0	1.0010715E+0	1.0009180E+0	1.0007954E+0
4	1.0006958E+0	1.0006138E+0	1.0005455E+0	1.0004880E+0	1.0004391E+0
5	1.0003973E+0	1.0003611E+0	1.0003297E+0	1.0003022E+0	1.0002780E+0
6	1.0002566E+0	1.0002376E+0	1.0002206E+0	1.0002054E+0	1.0001917E+0
7	1.0001793E+0	1.0001681E+0	1.0001579E+0	1.0001486E+0	1.0001401E+0
8	1.0001323E+0	1.0001252E+0	1.0001186E+0	1.0001125E+0	1.0001069E+0
9	1.0001017E+0	1.0000968E+0	1.0000923E+0	1.0000881E+0	1.0000842E+0
10	1.0000805E+0	1.0000771E+0	1.0000739E+0	1.0000709E+0	1.0000680E+0
11	0.0000000E-1	1.2283697E+0	1.3479931E+0	1.1185953E+0	1.0651144E+0
12	1.0417408E+0	1.0291903E+0	1.0216137E+0	1.0166703E+0	1.0132592E+0
13	1.0108032E+0	1.0089747E+0	1.0075759E+0	1.0064815E+0	1.0056090E+0
14	1.0049019E+0	1.0043210E+0	1.0038377E+0	1.0034313E+0	1.0030864E+0
15	1.0027910E+0	1.0025362E+0	1.0023148E+0	1.0021212E+0	1.0019509E+0
16	1.0018004E+0	1.0016667E+0	1.0015473E+0	1.0014403E+0	1.0013441E+0
17	1.0012572E+0	1.0011784E+0	1.0011069E+0	1.0010417E+0	1.0009820E+0
18	1.0009274E+0	1.0008772E+0	1.0008310E+0	1.0007883E+0	1.0007488E+0
19	1.0007122E+0	1.0006783E+0	1.0006467E+0	1.0006173E+0	1.0005898E+0
20	1.0005642E+0	1.0005401E+0	1.0005176E+0	1.0004965E+0	1.0004766E+0
21	0.0000000E-1	0.0000000E-1	1.5487410E+0	1.5514907E+0	1.2169958E+0
22	1.1278604E+0	1.0859450E+0	1.0622267E+0	1.0473226E+0	1.0372834E+0
23	1.0301737E+0	1.0249427E+0	1.0209762E+0	1.0178938E+0	1.0154491E+0
24	1.0134764E+0	1.0118610E+0	1.0105211E+0	1.0093970E+0	1.0084447E+0
25	1.0076307E+0	1.0069294E+0	1.0063208E+0	1.0057892E+0	1.0053222E+0
26	1.0049096E+0	1.0045433E+0	1.0042166E+0	1.0039240E+0	1.0036609E+0
27	1.0034234E+0	1.0032084E+0	1.0030130E+0	1.0028350E+0	1.0026723E+0
28	1.0025232E+0	1.0023863E+0	1.0022603E+0	1.0021440E+0	1.0020364E+0
29	1.0019368E+0	1.0018443E+0	1.0017583E+0	1.0016781E+0	1.0016034E+0
30	1.0015335E+0	1.0014681E+0	1.0014068E+0	1.0013492E+0	1.0012952E+0
31	0.0000000E-1	0.0000000E-1	0.0000000E-1	1.8132470E+0	1.7341793E+0
32	1.3129368E+0	1.1926253E+0	1.1335843E+0	1.0990625E+0	1.0767891E+0
33	1.0614544E+0	1.0503922E+0	1.0421237E+0	1.0357674E+0	1.0307682E+0
34	1.0267612E+0	1.0234973E+0	1.0208018E+0	1.0185489E+0	1.0166460E+0
35	1.0150237E+0	1.0136290E+0	1.0124210E+0	1.0113677E+0	1.0104436E+0
36	1.0096282E+0	1.0089052E+0	1.0082610E+0	1.0076845E+0	1.0071665E+0
37	1.0066994E+0	1.0062766E+0	1.0058927E+0	1.0055431E+0	1.0052238E+0
38	1.0049314E+0	1.0046629E+0	1.0044158E+0	1.0041879E+0	1.0039772E+0
39	1.0037821E+0	1.0036010E+0	1.0034326E+0	1.0032758E+0	1.0031295E+0
40	1.0029928E+0	1.0028649E+0	1.0027450E+0	1.0026325E+0	1.0025268E+0
41	0.0000000E-1	0.0000000E-1	0.0000000E-1	0.0000000E-1	2.0437639E+0
42	1.9004225E+0	1.4043927E+0	1.2565577E+0	1.1819523E+0	1.1373397E+0
43	1.1080120E+0	1.0874961E+0	1.0724910E+0	1.0611394E+0	1.0523200E+0
44	1.0453178E+0	1.0396576E+0	1.0350119E+0	1.0311487E+0	1.0278996E+0
45	1.0251394E+0	1.0227737E+0	1.0207302E+0	1.0189523E+0	1.0173956E+0
46	1.0160245E+0	1.0148105E+0	1.0137303E+0	1.0127649E+0	1.0118984E+0
47	1.0111177E+0	1.0104117E+0	1.0097713E+0	1.0091884E+0	1.0086564E+0
48	1.0081695E+0	1.0077227E+0	1.0073117E+0	1.0069327E+0	1.0065826E+0
49	1.0062584E+0	1.0059577E+0	1.0056782E+0	1.0054179E+0	1.0051752E+0
50	1.0049485E+0	1.0047364E+0	1.0045377E+0	1.0043513E+0	1.0041761E+0

AREA MATRIX 2

51	0.0000000E-1	0.0000000E-1	0.0000000E-1	0.0000000E-1	0.0000000E-1
52	2.2507778E+0	2.0537266E+0	1.4912860E+0	1.3187503E+0	1.2299409E+0
53	1.1759596E+0	1.1399739E+0	1.1144930E+0	1.0956564E+0	1.0812706E+0
54	1.0699985E+0	1.0609806E+0	1.0536404E+0	1.0475779E+0	1.0425076E+0
55	1.0382206E+0	1.0345611E+0	1.0314106E+0	1.0286778E+0	1.0262911E+0
56	1.0241937E+0	1.0223403E+0	1.0206940E+0	1.0192249E+0	1.0179081E+0
57	1.0167233E+0	1.0156531E+0	1.0146831E+0	1.0138012E+0	1.0129970E+0
58	1.0122614E+0	1.0115869E+0	1.0109669E+0	1.0103956E+0	1.0098680E+0
59	1.0093798E+0	1.0089270E+0	1.0085065E+0	1.0081150E+0	1.0077501E+0
60	1.0074093E+0	1.0070907E+0	1.0067922E+0	1.0065122E+0	1.0062492E+0
61	0.0000000E-1	0.0000000E-1	0.0000000E-1	0.0000000E-1	0.0000000E-1
62	0.0000000E-1	2.4402846E+0	2.1966089E+0	1.5739761E+0	1.3789493E+0
63	1.2770737E+0	1.2143754E+0	1.1721238E+0	1.1419188E+0	1.1193988E+0
64	1.1020677E+0	1.0883934E+0	1.0773846E+0	1.0683723E+0	1.0608894E+0
65	1.0546007E+0	1.0492597E+0	1.0446815E+0	1.0407249E+0	1.0372804E+0
66	1.0342621E+0	1.0316013E+0	1.0292431E+0	1.0271426E+0	1.0252633E+0
67	1.0235748E+0	1.0220518E+0	1.0206732E+0	1.0194211E+0	1.0182804E+0
68	1.0172382E+0	1.0162833E+0	1.0154062E+0	1.0145986E+0	1.0138533E+0
69	1.0131640E+0	1.0125252E+0	1.0119321E+0	1.0113804E+0	1.0108662E+0
70	1.0103863E+0	1.0099377E+0	1.0095176E+0	1.0091238E+0	1.0087540E+0
71	0.0000000E-1	0.0000000E-1	0.0000000E-1	0.0000000E-1	0.0000000E-1
72	0.0000000E-1	0.0000000E-1	2.6160946E+0	2.3308966E+0	1.6528954E+0
73	1.4371453E+0	1.3231526E+0	1.2523072E+0	1.2041513E+0	1.1694587E+0
74	1.1434121E+0	1.1232399E+0	1.1072320E+0	1.0942763E+0	1.0836184E+0
75	1.0747294E+0	1.0672279E+0	1.0608323E+0	1.0553303E+0	1.0505593E+0
76	1.0463929E+0	1.0427310E+0	1.0394941E+0	1.0366177E+0	1.0340494E+0
77	1.0317461E+0	1.0296721E+0	1.0277975E+0	1.0260973E+0	1.0245503E+0
78	1.0231383E+0	1.0218460E+0	1.0206601E+0	1.0195691E+0	1.0185630E+0
79	1.0176333E+0	1.0167722E+0	1.0159732E+0	1.0152303E+0	1.0145385E+0
80	1.0138931E+0	1.0132900E+0	1.0127255E+0	1.0121965E+0	1.0117000E+0
81	0.0000000E-1	0.0000000E-1	0.0000000E-1	0.0000000E-1	0.0000000E-1
82	0.0000000E-1	0.0000000E-1	0.0000000E-1	2.7808086E+0	2.4579515E+0
83	1.7284507E+0	1.4934227E+0	1.3681112E+0	1.2896136E+0	1.2358788E+0
84	1.1969196E+0	1.1674999E+0	1.1445941E+0	1.1263283E+0	1.1114784E+0
85	1.0992115E+0	1.0889409E+0	1.0802422E+0	1.0728008E+0	1.0663791E+0
86	1.0607941E+0	1.0559033E+0	1.0515935E+0	1.0477745E+0	1.0443729E+0
87	1.0413290E+0	1.0385935E+0	1.0361254E+0	1.0338904E+0	1.0318597E+0
88	1.0300088E+0	1.0283167E+0	1.0267657E+0	1.0253401E+0	1.0240268E+0
89	1.0228142E+0	1.0216920E+0	1.0206514E+0	1.0196846E+0	1.0187848E+0
90	1.0179459E+0	1.0171623E+0	1.0164294E+0	1.0157428E+0	1.0150987E+0
91	0.0000000E-1	0.0000000E-1	0.0000000E-1	0.0000000E-1	0.0000000E-1
92	0.0000000E-1	0.0000000E-1	0.0000000E-1	0.0000000E-1	2.9362953E+0
93	2.5788161E+0	1.8010005E+0	1.5478990E+0	1.4119472E+0	1.3262279E+0
94	1.2672043E+0	1.2241816E+0	1.1915336E+0	1.1659995E+0	1.1455526E+0
95	1.1288651E+0	1.1150303E+0	1.1034081E+0	1.0935335E+0	1.0850612E+0
96	1.0777296E+0	1.0713366E+0	1.0657243E+0	1.0607674E+0	1.0563651E+0
97	1.0524359E+0	1.0489129E+0	1.0457408E+0	1.0428737E+0	1.0402730E+0
98	1.0379061E+0	1.0357454E+0	1.0337672E+0	1.0319512E+0	1.0302800E+0
99	1.0287384E+0	1.0273130E+0	1.0259924E+0	1.0247665E+0	1.0236263E+0
100	1.0225639E+0	1.0215723E+0	1.0206453E+0	1.0197773E+0	1.0189635E+0

AREA MATRIX 3

101	0.0000000E-1	0.0000000E-1	0.0000000E-1	0.0000000E-1	0.0000000E-1
102	0.0000000E-1	0.0000000E-1	0.0000000E-1	0.0000000E-1	0.0000000E-1
103	3.0839513E+0	2.6943072E+0	1.8708538E+0	1.6006989E+0	1.4546901E+0
104	1.3621257E+0	1.2980720E+0	1.2511699E+0	1.2154287E+0	1.1873665E+0
105	1.1648137E+0	1.1463454E+0	1.1309859E+0	1.1180446E+0	1.1070187E+0
106	1.0975339E+0	1.0893058E+0	1.0821144E+0	1.0757873E+0	1.0701873E+0
107	1.0652041E+0	1.0607479E+0	1.0567453E+0	1.0531352E+0	1.0498669E+0
108	1.0468977E+0	1.0441914E+0	1.0417173E+0	1.0394491E+0	1.0373642E+0
109	1.0354431E+0	1.0336688E+0	1.0320265E+0	1.0305032E+0	1.0290875E+0
110	1.0277695E+0	1.0265401E+0	1.0253917E+0	1.0243170E+0	1.0233099E+0
111	0.0000000E-1	0.0000000E-1	0.0000000E-1	0.0000000E-1	0.0000000E-1
112	0.0000000E-1	0.0000000E-1	0.0000000E-1	0.0000000E-1	0.0000000E-1
113	0.0000000E-1	3.2248527E+0	2.8050783E+0	1.9382753E+0	1.6519436E+0
114	1.4963844E+0	1.3973061E+0	1.3284532E+0	1.2778393E+0	1.2391292E+0
115	1.2086329E+0	1.1840464E+0	1.1638530E+0	1.1470120E+0	1.1327852E+0
116	1.1206342E+0	1.1101572E+0	1.1010482E+0	1.0930704E+0	1.0860374E+0
117	1.0798008E+0	1.0742412E+0	1.0692612E+0	1.0647807E+0	1.0607333E+0
118	1.0570637E+0	1.0537250E+0	1.0506779E+0	1.0478887E+0	1.0453283E+0
119	1.0429721E+0	1.0407984E+0	1.0387885E+0	1.0369262E+0	1.0351971E+0
120	1.0335885E+0	1.0320894E+0	1.0306900E+0	1.0293814E+0	1.0281559E+0
121	0.0000000E-1	0.0000000E-1	0.0000000E-1	0.0000000E-1	0.0000000E-1
122	0.0000000E-1	0.0000000E-1	0.0000000E-1	0.0000000E-1	0.0000000E-1
123	0.0000000E-1	0.0000000E-1	3.3598496E+0	2.9116611E+0	2.0034926E+0
124	1.7017463E+0	1.5370808E+0	1.4317821E+0	1.3583370E+0	1.3041632E+0
125	1.2625984E+0	1.2297559E+0	1.2032039E+0	1.1813389E+0	1.1630588E+0
126	1.1475802E+0	1.1343308E+0	1.1228829E+0	1.1129099E+0	1.1041589E+0
127	1.0964305E+0	1.0895656E+0	1.0834358E+0	1.0779365E+0	1.0729815E+0
128	1.0684991E+0	1.0644294E+0	1.0607221E+0	1.0573342E+0	1.0542292E+0
129	1.0513758E+0	1.0487469E+0	1.0463191E+0	1.0440720E+0	1.0419878E+0
130	1.0400507E+0	1.0382471E+0	1.0365647E+0	1.0349928E+0	1.0335217E+0
131	0.0000000E-1	0.0000000E-1	0.0000000E-1	0.0000000E-1	0.0000000E-1
132	0.0000000E-1	0.0000000E-1	0.0000000E-1	0.0000000E-1	0.0000000E-1
133	0.0000000E-1	0.0000000E-1	0.0000000E-1	3.4896275E+0	3.0144953E+0
134	2.0667015E+0	1.7502103E+0	1.5768313E+0	1.4655740E+0	1.3877231E+0
135	1.3301273E+0	1.2858132E+0	1.2507060E+0	1.2222527E+0	1.1987672E+0
136	1.1790888E+0	1.1623913E+0	1.1480703E+0	1.1356729E+0	1.1248535E+0
137	1.1153435E+0	1.1069311E+0	1.0994470E+0	1.0927544E+0	1.0867416E+0
138	1.0813164E+0	1.0764024E+0	1.0719353E+0	1.0678609E+0	1.0641333E+0
139	1.0607132E+0	1.0575669E+0	1.0546651E+0	1.0519826E+0	1.0494974E+0
140	1.0471901E+0	1.0450439E+0	1.0430438E+0	1.0411766E+0	1.0394306E+0
141	0.0000000E-1	0.0000000E-1	0.0000000E-1	0.0000000E-1	0.0000000E-1
142	0.0000000E-1	0.0000000E-1	0.0000000E-1	0.0000000E-1	0.0000000E-1
143	0.0000000E-1	0.0000000E-1	0.0000000E-1	0.0000000E-1	3.6147487E+0
144	3.1139487E+0	2.1280718E+0	1.7974298E+0	1.6156874E+0	1.4987063E+0
145	1.4166179E+0	1.3557261E+0	1.3087593E+0	1.2714631E+0	1.2411687E+0
146	1.2161111E+0	1.1950736E+0	1.1771892E+0	1.1618225E+0	1.1484973E+0
147	1.1368491E+0	1.1265947E+0	1.1175102E+0	1.1094167E+0	1.1021693E+0
148	1.0956496E+0	1.0897596E+0	1.0844182E+0	1.0795569E+0	1.0751180E+0
149	1.0710527E+0	1.0673188E+0	1.0638804E+0	1.0607062E+0	1.0577691E+0
150	1.0550457E+0	1.0525150E+0	1.0501591E+0	1.0479618E+0	1.0459088E+0

AREA MATRIX 4

151	0.0000000E-1	0.0000000E-1	0.0000000E-1	0.0000000E-1	0.0000000E-1
152	0.0000000E-1	0.0000000E-1	0.0000000E-1	0.0000000E-1	0.0000000E-1
153	0.0000000E-1	0.0000000E-1	0.0000000E-1	0.0000000E-1	0.0000000E-1
154	3.7356811E+0	3.2103332E+0	2.1877515E+0	1.8434897E+0	1.6536981E+0
155	1.5312051E+0	1.4450322E+0	1.3809594E+0	1.3314289E+0	1.2920141E+0
156	1.2599350E+0	1.2333509E+0	1.2109916E+0	1.1919510E+0	1.1755641E+0
157	1.1613321E+0	1.1488727E+0	1.1378885E+0	1.1281442E+0	1.1194515E+0
158	1.1116578E+0	1.1046381E+0	1.0982892E+0	1.0925251E+0	1.0872736E+0
159	1.0824734E+0	1.0780728E+0	1.0740271E+0	1.0702981E+0	1.0668526E+0
160	1.0636617E+0	1.0607004E+0	1.0579466E+0	1.0553808E+0	1.0529860E+0
161	0.0000000E-1	0.0000000E-1	0.0000000E-1	0.0000000E-1	0.0000000E-1
162	0.0000000E-1	0.0000000E-1	0.0000000E-1	0.0000000E-1	0.0000000E-1
163	0.0000000E-1	0.0000000E-1	0.0000000E-1	0.0000000E-1	0.0000000E-1
164	0.0000000E-1	3.8528193E+0	3.3039156E+0	2.2458703E+0	1.8884668E+0
165	1.6909098E+0	1.5630969E+0	1.4729790E+0	1.4058307E+0	1.3538188E+0
166	1.3123507E+0	1.2785396E+0	1.2504720E+0	1.2268264E+0	1.2066589E+0
167	1.1892764E+0	1.1741581E+0	1.1609047E+0	1.1492053E+0	1.1388135E+0
168	1.1295319E+0	1.1212007E+0	1.1136884E+0	1.1068868E+0	1.1007053E+0
169	1.0950678E+0	1.0899100E+0	1.0851771E+0	1.0808220E+0	1.0768044E+0
170	1.0730891E+0	1.0696456E+0	1.0664473E+0	1.0634709E+0	1.0606957E+0
171	0.0000000E-1	0.0000000E-1	0.0000000E-1	0.0000000E-1	0.0000000E-1
172	0.0000000E-1	0.0000000E-1	0.0000000E-1	0.0000000E-1	0.0000000E-1
173	0.0000000E-1	0.0000000E-1	0.0000000E-1	0.0000000E-1	0.0000000E-1
174	0.0000000E-1	0.0000000E-1	3.9664995E+0	3.3949262E+0	2.3025426E+0
175	1.9324305E+0	1.7273656E+0	1.5944082E+0	1.5004729E+0	1.4303463E+0
176	1.3759290E+0	1.3324684E+0	1.2969745E+0	1.2674640E+0	1.2425657E+0
177	1.2212994E+0	1.2029447E+0	1.1869600E+0	1.1729295E+0	1.1605291E+0
178	1.1495020E+0	1.1396420E+0	1.1307820E+0	1.1227848E+0	1.1155369E+0
179	1.1089434E+0	1.1029247E+0	1.0974131E+0	1.0923512E+0	1.0876896E+0
180	1.0833856E+0	1.0794024E+0	1.0757078E+0	1.0722739E+0	1.0690758E+0
181	0.0000000E-1	0.0000000E-1	0.0000000E-1	0.0000000E-1	0.0000000E-1
182	0.0000000E-1	0.0000000E-1	0.0000000E-1	0.0000000E-1	0.0000000E-1
183	0.0000000E-1	0.0000000E-1	0.0000000E-1	0.0000000E-1	0.0000000E-1
184	0.0000000E-1	0.0000000E-1	0.0000000E-1	4.0770110E+0	3.4835655E+0
185	2.3578696E+0	1.9754436E+0	1.7631061E+0	1.6251644E+0	1.5275290E+0
186	1.4545138E+0	1.3977615E+0	1.3523651E+0	1.3152346E+0	1.2843193E+0
187	1.2582001E+0	1.2358617E+0	1.2165575E+0	1.1997255E+0	1.1849343E+0
188	1.1718469E+0	1.1601964E+0	1.1497683E+0	1.1403884E+0	1.1319139E+0
189	1.1242262E+0	1.1172264E+0	1.1108313E+0	1.1049702E+0	1.0995829E+0
190	1.0946177E+0	1.0900299E+0	1.0857810E+0	1.0818372E+0	1.0781690E+0
191	0.0000000E-1	0.0000000E-1	0.0000000E-1	0.0000000E-1	0.0000000E-1
192	0.0000000E-1	0.0000000E-1	0.0000000E-1	0.0000000E-1	0.0000000E-1
193	0.0000000E-1	0.0000000E-1	0.0000000E-1	0.0000000E-1	0.0000000E-1
194	0.0000000E-1	0.0000000E-1	0.0000000E-1	0.0000000E-1	4.1846049E+0
195	3.5700093E+0	2.4119416E+0	2.0175630E+0	1.7981685E+0	1.6553901E+0
196	1.5541629E+0	1.4783419E+0	1.4193203E+0	1.3720407E+0	1.3333171E+0
197	1.3010329E+0	1.2737228E+0	1.2503377E+0	1.2301055E+0	1.2124448E+0
198	1.1969086E+0	1.1831478E+0	1.1708857E+0	1.1598996E+0	1.1500087E+0
199	1.1410644E+0	1.1329435E+0	1.1255432E+0	1.1187767E+0	1.1125703E+0
200	1.1068613E+0	1.1015958E+0	1.0967271E+0	1.0922149E+0	1.0880238E+0

AREA MATRIX 5

201	0.0000000E-1	0.0000000E-1	0.0000000E-1	0.0000000E-1	0.0000000E-1
202	0.0000000E-1	0.0000000E-1	0.0000000E-1	0.0000000E-1	0.0000000E-1
203	0.0000000E-1	0.0000000E-1	0.0000000E-1	0.0000000E-1	0.0000000E-1
204	0.0000000E-1	0.0000000E-1	0.0000000E-1	0.0000000E-1	0.0000000E-1
205	4.2895007E+0	3.6544128E+0	2.4648393E+0	2.0588405E+0	1.8325877E+0
206	1.6851085E+0	1.5803896E+0	1.5018400E+0	1.4406100E+0	1.3914968E+0
207	1.3512206E+0	1.3176014E+0	1.2891289E+0	1.2647213E+0	1.2435817E+0
208	1.2251098E+0	1.2088439E+0	1.1944230E+0	1.1815606E+0	1.1700265E+0
209	1.1596332E+0	1.1502267E+0	1.1416793E+0	1.1338842E+0	1.1267513E+0
210	1.1202041E+0	1.1141773E+0	1.1086148E+0	1.1034681E+0	1.0986951E+0
211	0.0000000E-1	0.0000000E-1	0.0000000E-1	0.0000000E-1	0.0000000E-1
212	0.0000000E-1	0.0000000E-1	0.0000000E-1	0.0000000E-1	0.0000000E-1
213	0.0000000E-1	0.0000000E-1	0.0000000E-1	0.0000000E-1	0.0000000E-1
214	0.0000000E-1	0.0000000E-1	0.0000000E-1	0.0000000E-1	0.0000000E-1
215	0.0000000E-1	4.3918918E+0	3.7369137E+0	2.5166352E+0	2.0993232E+0
216	1.8663956E+0	1.7143418E+0	1.6062241E+0	1.5250176E+0	1.4616362E+0
217	1.4107357E+0	1.3689451E+0	1.3340228E+0	1.3044149E+0	1.2790077E+0
218	1.2569805E+0	1.2377144E+0	1.2207334E+0	1.2056651E+0	1.1922136E+0
219	1.1801411E+0	1.1692539E+0	1.1593927E+0	1.1504254E+0	1.1422413E+0
220	1.1347470E+0	1.1278634E+0	1.1215227E+0	1.1156667E+0	1.1102450E+0
221	0.0000000E-1	0.0000000E-1	0.0000000E-1	0.0000000E-1	0.0000000E-1
222	0.0000000E-1	0.0000000E-1	0.0000000E-1	0.0000000E-1	0.0000000E-1
223	0.0000000E-1	0.0000000E-1	0.0000000E-1	0.0000000E-1	0.0000000E-1
224	0.0000000E-1	0.0000000E-1	0.0000000E-1	0.0000000E-1	0.0000000E-1
225	0.0000000E-1	0.0000000E-1	4.4919495E+0	3.8176350E+0	2.5673947E+0
226	2.1390543E+0	1.8996223E+0	1.7431108E+0	1.6316810E+0	1.5478843E+0
227	1.4824049E+0	1.4297605E+0	1.3864915E+0	1.3502963E+0	1.3195786E+0
228	1.2931937E+0	1.2702975E+0	1.2502535E+0	1.2325716E+0	1.2168681E+0
229	1.2028383E+0	1.1902369E+0	1.1788641E+0	1.1685555E+0	1.1591746E+0
230	1.1506072E+0	1.1427567E+0	1.1355412E+0	1.1288905E+0	1.1227445E+0
231	0.0000000E-1	0.0000000E-1	0.0000000E-1	0.0000000E-1	0.0000000E-1
232	0.0000000E-1	0.0000000E-1	0.0000000E-1	0.0000000E-1	0.0000000E-1
233	0.0000000E-1	0.0000000E-1	0.0000000E-1	0.0000000E-1	0.0000000E-1
234	0.0000000E-1	0.0000000E-1	0.0000000E-1	0.0000000E-1	0.0000000E-1
235	0.0000000E-1	0.0000000E-1	0.0000000E-1	4.5898264E+0	3.8966868E+0
236	2.6171772E+0	2.1780731E+0	1.9322952E+0	1.7714353E+0	1.6567740E+0
237	1.5704499E+0	1.5029224E+0	1.4485750E+0	1.4038615E+0	1.3664220E+0
238	1.3346186E+0	1.3072767E+0	1.2835296E+0	1.2627232E+0	1.2443538E+0
239	1.2280270E+0	1.2134293E+0	1.2003082E+0	1.1884579E+0	1.1777090E+0
240	1.1679210E+0	1.1589759E+0	1.1507742E+0	1.1432312E+0	1.1362746E+0
241	0.0000000E-1	0.0000000E-1	0.0000000E-1	0.0000000E-1	0.0000000E-1
242	0.0000000E-1	0.0000000E-1	0.0000000E-1	0.0000000E-1	0.0000000E-1
243	0.0000000E-1	0.0000000E-1	0.0000000E-1	0.0000000E-1	0.0000000E-1
244	0.0000000E-1	0.0000000E-1	0.0000000E-1	0.0000000E-1	0.0000000E-1
245	0.0000000E-1	0.0000000E-1	0.0000000E-1	0.0000000E-1	4.6856591E+0
246	3.9741686E+0	2.6660366E+0	2.2164158E+0	1.9644401E+0	1.7993336E+0
247	1.6815165E+0	1.5927237E+0	1.5231952E+0	1.4671832E+0	1.4210573E+0
248	1.3824003E+0	1.3495344E+0	1.3212552E+0	1.2966742E+0	1.2751203E+0
249	1.2560765E+0	1.2391379E+0	1.2239823E+0	1.2103503E+0	1.1980304E+0
250	1.1868483E+0	1.1766594E+0	1.1673421E+0	1.1587941E+0	1.1509280E+0

AREA MATRIX 6

251	0.0000000E-1	0.0000000E-1	0.0000000E-1	0.0000000E-1	0.0000000E-1
252	0.0000000E-1	0.0000000E-1	0.0000000E-1	0.0000000E-1	0.0000000E-1
253	0.0000000E-1	0.0000000E-1	0.0000000E-1	0.0000000E-1	0.0000000E-1
254	0.0000000E-1	0.0000000E-1	0.0000000E-1	0.0000000E-1	0.0000000E-1
255	0.0000000E-1	0.0000000E-1	0.0000000E-1	0.0000000E-1	0.0000000E-1
256	4.7795707E+0	4.0501702E+0	2.7140219E+0	2.2541158E+0	1.9960808E+0
257	1.8268233E+0	1.7059214E+0	1.6147150E+0	1.5432297E+0	1.4855894E+0
258	1.4380813E+0	1.3982326E+0	1.3643259E+0	1.3351283E+0	1.3097297E+0
259	1.2874425E+0	1.2677368E+0	1.2501973E+0	1.2344936E+0	1.2203594E+0
260	1.2075775E+0	1.1959690E+0	1.1853852E+0	1.1757013E+0	1.1668118E+0
261	0.0000000E-1	0.0000000E-1	0.0000000E-1	0.0000000E-1	0.0000000E-1
262	0.0000000E-1	0.0000000E-1	0.0000000E-1	0.0000000E-1	0.0000000E-1
263	0.0000000E-1	0.0000000E-1	0.0000000E-1	0.0000000E-1	0.0000000E-1
264	0.0000000E-1	0.0000000E-1	0.0000000E-1	0.0000000E-1	0.0000000E-1
265	0.0000000E-1	0.0000000E-1	0.0000000E-1	0.0000000E-1	0.0000000E-1
266	0.0000000E-1	4.8716723E+0	4.1247732E+0	2.7611783E+0	2.2912039E+0
267	2.0272396E+0	1.8539208E+0	1.7300008E+0	1.6364327E+0	1.5630324E+0
268	1.5037980E+0	1.4549365E+0	1.4139202E+0	1.3789936E+0	1.3488955E+0
269	1.3226950E+0	1.2996881E+0	1.2793325E+0	1.2612027E+0	1.2449602E+0
270	1.2303321E+0	1.2170957E+0	1.2050674E+0	1.1940947E+0	1.1840494E+0
271	0.0000000E-1	0.0000000E-1	0.0000000E-1	0.0000000E-1	0.0000000E-1
272	0.0000000E-1	0.0000000E-1	0.0000000E-1	0.0000000E-1	0.0000000E-1
273	0.0000000E-1	0.0000000E-1	0.0000000E-1	0.0000000E-1	0.0000000E-1
274	0.0000000E-1	0.0000000E-1	0.0000000E-1	0.0000000E-1	0.0000000E-1
275	0.0000000E-1	0.0000000E-1	0.0000000E-1	0.0000000E-1	0.0000000E-1
276	0.0000000E-1	0.0000000E-1	4.9620646E+0	4.1980520E+0	2.8075469E+0
277	2.3277084E+0	2.0579371E+0	1.8806415E+0	1.7537662E+0	1.6578855E+0
278	1.5826095E+0	1.5218136E+0	1.4716258E+0	1.4294651E+0	1.3935382E+0
279	1.3625569E+0	1.3355692E+0	1.3118558E+0	1.2908618E+0	1.2721519E+0
280	1.2553797E+0	1.2402657E+0	1.2265820E+0	1.2141404E+0	1.2027845E+0
281	0.0000000E-1	0.0000000E-1	0.0000000E-1	0.0000000E-1	0.0000000E-1
282	0.0000000E-1	0.0000000E-1	0.0000000E-1	0.0000000E-1	0.0000000E-1
283	0.0000000E-1	0.0000000E-1	0.0000000E-1	0.0000000E-1	0.0000000E-1
284	0.0000000E-1	0.0000000E-1	0.0000000E-1	0.0000000E-1	0.0000000E-1
285	0.0000000E-1	0.0000000E-1	0.0000000E-1	0.0000000E-1	0.0000000E-1
286	0.0000000E-1	0.0000000E-1	0.0000000E-1	5.0508394E+0	4.2700747E+0
287	2.8531657E+0	2.3636556E+0	2.0881927E+0	1.9070000E+0	1.7772287E+0
288	1.6790817E+0	1.6019674E+0	1.5396408E+0	1.4881524E+0	1.4448692E+0
289	1.4079610E+0	1.3761127E+0	1.3483522E+0	1.3239447E+0	1.3023233E+0
290	1.2830431E+0	1.2657499E+0	1.2501579E+0	1.2360338E+0	1.2231851E+0
291	0.0000000E-1	0.0000000E-1	0.0000000E-1	0.0000000E-1	0.0000000E-1
292	0.0000000E-1	0.0000000E-1	0.0000000E-1	0.0000000E-1	0.0000000E-1
293	0.0000000E-1	0.0000000E-1	0.0000000E-1	0.0000000E-1	0.0000000E-1
294	0.0000000E-1	0.0000000E-1	0.0000000E-1	0.0000000E-1	0.0000000E-1
295	0.0000000E-1	0.0000000E-1	0.0000000E-1	0.0000000E-1	0.0000000E-1
296	0.0000000E-1	0.0000000E-1	0.0000000E-1	0.0000000E-1	5.1380806E+0
297	4.3409037E+0	2.8980699E+0	2.3990700E+0	2.1180244E+0	1.9330099E+0
298	1.8003988E+0	1.7000293E+0	1.6211122E+0	1.5572840E+0	1.5045196E+0
299	1.4601348E+0	1.4222633E+0	1.3895635E+0	1.3610439E+0	1.3359544E+0
300	1.3137162E+0	1.2938752E+0	1.2760694E+0	1.2600069E+0	1.2454491E+0

AREA MATRIX 7

301	0.0000000E-1	0.0000000E-1	0.0000000E-1	0.0000000E-1	0.0000000E-1
302	0.0000000E-1	0.0000000E-1	0.0000000E-1	0.0000000E-1	0.0000000E-1
303	0.0000000E-1	0.0000000E-1	0.0000000E-1	0.0000000E-1	0.0000000E-1
304	0.0000000E-1	0.0000000E-1	0.0000000E-1	0.0000000E-1	0.0000000E-1
305	0.0000000E-1	0.0000000E-1	0.0000000E-1	0.0000000E-1	0.0000000E-1
306	0.0000000E-1	0.0000000E-1	0.0000000E-1	0.0000000E-1	0.0000000E-1
307	5.2238649E+0	4.4105963E+0	2.9422917E+0	2.4339744E+0	2.1474492E+0
308	1.9586841E+0	1.8232865E+0	1.7207361E+0	1.6400497E+0	1.5747477E+0
309	1.5207307E+0	1.4752642E+0	1.4364465E+0	1.4029102E+0	1.3736445E+0
310	1.3478845E+0	1.3250398E+0	1.3046470E+0	1.2863367E+0	1.2698110E+0
311	0.0000000E-1	0.0000000E-1	0.0000000E-1	0.0000000E-1	0.0000000E-1
312	0.0000000E-1	0.0000000E-1	0.0000000E-1	0.0000000E-1	0.0000000E-1
313	0.0000000E-1	0.0000000E-1	0.0000000E-1	0.0000000E-1	0.0000000E-1
314	0.0000000E-1	0.0000000E-1	0.0000000E-1	0.0000000E-1	0.0000000E-1
315	0.0000000E-1	0.0000000E-1	0.0000000E-1	0.0000000E-1	0.0000000E-1
316	0.0000000E-1	0.0000000E-1	0.0000000E-1	0.0000000E-1	0.0000000E-1
317	0.0000000E-1	5.3082632E+0	4.4792055E+0	2.9858613E+0	2.4683898E+0
318	2.1764829E+0	1.9840349E+0	1.8459012E+0	1.7412095E+0	1.6587857E+0
319	1.5920363E+0	1.5367890E+0	1.4902597E+0	1.4505123E+0	1.4161538E+0
320	1.3861546E+0	1.3597351E+0	1.3362937E+0	1.3153578E+0	1.2965509E+0
321	0.0000000E-1	0.0000000E-1	0.0000000E-1	0.0000000E-1	0.0000000E-1
322	0.0000000E-1	0.0000000E-1	0.0000000E-1	0.0000000E-1	0.0000000E-1
323	0.0000000E-1	0.0000000E-1	0.0000000E-1	0.0000000E-1	0.0000000E-1
324	0.0000000E-1	0.0000000E-1	0.0000000E-1	0.0000000E-1	0.0000000E-1
325	0.0000000E-1	0.0000000E-1	0.0000000E-1	0.0000000E-1	0.0000000E-1
326	0.0000000E-1	0.0000000E-1	0.0000000E-1	0.0000000E-1	0.0000000E-1
327	0.0000000E-1	0.0000000E-1	5.3913403E+0	4.5467804E+0	3.0288066E+0
328	2.5023360E+0	2.2051403E+0	2.0090738E+0	1.8682519E+0	1.7614565E+0
329	1.6773257E+0	1.6091542E+0	1.5526978E+0	1.5051240E+0	1.4644624E+0
330	1.4292955E+0	1.3985747E+0	1.3715064E+0	1.3474776E+0	1.3260072E+0
331	0.0000000E-1	0.0000000E-1	0.0000000E-1	0.0000000E-1	0.0000000E-1
332	0.0000000E-1	0.0000000E-1	0.0000000E-1	0.0000000E-1	0.0000000E-1
333	0.0000000E-1	0.0000000E-1	0.0000000E-1	0.0000000E-1	0.0000000E-1
334	0.0000000E-1	0.0000000E-1	0.0000000E-1	0.0000000E-1	0.0000000E-1
335	0.0000000E-1	0.0000000E-1	0.0000000E-1	0.0000000E-1	0.0000000E-1
336	0.0000000E-1	0.0000000E-1	0.0000000E-1	0.0000000E-1	0.0000000E-1
337	0.0000000E-1	0.0000000E-1	0.0000000E-1	5.4731565E+0	4.6133662E+0
338	3.0711536E+0	2.5358317E+0	2.2334356E+0	2.0338115E+0	1.8903473E+0
339	1.7814839E+0	1.6956752E+0	1.6261056E+0	1.5684603E+0	1.5198593E+0
340	1.4782987E+0	1.4423364E+0	1.4109056E+0	1.3831986E+0	1.3585917E+0
341	0.0000000E-1	0.0000000E-1	0.0000000E-1	0.0000000E-1	0.0000000E-1
342	0.0000000E-1	0.0000000E-1	0.0000000E-1	0.0000000E-1	0.0000000E-1
343	0.0000000E-1	0.0000000E-1	0.0000000E-1	0.0000000E-1	0.0000000E-1
344	0.0000000E-1	0.0000000E-1	0.0000000E-1	0.0000000E-1	0.0000000E-1
345	0.0000000E-1	0.0000000E-1	0.0000000E-1	0.0000000E-1	0.0000000E-1
346	0.0000000E-1	0.0000000E-1	0.0000000E-1	0.0000000E-1	0.0000000E-1
347	0.0000000E-1	0.0000000E-1	0.0000000E-1	0.0000000E-1	5.5537676E+0
348	4.6790052E+0	3.1129264E+0	2.5688940E+0	2.2613817E+0	2.0582585E+0
349	1.9121954E+0	1.8012982E+0	1.7138393E+0	1.6428945E+0	1.5840798E+0
350	1.5344683E+0	1.4920230E+0	1.4552779E+0	1.4231482E+0	1.3948124E+0

AREA MATRIX 8

351	0.0000000E-1	0.0000000E-1	0.0000000E-1	0.0000000E-1	0.0000000E-1
352	0.0000000E-1	0.0000000E-1	0.0000000E-1	0.0000000E-1	0.0000000E-1
353	0.0000000E-1	0.0000000E-1	0.0000000E-1	0.0000000E-1	0.0000000E-1
354	0.0000000E-1	0.0000000E-1	0.0000000E-1	0.0000000E-1	0.0000000E-1
355	0.0000000E-1	0.0000000E-1	0.0000000E-1	0.0000000E-1	0.0000000E-1
356	0.0000000E-1	0.0000000E-1	0.0000000E-1	0.0000000E-1	0.0000000E-1
357	0.0000000E-1	0.0000000E-1	0.0000000E-1	0.0000000E-1	0.0000000E-1
358	5.6332252E+0	4.7437366E+0	3.1541478E+0	2.6015392E+0	2.2889911E+0
359	2.0824244E+0	1.9338041E+0	1.8209057E+0	1.7318230E+0	1.6595251E+0
360	1.5995595E+0	1.5489534E+0	1.5056372E+0	1.4681213E+0	1.4353034E+0
361	0.0000000E-1	0.0000000E-1	0.0000000E-1	0.0000000E-1	0.0000000E-1
362	0.0000000E-1	0.0000000E-1	0.0000000E-1	0.0000000E-1	0.0000000E-1
363	0.0000000E-1	0.0000000E-1	0.0000000E-1	0.0000000E-1	0.0000000E-1
364	0.0000000E-1	0.0000000E-1	0.0000000E-1	0.0000000E-1	0.0000000E-1
365	0.0000000E-1	0.0000000E-1	0.0000000E-1	0.0000000E-1	0.0000000E-1
366	0.0000000E-1	0.0000000E-1	0.0000000E-1	0.0000000E-1	0.0000000E-1
367	0.0000000E-1	0.0000000E-1	0.0000000E-1	0.0000000E-1	0.0000000E-1
368	0.0000000E-1	5.7115776E+0	4.8075969E+0	3.1948390E+0	2.6337826E+0
369	2.3162756E+0	2.1063184E+0	1.9551806E+0	1.8403124E+0	1.7496311E+0
370	1.6760011E+0	1.6149025E+0	1.5633170E+0	1.5191432E+0	1.4808683E+0
371	0.0000000E-1	0.0000000E-1	0.0000000E-1	0.0000000E-1	0.0000000E-1
372	0.0000000E-1	0.0000000E-1	0.0000000E-1	0.0000000E-1	0.0000000E-1
373	0.0000000E-1	0.0000000E-1	0.0000000E-1	0.0000000E-1	0.0000000E-1
374	0.0000000E-1	0.0000000E-1	0.0000000E-1	0.0000000E-1	0.0000000E-1
375	0.0000000E-1	0.0000000E-1	0.0000000E-1	0.0000000E-1	0.0000000E-1
376	0.0000000E-1	0.0000000E-1	0.0000000E-1	0.0000000E-1	0.0000000E-1
377	0.0000000E-1	0.0000000E-1	0.0000000E-1	0.0000000E-1	0.0000000E-1
378	0.0000000E-1	0.0000000E-1	5.7888695E+0	4.8706206E+0	3.2350198E+0
379	2.6656385E+0	2.3432461E+0	2.1299494E+0	1.9763321E+0	1.8595238E+0
380	1.7672683E+0	1.6923263E+0	1.6301118E+0	1.5775616E+0	1.5325430E+0
381	0.0000000E-1	0.0000000E-1	0.0000000E-1	0.0000000E-1	0.0000000E-1
382	0.0000000E-1	0.0000000E-1	0.0000000E-1	0.0000000E-1	0.0000000E-1
383	0.0000000E-1	0.0000000E-1	0.0000000E-1	0.0000000E-1	0.0000000E-1
384	0.0000000E-1	0.0000000E-1	0.0000000E-1	0.0000000E-1	0.0000000E-1
385	0.0000000E-1	0.0000000E-1	0.0000000E-1	0.0000000E-1	0.0000000E-1
386	0.0000000E-1	0.0000000E-1	0.0000000E-1	0.0000000E-1	0.0000000E-1
387	0.0000000E-1	0.0000000E-1	0.0000000E-1	0.0000000E-1	0.0000000E-1
388	0.0000000E-1	0.0000000E-1	0.0000000E-1	5.8651429E+0	4.9328395E+0
389	3.2747090E+0	2.6971206E+0	2.3699130E+0	2.1533256E+0	1.9972653E+0
390	1.8785455E+0	1.7847391E+0	1.7085045E+0	1.6451904E+0	1.5916897E+0
391	0.0000000E-1	0.0000000E-1	0.0000000E-1	0.0000000E-1	0.0000000E-1
392	0.0000000E-1	0.0000000E-1	0.0000000E-1	0.0000000E-1	0.0000000E-1
393	0.0000000E-1	0.0000000E-1	0.0000000E-1	0.0000000E-1	0.0000000E-1
394	0.0000000E-1	0.0000000E-1	0.0000000E-1	0.0000000E-1	0.0000000E-1
395	0.0000000E-1	0.0000000E-1	0.0000000E-1	0.0000000E-1	0.0000000E-1
396	0.0000000E-1	0.0000000E-1	0.0000000E-1	0.0000000E-1	0.0000000E-1
397	0.0000000E-1	0.0000000E-1	0.0000000E-1	0.0000000E-1	0.0000000E-1
398	0.0000000E-1	0.0000000E-1	0.0000000E-1	0.0000000E-1	5.9404371E+0
399	4.9942837E+0	3.3139240E+0	2.7282415E+0	2.3962864E+0	2.1764548E+0
400	2.0179865E+0	1.8973828E+0	1.8020477E+0	1.7245391E+0	1.6601412E+0

AREA MATRIX 9

401	0.0000000E-1	0.0000000E-1	0.0000000E-1	0.0000000E-1	0.0000000E-1
402	0.0000000E-1	0.0000000E-1	0.0000000E-1	0.0000000E-1	0.0000000E-1
403	0.0000000E-1	0.0000000E-1	0.0000000E-1	0.0000000E-1	0.0000000E-1
404	0.0000000E-1	0.0000000E-1	0.0000000E-1	0.0000000E-1	0.0000000E-1
405	0.0000000E-1	0.0000000E-1	0.0000000E-1	0.0000000E-1	0.0000000E-1
406	0.0000000E-1	0.0000000E-1	0.0000000E-1	0.0000000E-1	0.0000000E-1
407	0.0000000E-1	0.0000000E-1	0.0000000E-1	0.0000000E-1	0.0000000E-1
408	0.0000000E-1	0.0000000E-1	0.0000000E-1	0.0000000E-1	0.0000000E-1
409	6.0147888E+0	5.0549814E+0	3.3526815E+0	2.7590134E+0	2.4223756E+0
410	2.1993447E+0	2.0385019E+0	1.9160406E+0	1.8191983E+0	1.7404336E+0
411	0.0000000E-1	0.0000000E-1	0.0000000E-1	0.0000000E-1	0.0000000E-1
412	0.0000000E-1	0.0000000E-1	0.0000000E-1	0.0000000E-1	0.0000000E-1
413	0.0000000E-1	0.0000000E-1	0.0000000E-1	0.0000000E-1	0.0000000E-1
414	0.0000000E-1	0.0000000E-1	0.0000000E-1	0.0000000E-1	0.0000000E-1
415	0.0000000E-1	0.0000000E-1	0.0000000E-1	0.0000000E-1	0.0000000E-1
416	0.0000000E-1	0.0000000E-1	0.0000000E-1	0.0000000E-1	0.0000000E-1
417	0.0000000E-1	0.0000000E-1	0.0000000E-1	0.0000000E-1	0.0000000E-1
418	0.0000000E-1	0.0000000E-1	0.0000000E-1	0.0000000E-1	0.0000000E-1
419	0.0000000E-1	6.0882325E+0	5.1149593E+0	3.3909971E+0	2.7894476E+0
420	2.4481893E+0	2.2220023E+0	2.0588173E+0	1.9345238E+0	1.8361950E+0
421	0.0000000E-1	0.0000000E-1	0.0000000E-1	0.0000000E-1	0.0000000E-1
422	0.0000000E-1	0.0000000E-1	0.0000000E-1	0.0000000E-1	0.0000000E-1
423	0.0000000E-1	0.0000000E-1	0.0000000E-1	0.0000000E-1	0.0000000E-1
424	0.0000000E-1	0.0000000E-1	0.0000000E-1	0.0000000E-1	0.0000000E-1
425	0.0000000E-1	0.0000000E-1	0.0000000E-1	0.0000000E-1	0.0000000E-1
426	0.0000000E-1	0.0000000E-1	0.0000000E-1	0.0000000E-1	0.0000000E-1
427	0.0000000E-1	0.0000000E-1	0.0000000E-1	0.0000000E-1	0.0000000E-1
428	0.0000000E-1	0.0000000E-1	0.0000000E-1	0.0000000E-1	0.0000000E-1
429	0.0000000E-1	0.0000000E-1	6.1608008E+0	5.1742422E+0	3.4288855E+0
430	2.8195550E+0	2.4737362E+0	2.2444345E+0	2.0789382E+0	1.9528370E+0
431	0.0000000E-1	0.0000000E-1	0.0000000E-1	0.0000000E-1	0.0000000E-1
432	0.0000000E-1	0.0000000E-1	0.0000000E-1	0.0000000E-1	0.0000000E-1
433	0.0000000E-1	0.0000000E-1	0.0000000E-1	0.0000000E-1	0.0000000E-1
434	0.0000000E-1	0.0000000E-1	0.0000000E-1	0.0000000E-1	0.0000000E-1
435	0.0000000E-1	0.0000000E-1	0.0000000E-1	0.0000000E-1	0.0000000E-1
436	0.0000000E-1	0.0000000E-1	0.0000000E-1	0.0000000E-1	0.0000000E-1
437	0.0000000E-1	0.0000000E-1	0.0000000E-1	0.0000000E-1	0.0000000E-1
438	0.0000000E-1	0.0000000E-1	0.0000000E-1	0.0000000E-1	0.0000000E-1
439	0.0000000E-1	0.0000000E-1	0.0000000E-1	6.2325242E+0	5.2328539E+0
440	3.4663606E+0	2.8493459E+0	2.4990242E+0	2.2666477E+0	2.0988701E+0
441	0.0000000E-1	0.0000000E-1	0.0000000E-1	0.0000000E-1	0.0000000E-1
442	0.0000000E-1	0.0000000E-1	0.0000000E-1	0.0000000E-1	0.0000000E-1
443	0.0000000E-1	0.0000000E-1	0.0000000E-1	0.0000000E-1	0.0000000E-1
444	0.0000000E-1	0.0000000E-1	0.0000000E-1	0.0000000E-1	0.0000000E-1
445	0.0000000E-1	0.0000000E-1	0.0000000E-1	0.0000000E-1	0.0000000E-1
446	0.0000000E-1	0.0000000E-1	0.0000000E-1	0.0000000E-1	0.0000000E-1
447	0.0000000E-1	0.0000000E-1	0.0000000E-1	0.0000000E-1	0.0000000E-1
448	0.0000000E-1	0.0000000E-1	0.0000000E-1	0.0000000E-1	0.0000000E-1
449	0.0000000E-1	0.0000000E-1	0.0000000E-1	0.0000000E-1	6.3034315E+0
450	5.2908165E+0	3.5034357E+0	2.8788299E+0	2.5240609E+0	2.2886481E+0

AREA MATRIX 10

451	0.0000000E-1	0.0000000E-1	0.0000000E-1	0.0000000E-1	0.0000000E-1
452	0.0000000E-1	0.0000000E-1	0.0000000E-1	0.0000000E-1	0.0000000E-1
453	0.0000000E-1	0.0000000E-1	0.0000000E-1	0.0000000E-1	0.0000000E-1
454	0.0000000E-1	0.0000000E-1	0.0000000E-1	0.0000000E-1	0.0000000E-1
455	0.0000000E-1	0.0000000E-1	0.0000000E-1	0.0000000E-1	0.0000000E-1
456	0.0000000E-1	0.0000000E-1	0.0000000E-1	0.0000000E-1	0.0000000E-1
457	0.0000000E-1	0.0000000E-1	0.0000000E-1	0.0000000E-1	0.0000000E-1
458	0.0000000E-1	0.0000000E-1	0.0000000E-1	0.0000000E-1	0.0000000E-1
459	0.0000000E-1	0.0000000E-1	0.0000000E-1	0.0000000E-1	0.0000000E-1
460	6.3735499E+0	5.3481512E+0	3.5401232E+0	2.9080162E+0	2.5488537E+0
461	0.0000000E-1	0.0000000E-1	0.0000000E-1	0.0000000E-1	0.0000000E-1
462	0.0000000E-1	0.0000000E-1	0.0000000E-1	0.0000000E-1	0.0000000E-1
463	0.0000000E-1	0.0000000E-1	0.0000000E-1	0.0000000E-1	0.0000000E-1
464	0.0000000E-1	0.0000000E-1	0.0000000E-1	0.0000000E-1	0.0000000E-1
465	0.0000000E-1	0.0000000E-1	0.0000000E-1	0.0000000E-1	0.0000000E-1
466	0.0000000E-1	0.0000000E-1	0.0000000E-1	0.0000000E-1	0.0000000E-1
467	0.0000000E-1	0.0000000E-1	0.0000000E-1	0.0000000E-1	0.0000000E-1
468	0.0000000E-1	0.0000000E-1	0.0000000E-1	0.0000000E-1	0.0000000E-1
469	0.0000000E-1	0.0000000E-1	0.0000000E-1	0.0000000E-1	0.0000000E-1
470	0.0000000E-1	6.4429054E+0	5.4048780E+0	3.5764351E+0	2.9369138E+0
471	0.0000000E-1	0.0000000E-1	0.0000000E-1	0.0000000E-1	0.0000000E-1
472	0.0000000E-1	0.0000000E-1	0.0000000E-1	0.0000000E-1	0.0000000E-1
473	0.0000000E-1	0.0000000E-1	0.0000000E-1	0.0000000E-1	0.0000000E-1
474	0.0000000E-1	0.0000000E-1	0.0000000E-1	0.0000000E-1	0.0000000E-1
475	0.0000000E-1	0.0000000E-1	0.0000000E-1	0.0000000E-1	0.0000000E-1
476	0.0000000E-1	0.0000000E-1	0.0000000E-1	0.0000000E-1	0.0000000E-1
477	0.0000000E-1	0.0000000E-1	0.0000000E-1	0.0000000E-1	0.0000000E-1
478	0.0000000E-1	0.0000000E-1	0.0000000E-1	0.0000000E-1	0.0000000E-1
479	0.0000000E-1	0.0000000E-1	0.0000000E-1	0.0000000E-1	0.0000000E-1
480	0.0000000E-1	0.0000000E-1	6.5115221E+0	5.4610157E+0	3.6123827E+0
481	0.0000000E-1	0.0000000E-1	0.0000000E-1	0.0000000E-1	0.0000000E-1
482	0.0000000E-1	0.0000000E-1	0.0000000E-1	0.0000000E-1	0.0000000E-1
483	0.0000000E-1	0.0000000E-1	0.0000000E-1	0.0000000E-1	0.0000000E-1
484	0.0000000E-1	0.0000000E-1	0.0000000E-1	0.0000000E-1	0.0000000E-1
485	0.0000000E-1	0.0000000E-1	0.0000000E-1	0.0000000E-1	0.0000000E-1
486	0.0000000E-1	0.0000000E-1	0.0000000E-1	0.0000000E-1	0.0000000E-1
487	0.0000000E-1	0.0000000E-1	0.0000000E-1	0.0000000E-1	0.0000000E-1
488	0.0000000E-1	0.0000000E-1	0.0000000E-1	0.0000000E-1	0.0000000E-1
489	0.0000000E-1	0.0000000E-1	0.0000000E-1	0.0000000E-1	0.0000000E-1
490	0.0000000E-1	0.0000000E-1	0.0000000E-1	6.5794233E+0	5.5165824E+0
491	0.0000000E-1	0.0000000E-1	0.0000000E-1	0.0000000E-1	0.0000000E-1
492	0.0000000E-1	0.0000000E-1	0.0000000E-1	0.0000000E-1	0.0000000E-1
493	0.0000000E-1	0.0000000E-1	0.0000000E-1	0.0000000E-1	0.0000000E-1
494	0.0000000E-1	0.0000000E-1	0.0000000E-1	0.0000000E-1	0.0000000E-1
495	0.0000000E-1	0.0000000E-1	0.0000000E-1	0.0000000E-1	0.0000000E-1
496	0.0000000E-1	0.0000000E-1	0.0000000E-1	0.0000000E-1	0.0000000E-1
497	0.0000000E-1	0.0000000E-1	0.0000000E-1	0.0000000E-1	0.0000000E-1
498	0.0000000E-1	0.0000000E-1	0.0000000E-1	0.0000000E-1	0.0000000E-1
499	0.0000000E-1	0.0000000E-1	0.0000000E-1	0.0000000E-1	0.0000000E-1
500	0.0000000E-1	0.0000000E-1	0.0000000E-1	0.0000000E-1	6.6466308E+0

INVERSE AREA MATRIX 1

1	1.2732395E+0	-1.1690219E+0	1.7050617E-1	-1.3705760E-1	-4.2965059E-3
2	-2.9678093E-2	-1.2260348E-2	-1.2206130E-2	-8.5121852E-3	-7.1433272E-3
3	-5.7399487E-3	-4.8211275E-3	-4.0691575E-3	-3.4926999E-3	-3.0264345E-3
4	-2.6490453E-3	-2.3376205E-3	-2.0782017E-3	-1.8596348E-3	-1.6738346E-3
5	-1.5145436E-3	-1.3769556E-3	-1.2572978E-3	-1.1525855E-3	-1.0604294E-3
6	-9.7889950E-4	-9.0642275E-4	-8.4170682E-4	-7.8368197E-4	-7.3145664E-4
7	-6.8428293E-4	-6.4152977E-4	-6.0266160E-4	-5.6722161E-4	-5.3481817E-4
8	-5.0511406E-4	-4.7781757E-4	-4.5267537E-4	-4.2946659E-4	-4.0799797E-4
9	-3.8809979E-4	-3.6962252E-4	-3.5243405E-4	-3.3641723E-4	-3.2146795E-4
10	-3.0749341E-4	-2.9441068E-4	-2.8214544E-4	-2.7063100E-4	-2.5980729E-4
11	0.0000000E-1	8.1408716E-1	-7.0856510E-1	1.0406641E-1	-9.0639149E-2
12	-5.9025008E-3	-2.1753615E-2	-1.0134980E-2	-9.7666299E-3	-7.1020370E-3
13	-5.9941813E-3	-4.9034743E-3	-4.1592971E-3	-3.5485056E-3	-3.0717584E-3
14	-2.6825925E-3	-2.3641034E-3	-2.0989953E-3	-1.8763174E-3	-1.6873307E-3
15	-1.5255936E-3	-1.3860848E-3	-1.2649076E-3	-1.1589789E-3	-1.0658402E-3
16	-9.8350940E-4	-9.1037466E-4	-8.4511406E-4	-7.8663525E-4	-7.3402910E-4
17	-6.8653405E-4	-6.4350818E-4	-6.0440740E-4	-5.6876799E-4	-5.3619282E-4
18	-5.0634017E-4	-4.7891467E-4	-4.5366000E-4	-4.3035280E-4	-4.0879775E-4
19	-3.8882343E-4	-3.7027887E-4	-3.5303075E-4	-3.3696091E-4	-3.2196437E-4
20	-3.0794759E-4	-2.9482702E-4	-2.8252781E-4	-2.7098278E-4	-2.6013149E-4
21	0.0000000E-1	0.0000000E-1	6.4568574E-1	-5.5247599E-1	8.4303094E-2
22	-7.2458873E-2	-4.8626627E-3	-1.7881591E-2	-8.5546519E-3	-8.2864427E-3
23	-6.1209033E-3	-5.2083367E-3	-4.3027464E-3	-3.6771905E-3	-3.1598032E-3
24	-2.7523055E-3	-2.4172732E-3	-2.1411481E-3	-1.9098678E-3	-1.7144700E-3
25	-1.5477516E-3	-1.4043667E-3	-1.2801227E-3	-1.1717462E-3	-1.0766329E-3
26	-9.9269556E-4	-9.1824265E-4	-8.5189232E-4	-7.9250625E-4	-7.3913983E-4
27	-6.9100378E-4	-6.4743441E-4	-6.0787034E-4	-5.7183406E-4	-5.3891732E-4
28	-5.0876939E-4	-4.8108758E-4	-4.5560955E-4	-4.3210698E-4	-4.1038045E-4
29	-3.9025510E-4	-3.7157712E-4	-3.5421077E-4	-3.3803586E-4	-3.2294570E-4
30	-3.0884528E-4	-2.9564979E-4	-2.8328332E-4	-2.7167777E-4	-2.6077190E-4
31	0.0000000E-1	0.0000000E-1	0.0000000E-1	5.5149684E-1	-4.6795740E-1
32	7.3412978E-2	-6.2002310E-2	-3.9897793E-3	-1.5445017E-2	-7.4437442E-3
33	-7.2665423E-3	-5.4115435E-3	-4.6335861E-3	-3.8524330E-3	-3.3102475E-3
34	-2.8590699E-3	-2.5018098E-3	-2.2065955E-3	-1.9621254E-3	-1.7564503E-3
35	-1.5819593E-3	-1.4324977E-3	-1.3034827E-3	-1.1913051E-3	-1.0931369E-3
36	-1.0067196E-3	-9.3023689E-4	-8.6221192E-4	-8.0143421E-4	-7.4690352E-4
37	-6.9778733E-4	-6.5338803E-4	-6.1311738E-4	-5.7647647E-4	-5.4303988E-4
38	-5.1244298E-4	-4.8437178E-4	-4.5855467E-4	-4.3475574E-4	-4.1276925E-4
39	-3.9241511E-4	-3.7353511E-4	-3.5598984E-4	-3.3965602E-4	-3.2442431E-4
40	-3.1019748E-4	-2.9688882E-4	-2.8442079E-4	-2.7272388E-4	-2.6173565E-4
41	0.0000000E-1	0.0000000E-1	0.0000000E-1	0.0000000E-1	4.8929332E-1
42	-4.1313009E-1	6.6097311E-2	-5.5013343E-2	-3.3483466E-3	-1.3742009E-2
43	-6.6284947E-3	-6.5162403E-3	-4.8755286E-3	-4.1940667E-3	-3.5023177E-3
44	-3.0214343E-3	-2.6194506E-3	-2.3000885E-3	-2.0352535E-3	-1.8152183E-3
45	-1.6295113E-3	-1.4714836E-3	-1.3357327E-3	-1.2182303E-3	-1.1157950E-3
46	-1.0259287E-3	-9.4663171E-4	-8.7629179E-4	-8.1359530E-4	-7.5746309E-4
47	-7.0700150E-4	-6.6146513E-4	-6.2022808E-4	-5.8276152E-4	-5.4861605E-4
48	-5.1740773E-4	-4.8880688E-4	-4.6252908E-4	-4.3832789E-4	-4.1598888E-4
49	-3.9532475E-4	-3.7617126E-4	-3.5838395E-4	-3.4183530E-4	-3.2641236E-4
50	-3.1201487E-4	-2.9855350E-4	-2.8594849E-4	-2.7412843E-4	-2.6302923E-4

INVERSE AREA MATRIX 2

51	0.0000000E-1	0.0000000E-1	0.0000000E-1	0.0000000E-1	0.0000000E-1
52	4.4429086E-1	-3.7391210E-1	6.0691203E-2	-4.9929684E-2	-2.8733927E-3
53	-1.2472932E-2	-6.0055526E-3	-5.9388584E-3	-4.4558943E-3	-3.8464897E-3
54	-3.2220767E-3	-2.7880015E-3	-2.4239248E-3	-2.1340819E-3	-1.8931223E-3
55	-1.6924631E-3	-1.5227193E-3	-1.3779550E-3	-1.2533296E-3	-1.1452326E-3
56	-1.0508075E-3	-9.6780822E-4	-8.9443412E-4	-8.2923146E-4	-7.7101382E-4
57	-7.1880511E-4	-6.7179582E-4	-6.2930976E-4	-5.9077826E-4	-5.5572017E-4
58	-5.2372603E-4	-4.9444551E-4	-4.6757738E-4	-4.4286141E-4	-4.2007183E-4
59	-3.9901191E-4	-3.7950962E-4	-3.6141392E-4	-3.4459177E-4	-3.2892561E-4
60	-3.1431121E-4	-3.0065589E-4	-2.8787704E-4	-2.7590078E-4	-2.6466091E-4
61	0.0000000E-1	0.0000000E-1	0.0000000E-1	0.0000000E-1	0.0000000E-1
62	0.0000000E-1	4.0978827E-1	-3.4407951E-1	5.6464440E-2	-4.6022848E-2
63	-2.5127213E-3	-1.1484285E-2	-5.5136296E-3	-5.4793734E-3	-4.1179768E-3
64	-3.5642805E-3	-2.9924426E-3	-2.5952270E-3	-2.2612261E-3	-1.9949895E-3
65	-1.7732584E-3	-1.5883132E-3	-1.4315998E-3	-1.2977294E-3	-1.1822958E-3
66	-1.0820130E-3	-9.9427796E-4	-9.1704283E-4	-8.4866419E-4	-7.8781399E-4
67	-7.3340733E-4	-6.8455080E-4	-6.4050264E-4	-6.0064266E-4	-5.6444873E-4
68	-5.3147863E-4	-5.0135560E-4	-4.7375700E-4	-4.4840509E-4	-4.2505972E-4
69	-4.0351229E-4	-3.8358089E-4	-3.6510625E-4	-3.4794843E-4	-3.3198404E-4
70	-3.1710394E-4	-3.0321126E-4	-2.9021983E-4	-2.7805272E-4	-2.6664111E-4
71	0.0000000E-1	0.0000000E-1	0.0000000E-1	0.0000000E-1	0.0000000E-1
72	0.0000000E-1	0.0000000E-1	3.8224917E-1	-3.2040439E-1	5.3033000E-2
73	-4.2901703E-2	-2.2317024E-3	-1.0688389E-2	-5.1147190E-3	-5.1040252E-3
74	-3.8395931E-3	-3.3302196E-3	-2.8006204E-3	-2.4331748E-3	-2.1236143E-3
75	-1.8766740E-3	-1.6707493E-3	-1.4987924E-3	-1.3529055E-3	-1.2281324E-3
76	-1.1204117E-3	-1.0267159E-3	-9.4464533E-4	-8.7231127E-4	-8.0819723E-4
77	-7.5107704E-4	-6.9994841E-4	-6.5398543E-4	-6.1250194E-4	-5.7492380E-4
78	-5.4076733E-4	-5.0962256E-4	-4.8113996E-4	-4.5501997E-4	-4.3100452E-4
79	-4.0887030E-4	-3.8842321E-4	-3.6949382E-4	-3.5193371E-4	-3.3561235E-4
80	-3.2041457E-4	-3.0623842E-4	-2.9299336E-4	-2.8059875E-4	-2.6898261E-4
81	0.0000000E-1	0.0000000E-1	0.0000000E-1	0.0000000E-1	0.0000000E-1
82	0.0000000E-1	0.0000000E-1	0.0000000E-1	3.5960763E-1	-3.0102493E-1
83	5.0170659E-2	-4.0335269E-2	-2.0076583E-3	-1.0031219E-2	-4.7841595E-3
84	-4.7909121E-3	-3.6059224E-3	-3.1326622E-3	-2.6377916E-3	-2.2949019E-3
85	-2.0056020E-3	-1.7747291E-3	-1.5820248E-3	-1.4209789E-3	-1.2842256E-3
86	-1.1671587E-3	-1.0659975E-3	-9.7792529E-4	-9.0070857E-4	-8.3258916E-4
87	-7.7215500E-4	-7.1826401E-4	-6.6998229E-4	-6.2653999E-4	-5.8729723E-4
88	-5.5171835E-4	-5.1935188E-4	-4.8981494E-4	-4.6278095E-4	-4.3796983E-4
89	-4.1514020E-4	-3.9408306E-4	-3.7461662E-4	-3.5658214E-4	-3.3984045E-4
90	-3.2426913E-4	-3.0976006E-4	-2.9621748E-4	-2.8355632E-4	-2.7170076E-4
91	0.0000000E-1	0.0000000E-1	0.0000000E-1	0.0000000E-1	0.0000000E-1
92	0.0000000E-1	0.0000000E-1	0.0000000E-1	0.0000000E-1	3.4056520E-1
93	-2.8478238E-1	4.7733379E-2	-3.8177360E-2	-1.8254498E-3	-9.4775459E-3
94	-4.5052996E-3	-4.5251891E-3	-3.4066974E-3	-2.9634518E-3	-2.4976863E-3
95	-2.1754134E-3	-1.9031937E-3	-1.6859116E-3	-1.5044301E-3	-1.3526790E-3
96	-1.2237333E-3	-1.1132762E-3	-1.0177597E-3	-9.3454240E-4	-8.6152906E-4
97	-7.9707053E-4	-7.3984211E-4	-6.8877221E-4	-6.4298443E-4	-6.0175611E-4
98	-5.6448648E-4	-5.3067246E-4	-4.9988989E-4	-4.7177895E-4	-4.4603259E-4
99	-4.2238743E-4	-4.0061634E-4	-3.8052259E-4	-3.6193502E-4	-3.4470408E-4
100	-3.2869862E-4	-3.1380319E-4	-2.9991580E-4	-2.8694610E-4	-2.7481375E-4

INVERSE AREA MATRIX 3

101	0.0000000E-1	0.0000000E-1	0.0000000E-1	0.0000000E-1	0.0000000E-1
102	0.0000000E-1	0.0000000E-1	0.0000000E-1	0.0000000E-1	0.0000000E-1
103	3.2425933E-1	-2.7091292E-1	4.5624106E-2	-3.6330429E-2	-1.6747054E-3
104	-9.0033501E-3	-4.2665057E-3	-4.2964294E-3	-3.2345841E-3	-2.8167058E-3
105	-2.3757261E-3	-2.0710252E-3	-1.8134122E-3	-1.6077826E-3	-1.4359511E-3
106	-1.2922148E-3	-1.1700204E-3	-1.0652948E-3	-9.7468652E-4	-8.9570196E-4
107	-8.2636304E-4	-7.6511294E-4	-7.1070109E-4	-6.6211587E-4	-6.1852982E-4
108	-5.7926059E-4	-5.4374083E-4	-5.1149536E-4	-4.8212348E-4	-4.5528519E-4
109	-4.3069028E-4	-4.0808975E-4	-3.8726882E-4	-3.6804140E-4	-3.5024554E-4
110	-3.3373968E-4	-3.1839964E-4	-3.0411608E-4	-2.9079238E-4	-2.7834289E-4
111	0.0000000E-1	0.0000000E-1	0.0000000E-1	0.0000000E-1	0.0000000E-1
112	0.0000000E-1	0.0000000E-1	0.0000000E-1	0.0000000E-1	0.0000000E-1
113	0.0000000E-1	3.1009168E-1	-2.5888999E-1	4.3774546E-2	-3.4726609E-2
114	-1.5481339E-3	-8.5916536E-3	-4.0594098E-3	-4.0970891E-3	-3.0842049E-3
115	-2.6880744E-3	-2.2684905E-3	-1.9789612E-3	-1.7339945E-3	-1.5384731E-3
116	-1.3750326E-3	-1.2382809E-3	-1.1219839E-3	-1.0222765E-3	-9.3597536E-4
117	-8.6071369E-4	-7.9461379E-4	-7.3619817E-4	-6.8427999E-4	-6.3789921E-4
118	-5.9627060E-4	-5.5874660E-4	-5.2478873E-4	-4.9394600E-4	-4.6583803E-4
119	-4.4014203E-4	-4.1658246E-4	-3.9492282E-4	-3.7495913E-4	-3.5651458E-4
120	-3.3943527E-4	-3.2358668E-4	-3.0885074E-4	-2.9512347E-4	-2.8231297E-4
121	0.0000000E-1	0.0000000E-1	0.0000000E-1	0.0000000E-1	0.0000000E-1
122	0.0000000E-1	0.0000000E-1	0.0000000E-1	0.0000000E-1	0.0000000E-1
123	0.0000000E-1	0.0000000E-1	2.9763237E-1	-2.4833728E-1	4.2134963E-2
124	-3.3317048E-2	-1.4404852E-3	-8.2300932E-3	-3.8778400E-3	-3.9215714E-3
125	-2.9515274E-3	-2.5742714E-3	-2.1733731E-3	-1.8970897E-3	-1.6631901E-3
126	-1.4765275E-3	-1.3204547E-3	-1.1898474E-3	-1.0787482E-3	-9.8347213E-4
127	-9.0098176E-4	-8.2902030E-4	-7.6579717E-4	-7.0990375E-4	-6.6020862E-4
128	-6.1579667E-4	-5.7591941E-4	-5.3995964E-4	-5.0740411E-4	-4.7782293E-4
129	-4.5085353E-4	-4.2618820E-4	-4.0356425E-4	-3.8275621E-4	-3.6356955E-4
130	-3.4583566E-4	-3.2940775E-4	-3.1415748E-4	-2.9997220E-4	-2.8675268E-4
131	0.0000000E-1	0.0000000E-1	0.0000000E-1	0.0000000E-1	0.0000000E-1
132	0.0000000E-1	0.0000000E-1	0.0000000E-1	0.0000000E-1	0.0000000E-1
133	0.0000000E-1	0.0000000E-1	0.0000000E-1	2.8656354E-1	-2.3897773E-1
134	4.0668115E-2	-3.2065583E-2	-1.3478967E-3	-7.9094371E-3	-3.7171440E-3
135	-3.7656339E-3	-2.8334676E-3	-2.4727671E-3	-2.0883526E-3	-1.8237473E-3
136	-1.5996236E-3	-1.4207950E-3	-1.2712478E-3	-1.1460906E-3	-1.0396092E-3
137	-9.4827622E-4	-8.6918235E-4	-8.0016709E-4	-7.3951632E-4	-6.8588187E-4
138	-6.3818100E-4	-5.9553804E-4	-5.5723685E-4	-5.2268692E-4	-4.9139723E-4
139	-4.6295651E-4	-4.3701790E-4	-4.1328701E-4	-3.9151253E-4	-3.7147872E-4
140	-3.5299945E-4	-3.3591338E-4	-3.2008003E-4	-3.0537656E-4	-2.9169515E-4
141	0.0000000E-1	0.0000000E-1	0.0000000E-1	0.0000000E-1	0.0000000E-1
142	0.0000000E-1	0.0000000E-1	0.0000000E-1	0.0000000E-1	0.0000000E-1
143	0.0000000E-1	0.0000000E-1	0.0000000E-1	0.0000000E-1	2.7664441E-1
144	-2.3060226E-1	3.9345458E-2	-3.0944800E-2	-1.2674706E-3	-7.6226421E-3
145	-3.5737481E-3	-3.6260003E-3	-2.7276265E-3	-2.3815826E-3	-2.0118375E-3
146	-1.7576162E-3	-1.5421996E-3	-1.3703541E-3	-1.2266311E-3	-1.1063440E-3
147	-1.0039944E-3	-9.1619433E-4	-8.4014774E-4	-7.7377943E-4	-7.1544296E-4
148	-6.6384370E-4	-6.1794202E-4	-5.7689724E-4	-5.4002189E-4	-5.0674914E-4
149	-4.7660773E-4	-4.4920291E-4	-4.2420181E-4	-4.0132190E-4	-3.8032197E-4
150	-3.6099498E-4	-3.4316230E-4	-3.2666907E-4	-3.1138045E-4	-2.9717853E-4

INVERSE AREA MATRIX 4

151	0.0000000E-1	0.0000000E-1	0.0000000E-1	0.0000000E-1	0.0000000E-1
152	0.0000000E-1	0.0000000E-1	0.0000000E-1	0.0000000E-1	0.0000000E-1
153	0.0000000E-1	0.0000000E-1	0.0000000E-1	0.0000000E-1	0.0000000E-1
154	2.6768880E-1	-2.2304972E-1	3.8144684E-2	-2.9933495E-2	-1.1969952E-3
155	-7.3642346E-3	-3.4448606E-3	-3.5000985E-3	-2.6321090E-3	-2.2991467E-3
156	-1.9425573E-3	-1.6976395E-3	-1.4900347E-3	-1.3244581E-3	-1.1859689E-3
157	-1.0700627E-3	-9.7143377E-4	-8.8681867E-4	-8.1352242E-4	-7.4954593E-4
158	-6.9330320E-4	-6.4354740E-4	-5.9927738E-4	-5.5968370E-4	-5.2410454E-4
159	-4.9199424E-4	-4.6289918E-4	-4.3643943E-4	-4.1229462E-4	-3.9019284E-4
160	-3.6990196E-4	-3.5122275E-4	-3.3398329E-4	-3.1803455E-4	-3.0324676E-4
161	0.0000000E-1	0.0000000E-1	0.0000000E-1	0.0000000E-1	0.0000000E-1
162	0.0000000E-1	0.0000000E-1	0.0000000E-1	0.0000000E-1	0.0000000E-1
163	0.0000000E-1	0.0000000E-1	0.0000000E-1	0.0000000E-1	0.0000000E-1
164	0.0000000E-1	2.5955019E-1	-2.1619363E-1	3.7048060E-2	-2.9014978E-2
165	-1.1347558E-3	-7.1298910E-3	-3.3282686E-3	-3.3858798E-3	-2.5453979E-3
166	-2.2241959E-3	-1.8794853E-3	-1.6429590E-3	-1.4424088E-3	-1.2824955E-3
167	-1.1487387E-3	-1.0367967E-3	-9.4153773E-4	-8.5980999E-4	-7.8900953E-4
168	-7.2720568E-4	-6.7286677E-4	-6.2478896E-4	-5.8200570E-4	-5.4373568E-4
169	-5.0934010E-4	-4.7829238E-4	-4.5015478E-4	-4.2456072E-4	-4.0120109E-4
170	-3.7981355E-4	-3.6017418E-4	-3.4209075E-4	-3.2539744E-4	-3.0995047E-4
171	0.0000000E-1	0.0000000E-1	0.0000000E-1	0.0000000E-1	0.0000000E-1
172	0.0000000E-1	0.0000000E-1	0.0000000E-1	0.0000000E-1	0.0000000E-1
173	0.0000000E-1	0.0000000E-1	0.0000000E-1	0.0000000E-1	0.0000000E-1
174	0.0000000E-1	0.0000000E-1	2.5211146E-1	-2.0993316E-1	3.6041284E-2
175	-2.8175908E-2	-1.0794047E-3	-6.9161471E-3	-3.2221942E-3	-3.2816915E-3
176	-2.4662640E-3	-2.1557021E-3	-1.8217826E-3	-1.5928708E-3	-1.3987285E-3
177	-1.2439608E-3	-1.1145068E-3	-1.0061714E-3	-9.1398060E-4	-8.3488374E-4
178	-7.6635926E-4	-7.0653841E-4	-6.5393869E-4	-6.0739513E-4	-5.6597253E-4
179	-5.2891500E-4	-4.9560463E-4	-4.6553208E-4	-4.3827400E-4	-4.1347589E-4
180	-3.9083885E-4	-3.7010924E-4	-3.5107053E-4	-3.3353690E-4	-3.1734803E-4
181	0.0000000E-1	0.0000000E-1	0.0000000E-1	0.0000000E-1	0.0000000E-1
182	0.0000000E-1	0.0000000E-1	0.0000000E-1	0.0000000E-1	0.0000000E-1
183	0.0000000E-1	0.0000000E-1	0.0000000E-1	0.0000000E-1	0.0000000E-1
184	0.0000000E-1	0.0000000E-1	0.0000000E-1	2.4527773E-1	-2.0418679E-1
185	3.5112672E-2	-2.7405480E-2	-1.0298687E-3	-6.7201921E-3	-3.1251927E-3
186	-3.1861849E-3	-2.3937002E-3	-2.0928203E-3	-1.7687571E-3	-1.5467920E-3
187	-1.3585008E-3	-1.2084325E-3	-1.0829101E-3	-9.7787203E-4	-8.8848804E-4
188	-8.1179951E-4	-7.4535993E-4	-6.8735691E-4	-6.3635273E-4	-5.9121781E-4
189	-5.5104547E-4	-5.1510296E-4	-4.8279136E-4	-4.5361706E-4	-4.2716979E-4
190	-4.0310607E-4	-3.8113628E-4	-3.6101470E-4	-3.4253157E-4	-3.2550688E-4
191	0.0000000E-1	0.0000000E-1	0.0000000E-1	0.0000000E-1	0.0000000E-1
192	0.0000000E-1	0.0000000E-1	0.0000000E-1	0.0000000E-1	0.0000000E-1
193	0.0000000E-1	0.0000000E-1	0.0000000E-1	0.0000000E-1	0.0000000E-1
194	0.0000000E-1	0.0000000E-1	0.0000000E-1	0.0000000E-1	2.3897119E-1
195	-1.9888780E-1	3.4252570E-2	-2.6694837E-2	-9.8528375E-4	-6.5397190E-3
196	-3.0360770E-3	-3.0982475E-3	-2.3268733E-3	-2.0348492E-3	-1.7198323E-3
197	-1.5042356E-3	-1.3213125E-3	-1.1755559E-3	-1.0536427E-3	-9.5163249E-4
198	-8.6482737E-4	-7.9035276E-4	-7.2583093E-4	-6.6950105E-4	-6.1996637E-4
199	-5.7612969E-4	-5.3711042E-4	-5.0219699E-4	-4.7080786E-4	-4.4246378E-4
200	-4.1676647E-4	-3.9338252E-4	-3.7203082E-4	-3.5247289E-4	-3.3450516E-4

INVERSE AREA MATRIX 5

201	0.0000000E-1	0.0000000E-1	0.0000000E-1	0.0000000E-1	0.0000000E-1
202	0.0000000E-1	0.0000000E-1	0.0000000E-1	0.0000000E-1	0.0000000E-1
203	0.0000000E-1	0.0000000E-1	0.0000000E-1	0.0000000E-1	0.0000000E-1
204	0.0000000E-1	0.0000000E-1	0.0000000E-1	0.0000000E-1	0.0000000E-1
205	2.3312737E-1	-1.9398102E-1	3.3452922E-2	-2.6036640E-2	-9.4494690E-4
206	-6.3728155E-3	-2.9538627E-3	-3.0169537E-3	-2.2650879E-3	-1.9812014E-3
207	-1.6745241E-3	-1.4647914E-3	-1.2868147E-3	-1.1450309E-3	-1.0264444E-3
208	-9.2722616E-4	-8.4279987E-4	-7.7036840E-4	-7.0761726E-4	-6.5283305E-4
209	-6.0465667E-4	-5.6202070E-4	-5.2406852E-4	-4.9010804E-4	-4.5957367E-4
210	-4.3199937E-4	-4.0699789E-4	-3.8424506E-4	-3.6346760E-4	-3.4443367E-4
211	0.0000000E-1	0.0000000E-1	0.0000000E-1	0.0000000E-1	0.0000000E-1
212	0.0000000E-1	0.0000000E-1	0.0000000E-1	0.0000000E-1	0.0000000E-1
213	0.0000000E-1	0.0000000E-1	0.0000000E-1	0.0000000E-1	0.0000000E-1
214	0.0000000E-1	0.0000000E-1	0.0000000E-1	0.0000000E-1	0.0000000E-1
215	0.0000000E-1	2.2769231E-1	-1.8942033E-1	3.2706940E-2	-2.5424752E-2
216	-9.0828066E-4	-6.2178814E-3	-2.8777258E-3	-2.9415260E-3	-2.2077588E-3
217	-1.9313816E-3	-1.6324232E-3	-1.4281117E-3	-1.2547105E-3	-1.1166015E-3
218	-1.0010931E-3	-9.0445879E-4	-8.2223486E-4	-7.5169566E-4	-6.9058515E-4
219	-6.3723371E-4	-5.9031705E-4	-5.4879521E-4	-5.1183370E-4	-4.7875840E-4
220	-4.4901845E-4	-4.2216002E-4	-3.9780600E-4	-3.7564076E-4	-3.5539826E-4
221	0.0000000E-1	0.0000000E-1	0.0000000E-1	0.0000000E-1	0.0000000E-1
222	0.0000000E-1	0.0000000E-1	0.0000000E-1	0.0000000E-1	0.0000000E-1
223	0.0000000E-1	0.0000000E-1	0.0000000E-1	0.0000000E-1	0.0000000E-1
224	0.0000000E-1	0.0000000E-1	0.0000000E-1	0.0000000E-1	0.0000000E-1
225	0.0000000E-1	0.0000000E-1	2.2262049E-1	-1.8516687E-1	3.2008864E-2
226	-2.4853994E-2	-8.7480663E-4	-6.0735665E-3	-2.8069714E-3	-2.8713069E-3
227	-2.1543898E-3	-1.8849687E-3	-1.5931806E-3	-1.3938994E-3	-1.2247459E-3
228	-1.0900481E-3	-9.7739771E-4	-8.8316297E-4	-8.0298486E-4	-7.3420397E-4
229	-6.7461850E-4	-6.2259941E-4	-5.7685464E-4	-5.3636971E-4	-5.0033064E-4
230	-4.6807996E-4	-4.3908045E-4	-4.1288957E-4	-3.8913964E-4	-3.6752292E-4
231	0.0000000E-1	0.0000000E-1	0.0000000E-1	0.0000000E-1	0.0000000E-1
232	0.0000000E-1	0.0000000E-1	0.0000000E-1	0.0000000E-1	0.0000000E-1
233	0.0000000E-1	0.0000000E-1	0.0000000E-1	0.0000000E-1	0.0000000E-1
234	0.0000000E-1	0.0000000E-1	0.0000000E-1	0.0000000E-1	0.0000000E-1
235	0.0000000E-1	0.0000000E-1	0.0000000E-1	2.1787317E-1	-1.8118763E-1
236	3.1353762E-2	-2.4319962E-2	-8.4412525E-4	-5.9387232E-3	-2.7410092E-3
237	-2.8057358E-3	-2.1045572E-3	-1.8416025E-3	-1.5564974E-3	-1.3618992E-3
238	-1.1967021E-3	-1.0651812E-3	-9.5519290E-4	-8.6319361E-4	-7.8492181E-4
239	-7.1777976E-4	-6.5961610E-4	-6.0883959E-4	-5.6418815E-4	-5.2467099E-4
240	-4.8949320E-4	-4.5801278E-4	-4.2970522E-4	-4.0413845E-4	-3.8095355E-4
241	0.0000000E-1	0.0000000E-1	0.0000000E-1	0.0000000E-1	0.0000000E-1
242	0.0000000E-1	0.0000000E-1	0.0000000E-1	0.0000000E-1	0.0000000E-1
243	0.0000000E-1	0.0000000E-1	0.0000000E-1	0.0000000E-1	0.0000000E-1
244	0.0000000E-1	0.0000000E-1	0.0000000E-1	0.0000000E-1	0.0000000E-1
245	0.0000000E-1	0.0000000E-1	0.0000000E-1	0.0000000E-1	2.1341715E-1
246	-1.7745437E-1	3.0737390E-2	-2.3818885E-2	-8.1590037E-4	-5.8123687E-3
247	-2.6793340E-3	-2.7443320E-3	-2.0578972E-3	-1.8009729E-3	-1.5221154E-3
248	-1.3318906E-3	-1.1703897E-3	-1.0418363E-3	-9.3433500E-4	-8.4442433E-4
249	-7.6793396E-4	-7.0232368E-4	-6.4548929E-4	-5.9587480E-4	-5.5224612E-4
250	-5.1363456E-4	-4.7926302E-4	-4.4850391E-4	-4.2084455E-4	-3.9586269E-4

INVERSE AREA MATRIX 6

251	0.0000000E-1	0.0000000E-1	0.0000000E-1	0.0000000E-1	0.0000000E-1
252	0.0000000E-1	0.0000000E-1	0.0000000E-1	0.0000000E-1	0.0000000E-1
253	0.0000000E-1	0.0000000E-1	0.0000000E-1	0.0000000E-1	0.0000000E-1
254	0.0000000E-1	0.0000000E-1	0.0000000E-1	0.0000000E-1	0.0000000E-1
255	0.0000000E-1	0.0000000E-1	0.0000000E-1	0.0000000E-1	0.0000000E-1
256	2.0922381E-1	-1.7394274E-1	3.0156068E-2	-2.3347511E-2	-7.8984727E-4
257	-5.6936564E-3	-2.6215110E-3	-2.6866807E-3	-2.0140951E-3	-1.7628113E-3
258	-1.4898109E-3	-1.3036819E-3	-1.1456438E-3	-1.0198699E-3	-9.1469849E-4
259	-8.2674452E-4	-7.5192331E-4	-6.8774851E-4	-6.3216008E-4	-5.8363502E-4
260	-5.4096548E-4	-5.0320342E-4	-4.6958841E-4	-4.3950636E-4	-4.1245566E-4
261	0.0000000E-1	0.0000000E-1	0.0000000E-1	0.0000000E-1	0.0000000E-1
262	0.0000000E-1	0.0000000E-1	0.0000000E-1	0.0000000E-1	0.0000000E-1
263	0.0000000E-1	0.0000000E-1	0.0000000E-1	0.0000000E-1	0.0000000E-1
264	0.0000000E-1	0.0000000E-1	0.0000000E-1	0.0000000E-1	0.0000000E-1
265	0.0000000E-1	0.0000000E-1	0.0000000E-1	0.0000000E-1	0.0000000E-1
266	0.0000000E-1	2.0526832E-1	-1.7063165E-1	2.9606588E-2	-2.2903021E-2
267	-7.6572323E-4	-5.5818525E-3	-2.5671638E-3	-2.6324216E-3	-1.9728778E-3
268	-1.7268840E-3	-1.4593890E-3	-1.2771057E-3	-1.1223202E-3	-9.9915655E-4
269	-8.9617320E-4	-8.1005697E-4	-7.3680360E-4	-6.7397731E-4	-6.1955956E-4
270	-5.7205832E-4	-5.3029033E-4	-4.9332699E-4	-4.6042346E-4	-4.3097833E-4
271	0.0000000E-1	0.0000000E-1	0.0000000E-1	0.0000000E-1	0.0000000E-1
272	0.0000000E-1	0.0000000E-1	0.0000000E-1	0.0000000E-1	0.0000000E-1
273	0.0000000E-1	0.0000000E-1	0.0000000E-1	0.0000000E-1	0.0000000E-1
274	0.0000000E-1	0.0000000E-1	0.0000000E-1	0.0000000E-1	0.0000000E-1
275	0.0000000E-1	0.0000000E-1	0.0000000E-1	0.0000000E-1	0.0000000E-1
276	0.0000000E-1	0.0000000E-1	2.0152902E-1	-1.6750271E-1	2.9086142E-2
277	-2.2482956E-2	-7.4332019E-4	-5.4763176E-3	-2.5159646E-3	-2.5812407E-3
278	-1.9340064E-3	-1.6929868E-3	-1.4306786E-3	-1.2520152E-3	-1.1002920E-3
279	-9.7958557E-4	-8.7866206E-4	-7.9427587E-4	-7.2249856E-4	-6.6094199E-4
280	-6.0762665E-4	-5.6108969E-4	-5.2017099E-4	-4.8396020E-4	-4.5172720E-4
281	0.0000000E-1	0.0000000E-1	0.0000000E-1	0.0000000E-1	0.0000000E-1
282	0.0000000E-1	0.0000000E-1	0.0000000E-1	0.0000000E-1	0.0000000E-1
283	0.0000000E-1	0.0000000E-1	0.0000000E-1	0.0000000E-1	0.0000000E-1
284	0.0000000E-1	0.0000000E-1	0.0000000E-1	0.0000000E-1	0.0000000E-1
285	0.0000000E-1	0.0000000E-1	0.0000000E-1	0.0000000E-1	0.0000000E-1
286	0.0000000E-1	0.0000000E-1	0.0000000E-1	1.9798689E-1	-1.6453982E-1
287	2.8592254E-2	-2.2085160E-2	-7.2245874E-4	-5.3764916E-3	-2.4676270E-3
288	-2.5328626E-3	-1.8972718E-3	-1.6609399E-3	-1.4035297E-3	-1.2282811E-3
289	-1.0794477E-3	-9.6105929E-4	-8.6207917E-4	-7.7932516E-4	-7.0894053E-4
290	-6.4858202E-4	-5.9630700E-4	-5.5068012E-4	-5.1056310E-4	-4.7506283E-4
291	0.0000000E-1	0.0000000E-1	0.0000000E-1	0.0000000E-1	0.0000000E-1
292	0.0000000E-1	0.0000000E-1	0.0000000E-1	0.0000000E-1	0.0000000E-1
293	0.0000000E-1	0.0000000E-1	0.0000000E-1	0.0000000E-1	0.0000000E-1
294	0.0000000E-1	0.0000000E-1	0.0000000E-1	0.0000000E-1	0.0000000E-1
295	0.0000000E-1	0.0000000E-1	0.0000000E-1	0.0000000E-1	0.0000000E-1
296	0.0000000E-1	0.0000000E-1	0.0000000E-1	0.0000000E-1	1.9462521E-1
297	-1.6172878E-1	2.8122737E-2	-2.1707735E-2	-7.0298345E-4	-5.2818816E-3
298	-2.4218990E-3	-2.4870446E-3	-1.8624891E-3	-1.6305849E-3	-1.3778092E-3
299	-1.2057889E-3	-1.0596880E-3	-9.4349108E-4	-8.4634822E-4	-7.6513724E-4
300	-6.9606924E-4	-6.3684344E-4	-5.8555208E-4	-5.4078580E-4	-5.0142699E-4

INVERSE AREA MATRIX 7

301	0.0000000E-1	0.0000000E-1	0.0000000E-1	0.0000000E-1	0.0000000E-1
302	0.0000000E-1	0.0000000E-1	0.0000000E-1	0.0000000E-1	0.0000000E-1
303	0.0000000E-1	0.0000000E-1	0.0000000E-1	0.0000000E-1	0.0000000E-1
304	0.0000000E-1	0.0000000E-1	0.0000000E-1	0.0000000E-1	0.0000000E-1
305	0.0000000E-1	0.0000000E-1	0.0000000E-1	0.0000000E-1	0.0000000E-1
306	0.0000000E-1	0.0000000E-1	0.0000000E-1	0.0000000E-1	0.0000000E-1
307	1.9142915E-1	-1.5905705E-1	2.7675647E-2	-2.1349001E-2	-6.8475901E-4
308	-5.1920519E-3	-2.3785582E-3	-2.4435724E-3	-1.8294952E-3	-1.6017814E-3
309	-1.3533994E-3	-1.1844370E-3	-1.0409249E-3	-9.2680381E-4	-8.3140122E-4
310	-7.5165175E-4	-6.8383084E-4	-6.2567797E-4	-5.7531841E-4	-5.3136744E-4
311	0.0000000E-1	0.0000000E-1	0.0000000E-1	0.0000000E-1	0.0000000E-1
312	0.0000000E-1	0.0000000E-1	0.0000000E-1	0.0000000E-1	0.0000000E-1
313	0.0000000E-1	0.0000000E-1	0.0000000E-1	0.0000000E-1	0.0000000E-1
314	0.0000000E-1	0.0000000E-1	0.0000000E-1	0.0000000E-1	0.0000000E-1
315	0.0000000E-1	0.0000000E-1	0.0000000E-1	0.0000000E-1	0.0000000E-1
316	0.0000000E-1	0.0000000E-1	0.0000000E-1	0.0000000E-1	0.0000000E-1
317	0.0000000E-1	1.8838554E-1	-1.5651350E-1	2.7249252E-2	-2.1007466E-2
318	-6.6766707E-4	-5.1066159E-3	-2.3374077E-3	-2.4022554E-3	-1.7981449E-3
319	-1.5744044E-3	-1.3301955E-3	-1.1641348E-3	-1.0230799E-3	-9.1092856E-4
320	-8.1717735E-4	-7.3881465E-4	-6.7217708E-4	-6.1504230E-4	-5.6556695E-4
321	0.0000000E-1	0.0000000E-1	0.0000000E-1	0.0000000E-1	0.0000000E-1
322	0.0000000E-1	0.0000000E-1	0.0000000E-1	0.0000000E-1	0.0000000E-1
323	0.0000000E-1	0.0000000E-1	0.0000000E-1	0.0000000E-1	0.0000000E-1
324	0.0000000E-1	0.0000000E-1	0.0000000E-1	0.0000000E-1	0.0000000E-1
325	0.0000000E-1	0.0000000E-1	0.0000000E-1	0.0000000E-1	0.0000000E-1
326	0.0000000E-1	0.0000000E-1	0.0000000E-1	0.0000000E-1	0.0000000E-1
327	0.0000000E-1	0.0000000E-1	1.8548263E-1	-1.5408819E-1	2.6842000E-2
328	-2.0681799E-2	-6.5160371E-4	-5.0252292E-3	-2.2982720E-3	-2.3629240E-3
329	-1.7683087E-3	-1.5483425E-3	-1.3081036E-3	-1.1448013E-3	-1.0060826E-3
330	-8.9580358E-4	-8.0362205E-4	-7.2657742E-4	-6.6106456E-4	-6.0489742E-4
331	0.0000000E-1	0.0000000E-1	0.0000000E-1	0.0000000E-1	0.0000000E-1
332	0.0000000E-1	0.0000000E-1	0.0000000E-1	0.0000000E-1	0.0000000E-1
333	0.0000000E-1	0.0000000E-1	0.0000000E-1	0.0000000E-1	0.0000000E-1
334	0.0000000E-1	0.0000000E-1	0.0000000E-1	0.0000000E-1	0.0000000E-1
335	0.0000000E-1	0.0000000E-1	0.0000000E-1	0.0000000E-1	0.0000000E-1
336	0.0000000E-1	0.0000000E-1	0.0000000E-1	0.0000000E-1	0.0000000E-1
337	0.0000000E-1	0.0000000E-1	0.0000000E-1	1.8270992E-1	-1.5177224E-1
338	2.6452500E-2	-2.0370810E-2	-6.3647730E-4	-4.9475836E-3	-2.2609947E-3
339	-2.3254263E-3	-1.7398711E-3	-1.5234958E-3	-1.2870399E-3	-1.1263639E-3
340	-9.8986976E-4	-8.8137337E-4	-7.9068623E-4	-7.1489635E-4	-6.5045414E-4
341	0.0000000E-1	0.0000000E-1	0.0000000E-1	0.0000000E-1	0.0000000E-1
342	0.0000000E-1	0.0000000E-1	0.0000000E-1	0.0000000E-1	0.0000000E-1
343	0.0000000E-1	0.0000000E-1	0.0000000E-1	0.0000000E-1	0.0000000E-1
344	0.0000000E-1	0.0000000E-1	0.0000000E-1	0.0000000E-1	0.0000000E-1
345	0.0000000E-1	0.0000000E-1	0.0000000E-1	0.0000000E-1	0.0000000E-1
346	0.0000000E-1	0.0000000E-1	0.0000000E-1	0.0000000E-1	0.0000000E-1
347	0.0000000E-1	0.0000000E-1	0.0000000E-1	0.0000000E-1	1.8005795E-1
348	-1.4955768E-1	2.6079496E-2	-2.0073429E-2	-6.2220676E-4	-4.8734028E-3
349	-2.2254356E-3	-2.2896261E-3	-1.7127279E-3	-1.4997747E-3	-1.2669287E-3
350	-1.1087571E-3	-9.7438460E-4	-8.6758789E-4	-7.7832557E-4	-7.0373196E-4

INVERSE AREA MATRIX 8

351	0.0000000E-1	0.0000000E-1	0.0000000E-1	0.0000000E-1	0.0000000E-1
352	0.0000000E-1	0.0000000E-1	0.0000000E-1	0.0000000E-1	0.0000000E-1
353	0.0000000E-1	0.0000000E-1	0.0000000E-1	0.0000000E-1	0.0000000E-1
354	0.0000000E-1	0.0000000E-1	0.0000000E-1	0.0000000E-1	0.0000000E-1
355	0.0000000E-1	0.0000000E-1	0.0000000E-1	0.0000000E-1	0.0000000E-1
356	0.0000000E-1	0.0000000E-1	0.0000000E-1	0.0000000E-1	0.0000000E-1
357	0.0000000E-1	0.0000000E-1	0.0000000E-1	0.0000000E-1	0.0000000E-1
358	1.7751820E-1	-1.4743730E-1	2.5721855E-2	-1.9788692E-2	-6.0872007E-4
359	-4.8024382E-3	-2.1914687E-3	-2.2554009E-3	-1.6867857E-3	-1.4770982E-3
360	-1.2477020E-3	-1.0919218E-3	-9.5957567E-4	-8.5440187E-4	-7.6649999E-4
361	0.0000000E-1	0.0000000E-1	0.0000000E-1	0.0000000E-1	0.0000000E-1
362	0.0000000E-1	0.0000000E-1	0.0000000E-1	0.0000000E-1	0.0000000E-1
363	0.0000000E-1	0.0000000E-1	0.0000000E-1	0.0000000E-1	0.0000000E-1
364	0.0000000E-1	0.0000000E-1	0.0000000E-1	0.0000000E-1	0.0000000E-1
365	0.0000000E-1	0.0000000E-1	0.0000000E-1	0.0000000E-1	0.0000000E-1
366	0.0000000E-1	0.0000000E-1	0.0000000E-1	0.0000000E-1	0.0000000E-1
367	0.0000000E-1	0.0000000E-1	0.0000000E-1	0.0000000E-1	0.0000000E-1
368	0.0000000E-1	1.7508298E-1	-1.4540462E-1	2.5378549E-2	-1.9515729E-2
369	-5.9595308E-4	-4.7344650E-3	-2.1589803E-3	-2.2226399E-3	-1.6619599E-3
370	-1.4553934E-3	-1.2292983E-3	-1.0758048E-3	-9.4539642E-4	-8.4177433E-4
371	0.0000000E-1	0.0000000E-1	0.0000000E-1	0.0000000E-1	0.0000000E-1
372	0.0000000E-1	0.0000000E-1	0.0000000E-1	0.0000000E-1	0.0000000E-1
373	0.0000000E-1	0.0000000E-1	0.0000000E-1	0.0000000E-1	0.0000000E-1
374	0.0000000E-1	0.0000000E-1	0.0000000E-1	0.0000000E-1	0.0000000E-1
375	0.0000000E-1	0.0000000E-1	0.0000000E-1	0.0000000E-1	0.0000000E-1
376	0.0000000E-1	0.0000000E-1	0.0000000E-1	0.0000000E-1	0.0000000E-1
377	0.0000000E-1	0.0000000E-1	0.0000000E-1	0.0000000E-1	0.0000000E-1
378	0.0000000E-1	0.0000000E-1	1.7274530E-1	-1.4345376E-1	2.5048645E-2
379	-1.9253751E-2	-5.8384843E-4	-4.6692802E-3	-2.1278677E-3	-2.1912429E-3
380	-1.6381741E-3	-1.4345941E-3	-1.2116615E-3	-1.0603574E-3	-9.3180459E-4
381	0.0000000E-1	0.0000000E-1	0.0000000E-1	0.0000000E-1	0.0000000E-1
382	0.0000000E-1	0.0000000E-1	0.0000000E-1	0.0000000E-1	0.0000000E-1
383	0.0000000E-1	0.0000000E-1	0.0000000E-1	0.0000000E-1	0.0000000E-1
384	0.0000000E-1	0.0000000E-1	0.0000000E-1	0.0000000E-1	0.0000000E-1
385	0.0000000E-1	0.0000000E-1	0.0000000E-1	0.0000000E-1	0.0000000E-1
386	0.0000000E-1	0.0000000E-1	0.0000000E-1	0.0000000E-1	0.0000000E-1
387	0.0000000E-1	0.0000000E-1	0.0000000E-1	0.0000000E-1	0.0000000E-1
388	0.0000000E-1	0.0000000E-1	0.0000000E-1	1.7049883E-1	-1.4157937E-1
389	2.4731291E-2	-1.9002040E-2	-5.7235471E-4	-4.6066990E-3	-2.0980379E-3
390	-2.1611190E-3	-1.6153588E-3	-1.4146401E-3	-1.1947411E-3	-1.0455357E-3
391	0.0000000E-1	0.0000000E-1	0.0000000E-1	0.0000000E-1	0.0000000E-1
392	0.0000000E-1	0.0000000E-1	0.0000000E-1	0.0000000E-1	0.0000000E-1
393	0.0000000E-1	0.0000000E-1	0.0000000E-1	0.0000000E-1	0.0000000E-1
394	0.0000000E-1	0.0000000E-1	0.0000000E-1	0.0000000E-1	0.0000000E-1
395	0.0000000E-1	0.0000000E-1	0.0000000E-1	0.0000000E-1	0.0000000E-1
396	0.0000000E-1	0.0000000E-1	0.0000000E-1	0.0000000E-1	0.0000000E-1
397	0.0000000E-1	0.0000000E-1	0.0000000E-1	0.0000000E-1	0.0000000E-1
398	0.0000000E-1	0.0000000E-1	0.0000000E-1	0.0000000E-1	1.6833778E-1
399	-1.3977658E-1	2.4425712E-2	-1.8759943E-2	-5.6142568E-4	-4.5465536E-3
400	-2.0694063E-3	-2.1321855E-3	-1.5934508E-3	-1.3954767E-3	-1.1784907E-3

INVERSE AREA MATRIX 9

401	0.0000000E-1	0.0000000E-1	0.0000000E-1	0.0000000E-1	0.0000000E-1
402	0.0000000E-1	0.0000000E-1	0.0000000E-1	0.0000000E-1	0.0000000E-1
403	0.0000000E-1	0.0000000E-1	0.0000000E-1	0.0000000E-1	0.0000000E-1
404	0.0000000E-1	0.0000000E-1	0.0000000E-1	0.0000000E-1	0.0000000E-1
405	0.0000000E-1	0.0000000E-1	0.0000000E-1	0.0000000E-1	0.0000000E-1
406	0.0000000E-1	0.0000000E-1	0.0000000E-1	0.0000000E-1	0.0000000E-1
407	0.0000000E-1	0.0000000E-1	0.0000000E-1	0.0000000E-1	0.0000000E-1
408	0.0000000E-1	0.0000000E-1	0.0000000E-1	0.0000000E-1	0.0000000E-1
409	1.6625688E-1	-1.3804095E-1	2.4131196E-2	-1.8526865E-2	-5.5101968E-4
410	-4.4886906E-3	-2.0418958E-3	-2.1043668E-3	-1.5723924E-3	-1.3770538E-3
411	0.0000000E-1	0.0000000E-1	0.0000000E-1	0.0000000E-1	0.0000000E-1
412	0.0000000E-1	0.0000000E-1	0.0000000E-1	0.0000000E-1	0.0000000E-1
413	0.0000000E-1	0.0000000E-1	0.0000000E-1	0.0000000E-1	0.0000000E-1
414	0.0000000E-1	0.0000000E-1	0.0000000E-1	0.0000000E-1	0.0000000E-1
415	0.0000000E-1	0.0000000E-1	0.0000000E-1	0.0000000E-1	0.0000000E-1
416	0.0000000E-1	0.0000000E-1	0.0000000E-1	0.0000000E-1	0.0000000E-1
417	0.0000000E-1	0.0000000E-1	0.0000000E-1	0.0000000E-1	0.0000000E-1
418	0.0000000E-1	0.0000000E-1	0.0000000E-1	0.0000000E-1	0.0000000E-1
419	0.0000000E-1	1.6425128E-1	-1.3636841E-1	2.3847091E-2	-1.8302258E-2
420	-5.4109904E-4	-4.4329700E-3	-2.0154361E-3	-2.0775939E-3	-1.5521310E-3
421	0.0000000E-1	0.0000000E-1	0.0000000E-1	0.0000000E-1	0.0000000E-1
422	0.0000000E-1	0.0000000E-1	0.0000000E-1	0.0000000E-1	0.0000000E-1
423	0.0000000E-1	0.0000000E-1	0.0000000E-1	0.0000000E-1	0.0000000E-1
424	0.0000000E-1	0.0000000E-1	0.0000000E-1	0.0000000E-1	0.0000000E-1
425	0.0000000E-1	0.0000000E-1	0.0000000E-1	0.0000000E-1	0.0000000E-1
426	0.0000000E-1	0.0000000E-1	0.0000000E-1	0.0000000E-1	0.0000000E-1
427	0.0000000E-1	0.0000000E-1	0.0000000E-1	0.0000000E-1	0.0000000E-1
428	0.0000000E-1	0.0000000E-1	0.0000000E-1	0.0000000E-1	0.0000000E-1
429	0.0000000E-1	0.0000000E-1	1.6231656E-1	-1.3475523E-1	2.3572797E-2
430	-1.8085622E-2	-5.3162964E-4	-4.3792633E-3	-1.9899627E-3	-2.0518037E-3
431	0.0000000E-1	0.0000000E-1	0.0000000E-1	0.0000000E-1	0.0000000E-1
432	0.0000000E-1	0.0000000E-1	0.0000000E-1	0.0000000E-1	0.0000000E-1
433	0.0000000E-1	0.0000000E-1	0.0000000E-1	0.0000000E-1	0.0000000E-1
434	0.0000000E-1	0.0000000E-1	0.0000000E-1	0.0000000E-1	0.0000000E-1
435	0.0000000E-1	0.0000000E-1	0.0000000E-1	0.0000000E-1	0.0000000E-1
436	0.0000000E-1	0.0000000E-1	0.0000000E-1	0.0000000E-1	0.0000000E-1
437	0.0000000E-1	0.0000000E-1	0.0000000E-1	0.0000000E-1	0.0000000E-1
438	0.0000000E-1	0.0000000E-1	0.0000000E-1	0.0000000E-1	0.0000000E-1
439	0.0000000E-1	0.0000000E-1	0.0000000E-1	1.6044864E-1	-1.3319797E-1
440	2.3307762E-2	-1.7876497E-2	-5.2258047E-4	-4.3274526E-3	-1.9654165E-3
441	0.0000000E-1	0.0000000E-1	0.0000000E-1	0.0000000E-1	0.0000000E-1
442	0.0000000E-1	0.0000000E-1	0.0000000E-1	0.0000000E-1	0.0000000E-1
443	0.0000000E-1	0.0000000E-1	0.0000000E-1	0.0000000E-1	0.0000000E-1
444	0.0000000E-1	0.0000000E-1	0.0000000E-1	0.0000000E-1	0.0000000E-1
445	0.0000000E-1	0.0000000E-1	0.0000000E-1	0.0000000E-1	0.0000000E-1
446	0.0000000E-1	0.0000000E-1	0.0000000E-1	0.0000000E-1	0.0000000E-1
447	0.0000000E-1	0.0000000E-1	0.0000000E-1	0.0000000E-1	0.0000000E-1
448	0.0000000E-1	0.0000000E-1	0.0000000E-1	0.0000000E-1	0.0000000E-1
449	0.0000000E-1	0.0000000E-1	0.0000000E-1	0.0000000E-1	1.5864375E-1
450	-1.3169348E-1	2.3051475E-2	-1.7674459E-2	-5.1392333E-4	-4.2774294E-3

INVERSE AREA MATRIX 10

451	0.0000000E-1	0.0000000E-1	0.0000000E-1	0.0000000E-1	0.0000000E-1
452	0.0000000E-1	0.0000000E-1	0.0000000E-1	0.0000000E-1	0.0000000E-1
453	0.0000000E-1	0.0000000E-1	0.0000000E-1	0.0000000E-1	0.0000000E-1
454	0.0000000E-1	0.0000000E-1	0.0000000E-1	0.0000000E-1	0.0000000E-1
455	0.0000000E-1	0.0000000E-1	0.0000000E-1	0.0000000E-1	0.0000000E-1
456	0.0000000E-1	0.0000000E-1	0.0000000E-1	0.0000000E-1	0.0000000E-1
457	0.0000000E-1	0.0000000E-1	0.0000000E-1	0.0000000E-1	0.0000000E-1
458	0.0000000E-1	0.0000000E-1	0.0000000E-1	0.0000000E-1	0.0000000E-1
459	0.0000000E-1	0.0000000E-1	0.0000000E-1	0.0000000E-1	0.0000000E-1
460	1.5689843E-1	-1.3023884E-1	2.2803466E-2	-1.7479116E-2	-5.0563248E-4
461	0.0000000E-1	0.0000000E-1	0.0000000E-1	0.0000000E-1	0.0000000E-1
462	0.0000000E-1	0.0000000E-1	0.0000000E-1	0.0000000E-1	0.0000000E-1
463	0.0000000E-1	0.0000000E-1	0.0000000E-1	0.0000000E-1	0.0000000E-1
464	0.0000000E-1	0.0000000E-1	0.0000000E-1	0.0000000E-1	0.0000000E-1
465	0.0000000E-1	0.0000000E-1	0.0000000E-1	0.0000000E-1	0.0000000E-1
466	0.0000000E-1	0.0000000E-1	0.0000000E-1	0.0000000E-1	0.0000000E-1
467	0.0000000E-1	0.0000000E-1	0.0000000E-1	0.0000000E-1	0.0000000E-1
468	0.0000000E-1	0.0000000E-1	0.0000000E-1	0.0000000E-1	0.0000000E-1
469	0.0000000E-1	0.0000000E-1	0.0000000E-1	0.0000000E-1	0.0000000E-1
470	0.0000000E-1	1.5520948E-1	-1.2883137E-1	2.2563299E-2	-1.7290107E-2
471	0.0000000E-1	0.0000000E-1	0.0000000E-1	0.0000000E-1	0.0000000E-1
472	0.0000000E-1	0.0000000E-1	0.0000000E-1	0.0000000E-1	0.0000000E-1
473	0.0000000E-1	0.0000000E-1	0.0000000E-1	0.0000000E-1	0.0000000E-1
474	0.0000000E-1	0.0000000E-1	0.0000000E-1	0.0000000E-1	0.0000000E-1
475	0.0000000E-1	0.0000000E-1	0.0000000E-1	0.0000000E-1	0.0000000E-1
476	0.0000000E-1	0.0000000E-1	0.0000000E-1	0.0000000E-1	0.0000000E-1
477	0.0000000E-1	0.0000000E-1	0.0000000E-1	0.0000000E-1	0.0000000E-1
478	0.0000000E-1	0.0000000E-1	0.0000000E-1	0.0000000E-1	0.0000000E-1
479	0.0000000E-1	0.0000000E-1	0.0000000E-1	0.0000000E-1	0.0000000E-1
480	0.0000000E-1	0.0000000E-1	1.5357392E-1	-1.2746856E-1	2.2330567E-2
481	0.0000000E-1	0.0000000E-1	0.0000000E-1	0.0000000E-1	0.0000000E-1
482	0.0000000E-1	0.0000000E-1	0.0000000E-1	0.0000000E-1	0.0000000E-1
483	0.0000000E-1	0.0000000E-1	0.0000000E-1	0.0000000E-1	0.0000000E-1
484	0.0000000E-1	0.0000000E-1	0.0000000E-1	0.0000000E-1	0.0000000E-1
485	0.0000000E-1	0.0000000E-1	0.0000000E-1	0.0000000E-1	0.0000000E-1
486	0.0000000E-1	0.0000000E-1	0.0000000E-1	0.0000000E-1	0.0000000E-1
487	0.0000000E-1	0.0000000E-1	0.0000000E-1	0.0000000E-1	0.0000000E-1
488	0.0000000E-1	0.0000000E-1	0.0000000E-1	0.0000000E-1	0.0000000E-1
489	0.0000000E-1	0.0000000E-1	0.0000000E-1	0.0000000E-1	0.0000000E-1
490	0.0000000E-1	0.0000000E-1	0.0000000E-1	1.5198901E-1	-1.2614810E-1
491	0.0000000E-1	0.0000000E-1	0.0000000E-1	0.0000000E-1	0.0000000E-1
492	0.0000000E-1	0.0000000E-1	0.0000000E-1	0.0000000E-1	0.0000000E-1
493	0.0000000E-1	0.0000000E-1	0.0000000E-1	0.0000000E-1	0.0000000E-1
494	0.0000000E-1	0.0000000E-1	0.0000000E-1	0.0000000E-1	0.0000000E-1
495	0.0000000E-1	0.0000000E-1	0.0000000E-1	0.0000000E-1	0.0000000E-1
496	0.0000000E-1	0.0000000E-1	0.0000000E-1	0.0000000E-1	0.0000000E-1
497	0.0000000E-1	0.0000000E-1	0.0000000E-1	0.0000000E-1	0.0000000E-1
498	0.0000000E-1	0.0000000E-1	0.0000000E-1	0.0000000E-1	0.0000000E-1
499	0.0000000E-1	0.0000000E-1	0.0000000E-1	0.0000000E-1	0.0000000E-1
500	0.0000000E-1	0.0000000E-1	0.0000000E-1	0.0000000E-1	1.5045217E-1

References

1. M. Stanisavljevic and N. Konjevic, *Fizika*, **4**, 13 (1972).
2. R. N. Bracewell, *Aust. J. Phys.*, **9**, 198 (1956).
3. H. N. Olsen, *Phys. Fluids*, **2**, 614 (1959).
4. C. J. Cremers and R. C. Birkebak, *Appl. Opt.*, **5**, 1059 (1956).
5. D. J. Kalnicky, R. N. Kniseley, and V. A. Fassel, *Spectrochim. Acta, Part B*, **30**, 511 (1975).
6. C. R. Yokley and J. B. Shumaker, *Rev. Sci. Instrum.*, **34**, 551 (1963).
7. D. R. Paquette and W. L. Wiese, *Appl. Opt.*, **3**, 291 (1964).
8. C. D. Maldonado, A. P. Caron, and H. N. Olsen, *J. Opt. Soc. Am.*, **55**, 1247 (1965).
9. C. D. Maldonado and H. N. Olsen, *J. Opt. Soc. Am.*, **56**, 1305 (1966).
10. P. W. J. M. Boumans, *Theory of Spectrochemical Excitation*, Hilger and Watts, London (1966).
11. H. W. Emmons, *Phys. Fluids*, **10**, 1125 (1967).
12. L. I. Grechikhin and V. D. Shimanovich, *Opt. Spectrosc.*, **15**, 358 (1961).
13. J. F. Bott, *J. Quant. Spectrosc. Radiat. Transfer.* **6**, 807 (1966).
14. R. J. Decker and P. A. McFadden, *Spectrochim. Acta, Part B*, **30**, 1 (1975).
15. D. J. Kalnicky, V. A. Fassel, and R. N. Kniseley, *Appl. Spectrosc.*, **31**, 137 (1977).
16. R. D. Sacks and J. P. Walters, *Anal. Chem.*, **42**, 61 (1970).
17. W. S. Eaton, Ph.D. thesis, University of Wisconsin (1975) (University microfilms 75-12893).
18. J. P. Walters and S. A. Goldstein, How and what to sample in the analytical gap, sampling, standards, and homogeneity, *ASTM STP*, **540**, 45 (1973).
19. D. Ekimoff and J. P. Walters, *Anal. Chem.*, **53**, 1644 (1981).
20. R. D. Sacks, Ph.D. thesis, University of Wisconsin, Madison (1969) (University microfilms 70-3687).
21. S. A. Goldstein, Ph.D. thesis, University of Wisconsin, Madison (1973) (University microfilms 73-20996).
22. S. A. Goldstein and J. P. Walters, *Spectrochim. Acta, Part B*, **31**, 201 (1976).
23. S. A. Goldstein and J. P. Walters, *Spectrochim. Acta, Part B*, **31**, 295 (1976).
24. J. P. Walters, R. J. Klueppel, D. M. Coleman, W. S. Eaton, S. A. Goldstein, and R. D. Sacks, *Spectrochim. Acta, Part B*, **33**, 1 (1978).
25. R. J. Klueppel and J. P. Walters, personal communication.
26. K. C. Lapworth, *J. Quant. Spectrosc. Radiat. Transfer*, **16**, 357 (1976).
27. W. J. Pearce in *Conference on Extremely High Temperatures* (H. Fischer and L. C. Mansur, eds.), p. 123, John Wiley, New York (1958).
28. C. E. Harvey, *Spectrochemical Procedures*, Applied Research Laboratories, Glendale, California (1950).
29. M. P. Freeman and S. Katz, *J. Opt. Soc. Am.*, **50**, 826 (1960).
30. P. J. Dickerman and R. W. Deuel, *Rev. Sci. Instrum.*, **35**, 978 (1964).
31. L. A. Luizova, *Opt. Spectrosc.*, **38**, 362 (1975).
32. G. H. Dieke and R. D. Cowan, *Rev. Mod. Phys.*, **20**, 418 (1948).
33. W. Braun, A. M. Bass, and D. D. Davis, *J. Opt. Soc. Am.*, **60**, 166 (1970).
34. A. Scheeline, Ph.D. thesis (University Microfilms 79-02424), University of Wisconsin, Madison, 1978.
35. D. M. Coleman, Ph.D. thesis, University of Wisconsin, Madison (1976) (University microfilms 77-3393).
36. D. M. Coleman and J. P. Walters, *J. Appl. Phys. Lett.*, **48**, 3297 (1977).
37. V. M. Kock and J. Richter, *Ann. Phys.*, **24**, 30 (1969).
38. D. W. Blair, *J. Quant. Spectrosc. Radiat. Transfer*, **14**, 325 (1974).
39. W. L. Barr, *J. Opt. Soc. Am.*, **52**, 885 (1962).
40. W. G. Braun, *Rev. Sci. Instrum.*, **36**, 802 (1965)
41. R. Mavrodineonu and H. Boiteux, *Flame Spectroscopy*, p. 518, John Wiley, New York (1965).

Index

Abbott bichromatic analyzer
  ABA-100, 37-54
    absorbance difference, measurement of, 41
    absorbance linearity, 46-47
    absorbance reproducibility, 47
    automation, 51
    circuit for analog-to-digital conversion, 40-42
    cuvette, 41
    design principles, 38-46
    dilution ratio, precision of, 49
    filter factor, 43
    filter pair, 40, 44, 52
    filter wheel, 40, 42
    functions, 46-51
    hemolysis as a problem, 50
    linearity, 46-47
    module, 38
    optics, 39-40
    quality control, 51
    resistance capacitance, 41-42
    sample evaporation, 48
    specifications, listed, 46
    temperature of reaction, 46-48
    turbidity as a problem, 49-50
    uncertainty, photometric, 46
    viscosity effect, 48
    volume measurement, 48
  ABA-200, 37, 45
  Liston design, 37, 39
Abel inversion, 295-372
  absorption, 340-350
    deconvolution, 341
  applications for, 299
    dc arcs, 299
    plasma, inductively coupled, 299
    spark discharge, stabilized, 299
Abel inversion (*continued*)
  area matrix, *see* Area matrix
  definitions, 311, 348
  depth-of-field region, 300
  distortion, 300
  edge-on observation, 300
  emission
    profile, radial, 299
    spatially unseparated, 340-350
  failure, catastrophic, 337
  fundamentals, 297-300
  identity matrix, 310
  measurement-noise, 337-340
  misalignment, instrumental, 328-336
  negative emissivity, calculation of, 297
  noise problem, 337-340
    and profile shape, 338-339
  optics
    astigmatic, 299
    stigmatic, 299
  plasma discharge, spatial resolution of, 298
  profile, 317-322
    and noise, 337-339
    radial, 299
    strictly emitting, 308-311
  regional area, calculation of, 308
  ring/zone discharge model, 308
  self-absorption theory, 311-316
    background correction, 323-328
    Beer's law, 312
    expression, mathematical, 313-315
    hot-core model, 312
    interconversion information, 315
    lateral intensity profile, 312
    mirror reflectivity, 313
    models, 317
    profile, 317-322

Abel inversion (*continued*)
radial absorption profile, 312
radial emission profile, 312
simple model, 312
spark wander, 328-336
square array, 300
subroutines with "pinwheel" structure, 296
Absorption, 340-350
deconvolution, 341
definitions, 348
profile
radial, 312
radial-to-lateral conversion, 315
See also Self-absorption
'aca', *see* DuPont automatic clinical analyzer
AES, *see* Auger spectroscopy
Alanine amino transferase, 38, 43, 44
Albumin method, 71, 73
Algebra, linear
definitions, 79
matrix, 79
review, 79-87
transpose, 79, 81
vector, 79
Algorithm for nonlinear data
description, 160-161
theory, 160-161
Alkaline phosphatase, 44
Allen base-line correction, 29, 31
ALT, *see* Alanine amino transferase
Aluminum electrode, 220-224, 277
and seawater, 220
brass, 245
in seawater, 246
corrosion by chloride ion, 222
in borate solution, 223
in hydrogen fluoride liquid, 223-224
oxide, anodic film on, 220-223
pitting potential, 222
polarization, potentiostatic, 222
trans-Aminase, 12
Ammonium ion, 223
Analysis, bichromatic, 37-54, 60
Analyzer, automated, *see* individual analyzers
Anthracene, 101, 103, 111
Apple II 6502 (48K) microprocessor, 216
Area matrix (in Abel inversion)
angles in radians, 302
coefficients, 303
computation, 300-308
flow chart, 307
Area matrix (*continued*)
definitions, 301
depth-of-field, 301
discharge, 301
ring, radial, 301
slice, axial, 301
zone, lateral, 301
depth-of-field correction, 307-308
inverse, 303-306
property, 303
Argon-ion
beam, 260
bombardment, 254, 258, 272
depth profile on tinplate, 258, 262, 263
etching, 252, 253, 259, 271, 272
AST assay, 12, 14, 23-24
and NADH, 23-24
interferents
bilirubin, 23
hemoglobin, 23
turbidity, 23
Auger spectroscopy, 207
electron beam damage, 209

Background correction and self-absorption in Abel inversion, 323-328
Beer's law, 33, 88, 312, 344, 347
Benztriazole for corrosion inhibition, 245
Bilirubin, 10, 11, 17-23, 45, 50, 68, 71, 73
analysis, bichromatic, 18
and turbidity, 32
assay by two wavelengths, 1
blank correction, 18, 19
hemolyzed, 18, 19
in fetal hemolytic disease, 31
in kernicterus, 31
in neonates, 31
interferents, 17, 23
nonhemolyzed, 19
on STAC analyzer, 17-19
total, 17-19
Bilirubinometer, 31-32
and turbidity, 32
Bismuth, 277
Brass electrode, 220, 245, 246
BRIJ-35, 57

Cadmium, 277
Calcium, 9
assay, 14-17
blank correction in polychromatic analysis, 16
interference by turbidity, 14

Calcium (*continued*)
method, 68, 71, 73
on STAC analyzer, 14-17
Calomel electrode, saturated, 208
Carleazole, 111
Carbon electrode, 218-220
fluorine gas production, 218
glassy, 220, 278
modified, 268
Carbon monoxide, 32
Carboxyhemoglobin, 32
Catecholamine
metabolites in urine, 31
Chlor-alkali cell, 249
Chloride ion, 69, 71, 73, 222
Cholesterol, 69, 71, 73
Chromium
chromium–iron alloy, 234-235
chromium–nickel stainless steel, 238
electrode, 227-230
chromium–cobalt alloy, 229
film on, 229
plating process, 229
metallic, 237
steel, 236
Chromophore, 4
Chrysene, 101-103, 111
Colorimetry
bichromatic, 1, 4, 37-54
general theory, 4-7
polychromatic, 1-25
selection of wavelength, 7-8
trichromatic, 7
Conduction, ionic, 209
Convolution, 161
Copper, 275
alloy with
nickel, 245
titanium, 245
corrosion inhibition, 244-245
by benztriazole, 245
by mercaptobenzothiazole, 245
electrode, 220, 244-246
oxide solar cell, 244
underpotential deposition on platinum electrode, 275-276
Core electron, 208
Creatine kinase, 44
Current-voltage curve, 206
Curve fitting, 215, 218

Data analysis, 215-218
analog ratemeter, 216
Data analysis (*continued*)
collection arrangement, 216
computer, 215-216
curve fitting, 215, 218
digital ratemeter, 216
experimental, 178-180
fluorescent compounds, 180
Fourier transform method, 218
instability, *see* Ill-conditionedness
multicomponent, matrix-formatted, 75-140; *see* Matrix
nonlinear, algorithm for, 145-147
reduction
questionnaire response, 78
research, 75
stategy in analytical chemistry, 75-78
factor analysis, 75-77
pattern recognition, 75-78
rows versus columns, 76
smoothing method, 217-218
source, 180
Decay curve, 142-143
kinetics, 144
law, 144
Deconvolution, 341
iterative, 143
Discharge wander, 328-337
algorithm, 331
distribution, 331
modeling, 329-330
DuPont automatic clinical analyzer ('aca'), 55-74
accuracy, 62
advantages, 72-74
bichromatic analysis, 55-74
calibration, 62-64
disadvantages, 74
errors, 63-64
functions, 59
header, 56-57
instrument, 57-59
interference, 69
measurement principle, 64-72
chromophore spectrum, 67-72
implementation, 65-66
reaction curve, 64, 65
reaction time-course, 66-67
measurement system, 59-64
electro-optical system, 60-61
technique, 60
methods, 73
optical diagram, 58
output result, 62-64

DuPont automatic clinical analyzer ('aca') (*continued*)
pack
envelope, 57
filling, 57-58
performance, 72
sample handling, 57-58
source drift, 62
test packs, analytical, 55-57
zero absorbance requirement, 61-62
DuPont curve resolver, 215

Eigenvalue, 85-86, 98
eigenvalue–eigenvector equation, 87
theory of unsymmetric bilinear form, 90
Eigenvector, *see* Eigenvalue
Electrode
behavior, 205
current-voltage curve, 206
data analysis, 215-218
deposition, covalently bonded, 265-270
film on, 206, 209-211, 220-223, 229, 232-234, 240-244, 247, 259-264, 270-273, 276-277
ion-selective, 270
modified, 264-265
noble metal, 270-277
potential, 208
reactions, 205
studies of surface, 205-293; *see* X-ray photoelectron spectroscopy
transfer to a spectrophotometer, 209-215
anaerobic, 211-215
cell design, 211-215
glass electrochemical cell, 213
oxide film, air-formed, 215
vacuum chamber, 212
film change, 209-211
film decomposition, 209-211
vacuum, effect on, 209
valence band on, 208
water, 210
X-ray photoelectron spectroscopy, 206
See also individual electrodes
Electrolyte, solid, 270
Ellipsometry, 206
Emission
data, 182
definition, 348
distribution, 348
Emission (*continued*)
response function, multiple, 141-204
nonlinear estimation of, 141-204
scattering, secondary, 158-159
spatially unseparated, 340-350
Emissivity, 297
Energy transfer, 144
Erythrosin, 266
ESCA, *see* X-ray photoelectron spectroscopy
Ethanol method, 68, 71, 73
Excitation
convolved, nonlinear, estimation of, 141-204
data, 182-183

Factor analysis, 75-78
applications, 77
Fluoranthene, 101-103, 111
Fluorescence
concentration, 157-158
data, 197-202
decay curve, 142-143
emission, 87-103
properties, 87-88
excitation, 87-108
instrumentation, 78
intensity, 88
observed, 157-158
least squares theory for emission–excitation matrix, 105-107
lifetime, 145, 147
linear programming analysis, 107-109
matrix, 87-116,
matrix of emission–excitation, 103-116
application, 103-116
simplex method, 107-109
theory, 103-116
mixture, binary
computer synthesized, 97
projection, isometric, 99-100
multicomponent capabilities, 88
photons per flash, 155; *see* Photon
qualitative analysis, 97-103
quantitative analysis, 109-116
experimental, 110-116
simulated, 109-110
scattering
Rayleigh, 158-159
secondary emission, 158-159

Fluorescence (*continued*)
species, 91-97
categories, 95
time-correlated single-photon method, 147-148
Fluorine, 111, 218, 219
Fourier transform method, 146, 218

Gallium arsenide
film, 259-264
oxide, anodic, 259-264
semiconductor, 259
spectrum, 261-262
Galton, Francis, 76
Glassy carbon electrode, *see* Carbon electrode
Glucose assay, 66-69, 71, 73
chemistry, 8-9
instrumental, 8, 13-14
γ-Glutamyltranspeptidase, 44
Glycerol, 22
Gold
electrode, 206, 210, 227
modified, 264, 268-270
oxide film, 210, 276-277
spectrum, 276
Graphite fluoride electrode, 219
Grid search algorithm, 161-165, 181-182
convergence criteria, 164
convergence test, 163-164
data
convolved, 164-165
set, required, 162
simulated, 181-182
estimate, initial, 162
ill-conditionedness, 164
modeling function, 162
peripheral error sum, 163
shortcomings, 162

Hemoglobin, 13, 32
Hemolysis as a problem in analysis, 50
Heparin, 52
Hydrocarbon mixture in urine, analysis of, 110-116
Hydrogen fluoride, 223-224
Hydrotalcite, 220
4-Hydroxybenzaldehyde, 31

Ill-conditionedness, 179, 198
Immunoassay, enzyme multiplied, 52
Indium, 253
oxide electrode, 267
Infrared spectroscopy, 206
Interference
in assay, clinical, 7
equation for, 6
Iridium electrode
oxide film on, 277
Iron
alloy, 234-235
electrode, 230-239
iron–chromium alloy, 235
iron–magnetite powder, 233
iron–molybdenum alloy, 234
metallic, 232-234
oxide film on electrode, 232, 233
passivation, 233
by nitric acid, 230
polarization, anodic, 231
valence band, 233
See also Stainless steel

Kernicterus, 31

Lactate dehydrogenase, 44
Lactic acid method, 66-69, 71, 73
Laplace transform method, 146
Lead, 247, 277, 278
Least squares analysis, 112, 114, 116, 146
of fluorescence emission–excitation matrix, 105-107
Linear programming analysis, 107-109
Lipase, 52
Liston design, 37, 39
Lithium, 208
Luminescence
decay of component
one, 142
two, 143
process, 143-145
time-decay measurement, 143

Magnesium, 70, 71, 73
electrode, 220-224
hydrotalcite formation on, 220
Magnesium chloride, 220
Magnesium hydroxide, 221
Magnetite–iron powder, 233
Manganese dioxide electrode, 230
Marquardt's algorithm, 170-178
confidence interval, criteria for, 177

Marquardt's algorithm (*continued*)
convergence
characteristics, 193-196
criteria, 176
rate, 196-197
tests, 175-176
data
convolved, 178
simulated, 185-193
listed, 187-191
set requirement, 175
default value, 176
fluorescence data, 199-200
initial estimate, 175, 186
modeling function, 175
nonlinear data sets, 170
Marquardt method, 146, 147
Matrix
arithmetic of, 80-81
addition, 80
multiplication, scalar, 80, 81
properties
associative, 81
commutative, 81
distributive, 81
subtraction, 80
basis, 83-84, 87
definitions, 87
emission–excitation, 103-116
formatted multicomponent data
algebra
linear, 79-87
matrix, 80-85
application, 103-116
description, 78-79
effectiveness, 116-117
eigenvalue, 85-86
eigenvector, 85-86
Fortran subroutine for analysis
qualitative, 118-123
quantitative, 123-139
future use, 117-118
glossary of terms, 86-87
theory, 103-116
identity matrix, 84-85, 310
inverse matrix, 84-85
rank, 83-84
raw-reduced, 83
solution of a system of linear equations, 81-83
unit matrix, 84-85
Maximum likelihood gradient method, 146
Measurement–noise, 337-340
Mercaptobenzothiazole, 245
Metal, *see* individual metals
noble, 270-277
Methanol, 274
Method of moments, 146-147
Method of steepest descent, 146-147
Methylcyanide, 273
N-Methyl-6-methoxy-quinolinium chloride, 180
Methylpyridinium, 267
N-Methyl-quinolinium chloride, 180
MFMDT, *see* Matrix, formatted multicomponent data technique
Microcomputer, 3
Misalignment, instrumental, 328-337
and Abel inversion, 328-337
Molybdenum electrode, 247-249
molybdenum–iron alloy, 234
molybdenum–nickel alloy, 244
oxidation, 247
polarization, 248
Moments, algorithm, 165-170
convergence
characteristics, 193-196
criteria, 170
rate, 196-197
test, 169-170
errors, 170
data
convolved, 170
set requirement, 169
simulated, 182-184
emission function, 166
excitation function, 166
initial estimates, 167-169
errors, 168
method of moments, 165-170
modeling function, 167
short-comings, 169
Monochromator, grating
bandpass selection, 159

NADH, 23-24, 42, 43
absorbance, 66
buffered, 47
Naphthalene, 111
Nickel
alloy, 244
nickel–chromium stainless steel, 238
nickel–copper, 244, 245
nickel–molybdenum, 244

Nickel (*continued*)
nickel–palladium, 244
nickel–silicon, 244
nickel–titanium, 244
current–voltage curve, 240
electrode, 240–244
film, passive, 242, 243
metal, 240–242
molten salt system, 242–243
oxide, 234
polarization, 241
stress corrosion cracking, 244
Niobium electrode, 247
p-Nitroaniline, 42
p-Nitrophenol, 42
Noble metal system, 277

Oxidation, potentiostatic
in miniature cell, 211
Oxygen electrode, 219
in acid solution, 219

Paint film, 278-279
Palladium
oxide film, 277
palladium–nickel alloy, 244
Parameter estimation, nonlinear, 141-204
Fourier transform, 146
Laplace transformation, 146
least squares, 146
Marquardt method, 146
maximum likelihood gradient method, 146
method of steepest descent, 146
moments method, 146
Passivation, 230, 233
discovery by Faraday, 230
of stainless steel, 235-237
Pattern recognition, 75-78
application, 77
Perchlorate ion, 223
Perylene, 101-103, 111
Phenanthrene, 111
Phosphomolybdate absorbance, 67
Phosphorus, 70, 71, 73
method, 67, 71, 73
Photon, counting method
algorithm, 160-161
concentration, 159-160
constant fraction discriminator, 156
counter for, 153

Photon, counting method (*continued*)
data handling, 160-178
discriminator, constant fraction, 156
excitation source, 154-155
linearity, 159-160
monochromator, 155
optics, 155
photomultiplier tube, 156
pile-up, 151-152
start line, 156
stop line, 156
theory, 148-151
time correlated, 147-148
time-to-amplitude converter, 152-154
timing filter amplifier, 157
Plasma discharge
definitions, 301
spatial resolution, 298
Platinum electrode, 205, 206, 265
and aqua regia, 273
coated, 270
derivatized, 269
and electro-oxidation, 274
lead oxidation on, 276
and methanol, 274
and methylcyanide, 273
modified, 268-270
in molten salt system, 273
oxide film on, 270-273
polymer adsorption, 269
spectrum, 271
sulfide film on, 273
underpotential deposition of copper on, 275-276
X-ray photoreduction, 272
Polarization, 241, 248, 250
anodic, 231, 237-239, 256-257
galvanostatic, 209
potentiostatic, 209
Polyacetonitrile, 265
Polytetrahydrofuran, 265
Porphyrin compounds, 103, 104, 111-116
Profile, *see* Abel inversion
Protein
cerebrospinal, 68, 71, 73
method, 70, 71, 73
Pyrene, 101-103, 111

Questionnaire response
analysis, graphical, 78
Quinine sulfate, 180

Raman spectroscopy, 206
Rank annihilation method, 108
Ratemeter, 216
Rayleigh scattering, 39, 158-159
Relaxation oscillator, 154
Ruthenium
  dioxide electrode, 249
  oxide electrode, 268

Sea water, 220, 246
SCE, *see* Calomel, electrode saturated,
Self-absorption, *see* Abel inversion
  and background correction, 327-328
  examples
    Abel inversion, 316-323
    models, 317
    profile, 317-322
  theory
    and Abel inversion, 311-316
    expression, mathematical, 312-315
Silicon–nickel alloy, 244
Simplex method, 107-109, 112, 114, 116
Smoothing method, 217-218
Spark wander, 328-337
  algorithm, 331
  distribution, 331
  modeling, 329, 330
Spectrophotometry
  and analytical chemistry, 28-30
  bichromatic, 37-54
  by multiple wavelength, 1-54
  correction, 29
  definitions, 28
  derivative, 28
  dual-beam, 28
  dual-wavelength, 28, 30
  monochromatic, 28
  multichromatic, 28
  multiple, 27-35
  polychromatic, 1-25
Spectroscopy, spatially resolved, *see* Abel inversion
Stainless steel, *see* Steel, stainless
Steel, stainless, 235-239
  film, colored, 238
  passivation, 235-237
  polarization, anodic, 237-239
  stress corrosion, 239
  surface treatment, 236-237
Stress corrosion, 239
  cracking, 244
Substrate depletion, hidden, 12-13
Surlyn, 57, 59
Synephrine, 31

Tantalum
  electrode, 250
  metal foil, 250
  oxide, 250
Taylor series
  expansion, truncated, 171
Technicon STAC analyzer, 1-25
  bichromatic analysis, equation for, 6
  assay for
    AST, 12, 14, 23-24
    glucose, 8, 13-14
    triglyceride, 10, 14, 22-23
  design, 2-4
    modules, 2-4
  polychromatic analysis, 1-25
    classification, 8-13
    correction for interference, *see* Interference
    examples
      bilirubin, total, 17-19
      calcium, 9, 14-17
      uric acid, 19-21
  substrate depletion, detection of, 12-13
  theory, general, 4-8
    wavelength selection, 7-8
Thallium oxide, 270
Thionine, 265
Time-to-amplitude converter, 152-154
Tin
  alloy, 259
  and erythrosin, 266
  electrode, 252-259, 274
    oxidized surface, 252-256
  etched, 253
  oxide, 252, 274
    derivatized, 266
    modified, 266-267
    tin–platinum electrode, 274
  polarization, anodic, 256-257
  spectrum, 257
  tin–nickel alloy, 259
  valence band, 256
  See also Tinplate
Tinplate, 258
  and sodium dichromate, 258
  layer, passive, 258

Titanium
alloy, 224-225
dioxide, 225-226
electrode, 224-226, 267
metal, 224-225
titanium–copper alloy, 245
titanium–nickel alloy, 244
Trace metal analysis, 277-278
Transpose, 79, 81, 87
Triglyceride, 10, 11, 14, 22-23
bichromatic analysis, 22
blank correction, 23
conversion to glycerol, 22
Tungsten
electrode, 250-252
film thickness, 251
oxide, 250
polarization, 250
spectrum, 251
tungsten–halogen lamp, 3
Turbidity as a problem in analysis, 14, 23, 32, 49-50
Tween-20, 57

Underpotential deposition, a phenomenon, 275
University IBM 370/168 computer, 215, 216

Uric acid, 11, 19-21
interference by bilirubin, 20-21
correction for, 21
uricase reaction, 20
Uricase, 20

Vanadium pentoxide electrode, 226
reserve cell, 226
Vector, 79, 87
multiplication, 80
See also Eigenvector

Wavelength, multiple (in clinical chemistry), 30-33

XPS, *see* X-ray photoelectron spectroscopy
X-ray photoelectron spectroscopy
of electrode surfaces, 205-293
oxidation, potentiostatic, 211
oxygen spectrum, 217
reduction, galvanostatic, 210
X-ray photoreduction of platinum, 272

Zinc
electrode, 247
in battery anode, 247